SCUOLA INTERNAZIONALE SUPERIORE DI STUDI AVANZATI

DOCTORAL THESIS

Shape Dependence of Holographic Entanglement Entropy in AdS/BCFT and in Hyperscaling Violating Spacetimes

---

Author:
Jacopo Sisti

Supervisor:
Asst. prof. Erik Tonni

A thesis submitted in fulfillment of the requirements
for the degree of Doctor of Philosophy

in the

PhD Course in Statistical Physics

Contents

Introduction

Physics aims to describe the behaviour of systems due to the interaction between them. When two systems interact, their state changes, and the effect of this interaction is reflected in correlations. The nature of the correlations can be either classical or quantum. Understanding quantum correlations, i.e., correlations that cannot be realised in classical systems, is a fundamental question in physics. *Quantum entanglement* is the most famous manifestation of this phenomenon, and its interpretation has been widely discussed since the early days of quantum mechanics [1, 2]. Nowadays, it has become a powerful resource in quantum information since it allows us to perform tasks that would be otherwise impossible, or inefficient, in a classical setting such as quantum teleportation [3] and quantum error correction [4]. Quantifying entanglement of a quantum state became an essential task that has been solved for bipartite systems in pure states. In that case, the good measure of entanglement is the *entanglement entropy* [5], i.e., the von Neumann entropy of the *reduced density matrix* obtained by tracing over the degrees of freedom of one of the two subsystems.

Entanglement entropy has revealed unexpected connections between quantum entanglement and the most disparate areas of Physics. The first example is the black-hole physics, where this quantity seems to play a fundamental role in understanding the origin of the Bekenstein-Hawking entropy of black holes [6–9]. In 1986 Bombelli, Koul, Lee and Sorkin [10] computed the entropy associated with the reduced density matrix obtained by tracing over the degrees of freedom of a quantum field that are inside the horizon, and they interpreted that quantity as a contribution to the total Bekenstein-Hawking entropy. On the other hand, Srednicki [11] showed that the entanglement entropy of a sphere is proportional to the area of the boundary also for fields in flat spacetime. This result enhanced the belief that entanglement entropy could be the way to understand and compute the black hole entropy. Entanglement entropy is a divergent quantity that must be regularized in some way. By employing a UV regulator, the divergence structure, whose the area law term represents the leading contribution, has been extensively studied [12–16]. However, the great interest in the entanglement entropy in the high-energy context came to a sudden halt after the discovery of D-branes [17], which triggered a new and more efficient way to compute the black-hole entropy [18].

On the contrary, the interest in this quantity has grown in condensed matter and statistical physics (see [19–21] for some reviews) because it turned out to be a very effective method to probe quantum phase transitions [22]. This kind of transitions occurs at zero temperature and is characterised by the appearance of long-range correlations, which are not due to thermal fluctuations but to the structure of a strongly entangled ground state. In particular, in $(1+1)-$dimensions the entanglement entropy in systems at criticality shows a logarithmic violation of the area law driven by the central charge [13, 23, 24]. This critical behaviour makes the entanglement entropy a good quantity to infer the universality class of spin chains from numerical computations. Furthermore, more recently, some experimental groups have conducted pioneering experiments to capture some features of quantum entanglement [25–27]. In $(2+1)-$dimensional systems, the entanglement entropy of a region A is $S_A = aP_A/\varepsilon - F_A + \mathcal{O}(\varepsilon)$ where ε is the UV cutoff. In the area law term, P_A is the perimeter of the *entangling curve*, which divides A from the rest of the system, and a is a non-universal quantity. The subleading term F_A is finite as $\varepsilon \to 0$ whenever the region is smooth, while it diverges logarithmically if corners in the entangling surface occur [28]. This subleading term, being non-local, provides a universal characterization of the many-particle quantum entanglement in the ground state of topologically ordered systems with a mass gap [29, 30].

In the seminal works [31, 32], Ryu and Takayanagi redeemed the entanglement entropy in the study of black holes and quantum gravity. In the context of the AdS/CFT duality conjectured by Maldacena [33], they proposed a way to compute the entanglement entropy of a spatial region in field theories which admit a holographic dual. Such theories can be described in terms of a gravitational theory with an additional dimension whose boundary is the manifold in which the field theory is defined. The great advantage lies in the fact that, in the strong coupling and large N regime, the gravitational theory becomes classical. In this framework, the entanglement entropy is given by the area of the minimal surface in the gravity theory anchored to the spatial region defined on the boundary. The Ryu-Takayanagi (RT) formula (and its covariant generalization [34] due to Hubeny, Rangamani, and Takayanagi (HRT)) turned out to be extremely useful for two different purposes. On one side, it provides a very powerful tool to quantify the entanglement in strongly coupled field theories. On the other one, the RT formula can be interpreted as a generalization of the Bekenstein-Hawking entropy of black holes, revealing a renewed connection between entanglement and gravity. In [35–37] it has been argued that the essential building block of the spacetime geometry should be related to the entanglement structure of the quantum state in the QFT. In particular, Maldacena and Susskind [38] observed that the Einstein-Rosen bridge (ER) is related to the entanglement structure suggested by the Einstein-Podolsky-Rosen (EPR) gendanken experiment coining the equality "ER=EPR". Successively, in [39–41], entanglement has been shown to be a fundamental feature for the bulk-reconstruction program in AdS/CFT initiated in [42, 43]. Within this program, another quantity whose interest is growing during the recent years is the holographic complexity [44–48], emerged to understand the growth of the Einstein-Rosen bridge for AdS black holes in terms of quantum complexity [49–51] in the dual boundary CFT. Many interesting works have been done to extend the holographic dictionary with this quantity [52–55].

From the point of view of the field theory, a very interesting question is the study of the *shape dependence* of the entanglement entropy. In its expansion in terms of the UV cutoff, the leading term of the entanglement entropy is proportional to the area. On the other hand, in general, other subleading terms may occur. These terms depend on the dimensionality of the spacetime and the shape of the region. It turns out that different information can be extracted by studying the shape dependence. For instance, when the subsystem is a (hyper)sphere it has been shown that the subleading term leads to define a quantity which monotonically decreases along the renormalization group flow [56–62]. Moreover, when the region contains a conical singularity, the entanglement entropy provides the coefficient characterising the two-point function of the stress-energy tensor [63–66]. However, studying the shape dependence is a formidable task, even in free theories.

In the framework of $\text{AdS}_4/\text{CFT}_3$ the computation is simplified by the RT (and HRT) formula, and interesting results have been obtained for small perturbations about circular regions [65, 67–74]. In the holographic framework, when A has a generic shape, analytic expressions for F_A can be written where the *Willmore functional* [75] plays an important role. The first result has been found in [76] for the static case where the gravitational background is AdS_4. This analysis has been further developed in [77] and then extended to a generic asymptotically AdS_4 spacetime in [78].

In this thesis, we study the shape dependence of entanglement entropy in holographic theories which are dual to *three-dimensional conformal field theories with boundary* (BCFT_3), and to three-dimensional field theories which displays anisotropic scale invariance (called *Lifshitz* theories) and *violation of the hyperscaling relations*.

Conformal field theories in the presence of boundaries (BCFTs) have been largely studied in the literature [79–81] in $(1+1)-$dimensional systems, and also in higher dimensions [82–85]. In the former case, the subleading term of entanglement entropy is related to the *boundary entropy* introduced by Affleck and Ludwig [86], which is a monotonically decreasing quantity along the boundary RG flow [86, 87]. In three dimensions, the effective action of a BCFT contains divergent logarithmic terms that are related to conformal anomalies localised on the boundary. For this dimensionality, there are two independent anomalies: one depends on the intrinsic curvature of the boundary, while the other one depends on the extrinsic curvature. The coefficient of the former represents the analogous of the boundary entropy since it decreases along the boundary RG flow [88], while the interpretation of the other one is not clear so far. In this case, understanding the role of entanglement entropy is still an open problem, and one of the aims of this thesis is to take a step forward these issues by employing the holographic setup. The holographic dual of BCFTs ($\text{AdS}_{d+2}/\text{BCFT}_{d+1}$) has been proposed by Takayanagi in [89] and studied further in [90, 91]. In this setup, the boundary of the BCFT is extended into the bulk of the gravitational spacetime, and this extension represents an additional boundary of the gravitational dual. The spacetime metric and the extended boundary are determined from the extremization of a gravitational action which also contains some matter field localized on the additional boundary. The matter content has the role of fixing the boundary conditions in the BCFT_{d+1}. Also, we mention that boundaries can be viewed as a special case of *defects*. Quantum field theory in the presence of defects is a very interesting subject both from a theoretical point of view [92–96] and for the applications in statistical and condensed matter physics. For instance, it allow us studying the Kondo effect [97, 98], quantum wires [99, 100], and the topological state of matters [101–103]. Holography in the presence of defects has been studied also in [104–106], and then applied to condensed matter problems in [107–112]

Many condensed matter systems at the critical point of a quantum phase transition exhibit a critical behaviour with anisotropic scaling characterised by the Lifshitz exponent ζ [113–117] and hyperscaling violation [118]. In recent years, there has been a certain attempt to study this kind of critical points within the AdS/CFT correspondence. Bottom-up approaches have been employed to obtain gravitational backgrounds capturing the anisotropic Lifshitz scaling [119–121] and the hyperscaling violation [122–126]. Further studies have been performed also in [127–139]. Interestingly, in [125] the authors have observed that for a precise value of the hyperscaling exponent (see Sec. 1.5.2 for details) the holographic entanglement entropy displays a logarithmic violation of the area law, even in dimensions higher than two. Since this behaviour has been associated with the presence of a Fermi surface for weakly-interacting fermionic systems [140, 141], gravitational backgrounds with hyperscaling exponents are also good candidates to describe systems with a Fermi surface at strong coupling. By employing the RT formula, the holographic entanglement entropy has been studied in many works, both in static backgrounds [125, 126, 142–146] and in Vaidya spacetimes [147–151]. However, we remark that spherical regions and infinite strips are the only smooth regions considered in these studies. In the last chapter of this thesis, we will study the holographic entanglement entropy for generic shapes, performing both analytical and numerical computations.

This thesis is organized as follows.

In chapter 1, we introduce the basic concepts needed to understand the subsequent chapters. After a brief discussion of entanglement and entanglement entropy, we will focus on conformal field theories reviewing the divergence structure of entanglement entropy in terms of the UV cutoff and discussing in detail the three-dimensional case. After that, we introduce boundary conformal field theories, and we will discuss the entanglement in two and three dimensional flat spacetimes in the presence of boundaries. Particular attention is paid to the holographic computation of entanglement entropy and the AdS/BCFT setup introduced by Takayanagi. Holographic theories with Lifshitz dynamical exponents and which display a violation of the hyperscaling relations are presented. Finally, we will discuss the numerical tool we employ throughout this thesis, namely Surface Evolver [152, 153], an open-source program able to find an approximation of the minimal surfaces once boundary conditions and a simple ansatz are given.

The subsequent chapters 2, 3 and 4 contain the original contributions of this work, and are based on the following articles

- D. Seminara, J. Sisti and E. Tonni, "Corner contributions to holographic entanglement entropy in AdS4/BCFT3," JHEP **1711** (2017) 076 [arXiv:1708.05080 [hep-th]] [154]

- D. Seminara, J. Sisti and E. Tonni, "Holographic entanglement entropy in $\mathrm{AdS}_4/\mathrm{BCFT}_3$ and the Willmore functional," JHEP **1808** (2018) 164 [arXiv:1805.11551 [hep-th]] [155]

- G. Cavini, D. Seminara, J. Sisti and E. Tonni, "On shape dependence of holographic entanglement entropy in $\mathrm{AdS}_4/\mathrm{CFT}_3$ with Lifshitz scaling and hyperscaling violation," [arXiv:1907.10030 [hep-th]] [156]

In chapter 2, based on [154] and [155], we study the shape dependence of holographic entanglement entropy in $\mathrm{AdS}_4/\mathrm{BCFT}_3$ for smooth regions disjoint from the boundary. One of the main results is the analytic formula for the subleading term F_A given in terms of the normal vector to the minimal surface. This result, valid for any extremal surface in an asymptotically AdS_4 spacetime bounded by a generic boundary, generalizes the ones of [76, 78], and when the spacetime is AdS_4 bounded by a boundary it reduces to the Willmore functional with an appropriate boundary term. The other important results are the explicit computation of the holographic entanglement entropy corresponding to strips parallel to flat boundaries and disks disjoint from flat or circular boundaries in the vacuum of the BCFT_3. We observe transitions between extremal surfaces depending both on the distance of the region from the boundary and on the boundary condition (parametrized by the matter content). More interestingly, these results show that for certain boundary conditions the entanglement entropy is not affected by the presence of the boundary. Finally, numerical results corresponding to elliptic regions are presented, which are also needed to check the various analytical formulas.

In chapter 3, based on [154] and [155], we study the case in which the entangling regions are non-smooth and, in particular, intersect the boundary at some isolated points. In this case, there is an additional subleading term which diverges logarithmically as the UV cutoff vanishes. Its coefficient is a universal function of the angles of intersection between the entangling curve and the boundary, and it encodes some information about the underlying BCFT. In particular, it depends on the boundary conditions. We obtain the analytic result for this *boundary corner function* within the $\mathrm{AdS}_4/\mathrm{BCFT}_3$ setup by employing two particular domains, i.e., the half-disk attached to the boundary and the infinite wedge with one edge on the boundary. This result generalizes the corner function of Drukker-Gross-Ooguri [157], which is recovered in the special case of vanishing matter field on the additional spacetime boundary. We will present a very appealing result in the expansion of the boundary corner function about the orthogonal intersection: the quadratic order of this expansion provides a coefficient that is proportional to the coefficient that appears in the one-point function of the stress-energy tensor. Since this result, obtained in the Takayanagi setup [89], does not hold if other proposals are employed [158–161], we hope that future studies of the boundary corner functions in BCFTs could give constraints on the validity of the different proposals. Furthermore, in this case, Surface Evolver has been employed to provide numerical checks of our analytic results.

In the last chapter 4, based on the work [156], we will present results on the shape dependence of the holographic entanglement entropy in four-dimensional gravitational backgrounds having a non-trivial Lifshitz scaling and a hyperscaling violation exponent. In particular, we will find how the divergent terms get modified by the hyperscaling exponent, showing that all the divergences depend on the geodesic curvature of the entangling curve. Also in this case, we obtain an analytic expression for the subleading term, which turns out to be finite whenever the entangling curve is smooth. The numerical tool Surface Evolver is employed to check our analytic results and to study the holographic entanglement entropy corresponding to ellipses in the vacuum state and in the thermal state.

All the details of the various computations are reported in the appendices A, B and C.

Chapter 1

Basic Concepts of Entanglement and Holography

In this chapter, we introduce the concept of entanglement entropy as a measure of the bipartite entanglement of pure states. After the general discussion of Sec. 1.1, we will focus on entanglement in conformal field theories (CFTs) in Sec. 1.1.1. We are mainly interested in $(2+1)-$dimensional systems, and in particular, the subleading term in the expansion of the entanglement entropy will be studied. In Sec. 1.2, we will place special emphasis in boundary conformal field theories (BCFTs), namely CFTs living in manifolds with boundaries. Furthermore, this thesis is devoted to studying some aspects of entanglement entropy in holographic field theories, which are field theories defined on the boundary of a gravitational spacetime. When a CFT is dual to a gravitational theory in the classical regime, the entanglement entropy can be computed as the area of the minimal surface anchored to the bipartition living on the boundary of the spacetime. Holography and holographic entanglement entropy (HEE) are introduced in Sec. 1.3. In Sec. 1.4, the AdS/BCFT duality is considered, and the holographic entanglement entropy in this setup is discussed. Then, in Sec. 1.5, we consider theories with Lifshitz scaling and hyperscaling violation, which are interesting because they provide a dual for some condensed matter systems, and for a certain value of the hyperscaling exponent their characteristics are compatible with systems that have a Fermi surface. The last section 1.6 is dedicated to the software Surface Evolver, a numerical tool able to find a very accurate approximation of the minimal surfaces, and which will be employed throughout this thesis.

1.1 Entanglement Entropy

In this section, we define the concept of entanglement and entanglement entropy in quantum mechanics. After a general introduction, we focus on entanglement in quantum field theory. For a more detailed discussion we refer to [19–21, 162, 163].

Consider a generic quantum system described by a pure state $|\Psi\rangle$ normalized to unity with density matrix $\rho = |\Psi\rangle\langle\Psi|$. Suppose also that the Hilbert space $\mathcal{H}$ associated to the system can be factorized in two parts A and B, i.e., $\mathcal{H} = \mathcal{H}_A \otimes \mathcal{H}_B$, of dimension d_A and d_B.

For example, $|\Psi\rangle$ may correspond to the state of two different particles or spins A and B, or to the ground state of a lattice system where A and B represent a bipartition of the whole system. The Schmidt decomposition theorem allows us writing the pure state $|\Psi\rangle$ as

$$|\Psi\rangle = \sum_i c_i \, |i\rangle_A \otimes |i\rangle_B \tag{1.1.1}$$

for a particular choice of orthonormal vectors $\{|i\rangle_A\} \subset \mathcal{H}_A$ and $\{|i\rangle_B\} \subset \mathcal{H}_B$ with $i = 1, \dots, \min[d_A, d_B]$. Notice that the choice of these orthonormal sets is state-dependent, namely if we consider another pure state then also the vectors in the Schmidt decomposition will change accordingly. Another property of (1.1.1) is that the coefficients c_i, which are constrained to satisfy the normalization condition $\sum_i |c_i|^2 = 1$, can be chosen real and non-negative.

The two subsystems A and B are said *entangled* if there are at least two non-vanishing c_i, while is not entangled otherwise, i.e. if it exist $i = \bar{i}$ such that $c_{\bar{i}} = 1$ and $c_i = 0$ for any $i \neq \bar{i}$.

Out of the decomposition (1.1.1), it is possible to define the non-negative quantity $S_{A|B} \equiv -\sum_i |c_i|^2 \log |c_i|^2$. This quantity vanishes if and only if $c_{\bar{i}} = 1$ and $c_i = 0$ for $i \neq \bar{i}$, and it acquires its maximum value when all the c_i are equal. This observations suggests to consider $S_{A|B}$ as a measure of the entanglement between A and B.

For any pure state $|\Psi\rangle$, it is possible to rewrite $S_{A|B}$ in a basis-independent form as it follows. First, one defines the reduced density matrix associated with the subsystem A (or, equivalently to B) as

$$\rho_A = \mathrm{Tr}_B \rho \tag{1.1.2}$$

where Tr_B is the trace over the degrees of freedom of the subsystem B. Then, one computes the von-Neumann entropy associated to ρ_A (or ρ_B):

$$S_A = -\mathrm{Tr}_A \rho_A \log \rho_A . \tag{1.1.3}$$

In the literature, this quantity is known as *entanglement entropy* [10–13, 22, 23]. Entanglement entropy is a good measure of the amount of entanglement of bipartitions in pure states, and in particular is a decreasing quantity under local operations on A and B and classical communication between A and B (LOCC) [19]. Furthermore, it is also straightforward to notice that for pure states $S_A = S_B = S_{A|B}$.

However, for mixed states, entanglement entropy is not a measure of entanglement because it is sensible also to classical correlations. Moreover, in this case $S_A \neq S_B$. For mixed states, other quantities can be studied to provide a measure of the amount of entanglement like the *negativity* [164, 165] and the *entanglement of purification* [166].

Another quantity of interest related to entanglement entropy is the *mutual information*

$$I(A:B) = S_A + S_B - S_{A\cup B} \tag{1.1.4}$$

Entanglement entropy has a certain number of remarkable inequalities valid for any state:

- Positivity:

$$S_A \geq 0 \tag{1.1.5}$$

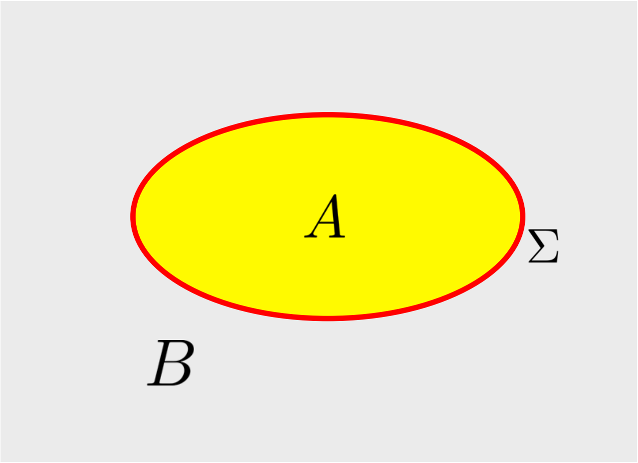

Figure 1.1: Example of bipartition of a spatial-slice at constant time of the manifold $\mathcal{M}_{d+1}$ (in this figure $d = 2$). The two regions A and B are separated by the entangling surface Σ, which in this case is the red curve.

- Subadditivity:
$$I(A:B) \geq 0 \tag{1.1.6}$$
- Strong subadditivity:
$$S_A + S_B \geq S_{A\cup C} + S_{A\cap C} \tag{1.1.7}$$
- Araki-Lieb:
$$|S_A - S_B| \leq S_{A\cup B} \tag{1.1.8}$$

where we have supposed that the Hilbert space $\mathcal{H}$ admits the factorization $\mathcal{H} = \mathcal{H}_A \otimes \mathcal{H}_B \otimes \mathcal{H}_C$.

Generalization of the entanglement entropy (1.1.3) are the so-called *Rényi entropies* defined as
$$S_A^{(n)} = \frac{1}{1-n} \log \mathrm{Tr}_A \, \rho_A^n \tag{1.1.9}$$
which reduce to (1.1.3) in the limit $n \to 1$. Rényi entropies are extremely interesting quantities because knowing them for any integer value of n up to the dimension of the subsystem A is equivalent to know the spectrum of the reduced density matrix ρ_A (the *entanglement spectrum*), which in general is much more difficult to exploit. Furthermore, the usual method to compute the entanglement entropy in quantum field theory is to find the Rényi entropies for any integer n, and then perform the analytic continuation to real values of n to take the limit $n \to 1$ [12, 23]. This procedure, which is described in the next section, is called *replica trick*, and it has been introduced for the first time in the context of spin glasses [167].

1.1.1 Entanglement entropy in quantum field theory

As discussed above, entanglement entropy quantifies the entanglement between two complementary subsystems. From now on, we will consider only spatial bipartitions, namely the subsystems A and B are meant to be complementary subsets of a Cauchy slice of the spacetime manifold $\mathcal{M}_{d+1}$, see Fig. 1.1. The two regions A and B are separated by a $(d-1)-$dimensional hypersurface which will be called *entangling surface* $\Sigma \equiv \partial A \cap \partial B$.

Here we discuss the usual approach to the computation of entanglement entropy in quantum field theory, which relies on the replica trick. For this reason, by following [12, 13, 23, 24] we describe the procedure to compute the Rényi entropies (1.1.9).

Let us consider a $(d+1)-$dimensional quantum field theory in the Euclidean formulation defined on a manifold $\mathcal{M}_{d+1}$ and described by a path integral over the field $\varphi(t_E, \boldsymbol{x})$ with action S. The field φ can represent a collection of different fundamental fields. In the path integral formulation, the density matrix corresponding to the ground state ρ reads

$$\rho_{\varphi_+\varphi_-} = \frac{1}{Z[\mathcal{M}_{d+1}]} \int_{t_E \to -\infty}^{t_E \to +\infty} \mathcal{D}\varphi \prod_{\boldsymbol{x}} \delta\left(\varphi(+0, \boldsymbol{x}) - \varphi_+(\boldsymbol{x})\right) \prod_{\boldsymbol{x}} \delta\left(\varphi(-0, \boldsymbol{x}) - \varphi_-(\boldsymbol{x})\right) e^{-S[\varphi]} \tag{1.1.10}$$

where $Z[\mathcal{M}_{d+1}]$ is the partition function needed to enforce the normalization $\mathrm{Tr}\rho = 1$. The products of delta functions enforce the boundary condition on the field φ at the Euclidean time $t_E = 0$, while the minus and plus correspond to the ket and bra, respectively.

Now, the reduced density matrix ρ_A can be written in this formalism by merely restricting the product of deltas to the region $x \in A$. We obtain

$$\rho_{A,\varphi_+\varphi_-} = \frac{1}{Z[\mathcal{M}_{d+1}]} \int_{t_E \to -\infty}^{t_E \to +\infty} \mathcal{D}\varphi \prod_{\boldsymbol{x}\in A} \delta\left(\varphi(+0, \boldsymbol{x}) - \varphi_+(\boldsymbol{x})\right) \prod_{\boldsymbol{x}\in A} \delta\left(\varphi(-0, x) - \varphi_-(\boldsymbol{x})\right) e^{-S[\varphi]}. \tag{1.1.11}$$

The quantity $\mathrm{Tr}\rho_A^n$ is obtained by taking the product of the n copies of (1.1.11) $\rho_{A,\varphi_+^{(i)}\varphi_-^{(i)}}$ for $i = 1, \dots, n$, and tracing over all the $\{\varphi_+^{(i)}\varphi_-^{(i)}\}$ subjected to the constraints $\varphi_-^{(i)} = \varphi_+^{(i+1)}$ for $i = 1, n-1$ and $\varphi_+^{(1)} = \varphi_-^{(n)}$. It is possible to realize that this construction is equivalent to the computation of the partition function on a manifold $\mathcal{M}_{n,d+1}$, which is the $n-$fold branched cover of $\mathcal{M}_{d+1}$. For $d = 1$ these manifolds have the structure of $n-$sheeted Riemann surfaces and, for the single interval, the resulting manifold is depicted in Fig. 1.2.

Thus, the Rényi entropies (1.1.9) in quantum field theory are given by

$$S_A^{(n)} = \frac{1}{1-n} \log\left(\frac{Z[\mathcal{M}_{n,d+1}]}{Z[\mathcal{M}_{d+1}]^n}\right). \tag{1.1.12}$$

As it was anticipated above, the knowledge of (1.1.3) or (1.1.12) in field theory leads us to obtain the entanglement entropy by taking the limit $n \to 1$. In general, analytic continuations may be very complicated and even not unique. However, the Carlson's theorem ensures that a function $f = f(n)$ defined on integers and that, in addition, is bounded by $f < ce^{\pi|n|}$ for $\mathrm{Re}(n) > 1/2$ admits a unique analytic continuation [168]. This allows us to use the replica trick method in most of the situations.

Entanglement entropy as defined by the analytic continuation of (1.1.12) is typically a UV-divergent quantity, which has to be regularised by introducing a short-length scale cutoff ε. On a physical ground, the divergence is due to the short-range correlations that characterize any state in a local quantum field theory. Since we took a spatial bipartition of the manifold $\mathcal{M}_{d+1}$, we expect that the leading contribution to the divergence comes from the EPR pairs

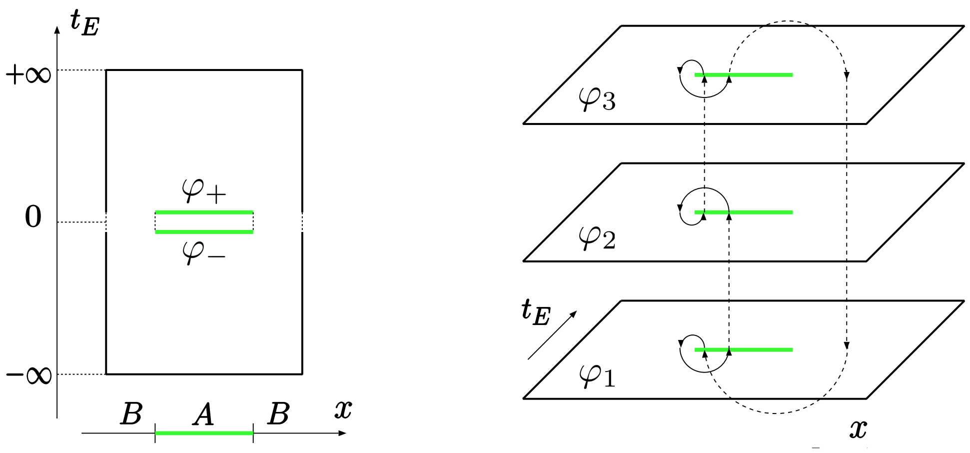

Figure 1.2: Illustration of the replica trick for the 2-dimensional case. Left: Cartoon of the path integral representation of the reduced density matrix $\rho_{A,\varphi_-\,\varphi_+}$ when A is a single interval. Right: Picture of the $n-$sheeted Riemann surface corresponding to the single interval A and $n = 3$. This figure is a modification of Fig. 1 of [32].

that bestride the entangling surface. Since the number of such EPR pairs is proportional to the area of the entangling surface, the main contribution to the entanglement entropy follows the well-known *area law* [11, 12]

$$S_A = a_{d-1}\frac{\text{Area}[\partial A]}{\varepsilon^{d-1}} + \dots \tag{1.1.13}$$

where a_{d-1} is a dimensionless coefficient depending on the regularization scheme employed. We mention that a rigorous proof of the area law in gapped two-dimensional systems has been proved in [169].

Besides the leading divergence (1.1.13), there are other divergent contributions that depend on the dimensionality. In the following, we restrict, for the sake of simplicity, to the case of *conformal field theories*, which have no other scales than the size of the region. In terms of the UV cutoff, the expansion of S_A has the form (see for example [68] for $d = 3$):

$$S_A = \begin{cases} a_{d-1}\left(\frac{\mu}{\varepsilon}\right)^{d-1} + a_{d-3}\left(\frac{\mu}{\varepsilon}\right)^{d-3} + \dots + a_{\log}\log\left(\frac{\mu}{\epsilon}\right) + \mathcal{O}(1) & \text{for } d \text{ odd} \\ a_{d-1}\left(\frac{\mu}{\varepsilon}\right)^{d-1} + a_{d-3}\left(\frac{\mu}{\varepsilon}\right)^{d-3} + \dots + (-1)^{d/2}F_A + \mathcal{O}(\varepsilon) & \text{for } d \text{ even} \end{cases} \tag{1.1.14}$$

where μ is a measure of the size of the region A. The coefficients a_i in the expansion (1.1.14) can be written as integrals over the entangling surface Σ of local quantities constructed in terms of the Riemann curvature of the spacetime and the extrinsic curvature of Σ. While the a_i are all scheme-dependent quantities fixed by the geometry of the entangling surface, the non-trivial information about the state ρ and the bipartition $\mathcal{H}_A \otimes \mathcal{H}_B$ is encoded in the quantities $a_{\log}$ and F_A for d odd and even, respectively. In particular, it has been shown in [56–62] that these coefficients play a fundamental role in defining quantities that decrease along the renormalization group flow, which generalize the c-theorem in two dimensions [170] to higher dimensions. In Sec. 1.1.2, we will give more details on the entropic F-theorem valid in three-dimensional quantum field theories.

From the first expansion in (1.1.14), we notice that in two-dimensional CFTs ($d = 1$) the area law is violated by a logarithmic correction. In particular, it has been shown in [13] (see also [23]) that when A is a single interval of length ℓ in the vacuum state

$$S_A = \frac{c}{3} \log \left(\frac{\ell}{\varepsilon} \right) + \mathcal{O}(1) \tag{1.1.15}$$

where c is the central charge of the CFT. Two-dimensional CFTs are the theories where entanglement entropy can be computed more easily. In [23, 24], results for finite systems and infinite systems in thermal states has been found. Furthermore, studies when the region A is made of two disjoint intervals have been done in [171–174]. The entanglement entropy (and Rény entropies) when A is made of $n-$disjoint intervals has also been found for the free Dirac fermion in [175]. When the theory is not conformal, the computation is much more involved also for free theories, and closed forms cannot be found. Single intervals for free massive fermions and scalars have been studied in [175, 176].

In this thesis, we are mainly interested in the three-dimensional case ($d = 2$), and the entanglement entropy for this case is discussed in the following subsection.

Now, for completeness, we briefly discuss the case $d = 3$. According to the general expansion (1.1.14), in four dimensions the leading term is the area law, and the first subleading term is a logarithmic divergence. Logarithmic divergences are very important terms since their coefficients are universal quantities, independent of the regularization scheme adopted. For example, in four dimensions, the coefficient $a_{\log}$ is made of two distinct contributions proportional to the two types of *conformal anomalies* a and c [68].

The logarithmic terms will occupy a special place in this thesis, and they will be studied in chapter 3 in the context of AdS$_4$/BCFT$_3$.

1.1.2 Entanglement entropy in CFT$_3$

For three-dimensional systems ($d = 2$), the entangling surface is a curve, called *entangling curve*, and we will refer to its perimeter as $P_{A,B}$. The expansion of S_A in this case is

$$S_A = a_1 \frac{P_{A,B}}{\varepsilon} - F_A + \mathcal{O}(\epsilon). \tag{1.1.16}$$

The leading term, which depends on the cutoff ε, is the area law term introduced above and the coefficient a_1 is a constant that depends on the regularization scheme. The subleading term F_A, which is finite whenever the entangling curve is smooth, is the quantity of our interest and will be extensively studied throughout this thesis in the holographic context. In particular, we will study the *shape dependence* of F_A on the domain A. It turns out that different configurations may give different information about the underlying CFT. For example, when the region A is a disk of radius R, F_A provides an analog of the Zamolodchikov $c-$function in the three-dimensional case when the CFT is perturbed by a relevant deformation [59, 60, 177]. More precisely, in [60] it has been shown that the dimensionless quantity $\mathfrak{F}_A = (R\partial_R - 1)F_A$ is a monotonically decreasing function along the RG flow, and it is a constant at the fixed points, i.e., $\mathfrak{F}'_A = R\partial^2_R F_A \leqslant 0$. Hence, $\mathfrak{F}^{(IR)}_A \leqslant \mathfrak{F}^{(UV)}_A$. We stress that F_A depends implicitly on the regularization scheme, and only differences of F_A can be directly related to physical

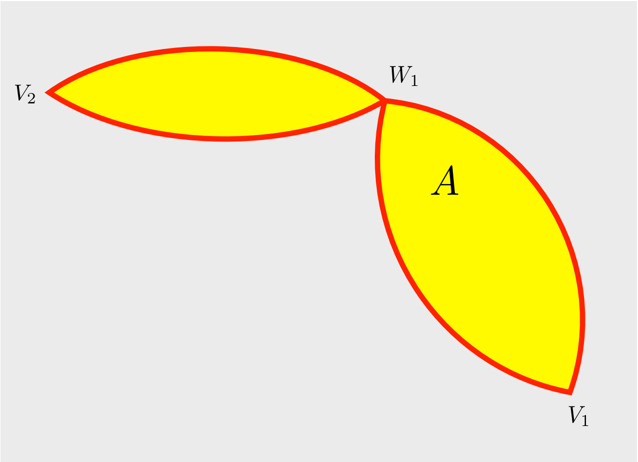

Figure 1.3: Entangling curve with isolated singularities. The vertices V_1 and V_2 are made by two lines which join forming opening angles θ_1 and θ_2. The vertex W_1, characterised by three angles $\vec{\phi}$, is made by four lines joining at the same point.

quantities. For this reason, in [177] the mutual information (1.1.4) has been considered to obtain a physical quantity analogous to the c-function. Another important case, which we discuss in the following, is when the entangling surface is not smooth and isolated *corners* occur.

Singular entangling surfaces

The result (1.1.14) is valid only in the case of smooth entangling surfaces. In the presence of singularities, the structure of the divergences may change.

Here, we focus on $d = 2$, and we consider entangling surfaces with the two types of corners depicted in Fig. (1.3). The $V-$types are corners made by two lines which join at the vertices V_i and which are fully characterized by the opening angles θ_k. The $W-$type are corners made by four lines joining at the vertices W_i, and they are determined by three angles labeled in the following with $\vec{\phi}_{W_i}$. When corners occur, the entanglement entropy shows additional contributions that logarithmically diverge as $\varepsilon \to 0^+$, i.e.

$$S_A = b\,\frac{P_A}{\varepsilon} - \tilde{f}_{\text{tot}} \log(P_A/\varepsilon) + O(1) \tag{1.1.17}$$

where

$$\tilde{f}_{\text{tot}} = \sum_{V_k} \tilde{f}(\theta_{V_k}) + \sum_{W_r} \widetilde{\mathsf{F}}(\vec{\phi}_{W_r}) \tag{1.1.18}$$

are the contributions of the two types of corners. The non-trivial functions $\tilde{f}(\theta_{V_k})$ and $\widetilde{\mathsf{F}}(\vec{\phi}_{W_r})$ are universal (independent of the regularization scheme), and they depend both on the angles characterising the corners and on the underlying CFT.

In the following, we consider only the $V-$type corners postponing the study of the others to the end of chapter 3, where an holographic discussion of the $W-$type has been made. Since for pure states $S_A = S_B$, the function $\tilde{f}(\theta_i)$ satisfies $\tilde{f}(\theta_i) = \tilde{f}(\pi - \theta_i)$ and vanishes in the smooth limit $\theta_i \to \pi$. Furthermore, by employing the strong subadditivity on suitable domains it has been shown that $\tilde{f}(\theta)$ must be a positive and convex decreasing function of θ [178], i.e.,

$$\tilde{f}''(\theta) \geqslant 0. \tag{1.1.19}$$

Furthermore, the above properties imply that about the angle $\theta = \pi$ the function $\tilde{f}(\theta)$ is quadratic, namely

$$\tilde{f}(\theta) = \frac{\tilde{f}''(\pi)}{2}(\pi - \theta)^2 + \dots \tag{1.1.20}$$

where $\tilde{f}''(\pi) \geqslant 0$.

Analytic results for $\tilde{f}$ have been found for free bosons and fermions [28, 179, 180], and in the holographic context [157, 178]. Other interesting studies have been done in [181–186].

A very appealing result relates the corner function $\tilde{f}(\theta)$ to the stress-energy tensor of the underlying CFT. More precisely, a universal relation between $f''(\pi)$ in the expansion (1.1.20) and the coefficient which characterises the two-point function of the stress-energy tensor has been conjectured in [63, 64]. This relation reads

$$\frac{f''(\pi)}{C_T} = \frac{\pi^2}{12} \tag{1.1.21}$$

where C_T is defined by

$$\langle T_{\mu\nu}(x)\, T_{\rho\sigma}(0)\rangle = \frac{C_T}{|x|^6}\, \mathcal{I}_{\mu\nu,\rho\sigma}(x) \tag{1.1.22}$$

being $\mathcal{I}_{\mu\nu,\rho\sigma}(x)$ a dimensionless tensor fixed by the conformal invariance [187]. The relation (1.1.21) holds in any conformal field theory, and it can be generalized to higher dimensions by considering the singular contribution coming from conical singularities in the entangling surface [64, 188]. The proof of (1.1.21) and its higher-dimensional generalizations have been given in [65, 66].

In chapter 3, we will study the holographic entanglement entropy for holographic boundary conformal field theories finding a relation (see equation (3.4.6)) which connects the corner function corresponding to regions A intersecting the boundary of the BCFT$_3$ and the one-point function of the stress-energy tensor. This observation, valid in the AdS$_4$/BCFT$_3$ setup proposed by Takayanagi [89], leads to the conjecture of a possible universal relation in three-dimensional BCFTs similar to (1.1.21).

We conclude this section by mentioning that in higher dimensions different kinds of singularities exist and they have been studied in holography and field theories [189, 190], and also numerically in lattice theories [191, 192].

1.2 Entanglement and Boundary Conformal Field Theory

Up to now, we have considered systems that extend to infinity or defined on compact manifolds. However, systems may be finite or may contain defects that break part of the symmetry characterizing the bulk. For a recent review on this topic, we refer to [193]. In this section, we will consider the case of conformal field theory with boundaries.

Boundary conformal field theory was founded by Cardy who studied the two-dimensional case [79–81], which represents the most known example so far. Besides their simplicity, two-dimensional BCFTs play an important role both in statistical physics [194] and in string theory [195–198], where they provide a general framework to study open strings and led to the discovery of D-branes [17].

We recall that CFTs are completely determined by the spectrum of local primary operators and the OPE coefficients. In fact, in principle by employing the OPE any n-point correlation function can be expressed as the expectation value of one-point functions, which are all vanishing except the one corresponding to the identity operator. On the other hand, the absence of non-trivial one-point functions is due to the translational symmetry (together with the scaling symmetry), which is partially broken in the presence of a boundary. Hence, in the presence of a boundary, the one-point functions join the conformal data that specify a given BCFT.

In most of this thesis, we will consider systems with a plane or a spherical boundary. This kind of boundaries has the properties to break (once appropriate conditions on fields are imposed) the least amount of symmetry, i.e., in this case, the conformal group $SO(d+2,1)$ is broken to the subgroup $SO(d+1,1)$. In the following we consider Euclidean conformal field theories defined on the manifold $\mathcal{M}_{d+1} = \mathbb{R}^+ \times \mathbb{R}^d$, described by the Cartesian coordinates $y^\mu = (x, \boldsymbol{y})$ with boundary located at $x = 0$. A systematic study on the form of one and two-point functions in these theories has been done in [84, 85]. From their analysis, it turns out that the form of the one-point functions of an operator with scale dimension η is completely fixed by the conformal symmetry, and it reads

$$\langle \mathcal{O}(y) \rangle = \frac{C_{\mathcal{O},\alpha}}{(2\,x)^\eta} \tag{1.2.1}$$

where α label the conformal boundary conditions, and $C_{\mathcal{O},\alpha}$ is non-vanishing only for scalar operators. In particular, the one-point function of the *stress-energy tensor* vanishes[1], i.e., $\langle T_{\mu\nu} \rangle = 0$. Boundary conformal field theories are completely determined once all the $C_{\mathcal{O},\alpha}$ and the (bulk) OPEs coefficients are known. It is therefore of the utmost importance to classify all the consistent boundary conditions.

In two-dimensions Cardy initiated this task writing constraints that the coefficients of the one-point function must satisfy (Cardy constraints) [80, 81]. Solving those constraints is in general very hard, and complete sets of possible boundary conditions can be found only in special cases, like in rational CFTs (RCFTs). In this thesis, we will not consider this topic, and we refer the interested reader to the exhaustive reference [198]. Besides the one-point

---

[1] We recall that the one-point function of the stress tensor is the variation of the effective action W with respect to the background metric, in Euclidean signature $\langle T_{\mu\nu} \rangle = -\frac{2}{\sqrt{g}} \frac{\delta W}{\delta g^{\mu\nu}}$.

functions, another very interesting quantity, which can be defined in 2-dimensional BCFTs, is the *boundary entropy* [86]. This represents the entropy associated to the boundary states $|B_\alpha\rangle$, i.e. $g_\alpha = \langle 0|B_\alpha\rangle$, and it is has been argued in [86] and proved in [87] to be a decreasing quantity along the boundary RG flow. Thus, it is a measure of the boundary degrees of freedom, and it plays the same role of the central charge c for the bulk of the system. In Sec. 1.2.1, we will discuss the analogue of the boundary entropy in the three-dimensional case.

In contrast to the one-point functions (1.2.1), the form of the two-point functions is not fixed by symmetry, and analogously to 4-point function on the infinite space, it depends on undetermined functions of conformal ratios. For example for scalar fields one obtains [84, 85]

$$\langle \mathcal{O}_i(y)\mathcal{O}_j(y')\rangle = \frac{1}{(2x)^{\eta_i}(2x')^{\eta_j}} f_{ij}(\xi) \qquad\qquad \xi = \frac{(y-y')^2}{4\,x\,x'} \tag{1.2.2}$$

where the functions f_{ij} depend on the specific BCFT we consider.

As an example, we consider the free massless scalar field in $(d+1)$ dimensions on the upper half-space. The action reads

$$\mathcal{I} = \int_{\mathcal{M}} d^{d+1}y\,\mathcal{L} = \frac{1}{2}\int_{\mathcal{M}} d^{d+1}y\,\partial^\mu\varphi\partial_\mu\varphi \tag{1.2.3}$$

whose extremization leads to the equation of motion and the two possible conformal boundary conditions

$$\partial^2\varphi = 0 \qquad\qquad \begin{cases} \varphi|_{\partial\mathcal{M}} = 0 & \qquad\qquad \text{Dirichlet b.c.} \\ \partial_\perp\varphi|_{\partial\mathcal{M}} = 0 & \qquad\qquad \text{Neumann b.c.} \end{cases} \tag{1.2.4}$$

where $\partial_\perp$ represents the derivative in the direction perpendicular to the boundary. The two different boundary conditions lead to different field theories, which both show different aspects with respect to the theory in the infinite space. For instance, the two-point function is modified and shows a dependence on the boundary conditions

$$\langle\varphi(y)\varphi(y')\rangle = \frac{1}{S_d}\frac{1}{d-1}\left(\frac{1}{|y-y'|^{d-1}} \pm \frac{1}{|y-\tilde{y}'|^{d-1}}\right) \tag{1.2.5}$$

where S_d is the volume of the hypersphere in d dimensions and $\tilde{y} = (-x, \boldsymbol{y})$. In (1.2.5), the ± sign corresponds to the two different boundary conditions, i.e., + for Neumann and − for Dirichlet. We note that (1.2.5) is in agreement with the general result (1.2.2) with $f_{\varphi\varphi} = \xi^{(d-1)/2} \pm [\xi+1]^{(d-1)/2}$. More interestingly, imposing boundary conditions on $x = 0$ implies that the one-point functions do not vanish, because the translational symmetry in the direction perpendicular to $\partial\mathcal{M}_{d+1}$ is broken. The limit $x \to x'$ of (1.2.5) and the usual subtraction of the divergences leads to[2] [84]

$$\langle\varphi^2(y)\rangle = \pm\frac{1}{S_d}\frac{1}{d-1}\frac{1}{|2x|^{d-1}} \tag{1.2.6}$$

in agreement with the general result (1.2.1) with $C_{\varphi^2} = \pm[S_d(d-1)]^{-1}$.

---

[2] We notice that the one-point function $\langle\varphi(x)\rangle$, and more in general any one-point function given by an odd power of the fundamental field $\varphi(x)$, vanishes since both the action (1.2.3) and the boundary condition (1.2.4) are $\mathbb{Z}_2$ invariant.

1.2.1 Curved boundaries and boundary quantum anomalies

So far, we have discussed the case of flat boundaries, for which the one-point function of the stress-energy tensor vanishes. Here, we consider the case of deformed boundaries and how this deformation affects $\langle T_{\mu\nu}\rangle$.

A generic codimesion-one surface is characterised by the first (induced metric) and second (extrinsic curvature) fundamental forms

$$h_{\mu\nu} = g_{\mu\nu} - n_\mu n_\nu \qquad\qquad k_{\mu\nu} = h^\alpha_\mu h^\beta_\nu \nabla_\alpha n_\beta \tag{1.2.7}$$

where n_μ is the normal vector to the hypersurface. When the boundary is curved, also the residual symmetry is in general broken, and we cannot conclude that the one-point function of the stress tensor vanishes. In fact, it turns out to be a function of the geodesic distance from the boundary X. In this case, the whole form of the one-point function is not fixed by symmetry consideration. However, it is possible to study its near-boundary behaviour [199]

$$\langle T_{\mu\nu}(y)\rangle = \frac{A_T}{X^{d-1}}\kappa_{\mu\nu} + \dots \tag{1.2.8}$$

where $\kappa_{\mu\nu} = k_{\mu\nu} - k/(d-1)h_{\mu\nu}$ is the traceless part of the extrinsic curvature $k_{\mu\nu}$. The dots stand for the subleading pieces in the expansion in terms of $X\,\kappa_{\mu\nu}$. Notice also that since $\kappa_{\mu\nu}$ is traceless, the stress-energy tensor is traceless as well (at leading order). The coefficient A_T has been found for free theories in four dimensions [199], and in any dimension for the free scalar [200]. The holographic computation has been done in our work [154], and it will be discussed in detail in Sec. 3.3.

The presence of a boundary also modifies the conformal anomaly of the theory. In a CFT the conformal anomaly is the non-vanishing of the expectation value of the trace of the stress-energy tensor due to quantum effects. For an extensive discussion of anomalies in quantum field theory we refer to [201–204]. In this thesis, we are interested in anomalies that arise when a gravitational background field is turned on. In the presence of conformal anomalies, the trace of the one-point function of the stress tensor becomes a function of local geometric quantities whose integrals are conformal invariants. For CFTs in infinite or closed manifolds, this condition implies that conformal anomalies occur only in even-dimensional spacetime since they can depend only on combinations of the Riemann tensor which has energy dimension two. Furthermore, they vanish in flat space. In the presence of a curved boundary, there may be additional contributions localized at the edge of the system. In the following, we report the trace-anomaly in $d = 1$

$$\langle T^\mu_\mu(y)\rangle^{(d=1)} = \frac{c}{24\pi}\left(\mathcal{R} + 2k\,\delta\left(\partial\mathcal{M}_2\right)\right) \tag{1.2.9}$$

and $d = 2$ [88, 205]

$$\langle T^\mu_\mu(y)\rangle^{(d=2)} = \frac{1}{4\pi}\left(-\mathfrak{a}\,\mathcal{R} + \mathfrak{q}\,\mathrm{Tr}\kappa^2\right)\delta\left(\partial\mathcal{M}_3\right) \tag{1.2.10}$$

where $x = 0$ define the boundary in a suitable coordinate system. The quantity $\langle T^{\mu}_{\ \mu}\rangle$ has been studied also in BCFT$_4$ [206, 207]. We notice that in $d = 1$ the contribution of the

	$\mathfrak{a}$	$\mathfrak{q}$	Boundary conditions
Free scalar boson	$-\frac{1}{96}$	$\frac{1}{64}$	Neumann
Free scalar boson	$\frac{1}{96}$	$\frac{1}{64}$	Dirichlet
Free dirac fermion	0	$\frac{1}{32}$	Mixed

Table 1.1: In this table the values of $\mathfrak{a}$ and $\mathfrak{q}$ are reported for the free scalar and free fermion [208].

boundary to the anomaly makes the integral of (1.2.9) conformal invariant in agreement with the Gauss-Bonnet theorem, but it does not add any new charge.

In three dimensions, the situation is much more interesting because the presence of the boundary uncovers the two boundary charges $\mathfrak{a}$ and $\mathfrak{q}$. These charges have been computed for the free scalar [88, 91] and fermion in [208] (we postpone the discussion for the holographic computation of those charges to Sec. 1.4). The central charge $\mathfrak{a}$ has been shown to be a decreasing quantity under the boundary renormalization group flow in [88]. Thus, it plays the role of the boundary entropy in three dimensions, and it represents a measure of the boundary number degrees of freedom. Regarding $\mathfrak{q}$, it turns out to be proportional to A_T in (1.2.8), namely $\mathfrak{q} = -2\pi A_T$ [200]. In table 1.1 the known boundary charges $\mathfrak{a}$ and $\mathfrak{q}$ are reported [208].

1.2.2 Entanglement entropy in BCFTs

One of the main aims of this dissertation is making progress in understanding how boundaries affect the entanglement entropy.

In two-dimensional conformal field theory, it has been found that when the region A is an interval of length ℓ adjacent to the boundary in the vacuum state, the entanglement entropy has the following form [23]

$$S_A^{(\text{BCFT})} = \frac{c}{6} \log \frac{\ell}{\varepsilon} + c_\alpha + \mathcal{O}(\varepsilon). \tag{1.2.11}$$

We notice that the coefficient in front of the logarithmic divergence is again proportional to the central charge but, since the entangling surface is made by one single point, is the half of the case of equation (1.1.15). In contrast to the leading term, which does not give any information about the boundary conditions, the subleading term c_α strongly depends on them. In particular, the combination $S_A^{(\text{BCFT})} - S_A^{(\text{CFT})}/2$ gives the Affleck-Ludwig boundary entropy $\log g_\alpha$ [23] discussed above. Furthermore, in [209] the entanglement entropy has been employed to obtain a quantity that is monotonically decreasing along the boundary RG flow on the same footing of the "entropic c-functions" in infinite systems discussed in 1.1.1.

In three and four dimensions, results in free boundary quantum field theories have been found in [208, 210], where the authors employed the heat kernel method to obtain the Rényi entropies corresponding to entangling surfaces orthogonal to flat boundaries which divide the space in two identical parts.

In BCFT$_3$, when the region A is smooth and disjoint from the boundary, the entanglement entropy is expected to have the form

$$S_A \,=\, b\,\frac{P_{A,B}}{\varepsilon} - F_{A,\alpha} + \mathcal{O}(\varepsilon) \tag{1.2.12}$$

where $F_{A,\alpha}$ is finite as $\varepsilon \to 0^+$. The expansion (1.2.12) is very similar to the one in CFT$_3$ (1.1.16) but here $F_{A,\alpha}$ shows a dependence on the boundary conditions labelled by α (besides the dependence on the shape of the region A). This case will be studied in details in chapter 2 where we employ the AdS$_4$/BCFT$_3$ setup introduced in Sec. 1.4 correspondence to find results for circular and elliptical regions disjoint from the boundary. To our best knowledge no results are available in CFT for this case.

Another compelling case is when the region A intersects the boundary at isolated points. In this case, the expansion (1.2.12) is modified by the occurrence of a logarithmic divergence

$$S_A \,=\, b\,\frac{P_{A,B}}{\varepsilon} - f_{\alpha,\text{tot}}\log(P_{A,B}/\varepsilon) + \mathcal{O}(1) \tag{1.2.13}$$

where the coefficient $f_{\alpha,\text{tot}}$ is, in general, a function of the angles which characterises the intersection between the entangling curve and the boundary, and it also depends on the boundary condition α. If more than one intersection occurs, $f_{\alpha,\text{tot}}$ is the sum of the various functions corresponding to the individual intersections. Here, we do not give any further details on $f_{\alpha,\text{tot}}$ because a detailed discussion is the subject of the chapter 3, where analytic results in the holographic framework regarding that function are obtained. In [208, 210], the explicit value of $f_{\alpha,\text{tot}}$ has been found for an orthogonal intersection between the entangling curve and the boundary both for the free scalar and the free Dirac fermion. For the former one, $f^{\text{bos}}_{\alpha,\text{orth}} = \pm 1/24$ where ± corresponds to Dirichlet and Neumann boundary conditions respectively, while for the free fermion with mixed boundary condition the coefficient vanishes $f^{\text{ferm}}_{\alpha,\text{orth}} = 0$.

In chapter 3, we will find the boundary corner function $f_\alpha(\gamma)$ for arbitrary angles $\gamma \in [0, \pi]$ within the holographic setup of Takayanagi [89].

1.3 Holographic Entanglement Entropy

Computing the entanglement entropy in quantum field theory is a formidable task. An exception is represented by $(d+1)-$dimensional quantum field theories that are dual to $(d+2)$-dimensional gravitational theories, which provide weakly coupled and calculable gravitational descriptions of certain strongly coupled field theories.

In these cases, the field theory on a manifold $\mathcal{M}_{d+1}$ is defined on the boundary of a gravitational spacetime $\mathcal{G}_{d+2} \times \mathcal{Y}$ where $\mathcal{Y}$ is eventually a compact space. The first and most known example of this kind of dualities was discovered by Maldacena [33] and it relates the 4-dimensional $\mathcal{N} = 4$ superconformal field theory with gauge group $SU(N)$ to type IIB superstring theory on $AdS_5 \times S^5$. Further studies have been performed in [211, 212], and for a review we refer to [213]. AdS/CFT dualities have been discovered also in three dimensions (ABJM) [214], in two dimensions [215] and in six dimensions [216].

Even though for generic coupling g_{YM} and N of the CFT these dualities are very complicated, they simplify in specific limits. When $N \to +\infty$ (*large N limit*) the gravitational theory reduces to classical string theory, which further simplifies to classical theory of gravity in the *strong coupling limit* $g_{YM} \to +\infty$. In this thesis, we always consider the dualities in the large N and strong coupling limit.

When the $(d+1)-$dimensional conformal field theory is in its vacuum state, the dual gravitational theory is given by a manifold $\mathcal{G}_{d+2} \times \mathcal{Y}$ where $\mathcal{G}_{d+2}$ is equipped with the AdS_{d+2} background metric. The compact space $\mathcal{Y}$ is not important for our purposes and in the following will be ignored. The AdS_{d+2} metric in Poincaré coordinates reads

$$ds^2 = \frac{R^2_{\text{AdS}}}{z^2}\left(-dt^2 + d\boldsymbol{x}^2 + dz^2\right), \tag{1.3.1}$$

where $\boldsymbol{x} = (x_1, \dots, x_d)$ and R_{AdS} is the AdS radius. The line element (1.3.1) diverges on the plane $z = 0$, where the $(d+1)$-dimensional CFT lives. The duality can be schematically stated by the equality between the partition functions of the two theories [211, 212]

$$e^{-S_{\text{grav}}[\phi^I_{(0)}(x)]} = \left\langle e^{\int d^dx\ \phi^I_{(0)}(x)\mathcal{O}_I(x)}\right\rangle_{\text{CFT}}$$

where S_{grav} is the (super)gravity action, $\phi^I_{(0)}(x)$ is the boundary limit of the classical solution of the fields in the gravity theory, and $\mathcal{O}_I(x)$ are scaling operators of the CFT duals to the bulk fields ϕ^I. In the following, we will refer to the CFT as the boundary theory, while the gravitational theory will be called bulk theory.

By employing the AdS/CFT correspondence, it is possible to compute CFT observables by performing computation in the gravity side, which is classical in the limit of our interest. For example, the (connected) correlation functions of primary operators are given by

$$\langle \mathcal{O}_{I_1}(x_1)\cdots\mathcal{O}_{I_n}(x_n)\rangle_{CFT} = -\frac{\delta}{\delta\phi^{I_1}_{(0)}(x_1)}\cdots\frac{\delta}{\delta\phi^{I_n}_{(0)}(x_n)} S[\phi^I_{(0)}(x)]\Bigg|_{\phi^I_{(0)}=0}.$$

Other interesting quantities are the Wilson loops whose holographic description has been firstly studied in [217] and the entanglement entropy, whose holographic dual will be described in 1.3.1 for the static case [31, 32] and 1.3.2 for the general one [34].

Similarly to what happens in field theory, the computation of observables in the bulk theory leads to divergences that must be regularized. In the gravity side, the divergences arise because the spacetime is not compact and the classical action diverges. In order to regularize them, we introduce an infrared cutoff ε which restricts the spacetime to the part $z \geq \varepsilon$. The IR cutoff ε corresponds in the boundary theory to a UV regulator. Furthermore, the renormalization procedure, which has been systematically studied in [218–220], can be entirely performed in the bulk theory. We mention that also the renormalization group has been extensively studied in the holographic context [221, 222].

1.3.1 Holographic entanglement entropy: static case

The gravitational dual of entanglement entropy has been conjectured by Ryu and Takayanagi [31, 32]. This subsection is devoted to discussing the holographic entanglement entropy and its properties for static spacetimes.

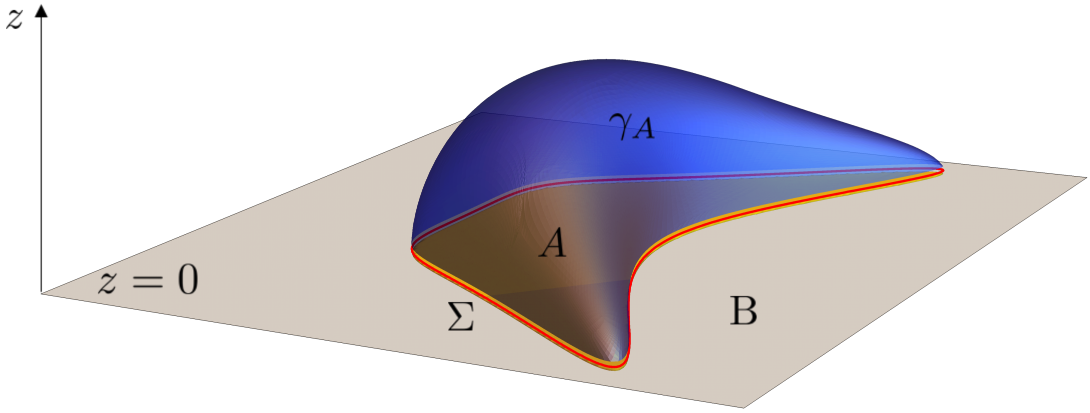

Figure 1.4: Example of minimal surface in the Cauchy slice $t = 0$ of the AdS$_4$ spacetime (1.3.1). The surface γ_A is anchored to the entangling curve Σ that divides the two complementary regions A and B. The entanglement entropy S_A is given by the Ryu-Takayanagi formula (1.3.2).

Let us consider a Cauchy slice $\mathcal{C}_{d+1}$ of the manifold $\mathcal{G}_{d+2}$ with asymptotic boundary $\partial\mathcal{G}_{d+2} = \mathcal{M}_{d+1}$. For instance, if the manifold is equipped with the metric (1.3.1) we can consider the time-slice $t = 0$. Then, we consider a bipartition $\{A, B\}$ of the boundary $\mathcal{M}_{d+1}$. The entanglement entropy corresponding to the region A is given by

$$S_A = \min_{\gamma_A \sim A} \frac{\mathcal{A}[\gamma_A]}{4G_N^{(d+2)}} \tag{1.3.2}$$

where $\mathcal{A}[\gamma_A]$ is the area of a d-dimensional (codimension-2) hypersurface γ_A *homologous* to the region A, see Fig. 1.4. A hypersurface γ_A is said to be homologous to the region A if it is smoothly retractable to A, or more correctly if it exists a smooth spacelike codimension-one surface bounded by γ_A and the region A. In particular, the boundary of $\partial\gamma_A$ coincides with the entangling surface ∂A. The formula (1.3.2) states that, among all the hypersurfaces which respect the homologous constraint, we have to pick up the one which has the *minimal area*. Finally, $G_N^{(d+2)}$ is the Newton gravitational constant in $d+2$ dimensions. Since the minimal (or extremal in general) hypersurface $\hat{\gamma}_A$ reaches the conformal infinity of the asymptotically AdS spacetime, its area diverges. In order to regularize the divergence we restrict the integration of the area of $\hat{\gamma}_A$ to the hypersurface $\hat{\gamma}_\varepsilon \equiv \hat{\gamma}_A \cap \{z \geqslant 0\}$, where $\varepsilon > 0$ is the UV cutoff. In the following, for simplicity will we use use the term surface instead of hypersurface.

A minimal surface is a particular case of *extremal surface*, which is a surface that extremizes the area functional

$$\mathcal{A}[\gamma_A] = \int \sqrt{h}\, d^d\sigma. \tag{1.3.3}$$

In the following, we will use the symbol $\hat{\gamma}_A$ for the extremal surfaces anchored to A. The extremal surfaces in asymptotically AdS background share the important property to be orthogonal to the conformal boundary $\mathcal{M}_{d+1}$ [67]. This property will be proved in chapter 4 in the context of the more general metrics with hyperscaling exponent (see appendix C.2).

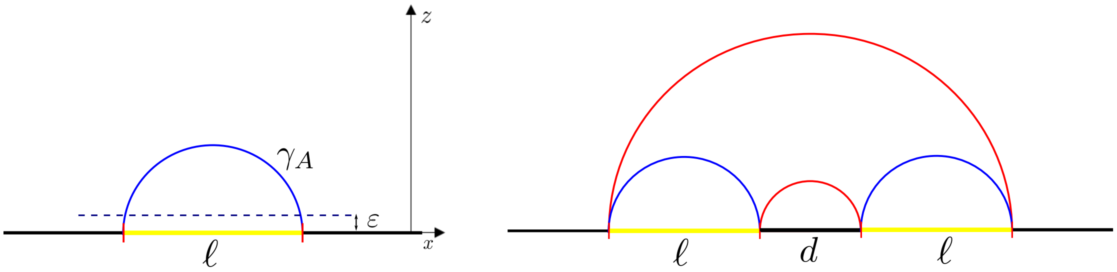

Figure 1.5: Left: Single interval of length ℓ in the AdS$_3$/CFT$_2$ setup. The minimal surface $\hat{\gamma}_A$ is the geodesics which connects the extrema of the interval. The straight dashed line $z = \varepsilon$ represents the cutoff in the gravity side. Right: Extremal surfaces anchored two the two intervals of length ℓ separated by the distance d. Above the critical value $(d/\ell)_{\text{crit}}$ the minimal surface is given by the blue geodesics, while below $(d/\ell)_{\text{crit}}$ the correct surface is made by the red ones.

For a given region A on $\mathcal{M}_{d+1}$ there could be more than one extremal surfaces consistent with the homology constraint. In those cases, by varying the shape of the region A, a *transition between extremal surfaces* may happen. In fact two distinct extremal surfaces, of which is one minimal, can have the same area once the region A is appropriately modified. Modifying the region further can exchange the role between the two surfaces, i.e., the extremal one can become the global minimum at the expense of the other. The simplest example of transitions occurs for two disjoint intervals in AdS$_3$/CFT$_2$, and it will be analysed in Sec. 1.3.1.

The Ryu-Takayanagi formula (1.3.2) has passed many consistency checks. For instance, it is able to reproduce the structure (1.1.14), and the minimality condition implies the strong subadditivity constraint introduced in Sec. 1.1 [223]. Furthermore, (1.3.2) has been proved for spherical domains in the vacuum state in [224]. There, the authors employed a conformal map between the CFT on flat spacetime and on a hyperbolic geometry. In this way, the vacuum state of the former geometry is mappedto a thermal state in the latter one. In particular, they showed that the entanglement entropy of the sphere is mapped to the thermal entropy of the hyperbolic geometry. If the CFT admits a holographic dual, by employing the AdS/CFT dictionary, it is possible to compute the thermodynamic entropy as the horizon entropy of a certain topological black hole, which is mapped back into the RT surface by applying the inverse mapping. The general proof of the Ryu-Takayanagi formula has been finally derived from the holographic dictionary in [225] (see also previous attempts in [226, 227]).

Before going to some examples in AdS$_3$/CFT$_2$, we mention that a reformulation of the holographic entanglement entropy formula (1.3.2) has been recently proposed through particular flows [228] called bit threads. Exploring the various features of the holographic entanglement entropy through this approach seems very insightful [229, 230], but a detailed description of this method is beyond the scope of this thesis.

Below we discuss some example in AdS$_3$/CFT$_2$.

HEE in AdS$_3$/CFT$_2$: single interval in the vacuum state

Let us consider the case of single interval $A = \{\mathbb{R} : -\ell/ \leq x \leq \ell/2\}$ on the Cauchy slice $t = 0$ of the asymptotic boundary of the AdS$_3$ spacetime described by the metric (1.3.1).

The minimal surface, which respects the homology constraint, is the geodesic $z(x) = \sqrt{(\ell/2)^2 - x^2}$ with $x \in (-\ell/2, \ell/2)$ [31, 32] depicted on the left side of Fig. 1.5. As discussed above, the integration of the area (1.3.3) must be performed on the restricted part $z \geqslant \varepsilon$. The holographic entanglement entropy is given by the formula (1.3.2), and we find

$$S_A = 2\frac{R_{\text{AdS}}}{4G_N^{(3)}}\int_{\varepsilon}^{\ell/2} dz\, \frac{\ell/2}{z\sqrt{\left(\frac{\ell}{2}\right)^2 - z^2}} = \frac{R_{\text{AdS}}}{2G_N^{(3)}}\log\left(\frac{\ell + \sqrt{\ell^2 - 4\varepsilon^2}}{2\varepsilon}\right) = \frac{R_{\text{AdS}}}{2G_N^{(3)}}\log\left(\frac{\ell}{\epsilon}\right) + \mathcal{O}\left(\varepsilon^2\right). \tag{1.3.4}$$

By employing the Brown-Henneaux formula for the central charge [215]

$$c = 3\frac{R_{\text{AdS}}}{2G_N^{(3)}} \tag{1.3.5}$$

we find the well-known CFT result (1.1.15). We stress that, even though we have found the same result of (1.1.15), the holographic computation is valid only for large central charges $c \gg 1$.

HEE in AdS$_3$/CFT$_2$: disjoint intervals in the vacuum state

Interesting cases are the ones in which the region A is made of two or more disjoint components, in which the transitions between extremal surfaces discussed above may occur. For the sake of simplicity, we analyse the case of two disjoint intervals. Now A is as represented on the right side of Fig. 1.5. In this case, there are two possible extremal solutions, i.e., the red and the blue surface, that compete. Which one is the global minimum depends on the ratio d/ℓ. The area of the surfaces corresponding to the two situations can be easily found by adapting the computation in (1.3.4). One obtains

$$\mathcal{A}_{\text{red}} = 2R_{\text{AdS}}\log\left(\frac{d}{\varepsilon}\right) + 2R_{\text{AdS}}\log\left(\frac{2\ell + d}{\varepsilon}\right) + \mathcal{O}\left(\varepsilon^2\right) \tag{1.3.6}$$

$$\mathcal{A}_{\text{blue}} = 4R_{\text{AdS}}\log\left(\frac{\ell}{\varepsilon}\right) + \mathcal{O}\left(\varepsilon^2\right). \tag{1.3.7}$$

We see that in the limit $\varepsilon \to 0$, $\mathcal{A}_{\text{red}}$ and $\mathcal{A}_{\text{blue}}$ are equal at $(d/\ell)_{\text{crit}} = (\sqrt{2} - 1)$, value at which the transition between the two extremal surface occurs. As a consequence, when $d/\ell \geq (d/\ell)_{\text{crit}}$ the minimal surface is the blue one, while when $d/\ell \leq (d/\ell)_{\text{crit}}$ we must consider the red surface. The mutual information reads

$$I(A:B) = \begin{cases} \dfrac{c}{3}\log\left(\dfrac{\ell^2}{d(2\ell + d)}\right) & d/\ell < (d/\ell)_{\text{crit}} \\ 0 & d/\ell > (d/\ell)_{\text{crit}} \end{cases} \tag{1.3.8}$$

which (1.3.8) is a continuous function of d/ℓ, but it is not derivable at $(d/\ell)_{\text{crit}}$, where it vanishes and the transition takes place. This behaviour is a large c effect that has not been observed for finite values of the central charge [171–174]. In particular, it is expected to be smoothed out by quantum corrections [231].

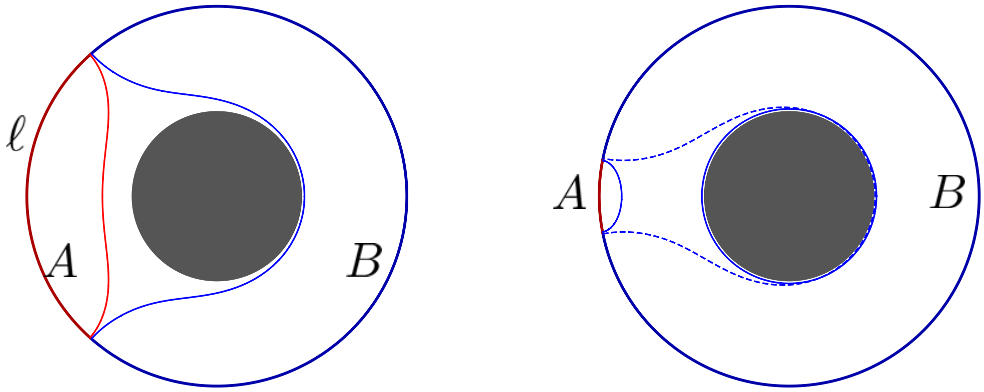

Figure 1.6: Left: Single interval in the BTZ black hole metric (1.3.9). The homology constraint implies that the minimal surface corresponding to the region A is the red geodesics, while the one corresponding to the region B is the blue one. Right: When the region B is sufficiently large, i.e., $\theta_0 > \theta_{0,\text{crit}}$, the minimal surface is made by the two disjoint components depicted with the continuous blue lines. When $\theta_0 < \theta_{0,\text{crit}}$ the minimal surface is given by the dashed blue line.

HEE in AdS$_3$/CFT$_2$: single interval in the thermal state

Before concluding this subsection, we consider the case of the BTZ black hole in AdS$_3$/CFT$_2$, which is dual to the CFT$_2$ on the circle of length L in the thermal state with inverse temperature β. The BTZ black hole metric (we set for simplicity $R_{\text{AdS}} = 1$) is given by [232]

$$ds^2 = -(r^2 - r_h^2)dt^2 + \frac{1}{r^2 - r_h^2}dr^2 + r^2 d\theta \tag{1.3.9}$$

where the asymptotic boundary is at $r \to +\infty$, and where r_h sets the position of the horizon given by $r_h = R_{\text{AdS}}L/\beta$. The extremal surfaces anchored to the extrema of the interval A of length ℓ have been found in [31, 32] (see also [233]), and their profile $r = r(\theta)$ reads

$$r(\theta) = r_h \left[1 - \frac{\cosh^2\left(\frac{r_h}{R_{\text{AdS}}}\theta\right)}{\cosh^2\left(\frac{r_h}{R_{\text{AdS}}}\theta_0\right)}\right]^{-\frac{1}{2}} \tag{1.3.10}$$

where θ_0 is a parameter whose value corresponds to the absolute value of θ when $r \to +\infty$.

This is the simplest case in which the homology constraint plays a crucial role. In Fig. 1.6, we show two possible extremal surfaces anchored to the extrema of the interval A of length ℓ. The two geodesics are given by the equation (1.3.10) with two different values of θ_0, i.e. $\theta_0^{(A)} = \pi\ell/L$ and $\theta_0^{(B)} = \pi - \theta_0^{(A)}$. The length of the two geodesics depends on the parameter θ_0, and it is given by [31, 32, 233]

$$S(\theta_0) = \frac{c}{3}\log\left(2\frac{r_\infty}{r_h}\sinh\left(r_h\theta_0\right)\right) \tag{1.3.11}$$

where r_∞ is the cutoff. We notice that if $\theta_0^{(A)} < \pi/2$, the red geodesics is shorter than the blue one. However, the red geodesic provides the entanglement entropy only for the region A. In fact, since the surface cannot be smoothly retracted to B due to the presence of the black hole, it does not respect the homology constraint if the entanglement entropy of the region B is considered. Thus, S_B is given by (1.3.11) with $\theta_0 = \theta_0^B$ even though it is longer than the one corresponding to $\theta_0 = \theta_0^A$. In particular, the homology constraint leads to $S_A \neq S_B$ for the thermal state, in agreement with the general expectation regarding the entanglement entropy of mixed states.

The BTZ black hole provides another kind of transitions between minimal surfaces, which gives rise to the *entanglement plateaux* [233]. On the right side of Fig. 1.6, the case of very large regions B is depicted. In this case, it turns out that the corresponding minimal surface may not be given by the dashed blue geodesic as in the previous example. In fact, there is another good candidate (respecting the homology constraint) for S_B. When the region B is sufficiently large, S_B is given by the sum of the two disconnected geodesics depicted in continuous blue lines: the one anchored to the extrema of the interval and that is the same as the one corresponding to A, and the one which wraps the black-hole horizon [233]. Thus, by comparing the length of the two configurations we find the entanglement entropy of B, which reads

$$S_B = \begin{cases} \dfrac{c}{3}\log\left(2\dfrac{r_\infty}{r_h}\sinh\left(r_h\theta_0^{(B)}\right)\right) & \theta_0^{(B)} < \theta_{0,\text{crit}} \\ \dfrac{c}{3}\pi r_h + \dfrac{c}{3}\log\left(2\dfrac{r_\infty}{r_h}\sinh\left(r_h(\pi-\theta_0^{(B)})\right)\right) & \theta_0^{(B)} > \theta_{0,\text{crit}} \end{cases} \tag{1.3.12}$$

where the critical angle is given by $\theta_{0,\text{crit}} = \coth^{-1}(2\coth(\pi r_h) - 1)/r_h$ [233]. In particular, in the limiting case in which the region B is the whole circle, the entanglement entropy is proportional to the area of the horizon, which is the dual of the thermal entropy of the CFT. Furthermore, we observe that if we do not take into account the disconnect solution, the holographic entanglement entropy will not respect the Araki-Lieb inequality since $|S_A - S_B|$ would diverge as $\theta_0 \to 0$, while $S_{A\cup B}$ gives the thermal entropy which is finite. Finally, we observe that the holographic entanglement entropy saturates the Araki-Lieb inequality when $\theta_0 > \theta_{0,\text{crit}}$.

1.3.2 Holographic entanglement entropy: time-dependent case

In the Ryu-Takayanagi prescription (1.3.2) is necessary to fix a Cauchy slice. In fact, the minimality condition makes sense only for Riemannian metrics, since for Lorentzian spaces minimal surfaces do not exist in general. This is the reason for which we assumed static spacetime so far. In fact, in those cases, the choice of a preferred time-slice is suggested by the existence of a time-like killing vector. In contrast, for time-dependent backgrounds, there are no preferred Cauchy time-slices, and the Ryu-Takayanagi formula (1.3.2) is not directly applicable.

The holographic prescription for computing the entanglement entropy in general spacetimes, which includes time-dependent metrics, has been proposed in [34] and it is called the Hubeny-Rangamani-Takayanagi (HRT) formula. In the following, we introduce this prescription.

Let us take a codimension-2 spacelike surface γ_A anchored to ∂A at a certain boundary time. The surface γ_A has two unit normal vectors orthogonal to each other, which we denote

$n^{(1)}$, $n^{(2)}$ and with normalization $n^{(1)} \cdot n^{(1)} = 1$ and $n^{(2)} \cdot n^{(2)} = -1$. Thus, $n^{(1)}$ is space-like, while $n^{(2)}$ is time-like. The first fundamental form can be constructed out of the unit normal vectors

$$h_{AB} = g_{AB} - n^{(1)}_A n^{(1)}_B + n^{(2)}_A n^{(2)}_B \tag{1.3.13}$$

and the two extrinsic curvatures read

$$K^{(i)}_{AB} = h^M_A \, h^N_B \, \nabla_M n^{(i)}_N \qquad i = 1, 2 \tag{1.3.14}$$

where ∇_M is the unique covariant derivative with respect to the metric g_{AB}. The HRT prescription requires that the surface, whose area provides S_A, is the extremal surface with the smallest area (if more than one extremal surface exists) which respects the homology constraint. The extremality condition of a codimension-2 surface is equivalent to the vanishing of the trace of both the extrinsic curvatures (1.3.14), i.e. $h^{AB} K^{(i)}_{AB} = 0$. We stress that for generic spacetimes the extremal surface with the smallest area may not be the minimal surface.

The HRT proposal has been employed for studying the evolution of entanglement entropy in the holographic setup. For instance, the Vaidya metrics provide simple models for the black hole formation where the holographic entanglement entropy has been largely studied [148, 149, 234–239]. This proposal will be considered in chapter 4.

We conclude this subsection discussing an alternative way to compute the holographic entanglement entropy which is equivalent to the HRT prescription, i.e. the *maxmin construction* [240]. Given a spatial boundary region $A \subset \mathcal{M}_{d+1}$ and its complement B, we consider a bulk Cauchy slice $\mathcal{C}^{(\text{guess})}_{d+1}$ such that $\partial \mathcal{C}^{(\text{guess})}_{d+1} = A \cup B$. Since $\mathcal{C}^{(\text{guess})}_{d+1}$ is space-like, one can compute the minimal surface $\hat{\gamma}^{(\text{guess})}_A \subset \mathcal{C}^{(\text{guess})}_{d+1}$ homologous to A. Then, one varies the Cauchy slice finding all the corresponding minimal surfaces. Among the whole family of minimal surfaces, the prescription requires to consider the one with the maximal area $\hat{\gamma}^{\text{maxmin}}_A$. Thus, the entanglement entropy is computed by employing the formula (1.3.2) where $\hat{\gamma}^{\text{maxmin}}_A$ takes the place of $\hat{\gamma}_A$. Even though the maxmin construction may be more involved to employ in explicit computations, it can be very useful to prove general statements. For istance, it has been used to prove the strong subadditivity inequality (1.1.7) for generic spacetimes [240].

1.3.3 Holographic entanglement entropy in AdS$_4$/CFT$_3$

In this subsection, we discuss in detail the holographic entanglement entropy in AdS$_4$/CFT$_3$, which is the case of interest of this dissertation. Let us consider an arbitrary background metric that is asymptotically AdS$_4$ (AAdS$_4$). In this case, the holographic entanglement entropy of a region A is

$$S_A = \frac{R^2_{\text{AdS}}}{4G_N} \left(\frac{P_{A,B}}{\varepsilon} - F_A + \mathcal{O}(\varepsilon) \right) \tag{1.3.15}$$

where for simplicity we used the same notation F_A for the subleading term divided by $R^2_{\text{Ads}}/(4G_N)$. The leading term is independent of the behaviour of the metric in the deep interior of the bulk and depends only on its asymptotic characteristics. In contrast, the finite term F_A is sensible on all the details of the metric.

When the metric is empty AdS$_4$, it is possible to obtain analytic solutions for the minimal surfaces in the case in which the region A have particular symmetries, i.e. when it is the half-plane, a disk or a strip, and when it is made by two disjoint disks [241–245]. The case with corners will be discussed in 1.3.3. In the time-slice $t = 0$, we consider the region A on the AdS boundary $z = 0$ to be the half-plane $A = \{x \geqslant 0,\ \forall\, y\}$. By symmetry, the corresponding minimal surface is a half-plane orthogonal to the boundary $z = 0$, i.e. $\hat{\gamma}_A = \{x = 0,\ \forall\,(y,z)\}$, and its area is

$$\mathcal{A}[\hat{\gamma}_{A,\varepsilon}] = \int_{\hat{\gamma}_{A,\varepsilon}} \sqrt{h} = \int_{\varepsilon}^{+\infty} dz \int_{-L/2}^{L/2} dy\, \frac{R^2_{\text{AdS}}}{z^2} dz dy = R^2_{\text{AdS}} \frac{L}{\varepsilon} \tag{1.3.16}$$

where, as discussed above, we have restricted $\hat{\gamma}_A$ to the part of AdS $z \geqslant \varepsilon$, and we introduced the IR cutoff L because the region A is infinite. In this case, we observe that S_A contains only the area-law term in (1.3.15), i.e. $F_A = 0$.

The minimal surface anchored to a disk of radius R can be obtained by the one anchored to the half-disk by employ a conformal mapping [246]. This mapping is studied in appendix A.1 and it will be applied to the case of AdS$_4$/BCFT$_3$ in chapter 2 (for the current case consider equation (A.1.4) with $\alpha = \pi/2$ and $R_Q = R$). In particular, the minimal surface turns out to be the hemisphere $x^2 + y^2 + z^2 = R^2$. The area can be easily computed, and it reads [31, 32, 217, 247]

$$\mathcal{A}[\hat{\gamma}_{A,\varepsilon}] = R^2_{\text{AdS}} \left(\frac{\pi R}{\varepsilon} - 2\pi \right) \tag{1.3.17}$$

from which we read $F_A = 2\pi$. The strip domain will be studied in the Sec. 1.5.2 for the more general hvLif$_4$ background metric, and here we report only the result F_A in the AdS$_4$ metric, which reads [31, 32]

$$F_A = 4\pi \frac{\Gamma^2\left(\frac{3}{4}\right)}{\Gamma^2\left(\frac{1}{4}\right)} \frac{L}{\ell} \tag{1.3.18}$$

where ℓ is the width of the strip and L is the IR cutoff as in the case of the half-plane. For general shapes, finding the holographic entanglement entropy is very complicated and usually one considers perturbation about half-space or spherical regions as in [65, 67–73].

In the context of AdS$_4$/CFT$_3$, an analytic formula for F_A valid for generic shape of the region A has been found [76, 77], which expresses this subleading term as a functional over the minimal surface $\hat{\gamma}_A$. In the time-slice $t = 0$, we consider an extremal (not necessarily minimal) surface $\hat{\gamma}_A$ which is described by the unit-normal vector n_μ and with extrinsic curvature $K_{\mu\nu} = h_\mu{}^\alpha h_\nu{}^\beta \nabla_\alpha n_\beta$. The surface $\hat{\gamma}_A \subset \mathbb{H}^3$ can be also embedded in the upper half-space $\mathbb{R}^3 \cap \{z \geqslant 0\}$, i.e. the flat space with metric $ds^2 = dx^2 + dy^2 + dz^2$. This can be achieved by applying the Weyl transformation $e^{-2\varphi} g_{\mu\nu} = \delta_{\mu\nu}$ where $g_{\mu\nu}$ is given by (1.3.1) with $t = 0$ and $\varphi = -\log(R_{\text{AdS}}/z)$. The subleading term F_A is then written as the functional over the extremal surface [76, 77]

$$F_A[\hat{\gamma}_A] = \mathcal{W}[\hat{\gamma}_A], \qquad \mathcal{W}[\gamma] = \int_\gamma \frac{1}{4} \left(\text{Tr} \widetilde{K} \right)^2 d\tilde{\mathcal{A}} \tag{1.3.19}$$

where $\widetilde{K}_{\mu\nu}$ is the extrinsic curvature of $\hat{\gamma}_A$ as embedded in $\mathbb{R}^3$. The functional $\mathcal{W}[\gamma]$ over the surface $\gamma \subset \mathbb{R}^3$ is known in mathematics as the *Willmore functional*, or Willmore energy [75], and it has the interesting property to be conformal invariant. This functional has also applications in biology where cell membranes are known to reach configurations which minimize the Willmore energy [248]. We stress that despite in (1.3.19) the quantity F_A is computed by means of a functional defined in $\mathbb{R}^3$, the result (1.3.19) corresponds to the subleading term of $\mathcal{A}[\hat{\gamma}_A]$ in AdS$_4$. We notice that, since the metric in (1.3.19) is flat, F_A turns out to be a finite quantity for any smooth $\hat{\gamma}_A$, and the integration in the functional can be performed without the introduction of any cutoff. Furthermore, equations (1.3.18) imply that F_A is a non-negative quantity in the empty AdS$_4$ case.

An interesting bound on F_A can be proved with the help of this functional [76, 78]. It can be shown that $\mathcal{W}[\gamma] \geqslant 4\pi$ whenever γ is a closed surface [75]. Of course, the extremal surfaces we are interested in are not closed because they have a boundary $\partial\hat{\gamma}_A = \partial A$. However, as argued in [76, 78], given any surface $\gamma_A \subset \mathbb{R}^3 \cap \{z \geqslant 0\}$ with boundary ∂A at $z = 0$ it is possible to consider the corresponding surface $\gamma_{A,\text{double}} = \hat{\gamma}_A \cup \gamma'_A$ where γ'_A is the mirror image of $\hat{\gamma}_A$ in the part of $\mathbb{R}^3$ with $z \leqslant 0$. We notice that, since any extremal surface $\hat{\gamma}_A$ is orthogonal to the plane $z = 0$, the doubled surface $\gamma_{A,\text{double}} = \hat{\gamma}_A \cup \gamma'_A$ is smooth. Thus, since γ_{double} is closed, $\mathcal{W}[\gamma_{A,\text{double}}] \geqslant 4\pi$ which, in turn, implies

$$F_A[\hat{\gamma}_A] = \mathcal{W}[\hat{\gamma}_A] \geqslant 2\pi \tag{1.3.20}$$

for any region A.

The result (1.3.18) has been generalized to arbitrary asymptotically AdS$_4$ metrics $g_{\mu\nu}$ in [78]. The steps leading to the analytic formula for F_A will be discussed in Sec. 2.1 where we will consider the AdS$_4$/BCFT$_3$ case. Below, we report the result for static AAdS$_4$ spacetimes only.

Let us consider an asymptotically AdS$_4$ spacetime with metric $g_{\mu\nu}$ in the time-slice $t = 0$. We define a conformally equivalent metric $\tilde{g}_{\mu\nu}$ which corresponds to the Euclidean space $\widetilde{\mathcal{M}}_3$ asymptotically flat close to the conformal boundary of $g_{\mu\nu}$, i.e.,

$$g_{\mu\nu} \,=\, e^{2\varphi}\, \tilde{g}_{\mu\nu}. \tag{1.3.21}$$

The generalization of the functional (1.3.18) reads

$$F_A[\hat{\gamma}_A] = \int_{\hat{\gamma}_A} \left(\frac{1}{2}\big(\mathrm{Tr}\widetilde{K}\big)^2 + \widetilde{\nabla}^2\varphi - e^{2\varphi} - \tilde{n}^\mu \tilde{n}^\nu\, \widetilde{\nabla}_\mu \widetilde{\nabla}_\nu \varphi \right) d\tilde{\mathcal{A}} \tag{1.3.22}$$

and it reduces to (1.3.18) when $\tilde{g}_{\mu\nu} = \delta_{\mu\nu}$ and $\varphi = -\log(R_{\text{AdS}}/z)$. We notice that, in this case, F_A is not always positive and its sign depends both on the region A and on the metric $g_{\mu\nu}$.

The functionals (1.3.18) and (1.3.22) are finite as far as the surface $\hat{\gamma}_A$ is smooth, i.e. for non-singular entangling curves. In [78] the functional (1.3.22) has been studied for different kinds of metrics, namely black hole and domain wall, and for generic shapes of the region A. Furthermore, a functional valid for time-dependent spacetimes has also been discussed. In this chapter, we do not consider this case because it will be analysed in detail in chapter 4.

Corners in HHE in AdS$_4$/CFT$_3$

So far, we have restricted our analysis to smooth entangling regions for which the subleading term F_A is finite. Here, we consider the holographic entanglement entropy of domains with corners in AdS$_4$/CFT$_3$. As introduced in Sec. 1.1.2, in the presence of isolated corners, the area of the minimal surfaces shows a logarithmic divergence

$$\mathcal{A}[\hat{\gamma}_\varepsilon] = R^2_{\text{AdS}} \left(\frac{P_A}{\varepsilon} - \widetilde{F}_{\text{tot}} \log(P_A/\varepsilon) + O(1) \right) \tag{1.3.23}$$

where

$$\widetilde{F}_{\text{tot}} = \sum_{V_k} \widetilde{F}(\theta_{V_k}) + \sum_{W_r} \widetilde{\mathcal{F}}(\vec{\phi}_{W_r}). \tag{1.3.24}$$

We note that $\widetilde{F}$ and $\widetilde{\mathcal{F}}$ in (1.3.24) are the holographic analogue of the corner functions (1.1.18). In this section we will focus only on $\widetilde{F}$, postponing the discussion of $\widetilde{\mathcal{F}}$ to the Sec. 3.5.

The analytic expression of the coefficient $\widetilde{F}$ of the logarithmic divergence has been found in [157] in the context of Wilson loops. We take A to be the infinite wedge of opening angle θ defined as $A = \{(x, y) = (\rho \sin\phi, \rho\cos\phi) \,|\, \rho \in (0, +\infty), \phi \in (-\theta, \theta)\}$. Yhe scale invariance of the region suggests the following ansatz for the profile of $\hat{\gamma}_A$

$$z = \frac{\rho}{q(\phi)} \tag{1.3.25}$$

where $q(\phi)$ is an undetermined function. By plugging equation (1.3.25) in the area functional (1.3.3), one observes that, since the coordinate ϕ is cyclic, it is possible to obtain a conservation law. By employing this conservation law, the function $q(\phi)$ and, in turn, the area of the minimal surface can be found analytically. In this way, the function $\widetilde{F}$ and the opening angle θ have been found in terms of the parameter $q_0 = q(0)$

$$\widetilde{F}(\theta) \;\equiv\; 2\, F(q_0) \tag{1.3.26}$$

where

$$F(q_0) \equiv \frac{\mathbb{E}(\tilde{q}_0^2) - (1 - \tilde{q}_0^2)\mathbb{K}(\tilde{q}_0^2)}{\sqrt{1 - 2\tilde{q}_0^2}} \tag{1.3.27}$$

and the opening angle θ of the wedge is given by

$$\frac{\theta}{2} \;=\; \tilde{q}_0 \sqrt{\frac{1 - 2\tilde{q}_0^2}{1 - \tilde{q}_0^2}} \,\Big[\, \Pi\big(1 - \tilde{q}_0^2, \tilde{q}_0^2\big) - \mathbb{K}\big(\tilde{q}_0^2\big) \Big] \;\equiv\; P_0(q_0) \tag{1.3.28}$$

where the positive parameter $\tilde{q}_0 \in (0, 1/2)$ is related to q_0 as

$$\tilde{q}_0^2 \equiv \frac{q_0^2}{1 + 2q_0^2} \qquad q_0 > 0. \tag{1.3.29}$$

The functions $\mathbb{K}(m)$, $\mathbb{E}(m)$ and $\Pi(n, m)$ are the complete elliptic integrals of the first, second, and third kind respectively. From (1.3.26) and (1.3.28), one can plot the curve $\widetilde{F}(\theta)$ parametrically in terms of $q_0 > 0$, finding the blue curve shown in Fig. 1.8.

Since $S_A = S_B$ for pure states, for the argument of the corner function $\widetilde{F}(\theta)$ we have $\theta \in (0, \pi]$. Hereafter, whenever $\theta \in (0, 2\pi)$ we mean $\widetilde{F}(\theta) = \widetilde{F}(\min[\theta, 2\pi - \theta])$.

In the remaining part of this section, we study a simple domain whose holographic entanglement entropy is given by (1.3.23) with $\widetilde{F}_{\text{tot}} = \widetilde{F}$. In this example studied in our work [154], ∂A has a single vertex with two edges, and thus only one term occurs in (1.3.24).

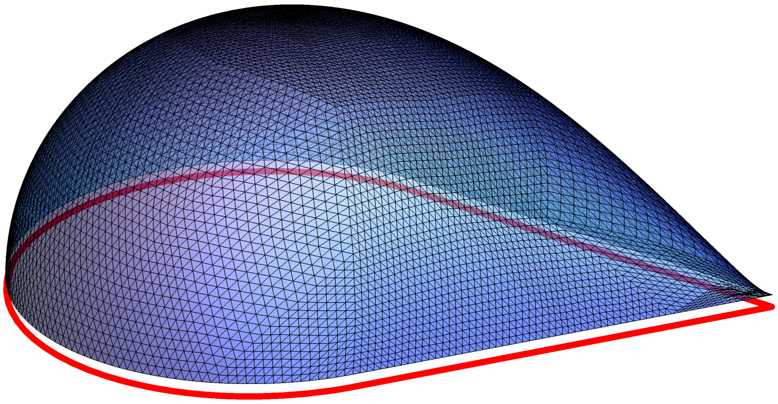

Figure 1.7: Triangulated surface in $\mathbb{H}_3$ which approximates the minimal area surface $\hat{\gamma}_A$ corresponding to a single drop region A in the $z = 0$ plane. The boundary ∂A (red curve) lies in the $z = 0$ plane and it is characterised by $L = 1$ and $\theta = \pi/3$. The UV cutoff is $\varepsilon = 0.03$. The triangulation has been obtained with Surface Evolver by setting ∂A at $z = \varepsilon$.

We consider the finite domain A similar to a two-dimensional drop. It is constructed by taking the infinite wedge with opening angle $\theta < \pi$ (whose tip is denoted by P) and the disk of radius R which is tangent to both the edges of the wedge. The distance between the two intersection points and P is $L = R\cot(\theta/2)$. Considering the circular sector given by the intersection of the infinite wedge with the disk centered in P with radius L, our drop region A is obtained as the union between this circular sector and the disk of radius R tangent to the edges of the infinite wedge introduced above. This domain can be characterised by the parameters L and θ. Its boundary ∂A is a smooth curve except for the vertex P, where two edges join, whose length is $P_A = 2L + R(\pi + \theta)$. An example of drop domain is the region in the plane enclosed by the red curve in Fig. 1.7.

The holographic entanglement entropy of a drop region A in the $z = 0$ plane is obtained by computing the area $\mathcal{A}[\hat{\gamma}_\varepsilon]$ from the minimal surface $\hat{\gamma}_A$ embedded in $\mathbb{H}_3$ which is anchored to ∂A, as prescribed by (1.3.2). The result is (1.3.23) with $\widetilde{F}_{\text{tot}} = \widetilde{F}(\theta)$, being $\widetilde{F}(\theta)$ the corner function given by (1.3.26) and (1.3.28). Here, we anticipate the numerical tool we have used throughout this thesis, namely *Surface Evolver* [152, 153], which has been applied in the context of holography for the first time in [78, 245]. Evolver is an optimization problem software that is able to obtain a triangulated surface as an accurate approximation of extremal surfaces, once the background metric and the boundary conditions together with a very simple ansatz fixing the topology are given. This software will be discussed in detail in Sec. 1.6, and in the remaining of this section we show the result of our analysis in studying the corner function $\widetilde{F}$ by means of the drop domain introduced above. The main advantage of our choice for A is that we can vary the opening angle θ in a straightforward way. The minimal area surfaces $\hat{\gamma}_A$ corresponding to regular polygons, and other finite domains with three or more vertices have been studied in [245].

In Fig. 1.7 we show a refined triangulation which approximates the minimal surface $\hat{\gamma}_A$ anchored to a single drop domain. Some technical details about the construction of this kind

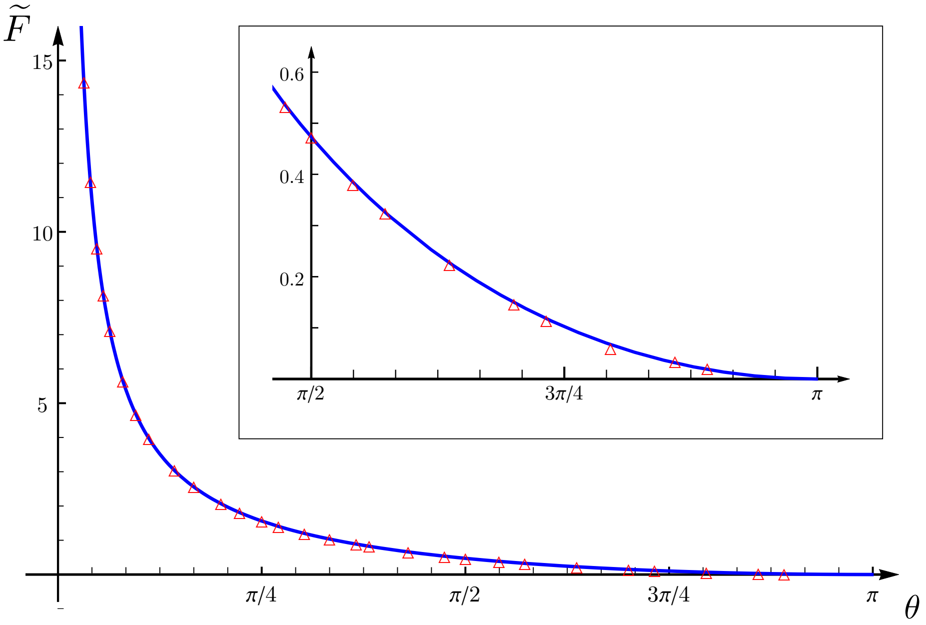

Figure 1.8: Corner function for a vertex with two edges in $\mathrm{AdS}_4/\mathrm{CFT}_3$. The blue curve corresponds to the analytic expression given by (1.3.26) and (1.3.28) found in [157]. The points labeled by the red triangles have been found through the numerical analysis based on Surface Evolver (see appendix 1.6). The inset highlights the domain corresponding to opening angles close to π.

of triangulations are discussed in Sec. 1.6 (see also [245]).

As explained in the Sec. 1.6, by fitting the numerical data for $\mathcal{A}[\hat{\gamma}_\varepsilon]$ obtained for various ε at fixed values of θ and L, we find a numerical value for the corner function which can be compared to the corresponding value coming from the analytic expression of $\widetilde{F}(\theta)$ given by (1.3.26) and (1.3.28). Repeating this analysis for different values of θ, we have obtained the results shown in Fig. 1.8, where the blue solid curve is the analytic curve $\widetilde{F}(\theta)$ found in [157], while the points marked by the red triangles have been found through our numerical analysis. The agreement is exceptionally good in the range of θ that has been explored, and it represents a good benchmark for our studies in the following chapters.

1.4 AdS/BCFT duality

In this section, we introduce the holographic dual of a BCFT on $\mathcal{M}_{d+1}$ following Takayanagi [89] and the subsequent works [90, 91].

In this prescription, the gravitational theory is an asymptotically AdS_{d+2} spacetime $\mathcal{G}_{d+2}$ restricted by the occurrence of a $(d+1)$-dimensional hypersurface $\mathcal{Q}$ in the bulk whose boundary coincides with the boundary of the BCFT_{d+1}, i.e. $\partial\mathcal{G}_{d+2} = \mathcal{M}_{d+1} \cup \mathcal{Q}$ and $\partial\mathcal{Q} = \partial\mathcal{M}_{d+1}$. Thus, $\mathcal{Q}$ is the extension of the boundary of the BCFT_{d+1} in the bulk. The metric of $\mathcal{G}_{d+2}$ and the shape of $\mathcal{Q}$ are fixed by requiring the extremization of the following gravitational action [89, 90]

$$\mathcal{I} = \frac{1}{16\pi G_{\mathrm{N}}} \int_{\mathcal{G}_{d+2}} \sqrt{-g}\,(R - 2\Lambda) + \frac{1}{8\pi G_{\mathrm{N}}} \int_{\partial\mathcal{G}_{d+2}} \sqrt{-h}\,K + \mathcal{I}_{\mathcal{Q}} \tag{1.4.1}$$

being $\Lambda = -\frac{d(d+1)}{2R^2_{\mathrm{AdS}}}$ the negative cosmological constant, $h_{\mu\nu}$ the induced metric on $\partial\mathcal{G}_{d+2}$ and $K = h^{\mu\nu}K_{\mu\nu}$ the trace of the extrinsic curvature $K_{\mu\nu}$ of $\partial\mathcal{G}_{d+2}$. We stress that, since $\partial\mathcal{G}_{d+2}$ is made of two components joined along the boundary of the BCFT_{d+1}, the manifold $\partial\mathcal{G}_{d+2}$ is in general non-smooth. The boundary term $\mathcal{I}_{\mathcal{Q}}$ describes some matter fields localised on $\mathcal{Q}$. In the action the boundary term on $\mathcal{M}_{d+1} \cap \mathcal{Q}$, needed because $\partial\mathcal{G}_{d+2}$ is non-smooth [249, 250], and the ones introduced by the holographic renormalisation procedure [219, 220, 251, 252] have been omitted because they are not relevant in the following analysis.

The variation of the first term (1.4.1) gives the Einstein equations plus a boundary term

$$\begin{aligned}\delta\mathcal{I}_{\mathrm{bulk}} =& \frac{1}{16\pi_{\mathrm{N}}} \int_{\mathcal{G}_{d+2}} \sqrt{-g}\left(R_{\mu\nu} - \frac{1}{2}g_{\mu\nu} + \Lambda g_{\mu\nu}\right)\delta g^{\mu\nu} \\ &+ \frac{1}{8\pi G_{\mathrm{N}}} \int_{\partial\mathcal{G}_{d+2}} \sqrt{-h}\frac{1}{2}n^{\mu}\left(\nabla^{\nu}\delta g_{\mu\nu} - g^{\nu\lambda}\nabla_{\mu}\delta g_{\nu\lambda}\right)\end{aligned} \tag{1.4.2}$$

while the variation of the extrinsic curvature reads[3]

$$\delta K = \frac{1}{2}K_{\mu\nu}\delta h^{\mu\nu} - \frac{1}{2}n^{\mu}\left(\nabla^{\nu}\delta g_{\mu\nu} - g^{\nu\lambda}\nabla_{\mu}\delta g_{\nu\lambda}\right) + \mathcal{D}_{\mu}c^{\mu} \tag{1.4.3}$$

where $\mathcal{D}_{\mu}$ is the covariant derivative with respect $h_{\mu\nu}$ and $c^{\mu} = -1/2h^{\mu\lambda}n^{\nu}\delta g_{\nu\lambda}$. We observe that the second term of (1.4.2) is cancelled against the second one in (1.4.3). Thus, the total variation becomes

$$\begin{aligned}\delta\mathcal{I} =& \frac{1}{16\pi G_{\mathrm{N}}} \int_{\mathcal{G}_{d+2}} \sqrt{-g}\left(R_{\mu\nu} - \frac{1}{2}g_{\mu\nu} + \Lambda g_{\mu\nu}\right)\delta g^{\mu\nu} \\ &+ \frac{1}{8\pi G_{\mathrm{N}}} \int_{\partial\mathcal{G}_{d+2}} \sqrt{-h}\left[\frac{1}{2}\left(K_{\mu\nu} - h_{\mu\nu}K\right)\delta h^{\mu\nu} + \mathcal{D}_{\mu}c^{\mu}\right] + \delta I_{\mathcal{Q}}.\end{aligned} \tag{1.4.4}$$

The first line of (1.4.4) gives the well-known Einstein equations in the presence of the cosmological constant Λ, while the second line is the boundary term that sets the boundary conditions. The boundary of $\mathcal{G}_{d+2}$ is made of two components $\mathcal{M}_{d+1}$ and $\mathcal{Q}$: on the former component, we impose the Dirichlet boundary conditions $\delta h_{\mu\nu} = 0$ as usual, while on the

---

[3] A nice compendium of useful formulas can be found in http://jacobi.luc.edu/notes.html.

latter one $\mathcal{Q}$ we impose the Neumann boundary conditions. In particular, the equations that describe the spacetime are

$$R_{\mu\nu} - \frac{1}{2} g_{\mu\nu} + \Lambda g_{\mu\nu} = 0 \tag{1.4.5}$$

$$K_{\mu\nu} - h_{\mu\nu} K = 8\pi G_N T^{\mathcal{Q}}_{\mu\nu}\big|_{\mathcal{Q}} \tag{1.4.6}$$

where $T^{\mathcal{Q}}_{\mu\nu} = 2/\sqrt{-h}\,\delta\mathcal{I}_{\mathcal{Q}}/\delta h^{\mu\nu}$.

In the following we focus on the simplest case where $\mathcal{I}_{\mathcal{Q}}$ in (1.4.1) is given by

$$\mathcal{I}_{\mathcal{Q}} = -\frac{T}{8\pi G_{\mathrm{N}}} \int_{\mathcal{Q}} \sqrt{-h} \tag{1.4.7}$$

being T a constant real parameter characterising the hypersurface $\mathcal{Q}$. Furthermore, we will consider only on static backgrounds.

1.4.1 Vacuum state on the half-space

In this subsection we discuss the simplest case of $\mathrm{AdS}_{d+2}/\mathrm{BCFT}_{d+1}$ duality, namely when the BCFT_{d+1} is in its ground state and the boundary $\partial\mathcal{M}_{d+1}$ is a flat $d-$dimensional hyperplane. Under these hypothesis, the equations (1.4.5) with (1.4.7) can be solved exactly [89, 90]. We introduce the Cartesian coordinates $(t, x, \vec{y}\,)$ in the $(d+1)-$dimensional Minkowski spacetime such that the BCFT_{d+1} is defined in $x \geqslant 0$, and its boundary corresponds to $x = 0$. In this simple case the spacetime is completely determined by the trace of (1.4.6) $K = (d+1)/dT$. In [89], by solving this equation, the author found that the gravitational spacetime $\mathcal{G}_{d+2}$ dual to the ground state of the BCFT_{d+1} is AdS_{d+2}, whose metric in Poincaré coordinates reads

$$ds^2 = \frac{R^2_{\mathrm{AdS}}}{z^2}\Big(-dt^2 + dz^2 + dx^2 + d\vec{y}^{\,2}\Big) \qquad z > 0 \tag{1.4.8}$$

restricted by the half-hyperplane $\mathcal{Q}$ given by[4]

$$\mathcal{Q}: \quad x = -(\cot\alpha)\, z \qquad \alpha \in (0,\pi). \tag{1.4.9}$$

Notice that the boundary of $\mathcal{Q}$ at $z = 0$ coincides with the boundary of the BCFT_{d+1}, which is the hyperplane $\{x = 0, z = 0\}$. On the left side of Fig. 1.9 a cartoon of the spacetime is depicted. In (1.4.9), the slope $\alpha \in (0,\pi)$ of the half-hyperplane $\mathcal{Q}$ is related to the parameter T in (1.4.7) as $T = (d/R_{\mathrm{AdS}})\cos\alpha$, and as it will be argued in the following it can be interpreted as the *dual of the boundary conditions* of the BCFT_{d+1}.

1.4.2 Vacuum state on the ball

The second setup that we will consider in this thesis is the BCFT_{d+1} defined on a ball of radius $R_{\mathcal{Q}}$. To discuss this setup we find it useful to switch to the Euclidean time $\tau = it$. The gravitational spacetime of this case can be obtained by performing a suitable reparametrization [246], which maps the hyperplane $x = 0$ at $z = 0$ into the ball of radius $R_{\mathcal{Q}}$ described

---

[4] Comparing our notation with the one adopted in [89, 90], we have $\tan\alpha = 1/\sinh(\rho_*/R_{\mathrm{AdS}})$, being $\rho_* \in \mathbb{R}$.

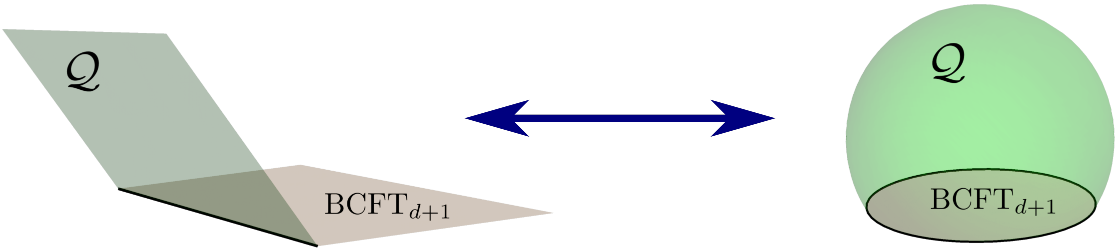

Figure 1.9: Cartoons of the holographic duals of BCFT_{d+1} with flat boundary (left) and spherical boundary (right). The two cases are related by a conformal transformation and the boundaries $\mathcal{Q}$ are given by equations (1.4.9) and (1.4.10), respectively.

by $\tau^2 + \vec{y}^2 + x^2 = R_{\mathcal{Q}}$. This transformation is discussed in detail in Appendix A.1 for the two-dimensional case, and it will be employ also in chapter 2. After the transformation the AdS metric (1.4.8) remains unchanged but the boundary $\mathcal{Q}$ (1.4.9) becomes the spherical cup [90]

$$\mathcal{Q}\ :\quad \tau^2 + \vec{y}^2 + (z - R_{\mathcal{Q}} \cot\alpha)^2 = R_{\mathcal{Q}}^2 \csc^2\alpha \qquad \alpha \in (0, \pi) \tag{1.4.10}$$

which ends on the hypersphere $\tau^2 + \vec{y}^2 + x^2 = R_{\mathcal{Q}}$, see the right side of Fig. 1.9. In order to exploit the symmetry of the system, we introduce the spherical coordinates in $(d+2)-$dimensions. The metric of the space-time reads $ds^2 = (dz^2 + d\rho^2 + \rho^2 d\Omega_d^2)$, where $d\Omega_d^2$ is the volume element of the $d-$dimensional hypersphere and $\rho \in [0, R_{\mathcal{Q}}]$ is the radial coordinate. Now, $\mathcal{Q}$ is described by

$$\rho_{\mathcal{Q}}(z) = \sqrt{(R_{\mathcal{Q}}\ \csc\alpha)^2 - (z - R_{\mathcal{Q}} \cot\alpha)^2}, \tag{1.4.11}$$

which corresponds to a spherical cap $\mathcal{Q}$ centered in $(\rho, z) = (0, R_{\mathcal{Q}} \cot\alpha)$ with radius $R_{\mathcal{Q}}/\sin\alpha$ (see the green surface in the left panel of Fig. 1.9). When $\alpha = \pi/2$, this spherical cap becomes the hemisphere $\rho^2 + z^2 = R_{\mathcal{Q}}^2$. By introducing the angular coordinate θ as $\tan\theta = z/\rho$, from (1.4.11) we find that the coordinates of a point of $\mathcal{Q}$ are $(\rho, z) = R_{\mathcal{Q}}\big(Q_\alpha(\theta), Q_\alpha(\theta)\tan\theta\big)$ with

$$Q_\alpha(\theta)\ \equiv\ \cos\theta \left(\cot\alpha\ \sin\theta + \sqrt{1 + (\cot\alpha\ \sin\theta)^2}\ \right) = \frac{\sqrt{\zeta^2 + (\sin\alpha)^2} + \zeta\cos\alpha}{(\zeta^2+1)\sin\alpha} \tag{1.4.12}$$

where in the last step we have introduced $\zeta \equiv \tan\theta$, that will be employed also in Sec. 2.3.1.

In the following, we will focus on the BCFT_3 $(d = 2)$, which is the case of our interest. We find it instructive computing the partition function on the ball, which can be easily found by evaluating the gravitational action (1.4.1) on the solution (1.4.8) restricted on the part of spacetime bounded by the boundary (1.4.11). After the introduction of the cutoff $z = \varepsilon$, we find

$$\begin{aligned}\mathcal{I}_E &= \frac{R_{\mathrm{AdS}}^2}{2G_N} \int_\varepsilon^{R_{\mathcal{Q}}\cot\frac{\alpha}{2}} \frac{\rho_{\mathcal{Q}}^3(z)}{z^4}\, dz - \frac{R_{\mathrm{AdS}}^2}{2G_N}\cos\alpha \int_\varepsilon^{R_{\mathcal{Q}}\cot\frac{\alpha}{2}} \frac{\sqrt{1+\rho_{\mathcal{Q}}'^2(z)}}{z^3}\rho_{\mathcal{Q}}^2(z)\, dz \\ &= \frac{R_{\mathrm{AdS}}^2}{2G_N}\left[\frac{R_{\mathcal{Q}}^3}{3\varepsilon^3} + \frac{R_{\mathcal{Q}}^2\cot\alpha}{\varepsilon^2} + \frac{R_{\mathcal{Q}}(\cot^2\alpha - 3)}{2\varepsilon} - \cot\alpha\log\left(\frac{R_{\mathcal{Q}}}{\varepsilon}\right) + f_\alpha\right]\end{aligned} \tag{1.4.13}$$

where f_α is the finite parte of the action which reads

$$f_\alpha = (\pi - \alpha) - \cot\alpha \left[\frac{3}{2} + \frac{\cot^2\alpha}{6} + \log(2\sin\alpha)\right]. \qquad (1.4.14)$$

The first integral in (1.4.13) comes from the bulk contribution to the action (1.4.1), while the second one from the boundary terms. The polynomial divergences in (1.4.13) can be removed by suitable counterterms, while the logarithmic divergence encodes the conformal anomaly. In particular, the trace of the stress-energy tensor can be obtained by taking the variation of the action under the Weyl rescaling $\delta g_{\mu\nu} = \delta R_{\mathcal{Q}} g_{\mu\nu}/R_{\mathcal{Q}}$. We find

$$\int \langle T^\mu_\mu \rangle = -R_{\mathcal{Q}} \frac{\partial \mathcal{I}_E}{\partial R_{\mathcal{Q}}} = \frac{R^2_{\text{AdS}}}{2G_N} \cot\alpha. \qquad (1.4.15)$$

By comparing (1.4.15) with equation (1.2.10) and by using $\mathcal{R} = 2/R_{\mathcal{Q}}$ for a sphere, we get the central charge $\mathfrak{a}$ [90]

$$\mathfrak{a} = -\frac{R^2_{\text{AdS}}}{4G_N} \cot\alpha. \qquad (1.4.16)$$

We notice that the charge $\mathfrak{q}$ does not appear in the boundary anomaly of the ball because $\kappa_{\mu\nu} = 0$.

We discussed in Sec. 1.2 that the charge $\mathfrak{a}$ is a measure of the boundary degrees of freedom of the theory. This fact suggests to interpret the holographic parameter α, or equivalently the tension T, as the dual of the boundary conditions of the BCFT$_3$. We will see in the next section how this parameter is related to the boundary entropy in the AdS$_3$/BCFT$_2$ setup.

We conclude this section mentioning other recent proposals of AdS/BCFT [158–161]. In those proposals, the boundary condition (1.4.6) is replaced by its trace $K = (d+1)/dT$. This condition is less restrictive than (1.4.6), and it admits in general more solutions. While for the flat and spherical boundaries, both kinds of the boundary conditions are satisfied by the solutions presented above, for a generic curved boundary the condition (1.4.6) induces a back-reaction on the metric. In particular, in the Takayanagi proposal [89] the solution for generic boundary will not be simply the AdS spacetime bounded by $\mathcal{Q}$, but a more complicate asymptotically AdS spacetime. In contrast, employing just the trace of (1.4.6) leads to a single equation that can be solved keeping the bulk metric pure AdS. The two proposals give, in general, different results. For instance, since the charge $\mathfrak{q}$ and the coefficient A_T require $\kappa_{\mu\nu} \neq 0$ to be uncovered, their value differs between the proposals, while the value of $\mathfrak{a}$ is the same. In the Takayanagi setup, generic boundaries have been studied by using the perturbation theory about the flat case [91]. We stress that our results on the entanglement entropy discussed in chapter 2 and the corner function derived in chapter 3 do not depend on the choice of the prescription. On the other hand, as it will be discussed in detail in chapter 3, the relation between the corner function and the one-point function of the stress-energy tensor observed in 3.4 is valid only in the Takayanagi's setup, since it also depends on A_T.

1.4.3 Holographic entanglement entropy in AdS/BCFT

In this section we discuss the holographic entanglement entropy in the AdS$_{d+2}$/BCFT$_{d+1}$ setup introduced in Sec. 1.4.

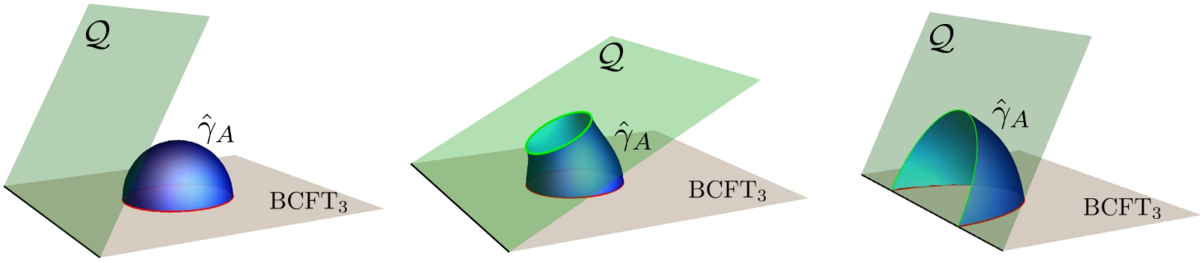

Figure 1.10: Left: When the domain A is sufficiently far from the boundary, the minimal surface $\hat{\gamma}_A$ is disconnected from $\mathcal{Q}$. Middle: When A is close to the boundary, a transition between extremal surfaces occurs, and the global minimum is represented by the surface which intersects $\mathcal{Q}$. Right: Case of entangling regions that intersect the boundary, the minimal surface is always connected to $\mathcal{Q}$.

Given a $(d+1)-$dimensional region A in the spatial slice $t=0$ of the BCFT$_{d+1}$[5], the corresponding holographic entanglement entropy is also given in this case by the formula (1.3.2), where the minimal area surface $\hat{\gamma}_A$ is anchored to the entangling surface $\partial A \cap \partial B$. However, in this case, the extremal area surfaces may also end on the spacetime boundary $\mathcal{Q}$, i.e., $\hat{\gamma}_A \cap \mathcal{Q} \neq 0$. Whenever $\hat{\gamma}_A \cap \mathcal{Q}$ is a non-trivial submanifold, since we do not impose any restriction on the intersection between $\hat{\gamma}_A$ and $\mathcal{Q}$, it is not difficult to show that $\hat{\gamma}_A$ intersects $\mathcal{Q}$ orthogonally along $\hat{\gamma}_A \cap \mathcal{Q}$, i.e., $\hat{\gamma}_A \perp \mathcal{Q}$.

In Fig. 1.10, we show two possible cases of minimal surface anchored to a disk in the spatial slice of BCFT$_3$. On the left, the minimal surface is disconnected from $\mathcal{Q}$ while in the middle part the submanifold $\hat{\gamma}_A \cap \mathcal{Q}$ is non-trivial. In general, whether $\hat{\gamma}_A$ intersects $\mathcal{Q}$ or not depends both on the entangling region A and the parameter α. In particular, when the spacetime is given by (1.4.8) subjected to the constraint (1.4.9) or (1.4.10), the disconnected case gives the same value of the entanglement entropy of the vacuum case without boundary, while the connected one is affected by the presence of the boundary.

As it will be discussed in details in Sec. 2.2 and 2.3 employing specific entangling regions in AdS$_4$/BCFT$_3$, when we change the distance of the region from the boundary keeping α fixed, a transition between the connected and the disconnected case occurs at a finite distance from the boundary. The simplest case in which such transitions happen is the single interval in AdS$_3$/BCFT$_2$ setup, and it will be discussed at the end of this subsection. This kind of transitions are analogous to the transitions discussed in Sec. 1.3.1. Transitions also occur if the region is kept fixed but α is changed toward smaller values. In particular, we will show in chapter 2 that for $d>1$ it exists a *critical value* of α denoted with α_{crit} below which any minimal surface (independently of the distance from the boundary) is disconnected from $\mathcal{Q}$.

On the right side of Fig. 1.10 we show the case in which the region A intersects the boundary. When $d=2$ as in the figure, the intersection is made of isolated points and the entangling curve creates corners with the spatial boundary of the BCFT$_3$. The case of

---

[5] With a slight abuse of notation, in the following we will denote in the same way $\mathcal{Q}$ and its spatial section.

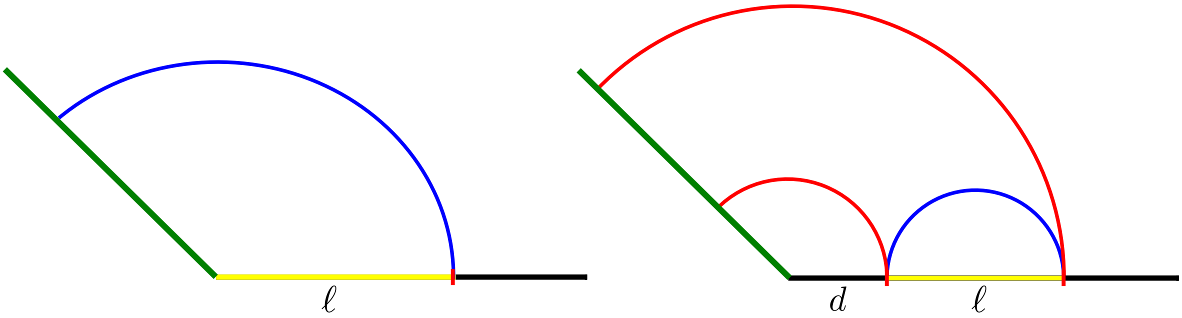

Figure 1.11: Left: Single interval of length ℓ adjacent to the boundary in $\mathrm{AdS}_3/\mathrm{BCFT}_2$. The minimal surface is the blue geodesics, which in Cartesian coordinates is part of the semicircle of radius ℓ centered on the spatial section of the boundary of the BCFT_2. Right: Single interval disjoint from the boundary. When $d/\ell < (d/\ell)_{\mathrm{crit}}$, the minimal surface is the one made by the two disconnected red geodesics. When $d/\ell > (d/\ell)_{\mathrm{crit}}$, the minimal surface is the blue connected geodesic.

entangling curves that intersect the boundary will be studied in detail in chapter 3. We will see that the corners give rise to an additional logarithmic divergence in agreement with the general discussion done in Sec. 1.2.2, whose coefficient depends on the slope α. When the entangling surface intersects the boundary, $\hat{\gamma}_A \cap \mathcal{Q} \neq 0$ for any value of α (also for $\alpha \leqslant \alpha_c$). However, we will show that α_c shows up in the behaviour of the boundary corner function in the limit of vanishing opening angle, namely for $\alpha > \alpha_c$ the function has a pole in that limit, while tends to a finite value for $\alpha \leqslant \alpha_c$.

We conclude this section by discussing two examples in the $\mathrm{AdS}_3/\mathrm{BCFT}_2$ setup: the single interval adjacent to the boundary and the one disjoint from it.

HEE in $\mathrm{AdS}_3/\mathrm{BCFT}_2$: Single interval in the vacuum

In the spatial slice $t = 0$, we consider the flat boundary case of Sec. 1.4.1 where the region A is an interval adjacent to the boundary of length ℓ. We saw in Sec. 1.3.1 that the minimal surfaces anchored to intervals in $\mathrm{AdS}_3/\mathrm{CFT}_2$ are semi-circles. Since the semi-circles of radius ℓ anchored to the end of the interval located at $(z, x) = (0, \ell)$ are orthogonal to the boundary $\mathcal{Q}$ (which is a straight line with slope parametrised by α) they are the minimal surfaces also for this case once we restrict them to the part of space-time $x \geq -(\cot\alpha)$ (see left side of Fig. 1.11). Thus, the entanglement entropy for this case is given by the following integral

$$S_A = \frac{c}{6}\int_{\sin^{-1}(\varepsilon/\ell)}^{\pi-\alpha} \frac{d\theta}{\sin\theta} = \frac{c}{6}\log\left(\frac{2\ell}{\epsilon}\right) + \frac{c}{6}\log\left[\cot\left(\frac{\alpha}{2}\right)\right] + \mathcal{O}\left(\varepsilon^2\right). \tag{1.4.17}$$

We notice that the factor of $c/6$ instead of $c/3$ comes from the fact that the geodesics reach the conformal boundary only at $(z, x) = (0, \ell)$, and this is in agreement with the BCFT result of [23] (see eq. (1.2.11)). Moreover, from (1.4.17) we can extract the boundary entropy which reads [90]

$$\log g_\alpha = \frac{c}{6}\log\left[2\cot\left(\frac{\alpha}{2}\right)\right]. \tag{1.4.18}$$

In [90], the same value of the boundary entropy has also been found from the computation of the partition function, analogously to the one discussed in the previous section. This match provides a non-trivial check of the AdS/BCFT correspondence, and it enforces the interpretation of α as the dual of the boundary conditions.

For an interval of length ℓ disjoint from the boundary, a transition analogous to the one studied in Sec. 1.3.1 occurs. On the right side of Fig. 1.11, the two competing extremal surfaces are depicted. The area of the disconnected case has been found in eq. (1.3.4) while the connected one can be easily computed from the result (1.4.17). One obtains

$$S_{\text{red}} = \frac{c}{3} \log\left(\frac{\ell}{\varepsilon}\right) + \frac{c}{6} \log\left[\frac{4d(\ell+d)}{\ell^2} \cot^2\left(\frac{\alpha}{2}\right)\right] + \mathcal{O}\left(\varepsilon^2\right) \tag{1.4.19}$$

$$S_{\text{blue}} = \frac{c}{3} \log\left(\frac{\ell}{\varepsilon}\right) + \mathcal{O}\left(\varepsilon^2\right). \tag{1.4.20}$$

Thus, we find the transition between the two different extremal surfaces at

$$\left(\frac{d}{\ell}\right)_{\text{crit}} = \frac{\sec\left(\frac{\alpha}{2}\right) - 1}{2}. \tag{1.4.21}$$

We note that the critical distance depends on the slope α and, in particular, when $\alpha = \pi/2$ we recover the critical distance of the disjoint interval case studied in Sec. 1.3.1 (once we apply the substitution $d \to d/2$).

1.5 Holographic theories with Lifshitz scaling and hyperscaling violation

In Sec. 1.3, we discussed the AdS/CFT correspondence as an example of holographic duality. In that case, the gravitational theory is dual to a relativistic field theory which possesses superconformal invariance. Furthermore, we mentioned that, when the gravitational theory is in the classical regime, the field theory is strongly coupled. It turns out that the strong/weak characteristic of the holographic duality is very useful for various applications to physical systems that cannot be described through perturbation theory. On the other hand, many physical systems of interest may be not supersymmetric or may possess intrinsic length scales like massive excitations. Even though in those cases exact gravity duals have not been discovered yet, many features of those systems can be realised within the gauge/gravity dualities. Examples are the AdS/QCD dualities where gravitational theories are employed to study the low-energy characteristic of the QCD, and the fluid/gravity correspondence whose aim is to study strongly-coupled relativistic fluids like the quark-gluon plasma. Another branch of the gauge/gravity duality is AdS/CMT, which studies gravitational theories able to mimic condensed matter systems like superfluid, superconductor and, more in general, systems that undergo to *quantum phase transitions*.

In this section, after a very brief discussion of quantum phase transitions, we are going to introduce the gravitational theories that are supposed to describe field theories with anisotropic Lifshitz scaling and theories displaying a violation of the hyperscaling relations. Furthermore, we will see that specific cases of those metrics present violation of the area law of entanglement entropy compatible with systems with a Fermi surface [140, 141].

Let us begin introducing the concept of quantum phase transition. Consider a quantum system described by a Hamiltonian $H(g)$ that depends on a dimensionless coupling g, and with ground state energy $E_0(g)$. A quantum critical point is a point g_c in the phase diagram in which a non-analyticity of $E_0(g)$ occurs. This non-analyticity highlights a level-crossing between the ground state and the first excited state. If there is an energy gap Δ, it vanishes at g_c as

$$\Delta \sim |g - g_c|^{\zeta\nu}. \tag{1.5.1}$$

In a second-order quantum phase transition, the characteristic length scale ξ diverges. About the critical point, its behaviour is given by

$$\xi \sim |g - g_c|^{-\nu} \qquad \Delta \sim \xi^{-\zeta}. \tag{1.5.2}$$

ζ and ν are the critical exponents and they are universal, being independent of most of the microscopic details of the systems. We note that this kind of phase transitions occurs at $T = 0$. At the critical point, the effective theory is scale-invariant. Nonetheless, an important observation is that the energy Δ and the correlation length ξ are not in general inversely related. The exponent ζ is called the *dynamical critical exponent*, and characterizes the scaling of the theory. In particular, when $\zeta = 1$ the effective theory is relativistic, while for $\zeta \neq 1$ the scaling is not relativistic. Systems that display this behaviour have been extensively studied in condensed matter [113–117], and the entanglement entropy in these theories has been considered in [181, 253–258].

1.5.1 Theories with anisotropic Lifshitz scaling

An example of effective field theories that display a non-relativistic scaling is the *Lifshitz field theory*, invariant under the following anisotropic scale

$$t \to \lambda^{\zeta} t \qquad y_i \to \lambda y_i \tag{1.5.3}$$

and where the dynamical exponent ζ fixes the dispersion relation $\omega \sim k^{\zeta}$. Scaling arguments imply that the thermal entropy density as a function of the temperature T scales as

$$s(T) \sim T^{\frac{d}{\zeta}}. \tag{1.5.4}$$

The simplest theory with an anisotropic scaling is the *Lifshitz field theory* with $\zeta = 2$

$$\mathcal{I} = \int dx^2 dt \left[(\partial_t \varphi)^2 - g(\nabla^2 \varphi)^2\right] \tag{1.5.5}$$

that has a line of critical points parametrised by the coupling g, and that it describes the critical behavior of various strongly coupled electron systems. For instance, the effective theory (1.5.5) arises in the description of certain liquid crystals [259], and quantum dimers [117]. We mention that $\zeta = 2$ is a special case since it allows for a non-relativistic conformal algebra called *Schroedinger algebra*. An interesting fact is that the non-relativistic conformal algebra is not able to fix completely the form of the two-point function, which can depend on the ratio $|\vec{y} - \vec{y}'|^2/(t - t')$.

The holographic spacetimes compatible with the scaling (1.5.3) have been found as solutions of the Einstein equations coupled to some appropriate matter [119, 121], and successively from string theory in [123, 260, 261] (see also [121] for related discussions). The metric compatible with the scaling property (1.5.3) has the form

$$ds^2 = \frac{1}{z^2}\left(-z^{2(1-\zeta)}dt^2 + d\vec{y}^2 + dz^2\right) \tag{1.5.6}$$

where we set for simplicity $R_{\text{AdS}} = 1$, and which reduces to the AdS metric for $\zeta = 1$. We notice that the line element (1.5.6) is invariant under the scale transformation

$$t \to \lambda^{\zeta} t \qquad y_i \to \lambda y_i \qquad z \to \lambda z. \tag{1.5.7}$$

Furthermore, this metric is non-singular everywhere, and its Ricci scalar is $\mathcal{R} = -2(\zeta^2+2\zeta+3)$.

As for the holographic entanglement entropy of this case, we observe that once we fix a constant time-slice of the metric (1.5.6), the background does not depend on the dynamical exponent ζ. As a consequence, the holographic entanglement entropy is the same as in AdS/CFT. The situation is different for the finite-temperature case. In fact, as we will see in chapter 4, the black hole metric depends on ζ through the blackening function. In particular, in Sec. 4.4.2 we will study the holographic entanglement entropy of a disk in the metric (1.5.6) for $d = 2$ (we anticipate that in Fig. 4.4 we show cases with different ζ). In addition, an analytic result in the limit $\zeta \to +\infty$ will be discussed.

1.5.2 Holographic theories with hyperscaling violation

Besides metric backgrounds with the Lifshitz exponent, it is possible to engineer a more general family of metrics parametrised by an additional parameter θ, called *hyperscaling violation exponent*. This kind of metrics, which we call asymptotic hivLif$_{d+2}$, emerges as a solution to the Einstein equations when both a dilaton and an abelian gauge field are introduced in the bulk. They have the asymptotic form [122]

$$ds^2 = \frac{1}{z^{2(d-\theta)/d}}\left(-z^{2(1-\zeta)}dt^2 + d\vec{y}^2 + dz^2\right). \tag{1.5.8}$$

We note that, in contrast to the metrics (1.5.6), the hivLif$_{d+2}$ metrics are not scale invariant since under the transformation 1.5.7 they scale as

$$ds^2 \to \lambda^{2\theta/d} ds^2. \tag{1.5.9}$$

In order to deal only with geometries admitting physically sensible dual field theories, the allowed values of the parameters in (1.5.8) must satisfy some constraints on the energy-momentum tensor computed via the Einstein equations $G_{MN} - \Lambda g_{MN} = T_{MN}$. In particular the Null Energy Condition (NEC)[6] is required, namely $T_{MN}V^M V^N \geqslant 0$ for any (future directed) null vector V^M. The NEC translates into the following constraints for θ and ζ [126]

$$\begin{cases} (d+\zeta-\theta)(\zeta-1) \geqslant 0 \\ (d-\theta)(d(\zeta-1)-\theta) \geqslant 0\,. \end{cases} \tag{1.5.10}$$

---

[6] The NEC is insensible to the cosmological constant; indeed for a null vector $G_{MN}V^M V^N = T_{MN}V^M V^N$.

We refer to Appendix C.1 for a detailed discussion of the NEC and its consequences in $d = 2$, which is the case we will explore in chapter 4. Further studies have been done in [123–126].

The metric (1.5.8) represents a candidate for the holographic description of theories that show a violation of hyperscaling [118]. When hyperscaling holds, the free energy scales as a function of the temperature by its naive dimensions. In particular, the thermal entropy density scales as $S \sim T^{d/\zeta}$. In order to show that θ actually drives the hyperscaling violation, we need to consider the finite temperature case described by the black hole metric

$$ds^2 = \frac{1}{z^{2(d-\theta)/d}}\left(-z^{2(1-\zeta)}f(z)dt^2 + d\vec{y}^2 + \frac{dz^2}{f(z)}\right) \qquad f(z) = 1 - \left(\frac{z}{z_h}\right)^{d+\zeta-\theta} \tag{1.5.11}$$

where z_h determines the location of the horizon. Notice that the metric (1.5.11) has the asymptotic form of (1.5.8). The temperature and the area of the black hole can be easily computed and are related to z_h by [126]

$$T = \frac{1}{4\pi}\frac{|d+\zeta-\theta|}{z_h^{\zeta}} \qquad\qquad \mathcal{A} = \frac{L^d}{z_h^{d-\theta}} \tag{1.5.12}$$

where we have introduced the infra-red cutoff L. Combining the two relations (1.5.12) to remove z_h and employing the Bekenstein-Hawking formula for the entropy of black holes, for the thermal density entropy $s(T)$ of the system we find the following scaling

$$s(T) \sim T^{(d-\theta)/\zeta} \tag{1.5.13}$$

which legitimises θ to be called the hyperscaling violation exponent. In particular, we observe that θ has the effect of modifying the effective dimension of the theory. In condensed matter physics, the hyperscaling violation has been studied for the first time by Fisher in [118]. Generically, they are gapless systems that do not possess conformal symmetries.

Now we discuss briefly the entanglement entropy in systems dual to the metric (1.5.11). The simplest region we can employ is the strip $A = \left\{\mathbb{R}^d : |x| \leqslant \ell/2, |y_i| \leqslant L/2 \; i = 1, \dots, d-1\right\}$ in the limit of $\ell \ll L$. By following [126], we consider the hvLif$_{d+2}$ gravitational background (1.5.8). In the regime $\ell \ll L$ the area functional evaluated on the surfaces γ_A characterised by the profile $z = z(x)$ reads

$$\mathcal{A}[\gamma_A] = L^{d-1}\int_{-\ell/2}^{\ell/2} \frac{\sqrt{1+(z')^2}}{z^{d-\theta}}\, dx\,. \tag{1.5.14}$$

Since the coordinate y_1 is cyclic, its conjugate momentum is conserved, namely

$$\frac{d}{dx}\left(\frac{1}{z^{d-\theta}}\frac{1}{\sqrt{1+(z')^2}}\right) = 0 \qquad \Longrightarrow \qquad \frac{1}{z^{d-\theta}\sqrt{1+(z')^2}} = \frac{1}{z_*^{d-\theta}} \tag{1.5.15}$$

where in the integration we have denoted by $z_* \equiv z(0)$ the value of the function $z(x)$ corresponding to the tip of the surface, where $z'(0) = 0$. The parameter z_* can also be expressed in terms of the width of the strip ℓ as follows

$$\frac{\ell}{2} = \int_0^{z_*}\frac{dz}{z'} = \int_0^{z_*}\frac{dz}{\sqrt{\left(z_*/z\right)^{2(d-\theta)} - 1}} = \frac{\sqrt{\pi}\,\Gamma\left(\frac{1}{2}+\frac{1}{2(d-\theta)}\right)}{\Gamma\left(\frac{1}{2(d-\theta)}\right)}\, z_*\,. \tag{1.5.16}$$

By integrating the conservation law (1.5.15), for the profile $x(z)$ one finds

$$x(z) = \frac{\ell}{2} - \frac{z_*}{d-\theta+1}\left(\frac{z}{z_*}\right)^{d-\theta+1} {}_2F_1\left(\frac{1}{2}\,,\frac{1}{2}+\frac{1}{2(d-\theta)}\,;\frac{3}{2}+\frac{1}{2(d-\theta)}\,;(z/z_*)^{2(d-\theta)}\right). \quad (1.5.17)$$

Introducing the usual cutoff $z \geqslant \varepsilon$, the area corresponding to the profile (1.5.17) can be easily computed by employing the conservation law (1.5.15)

$$\begin{aligned}\mathcal{A}[\hat{\gamma}_A] &= 2\frac{L^{d-1}}{z_*^{d-1-\theta}}\int_{\varepsilon/z_*}^{1}\frac{x^{-(d-\theta)}}{\sqrt{1-x^{2(d-\theta)}}}\,dx = \frac{2L^{d-1}}{d-\theta-1}\left[\frac{1}{\varepsilon^{d-1-\theta}} - \frac{\sqrt{\pi}\,\Gamma\left(\frac{d+1-\theta}{2(d-\theta)}\right)}{\Gamma\left(\frac{1}{2(d-\theta)}\right)}\frac{1}{z_*^{d-1-\theta}}\right] \\ &= \frac{2L^{d-1}}{d-\theta-1}\left[\frac{1}{\varepsilon^{d-1-\theta}} - \left(\frac{\sqrt{\pi}\,\Gamma\left(\frac{d+1-\theta}{2(d-\theta)}\right)}{\Gamma\left(\frac{1}{2(d-\theta)}\right)}\right)^{d-\theta}\left(\frac{2}{\ell}\right)^{d-1-\theta}\right], \qquad \theta < d-1\end{aligned} \quad (1.5.18)$$

where in the last step we employed (1.5.16). We notice that, since the asymptotic behaviour of (1.5.8) is different from the one of the AdS metric, the leading divergence got modified, and in particular it turns out to depend on θ. However, the scaling with respect to the size of the region follows the area law again. In chapter 4, we will study the divergences of the holographic entanglement entropy for generic shape for $d = 2$. We will find that all the divergent terms are completely fixed by the geodesic curvature of the entangling curve (see Sec. 4.1.1).

A very interesting case is when $\theta = d-1$. In fact, in this regime, the area law is violated by a logarithmic correction [125]. By performing the same integral as in (1.5.18), we find

$$\mathcal{A}[\hat{\gamma}_A] = 2L^{d-1}\log\left(\frac{\ell}{\varepsilon}\right) + \mathcal{O}(\varepsilon^2) \quad (1.5.19)$$

where we employed (1.5.16), which gives $\ell/2 = z_*$ in this case.

The violation of the area law has been found in weakly coupled fermionic systems [140, 141], and it is attributed to the presence of a Fermi surface. Hence, the hyperscaling violating metric (1.5.8) for $\theta = d-1$ is a good candidate to describe strongly coupled quantum systems with Fermi surfaces.

Chapter 4 is devoted to the study of holographic entanglement entropy in asymptotically hvLif$_4$ metrics. Besides the divergent structure of the area of the extremal surfaces in these backgrounds, we have found different ways to express the finite term in the expansion of the area as the cutoff ε vanishes. In particular, we will generalise the functional (1.3.22) valid for asymptotically AdS$_4$ metrics (see Sec. 4.1.2), and we will show that it is also possible to express the finite term as an integral over the boundary of the extremal surface when the metric is hvLif$_4$ (see Sec. 4.2). Finally, we will present numerical results for elliptic regions in both hvLif$_4$ (1.5.8), and in the presence of the black hole (1.5.11).

1.6 Numerical method: Surface Evolver

In this section, we will give details about the software we employed throughout this thesis to obtain the various numerical results. As anticipated in Sec. 1.3.3, our numerical analysis is based on *Surface Evolver*, a multipurpose optimisation software developed by Ken Brakke [152, 153]. This tool is employed here to find minimal-area surfaces embedded in three-dimensional spaces with AdS_4 or asymptotically hvLif_4 metrics on the constant time-slice $t = 0$. The constraints imposed on the minimal surfaces define the ones we are interested in.

In this thesis, we deal with two qualitatively different situations, depending on the occurrence of the boundary $\mathcal{Q}$ defined by (1.4.9) or (1.4.11). For the corner functions in $\mathrm{AdS}_4/\mathrm{CFT}_3$ discussed in Sec. 1.3.3 and the application to the chapter 4, where $\mathcal{Q}$ does not occur, we employed the standard prescription (1.3.2) for the holographic entanglement entropy. It requires to construct the minimal surface $\hat{\gamma}_A$ anchored to ∂A in the $z = 0$ plane. Instead, to compute the holographic entanglement entropy in $\mathrm{AdS}_4/\mathrm{BCFT}_3$ discussed in Sec. 1.4.3, the minimal area surface $\hat{\gamma}_A$ belongs to the region of $\mathbb{H}_3$ bounded by $\mathcal{Q}$ and may intersect it. Thus, while in the former case $\partial\hat{\gamma}_A = \partial A$, in the latter one $\partial\hat{\gamma}_A \subset \partial A$ and it can happen that $\partial\hat{\gamma}_A \cap \mathcal{Q} \neq \emptyset$. When $\partial\hat{\gamma}_A \cap \mathcal{Q} \neq \emptyset$, the minimisation procedure implemented by Surface Evolver leads to surfaces which are orthogonal to $\mathcal{Q}$ along $\hat{\gamma}_A \cap \mathcal{Q}$ in the final step of the evolution.

Surface Evolver constructs surfaces as unions of triangles; therefore, a smooth surface is approximated by a surface made by triangles obtained through a particular evolution. The initial step of the optimisation procedure is a very simple surface, made by a few triangles, which basically sets the topology. The initial surface evolves towards a configuration that is a local minimum of the area functional by both increasing the number of triangles and modifying the mesh in a proper way. For each step of the evolution, the software provides all the elements characterising the surface, like the coordinates of the vertices, the way to connect them, the normal vectors, the area of each triangle, the total number of triangles and the total area of the surface. We refer the interested reader also the appendix B of [245] for another discussion on the application of Surface Evolver to find minimal area surfaces in $\mathbb{H}_3$.

Since the area of a surface that reaches the boundary at $z = 0$ diverges, in our numerical analysis, we have defined the entangling curve $\partial A \cap \partial B$ (which coincides with ∂A for the domains considered in Sec. 1.3.3 to study the corner functions in $\mathrm{AdS}_4/\mathrm{CFT}_3$) at $z = \varepsilon$ and not at $z = 0$, as required in the prescription for the holographic entanglement entropy.

Once the final entangling curve $\partial A \cap \partial B$ has been fixed at $z = \varepsilon$, let us denote by $\gamma_\varepsilon^{\mathrm{SE}}$ the triangulated surface constructed by Surface Evolver at a generic step of the evolution and by $\tilde{\mathcal{A}}[\gamma_\varepsilon^{\mathrm{SE}}]$ the corresponding numerical value for its area provided by the software. We denote by $\tilde{\gamma}_\varepsilon^{\mathrm{SE}}$ the final configuration of the evolution and by $\tilde{\mathcal{A}}[\tilde{\gamma}_\varepsilon^{\mathrm{SE}}]$ the corresponding area given by Surface Evolver. The final step of the evolution depends on the required level of approximation. In our analysis the typical value of the UV cutoff is $\varepsilon = 0.03$, the area of the final surfaces is $O(10^2)$ (setting $R_{\mathrm{AdS}} = 1$) and we have stopped the evolution once the value of the area was stable up to small variations of order $O(10^{-2})$.

The evolution begins from a very simple trial surface, and it develops through some steps which improve the triangulation of the surface towards configurations with a smaller area. A way to improve the triangulation consists of moving the positions of the vertices without changing their total number according to a gradient descent method which decreases the total area of the surface. Another way is to refine the mesh of the surface by splitting each edge of a facet into two new edges and then connecting them. After a modification of this kind,

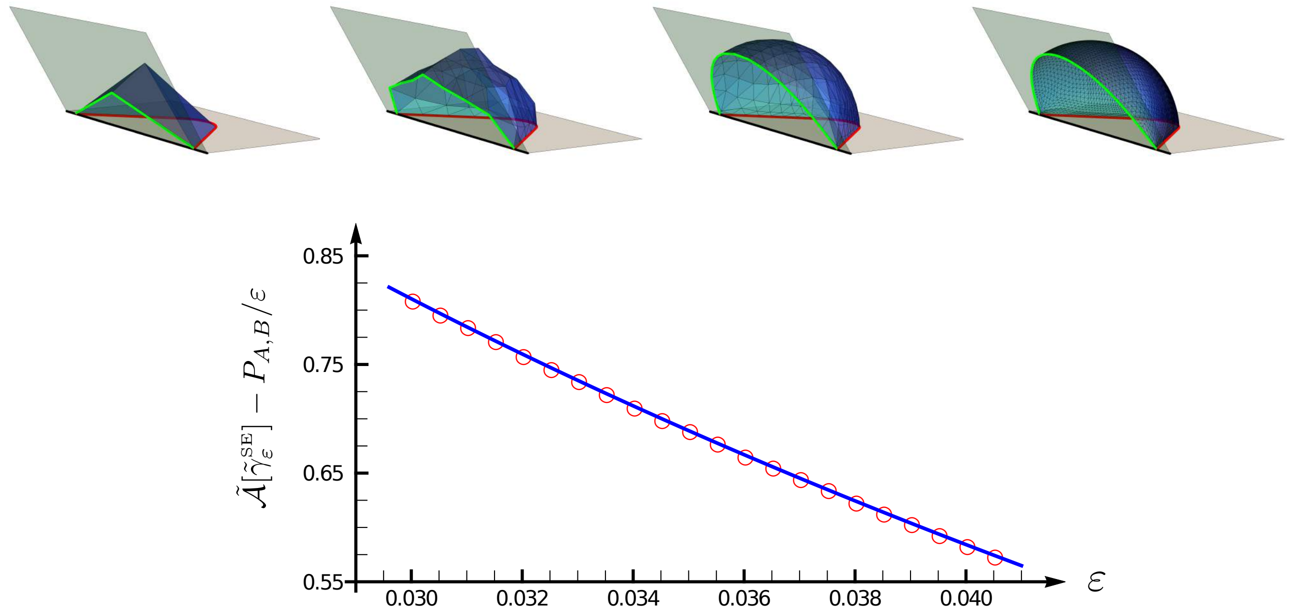

Figure 1.12: An example of the numerical analysis of the corner functions based on Surface Evolver. Top: Some stages of an evolution towards the minimal area surface anchored to the entangling curve given by the red line in the $z = 0$ half-plane, which has $\gamma = \pi/4$ and $L = 2.5$ (see also Fig. 3.6). Here $\alpha = \pi/3$. Bottom: Numerical data corresponding to the evolutions shown in the top panel for different values of ε. Fitting this data as discussed in Sec. 1.6, one finds the numerical value for the corner function to compare with the corresponding one obtained from the analytic expression $F_\alpha(\gamma)$ given by (3.2.7) and (3.2.12).

a facet is partitioned into four new facets; therefore, this step increases the total number of triangles.

The boundaries of the triangulated surfaces are treated differently during the evolution, depending on whether they belong to the half-plane $\mathcal{Q}$ or to the section of the spacetime given by $z = \varepsilon$ (for the surfaces studied in Sec. 1.3.3 only the latter situation occurs). The vertices on the entangling curve $\partial A \cap \partial B$ at $z = \varepsilon$ are kept fixed although their number increases during the refinements. Instead, the vertices of the curve $\partial\gamma_\varepsilon^{\mathrm{SE}} \cap \mathcal{Q}$ can move freely on $\mathcal{Q}$ during the evolution.

In the following as an example, we consider the case in which a region A intersects the boundary of the BCFT$_3$.

In the top part of Fig. 1.12 we show some steps of an evolution made by Surface Evolver towards the minimal area surface anchored to the entangling curve given by the red line in the $z = 0$ plane (see also Fig. 3.6). In this example $\partial\gamma_\varepsilon^{\mathrm{SE}} \cap \mathcal{Q} \neq \emptyset$. The initial step of the evolution is a trial surface made by six facets, while the last step shown in the figure is a triangulated surface with 6144 facets.

As anticipated in Sec. 1.4.3, when the region A intersects the boundary of the BCFT$_3$ a logarithmic divergence in the expansion of the area as $\varepsilon \to 0^+$ occurs. Here, we give details on the method we used in chapter 3 to extract its coefficient. Once the final step $\tilde{\gamma}_\varepsilon^{\mathrm{SE}}$ of the evolution corresponding to a given entangling curve at $z = \varepsilon$ is reached, one subtracts to $\tilde{\mathcal{A}}[\tilde{\gamma}_\varepsilon^{\text{SE}}]$ the area law term, which is given by either P_A/ε or $P_{A,B}/\varepsilon$. By repeating this analysis for various small values of ε, a list of numerical values is obtained. Fitting these data points through the function $a \log \varepsilon + b + c\,\varepsilon$, one finds the best fit for the parameters a, b and c. The value of a is the numerical result for the coefficient of the logarithmic divergence that we have compared against the corresponding theoretical prediction. In the bottom part of Fig. 1.12 we show an example of this procedure which corresponds to the domain A identified by the red curve in the top part of the same figure.

Chapter 2

Holographic entanglement entropy in AdS$_4$/BCFT$_3$ and the Willmore Functional

This chapter is devoted to the study of the shape dependence of entanglement entropy in holographic boundary conformal field theories in three dimensions. Throughout this chapter and the next one, we employ the setup proposed by Takayanagi in [89] that has been extensively discussed in Sec. 1.4 following the works [90, 91]. Even though this framework makes it possible to study also dynamical situations, we will focus for the sake of simplicity only on static spacetimes.

The strategy is to employ the holographic entanglement entropy formula (1.3.2) within the AdS/BCFT duality as described in Sec. 1.4.3. We remind that given a spatial region A in a Cauchy slice of the BCFT, the holographic entanglement entropy is determined by the minimal area hypersurface $\hat{\gamma}_A$ anchored to the entangling surface $\partial A \cap \partial B$. As discussed in Sec. 1.4.3, a peculiar feature of extremal hypersurfaces in the context of AdS/BCFT is that $\hat{\gamma}_A$ may intersect $\mathcal{Q}$. It is also important to remind that, since $\hat{\gamma}_A \cap \mathcal{Q}$ is not fixed, the extremization of the area functional leads to the condition that $\hat{\gamma}_A$ intersects $\mathcal{Q}$ orthogonally. In order to obtain a finite value for the area, we restrict the surface to the part $\hat{\gamma}_\varepsilon = \gamma_A \cap \{z \geqslant \varepsilon\}$, being ε the UV cutoff. The expansion of the area in terms of the cutoff ε gives

$$\mathcal{A}[\hat{\gamma}_\varepsilon] = \frac{P_{A,B}}{\varepsilon} - F_A + o(1). \tag{2.0.1}$$

This chapter aims to study the subleading term F_A of the holographic entanglement entropy (2.0.1) associated with spatial regions A having arbitrary shapes. Here, we will deal only with smooth entangling curves ∂A, which in particular do not intersect the boundary of the BCFT, postponing the case of singular entangling curves to chapter 3. In this case, F_A is finite and independent of the cutoff ε.

This chapter is organized as follows. In Sec. 2.1 we adapt the method employed in [76–78] for the holographic entanglement entropy in AdS$_4$/CFT$_3$ to the case with boundaries. This analysis leads to writing F_A as a functional evaluated on the surface $\hat{\gamma}_\varepsilon$ embedded in a three-dimensional Euclidean space with boundary which is asymptotically flat close to $z = 0$, generalising the functional (1.3.22). This result holds for any static gravitational background and any region, even when it is made by disjoint domains. Focusing on the simplest AdS$_4$/BCFT$_3$ setup, where the gravitational background is a part of $\mathbb{H}_3$ and the asymptotically flat space is a part of $\mathbb{R}^3$, in Sec. 2.1.1 we observe that the functional obtained for F_A becomes the Willmore functional [75] with a proper boundary term evaluated on the surface $\hat{\gamma}_\varepsilon$ embedded in $\mathbb{R}^3$. In the remaining part of the chapter, further simplifications are introduced by restricting to BCFT$_3$s whose spatial slice is either a half-plane (see Sec. 1.4.1) or a disk (see Sec. 1.4.2).

The analytic expression found for F_A is checked by considering some particular regions such that the corresponding F_A can be found analytically. In Sec. 2.2.1 we study the simplest configuration, namely the infinite strip parallel to a flat boundary (see also [158, 262]). Another interesting entangling region for which is possible to obtain analytic results is a disk disjoint from a boundary which is either flat or circular. In Sec. 2.3 we compute F_A analytically for these configurations and check the results against the numerical data obtained through Surface Evolver, the numerical tool introduced in Sec. 1.6. In Sec. 2.4 Surface Evolver is employed to find numerically F_A corresponding to some ellipses disjoint from a flat boundary.

In Appendix A.1 we report the mappings that are employed to study the disk disjoint from a flat boundary. Details on the derivation of the minimal surfaces anchored to the strips and the generalization to higher dimensions are collected in Appendix A.2. The Appendix A.3 contains the technical details for the derivation of the analytic results presented in Sec. 2.3 about a disk concentric to a circular boundary. In Appendix A.4 we further discuss the auxiliary surfaces corresponding to some extremal surfaces occurring in this chapter.

2.1 A formula for the finite term F_A

On the lines of [78], in the AdS$_4$/BCFT$_3$ setup described in Sec. 1.4, let us denote by $\mathcal{C}_3 \subset \mathcal{G}_4$ the three dimensional Riemannian space with metric $g_{\mu\nu}$ obtained by taking a constant time slice of the static asymptotically AdS$_4$ gravitational background. The boundary of $\mathcal{C}_3$ is the union of the conformal boundary, which is the constant time slice of the spacetime where the BCFT$_3$ is defined, and the surface $\mathcal{Q}$ delimiting the gravitational bulk.

Let us consider a two dimensional surface γ embedded into $\mathcal{C}_3$ whose boundary $\partial\gamma$ is made by either one or many disjoint closed curves. Denoting by n_μ the spacelike unit vector normal to γ, the metric induced on γ (first fundamental form) and the extrinsic curvature of γ (second fundamental form) are given respectively by

$$h_{\mu\nu} = g_{\mu\nu} - n_\mu n_\nu \qquad\qquad K_{\mu\nu} = h_\mu{}^\alpha h_\nu{}^\beta \, \nabla_\alpha n_\beta \tag{2.1.1}$$

where ∇_α is the torsionless covariant derivative compatible with $g_{\mu\nu}$. Furthermore, in the following, we will need the traceless part of the extrinsic curvature $\mathcal{K}_{\mu\nu} = K_{\mu\nu} - \frac{\mathrm{Tr}K}{2}\, h_{\mu\nu}$.

In our analysis $g_{\mu\nu}$ is conformally equivalent to the metric $\tilde{g}_{\mu\nu}$ corresponding to a Euclidean space $\widetilde{\mathcal{C}}_3$ which is asymptotically flat near the conformal boundary, namely

$$g_{\mu\nu} \,=\, e^{2\varphi}\, \tilde{g}_{\mu\nu} \tag{2.1.2}$$

where φ is a function of the coordinates. The two dimensional surface γ is also a submanifold of $\widetilde{\mathcal{C}}_3$. Denoting by $\tilde{n}_\mu$ the spacelike unit vector normal to $\gamma \subset \widetilde{\mathcal{C}}_3$, we have that $n_\mu = e^{\varphi}\, \tilde{n}_\mu$.

The fundamental forms in (2.1.1) can be written in terms of the fundamental forms $\tilde{h}_{\mu\nu}$ and $\widetilde{K}_{\mu\nu}$ characterising the embedding $\gamma \subset \widetilde{\mathcal{C}}_3$ as follows

$$h_{\mu\nu} \,=\, e^{2\varphi}\, \tilde{h}_{\mu\nu} \qquad\qquad K_{\mu\nu} = e^{\varphi}\big(\widetilde{K}_{\mu\nu} + \tilde{h}_{\mu\nu}\, \tilde{n}^{\lambda}\partial_{\lambda}\varphi\big). \tag{2.1.3}$$

A very useful identity we will employ in our analysis is the contracted Gauss-Codazzi relation [263]

$$\mathcal{R} - \big(\mathrm{Tr}K\big)^2 + \mathrm{Tr}K^2 = h^{\mu\rho}h^{\nu\sigma} \perp\! R_{\mu\nu\rho\sigma} \tag{2.1.4}$$

where $\mathcal{R}$ is the Ricci scalar, which provides the intrinsic curvature of γ, and $\perp R_{\mu\nu\rho\sigma} = h_{\mu}{}^{\alpha} h_{\nu}{}^{\beta} h_{\rho}{}^{\gamma} h_{\sigma}{}^{\lambda} R_{\alpha\beta\gamma\lambda}$ is the Riemann tensor of $g_{\mu\nu}$ projected on γ. Explicit contraction of the right-hand side of (2.1.4) gives

$$h^{\mu\rho}h^{\nu\sigma} \perp\! R_{\mu\nu\rho\sigma} = R - 2\, n^{\mu}n^{\nu} R_{\mu\nu} \,=\, -\,2\, n^{\mu}n^{\nu} G_{\mu\nu}\,, \tag{2.1.5}$$

where $G_{\mu\nu}$ is the Einstein tensor of $g_{\mu\nu}$.

The starting point is the following Weyl invariant quantity

$$\mathrm{Tr}\mathcal{K}^2\, d\mathcal{A} \,=\, \bigg(\mathrm{Tr}K^2 - \frac{1}{2}\big(\mathrm{Tr}K\big)^2\bigg)\, d\mathcal{A} \tag{2.1.6}$$

which holds because the area elements $d\mathcal{A} = \sqrt{h}\, d\Sigma$ of $\gamma \subset \mathcal{C}_3$ and $d\tilde{\mathcal{A}} = \sqrt{\tilde{h}}\, d\Sigma$ of $\gamma \subset \widetilde{\mathcal{C}}_3$ are related as $d\mathcal{A} = e^{2\varphi} d\tilde{\mathcal{A}}$, being $d\Sigma = d\sigma_1 d\sigma_2$, where σ_i are some local coordinates on γ.

By employing the Gauss-Codazzi relation (2.1.4), together with (2.1.5) to eliminate $\mathrm{Tr}K^2$ in (2.1.6), the Weyl invariance of the combination (2.1.6) can be rewritten as

$$\bigg(\frac{1}{2}\big(\mathrm{Tr}K\big)^2 - \mathcal{R} - 2\, n^{\mu}n^{\nu} G_{\mu\nu}\bigg)\, d\mathcal{A} = \bigg(\frac{1}{2}\big(\mathrm{Tr}\widetilde{K}\big)^2 - \widetilde{\mathcal{R}} - 2\, \tilde{n}^{\mu}\tilde{n}^{\nu} \widetilde{G}_{\mu\nu}\bigg)\, d\tilde{\mathcal{A}} \tag{2.1.7}$$

where the tilded quantities refer to the asymptotically flat metric $\tilde{g}_{\mu\nu}$. In the left and right side of (2.1.7), the same surface γ is embedded either in $\mathcal{C}_3$ or in $\widetilde{\mathcal{C}}_3$ respectively. The geometric quantity $\mathcal{R}$ and $G_{\mu\nu}$ transform under a Weyl transformation as

$$\mathcal{R} \,=\, e^{-2\varphi}\big(\widetilde{\mathcal{R}} - 2\, \widetilde{\mathcal{D}}^2\varphi\big) \tag{2.1.8}$$

$$G_{\mu\nu} \,=\, \widetilde{G}_{\mu\nu} - \widetilde{\nabla}_{\mu}\widetilde{\nabla}_{\nu}\varphi + \widetilde{\nabla}_{\mu}\varphi\, \widetilde{\nabla}_{\nu}\varphi + \tilde{g}_{\mu\nu}\widetilde{\nabla}^2\varphi \tag{2.1.9}$$

where $\widetilde{\mathcal{D}}_{\mu}$ is the covariant derivative constructed through $\tilde{h}_{\mu\nu}$ and $\widetilde{\mathcal{D}}^2$ the corresponding Laplacian operator. By plugging (2.1.8) and (2.1.9) into (2.1.7) and then integrating over γ, we find

$$0 \,=\, \int_{\gamma} \bigg(\widetilde{\mathcal{D}}^2\varphi - \widetilde{\nabla}^2\varphi + \tilde{n}^{\mu}\tilde{n}^{\nu}\, \widetilde{\nabla}_{\mu}\widetilde{\nabla}_{\nu}\varphi - \big(\tilde{n}^{\lambda}\partial_{\lambda}\varphi\big)^2 - \frac{1}{4}\big(\mathrm{Tr}\widetilde{K}\big)^2\bigg)\, d\tilde{\mathcal{A}} + \frac{1}{4}\int_{\gamma} \big(\mathrm{Tr}K\big)^2\, d\mathcal{A}\,. \tag{2.1.10}$$

Adding the area $\mathcal{A}[\gamma]$ to both sides of this identity, it becomes

$$\mathcal{A}[\gamma] \,=\, \int_{\gamma} \bigg(\widetilde{\mathcal{D}}^2\varphi - \widetilde{\nabla}^2\varphi + e^{2\varphi} + \tilde{n}^{\mu}\tilde{n}^{\nu}\, \widetilde{\nabla}_{\mu}\widetilde{\nabla}_{\nu}\varphi - \big(\tilde{n}^{\lambda}\partial_{\lambda}\varphi\big)^2 - \frac{1}{4}\big(\mathrm{Tr}\widetilde{K}\big)^2\bigg)\, d\tilde{\mathcal{A}} + \frac{1}{4}\int_{\gamma} \big(\mathrm{Tr}K\big)^2\, d\mathcal{A}\,. \tag{2.1.11}$$

We remark that (2.1.11) holds for a generic two dimensional surface embedded into the three dimensional Euclidean space given by (2.1.2).

The first term is a total derivative that reduces to a boundary integral. This observation leads to the following expression for the area $\mathcal{A}[\gamma]$ of the surface [78]

$$\begin{aligned}\mathcal{A}[\gamma] = &\oint_{\partial\gamma} \tilde{b}^{\mu}\partial_{\mu}\varphi \, d\tilde{s} + \frac{1}{4}\int_{\gamma} \left(\mathrm{Tr}K\right)^{2} d\mathcal{A} \\ &- \int_{\gamma} \left(\frac{1}{4}\big(\mathrm{Tr}\widetilde{K}\big)^{2} + \widetilde{\nabla}^{2}\varphi - e^{2\varphi} - \tilde{n}^{\mu}\tilde{n}^{\nu}\, \widetilde{\nabla}_{\mu}\widetilde{\nabla}_{\nu}\varphi + \big(\tilde{n}^{\lambda}\partial_{\lambda}\varphi\big)^{2} \right) d\tilde{\mathcal{A}}\end{aligned} \tag{2.1.12}$$

where $\tilde{b}^{\mu}$ is the unit vector on $\partial\gamma$ that is tangent to γ, orthogonal to $\partial\gamma$ and outward pointing with respect to γ.

If part of γ belongs to the conformal boundary at $z = 0$, the area (2.1.12) is infinite because of the behaviour of the metric $h_{\mu\nu}$ near the conformal boundary. In order to regularise the area, one introduces the UV cutoff ε and considers the part of γ given by $\gamma_{\varepsilon} \equiv \gamma \cap \{z \geqslant \varepsilon\}$. The curve $\partial\gamma_{\varepsilon}$ can be decomposed as $\partial\gamma_{\varepsilon} = \partial\gamma_{\mathcal{Q}} \cup \partial\gamma_{\parallel}$, where $\partial\gamma_{\mathcal{Q}} \equiv \gamma_{\varepsilon} \cap \mathcal{Q}$ and $\partial\gamma_{\parallel} \equiv \gamma_{\varepsilon} \cap \{z = \varepsilon\}$ are not necessarily closed lines. Consequently, for the surfaces γ_{ε} the boundary term in (2.1.12) can be written as

$$\oint_{\partial\gamma_{\varepsilon}} \tilde{b}^{\mu}\partial_{\mu}\varphi \, d\tilde{s} = \int_{\partial\gamma_{\parallel}} \tilde{b}^{\mu}\partial_{\mu}\varphi \, d\tilde{s} + \int_{\partial\gamma_{\mathcal{Q}}} \tilde{b}^{\mu}\partial_{\mu}\varphi \, d\tilde{s}. \tag{2.1.13}$$

Let us consider the integral over $\partial\gamma_{\parallel}$ in the r.h.s. of this expression. Since in our analysis $\varphi = -\log(z) + O(z^{a})$ with $a > 1$ as $z \to 0$, we need to know the behaviour of the component $\tilde{b}^{z}$ at $z = \varepsilon$ as $\varepsilon \to 0$. If $\tilde{b}^{z} = -1 + o(\varepsilon)$, for the integral over $\partial\gamma_{\parallel}$ in (2.1.13) we obtain the following expansion

$$\int_{\partial\hat{\gamma}_{\parallel}} \tilde{b}^{\mu}\partial_{\mu}\varphi \, d\tilde{s} = \frac{P_{A,B}}{\varepsilon} + o(1) \tag{2.1.14}$$

as $\varepsilon \to 0$, being $P_{A,B} = \mathrm{length}(\partial A \cap \partial B)$ the length of the entangling curve. The above expansion for $\tilde{b}^{z}$ holds for any surface, not necessarily minimal, which intersects the conformal boundary orthogonally [77]. This fact will be discussed in detail in the chapter 4 for the more general metric hvLif$_4$. The interested reader is referred to the corresponding appendix C.3, where the expansion (C.3.7) is derived.

Hereafter we will consider only this class of surfaces, which includes also the extremal surfaces.

By plugging (2.1.14) into (2.1.13) first and then substituting the resulting expression into (2.1.12), for the area of the surfaces γ_{ε} we find the following expansion

$$\begin{aligned}\mathcal{A}[\gamma_{\varepsilon}] = &\frac{P_{A,B}}{\varepsilon} + \int_{\partial\gamma_{\mathcal{Q}}} \tilde{b}^{\mu}\partial_{\mu}\varphi \, d\tilde{s} + \frac{1}{4}\int_{\gamma_{\varepsilon}} \left(\mathrm{Tr}K\right)^{2} d\mathcal{A} \\ &- \int_{\gamma_{\varepsilon}} \left(\frac{1}{4}\big(\mathrm{Tr}\widetilde{K}\big)^{2} + \widetilde{\nabla}^{2}\varphi - e^{2\varphi} - \tilde{n}^{\mu}\tilde{n}^{\nu}\, \widetilde{\nabla}_{\mu}\widetilde{\nabla}_{\nu}\varphi + \big(\tilde{n}^{\lambda}\partial_{\lambda}\varphi\big)^{2} \right) d\tilde{\mathcal{A}} + o(1)\end{aligned} \tag{2.1.15}$$

as $\varepsilon \to 0$. We remark that (2.1.15) also holds for surfaces γ_{ε} that are not extremal of the area functional. Furthermore, no restrictions are imposed along the curve $\partial\gamma_{\mathcal{Q}}$.

In order to compute the holographic entanglement entropy in AdS$_4$/BCFT$_3$ through (1.3.2), we must consider the minimal area surface $\hat{\gamma}_A$ which is anchored to the entangling curve $\partial A \cap \partial B$. This implies that $\hat{\gamma}_A$ intersects the surface $\mathcal{Q}$ orthogonally, whenever $\hat{\gamma}_A \cap \mathcal{Q} \neq \emptyset$. The expression (2.1.15) significantly simplifies for the extremal surfaces $\hat{\gamma}_\varepsilon \equiv \hat{\gamma}_A \cap \{z \geqslant \varepsilon\}$ (with a slight abuse of notation, sometimes we denote by $\hat{\gamma}_A$ also extremal surfaces which are not the global minimum). The local extrema of the area functional are the solutions of the following equation

$$\mathrm{Tr}K = 0 \qquad \Longleftrightarrow \qquad \big(\mathrm{Tr}\widetilde{K}\big)^2 = 4(\tilde{n}^\lambda \partial_\lambda \varphi)^2 \tag{2.1.16}$$

which, furthermore, intersect orthogonally $\mathcal{Q}$ whenever $\hat{\gamma}_A \cap \mathcal{Q} \neq \emptyset$. The second expression in (2.1.16) has been obtained by using the second formula in (2.1.3).

Plugging the extremality condition (2.1.16) into (2.1.15), we find the expansion of $\mathcal{A}[\hat{\gamma}_\varepsilon]$ as $\varepsilon \to 0$, which provides the holographic entanglement entropy of a region A in AdS$_4$/BCFT$_3$ for static gravitational backgrounds. It reads

$$\mathcal{A}[\hat{\gamma}_\varepsilon] \,=\, \frac{P_{A,B}}{\varepsilon} + \int_{\partial\hat{\gamma}_{\mathcal{Q}}} \tilde{b}^\mu \partial_\mu \varphi \, d\tilde{s} - \int_{\hat{\gamma}_\varepsilon} \left(\frac{1}{2}\big(\mathrm{Tr}\widetilde{K}\big)^2 + \widetilde{\nabla}^2 \varphi - e^{2\varphi} - \tilde{n}^\mu \tilde{n}^\nu \, \widetilde{\nabla}_\mu \widetilde{\nabla}_\nu \varphi \right) d\tilde{\mathcal{A}} + o(1) \tag{2.1.17}$$

where the leading divergence gives the expected area law term for the holographic entanglement entropy in AdS$_4$/BCFT$_3$. Comparing (2.1.17) with the expansion (2.0.1) expected for $\mathcal{A}[\hat{\gamma}_\varepsilon]$, we find that the subleading term is given by

$$F_A = \int_{\hat{\gamma}_\varepsilon} \left(\frac{1}{2}\big(\mathrm{Tr}\widetilde{K}\big)^2 + \widetilde{\nabla}^2 \varphi - e^{2\varphi} - \tilde{n}^\mu \tilde{n}^\nu \, \widetilde{\nabla}_\mu \widetilde{\nabla}_\nu \varphi \right) d\tilde{\mathcal{A}} - \int_{\partial\hat{\gamma}_{\mathcal{Q}}} \tilde{b}^\mu \partial_\mu \varphi \, d\tilde{s}. \tag{2.1.18}$$

This is one of the main results of this chapter. According to (2.1.18), the subleading term is made by two contributions: an integral over the whole minimal surface $\hat{\gamma}_\varepsilon$ and a line integral over the curve $\partial\hat{\gamma}_{\mathcal{Q}} = \hat{\gamma}_\varepsilon \cap \mathcal{Q}$. We also remark that the definition of $\mathcal{Q}$ has not been employed in the derivation of (2.1.18).

We observe that when the surface does not intersect $\mathcal{Q}$, the boundary term in (2.1.18) vanishes and we recover the functional (1.3.22) discussed in the previous chapter.

The first term in (2.1.18) is the same of equation (1.3.22) obtained in [78], where this analysis has been applied for the holographic entanglement entropy in AdS$_4$/CFT$_3$. The holographic entanglement entropy in AdS$_4$/BCFT$_3$ includes the additional term given by the line integral over $\partial\hat{\gamma}_{\mathcal{Q}}$. This term can be written in a more geometrical form by considering the transformation rule of the geodesic curvature k under Weyl transformations (see e.g. [77])

$$k \,=\, e^{-\varphi}\big(\tilde{k} + \tilde{b}^\mu \partial_\mu \varphi\big). \tag{2.1.19}$$

This formula allows to write the line integral over $\partial\gamma_{\mathcal{Q}}$ in (2.1.18) as follows

$$\int_{\partial\gamma_{\mathcal{Q}}} \tilde{b}^\mu \partial_\mu \varphi \, d\tilde{s} \,=\, \int_{\partial\gamma_{\mathcal{Q}}} k \, ds - \int_{\partial\gamma_{\mathcal{Q}}} \tilde{k}\, d\tilde{s}. \tag{2.1.20}$$

In the following we are going to consider backgrounds such that $\varphi = -\log(z)$ in (2.1.2). In these cases, the first and the last term of the integrand in the surface integral in (2.1.18) become respectively

$$\big(\mathrm{Tr}\widetilde{K}\big)^2 = \frac{4(\tilde{n}^z)^2}{z^2} \qquad \tilde{n}^\mu \tilde{n}^\nu\, \widetilde{\nabla}_\mu \widetilde{\nabla}_\nu \varphi = \frac{(\tilde{n}^z)^2}{z^2} + \frac{1}{z}\, \widetilde{\Gamma}^z_{\mu\nu}\, \tilde{n}^\mu \tilde{n}^\nu \tag{2.1.21}$$

where the first expression has been obtained from the second expression in (2.1.16) and $\widetilde{\Gamma}^z_{\mu\nu}$ are some components of the Christoffel connection compatible with $\tilde{g}_{\mu\nu}$.

2.1.1 Special case: AdS$_4$ with boundary

In the previous discussion, we did not specify the background metric at all, being the only requirement that $g_{\mu\nu}$ is asymptotically AdS$_4$ and $\tilde{g}_{\mu\nu}$ asymptotically flat. In the remaining part of this chapter, we focus on the simple gravitational background given by a part of AdS$_4$ delimited by $\mathcal{Q}$ and the conformal boundary. These cases are relevant because, as explained in Sec. 1.4, they are dual to the vacuum of BCFT$_3$ with flat or spherical boundaries. We recall that the time-slice $t = 0$ of the AdS$_4$ space-time reduces to the hyperbolic space $\mathbb{H}_3$, which in Cartesian coordinates reads

$$ds^2 = \frac{1}{z^2}\left(dz^2 + dx^2 + dy^2\right) \qquad z > 0. \tag{2.1.22}$$

Specialising the results of Sec. 2.1 to this background, we have $\mathcal{C}_3 = \mathbb{H}_3$, i.e. $g_{\mu\nu} = \frac{1}{z^2}\,\delta_{\mu\nu}$, which means that $\tilde{g}_{\mu\nu} = \delta_{\mu\nu}$ and $\varphi = -\log(z)$. In this case, drastic simplifications occur in (2.1.18) because $\widetilde{\nabla}^2\varphi - e^{2\varphi} = 0$ and all the components of the connection $\widetilde{\Gamma}^z_{\mu\nu}$ vanish identically. Thus, when the gravitational bulk is a proper subset of $\mathbb{H}_3$ delimited by the surface $\mathcal{Q}$ and the conformal boundary, the expression (2.1.18) for F_A reduces to

$$F_A \,=\, \frac{1}{4}\int_{\hat{\gamma}_\varepsilon} \big(\mathrm{Tr}\widetilde{K}\big)^2\, d\tilde{\mathcal{A}} + \int_{\partial\hat{\gamma}_{\mathcal{Q}}} \frac{\tilde{b}^z}{z}\, d\tilde{s} \,=\, \int_{\hat{\gamma}_\varepsilon} \frac{(\tilde{n}^z)^2}{z^2}\, d\tilde{\mathcal{A}} + \int_{\partial\hat{\gamma}_{\mathcal{Q}}} \frac{\tilde{b}^z}{z}\, d\tilde{s}. \tag{2.1.23}$$

The surface integral over $\hat{\gamma}_\varepsilon$ in the first expression is the Willmore functional of $\hat{\gamma}_\varepsilon \subset \mathbb{R}^3$. Notice that the curves $\partial\hat{\gamma}_{\mathcal{Q}}$ corresponding to some configurations may intersect the plane given by $z = \varepsilon$.

When the entangling curve is a smooth and closed line that does not intersect the spatial boundary of the BCFT$_3$, the limit $\varepsilon \to 0$ of (2.1.23) provides the following finite expression

$$F_A \,=\, \frac{1}{4}\int_{\hat{\gamma}_A} \big(\mathrm{Tr}\widetilde{K}\big)^2\, d\tilde{\mathcal{A}} + \int_{\partial\hat{\gamma}_{\mathcal{Q}}} \frac{\tilde{b}^z}{z}\, d\tilde{s} \,=\, \int_{\hat{\gamma}_A} \frac{(\tilde{n}^z)^2}{z^2}\, d\tilde{\mathcal{A}} + \int_{\partial\hat{\gamma}_{\mathcal{Q}}} \frac{\tilde{b}^z}{z}\, d\tilde{s} \tag{2.1.24}$$

which will be largely employed throughout this chapter.

Below we specialize the equation (2.1.24) to the flat boundary case.

Flat boundary

For this case, we remark that the line integral over $\partial\hat{\gamma}_{\mathcal{Q}}$ in (2.1.23) simplifies because $\tilde{b}^z = -\cos\alpha$ for all the points of $\partial\hat{\gamma}_{\mathcal{Q}}$. Furthermore, $\tilde{k} = 0$ in (2.1.20) in this setup, i.e. $\partial\hat{\gamma}_{\mathcal{Q}}$ is a geodesic of $\hat{\gamma}_A \in \mathbb{R}^3$. Thus, for any region A in the half-plane $x \geqslant 0$, we find

$$F_A \,=\, \int_{\hat{\gamma}_A} \frac{(\tilde{n}^z)^2}{z^2}\, d\tilde{\mathcal{A}} - (\cos\alpha)\int_{\partial\hat{\gamma}_{\mathcal{Q}}} \frac{1}{z}\, d\tilde{s}. \tag{2.1.25}$$

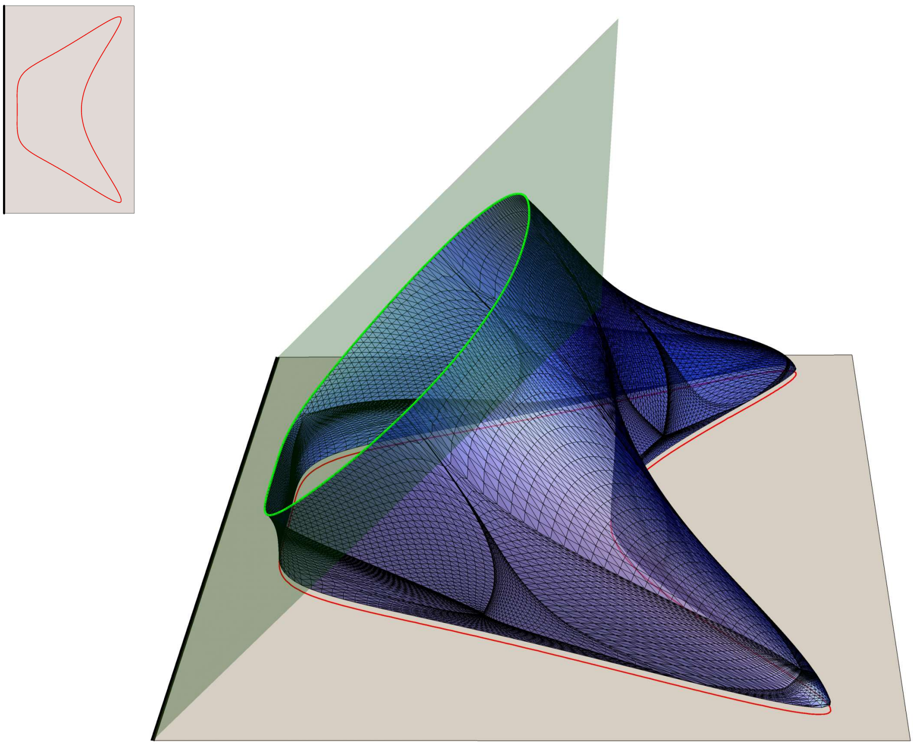

Figure 2.1: Extremal surface $\hat{\gamma}_\varepsilon$ constructed with Surface Evolver from a spatial domain A in the right half-plane (the grey half-plane) whose ∂A is the red curve, which is also highlighted in the inset. The gravitational bulk is the part of $\mathbb{H}_3$ defined by (2.1.22), whose boundary is made by the conformal boundary at $z = 0$ (the grey half-plane) and $\mathcal{Q}$ (the green half-plane defined in (1.4.9)). Here $\alpha = 3\pi/4$. The green curve corresponds to $\partial\hat{\gamma}_{\mathcal{Q}} = \hat{\gamma}_\varepsilon \cap \mathcal{Q}$, and $\hat{\gamma}_\varepsilon$ intersects $\mathcal{Q}$ orthogonally along this curve.

The two integrals in this expression are always positive, but their relative sign depends on the slope α. In particular, when $\alpha \geqslant \pi/2$ we have $F_A > 0$, while F_A can be negative when $\alpha < \pi/2$.

In Fig. 2.1 we show an explicit example where (2.1.25) can be applied. The entangling curve ∂A is the red curve in the $z = 0$ half-plane also highlighted in the inset. Surface Evolver has been employed to construct $\hat{\gamma}_\varepsilon$, as done in [154] for other regions in this AdS$_4$/BCFT$_3$ setup.

The AdS$_4$/BCFT$_3$ for the circular case has been discussed in Sec. 1.4.2, and F_A in (2.1.24) can be applied in this case as well. However, $\tilde{b}^z$ is not constant along $\hat{\gamma}_{\mathcal{Q}}$ and the simplification which leads to equation (2.1.25) is not available in this case.

2.2 Infinite strip domains

A simple domain which plays an important role in our analysis is the infinite strip of finite width ℓ which can be either adjacent to the boundary, namely such that one of its two edges coincides with the boundary $x = 0$, or parallel but disjoint from it by a distance d. The strip adjacent to the boundary has also been considered in [159]. In the following we present only the main results about the holographic entanglement entropy of these regions in AdS$_4$/BCFT$_3$, and their detailed derivation in AdS$_{d+2}$/BCFT$_{d+1}$ is reported in the appendix A.2.

2.2.1 Infinite strip adjacent to the boundary

Considering the rectangular domain $A = \{(x,y) \in \mathbb{R}^2 \,|\, 0 \leqslant x \leqslant \ell\,,\, 0 \leqslant y \leqslant L_\parallel\}$, the infinite strip adjacent to the boundary is obtained by taking $L_\parallel \gg \ell \gg \varepsilon$. These assumptions allow assuming the invariance under translations in the y direction and this symmetry drastically simplifies the problem of finding the minimal surface $\hat{\gamma}_A$ and its area because $\hat{\gamma}_A$ is completely characterised by its profile $z = z(x)$ obtained through a section at $y = \text{const}$.

The minimal area surface $\hat{\gamma}_A$ intersects the $z = 0$ half-plane orthogonally along the line $x = \ell$, and this leads to the linear divergence $L_\parallel/\varepsilon$ (area law term) in its area. Let us stress that the logarithmic divergence does not occur in this case.

When $\alpha \leqslant \pi/2$, two surfaces $\hat{\gamma}_A^{\,\text{dis}}$ and $\hat{\gamma}_A^{\,\text{con}}$ are local extrema of the area functional and the minimal surface $\hat{\gamma}_A$ is given by the global minimum. In particular, $\hat{\gamma}_A^{\,\text{dis}}$ is the half-plane given by $x = \ell$, therefore it remains orthogonal to the $z = 0$ plane and it does not intersect $\mathcal{Q}$ at a finite value of z, while $\hat{\gamma}_A^{\,\text{con}}$ bends in the bulk towards the half-plane $\mathcal{Q}$ until it intersects it orthogonally at a finite value z_* of the coordinate z. It is straightforward to observe that the solution $\hat{\gamma}_A^{\,\text{dis}}$ does not exist for $\alpha > \pi/2$.

The surface $\hat{\gamma}_A^{\,\text{con}}$ can be also viewed as the part identified by the constraint $x \geqslant -(\cot\alpha) z$ of the auxiliary minimal surface $\hat{\gamma}_{A,\text{aux}} \subset \mathbb{H}_3$ anchored to the auxiliary infinite strip $A_{\,\text{aux}} \subset \mathbb{R}^2$ which includes A and has one of its edges at $x = \ell$. In the appendix A.4 the width of A_{aux} has been computed (see (A.4.1) specialised to $d = 2$).

Focussing on a section at $y = \text{const}$ of $\hat{\gamma}_A^{\,\text{con}}$, which is characterised by the profile $z(x)$, let us denote by $P_* = (x_*, z_*)$ the intersection between this curve and the half-line (1.4.9) corresponding to $\mathcal{Q}$. In the half-plane described by the pair (z, x), we find it convenient to write the curve $z(x)$ of $\hat{\gamma}_A$ in a parametric form $P_\theta = (x(\theta), z(\theta))$ in terms of the angular variable $\theta \in [0, \pi - \alpha]$. The angular variable θ corresponds to the angle between the outgoing vector normal to the curve given by P_θ and the x semi-axis with $x \geqslant 0$. The parametric expressions P_θ must satisfy the boundary conditions $P_0 = (\ell, 0)$ and $P_{\pi-\alpha} = P_*$. Since P_* lies on $\mathcal{Q}$, we have $x_* = -\, z_* \cot\alpha$; therefore we can write its position as $P_* = z_*(-\cot\alpha\,, 1)$. In Fig. 2.2 we show the profile $z(x)$ corresponding to a given strip adjacent to the boundary for different values of the slope α of $\mathcal{Q}$. Notice that z_* is a decreasing function of α.

In the appendix A.2 we find that, for any given slope $\alpha \in (0, \pi)$, the coordinate z_* of P_* is related to the width ℓ of the strip as follows

$$z_* = \frac{\sqrt{\sin\alpha}}{\mathfrak{g}(\alpha)}\,\ell \tag{2.2.1}$$

where we have introduced

$$\mathfrak{g}(\alpha) \,\equiv\, \mathbb{E}\big(\pi/4 - \alpha/2\,|\,2\big) - \frac{\cos\alpha}{\sqrt{\sin\alpha}} + \frac{\Gamma\big(\frac{3}{4}\big)^2}{\sqrt{2\pi}} \tag{2.2.2}$$

being $\mathbb{E}(\phi|m)$ the elliptic integral of the second kind. The expressions (2.2.1) and (2.2.2) correspond respectively to (A.2.10) and (A.2.11) specialised to $d = 2$. In order to enlighten

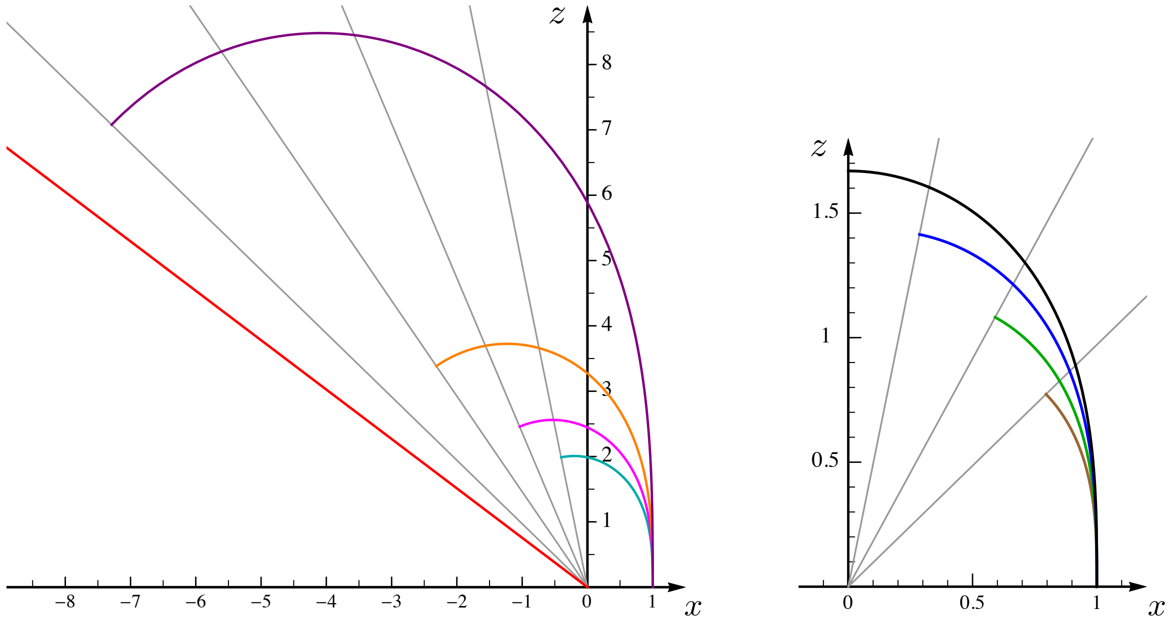

Figure 2.2: Sections of minimal surfaces $\hat{\gamma}_A$ corresponding to an infinite strip adjacent to the boundary whose width is $\ell = 1$ for different values of $\alpha > \alpha_c$, where α_c is given by (2.2.4). These curves are obtained from (2.2.5). The grey half-lines correspond to the sections of $\mathcal{Q}$ at $y = \text{const}$ obtained from (1.4.9) and the red one is associated to $\alpha = \alpha_c$. Each curve intersects orthogonally the corresponding section of $\mathcal{Q}$ at the point P_*, whose coordinate z_* along the z axis is (2.2.1).

the notation, in the main text we slightly change the notation with respect to the appendix A.2 by setting $\mathfrak{g}(\alpha) \equiv \mathfrak{g}_2(\alpha)$ (see (A.2.11)). In Fig. 2.3 the function $\mathfrak{g}(\alpha)$ and the ratio z_*/ℓ are shown in terms of $\alpha \in (0, \pi)$.

As for the function $\mathfrak{g}(\alpha)$ in (2.2.2), we find $\mathfrak{g}(\alpha) = -1/\sqrt{\alpha} + O(1)$ when $\alpha \to 0^+$ and $\mathfrak{g}(\alpha) = 1/\sqrt{\pi - \alpha} + O(1)$ as $\alpha \to \pi^-$. Moreover $\mathfrak{g}'(\alpha) = (\sin\alpha)^{-3/2}/2$ is positive in the whole domain $\alpha \in (0, \pi)$. These observations imply that $\mathfrak{g}(\alpha)$ has a unique zero, namely

$$\mathfrak{g}(\alpha_c) = 0 \tag{2.2.3}$$

where we have introduced α_c to label the unique solution of this transcendental equation. Solving (2.2.3) numerically, we find

$$\alpha_c \simeq \frac{\pi}{4.8525821} \simeq 0.647406. \tag{2.2.4}$$

Since $z_* > 0$ in (2.2.1), the condition (2.2.3) defines the critical value for the slope α characterising the range of validity of (2.2.1), which is well defined only for $\alpha \in (\alpha_c, \pi)$. Thus, for $\alpha \leqslant \alpha_c$ the solution $\hat{\gamma}_A^{\text{con}}$ does not exist and therefore $\hat{\gamma}_A = \hat{\gamma}_A^{\text{dis}}$. This is confirmed also by the fact that, by taking $\alpha \to \alpha_c^+$ in (2.2.1) we have $z_* \to +\infty$. The occurrence of the critical value (2.2.4) has been observed also in [159].

When $\alpha > \alpha_c$, the extremal surface $\hat{\gamma}_A^{\text{con}}$ is parametrically described by the following curve

$$P_\theta = \big(x(\theta)\,, z(\theta)\big) \;=\; \frac{\ell}{\mathfrak{g}(\alpha)} \left(\mathbb{E}\big(\pi/4 - \alpha/2\,|\,2\big) - \frac{\cos\alpha}{\sqrt{\sin\alpha}} + \mathbb{E}\big(\pi/4 - \theta/2\,|\,2\big)\,,\, \sqrt{\sin\theta} \right) \tag{2.2.5}$$

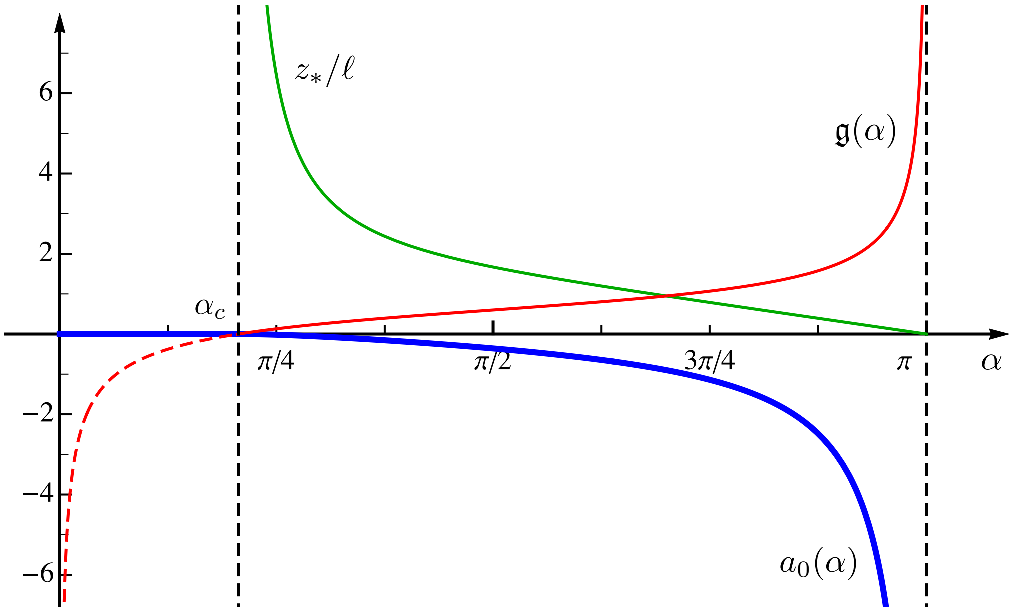

Figure 2.3: Infinite strip adjacent to the boundary: The red curve is $\mathfrak{g}(\alpha)$ in (2.2.2), which is positive for $\alpha \geqslant \alpha_c$ and negative for $\alpha \leqslant \alpha_c$, being α_c given by (2.2.4). The solid green curve corresponds to z_*/ℓ obtained from (2.2.1) and it diverges as $\alpha \to \alpha_c^+$. The solid blue line is the $O(1)$ term in the expansion (2.2.7) of the area $\mathcal{A}[\hat{\gamma}_\varepsilon]$.

where the independent angular parameter is $0 \leqslant \theta \leqslant \pi - \alpha$. The profile (2.2.5) corresponds to (A.2.14) specialised to $d = 2$. It is straightforward to check that (2.2.5) fulfils the required boundary conditions $P_0 = (\ell, 0)$ and $P_{\pi-\alpha} = P_* = z_*(-\cot\alpha\,, 1)$, with z_* given by (2.2.1). In Fig. 2.2 we show the profiles $z(x)$ for $\hat{\gamma}_A$ obtained from (2.2.5) which correspond to the same strip adjacent to the boundary in the $z = 0$ half-plane ($\ell = 1$ in the figure) and different values of α. As for the maximum value z_{max} reached by the coordinate z along the curve (2.2.5), we observe that $z_{\text{max}} = z_*$ when $\alpha \in [\pi/2, \pi)$, while $z_{\text{max}} > z_*$ for $\alpha \in (\alpha_c, \pi/2)$.

The expansion for $\varepsilon \to 0^+$ of the area of the extremal surface corresponding to the infinite strip adjacent to the boundary and characterised by the curve (2.2.5) restricted to $z \geqslant \varepsilon$ reads

$$\mathcal{A}[\hat{\gamma}_\varepsilon] \,=\, R^2_{\text{AdS}}\, L_{\parallel} \left(\frac{1}{\varepsilon} - \frac{\mathfrak{g}(\alpha)^2}{\ell} + O(\varepsilon^3) \right) \qquad \alpha > \alpha_c. \tag{2.2.6}$$

This expression is the special case $d = 2$ of (A.2.23). Comparing (2.2.6) with (2.0.1), we have that in this case $P_{A,B} = L_{\parallel}$, the logarithmic divergence does not occur and the $O(1)$ term is negative.

An important role in our analysis is played by the extremal surface $\hat{\gamma}_A^{\text{dis}}$ given by the vertical half-plane at $x = \ell$. By computing its area restricted to $\varepsilon \leqslant z \leqslant z_{\text{IR}}$, being $z_{\text{IR}} \gg \ell$ an infrared cutoff, one easily finds that $\mathcal{A}[\hat{\gamma}_\varepsilon] = R^2_{\text{AdS}} L_{\parallel}(1/\varepsilon - 1/z_{\text{IR}})$. Notice that the $O(1)$ term of this expression vanishes in the limit $z_{\text{IR}} \to +\infty$. This extremal surface exists only for $\alpha \leqslant \pi/2$ because when $\alpha > \pi/2$ the half-plane $\mathcal{Q}$ and the vertical infinite strip $x = \ell$ do not intersect orthogonally.

Summarising, for the minimal area surface $\hat{\gamma}_A$ we have that $\hat{\gamma}_A = \hat{\gamma}_A^{\text{dis}}$ when $\alpha \leqslant \alpha_c$ because (2.2.1) is not well defined. When $\alpha \in (\alpha_c, \pi/2]$, two extremal surfaces $\hat{\gamma}_A^{\text{dis}}$ and $\hat{\gamma}_A^{\text{con}}$ compete (the vertical half-plane at $x = \ell$ and the surface characterised by (2.2.5) respectively), while for $\alpha > \pi/2$ we have $\hat{\gamma}_A = \hat{\gamma}_A^{\text{con}}$ because $\hat{\gamma}_A^{\text{dis}}$ does not exist. As for the regime $\alpha \in (\alpha_c, \pi/2]$, since the $O(1)$ term in (2.2.6) is negative while it vanishes for $\hat{\gamma}_A^{\text{dis}}$, we conclude that $\hat{\gamma}_A = \hat{\gamma}_A^{\text{con}}$, given by (2.2.5).

Combining the above observations, we find that the expansion as $\varepsilon \to 0^+$ of the area of the minimal surface $\hat{\gamma}_A \cap \{z \geqslant \varepsilon\}$ corresponding to an infinite strip of width ℓ adjacent to the boundary for $\alpha \in (0, \pi)$ is

$$\mathcal{A}[\hat{\gamma}_\varepsilon] \;=\; R^2_{\text{AdS}}\, L_\parallel \left(\frac{1}{\varepsilon} + \frac{a_0(\alpha)}{\ell} + o(1) \right) \qquad a_0(\alpha) = \begin{cases} -\,\mathfrak{g}(\alpha)^2 & \alpha \geqslant \alpha_c \\ \;\;0 & \alpha \leqslant \alpha_c \end{cases} \tag{2.2.7}$$

where $\mathfrak{g}(\alpha)$ has been defined in (2.2.2) and α_c is its unique zero (2.2.4). The result (2.2.7) is the special case $d = 2$ of the expressions (A.2.23) and (A.2.26). Since α_c is defined by (2.2.3), the function $a_0(\alpha)$ in (2.2.7) is continuous and it corresponds to the blue solid curve in Fig. 2.3. Let us also observe that $\mathfrak{g}'(\alpha)$ is continuous but $\mathfrak{g}''(\alpha)$ is not continuous at $\alpha = \alpha_c$.

2.2.2 Infinite strip parallel to the boundary

The results for the infinite strip adjacent to the boundary discussed in Sec. 2.2 allow addressing also the holographic entanglement entropy of an infinite strip A parallel to the boundary and at a finite distance from it. In the appendix A.2.2 we discuss the analogue case in a BCFT$_{d+1}$. In the following, we report only the results of that analysis for $d = 2$.

The configuration of an infinite strip parallel to the boundary is characterised by the width ℓ_A of the strip and by its distance d_A from the boundary. By employing the translation invariance and the results of Sec. 2.2, one realises that $\hat{\gamma}_A$ is the global minimum obtained by comparing the area of two possible configurations $\hat{\gamma}_A^{\text{dis}}$ and $\hat{\gamma}_A^{\text{con}}$. The surface $\hat{\gamma}_A^{\text{dis}}$ is disconnected from $\mathcal{Q}$ and it connects the two parallel lines of ∂A through the bulk, while $\hat{\gamma}_A^{\text{con}}$ is made by two disjoint surfaces such that each of them connects an edge of ∂A to $\mathcal{Q}$. The two disjoint surfaces occurring in $\hat{\gamma}_A^{\text{con}}$ are like the ones described in Sec. 2.2; therefore $\hat{\gamma}_A^{\text{con}} \cap \mathcal{Q}$ is made by two parallel lines. The two configurations $\hat{\gamma}_A^{\text{dis}}$ and $\hat{\gamma}_A^{\text{con}}$ are depicted in Fig. 2.4 for a given value of α

For an infinite strip A at a finite distance from the boundary, $\hat{\gamma}_{A,\text{aux}}$ is the minimal surface in $\mathbb{H}_3$ anchored to $A_{\text{aux}} = A \cup A' \subset \mathbb{R}^2$, which is the union of two parallel and disjoint infinite strips in $\mathbb{R}^2$ [142]. The minimal surface $\hat{\gamma}_A$ is the part of $\hat{\gamma}_{A,\text{aux}}$ identified by the constraint $x \geqslant -(\cot\alpha) z$. The width of A' and the separation between A and A' are given by (A.4.3) specialised to the case $d = 2$.

As for the area of $\hat{\gamma}_\varepsilon$, we find

$$\mathcal{A}[\hat{\gamma}_\varepsilon] \;=\; R^2_{\text{AdS}}\, L_\parallel \left(\frac{2}{\varepsilon} + \frac{1}{\ell_A} \min\!\left[h_2\,,\, a_0(\alpha) \left(\frac{1}{\delta_A} + \frac{1}{\delta_A + 1} \right) \right] + o(1) \right) \qquad \delta_A \equiv \frac{d_A}{\ell_A} \tag{2.2.8}$$

where $a_0(\alpha)$ has been introduced in (2.2.7) and $h_2 \equiv -\,4\pi \big[\Gamma(\tfrac{3}{4})/\Gamma(\tfrac{1}{4})\big]^2$ comes from the $O(1)$ term of the holographic entanglement entropy of an infinite strip in CFT$_3$ [31, 32]. The

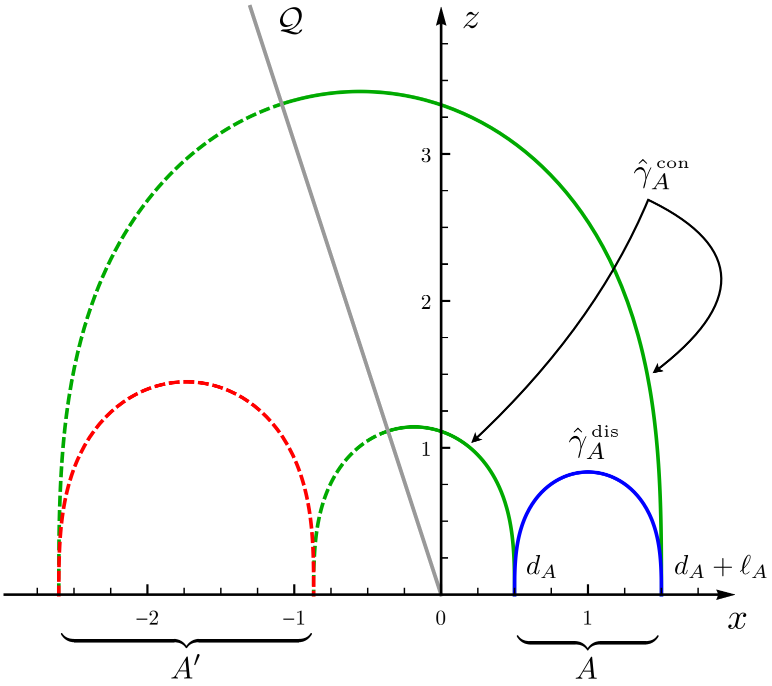

Figure 2.4: Infinite strip of width ℓ_A parallel to the boundary at distance d_A: Section of the surfaces $\hat{\gamma}_A^{\text{dis}}$ and $\hat{\gamma}_A^{\text{con}}$ (blue and green solid curve respectively) which are local extrema of the area functional. In this plot $\alpha > \alpha_c$. The auxiliary domain $A_{\text{aux}} = A \cup A'$ in $\mathbb{R}^2$ is made by two parallel infinite strips A and A'. The green dashed curves together with $\hat{\gamma}_A^{\text{con}}$ provide $\hat{\gamma}_{A,\text{aux}}$ when $\hat{\gamma}_A = \hat{\gamma}_A^{\text{con}}$, while the red dashed curve together with $\hat{\gamma}_A^{\text{dis}}$ gives $\hat{\gamma}_{A,\text{aux}}$ when $\hat{\gamma}_A = \hat{\gamma}_A^{\text{dis}}$.

expression (2.2.8) corresponds to the special case $d = 2$ of (A.2.29). When $\alpha \leqslant \alpha_c$, we have that $\hat{\gamma}_A = \hat{\gamma}_A^{\text{dis}}$ because $a_0(\alpha) = 0$ and $h_2 < 0$.

The critical configuration corresponds to the value $\delta_A = \delta_{A,c}$ such that the two terms occurring in the minimisation procedure in (2.2.8) provide the same result. By imposing this condition, one finds an algebraic equation of second order with only one positive root given by

$$\delta_{A,c} = \frac{1}{2}\left(\sqrt{4\left[a_0(\alpha)/h_2\right]^2 + 1} + 2\,a_0(\alpha)/h_2 - 1\right). \tag{2.2.9}$$

When $\delta_A \leqslant \delta_{A,c}$ the minimal surface is $\hat{\gamma}_A = \hat{\gamma}_A^{\text{con}}$, while for $\delta_A \geqslant \delta_{A,c}$ it is given by $\hat{\gamma}_A = \hat{\gamma}_A^{\text{dis}}$. The function (2.2.9) corresponds to the red curve in Fig. A.3 and it is meaningful for $\alpha \geqslant \alpha_c$.

2.2.3 Recovering the finite term from the modified Willmore functional

Before concluding this section, we show that the non-trivial expression for F_A corresponding to the regime $\alpha \geqslant \alpha_c$ in (2.2.7) can be recovered by evaluating (2.1.25) for $\hat{\gamma}_A^{\text{con}}$ as surface embedded in $\mathbb{R}^3$. The surface $\hat{\gamma}_A^{\text{con}}$ is described by the constraint $\mathcal{C} = 0$, being $\mathcal{C} \equiv z - z(x)$, and its unit normal vector $\tilde{n}_\mu = (\tilde{n}_z, \tilde{n}_x, \tilde{n}_y)$ can be found by first computing $\partial_\mu \mathcal{C}$ and then normalising the resulting vector. We find $\tilde{n}_\mu = (1, -z', 0)/\sqrt{1 + (z')^2}$. The area element in the surface integral occurring in (2.1.25) reads $d\tilde{\mathcal{A}} = \sqrt{1+(z')^2}\, dx\, dy$ in this case. Combining these observations, we get

$$\int_{\hat{\gamma}_A} \frac{(\tilde{n}^z)^2}{z^2}\, d\tilde{\mathcal{A}} = \int_{\hat{\gamma}_A} \frac{dx\, dy}{z^2 \sqrt{1+(z')^2}} \tag{2.2.10}$$

where we have not used yet the fact that $z(x)$ corresponds to $\hat{\gamma}_A$. Specifying (2.2.10) to the profile (2.2.5), we find $\sqrt{1+(z')^2} = 1/\sin\theta$ and $dx = \ell\sqrt{\sin\theta}\, d\theta/(2\mathfrak{g}(\alpha))$. By employing these observations, (2.2.10) becomes

$$\int_{\hat{\gamma}_A} \frac{(\tilde{n}^z)^2}{z^2}\, d\tilde{\mathcal{A}} = L_\parallel \frac{2\mathfrak{g}(\alpha)}{\ell} \int_0^{\pi-\alpha} \sqrt{\sin\theta}\, d\theta = L_\parallel \frac{\mathfrak{g}(\alpha)}{\ell} \left(\mathbb{E}\big(\pi/4 - \alpha/2 \,|\, 2\big) + \frac{\Gamma(\frac{3}{4})^2}{\sqrt{2\pi}} \right). \tag{2.2.11}$$

The integral over the line $\partial\hat{\gamma}_{\mathcal{Q}}$ in (2.1.25) significantly simplifies for these domains because $\partial\hat{\gamma}_{\mathcal{Q}}$ is the straight line given by $(z,x,y) = (z_*, x_*, y)$ with $-L_\parallel/2 \leqslant y \leqslant L_\parallel/2$, where $(x_*, z_*) = P_{\pi-\alpha}$ can be read from (2.2.5) and it corresponds to the green straight lines in Fig. **??**. Thus, the line integral in (2.1.25) gives

$$\int_{\partial\hat{\gamma}_{\mathcal{Q}}} \frac{1}{z}\, d\tilde{s} = \frac{L_\parallel}{z_*} = \frac{\mathfrak{g}(\alpha)}{\ell\sqrt{\sin\alpha}}\, L_\parallel \tag{2.2.12}$$

where (2.2.1) has been used in the last step.

Plugging (2.2.11) and (2.2.12) into the general expression (2.1.25), for an infinite strip of width ℓ adjacent to the boundary we find

$$F_A\big|_{\hat{\gamma}_A^{\text{con}}} = L_\parallel \frac{\mathfrak{g}(\alpha)}{\ell} \left[\left(\mathbb{E}\big(\pi/4 - \alpha/2 \,|\, 2\big) + \frac{\Gamma(\frac{3}{4})^2}{\sqrt{2\pi}} \right) - \frac{\cos\alpha}{\sqrt{\sin\alpha}} \right] = L_\parallel \frac{\mathfrak{g}(\alpha)^2}{\ell} \tag{2.2.13}$$

where the last result has been obtained by employing (2.2.2), and which agrees with the area (2.2.7) as expected. Notice that both the terms in (2.1.25) provide non-trivial contributions.

From the results discussed in this section, it is straightforward to find F_A when A is an infinite strip parallel to the flat boundary and at a finite distance from it through the formula (2.1.25), recovering the result presented in Sec. 2.2.2.

2.3 Disk disjoint from the boundary

In this section, we study the holographic entanglement entropy of a disk A at a finite distance from the boundary.

In the setup described in Sec. 1.4.2, in Sec. 2.3.1 we consider the case of a disk A concentric to the circular boundary because the symmetry of this configuration allows us to obtain an analytic expression for the profile characterising the minimal surface $\hat{\gamma}_A$ (in the left panel of Fig. 2.5 we show an example of $\hat{\gamma}_A$). The corresponding area $\mathcal{A}[\hat{\gamma}_\varepsilon]$ is computed in two ways: by the direct evaluation of the integral and by specifying the general formula (2.1.25) to this case. In Sec. 2.3.2, by employing the second transformation in (A.1.3) and the analytic results presented in Sec. 2.3.1, we study the holographic entanglement entropy of a disk disjoint from the flat boundary in the setup introduced in Sec. 2.1.1 (see the right panel of Fig. 2.5 for an example of $\hat{\gamma}_A$ in this setup). The two configurations in Fig. 2.5 have the same α and are related through the map (A.1.3) discussed in Appendix A.1.

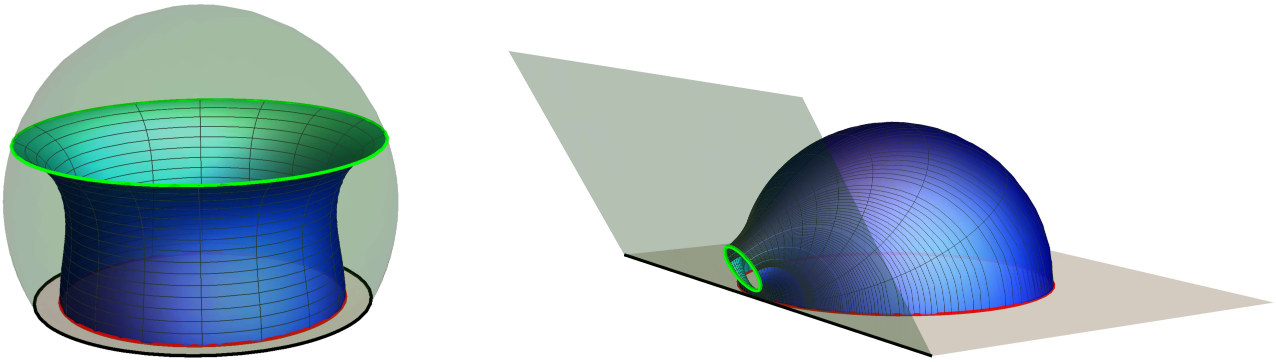

Figure 2.5: Left: Extremal area surface $\hat{\gamma}_A^{\text{con}}$ anchored to a disk A disjoint from a circular concentric boundary (see Sec. 1.4.2 and Sec. 2.3.1) where $\mathcal{Q}$ (green spherical dome) is described by (1.4.11). Here $\alpha = \pi/3$ and $R_\circ/R_\mathcal{Q} \sim 0.85$, which corresponds to $r_{\circ,\,\text{min}}$ (see Sec. 2.3.1). Right: Extremal surface $\hat{\gamma}_A^{\text{con}}$ anchored to a disk disjoint from a flat boundary (see Sec. 2.1.1 and Sec. 2.3.2). Here $\alpha = \pi/3$ and d/R can be obtained from the first expression in (2.3.22) with the value of $R_\circ/R_\mathcal{Q}$ of the left panel because the two configurations shown in these panels are related through (A.1.3).

2.3.1 Disk disjoint from a circular concentric boundary

In the AdS$_4$/BCFT$_3$ setup introduced in Sec. 1.4.2, let us consider a disk A with radius $R_\circ < R_\mathcal{Q}$ which is concentric to the boundary of the spatial slice of the spacetime. In Sec. 2.3.1 we obtain an analytic expression for the profile characterising $\hat{\gamma}_A$ and in Sec. 2.3.1 we evaluate the corresponding area $\mathcal{A}[\hat{\gamma}_\varepsilon]$. In the following, we report only the main results of this analysis. Their detailed derivation, which is closely related to the evaluation of the holographic entanglement entropy of an annulus in AdS$_4$/CFT$_3$ [243, 245] has been presented in Appendix A.3.

Profile of the extremal surfaces

Adopting the coordinate system (ρ, ϕ, z) introduced in Sec. 1.4.2, the invariance under rotations about the z-axis in the $z = 0$ plane implies that the local extrema of the area functional are described by the profiles of their sections at $\phi = \text{const}$.

For a given A, an extremal surface is a hemisphere anchored to the circle ∂A. Since it does not intersect $\mathcal{Q}$, this solution will be denoted by $\hat{\gamma}_A^{\text{dis}}$, while we will refer to the extremal surfaces that intersect $\mathcal{Q}$ orthogonally as $\hat{\gamma}_A^{\text{con}}$. The holographic entanglement entropy of A is provided by the surface corresponding to the global minimum of the area. Let us anticipate that we find at most two solutions $\hat{\gamma}_A^{\text{con}}$; hence we have at most three local extrema for a given disk A. The number of solutions depends on the value of α, as we will discuss in the following. By employing the analytic result that will be presented below, in the left panel of Fig. 2.6 we show the three profiles corresponding to $\hat{\gamma}_A^{\text{dis}}$ (black curve) and $\hat{\gamma}_A^{\text{con}}$ (blue and red curve) in an explicit case. The red curve provides the holographic entanglement entropy in this example.

We find it worth introducing an auxiliary surface that allows relating our problem to the

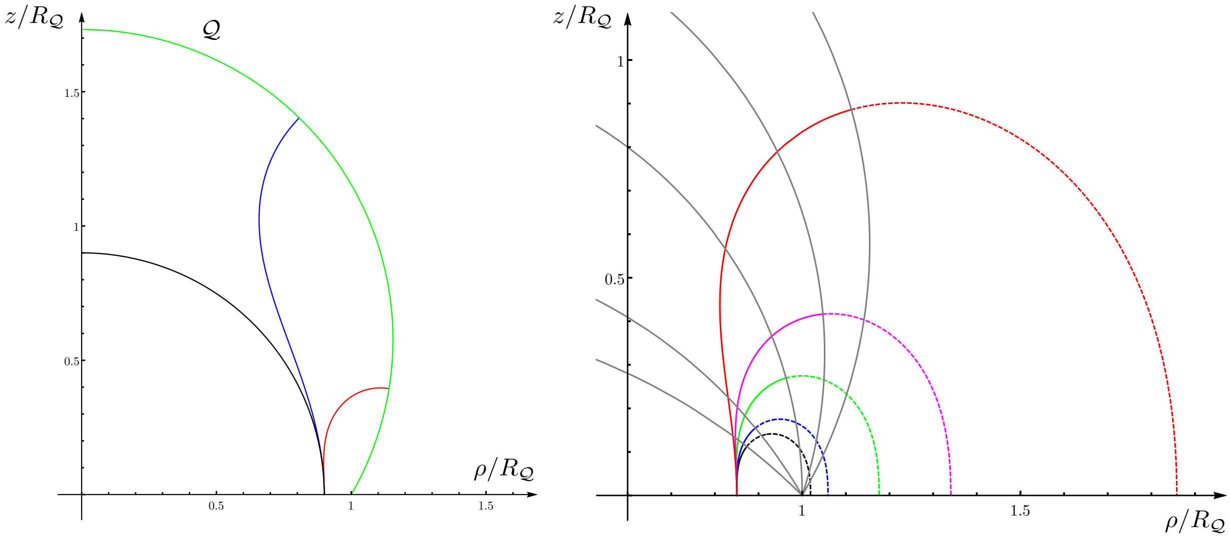

Figure 2.6: Sections of the extremal surfaces anchored to a disk A of radius $R_\circ$ disjoint from a circular concentric boundary with radius $R_{\mathcal{Q}}$ (see Sec. 2.3.1). Left: Profiles corresponding to the three extremal surfaces in the case of $R_\circ/R_{\mathcal{Q}} = 0.9$ and $\alpha = \pi/3$. The green curve represents $\mathcal{Q}$. The black curve corresponds to $\hat{\gamma}_A^{\text{dis}}$ (the hemisphere). The red curve and the blue curve correspond to $\hat{\gamma}_A^{\text{con}}$ and they have been obtained through the analytic results discussed in Sec. 2.3.1 and in Appendix A.3. The red curve provides the global minimum in this case. Right: Extremal surfaces $\hat{\gamma}_A^{\text{con}}$ having $R_\circ/R_{\mathcal{Q}} \simeq 0.85$ for different values of α: $\alpha = \pi/3$ (red), $\alpha = \pi/2.5$ (magenta), $\alpha = \pi/2$ (green), $\alpha = 2\pi/3$ (blue) and $\alpha = 3\pi/4$ (black). The dashed curves are the profiles of the auxiliary surfaces $\hat{\gamma}_{A,\,\text{aux}}^{\text{con}}$, with the same color code. All the profiles correspond to the smaller value of k whenever two surfaces $\hat{\gamma}_A^{\text{con}}$ exists. All the curves except for the red one provide the global minimum of the corresponding configuration.

one of finding the extremal surfaces in $\mathbb{H}_3$ anchored to an annulus, which has been already addressed in the literature. Given $\hat{\gamma}_A^{\text{con}}$, let us consider its unique surface $\hat{\gamma}_{A,\,\text{aux}}^{\text{con}}$ in the whole $\mathbb{H}_3$ such that $\hat{\gamma}_A^{\text{con}} \cup \hat{\gamma}_{A,\,\text{aux}}^{\text{con}}$ is an extremal area surface in $\mathbb{H}_3$ anchored to the annulus whose boundary is made by the two concentric circles with radii $R_\circ$ and $R_{\text{aux}} > R_\circ$. Thus, $\hat{\gamma}_A^{\text{con}}$ can be viewed as part of an extremal surface anchored to a proper annulus whose boundary is the union of two circles, one of which is ∂A. By using the solution that will be discussed in the following, in the right panel of Fig. 2.6 we fix A and we show the profiles associated to $\hat{\gamma}_A^{\text{con}}$ (solid curves) for various α and the ones for the corresponding extensions $\hat{\gamma}_{A,\,\text{aux}}^{\text{con}}$ (dashed curves). Other examples are shown in Fig. 2.8.

The profile of a section of $\hat{\gamma}_A^{\text{con}}$ at fixed ϕ can be written as $(\rho, z) = (\rho_\gamma(\theta), \rho_\gamma(\theta)\tan\theta)$, where the angular variable is defined as $\hat{z} \equiv \tan\theta = z/\rho$ (see Sec. 1.4.2). Considering the construction of the extremal surfaces in $\mathbb{H}_3$ anchored to an annulus reported in [245], we have that the curve $\rho_\gamma(\theta)$ can be written by introducing two branches as follows

$$\rho_\gamma(\theta) \;=\; \begin{cases} R_\circ \, e^{-q_{-,k}(\hat{z})} \\ R_{\text{aux}} \, e^{-q_{+,k}(\hat{z})} \end{cases} \tag{2.3.1}$$

with $R_{\textrm{aux}} > R_\circ$. The functions $q_{\pm,k}(\hat{z})$ are defined as

$$q_{\pm,k}(\hat{z}) \equiv \int_0^{\hat{z}} \frac{\lambda}{1+\lambda^2} \left(1 \pm \frac{\lambda}{\sqrt{k\,(1+\lambda^2)-\lambda^4}} \right) d\lambda \qquad 0 \leqslant \hat{z} \leqslant \hat{z}_m \tag{2.3.2}$$

being $k > 0$ and $\hat{z}_m^2 \equiv \big(k + \sqrt{k(k+4)}\,\big)/2$ the unique admissible root of the biquadratic equation coming from the expression under the square root in (2.3.2). Since $q_{\pm,k}(0) = 0$, the two branches in (2.3.1) give $\rho_\gamma = R_\circ$ and $\rho_\gamma = R_{\textrm{aux}}$ when $z = 0$.

The two branches characterised by $q_{\pm,k}(\hat{z})$ in (2.3.1) match at the point $P_m = (\rho_m, \hat{z}_m)$ associated to the maximum value of θ. The coordinates of P_m read (see also Appendix A.3)

$$\hat{z}_m^2 = \frac{k + \sqrt{k(k+4)}}{2} \qquad\qquad \rho_m = R_\circ\, e^{-q_{-,k}(\hat{z}_m)} = R_{\textrm{aux}}\, e^{-q_{+,k}(\hat{z}_m)}. \tag{2.3.3}$$

The last equality in the second expression follows from the continuity of the profile (2.3.1) and it gives

$$\frac{R_\circ}{R_{\textrm{aux}}} = e^{q_{-,k}(\hat{z}_m) - q_{+,k}(\hat{z}_m)} \tag{2.3.4}$$

which will be denoted by $\chi(\hat{z}_m)$ in the following. Being $\hat{z}_m$ given by the first expression in (2.3.3), from (2.3.4) we observe that the ratio $R_\circ/R_{\textrm{aux}}$ is a function of the parameter $k > 0$. Moreover, by employing (2.3.2) in (2.3.4), it is straightforward to observe that $R_\circ/R_{\textrm{aux}} < 1$.

The integral in (2.3.2) can be computed analytically, finding that $q_{\pm,k}(\hat{z})$ can be written in terms of the incomplete elliptic integrals of the first and third kind as follows

$$q_{\pm,k}(\hat{z}) = \frac{1}{2} \log(1+\hat{z}^2) \pm \kappa \sqrt{\frac{1-2\kappa^2}{\kappa^2-1}}\, \Big[\Pi\big(1-\kappa^2, \Omega(\hat{z}) | \kappa^2\big) - \mathbb{F}\big(\Omega(\hat{z})|\kappa^2\big) \Big] \tag{2.3.5}$$

where

$$\Omega(\hat{z}) \,\equiv\, \arcsin\left(\frac{\hat{z}/\hat{z}_m}{\sqrt{1+\kappa^2(\hat{z}^2/\hat{z}_m^2 - 1)}} \right) \qquad \kappa \equiv \sqrt{\frac{1+\hat{z}_m^2}{2+\hat{z}_m^2}}. \tag{2.3.6}$$

Let us remark that the above expressions depend on the positive parameters $R_\circ$ and k. The dependence on the parameters $R_{\mathcal{Q}}$ and α characterising the boundary occurs through the requirement that $\hat{\gamma}_A^{\textrm{con}} \perp \mathcal{Q}$.

Denoting by $P_* = (\rho_*, z_*)$ the point in the radial profile corresponding to the intersection between $\hat{\gamma}_A^{\textrm{con}}$ and $\mathcal{Q}$, in Appendix A.3 we have found that

$$\hat{z}_*^2 = \frac{k + \sqrt{k(k+4(\sin\alpha)^2)}}{2} \qquad\qquad \rho_* = R_{\mathcal{Q}}\, \frac{\sqrt{\hat{z}_*^2 + (\sin\alpha)^2} + \hat{z}_* \cos\alpha}{(\hat{z}_*^2+1)\sin\alpha} \tag{2.3.7}$$

where the first expression has been obtained by imposing that $\hat{\gamma}_A^{\textrm{con}}$ intersects $\mathcal{Q}$ orthogonally at P_*, while the second one comes from (1.4.12). In Appendix A.3.1 (see below (A.3.12)) we have also remarked that the orthogonality condition also implies that P_* belongs to the branch described $q_{-,k}$ when $\alpha \geqslant \pi/2$, while it belongs to the branch characterised by $q_{+,k}$ when $\alpha \leqslant \pi/2$. This observation and (2.3.1) specialised to P_* lead to

$$R_\circ = \rho_* \left(\frac{1+\eta_\alpha}{2}\, e^{q_{-,k}(\hat{z}_*)} + \frac{1-\eta_\alpha}{2}\, \chi(\hat{z}_m)\, e^{q_{+,k}(\hat{z}_*)} \right) \tag{2.3.8}$$

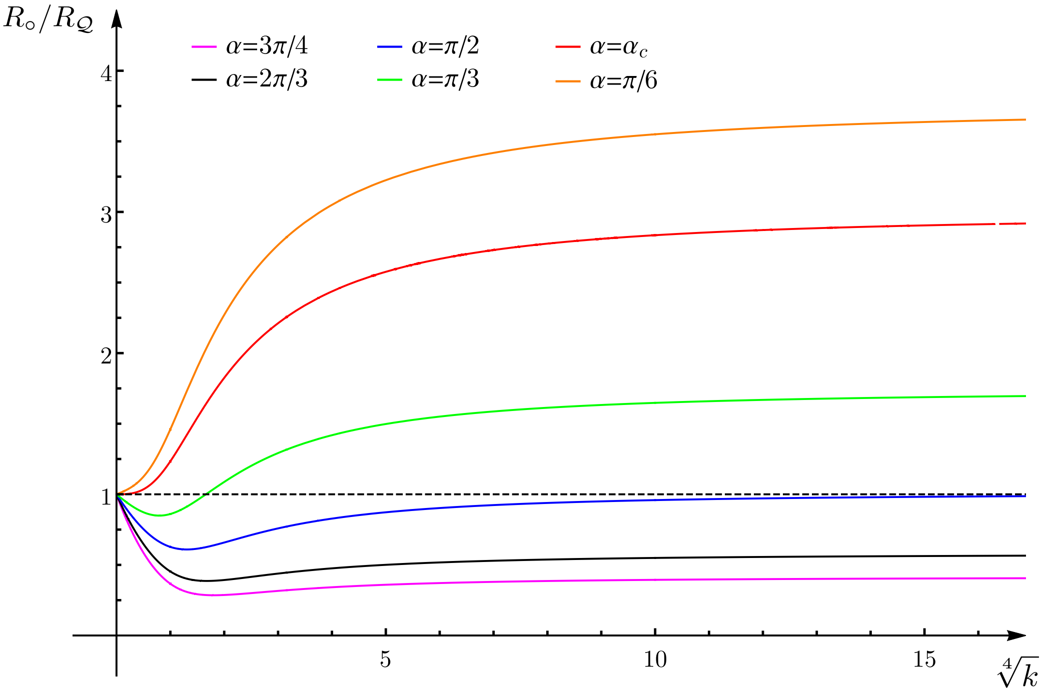

Figure 2.7: The ratio $R_\circ/R_Q$ providing $\hat{\gamma}_A^{\text{con}}$ as a function of $\sqrt[4]{k}$ from (2.3.9) for different values of α. The allowed configurations have $R_\circ/R_Q < 1$ and the black dashed line corresponds to the limiting value $R_\circ/R_Q = 1$. The asymptotic behaviours of these curves for $k \to 0$ and $k \to \infty$ are given by (2.3.10) and (2.3.11) respectively. For fixed values of $\alpha > \alpha_c$ and $R_\circ/R_Q < 1$, the number of extremal solutions $\hat{\gamma}_A^{\text{con}}$ is given by the number of intersections between the curve corresponding to α and the horizontal line characterised by the given value of $R_\circ/R_Q$.

where $\eta_\alpha \equiv -\,\text{sign}(\cot\alpha)$ and $\chi(\hat{z}_m)$ denotes the ratio in (2.3.4).

Notice that $e^{q_{-,k}(\hat{z}_*)} = \chi(\hat{z}_m)\, e^{q_{+,k}(\hat{z}_*)}$ for $\alpha = \pi/2$. Moreover, if we employ this observation into the second expression of (2.3.3), we find that $P_* = P_m$ when $\alpha = \pi/2$.

By using the expression of ρ_* in (2.3.7) into (2.3.8), we get the following relation

$$\frac{R_\circ}{R_Q} = \frac{\sqrt{\hat{z}_*^2 + (\sin\alpha)^2} + \hat{z}_*\cos\alpha}{(\hat{z}_*^2+1)\sin\alpha}\left(\frac{1+\eta_\alpha}{2}\, e^{q_{-,k}(\hat{z}_*)} + \frac{1-\eta_\alpha}{2}\,\chi(\hat{z}_m)\, e^{q_{+,k}(\hat{z}_*)}\right) \tag{2.3.9}$$

where $\hat{z}_*$ is the function of k and α given by the first formula in (2.3.7). The expression (2.3.9) tells us that $R_\circ/R_Q$ is a function of k and α, and it is used to find the value of the parameter k given the physical quantities $R_\circ, R_Q$ and α. In Fig. 2.7 we plot this function by employing $\sqrt[4]{k}$ as the independent variable and α as parameter. Since the disk A is a spatial subsystem of the disk with radius R_Q, the admissible configurations have $R_\circ/R_Q < 1$.

We find it worth discussing the behaviour of the curves $R_\circ/R_Q$ in (2.3.9) parameterised by α in the limiting regimes given by $k \to 0$ and $k \to \infty$. The technical details of this analysis have been reported in Appendix A.3.3.

The expansion of (2.3.9) for small k reads

$$\frac{R_\circ}{R_Q} = 1 - \mathfrak{g}(\alpha)\,\sqrt[4]{k} + \frac{\mathfrak{g}(\alpha)^2}{2}\,\sqrt{k} + o\big(\sqrt{k}\,\big) \tag{2.3.10}$$

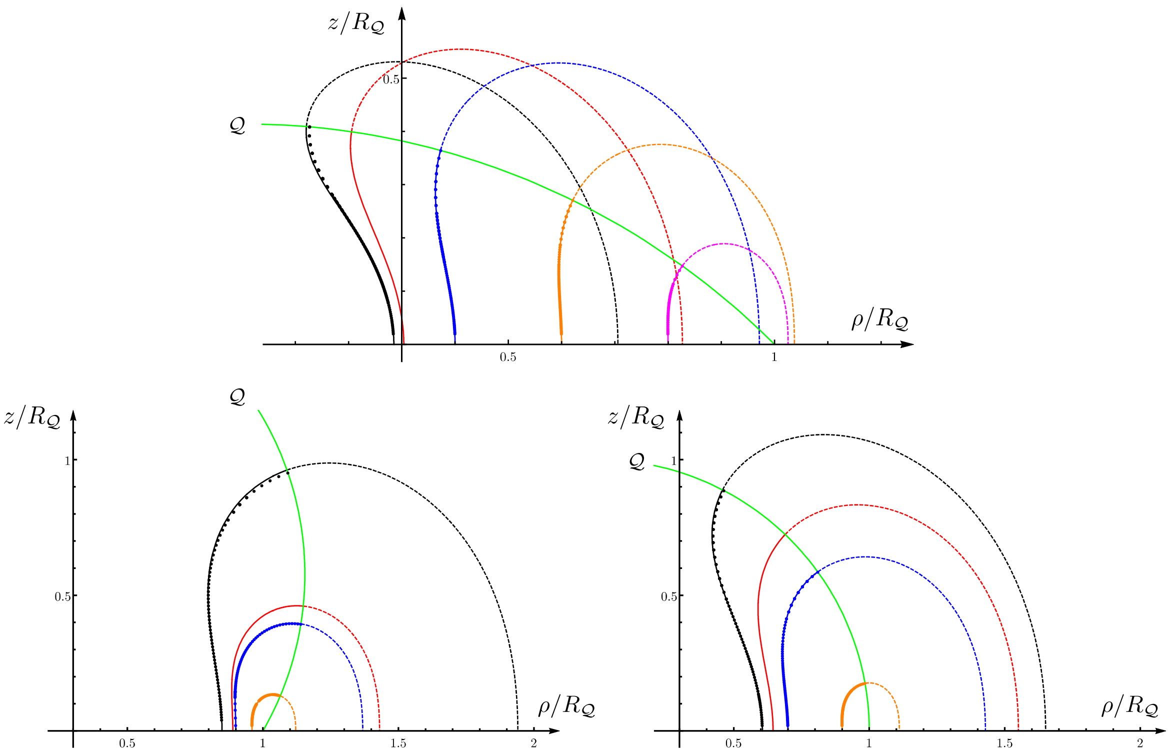

Figure 2.8: Radial profiles of extremal surfaces $\hat{\gamma}_A^{\text{con}}$ intersecting $\mathcal{Q}$ (green curve) orthogonally and anchored to a disk A of radius $R_\circ$ concentric to a circular boundary with radius $R_{\mathcal{Q}}$ (see Sec. 2.3.1). The value of α in the three panels is $\alpha = 3\pi/4$ (top), $\alpha = \pi/2$ (bottom, right) and $\alpha = \pi/3$ (bottom, left). The solid lines give $\hat{\gamma}_A^{\text{con}}$, while the dashed ones (with the same colour) give the corresponding auxiliary surface $\hat{\gamma}_{A,\,\text{aux}}^{\text{con}}$. The value of k associated to all the shown profiles is the minimum one, whenever two solutions occur (see Fig. 2.7). All the profiles except for the black one correspond to the global minimum. The red curves correspond to the critical value of the ratio $R_\circ/R_{\mathcal{Q}}$ where the area of the extremal surface $\hat{\gamma}_A^{\text{dis}}$ is equal to the minimum of the area of the extremal surfaces $\hat{\gamma}_A^{\text{con}}$. The points have been found by taking the $\phi = \text{const}$ section of the extremal surfaces constructed by Surface Evolver and they nicely agree with the corresponding analytic solutions.

where $\mathfrak{g}(\alpha)$ has been defined in (2.2.2). Since $\mathfrak{g}(\alpha) > 0$ only for $\alpha > \alpha_c$, being α_c the unique zero of $\mathfrak{g}(\alpha)$ introduced in Sec. 2.2.1, the expansion (2.3.10) tells us that, in the regime of small k, an extremal surface $\hat{\gamma}_A^{\text{con}}$ can be found only when $\alpha > \alpha_c$ because $R_\circ/R_{\mathcal{Q}} < 1$. From Fig. 2.7 we notice that this observation can be extended to the entire regime of k. Indeed, since $R_\circ/R_{\mathcal{Q}} \geqslant 1$ for the curves with $\alpha \leqslant \alpha_c$, we have that $\hat{\gamma}_A^{\text{con}}$ does not exist in this range of α.

In Appendix A.3.3 also the limit of (2.3.9) for large k has been discussed, finding that for any $\alpha \in (0, \pi)$ it reads

$$\lim_{k\to\infty} \frac{R_\circ}{R_{\mathcal{Q}}} = \cot(\alpha/2) \tag{2.3.11}$$

which gives the asymptotic value of the curves in Fig. 2.7 for large k.

When $\alpha > \alpha_c$ the curve $R_\circ/R_{\mathcal{Q}}$ has only one local minimum (see Fig. 2.7). Denoting by

$k_{\circ,\,\text{min}}$ and $r_{\circ,\,\text{min}}$ the values of k and $R_\circ/R_\mathcal{Q}$ characterising this point, we have that $r_{\circ,\,\text{min}} < \cot(\alpha/2)$. The plot of $r_{\circ,\,\text{min}}$ in terms of $\alpha > \alpha_c$ has been reported in Fig. 2.10 (black solid curve) where $\cot(\alpha/2)$ corresponds to the dashed blue curve.

These observations about the limits of $R_\circ/R_\mathcal{Q}$ and the numerical analysis of Fig. 2.7 allow to discuss the number of extremal surfaces $\hat{\gamma}_A^{\,\text{con}}$ in the various regimes of the parameters. When $\alpha \leqslant \alpha_c$ the solutions $\hat{\gamma}_A^{\,\text{con}}$ do not exist because $R_\circ/R_\mathcal{Q} \geqslant 1$. When $\alpha > \alpha_c$ also the global minimum $r_{\circ,\,\text{min}}$ of $R_\circ/R_\mathcal{Q}$ is an important parameter to consider. Indeed, for $\alpha_c < \alpha \leqslant \pi/2$ (see e.g. the green curve in Fig. 2.7) one has two distinct extremal surfaces $\hat{\gamma}_A^{\,\text{con}}$ when $r_{\circ,\,\text{min}} < R_\circ/R_\mathcal{Q} < 1$, one extremal surface when $R_\circ/R_\mathcal{Q} = r_{\circ,\,\text{min}}$ and none of them when $R_\circ/R_\mathcal{Q} < r_{\circ,\,\text{min}}$. For $\alpha > \pi/2$ also the asymptotic value (2.3.11) plays an important role. Indeed, when $\cot(\alpha/2) \leqslant R_\circ/R_\mathcal{Q} < 1$ we can find only one extremal surface $\hat{\gamma}_A^{\,\text{con}}$, when $r_{\circ,\,\text{min}} < R_\circ/R_\mathcal{Q} < \cot(\alpha/2)$ there are two solutions $\hat{\gamma}_A^{\,\text{con}}$, when $r_{\circ,\,\text{min}} = R_\circ/R_\mathcal{Q}$ we have again only one solution, while $\hat{\gamma}_A^{\,\text{con}}$ do not exist when $R_\circ/R_\mathcal{Q} < r_{\circ,\,\text{min}}$. Whenever two distinct solutions $\hat{\gamma}_A^{\,\text{con}}$ can be found, considering their values $k_1 < k_2$ for the parameter k, we have that $k_1 < k_{\circ,\,\text{min}} < k_2$ because $R_\circ/R_\mathcal{Q}$ has at most one local minimum for $k > 0$.

As for the extremal surface $\hat{\gamma}_A^{\,\text{dis}}$, which does not intersect $\mathcal{Q}$, its existence depends on the value of α because the condition that $\hat{\gamma}_A^{\,\text{dis}}$ does not intersect $\mathcal{Q}$ provides a non-trivial constraint when $\alpha < \pi/2$. In order to write this constraint, one first evaluates the z coordinate $z_\mathcal{Q}$ of the tip of $\mathcal{Q}$ by setting $\rho = 0$ in (1.4.11), finding that $z_\mathcal{Q}/R_\mathcal{Q} = \cot(\alpha/2)$. Then, being $\hat{\gamma}_A^{\,\text{dis}}$ a hemisphere, we must impose that $R_\circ \leqslant z_\mathcal{Q}$ and this leads to $R_\circ/R_\mathcal{Q} \leqslant \cot(\alpha/2)$.

Focusing on the regimes where at least one extremal surface $\hat{\gamma}_A^{\,\text{con}}$ exists and employing the above observations, we can plot the profile given by the section of $\hat{\gamma}_A^{\,\text{con}}$ at $\phi = \text{const}$ by using (2.3.1) and the related expressions. In Fig. 2.8 we show some radial profiles of $\hat{\gamma}_A^{\,\text{con}}$ (solid lines) and of the corresponding auxiliary surfaces $\hat{\gamma}_{A,\,\text{aux}}^{\,\text{con}}$ (dashed lines) obtained from the analytic expressions discussed above. These analytic results have also been checked numerically by employing Surface Evolver as done in [78, 154, 245] for other configurations. The data points in Fig. 2.8 correspond to the $\phi = \text{const}$ section of the extremal surfaces obtained numerically with Surface Evolver. The nice agreement between the solid curves and the data points provides a highly non-trivial check of our analytic results. We remark that Surface Evolver also constructs extremal surfaces that are not the global minimum corresponding to a given configuration.

A detailed discussion about the position of the auxiliary circle with respect to the circular boundary has been reported in Appendix A.4. Here let us notice that in the top panel, where $\alpha = 3\pi/4$, for the black curve and the blue curve we have $R_\text{aux} < R_\mathcal{Q}$.

In the above analysis, we have considered the case of a disk concentric to a circular boundary. Nonetheless, we can also study the case of a disk whose center does not coincide with the center of the circular boundary by combining the analytic expressions obtained for this configuration and the mapping discussed in Appendix A.1.

Area

Given a configuration characterised by a disk A of radius $R_\circ < R_\mathcal{Q}$ concentric to the spatial disk of radius $R_\mathcal{Q}$ and the value α for $\mathcal{Q}$, in Sec. 2.3.1 we have seen that we can find at most three local extrema of the area functional among the surfaces anchored to A: the hemisphere $\hat{\gamma}_A^{\text{dis}}$ and at most two surfaces $\hat{\gamma}_A^{\text{con}} \perp \mathcal{Q}$. Since for these three surfaces the expansion of the regularised area is given by the r.h.s. of (2.0.1) with $P_{A,B} = P_A = 2\pi R_\circ$, the holographic entanglement entropy of A can be found by comparing their subleading terms F_A. Let us denote by F_{con} the subleading term for the surfaces intersecting $\mathcal{Q}$ orthogonally discussed in Sec. 2.3.1. Since $F_A = 2\pi$ for the hemisphere [31, 32, 246], the holographic entanglement entropy of A is given by

$$\mathcal{A}[\hat{\gamma}_\varepsilon] = \frac{2\pi R_\circ}{\varepsilon} - \max\big(2\pi, \widehat{F}_{\text{con}}\big) + \mathcal{O}(\varepsilon) \tag{2.3.12}$$

where we have denoted by $\widehat{F}_{\text{con}}$ the maximum between the (at most) two values taken by F_{con} for the values of k corresponding to the local extrema $\hat{\gamma}_A^{\text{con}}$.

In Appendix A.3.2, we have computed F_{con} by employing two methods: a straightforward evaluation of the integral coming from the area functional and the general expression (2.1.24) specialized to the extremal surfaces $\hat{\gamma}_A^{\text{con}}$ of these configurations. Both these approaches lead to the following result

$$F_{\text{con}} = 2\pi \left[\frac{1+\eta_\alpha}{2}\, \mathcal{F}_k(\hat{z}_*) + \frac{1-\eta_\alpha}{2} \Big(2\, \mathcal{F}_k(\hat{z}_m) - \mathcal{F}_k(\hat{z}_*) \Big) \right] \tag{2.3.13}$$

where

$$\mathcal{F}_k(\hat{z}) \equiv \frac{\sqrt{k(1+\hat{z}^2) - \hat{z}^4}}{\sqrt{k}\, \hat{z}} - \frac{\mathbb{F}(\arcsin(\hat{z}/\hat{z}_m)\,|\, -\hat{z}_m^2 - 1) - \mathbb{E}(\arcsin(\hat{z}/\hat{z}_m)\,|\, -\hat{z}_m^2 - 1)}{\hat{z}_m} \tag{2.3.14}$$

and we recall that $\hat{z}_m$ and $\hat{z}_*$ are the values of $\hat{z}$ corresponding to the points P_m and P_* respectively (see Sec. 2.3.1). For $\hat{z} = \hat{z}_m$, we have

$$\mathcal{F}_k(\hat{z}_m) = \frac{\mathbb{E}(-\hat{z}_m^2 - 1) - \mathbb{K}(-\hat{z}_m^2 - 1)}{\hat{z}_m} \tag{2.3.15}$$

where $\mathbb{K}$ and $\mathbb{E}$ are the complete elliptic integral of the first and second kind respectively. Since $\hat{z}_m$ is a function of k (see (2.3.3)), the r.h.s. of (2.3.15) depends only on this parameter. Instead, since $\hat{z}_*$ depends on both k and α (see the first expression in (2.3.7)), we have that (2.3.13) defines a family of functions of k parameterised by $\alpha \in (\alpha_c, \pi)$.

We find it worth to discuss the limiting regimes of F_{con} in (2.3.13) for small and large values of k (the technical details of this analysis have been reported in Appendix A.3.3).

In the limit $k \to 0$, which corresponds to $R_\circ \to R_{\mathcal{Q}}$ (see (2.3.10) and Fig. 2.7), the expansion of F_{con} reads

$$F_{\text{con}} = \frac{2\pi\, \mathfrak{g}(\alpha)}{\sqrt[4]{k}} + \frac{\pi}{2} \left(\frac{\cot\alpha}{\sqrt{\sin\alpha}} + \mathbb{F}\big(\pi/4 - \alpha/2\,|\,2\big) + \frac{\Gamma^2\left(\frac{1}{4}\right)}{4\sqrt{2\pi}} \right) \sqrt[4]{k} + o\big(\sqrt[4]{k}\,\big). \tag{2.3.16}$$

Since the coefficient of the leading term is positive when $\alpha > \alpha_c$, negative when $\alpha < \alpha_c$ and zero when $\alpha = \alpha_c$, different qualitative behaviours are observed when $k \to 0$. In particular, for $\alpha = \alpha_c$ the subleading term is $o(1)$; therefore $F_{\text{con}} \to 0$.

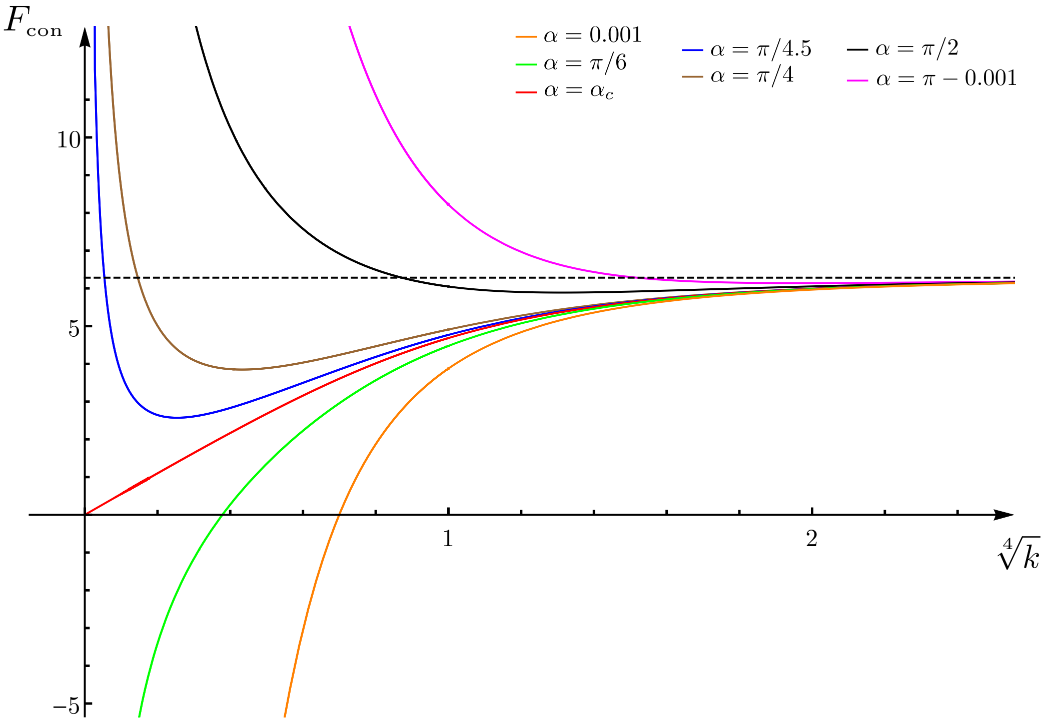

Figure 2.9: The subleading term F_{con} for the extremal surfaces $\hat{\gamma}_A^{\text{con}}$ which intersect $\mathcal{Q}$ orthogonally as a function of $\sqrt[4]{k}$ (see (2.3.13)). The horizontal dashed line corresponds to 2π, i.e. the value of F_A for the hemisphere $\hat{\gamma}_A^{\text{dis}}$, and it provides the asymptotic limit at large k for any value of α. The asymptotic behaviour for $k \to 0$ is given by (2.3.16). The curve with $\alpha = \alpha_c$ vanishes as $k \to 0$ and the slope of its tangent at $k = 0$ is given by the coefficient of the $O(\sqrt[4]{k}\,)$ term in (2.3.16). We numerically observe that for $\alpha \geqslant \alpha_c$ the values of k corresponding to the local minima coincide with the values of k of the local minima in Fig. 2.7.

By using (2.3.10), the expansion (2.3.16) can be written also as an expansion for $R_\circ/R_{\mathcal{Q}} \to 1$, finding that

$$F_{\text{con}} = \frac{2\pi\, \mathfrak{g}(\alpha)^2}{1 - R_\circ/R_{\mathcal{Q}}} - \pi\, \mathfrak{g}(\alpha)^2 + \mathcal{O}(1 - R_\circ/R_{\mathcal{Q}}). \tag{2.3.17}$$

In the limit $k \to \infty$ we have seen that (2.3.11) and in Appendix A.3.3 we find that $F_{\text{con}} \to 2\pi$ for every α.

In Fig. 2.9 we show F_{con} in terms of $\sqrt[4]{k}$ for different values of α. The horizontal dashed line corresponds to 2π, which is the value of the subleading term in the expansion of the area of the hemisphere $\hat{\gamma}_A^{\text{dis}}$. This value provides the asymptotic limit of all the curves, confirming the result obtained in Appendix A.3.3.

When $\alpha \leqslant \alpha_c$, from Fig. 2.9 we observe that $F_{\text{con}} < 2\pi$ for all values of k. Since in Sec. 2.3.1 we have shown that the local solutions $\hat{\gamma}_A^{\text{con}}$ do not exist in this regime, the curves F_{con} having $\alpha \leqslant \alpha_c$ do not occur in the computation of holographic entanglement entropy. Thus, for $\alpha \leqslant \alpha_c$ the holographic entanglement entropy is given by $\hat{\gamma}_A^{\text{dis}}$.

When $\alpha > \alpha_c$ we have that $F_{\text{con}} \to +\infty$ for $k \to 0$ and $F_{\text{con}} \to (2\pi)^-$ for $k \to \infty$. This

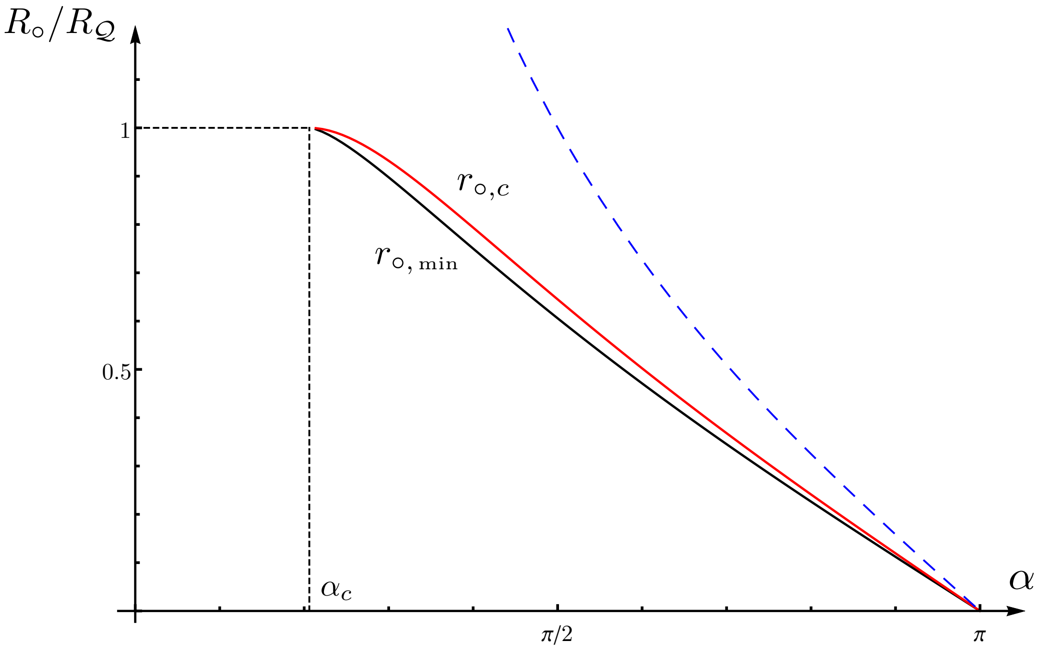

Figure 2.10: The solid black curve is the minimal value $r_{\circ,\,\mathrm{min}}$ of $R_\circ/R_{\mathcal{Q}}$, below which the local solutions $\hat{\gamma}_A^{\,\mathrm{con}}$ intersecting $\mathcal{Q}$ orthogonally do not exist (see also Fig. 2.7), in terms of $\alpha > \alpha_c$. The solid red curve gives the value $r_{\circ,c} > r_{\circ,\,\mathrm{min}}$ of $R_\circ/R_{\mathcal{Q}}$ for $\alpha > \alpha_c$ corresponding to the critical configuration where $\hat{\gamma}_A^{\,\mathrm{con}}$ and $\hat{\gamma}_A^{\,\mathrm{dis}}$ provide the same finite term F_A of the holographic entanglement entropy. The dashed blue curve is the asymptotic value (2.3.11).

implies that at least a local minimum exists. We observe numerically that F_{con} has only one local extremum for $k = k_{\circ,\,\mathrm{min}}$, i.e. the same value for k corresponding to the minimum of the ratio $R_\circ/R_{\mathcal{Q}}$. This observation and the fact that, whenever two solutions $\hat{\gamma}_A^{\,\mathrm{con}}$ can be found, for their values $k_1 < k_2$ of k we have $k_1 < k_{\circ,\,\mathrm{min}} < k_2$ lead to conclude that $F_{\mathrm{con}}(k_2) < 2\pi$. Hence, the holographic entanglement entropy is obtained by comparing 2π with F_{con} evaluated on k_1. When $\alpha > \alpha_c$, let us denote with $k = k_c$ the solution of $F_{\mathrm{con}} = 2\pi$, which can be found numerically and characterises the configuration where the subleading terms for $\hat{\gamma}_A^{\,\mathrm{con}}$ and $\hat{\gamma}_A^{\,\mathrm{dis}}$ take the same value. Since $k_c < k_{\circ,\,\mathrm{min}}$, the minimal surface providing the holographic entanglement entropy is $\hat{\gamma}_A^{\,\mathrm{con}}$ if $k_1 < k_c$ and $\hat{\gamma}_A^{\,\mathrm{dis}}$ if $k_1 > k_c$. Denoting by $r_{\circ,c}$ the value of the ratio $R_\circ/R_{\mathcal{Q}}$ for the critical configuration having $k = k_c$, in Fig. 2.10 we show $r_{\circ,\,\mathrm{min}} < r_{\circ,c}$ in terms of $\alpha \in (\alpha_c, \pi)$.

The solid curves in Fig. 2.11, which are parameterised by α, have been obtained by combining (2.3.9) and (2.3.13) through a parametric plot. The allowed configurations have $R_\circ/R_{\mathcal{Q}} < 1$. A vertical line having $R_\circ/R_{\mathcal{Q}} < 1$ can intersect twice a solid curve corresponding to a fixed value of $\alpha > \alpha_c$. These two intersection points provide the values of F_{con} (see Fig. 2.9) obtained from the two values of k given by the intersection of the horizontal line $R_\circ/R_{\mathcal{Q}}$ with the curve in Fig. 2.7 having the same α.

In Fig. 2.11, the value of $R_\circ/R_{\mathcal{Q}}$ corresponding to the intersection between F_{con} for a given α and the horizontal dashed line (whose height is 2π) is $r_{\circ,c}$ (see the red line in Fig. 2.10),

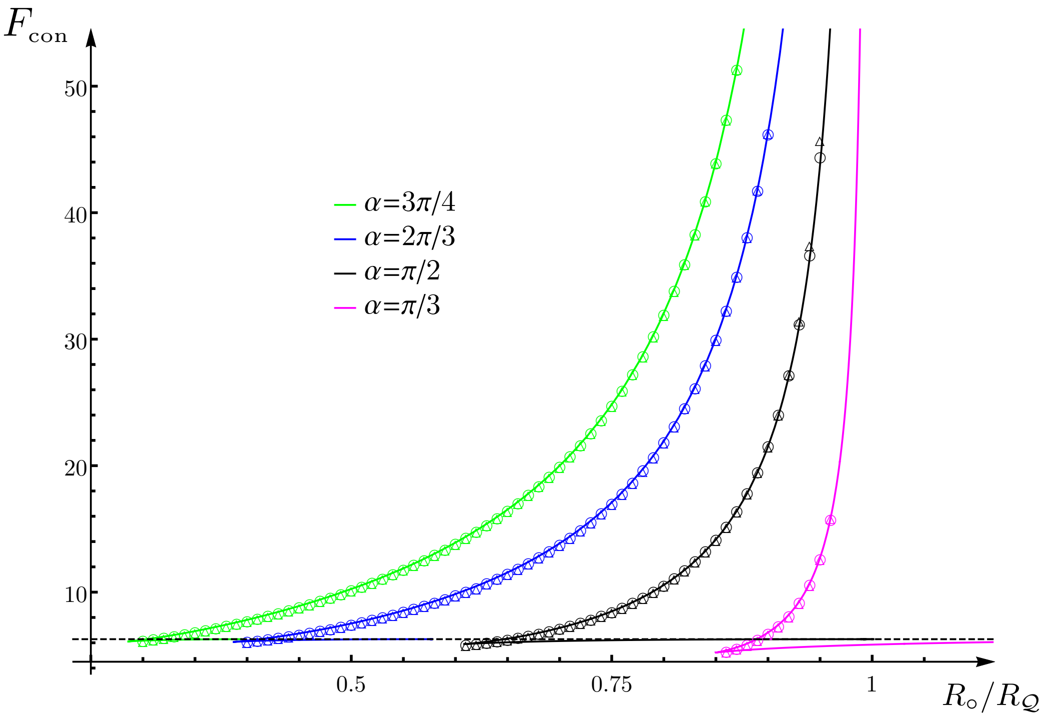

Figure 2.11: The subleading term F_{con} for the extremal surfaces $\hat{\gamma}_A^{\text{con}}$ intersecting orthogonally $\mathcal{Q}$ in terms of the ratio $R_\circ/R_{\mathcal{Q}}$, for some values of α. The allowed configurations have $R_\circ/R_{\mathcal{Q}} < 1$. The solid curves have been obtained by combining the analytic expressions (2.3.9) and (2.3.13). The horizontal dashed line corresponds to the value of the subleading term of the hemisphere $\hat{\gamma}_A^{\text{dis}}$, i.e. $F_A = 2\pi$. The data points are the numerical values obtained through Surface Evolver. The ones below the horizontal dashed line correspond to extremal surfaces that are not global minima. Different kind of markers are associated with the two different ways employed to extract F_{con} from the numerical data provided by Surface Evolver: either by subtracting the area law term from the area of the entire extremal surface (empty circles) or by applying the general formula (2.1.23) (empty triangles).

while $r_{\circ,\,\text{min}}$ is the value of $R_\circ/R_{\mathcal{Q}}$ corresponding to the cusp.

The analytic expression for F_{con} has been checked numerically with Surface Evolver, by adapting the method discussed in [154] to the configurations considered in this chapter. The numerical results are the data points in Fig. 2.11, where the two different kinds of markers (the empty circles and the empty triangles) correspond to two different ways to obtain the numerical value of F_{con} from the numerical data about the extremal surface $\hat{\gamma}_A^{\text{con}}$. One way is to evaluate $\hat{\mathcal{A}}_\varepsilon^{\text{SE}} - 2\pi R_\circ/\varepsilon$, being $\hat{\mathcal{A}}_\varepsilon^{\text{SE}}$ the numerical value of the area of the extremal surface $\hat{\gamma}_A^{\text{con}}$. The other method consists in finding F_{con} by plugging into (2.1.23) the geometrical quantities about $\hat{\gamma}_A^{\text{con}}$ required to employ this formula, which are also given by Surface Evolver.

Notice that Fig. 2.11 shows that the extremal surfaces $\hat{\gamma}_A^{\text{con}}$ do not exist when $R_\circ/R_{\mathcal{Q}} \to 0$. This means that the hemisphere $\hat{\gamma}_A^{\text{dis}}$ provides the holographic entanglement entropy in this regime, as expected.

The agreement between the solid curves and the data points in Fig. 2.11 provides a highly non-trivial confirmation of the analytic expressions obtained above.

The formula (2.3.13) can be found also by specialising the general result (2.1.24) to the extremal surfaces $\hat{\gamma}_A^{\text{con}}$ for the disks A that we are considering. The details of this computation have been reported in Appendix A.3.2, and in the following, we report only the main results. For the surface integral in (2.1.24) we find

$$\int_{\hat{\gamma}_A} \frac{(\tilde{n}^z)^2}{z^2}\, d\tilde{\mathcal{A}} \,=\, 2\pi \left(\frac{1+\eta_\alpha}{2}\, \mathcal{F}_{k,-}(\hat{z}_*) + \frac{1-\eta_\alpha}{2} \Big[\mathcal{F}_{k,+}(\hat{z}_m) + \mathcal{F}_{k,-}(\hat{z}_m) - \mathcal{F}_{k,+}(\hat{z}_*) \Big] \right) \tag{2.3.18}$$

where the functions $\mathcal{F}_{k,\pm}$ can be written in terms of the function $\mathcal{F}_k$ introduced in (2.3.14) as follows (the derivation of this identity is briefly discussed in Appendix A.3.2)

$$\mathcal{F}_{k,\pm}(\hat{z}) \,=\, \mathcal{F}_k(\hat{z}) - \frac{\sqrt{k(\hat{z}^2+1) - \hat{z}^4}}{\sqrt{k}\; \hat{z}\big(\hat{z}^2+1\big)} \pm \frac{\hat{z}^2}{\sqrt{k}\,(\hat{z}^2+1)}. \tag{2.3.19}$$

Since for $\hat{z} = \hat{z}_m$ the expression under the square root in (2.3.19) vanishes, it is straightforward to observe that, by plugging (2.3.19) into (2.3.18), one obtains (2.3.13) and an additive contribution which depends on $\hat{z}_*$ but that does not contain $\hat{z}_m$. This additive contribution is cancelled by the integral over the line $\partial\hat{\gamma}_{\mathcal{Q}} = \hat{\gamma}_A^{\text{con}} \cap \mathcal{Q}$ in (2.1.24), which gives

$$\int_{\partial\hat{\gamma}_{\mathcal{Q}}} \frac{\tilde{b}^z}{z}\, d\tilde{s} \,=\, 2\pi\, \frac{\sqrt{\hat{z}_*^2 + (\sin\alpha)^2}\;\hat{z}_* - \cos\alpha}{\hat{z}_*\,(\hat{z}_*^2+1)}. \tag{2.3.20}$$

This concludes our analysis of the disk concentric to a circular boundary. We remark that we can easily study disks which are not concentric to the circular boundary by combining the analytic expressions presented above with the mapping discussed in Appendix A.1.

2.3.2 Disk disjoint from a flat boundary

In the final part of this section we consider a disk A of radius R at a finite distance d from a flat boundary, in the AdS$_4$/BCFT$_3$ setup described in Sec. 1.4.1. By combining the results presented in Sec. 2.3.1 with the mapping (A.1.3) discussed in Appendix A.1, one can easily obtain the analytic expressions for the extremal surfaces anchored to ∂A and for the corresponding subleading term in the expansion of the area as $\varepsilon \to 0$.

The values of R and d are related to the parameters $R_\circ$ and $R_{\mathcal{Q}}$ characterising the configuration considered in Sec. 2.3.1 as follows

$$R = \frac{R_\circ\, R_{\mathcal{Q}}^2}{R_{\mathcal{Q}}^2 - R_\circ^2} \qquad\qquad d = \frac{R_{\mathcal{Q}}(R_{\mathcal{Q}} - R_\circ)}{2(R_{\mathcal{Q}} + R_\circ)}. \tag{2.3.21}$$

From these expressions it is straightforward to find that

$$\frac{d}{R} \,=\, \frac{(R_\circ/R_{\mathcal{Q}} - 1)^2}{2\, R_\circ/R_{\mathcal{Q}}} \qquad\qquad \frac{R_\circ}{R_{\mathcal{Q}}} \,=\, \frac{d}{R} + 1 - \sqrt{\frac{d}{R}\left(\frac{d}{R}+2\right)}. \tag{2.3.22}$$

Since the extremal surfaces anchored to a disk disjoint from the flat boundary in the setup of Sec. 1.4.1 are obtained by mapping the extremal surfaces described in Sec. 2.3.1 through (A.1.3), also for this configuration, we have at most three local extrema of the area functional,

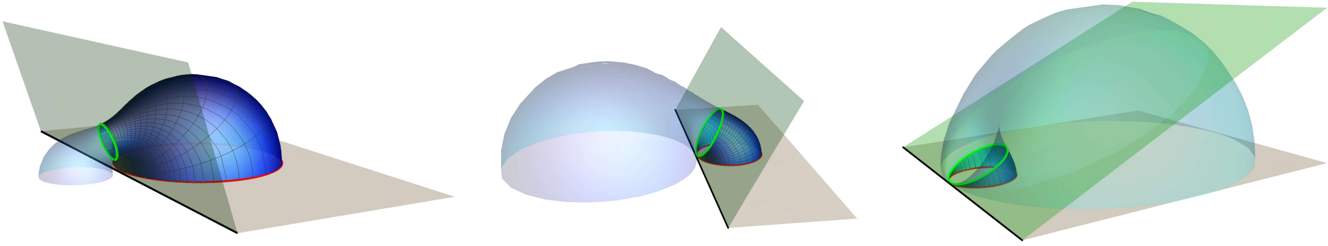

Figure 2.12: Extremal surfaces $\hat{\gamma}_A^{\text{con}}$ anchored to a disk of radius R (bounded by the red circle) at finite distance d from the flat boundary (see Sec. 2.3.2). Here $d/R \sim 0.042$ is fixed and different values of α are considered: $\alpha = \pi/2.5$ (left), $\alpha = 2\pi/3$ (middle) and $\alpha = 2.7$ (right). The surface $\hat{\gamma}_A^{\text{con}}$ intersects the green half-plane $\mathcal{Q}$ orthogonally along the green circle $\partial\hat{\gamma}_{\mathcal{Q}}$. The shaded surfaces correspond to the auxiliary surfaces $\hat{\gamma}_{A,\,\text{aux}}^{\text{con}}$ (see also Appendix A.4). The extremal surface $\hat{\gamma}_A^{\text{con}}$ is the global minimum when the corresponding F_A is larger than 2π. Here $F_A = 5.6$ (left), $F_A = 17.1$ (middle) and $F_A = 47.1$ (right). The surface in the left panel has the smallest area among the two solutions $\hat{\gamma}_A^{\text{con}}$ but the global minimum is the hemisphere $\hat{\gamma}_A^{\text{dis}}$ in this case.

depending on the ratio d/R: the hemisphere $\hat{\gamma}_A^{\text{dis}}$ and at most two solutions $\hat{\gamma}_A^{\text{con}}$ intersecting the half-plane $\mathcal{Q}$ orthogonally.

In Fig 2.12 we show some examples of $\hat{\gamma}_A^{\text{con}}$ for a fixed configuration of the disk A and three different slopes of $\mathcal{Q}$ (the green half-plane). In each panel, the shaded surface is the auxiliary surface $\hat{\gamma}_{A,\,\text{aux}}^{\text{con}}$ corresponding to $\hat{\gamma}_A^{\text{con}}$, which intersects orthogonally $\mathcal{Q}$ along $\partial\hat{\gamma}_{\mathcal{Q}}$ and is such that $\hat{\gamma}_A^{\text{con}} \cup \hat{\gamma}_{A,\,\text{aux}}^{\text{con}}$ is an extremal surface in $\mathbb{H}_3$ anchored to the two disjoint circles (one of them is ∂A). In Fig. 2.13 we show $\hat{\gamma}_A^{\text{con}}$ and the corresponding $\hat{\gamma}_{A,\,\text{aux}}^{\text{con}}$ for a fixed value of α and three different values of d/R. Notice that for some configurations $\hat{\gamma}_{A,\,\text{aux}}^{\text{con}}$ lies entirely outside the gravitational space-time bounded by $\mathcal{Q}$ (see e.g. the left panel and the middle panel of Fig 2.12), while for other ones part of $\hat{\gamma}_{A,\,\text{aux}}^{\text{con}}$ belongs to it. The latter case occurs when the auxiliary region $A_{\,\text{aux}}$ is a subset of the half-plane $x > 0$, where also A is defined.

For the extremal surfaces that we are considering, the leading term of $\mathcal{A}[\hat{\gamma}_\varepsilon]$ as $\varepsilon \to 0$ is the area law term $2\pi R/\varepsilon$ and the subleading finite term is $-\max(2\pi, \widehat{F}_{\text{con}})$, like in (2.3.12), where $\widehat{F}_{\text{con}}$ corresponds to the maximum between the values of F_{con} evaluated for the extrema $\hat{\gamma}_A^{\text{con}}$. The analytic expression of F_{con} as function of d/R can be obtained through a parametric plot involving F_{con} in (2.3.13), d/R in (2.3.22) and $R_\circ/R_{\mathcal{Q}}$ in (2.3.9). This procedure has been employed to find the solid black curves in Fig. 2.15, which correspond to a disk.

From (2.3.22), it is straightforward to observe that $d/R \to \infty$ corresponds to $R_\circ/R_{\mathcal{Q}} \to 0$, and $d/R \to 0$ to $R_\circ/R_{\mathcal{Q}} \to 1$. Thus, when $d/R \to \infty$ the hemisphere $\hat{\gamma}_A^{\text{dis}}$ is the minimal surface providing the holographic entanglement entropy (see also Sec. 2.3.1). In the opposite limiting regime $d/R \to 0$, the second expression in (2.3.22) implies that $R_\circ/R_{\mathcal{Q}} = 1 - \sqrt{2\,d/R} + d/R + O((d/R)^{3/2})$. Hence, from the expansion (2.3.17), it is straightforward to obtain that $F_{\text{con}} = 2\pi\, \mathfrak{g}(\alpha)^2/\sqrt{2d/R} + \mathcal{O}\big(\sqrt{d/R}\big)$ at leading order.

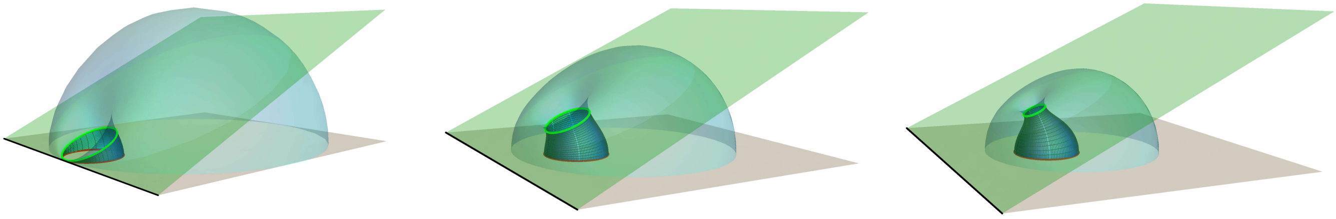

Figure 2.13: Extremal surfaces $\hat{\gamma}_A^{\text{con}}$ anchored to a disk (bounded by the red circle) of radius R at finite distance d from the flat boundary, like in Fig. 2.12. Here $\alpha = 2.7$ is fixed (like in the right panel of Fig. 2.12) and the different values of d/R are considered: $d/R \sim 0.042$ (left), $d/R \sim 1.6$ (middle) and $d/R \sim 2.243$ (right). The shaded surfaces correspond to $\hat{\gamma}_{A,\,\text{aux}}^{\text{con}}$ and for all the configurations of this figure part of $\hat{\gamma}_{A,\,\text{aux}}^{\text{con}}$ belongs to the gravitational space-time constraint by $x \geqslant -(\cot\alpha)z$ (see also Appendix A.4). The extremal surface $\hat{\gamma}_{A,\,\text{aux}}^{\text{con}}$ is a global minimum when its F_A is larger than 2π. The configuration in the left panel is the same as shown in the right panel of Fig. 2.12. In the remaining panels $F_A = 6.95$ (middle) and $F_A = 6.13$ (right).

2.4 On smooth domains disjoint from the boundary

Analytic expressions for the subleading term F_A in (2.0.1) can be obtained for configurations which are particularly simple or highly symmetric. Two important cases have been discussed in Sec. 2.2 and Sec. 2.3. In order to find analytic solutions for an extremal surface anchored to a generic entangling curve, typically a partial differential equation must be solved, which is usually a difficult task. Thus, it is useful to develop efficient numerical methods that allow us to study the shape dependence of F_A.

The crucial tool of our numerical analysis is Surface Evolver, which has been already employed to study the holographic entanglement entropy in AdS$_4$/CFT$_3$ [78, 245] and to check the corner functions in AdS$_4$/BCFT$_3$ in Sec. 1.3.3. Surface Evolver has been introduced in the previous chapter (see Sec. 1.6). In this chapter, we consider some regions disjoint from the boundary in AdS$_4$/BCFT$_3$. In Sec. 2.3.1 Surface Evolver has been used to check the analytic expressions numerically of the extremal surfaces and of F_A for a disk concentric to a circular boundary (see Fig. 2.8 and Fig. 2.11 respectively). In this section, we use Surface Evolver to study the extremal surfaces $\hat{\gamma}_A$ and the corresponding F_A for some simple domains which cannot be treated through analytic methods.

Considering the simple AdS$_4$/BCFT$_3$ setup described in Sec. 2.1.1, in Fig. 2.1 we showed the extremal surface corresponding to a region A with a complicated shape (the entangling curve is the red curve in the inset) which has been constructed by using Surface Evolver and which is very difficult to describe analytically.

In the same setup, let us consider, for simplicity, regions A delimited by ellipses at a distance d from the flat boundary with one of the semiaxis parallel to the flat boundary. These regions are given by the points $(x, y) \in \mathbb{R}^2$ with $x > 0$ such that $(x - d - R_\perp)^2/R_\parallel^2 + y^2/R_\perp^2 \leqslant 1$, where $R_\perp$ and $R_\parallel$ are the lengths of the semiaxis which are respectively orthogonal and parallel to the flat boundary $x = 0$. As for the extremal surfaces anchored to the entangling curve ∂A, either they are disconnected from the half-plane $\mathcal{Q}$ or they intersect it

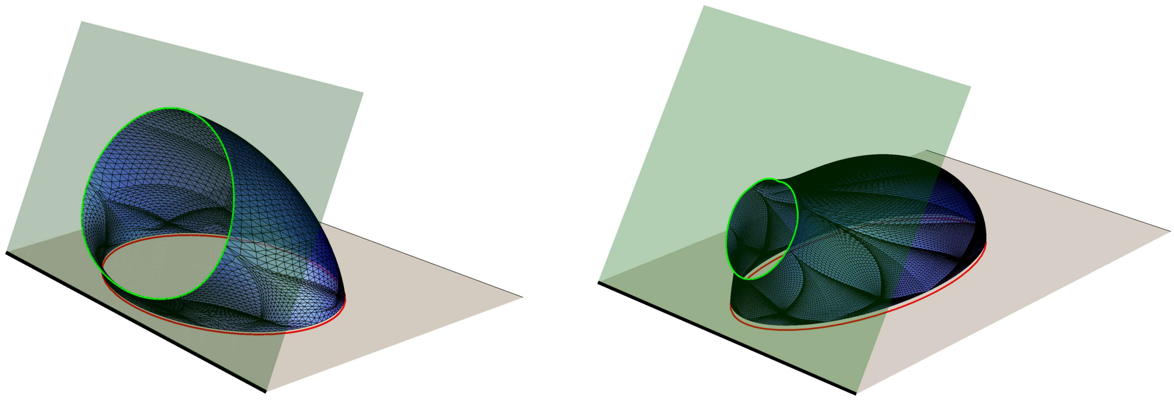

Figure 2.14: Extremal surfaces $\hat{\gamma}_A^{\text{con}}$ found with Surface Evolver in the gravitational setup described in Sec. 2.1.1. The extremal surfaces are anchored to the boundary of two different ellipses A (red curves) and intersect the half-plane $\mathcal{Q}$ with $\alpha = 2\pi/3$ (green half-plane) orthogonally. Here $\varepsilon = 0.03$. Denoting by $R_\perp$ and $R_\parallel$ the lengths of the semiaxis which are respectively orthogonal and parallel to the flat boundary, and by d the distance of ∂A from the flat boundary, we have $d/R_\perp = 0.2$ in both the panels. Instead, $R_\parallel = 2R_\perp$ in the left panel and $R_\parallel = 0.5R_\perp$ in the right panel.

orthogonally. The occurrence of this different kind of extremal surfaces and which of them gives the global minimum depend on the values of α, of the ratio $d/R_\perp$ and of the eccentricity of A. For some configurations only the solutions disconnected from $\mathcal{Q}$ are allowed, while for other configurations only the extremal surfaces intersecting $\mathcal{Q}$ exist, as discussed in a specific example in the final part of Sec. 2.3.1. In Fig. 2.14 we show two examples of extremal surfaces anchored to ellipses in the $z = 0$ half-plane (the red curves) which intersect $\mathcal{Q}$ orthogonally along the green line $\partial\hat{\gamma}_{\mathcal{Q}}$.

In Fig. 2.15 the values of the subleading term for extremal surfaces intersecting $\mathcal{Q}$ and anchored to various ellipses are plotted in terms of the ratio $d/R_\perp$. These data points have been obtained through Surface Evolver by first constructing the extremal surface $\hat{\gamma}_\varepsilon^{\text{SE}}$ anchored to the ellipses defined at $z = \varepsilon$ and then employing the information about $\hat{\gamma}_\varepsilon^{\text{SE}}$ provided by the code (in particular its area $\mathcal{A}[\hat{\gamma}_\varepsilon^{\text{SE}}]$ and its normal vectors) in two different ways. One way to extract the subleading term is to compute $P_A/\varepsilon - \mathcal{A}[\hat{\gamma}_\varepsilon^{\text{SE}}]$ (empty circles in Fig. 2.15). Another way is to evaluate (2.1.25) from the unit vector $\tilde{n}^\mu$ normal to $\hat{\gamma}_\varepsilon^{\text{SE}}$ (empty triangles in Fig. 2.15). The agreement between these two approaches provides a non-trivial check of the functional (2.1.25). The numerical analysis has been performed by adapting the method discussed in [154] to the configurations considered here.

The horizontal dashed lines in Fig. 2.15 correspond to the extremal surfaces that do not intersect $\mathcal{Q}$. Denoting by F_{dis} the subleading term in the expansion of $\mathcal{A}[\hat{\gamma}_\varepsilon^{\text{SE}}]$ for these surfaces, we have that F_A in (2.0.1) is finite and given by $F_A = \max(F_{\text{con}}, F_{\text{dis}})$. The relation $F_{\text{con}} = F_{\text{dis}}$ provides the critical value of $d/R_\perp$ characterising the transition in the holographic entanglement entropy between the surfaces connected to $\mathcal{Q}$ and the ones disjoint from $\mathcal{Q}$ (see the intersection between the curve identified by the data points and the horizontal dashed line having the same colour in Fig. 2.15, except for the magenta points, that must be compared with the red dashed line).

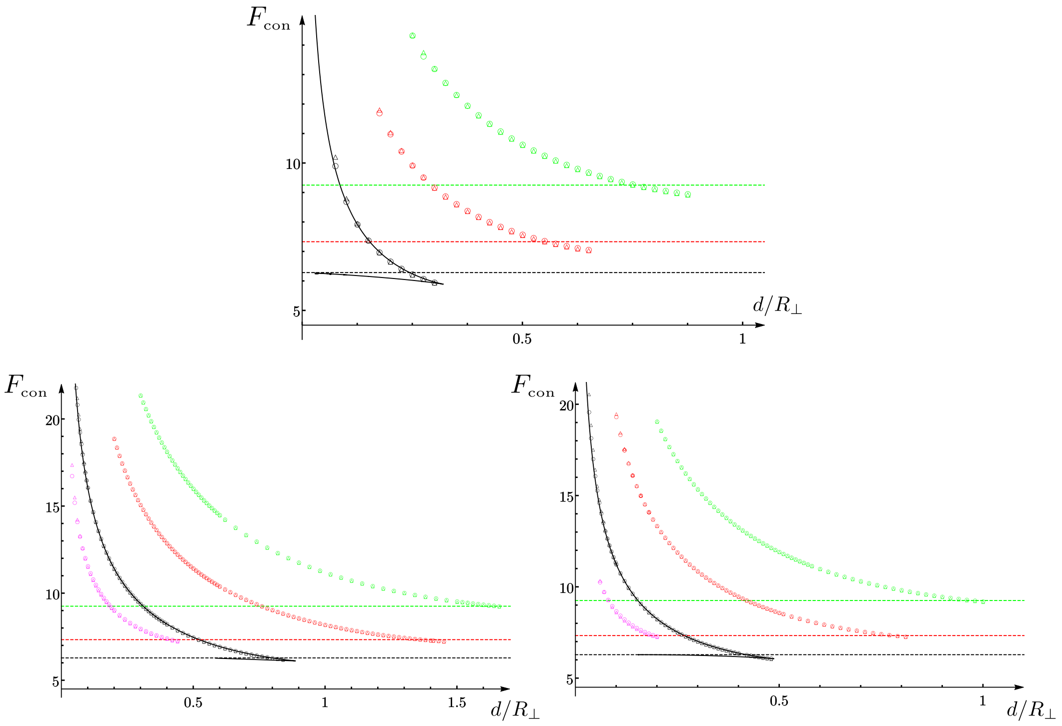

Figure 2.15: The subleading term $F_{\rm con}$ for the extremal surfaces $\hat{\gamma}_A^{\rm con}$ intersecting orthogonally the half-plane $\mathcal{Q}$ and anchored to ellipses at distance d from a flat boundary (see Fig. 2.14). A semiaxis of the ellipse is orthogonal to the flat boundary, and its length is $R_\perp$, while $R_\parallel$ is the length of the other one. The three panels are characterised by three diverse values of the slope α for the half-plane $\mathcal{Q}$ (see Fig. 2.14): $\alpha = \pi/2$ (top), $\alpha = 2\pi/3$ (bottom right) and $\alpha = 3\pi/4$ (bottom left). Different colours correspond to different eccentricities: $R_\parallel = 3R_\perp$ (green), $R_\parallel = 2R_\perp$ (red), $R_\parallel = R_\perp$ (black) and $R_\parallel = 0.5R_\perp$ (magenta). The solid black curves correspond to the analytic expressions obtained in Sec. 2.3.2 for disks. The dashed horizontal lines provide the value $F_A = F_{\rm dis}$ for the extremal surfaces disconnected from $\mathcal{Q}$. In particular, $F_{\rm dis} = 9.25$ (green), $F_{\rm dis} = 2\pi$ (black) and $F_{\rm dis} = 7.33$ (red and magenta).

The black points in Fig. 2.15 correspond to disks disjoint from a flat boundary and the solid black curves have been obtained through the analytic expressions discussed in Sec. 2.3 (see (2.3.13) and (2.3.22)). The nice agreement with the data points found with Surface Evolver is a strong check for the analytic expressions.

In Sec. 2.3 we have found that the critical value α_c (defined as the unique zero of (2.2.2)) for the slope of $\mathcal{Q}$ in the AdS$_4$/BCFT$_3$ setup of Sec. 2.1.1 is such that extremal surfaces anchored to a disk A disjoint from the flat boundary and intersecting $\mathcal{Q}$ orthogonally do not exist for $\alpha \leqslant \alpha_c$. We find it reasonable to conjecture the validity of this property (with same α_c) for any smooth region A disjoint from the boundary in the AdS$_4$/BCFT$_3$ setups described in Sec. 1.4.1 and Sec. 1.4.2.

We find it worth exploring the existence of bounds on the subleading term F_A. In the AdS$_4$/CFT$_3$ duality when the dual gravitational background is AdS$_4$, by employing a well known bound for the Willmore functional in $\mathbb{R}^3$, it has been shown that $F_A \geqslant 2\pi$ for any kind of spatial region, including the ones with singular ∂A and the ones made by disjoint components [78].

In the remaining part of this section, we discuss that, in the context of AdS$_4$/BCFT$_3$ and when the gravitational dual is the part of AdS$_4$ delimited by $\mathcal{Q}$ and the conformal boundary, for any kind of spatial region A disjoint from the boundary we have

$$F_A \geqslant 2\pi. \tag{2.4.1}$$

If A contains at least one corner, this bound is trivially satisfied because F_A diverges logarithmically and the coefficient of this divergence is positive, being determined by the corner function of [157].

For regions A with smooth ∂A, the subleading term F_A in (2.0.1) is finite and the corresponding minimal surface $\hat{\gamma}_A$ is such that either $\hat{\gamma}_A \cap \mathcal{Q} = \emptyset$ or $\hat{\gamma}_A \cap \mathcal{Q} \neq \emptyset$. In the former case $\hat{\gamma}_A$ is also a minimal surface in $\mathbb{H}_3$, therefore we can employ the observation made in [78] and discussed in Sec. 1.3.3 for AdS$_4$/CFT$_3$ and conclude that (2.4.1) holds.

If $\hat{\gamma}_A \cap \mathcal{Q} \neq \emptyset$, let us denote by $F_A = F_{\text{con}}$ the value of the subleading term corresponding to $\hat{\gamma}_A$. In these cases, we have two possibilities: either another extremal surface $\hat{\gamma}_A^{\text{dis}}$ such that $\hat{\gamma}_A^{\text{dis}} \cap \mathcal{Q} = \emptyset$ exists or not. In the former case, being $\hat{\gamma}_A$ the global minimum, we have that $F_{\text{con}} \geqslant F_{\text{dis}} \geqslant 2\pi$, where the last inequality is obtained from the observation of [78], as above.

The remaining configurations are the ones such that only the extremal surface $\hat{\gamma}_A$ with $\hat{\gamma}_A \cap \mathcal{Q} \neq \emptyset$ exists (see e.g. the explicit case discussed in the final part of Sec. 2.3.1). In these cases $\hat{\gamma}_A^{\text{dis}}$ does not occur because, by introducing the extremal surface $\hat{\gamma}_A^{(0)}$ in $\mathbb{H}_3$ anchored to ∂A, we have that $\hat{\gamma}_A^{(0)} \cap \mathcal{Q} \neq \emptyset$. Let us consider the part $\hat{\gamma}_A^{\angle} \subset \hat{\gamma}_A^{(0)}$ of $\hat{\gamma}_A^{(0)}$ belonging to the region of AdS$_4$ delimited by $\mathcal{Q}$ and the conformal boundary. We remark that $\hat{\gamma}_\varepsilon^{\angle}$ intersects $\mathcal{Q}$ but, typically, they are not orthogonal along their intersection. Restricting both $\hat{\gamma}_A^{(0)}$ and $\hat{\gamma}_A^{\angle}$ to $z \geqslant \varepsilon$, for the resulting surfaces $\hat{\gamma}_\varepsilon^{(0)}$ and $\hat{\gamma}_\varepsilon^{\angle}$ the expansion (2.0.1) holds with the same $P_{A,B}$ but different $O(1)$ terms, that will be denoted by $F_A^{(0)}$ and $F_A^{\angle}$ respectively. Notice that the observation of [78] here gives $F_A^{(0)} \geqslant 2\pi$. Since $\hat{\gamma}_A^{\angle} \subset \hat{\gamma}_A^{(0)}$, we have $\mathcal{A}[\hat{\gamma}_\varepsilon^{(0)}] \geqslant \mathcal{A}[\hat{\gamma}_\varepsilon^{\angle}]$, which implies $F_A^{(0)} \leqslant F_A^{\angle}$, being $P_{A,B}$ the same for $\hat{\gamma}_\varepsilon^{(0)}$ and $\hat{\gamma}_\varepsilon^{\angle}$. Since F_{con} corresponds to an extremal surface and $\hat{\gamma}_\varepsilon^{\angle}$ is not extremal, we can conclude that $F_{\text{con}} \geqslant F_A^{\angle}$. Collecting these observations, we find that $F_{\text{con}} \geqslant F_A^{\angle} \geqslant F_A^{(0)} \geqslant 2\pi$.

This completes our discussion about the validity of the inequality (2.4.1) for any spatial region A disjoint from the boundary, including the ones having singular ∂A or that are made by disjoint connected components. We find it worth remarking that the bound (2.4.1) does not hold in general when A is adjacent to the boundary because as we will see in the next chapter 3 the corner function is negative for some configurations.

2.5 Discussion

In this chapter we studied the shape dependence of the holographic entanglement entropy in AdS$_4$/BCFT$_3$, along the lines of [89–91, 154, 158, 160, 161, 262]. Considering the expansion of the holographic entanglement entropy as the UV cutoff vanishes, our main result is the analytic formula (2.1.18) for the subleading term F_A, which can be applied for any spatial region and any static gravitational background.

We have analysed some specific cases that admit an explicit solution of the minimal surfaces. Thus, in Sec. 2.2 we focused on the holographic dual of the vacuum state of BCFT_3 with a flat boundary. In this setup we found analytic expressions corresponding to infinite strips which can be either adjacent to the flat boundary (see Sec. 2.2.2) or parallel and disjoint from it (see Sec. 2.2.2). In these cases, we found a particular value of $\alpha = \alpha_c$ for which a *transition* between the extremal surfaces connected and disconnected to $\mathcal{Q}$ happens. More precisely, *when* $\alpha \leqslant \alpha_c$ *the connected solution does not exist.* We have also shown that the subleading term F_A can be recovered by employing the general formula (2.1.18), providing a first check. In the appendix A.2 details of the derivations and the generalization to higher dimensions are reported.

The second explicit result is the analytic study of the extremal surfaces anchored to disks disjoint from a boundary which is either flat or circular, when the gravitational background is a part of $\mathbb{H}_3$. The corresponding expression for the subleading term F_A has been obtained both by evaluating the area in the standard way and by specialising (2.1.18) to this configuration. The software Surface Evolver has also been employed to obtain a numerical check of the analytic formulas. By studying the limit regime of very large regions A when the BCFT_3 is a disk, we found again the same value $\alpha = \alpha_c$ below which the minimal surfaces are always disconnected from $\mathcal{Q}$. This result suggests that this value is valid for any region disjoint from the boundary, and it would be interesting to explore this fact further. Another question that is worth to address is understanding the meaning of this transition in the field theory. We hope to make progress on these questions in the future.

As for our last analytic result of this chapter, when the spatial section of the gravitational spacetime is a part of $\mathbb{H}_3$, we found the bound $F_A \geqslant 2\pi$ for any region A that does not intersect the boundary.

Finally, we employed the software Surface Evolver to obtain numerical results for elliptic entangling regions disjoint from the boundary providing a highly non-trivial check of the general formula (2.1.18).

Chapter 3

Corner Contributions to Holographic Entanglement Entropy in $\mathrm{AdS}_4/\mathrm{BCFT}_3$

In this chapter, we study the entanglement entropy in $\mathrm{AdS}_4/\mathrm{BCFT}_3$ when the entangling curve intersects the boundary of the BCFT_3, focusing on the flat boundary case. More specifically, we consider the holographic setup discussed in Sec. 1.4.1 in which the holographic spacetime is AdS_4 restricted by the boundary $\mathcal{Q}$ such that $x \geqslant -(\cot\alpha)z$ in Poincaré coordinates.

Given a generic BCFT_3, we shall focus on two-dimensional regions A whose boundaries ∂A contain some isolated vertices that are all located on the boundary of the spatial half-plane, which is the straight line $x = 0$. A prototypical example is the yellow domain on the left panel of Fig. 3.1. The entanglement entropy for this case has been briefly discussed in Sec. 1.2.2. We recall that for this kind of domains, the expansion of the entanglement entropy as $\varepsilon \to 0^+$ reads

$$S_A \,=\, b\,\frac{P_{A,B}}{\varepsilon} - f_{\alpha,\mathrm{tot}} \log(P_{A,B}/\varepsilon) + O(1) \tag{3.0.1}$$

where $P_{A,B} \equiv \mathrm{length}(\partial A \cap \partial B)$ is the length of the entangling curve (the red curves on the left and right panel of Fig. 3.1). In the rest of this chapter, we are interested in the coefficient of the logarithmic divergence in (3.0.1), which is expected to depend on the boundary conditions characterising the BCFT_3 in a highly non-trivial way. The index α labels the boundary conditions allowed by the conformal invariance in the underlying model.

In particular, we are going to consider domains A with vertices on the $x = 0$ line both of the types P_1, P_2 and Q_1 depicted in Fig. 3.1. The vertices of the P type are characterised only by an angle γ, while the Q vertices are determined by a pair $\vec{\omega}$ of opening angles.

For this class of regions A, the coefficient $f_{\alpha,\mathrm{tot}}$ of the logarithmic divergence in (3.0.1) is obtained by summing the contributions of all the corners on the boundary, namely

$$f_{\alpha,\mathrm{tot}} = \sum_{P_i} f_\alpha(\gamma_{P_i}) + \sum_{Q_j} \mathsf{F}_\alpha(\vec{\omega}_{Q_j}) \tag{3.0.2}$$

where f_α and F_α are corner functions that depend on the boundary conditions of the BCFT_3.

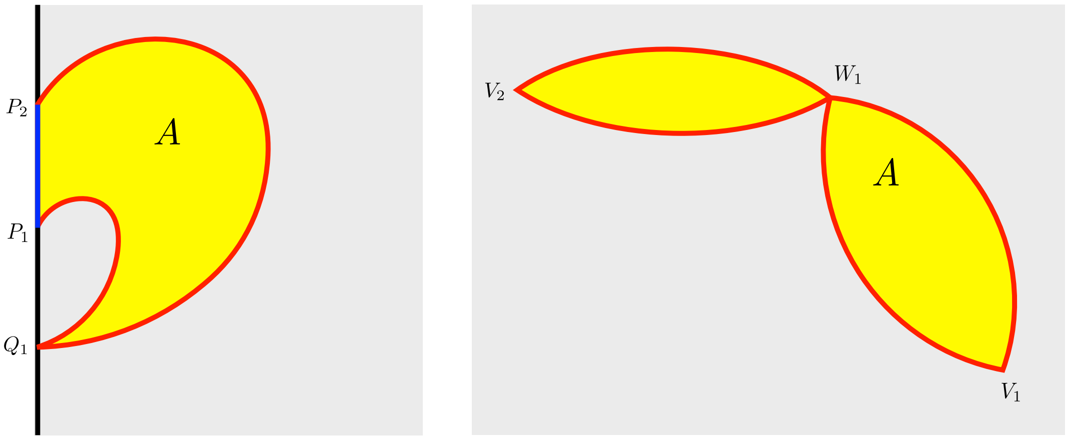

Figure 3.1: Examples of finite two-dimensional regions A (yellow domains) containing the kinds of corners considered in this chapter. Left: A is a domain in the plane with three corners and two different kinds of vertices. Right: A is a domain in the half-plane with three corners whose boundary ∂A intersects the boundary of the BCFT$_3$ (solid black line). The three vertices in ∂A are also on the boundary of the BCFT$_3$, and they belong to two different classes of vertices. In both panels, the red curve corresponds to the entangling curve $\partial A \cap \partial B$, whose length provides the area law term in (1.1.17) and in (3.0.1).

In the holographic framework, by employing the Ryu-Takayanagi formula (1.3.2) properly adapted to the AdS/BCFT setup as discussed in Sec. 1.4.3, we will find

$$\mathcal{A}[\hat{\gamma}_\varepsilon] = R^2_{\text{AdS}} \left(\frac{P_{A,B}}{\varepsilon} - F_{\alpha,\text{tot}} \log(P_{A,B}/\varepsilon) + O(1) \right) \tag{3.0.3}$$

where $P_{A,B}$ is the length of the entangling curve in the boundary at $z = 0$. We are mainly interested in the coefficient of the logarithmic divergence, which is given by the sum of the contributions from all the vertices of ∂A, namely

$$F_{\alpha,\text{tot}} = \sum_{P_i} F_\alpha(\gamma_{P_i}) + \sum_{Q_j} \mathcal{F}_\alpha(\omega_{Q_j}, \gamma_{Q_j}) \tag{3.0.4}$$

where the functions occurring in the sums depend on the slope α of the half-plane $\mathcal{Q}$ (1.4.9). We mainly refer to $F_\alpha(\gamma)$ and $\mathcal{F}_\alpha(\omega, \gamma)$ as the holographic corner functions in the presence of a boundary, although the proportionality constant $\frac{R^2_{\text{AdS}}}{4G_{\text{N}}}$ should be taken into account.

In this chapter, we find analytic expressions for the corner functions $F_\alpha(\gamma)$ and $\mathcal{F}_\alpha(\omega, \gamma)$. Numerical checks of these results are performed by constructing the minimal area surfaces corresponding to some finite domains containing corners. In the numerical analysis, we have employed the software Surface Evolver [152, 153] introduced in Sec. 1.6 to construct the minimal area surfaces. This numerical tool has been already used in [78, 245] to study the shape dependence of the holographic entanglement entropy in AdS$_4$/CFT$_3$, and in chapter 2 where entangling regions disjoint from the boundary in the AdS$_4$/BCFT$_3$ framework have been considered.

This chapter is organised as follows. In Sec. 3.1 the strong subadditivity is employed to find constraints for the corner functions $f_\alpha(\gamma)$ and $\mathsf{F}_\alpha(\omega, \gamma)$ in a generic BCFT$_3$. In Sec. 3.2

we describe the main result of this chapter, namely the holographic boundary corner function $F_\alpha(\gamma)$. We apply the prescription for the holographic entanglement entropy to two simple domains, i.e., the half-disk centered on the boundary (Sec. 3.2.1) and the infinite wedge (Sec. 3.2.2), whose area provides the analytic expression of $F_\alpha(\gamma)$. Furthermore, in Sec. 3.2.3 we will recover the boundary corner function also by employing the expression (2.1.25) for the subleading term F_A obtained the previous chapter. In Sec. 3.3, we find the one-point function of the stress-energy tensor in the presence of a curved boundary in the Takayanagi setup. By performing perturbation about the flat boundary case, we extract the coefficient A_T in (1.2.8) for any dimension $d \geqslant 1$. From this result and the analytical expression of $F_\alpha(\gamma)$, in Sec. 3.4 we discuss a proportionality relation between A_T and $F''_\alpha(\pi/2)$. In Sec. 3.5, we study transitions in the minimal surfaces both when the domain A has two corners with the same tip in AdS$_4$/CFT$_3$ (see the right side of Fig. 3.1), and in the presence of one corner of the Q-type depicted on the left side of Fig. 3.1. In particular, we will find the analytic formula for the corner function $\mathcal{F}_\alpha(\omega,\gamma)$. Throughout this chapter, the analytic results are double-checked against the numerical calculation obtained with Surface Evolver.

The main text of this chapter contains only the description of the main results. All the computational details and also some generalisations to an arbitrary number of spacetime dimensions have been collected and discussed in the appendices B.1, B.2, and B.3.

3.1 Constraining the corner functions

In this section, we employ the strong subadditivity of the entanglement entropy (1.1.7) to constrain the corner functions introduced in (3.0.2). Our analysis is similar to the one performed in [178] for the corner function $\tilde{f}(\theta)$ in (1.1.18).

Let us consider a BCFT$_3$ in its ground state and the domain A given by the infinite wedge adjacent to the boundary whose opening angle is γ. Thus, the complementary domain B is the infinite wedge with opening angle $\pi - \gamma$. Since the ground state is a pure state, we have $S_A = S_B$. Combining this property with (3.0.1) and (3.0.2) specialised to these complementary domains, we have

$$f_\alpha(\pi-\gamma) = f_\alpha(\gamma) \tag{3.1.1}$$

namely the corner function $f_\alpha(\gamma)$ is symmetric with respect to $\gamma = \pi/2$; therefore we are allowed to study this corner function for $0 < \gamma \leqslant \pi/2$. Hereafter we mainly consider $\gamma \in (0, \pi/2]$ for the argument of this corner function. Nonetheless, whenever $\gamma \in (0,\pi)$ in the following, we always mean $f_\alpha(\gamma) = f_\alpha(\min[\gamma, \pi-\gamma])$.

By assuming that $f_\alpha(\gamma)$ is smooth for $\gamma \in (0,\pi)$, the symmetry (3.1.1) implies that its expansion around $\gamma = \pi/2$ includes only even powers of $\gamma - \pi/2$, namely

$$f_\alpha(\gamma) = f_\alpha(\pi/2) + \frac{f''_\alpha(\pi/2)}{2}\,(\gamma-\pi/2)^2 + \dots \qquad \gamma \to \frac{\pi}{2}. \tag{3.1.2}$$

In the remaining part of this section, we discuss some constraints for the corner functions in (3.0.2) obtained by imposing that the strong subadditivity of the entanglement entropy is valid for particular configurations of adjacent domains.

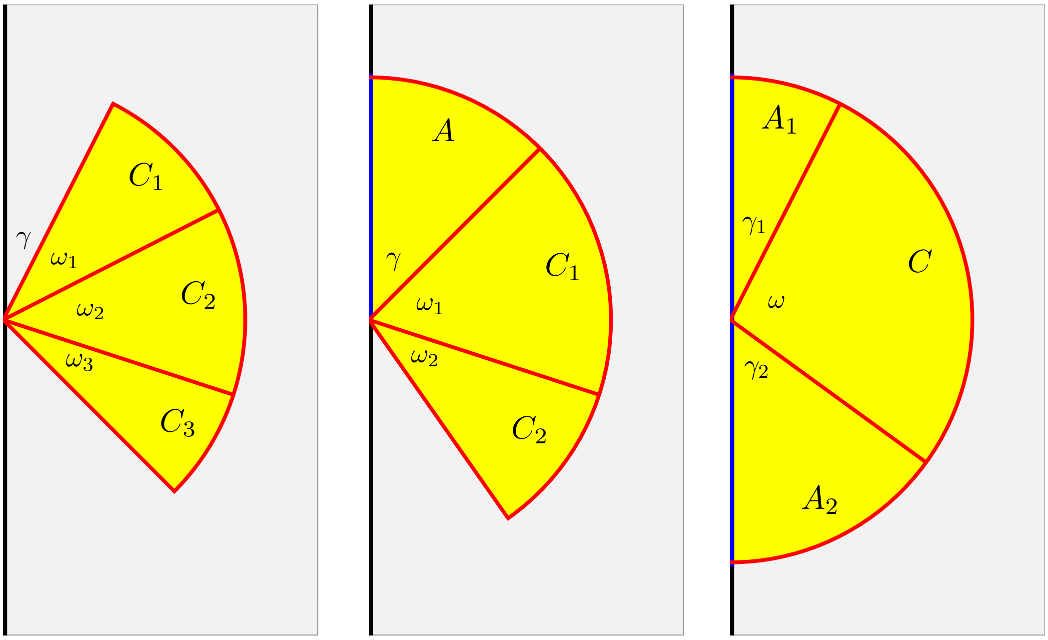

Figure 3.2: Configurations of adjacent domains containing corners (yellow regions) in the half-plane $x \geqslant 0$ (grey region) which have been used in Sec. 3.1 to constrain the corner functions through the strong subadditivity.

Consider the configuration of adjacent regions shown in the left panel of Fig. 3.2. The strong subadditivity inequality specialised to this case states that

$$S_{C_1 \cup C_2} + S_{C_2 \cup C_3} \geqslant S_{C_1 \cup C_2 \cup C_3} + S_{C_2}. \tag{3.1.3}$$

By employing the expressions (3.0.1) and (3.0.2), which provide the entanglement entropy of the domains occurring in this inequality, one observes that the area law terms and the logarithmic divergencies corresponding to vertices which are not on the boundary simplify. The remaining terms at leading order provide the following inequality

$$\mathsf{F}_\alpha(\omega_1+\omega_2+\omega_3,\gamma) - \mathsf{F}_\alpha(\omega_1+\omega_2,\gamma) \geqslant \mathsf{F}_\alpha(\omega_2+\omega_3,\gamma+\omega_1) - \mathsf{F}_\alpha(\omega_2,\gamma+\omega_1). \tag{3.1.4}$$

Multiplying both sides of this inequality by $1/\omega_3 > 0$ first and then taking the limit $\omega_3 \to 0^+$, one finds

$$\partial_\omega \, \mathsf{F}_\alpha(\omega_2+\omega_1,\gamma) \,\geqslant\, \partial_\omega \, \mathsf{F}_\alpha(\omega_2,\gamma+\omega_1). \tag{3.1.5}$$

Next we add $-\,\partial_\omega \mathsf{F}_\alpha(\omega_2,\gamma)$ to both sides of (3.1.5), then we multiply them by $1/\omega_1 > 0$ and finally take the limit $\omega_1 \to 0^+$. The resulting inequality reads

$$\partial^2_\omega \, \mathsf{F}_\alpha(\omega,\gamma) \,\geqslant\, \partial_\omega \partial_\gamma \, \mathsf{F}_\alpha(\omega,\gamma). \tag{3.1.6}$$

This property resembles to $\tilde{f}''(\omega) \geqslant 0$ for the corner function $\tilde{f}(\omega)$ in CFT$_3$ [178] discussed in Sec.1.1.2 (see equation (1.1.19)).

The second configuration of adjacent domains that we consider is the one depicted in the middle panel of Fig. 3.2. In this case, the constraint given by the strong subadditivity reads

$S_{A\cup C_1} + S_{C_1\cup C_2} \geqslant S_{A\cup C_1\cup C_2} + S_{C_1}$ and simplifications similar to the ones discussed in the previous case occur. In particular, the leading non-vanishing terms correspond to the vertex shared by the three domains. The resulting inequality reads

$$f_\alpha(\gamma+\omega_1+\omega_2) - f_\alpha(\gamma+\omega_1) \geqslant \mathsf{F}_\alpha(\omega_1+\omega_2,\gamma) - \mathsf{F}_\alpha(\omega_1,\gamma). \tag{3.1.7}$$

Multiplying both sides of this relation by $1/\omega_1 > 0$ and taking the limit $\omega_1 \to 0^+$, one obtains

$$\partial_\omega \mathsf{F}_\alpha(\omega,\gamma) \leqslant \partial_\gamma f_\alpha(\gamma+\omega). \tag{3.1.8}$$

Let us study also the configuration shown in the right panel of Fig. 3.2, where $\gamma_1+\omega+\gamma_2 = \pi$ and the strong subadditivity property provides the constraint $S_{A_1\cup C} + S_{A_2\cup C} \geqslant S_{A_1\cup A_2\cup C} + S_C$. By using (3.0.1) and (3.0.2) as done in the previous cases, we get another inequality among the corner functions corresponding to the vertex shared by the three adjacent domains

$$f_\alpha(\gamma_1+\omega) + f_\alpha(\gamma_2+\omega) \leqslant \mathsf{F}_\alpha(\omega,\gamma_1) \qquad \gamma_1 \leqslant \gamma_2. \tag{3.1.9}$$

Since $\gamma_2 + \omega = \pi - \gamma_1$, we can employ (3.1.1), finding that (3.1.9) can be written as

$$f_\alpha(\gamma+\omega) + f_\alpha(\gamma) \leqslant \mathsf{F}_\alpha(\omega,\gamma) \qquad \gamma \leqslant \frac{\pi-\omega}{2}. \tag{3.1.10}$$

We remark that the constraints (3.1.6), (3.1.8) and (3.1.10) hold whenever the entanglement entropy is given by (3.0.1) and (3.0.2), with corner functions which are regular enough to define the derivatives occurring in these inequalities.

3.2 The boundary corner function in AdS$_4$/BCFT$_3$

In this section we study the holographic boundary corner function $F_\alpha(\gamma)$ defined in (3.0.3) and (3.0.4). We will employ two simple entangling regions which allow us finding the analytic solution of the Ryu-Takayanagi minimal surface and the corresponding holographic entanglement entropy. The first domain we consider is the half-disk centered on the boundary (Sec. 3.2.1) from which we extract the quantity $F_\alpha(\pi/2)$. In the following subsection (Sec. 3.2.2) we study the infinite wedge that provides the whole boundary corner function $F_\alpha(\gamma)$.

3.2.1 Half-disk centered on the boundary

Let us consider the half-disk A of radius R whose center is located on the boundary of the BCFT$_3$., i.e. in Cartesian coordinates $A = \{(x,y)\in\mathbb{R}^2\,|\,x^2+y^2 \leqslant R^2,\, x \geqslant 0\}$. In BCFT$_3$ the entanglement entropy of this domain has been studied in [264], by using the method of [224].

In our AdS$_4$/BCFT$_3$ setup the constraint $z \geqslant -(\cot\alpha)z$ due to the occurrence of the half-plane $\mathcal{Q}$ must be taken into account. The key observation is that the hemisphere $x^2+y^2+z^2 = R^2$ in $\mathbb{H}_3$ intersects the half-plane $\mathcal{Q}$ orthogonally along a semi-circumference of radius R centered on the origin. As discussed in Sec. 1.3.1, this hemisphere is the minimal area surface anchored to the circular curve $x^2+y^2 = R^2$ in the $z = 0$ plane [31, 32, 217, 247]. Thus, the minimal surface $\hat{\gamma}_A$ corresponding to the half-disk A in presence of $\mathcal{Q}$ is part of the minimal

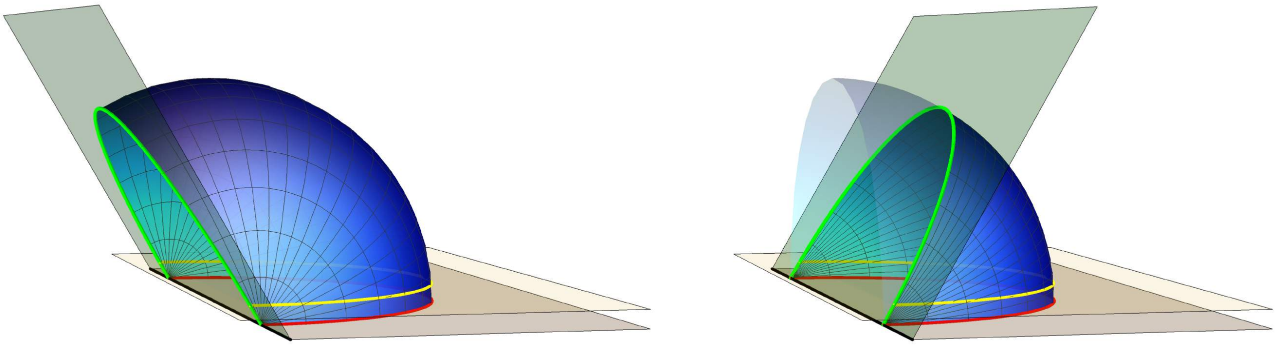

Figure 3.3: Minimal surfaces $\hat{\gamma}_A$ corresponding to the half-disk centered on the boundary. The green half-plane is $\mathcal{Q}$ in (1.4.9), while the grey half-plane is $z = 0$. In the left panel $\alpha < \pi/2$, while in the right panel $\alpha > \pi/2$. The green curve is $\hat{\gamma}_A \cap \mathcal{Q}$ and the red curve is the entangling curve $\partial A \cap \partial B$, whose length enters in the area law term of (3.2.1). The yellow half-plane is defined by $z = \varepsilon$, and the yellow curve corresponds to its intersection with $\hat{\gamma}_A$.

area surface $\hat{\gamma}_{A,\text{aux}} = \{(x, y, z) \in \mathbb{H}_3 \,|\, x^2 + y^2 + z^2 = R^2\}$ anchored to the boundary of the auxiliary domain $A_{\text{aux}} \subset \mathbb{R}^2 = \partial\mathbb{H}_3$ given by a disk of radius R which includes A as a proper subset. In particular $\hat{\gamma}_A$ is the part of $\hat{\gamma}_{A,\text{aux}}$ identified by the constraint $x \geqslant -(\cot\alpha)z$.

In Fig. 3.3 we show $\hat{\gamma}_A$ for a case having $\alpha < \pi/2$ in the left panel and for a case with $\alpha > \pi/2$ in the right panel. Notice that the boundary of $\hat{\gamma}_A$ is a continuous curve made by two arcs whose opening angles are equal to π: the arc in the $z = 0$ half-plane defined by $\{(x, y) \,|\, x^2 + y^2 = R^2,\ x \geqslant 0\}$ and the arc given by $\partial\hat{\gamma}_{\mathcal{Q}} \equiv \hat{\gamma}_A \cap \mathcal{Q}$.

Since $\hat{\gamma}_A$ reaches the boundary at $z = 0$, its area is infinite; therefore we have to introduce the cutoff $\varepsilon > 0$ and consider the area of the restricted surface $\hat{\gamma}_\varepsilon = \hat{\gamma}_A \cap \{z \geqslant \varepsilon\}$ as $\varepsilon \to 0^+$. The details of this computation have been reported in the appendix B.1. For a given $\alpha \in (0, \pi)$ we find

$$\mathcal{A}[\hat{\gamma}_\varepsilon] = R^2_{\text{AdS}} \left(\frac{\pi R}{\varepsilon} + 2(\cot\alpha)\log(R/\varepsilon) + O(1) \right). \tag{3.2.1}$$

This expression is a special case of (3.0.3) corresponding to $P_{A,B} = \pi R$ and $F_{\alpha,\text{tot}} = 2F_\alpha(\pi/2)$. Thus, we have

$$F_\alpha(\pi/2) = -\cot\alpha. \tag{3.2.2}$$

As consistency check, we observe that $F_{\pi/2}(\pi/2) = 0$. This is expected because (3.2.1) for $\alpha = \pi/2$ gives half of the area of the hemisphere $x^2 + y^2 + z^2 = R^2$ restricted to $z \geqslant \varepsilon$ in $\mathbb{H}_3$. Furthermore, by increasing the slope α of $\mathcal{Q}$ while A is kept fixed, the area $\mathcal{A}[\hat{\gamma}_\varepsilon]$ in (3.2.1) decreases because of the coefficient of the logarithmic divergence, as expected.

The result (3.2.2) can also be obtained by considering a bipartition whose entangling curve is a half straight line orthogonal to the boundary [161].

3.2.2 Infinite wedge adjacent to the boundary

Now we discuss the main result of this chapter. We compute the minimal surface $\hat{\gamma}_A$ corresponding to an infinite wedge with opening angle $\gamma \in (0, \pi/2]$ having one of its edges on the boundary of the BCFT$_3$. By evaluating the area of $\hat{\gamma}_\varepsilon$, an analytic expression for the

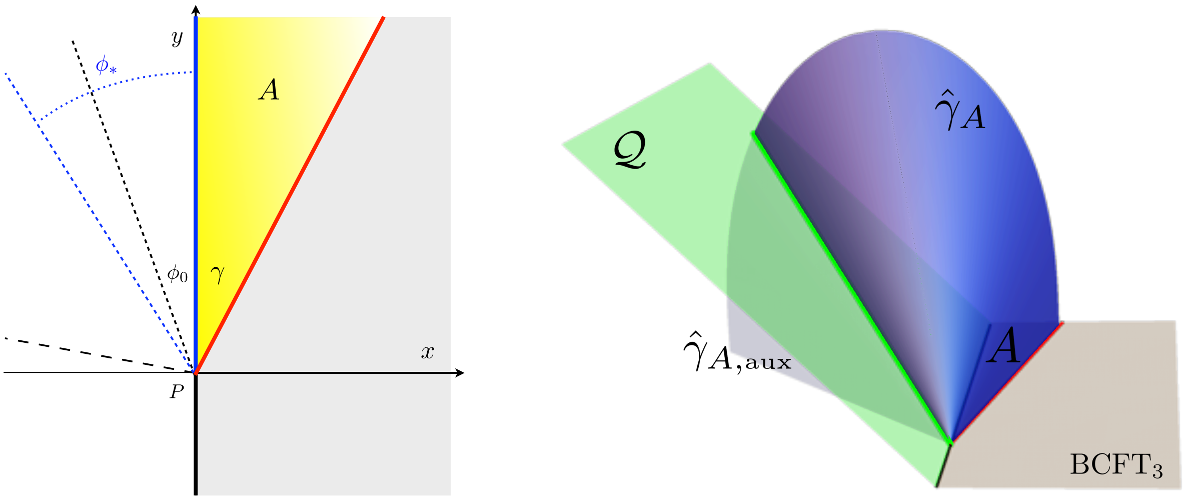

Figure 3.4: Left: The opening angles occurring in the construction of the minimal surface $\hat{\gamma}_A$ anchored to the infinite wedge A (the yellow region) adjacent to the boundary with opening angle γ. Here, $\alpha \in (0, \pi/2]$ while for the range $\alpha \in [\pi/2, \pi)$ see Fig. B.1. The entangling curve is the red straight line given by $\phi = \gamma$. The auxiliary wedge A_{aux} is the infinite wedge in $\mathbb{R}^2$ containing A whose tip is P and whose edges are the red half-line and the black dashed line with the largest dashing. The black dashed line with the smallest dashing at $\phi = \phi_0$ corresponds to the bisector of A_{aux}. The blue dashed half-line at $\phi = \phi_*$ corresponds to the projection of $\hat{\gamma}_A \cap \mathcal{Q}$ in the $z = 0$ plane. Right: Minimal surface $\hat{\gamma}_A$ anchored to the region A. The green half-plane is $\mathcal{Q}$, and it intersects $\hat{\gamma}_A$ along the green line.

corner function $F_\alpha(\gamma)$ occurring in (3.0.4) is obtained. In the following, we report only the main results of our analysis, while the technical details of their derivations are collected in the appendix B.2.

Let us adopt the polar coordinates (ρ, ϕ) given by $x = \rho \sin\phi$ and $y = \rho\cos\phi$ for the $t = \text{const}$ slice of the BCFT$_3$, in terms of which the region is $A = \big\{(\rho,\phi)\,|\, 0 \leqslant \phi \leqslant \gamma\,, \rho \leqslant L\big\}$ with $L \gg \varepsilon$. Since the wedge is infinite, we can look for the corresponding minimal surface $\hat{\gamma}_A$ among the surfaces described by the following ansatz

$$z = \frac{\rho}{q(\phi)} \tag{3.2.3}$$

where $q(\phi) > 0$, as already done in [157] to get the minimal surface in $\mathbb{H}_3$ anchored to an infinite wedge in $\mathbb{R}^2$.

The minimal surface $\hat{\gamma}_A$ can be found as part of an auxiliary minimal surface $\hat{\gamma}_{A,\text{aux}}$ embedded in $\mathbb{H}_3$ and anchored to an auxiliary infinite wedge $\hat{\gamma}_{A,\text{aux}}$ containing A and having the same edge $\{(\rho,\phi)\,|\,\phi = \gamma\}$. The minimal surface $\hat{\gamma}_A$ intersects orthogonally the half-plane at $z = 0$ along the edge $\{(\rho,\phi)\,|\,\phi = \gamma\}$ of A and the half-plane $\mathcal{Q}$ along the half-line given by $\phi = \phi_*$. As remarked for the previous case, $\hat{\gamma}_A$ is the part of $\hat{\gamma}_{A,\text{aux}}$ identified by the constraint $z \geqslant -(\cot\alpha)z$. For the infinite wedge A that we are considering, A_{aux} is a suitable infinite wedge in $\mathbb{R}^2$ and $\hat{\gamma}_{A,\text{aux}}$ is the corresponding minimal surface found in [157]. On the left side of Fig. 3.4 the auxiliary wedge A_{aux} is shown (see also B.1 in the appendix B.2), while on

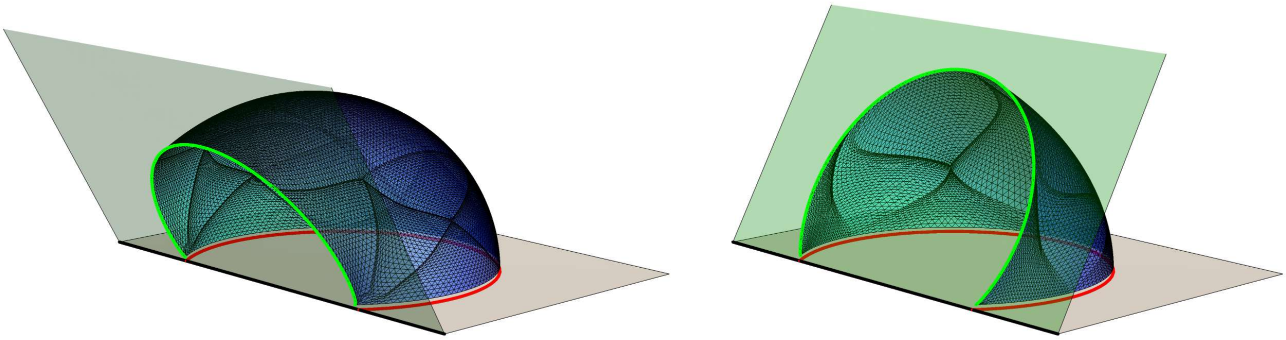

Figure 3.5: Minimal surfaces $\hat{\gamma}_A$ obtained with Surface Evolver corresponding to a region A given by the intersection between the grey half-plane at $z = 0$ and a disk of radius R whose center has coordinate $x > 0$. The entangling curve $\partial A \cap \partial B$ (red line) is an arc of circumference. The green half-plane is $\mathcal{Q}$ defined by (1.4.9), and the green curve corresponds to $\hat{\gamma}_A \cap \mathcal{Q}$. In the figure $\varepsilon = 0.03$, $R = 1$ and the center of the disk has coordinate $x = 0.6$. In the left panel $\alpha = \pi/3$, while in the right panel $\alpha = 2\pi/3$. The numerical data of the corner function $F_\alpha(\gamma)$ corresponding to this kind of domains are labeled by empty circles in Fig. 3.7.

the right side the minimal surface $\hat{\gamma}_A$ in dark blue is shown with the auxiliary surface $\hat{\gamma}_{A,\text{aux}}$ depicted with a lighter color.

Given the half-plane $\mathcal{Q}$ described by (1.4.9), whose slope is $\alpha \in (0, \pi)$, the angle ϕ_* which identifies the half-line $\hat{\gamma}_A \cap \mathcal{Q}$ can be defined by introducing the following positive function

$$s_*(\alpha, q_0) \equiv -\eta_\alpha \frac{\cot\alpha}{\sqrt{2}} \left\{ \frac{\sqrt{1 + 4(\sin\alpha)^2(q_0^4 + q_0^2)} - \cos(2\alpha)}{(\cos\alpha)^2 + q_0^4 + q_0^2} \right\}^{\frac{1}{2}} \qquad \eta_\alpha \equiv -\,\text{sign}(\cot\alpha) \tag{3.2.4}$$

where $q(\phi_0) \equiv q_0 > 0$ is the value of the function $q(\phi)$ at the angle $\phi = \phi_0$ corresponding to the bisector of the auxiliary wedge A_{aux}. We find it convenient to adopt q_0 as a parameter to define various quantities in the following. From (3.2.4), we find ϕ_* as

$$\phi_*(\alpha, q_0) = \eta_\alpha \arcsin[s_*(\alpha, q_0)]. \tag{3.2.5}$$

This result encodes the condition that $\hat{\gamma}_A$ intersects $\mathcal{Q}$ orthogonally, as explained in the appendix B.2.2.

To write the analytic expression for the opening angle γ of the infinite wedge in terms of the positive parameter q_0, let us introduce

$$q_*(\alpha, q_0) = \frac{|\cot\alpha\,|}{s_*(\alpha, q_0)} \tag{3.2.6}$$

where $s_*(\alpha, q_0) > 0$ is given by (3.2.4). For the opening angle γ of A we find

$$\gamma = P_0(q_0) + \eta_\alpha \Big(\arcsin[s_*(\alpha, q_0)] - P\big(q_*(\alpha, q_0), q_0\big) \Big) \tag{3.2.7}$$

where the function $P(q, q_0)$ is defined as

$$P(q, q_0) \equiv \frac{1}{q_0(1 + q_0^2)} \Big\{ (1 + 2q_0^2)\, \Pi\big(-1/Q_0^2\,,\, \sigma(q, q_0)\,\big|\, -Q_0^2\big) - q_0^2\, \mathbb{F}\big(\sigma(q, q_0)\,\big|\, -Q_0^2\big) \Big\} \tag{3.2.8}$$

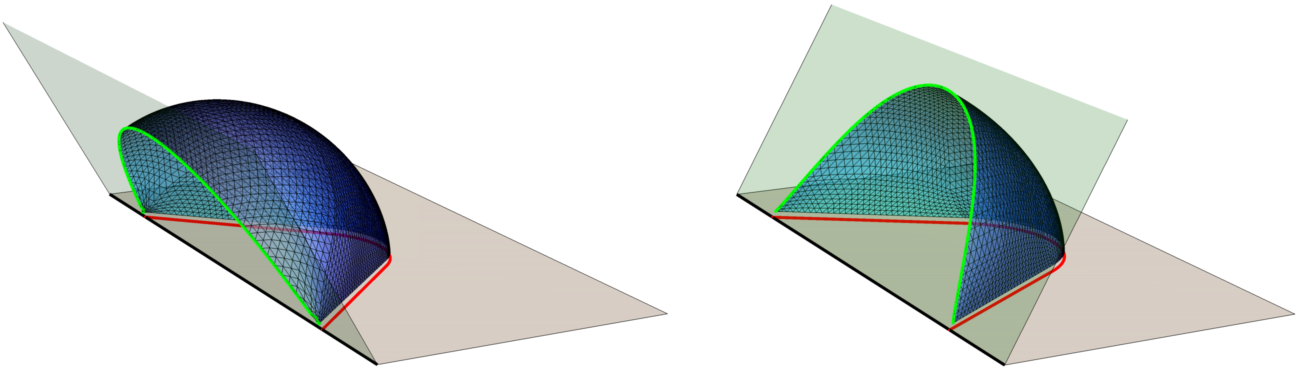

Figure 3.6: Minimal surfaces $\hat{\gamma}_A$ obtained with Surface Evolver corresponding to a region A delimited by the red curve (entangling curve $\partial A \cap \partial B$) in the grey half-plane at $z = 0$, which has been obtained by smoothly joining two segments of equal length L forming two equal corners with the boundary, whose opening angle is γ. The green half-plane is $\mathcal{Q}$ defined by (1.4.9), and the green curve corresponds to $\hat{\gamma}_A \cap \mathcal{Q}$. In the left panel $\alpha = \pi/3$, $L = 1$ and $\gamma = 0.8$, while in the right panel $\alpha = 2\pi/3$, $L = 1$ and $\gamma = 1$. The numerical data of the corner function $F_\alpha(\gamma)$ corresponding to this kind of domains are labeled by empty triangles in Fig. 3.7.

(in (B.2.9) we give the integral representation) being $\mathbb{F}(\phi|m)$ and $\Pi(n,\phi|m)$ the incomplete elliptic integrals of the first and third kind respectively, with

$$\sigma(q,q_0) \equiv \arctan\sqrt{\frac{q^2-q_0^2}{1+2q_0^2}} \qquad\qquad Q_0^2 \equiv \frac{q_0^2}{1+q_0^2} \in (0,1). \tag{3.2.9}$$

The function $P_0(q_0)$ in (3.2.7) is the limit $P(q,q_0) \to P_0(q_0)$ as $q \to +\infty$. The explicit expression of $P_0(q_0)$ in terms of the complete elliptic integrals has been written in (1.3.28). Here, we provide an equivalent form coming directly from (3.2.8), namely

$$P_0(q_0) = \frac{1}{q_0(1+q_0^2)}\left\{(1+2q_0^2)\,\Pi\left(-1/Q_0^2, -Q_0^2\right) - q_0^2\,\mathbb{K}\left(-Q_0^2\right)\right\} \tag{3.2.10}$$

being $\mathbb{K}(m)$ and $\Pi(n|m)$ the complete elliptic integrals of the first and third kind respectively.

As for the holographic entanglement of the infinite wedge A adjacent to the boundary, since $\hat{\gamma}_A$ reaches the boundary $z = 0$, its area is infinite; therefore we have to consider its restriction $\hat{\gamma}_\varepsilon = \hat{\gamma}_A \cap \{z \geqslant \varepsilon\}$ and take the limit $\varepsilon \to 0^+$.

We find that the expansion of the area $\mathcal{A}[\hat{\gamma}_\varepsilon]$ of $\hat{\gamma}_\varepsilon$ as $\varepsilon \to 0$ reads

$$\mathcal{A}[\hat{\gamma}_\varepsilon] = R^2_{\text{AdS}}\left(\frac{L}{\varepsilon} - F_\alpha(\gamma)\,\log(L/\varepsilon) + O(1)\right) \tag{3.2.11}$$

which is a special case of (3.0.3) and (3.0.4) with $P_{A,B} = L$ and $F_{\alpha,\text{tot}} = F_\alpha(\gamma)$. The leading linear divergence in (3.2.11) is the expected area law term and it comes from the part of $\hat{\gamma}_\varepsilon$ close the edge of A at $\phi = \gamma$. The occurrence of the wedge leads to the important logarithmic divergence, whose coefficient provides the corner function $F_\alpha(\gamma)$ we are interested in.

The corner function $F_\alpha(\gamma)$ has been computed in the appendix B.2.3 and the result is

$$F_\alpha = F(q_0) + \eta_\alpha\,\mathcal{G}\big(q_*(\alpha,q_0),q_0\big) \tag{3.2.12}$$

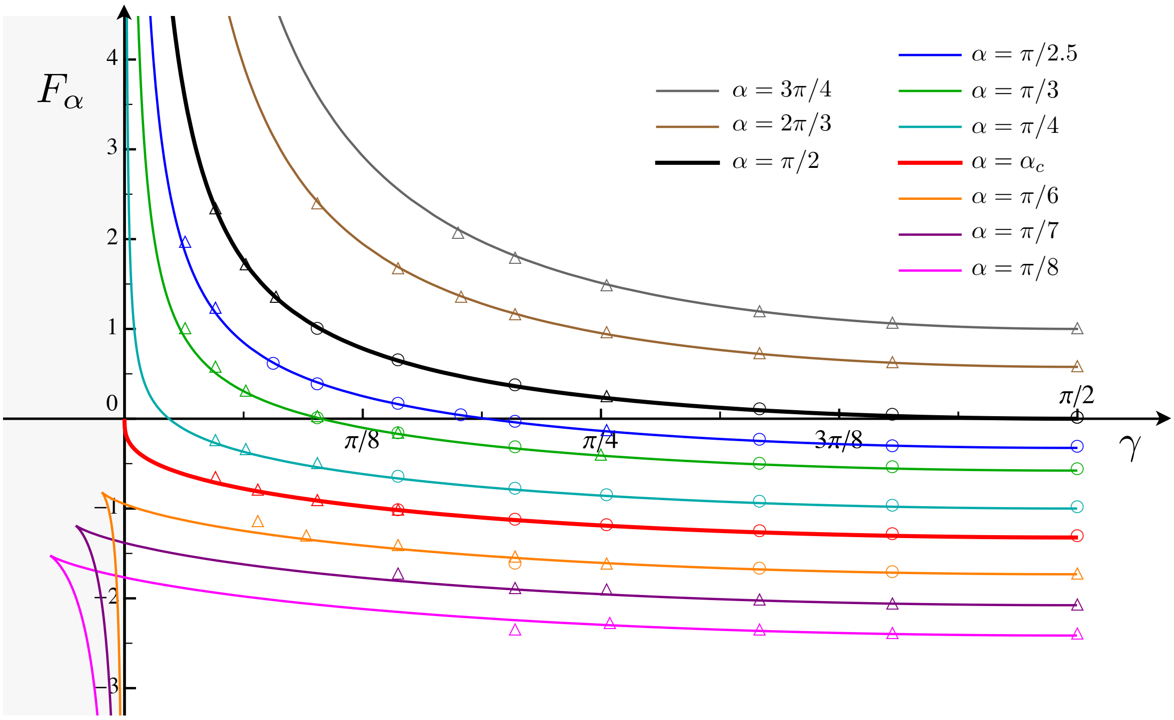

Figure 3.7: The corner function $F_\alpha(\gamma)$ for some values of the slope α of the half-plane $\mathcal{Q}$. The solid curves are obtained from the analytic expressions (3.2.7) and (3.2.12), which provide the corner function parametrically in terms of $q_0 > 0$ (see also Fig. 3.8). The marked points have been found through our numerical analysis based on Surface Evolver. The empty circles label the data points obtained from the domain A in Fig. 3.5, while empty triangles label the data points found by employing the domain A in Fig. 3.6. The same color has been adopted for the analytic curves and the data points corresponding to the same α.

where $F(q_0)$ has been introduced in (1.3.27) and the function $\mathcal{G}(q, q_0)$ is

$$\mathcal{G}(q,q_0) \equiv \sqrt{1+q_0^2}\,\left\{ \mathbb{F}\big(\sigma(q,q_0)\,\big|\,-Q_0^2\big) - \mathbb{E}\big(\sigma(q,q_0)\,\big|\,-Q_0^2\big) + \sqrt{\frac{(q^2+1)(q^2-q_0^2)}{(q_0^2+1)(q^2+q_0^2+1)}}\,\right\}. \tag{3.2.13}$$

The expression for $q_*(\alpha, q_0)$ to use in (3.2.12) is (3.2.6).

The main results of this chapter are (3.2.7) and (3.2.12), which provide the analytic expression of the corner function $F_\alpha(\gamma)$ in a parametric form in terms of $q_0 > 0$.

In Fig. 3.7 the solid curves corresponds to the corner function $F_\alpha(\gamma)$ for some values of α. As for the argument of the corner function $F_\alpha(\gamma)$, we remind that $\gamma \in (0, \pi/2]$. Nonetheless, whenever $\gamma \in (0, \pi)$ we mean $F_\alpha(\min[\gamma, \pi - \gamma])$.

In Fig. 3.8 we show the surface given by the corner function $F_\alpha(\gamma)$ in terms of the opening angle γ and the slope $\alpha \in (0, \pi)$. In this figure we have highlighted the sections corresponding to the curves reported in Fig. 3.7 and also the curve $F_\alpha(\pi/2)$ (yellow curve).

We have employed Surface Evolver to find an important numerical evidence of our analytic result. In this numerical analysis we have chosen domains A whose entangling curves $\partial A \cap \partial B$ correspond to the red solid curves in the $z = 0$ half-plane shown in Fig. 3.5 and in Fig. 3.6. In

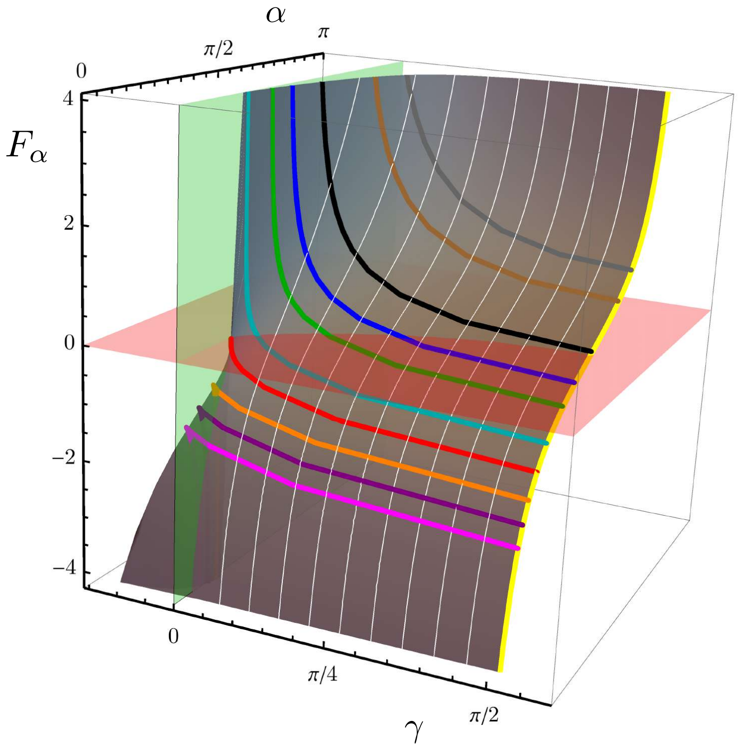

Figure 3.8: The corner function $F_\alpha(\gamma)$ given by (3.2.7) and (3.2.12) in terms of $\gamma \in (0, \pi/2]$ and $\alpha \in (0, \pi)$ (grey surface). The solid curves corresponding to the $\alpha =$ const sections are the same ones shown in Fig. 3.7, with the same colour code. The section $\gamma = \pi/2$ (yellow solid curve) is (3.2.2). In the left panel of Fig. B.2 we depict the intersection between the grey surface and the red plane and in the right panel of Fig. B.2 the intersection of the grey surface with the green plane is shown.

particular, in Fig. 3.5 we have that A is part of a disk which is not centered on the boundary and in Fig. 3.6 the region A is made by two finite wedges with an edge on the boundary and the same opening angle whose remaining edges are joined smoothly. In Fig. 3.5 and in Fig. 3.6 we show also the corresponding minimal surface $\hat{\gamma}_A$ constructed with Surface Evolver for a value $\alpha < \pi/2$ (left panels) and for a value $\alpha > \pi/2$ (right panels).

The marked points in Fig. 3.7 are the numerical values of the corner function $F_\alpha(\gamma)$ obtained through the numerical analysis based on the data obtained from Surface Evolver, as explained in the appendix 1.6. In particular, the empty circles and the empty triangles correspond to the domains A shown in Fig. 3.5 and in Fig. 3.6 respectively. It turns out that the domain A in Fig. 3.6 is more suitable to deal with small values of γ in our numerical approach. Excellent agreement is obtained with the analytic result for the values of α and γ considered in Fig. 3.7.

From Fig. 3.7 and Fig. 3.8 we observe that for the holographic corner function given by (3.2.7) and (3.2.12) we have that $F'_\alpha(\gamma) \leqslant 0$ and also $F''_\alpha(\gamma) \geqslant 0$ for any fixed value of the slope $\alpha \in (0, \pi)$. Furthermore, from Fig. 3.8 we also notice that $\partial_\alpha F_\alpha(\gamma) > 0$ for any fixed value of $\gamma \in (0, \pi/2]$. It would be interesting to understand whether these properties come from some more fundamental principles.

In Fig. 3.7 the curves corresponding to the critical value $\alpha = \alpha_c$ (red curve) given by (2.2.4) and to $\alpha = \pi/2$ (black curve) have been highlighted by employing thicker lines because these values separate the range of $\alpha \in (0, \pi)$ into three intervals for α where the corner function $F_\alpha(\gamma)$ has different features. In particular, when $\alpha \geqslant \pi/2$ we have that $F_\alpha(\gamma) \geqslant 0$, while when $\alpha \leqslant \alpha_c$ we have that $F_\alpha(\gamma) \leqslant 0$. In the intermediate range $\alpha \in (\alpha_c, \pi/2)$ the corner function does not have a definite sign in the whole range $\gamma \in (0, \pi/2]$ and, being $F'_\alpha(\gamma) < 0$, it has a unique zero $\gamma = \gamma_0$. The value γ_0 in terms of $\alpha \in [\alpha_c, \pi/2]$ found numerically is shown in the left panel of Fig. B.2.

From Fig. 3.7 we observe that the corner function $F_\alpha(\gamma)$ displays two qualitative different behaviours as $\gamma \to 0^+$. Indeed, $F_\alpha(\gamma) \to +\infty$ when $\alpha > \alpha_c$, while it reaches a finite (non-positive) value when $\alpha \leqslant \alpha_c$. In Sec. 3.2.2 quantitative results about the regimes $\gamma \to 0^+$ and $\gamma \to \pi/2$ of $F_\alpha(\gamma)$ are obtained.

It would be interesting to get a direct numerical confirmation of the occurrence of α_c through Surface Evolver or other methods. Unfortunately, we have not been able to push our numerical analysis to values of γ small enough to appreciate the qualitatively different behaviour of the corner function for $\alpha \leqslant \alpha_c$ and $\alpha > \alpha_c$.

Limiting regimes of the corner function

It is worth studying the corner function $F_\alpha(\gamma)$ in some particular regimes. In the following we report only the main results of our analysis, referring the reader to the appendices B.2.3 and B.2.4 for a detailed discussion of their derivations.

An important special value to consider is $\alpha = \pi/2$. In this case, it is straightforward to realise that the minimal surface $\hat{\gamma}_A$ is half of the auxiliary minimal surface $\hat{\gamma}_{A,\mathrm{aux}}$ in $\mathbb{H}_3$, which is anchored to the auxiliary infinite wedge A_{aux} with opening angle 2γ. Indeed, for every α we have that $\hat{\gamma}_{A,\mathrm{aux}}$ in $\mathbb{H}_3$ is smooth and symmetric with respect to the half-plane orthogonal to $z = 0$ passing through the bisector of A_{aux}; therefore $\hat{\gamma}_{A,\mathrm{aux}}$ intersects this half-plane orthogonally. When $\alpha = \pi/2$ the half-plane characterising this reflection symmetry coincides with $\mathcal{Q}$.

As for the corner function at $\alpha = \pi/2$, from the analytic expression (3.2.7) and (3.2.12) we find respectively that

$$\lim_{\alpha \to \pi/2} \gamma = P_0(q_0) \qquad\qquad \lim_{\alpha \to \pi/2} F_\alpha = F(q_0). \tag{3.2.14}$$

Further comments can be found in the closing remarks of the appendix B.2.3. Comparing (3.2.14) with (1.3.26) and (1.3.28) respectively, we obtain

$$\widetilde{F}(2\gamma) = 2\, F_{\pi/2}(\gamma). \tag{3.2.15}$$

Thus, the corner function found in [157] and discussed in Sec. 1.3.3 is recovered as the special case $\alpha = \pi/2$ of the corner function $F_\alpha(\gamma)$ given by (3.2.7) and (3.2.12).

Now we consider the limiting regimes of $\gamma \to 0$ and $\gamma \to \pi/2$, which correspond to $q_0 \to +\infty$ and $q_0 \to 0^+$ respectively (see the appendix B.2.4 for a detailed discussion).

Taking the limit $q_0 \to +\infty$ of (3.2.7) and (3.2.12), we obtain

$$\gamma = \frac{\mathfrak{g}(\alpha)}{q_0} + O(1/q_0^3) \qquad F_\alpha = \mathfrak{g}(\alpha)\, q_0 + O(1/q_0) \qquad q_0 \to +\infty \tag{3.2.16}$$

where $\mathfrak{g}(\alpha)$ is the same function introduced (2.2.2) and given by the red curve in Fig. 2.3. The appearance of $\mathfrak{g}(\alpha)$ can be explained from a relation between the strip and the infinite wedge in the limit $\gamma \to 0^+$. In appendix B.2.5 we perform a conformal transformation which relates the infinite wedge on the half-plane to the strip of width ℓ on the half-cylinder with semi-circumference L_0. In the limit $\gamma \to 0^+$ and $L_0 \to +\infty$ such that $\gamma L_0 = \ell$, the half-cylinder becomes the half-plane allowing us to identify the infinite wedge when $\gamma \to 0^+$ with the strip. The discussion reported in the appendix B.2.5 is a modification of the analogue one in AdS$_4$/CFT$_3$ [189, 247, 265], obtained by taking into account the presence of the boundary.

We remark that we have different behaviors of the corner function $F_\alpha(\gamma)$ as $\gamma \to 0^+$, depending on whether $\alpha \in (0, \alpha_c]$ or $\alpha \in (\alpha_c, \pi)$. Indeed, $\mathfrak{g}(\alpha)$ changes its sign at the critical value $\alpha = \alpha_c$ defined by (2.2.3), whose numerical value is (2.2.4). Since γ and q_0 must be strictly positive, while $\mathfrak{g}(\alpha) \leqslant 0$ for $\alpha \in (0, \alpha_c]$, the expansion of γ in (3.2.16) is meaningful in our setup only when $\alpha \in (\alpha_c, \pi)$. In this range, from the first expansion in (3.2.16) we find that $q_0 = \mathfrak{g}(\alpha)/\gamma + O(\gamma)$ as $\gamma \to 0$. Then, plugging this result into the second expansion of (3.2.16), we obtain

$$F_\alpha = \frac{\mathfrak{g}(\alpha)^2}{\gamma} + O(\gamma) \qquad \gamma \to 0^+ \qquad \alpha \in (\alpha_c, \pi). \tag{3.2.17}$$

When $\alpha = \alpha_c$ the second expansion in (3.2.17) tells us that

$$F_{\alpha_c}(0) = 0. \tag{3.2.18}$$

We can interpret this observation as a possible definition of α_c in terms of the corner function. The function $F_\alpha(0)$, which corresponds to finite values $\hat{q}_0$ of the parameter q_0 for a given α, can be found numerically in terms of $\alpha \in (0, \alpha_c)$ and the result of this analysis is shown in the right panel of Fig. B.2 in the appendix B.2. In particular, when $\alpha = \alpha_c$ we have (3.2.18).

From Fig. 3.7 we observe that in the range $\alpha \in [\alpha_c, \pi/2)$ the function $F_\alpha(\gamma)$ vanishes at a positive value γ_0 of the opening angle. When $\alpha = \alpha_c$ we have $\gamma_0 = 0$, as written in (3.2.18). By solving numerically the equation $F_\alpha(\gamma_0) = 0$ for $\alpha \in [\alpha_c, \pi/2)$, we find the function $\gamma_0(\alpha)$ shown in the left panel of Fig. B.2.

When $\alpha \in (0, \alpha_c)$ we have $\mathfrak{g}(\alpha) < 0$; therefore the expansions in (3.2.16) imply that $\gamma \to 0^-$ and $F_\alpha \to -\infty$ as $q_0 \to +\infty$. Since negative values of γ are meaningless in our context, we do not consider the limit in this case.

As for the regime $q_0 \to 0^+$, in the appendix B.2.4 we have computed the expansions of the opening angle γ and of the corner function F_α, which are given by (3.2.7) and (3.2.12) respectively, finding (B.2.47) and (B.2.51). From these results, we conclude that $\gamma \to \pi/2$ and also that

$$F_\alpha(\gamma) = -\cot\alpha + \frac{(\pi/2 - \gamma)^2}{2(\pi - \alpha)} + O\big((\pi/2 - \gamma)^4\big) \tag{3.2.19}$$

which agrees with the general expansion (3.1.2) for this kind of corner function. In particular, we have that with $F_\alpha(\pi/2) = -\cot\alpha$ and $F''_\alpha(\pi/2) = 1/(\pi-\alpha)$. The expression for $F_\alpha(\pi/2)$ confirms the expected result (3.2.2) obtained in Sec. 3.2.1 by considering the half-disk centered on the boundary. Let us remark that the method discussed in the appendix B.2.4 allows to computed also higher orders in (3.2.19). For instance, in (B.2.52) also the $O((\pi/2-\gamma)^4)$ term has been reported.

3.2.3 Corner function from the modified Willmore functional

In the previous chapter, the shape dependence of the holographic entanglement entropy for spacetimes with boundaries has been studied. The main result is the functional (2.1.18), which reduces (2.1.24) when the spacetime is part of AdS$_4$. The functional (2.1.18) and (2.1.24) corresponds to the subleading term in the expansion of the area $\mathcal{A}[\hat{\gamma}_A]$. As discussed in Sec. (2.1), whenever the region A is smooth, i.e., has no corners and does not intersect the boundary of the BCFT$_3$, F_A is finite in the limit $\varepsilon \to 0^+$. On the other hand, the expression (2.1.23) diverges logarithmically when it contains corners. In AdS$_4$/CFT$_3$, the emergence of the logarithmic divergence from the Willmore functional (1.3.18) for domains with corners has been studied in [78], where the corner function found in [157] has been recovered. In this section, we discuss the occurrence of the logarithmic divergence in (2.1.23) for singular domains in the AdS$_4$/BCFT$_3$ setup. Since we are interested in the flat boundary case, the functional we will employing below is (2.1.25) with the only modification that the integral will be taken over the restricted surface $\hat{\gamma}_\varepsilon$ to tame the logarithmic divergence, i.e.

$$F_A[\hat{\gamma}_\varepsilon] = \int_{\hat{\gamma}_\varepsilon} \frac{(\tilde{n}^z)^2}{z^2}\, d\tilde{\mathcal{A}} - (\cos\alpha)\int_{\partial\hat{\gamma}_{\varepsilon,\mathcal{Q}}} \frac{1}{z}\, d\tilde{s}. \tag{3.2.20}$$

Below, we show that the corner function $F_\alpha(\gamma)$ can also be obtained also from (2.1.25) once the cutoff ε is reintroduced by focusing on the half-disk and the infinite wedge domains.

Half-disk centered on the boundary

In the integral (3.2.20), we have two contributions, the surface and the boundary integrals. Let us observe that the former one provides a finite result as $\varepsilon \to 0$ because $\hat{\gamma}_\varepsilon$ is part of the hemisphere $\hat{\gamma}_A \cup \hat{\gamma}_{A,\,\mathrm{aux}}$ and, being the integrand positive, the integral over $\hat{\gamma}_\varepsilon$ is smaller than the integral over the entire hemisphere $\hat{\gamma}_A \cup \hat{\gamma}_{A,\,\mathrm{aux}}$, which is finite (see (1.3.17)). Thus, all the logarithmic divergence comes from the boundary integral in (3.2.20).

The intersection between $\hat{\gamma}_A$ and $\mathcal{Q}$ is given by the following semi-circle

$$\partial\hat{\gamma}_\mathcal{Q} : \begin{cases} x^2+y^2+z^2 = R^2 \\ z = -\,x\tan\alpha \end{cases}. \tag{3.2.21}$$

By employing the spherical coordinates

$$z = R\,\sin\theta\,\cos\phi \qquad x = -\,R\,\sin\theta\,\sin\phi \qquad y = R\,\cos\theta \tag{3.2.22}$$

one finds the following parametric representation of $\partial\hat{\gamma}_Q$

$$\partial\hat{\gamma}_Q: \quad (z,x,y) = R\big(\sin\theta\,\cos(\pi/2-\alpha)\,,\,-\sin\theta\,\sin(\pi/2-\alpha)\,,\,\cos\theta\big) \qquad \theta_\varepsilon \leqslant \theta \leqslant \pi-\theta_\varepsilon. \tag{3.2.23}$$

The angle θ_ε is given by the intersection of $\partial\hat{\gamma}_Q$ with the cutoff $z=\varepsilon$; therefore it can be found from the condition $\varepsilon = R\sin\theta_\varepsilon\cos(\pi/2-\alpha)$. Since the line element is $d\tilde{s} = R\,d\theta$, from (3.2.23) we easily obtain the following result for the line integral over $\partial\hat{\gamma}_Q$ in (3.2.20) for this configuration

$$\int_{\partial\hat{\gamma}_Q} \frac{\tilde{b}^z}{z}\,d\tilde{s} \;=\; -\cot\alpha\int_{\theta_\varepsilon}^{\pi-\theta_\varepsilon}\frac{1}{\sin\theta}\,d\theta \;=\; -\cot\alpha\,\log\big[\tan(\theta/2)\big]\Big|_{\theta_\varepsilon}^{\pi-\theta_\varepsilon}. \tag{3.2.24}$$

As $\varepsilon\to 0$, at the leading order we obtain

$$\int_{\partial\hat{\gamma}_Q}\frac{\tilde{b}^z}{z}\,d\tilde{s} \;=\; -2\cot\alpha\,\log(R/\varepsilon)+O(1) \tag{3.2.25}$$

as expected. Thus, the logarithmic divergence and its coefficient in (3.2.1) have been recovered by specifying the functional (3.2.20) to this configuration, finding that they come from the line integral over $\partial\hat{\gamma}_Q$.

Infinite wedge

Here we consider the infinite wedge. In this case, since showing that (3.2.20) reproduces the corner function $F_\alpha(\gamma)$ is more involved, we underly the main steps leaving the details to the appendix B.2.6.

First of all, we observe that, while for the half-disk centered on the flat boundary the logarithmic divergence in the expansion of $\mathcal{A}[\hat{\gamma}_\varepsilon]$ comes only from the line integral over $\partial\hat{\gamma}_Q$, for the infinite wedge both the surface integral over $\hat{\gamma}_\varepsilon$ and the line integral over $\partial\hat{\gamma}_Q$ provide a logarithmic divergence. In particular, for the line integral over $\partial\hat{\gamma}_Q$ we find

$$\int_{\partial\hat{\gamma}_Q}\frac{\tilde{b}^z}{z}\,d\tilde{s} \;=\; -\cot\alpha\,\sqrt{1+(\cos\alpha\,\cot\phi_*)^2}\;\log(L/\varepsilon)+\mathcal{O}(1). \tag{3.2.26}$$

Notice that, since for the half-disk centered on the flat boundary $\phi_* = \eta_\alpha\,\pi/2$, the expression (3.2.26) is consistent with (3.2.25) (where we recall that the factor of 2 occurs because the half-disk contains two corners).

The evaluation of the surface integral over $\hat{\gamma}_\varepsilon$ in (3.2.20) is less straightforward than (3.2.26) and it provides the following logarithmic divergent contribution

$$\int_{\hat{\gamma}_\varepsilon}\frac{(\tilde{n}^z)^2}{z^2}\,d\tilde{\mathcal{A}} \;=\; \mathcal{I}(q_*,q_0)\log(L/\varepsilon)+O(1) \tag{3.2.27}$$

whose coefficient is given by

$$\mathcal{I}(q_*,q_0) \equiv F(q_0)-\eta_\alpha\left(S(q_*,q_0)+\sqrt{\frac{(q_*-q_0)\,(q_*+q_0)\,(q_*^2+q_0^2+1)}{q_*^2+1}}\,\right) \tag{3.2.28}$$

where

$$S(q_*, q_0) \equiv \sqrt{q_0^2+1}\left[\mathbb{E}\left(i\,\text{arccsch}\,\frac{q_0}{\sqrt{q^2+1}}\,\bigg|\,\frac{-\,q_0^2}{q_0^2+1}\right) - \mathbb{F}\left(i\,\text{arccsch}\,\frac{q_0}{\sqrt{q^2+1}}\,\bigg|\,\frac{-\,q_0^2}{q_0^2+1}\right)\right]\Bigg|_{q_0}^{q_*}. \tag{3.2.29}$$

By combining (3.2.26) and (3.2.27) as prescribed by the formula (3.2.20) (see the Appendix B.2.6 for some technical details), we recover exactly the expression (3.2.12) for the corner function.

3.3 The coefficient A_T from holography

In this section we describe the holographic computation of the coefficient A_T defined in (3.4.3) in the AdS$_{d+2}$/BCFT$_{d+1}$ setup of [89]. The main result of our analysis is the analytic expression of A_T for arbitrary $d > 1$. The special case of $d = 2$ will be used in Sec. 3.4 to state a relation with the quantity $f''_\alpha(\pi/2)$ that appears in the expansion of the boundary corner function obtained in the previous section.

The AdS$_{d+2}$/BCFT$_{d+1}$ construction of [89] has been described by employing the following metric

$$ds^2 = d\xi^2 + \big[\cosh(\xi/R_{\text{AdS}})\big]^2\left(R_{\text{AdS}}^2\,\frac{-\,dt^2+d\zeta^2+d\vec{y}^{\,2}}{\zeta^2}\right) \qquad \zeta>0 \tag{3.3.1}$$

where $d\vec{y}^{\,2}$ is the Euclidean flat metric of $\mathbb{R}^{d-1}$. If $\xi \in \mathbb{R}$, then the metric (3.3.1) describes AdS$_{d+2}$. Indeed, the change of coordinates

$$z = \frac{\zeta}{\cosh(\xi/R_{\text{AdS}})} \qquad x = -\,\zeta\,\tanh(\xi/R_{\text{AdS}}) \tag{3.3.2}$$

brings the metric (3.3.1) into the usual form (1.4.8) in terms of the Poincaré coordinates. Notice that on a generic $\xi =$ const slice of (3.3.1) the induced metric is the Poincaré metric of AdS$_{d+1}$. In terms of the coordinates occurring in (3.3.1), the half-hyperplane $\mathcal{Q}$ corresponds to a particular $\xi =$ const slice. From (3.3.2), we have that the conformal boundary where the BCFT$_{d+1}$ is defined is given by $\xi \to -\infty$.

In order to make contact with the coordinates mainly employed throughout this thesis, we find it convenient to introduce the angular coordinate $\psi \in (0, \pi)$ as follows

$$\cot\psi \;=\; -\,\sinh(\xi/R_{\text{AdS}}). \tag{3.3.3}$$

From (3.3.2), it is straightforward to observe that

$$\frac{z}{x} = -\frac{1}{\sinh(\xi/R_{\text{AdS}})} = \tan\psi. \tag{3.3.4}$$

In terms of the angular coordinate $\psi \in (0, \pi)$ defined in (3.3.3), the metric (3.3.1) becomes

$$ds^2 = \frac{R_{\text{AdS}}^2}{(\sin\psi)^2}\left(d\psi^2 + \frac{-\,dt^2+d\zeta^2+d\vec{y}^{\,2}}{\zeta^2}\right). \qquad \zeta>0 \tag{3.3.5}$$

By employing the metric (3.3.5) in the $\mathrm{AdS}_{d+2}/\mathrm{BCFT}_{d+1}$ setup described in Sec. 1.4.3, where the boundary of the BCFT_{d+1} is a flat hyperplane, we have that the half-hyperplane $\mathcal{Q}$ in (1.4.9) is given by $\psi = \pi - \alpha$, with $\alpha \in (0, \pi)$, and the spacetime of the BCFT_{d+1} corresponds to the limit $\psi \to 0^+$. Indeed, (3.3.4) tells us that the limit $z \to 0^+$ for fixed $x > 0$ corresponds to $\psi \to 0^+$.

In order to find A_T for the $\mathrm{AdS}_{d+2}/\mathrm{BCFT}_{d+1}$ construction proposed in [89], one introduces a non-vanishing extrinsic curvature k_{ij} for the boundary of the BCFT_{d+1} and solves the Einstein equations with the Neumann boundary condition $K_{\mu\nu} = (K - T)h_{\mu\nu}$ proposed by [89] perturbatively in k_{ij}, considering only the first order in the perturbation.

Since we consider the first non-trivial order in the curvature of the boundary, the metric of the BCFT_{d+1} close to the boundary can be written as the follows

$$ds^2 = dx^2 + \big(\eta_{ij} - 2\, x\, k_{ij} + \dots \big)\, dY^i dY^j \tag{3.3.6}$$

where $Y^i = (t, \vec{y})$ and η_{ij} is the d dimensional Minkowski metric. The dots denote higher-order terms in the extrinsic curvature and in the distance x. In the literature, this gauge choice is sometimes called geodesic slicing.

In order to find the bulk metric corresponding to (3.3.6), in the following, we employ the ansatz recently suggested in [266] written in the coordinates adopted in (3.3.5). Also, in [91] a similar analysis has been performed. In particular, let us consider the perturbation of (3.3.5) given by

$$ds^2 = \frac{R^2_{\mathrm{AdS}}}{(\sin\psi)^2} \left(d\psi^2 + \frac{d\zeta^2 + \big(\eta_{ij} - 2\,\zeta \cos\psi\; p_d(\psi)\, \kappa_{ij}\big) dY^i dY^j}{\zeta^2} \right) + O(k^2) \tag{3.3.7}$$

where $\kappa_{ij} = k_{ij} - (k/d)\eta_{ij}$ is the traceless part of the extrinsic curvature and the boundary condition $p_d(0) = 1$ is imposed to recover (3.3.6) for the BCFT_{d+1}.

The metric (3.3.7) is a solution of the Einstein equations with negative cosmological constant up to $O(k^2)$ terms when $p_d(\theta)$ solves the following ordinary differential equation

$$\sin(2\psi)\, p_d''(\psi) - 2\big[\, (d-2)(\cos\psi)^2 + 2 \,\big]\, p_d'(\psi) \;=\; 0. \tag{3.3.8}$$

We remark that in (3.3.7) κ_{ij} occurs in the perturbation (and not k_{ij}) without loss of generality. Indeed, if we start with a metric like (3.3.7) where κ_{ij} is replaced by k_{ij} and η_{ij} by $\eta_{ij}[1 + \zeta \cos\psi\, q_d(\psi)\, k\,]$, being k the trace of k_{ij}, we would find that the Einstein equations at the first perturbative order in the extrinsic curvature provide again the equation (3.3.8) for $p_d(\psi)$ besides another equation for the function $q_d(\psi)$. Otherwise, if we start with an ansatz like (3.3.7) with κ_{ij} just replaced by k_{ij}, the Einstein equations to this order would lead to (3.3.8), as expected, and also the condition that $k = 0$.

The general solution of (3.3.8) reads

$$p_d(\psi) = B_d + \frac{C_d}{\cos\psi}\; {}_2F_1\big(-1/2\,, (1-d)/2\,; 1/2\,; (\cos\psi)^2 \,\big) \tag{3.3.9}$$

where B_d and C_d are integration constants. The requirement that (3.3.9) satisfies the boundary condition $p_d(0) = 1$ leads to

$$B_d = 1 - \frac{\sqrt{\pi}\, \Gamma(\frac{d+1}{2})}{\Gamma(\frac{d}{2})}\, C_d. \tag{3.3.10}$$

Thus, the solution of (3.3.8) fulfilling the constraint $p_d(0)=1$ can be written as

$$p_d(\psi)=1+C_d\,\mathcal{P}_d(\psi) \tag{3.3.11}$$

where

$$\mathcal{P}_d(\psi)\equiv\frac{1}{\cos\psi}\;{}_2F_1\big(-1/2\,,(1-d)/2\,;1/2\,;(\cos\psi)^2\,\big)-\frac{\sqrt{\pi}\,\Gamma(\frac{d+1}{2})}{\Gamma(\frac{d}{2})}. \tag{3.3.12}$$

We find important to remark that the combination $p_d(\psi)\cos\psi$ occurring in the metric is smooth for $\psi\in(0,\pi)$.

In the following we show that the constant C_d in (3.3.11) can be fixed in order to have that the half-hyperplane $\mathcal{Q}$ given by $\psi=\pi-\alpha$ is a solution of the Neumann boundary conditions $K_{ab}=(K-T)h_{ab}$ of [89] up to $O(k^2)$ terms.

Considering the metric $ds^2=g_{\mu\nu}dx^\mu dx^\nu$ defined in (3.3.7), the outward unit normal vector of the half-hyperplane $\mathcal{Q}$ is $n^\mu=L_{\text{AdS}}^{-1}(\sin\alpha,\vec{0}\,)$. As for the extrinsic curvature of $\mathcal{Q}$, we find that its non-vanishing components are given by

$$K_{\zeta\zeta}\;=\;\frac{R_{\text{AdS}}\,\sin\psi}{2\,\zeta^2}\;\partial_\psi\left(\frac{1}{\sin^2\psi}\right)\bigg|_{\psi=\pi-\alpha} \tag{3.3.13}$$

$$K_{Y^iY^j}\;=\;\frac{R_{\text{AdS}}\,\sin\psi}{2}\;\partial_\psi\left(\frac{1}{\zeta^2\sin^2\psi}\,\delta_{ij}-\frac{2\,p_d(\psi)\cos\psi}{\zeta\sin^2\psi}\;k_{ij}\right)\bigg|_{\psi=\pi-\alpha}. \tag{3.3.14}$$

Taking the trace of the Neumann boundary conditions, it is straightforward to observe that they can be written as $K_{ab}=(T/d)h_{ab}$. Since $T=(d/R_{\text{AdS}})\cos\alpha$ for the half-hyperplane $\mathcal{Q}$, the condition to impose in order to get the solution given by $\mathcal{Q}$ becomes $K_{ab}=(\cos\alpha/R_{\text{AdS}})h_{ab}$ at $\psi=\pi-\alpha$. At $O(k)$, the component having $(a,b)=(\zeta,\zeta)$ is identically satisfied, while the components with $(a,b)=(Y^i,Y^j)$ lead to the following equation

$$(\cot\alpha)\,p_d'(\pi-\alpha)+p_d(\pi-\alpha)\;=\;0. \tag{3.3.15}$$

Plugging (3.3.11) into (3.3.15), we obtain an equation for the integration constant C_d that can be easily solved. For $\alpha\in(0,\pi)$, we find

$$\begin{aligned}\frac{1}{C_d}\;&=\;-\,\mathcal{P}_d(\pi-\alpha)-\cot\alpha\;\partial_\psi\mathcal{P}_d(\psi)\big|_{\psi=\pi-\alpha}\\ &=\;\frac{1}{\cos\alpha}\;{}_2F_1\big(-1/2\,,(1-d)/2\,;1/2\,;(\cos\alpha)^2\,\big)-\frac{(\sin\alpha)^{d-1}}{\cos\alpha}+\frac{\sqrt{\pi}\,\Gamma(\frac{d+1}{2})}{\Gamma(\frac{d}{2})}.\end{aligned} \tag{3.3.16}$$

Let us observe that $C_d=1/(\pi-\alpha)^{d-1}+\dots$ when $\alpha\to\pi$ and also that

$$\partial_\alpha\big(1/C_d\big)\;=\;-\,(d-1)(\sin\alpha)^{d-2}. \tag{3.3.17}$$

Comparing (3.3.17) with (A.2.12) it is straightforward to observe that $\partial_\alpha\big(1/C_d\big)=\partial_\alpha\,\mathfrak{g}_{1/d}$. This observation suggests performing a direct comparison between (3.3.16) and (A.2.11), which provides the following intriguing relation

$$\frac{1}{C_d(\alpha)}=\mathfrak{g}_{1/d}(\alpha). \tag{3.3.18}$$

It would be interesting to explore whether this observation leads to some physical insights.

We find it worth considering the special cases of $d = 2$ and $d = 3$ explicitly. In AdS$_4$/BCFT$_3$, the expressions (3.3.12) and (3.3.16) give respectively

$$\mathcal{P}_2(\psi) = \tan\psi - \psi \tag{3.3.19}$$

and

$$C_2 = \frac{1}{\pi - \alpha}. \tag{3.3.20}$$

In the case of AdS$_5$/BCFT$_4$ we have that (3.3.12) simplifies to

$$\mathcal{P}_3(\psi) = \cos\psi + \sec\psi - 2 \tag{3.3.21}$$

and (3.3.16) leads to

$$C_3 = \frac{1}{2\,(1+\cos\alpha)}. \tag{3.3.22}$$

In the remaining part of this appendix, we show that the constant C_d is proportional to the constant A_T defined by (3.4.3).

According to the holographic prescription of [218], the expansion close to the boundary of the one-point function $\langle\, T_{ij}\,\rangle$ of the stress tensor in the BCFT$_3$ is given by

$$\langle\, T_{ij}\,\rangle \;=\; \frac{(d+1)R^d_{\text{AdS}}}{16\pi G_{\text{N}}}\,\lim_{z\to 0}\frac{g^{(1)}_{ij}}{z^{d-1}} \qquad x \to 0^+ \tag{3.3.23}$$

being $g^{(1)}_{ij}$ the $O(k)$ perturbation, which can be read from (3.3.7), finding

$$g^{(1)}_{ij} \;=\; -\,\frac{2\cos\psi\, p_d(\psi)}{(\sin\psi)^2\,\zeta}\,\kappa_{ij} \tag{3.3.24}$$

where $p_d(\psi)$ is (3.3.11) with the constant C_d given by (3.3.16)

In order to recover the expression (3.4.3) from (3.3.23), we have to exploit the relations among the various coordinates. In particular, from (3.3.3) we have that $\xi \to -\infty$ as $\psi \to 0^+$. Furthermore, taking this limit in the second expression in (3.3.2), one finds $\zeta \to x$. By considering the $O(\psi^{d+1})$ term in the expansion of $p_d(\psi)$ for $\psi \to 0$, we obtain

$$\lim_{z\to 0}\frac{g^{(1)}_{ij}}{z^{d-1}} \;=\; -\,\frac{2\,C_d}{(d+1)\,x^d}\,\kappa_{ij} \tag{3.3.25}$$

where we used that $z/x = \psi$ and $\zeta = x$ when $\psi \to 0^+$.

Finally, by plugging (3.3.25) into (3.3.23), we find that

$$\langle\, T_{ij}\,\rangle \;=\; \frac{A_T}{x^d}\,\kappa_{ij} + \dots \qquad x \to 0^+ \qquad\qquad A_T = -\frac{R^d_{\text{AdS}}}{8\pi G_{\text{N}}}\,C_d \tag{3.3.26}$$

which corresponds to the expected BCFT$_{d+1}$ behaviour (3.4.3). The proportionality relation between A_T and the integration constant C_d comes from the dual gravitational description of the BCFT$_{d+1}$ at strong coupling.

We can write A_T explicitly by employing the expression of C_d that can be read from (3.3.16). The result is

$$A_T \,=\, -\,\frac{R^d_{\mathrm{AdS}}}{8\pi G_{\mathrm{N}}}\left[\,\frac{1}{\cos\alpha}\;{}_2F_1\big(-1/2\,,(1-d)/2\,;1/2\,;(\cos\alpha)^2\,\big)-\frac{(\sin\alpha)^{d-1}}{\cos\alpha}+\frac{\sqrt{\pi}\;\Gamma(\frac{d+1}{2})}{\Gamma(\frac{d}{2})}\,\right]^{-1}. \tag{3.3.27}$$

We find worth remarking that A_T can be written also in terms of the function $\mathfrak{g}_d(\alpha)$ defined in (A.2.11). From (3.3.26) and the relation (3.3.18), we obtain

$$A_T \,=\, -\,\frac{R^d_{\mathrm{AdS}}}{8\pi G_{\mathrm{N}}}\,\frac{1}{\mathfrak{g}_{1/d}(\alpha)}. \tag{3.3.28}$$

The function $A_T(\alpha)$ is negative and decreasing function in the range $\alpha \in (0,\pi)$, Indeed, for $\alpha = 0$ we find

$$A_T\big|_{\alpha=0} \,=\, \frac{R^d_{\mathrm{AdS}}}{8\pi G_{\mathrm{N}}}\left(\frac{2\,\sqrt{\pi}\;\Gamma(\frac{d+1}{2})}{\Gamma(\frac{d}{2})}-\delta_{d,1}\right)^{-1} \tag{3.3.29}$$

which is negative for every value of d. Moreover, from (3.3.17) it is straightforward to observe that

$$\partial_\alpha A_T(\alpha) \,=\, \frac{R^d_{\mathrm{AdS}}}{8\pi G_{\mathrm{N}}}\,C_d^2\,\partial_\alpha(1/C_d) \,=\, -\,\frac{R^d_{\mathrm{AdS}}}{8\pi G_{\mathrm{N}}}\,(d-1)(\sin\alpha)^{d-2}\,C_d^2 \tag{3.3.30}$$

which implies $\partial_\alpha A_T(\alpha) \leqslant 0$ for $\alpha \in (0,\pi)$. Furthermore, let us notice that the behaviour of C_d as $\alpha \to \pi$ leads to conclude that $A_T(\alpha) = -\frac{R^d_{\mathrm{AdS}}}{8\pi G_{\mathrm{N}}}(\pi-\alpha)^{-(d-1)}$ in this limit.

In the special case of $d = 2$, the expression (3.3.27) of A_T simplifies to

$$A_T = -\,\frac{R^2_{\mathrm{AdS}}}{16\pi G_{\mathrm{N}}}\,\frac{2}{\pi-\alpha} \tag{3.3.31}$$

and this result will be crucial to observe the relation (3.4.6) presented in the next section.

The computation described above has been done for $d = 2$ and $d = 3$ also in [266] and non-smooth expressions for A_T have been found in the regime $\alpha \in (0,\pi)$.

3.4 Relations between the stress-energy tensor and the boundary corner function

In this section, we are going to explore possible universal relations among the corner functions and other quantities of the underlying BCFT_3 model.

In CFT_3, an important example of universal relation involves the corner function $\tilde{f}(\theta)$ and the two-point function (1.1.22) of the stress tensor T_{ij}, which has been discussed in Sec. 1.1.2[1]. We recall that by considering the coefficient $\tilde{\sigma} = \tilde{f}''(\pi)/2$ of the leading term in the expansion $\tilde{f}(\theta) = \tilde{\sigma}(\pi-\theta)^2 + \dots$ as $\theta \to \pi^-$, it has been found that [63, 265]

$$\frac{\tilde{\sigma}}{C_T} = \frac{\pi^2}{24}. \tag{3.4.1}$$

---

[1] In this section, we will use Latin indices for the components of the BCFT_{d+1}, while Greek indices are reserved for the bulk spacetime

In AdS$_4$/CFT$_3$ the holographic corner function is $\tilde{f}(\theta) = \frac{R^2_{\text{AdS}}}{4G_{\text{N}}}\,\widetilde{F}(\theta)$, as discussed in Sec. 1.3.3. Denoting by $\tilde{\sigma}_{\text{E}}$ the coefficient $\tilde{\sigma}$ for this holographic corner function in a bulk theory described by Einstein gravity, we have that $\tilde{\sigma}_{\text{E}} = \frac{R^2_{\text{AdS}}}{8G_{\text{N}}}\widetilde{F}''(\pi)$. Considering the corner function $F_\alpha(\gamma)$ in AdS$_4$/BCFT$_3$ given by (3.2.7) and (3.2.12), in Sec. 3.2.2 the relation (3.2.14) has been observed when $\alpha = \pi/2$. Taking the limit $\gamma \to \pi/2$ of (3.2.14) by employing (3.1.2) and $F_{\pi/2}(\frac{\pi}{2}) = 0$, one finds that $2\widetilde{F}''(\pi) = F''_{\pi/2}(\frac{\pi}{2})$. The latter relation and $F''_\alpha(\frac{\pi}{2}) = 1/(\pi-\alpha)$ (see (3.2.19)) evaluated for $\alpha = \pi/2$ provide $\sigma_{\text{E}} = \frac{R^2_{\text{AdS}}}{16G_{\text{N}}}\,F''_{\pi/2}(\frac{\pi}{2}) = \frac{R^2_{\text{AdS}}}{8\pi G_{\text{N}}}$. Then, by employing the holographic result $C_T = 3R^2_{\text{AdS}}/(\pi^3 G_{\text{N}}) = \frac{R^2_{\text{AdS}}}{16\pi G_{\text{N}}}(48/\pi^2)$ found in [267, 268], one obtains $\tilde{\sigma}_{\text{E}}/C_T = \pi^2/24$, which corresponds to (3.4.1) in the holographic setup determined by the Einstein gravity in the bulk. Thus, consistency has been found between (3.2.14) and the ratio (3.4.1).

We find it interesting to explore the possibility that universal relations also exist for BCFT$_3$. In Sec. 1.2.1 we have seen that in a BCFT$_3$ the presence of the boundary leads to a non-trivial Weyl anomaly localised on the boundary, which is given by [88, 205]

$$\langle\, T^{i}{}_{i}\,\rangle \;=\; \frac{1}{4\pi}\big(-\,\mathfrak{a}\,\mathcal{R} + \mathfrak{q}\,\mathrm{Tr}\kappa^2\,\big)\,\delta(\partial\mathcal{M}_3) \tag{3.4.2}$$

where $\delta(\partial\mathcal{M}_3)$ is the Dirac delta whose support is $\partial\mathcal{M}_3$. Furthermore, we discussed that the one-point function of the stress-tensor is non-trivial when the boundary is curved and, in terms of the proper distance X from $\partial\mathcal{M}_3$, it is given by [199]

$$\langle\, T_{\mu\nu}\,\rangle \;=\; \frac{A_T}{X^2}\,\kappa_{ij} + \dots \qquad X \to 0^+ \tag{3.4.3}$$

In the above equations, $\mathcal{R}$ is the Ricci scalar corresponding to the induced metric h_{ij} on $\partial\mathcal{M}_3$ and κ_{ij} is the traceless part of the extrinsic curvature of $\mathcal{M}_3$. The constants $\mathfrak{a}$ and $\mathfrak{q}$ are the boundary central charges, which depends on the underlying model and also on the conformally invariant boundary conditions characterising the BCFT$_3$, which have been computed for some free models in [88, 91, 208]. The coefficient A_T has been computed in four dimensions in [199] and it has been found to be proportional to $\mathfrak{q}$ in [200].

Let us focus on the holographic corner function $f_\alpha(\gamma) = \frac{R^2_{\text{AdS}}}{4G_{\text{N}}}\,F_\alpha(\gamma)$, where $F_\alpha(\gamma)$ is given by (3.2.7) and (3.2.12).

Let us recall that in the AdS/BCFT construction discussed in [89], the Neumann boundary conditions given by $K_{\mu\nu} = (K - T)h_{\mu\nu}$ have been imposed to define the hypersurface $\mathcal{Q}$ in the bulk delimiting the gravitational spacetime. Instead, in [158–160] it has been proposed to employ the less restrictive boundary condition $K = \frac{d+1}{d}\,T$ to find $\widetilde{\mathcal{Q}}$. When the boundary of the BCFT$_3$ is flat, both these prescriptions provides the half-plane $\widetilde{\mathcal{Q}} = \mathcal{Q}$ given by (1.4.9).

In Sec. 1.4.2, by following [90] we found for a BCFT$_3$ defined on the three-dimensional sphere (in the Euclidean signature) that [90][2]

$$\mathfrak{a} = \frac{R^2_{\text{AdS}}}{4G_{\text{N}}}\,(-\cot\alpha) \tag{3.4.4}$$

which means that $\mathfrak{a} = f_\alpha(\pi/2)$ in the holographic setup. Recently, in [269] the authors showed by employing the method of [224] that the relation $\mathfrak{a} = f_\alpha(\pi/2)$ is actually true for a generic

---

[2] Comparing with the notation of [90], we find that $(-\,c_{bdy}/6)\big|_{\text{there}} = \mathfrak{a}$.

BCFT$_3$. On the other hand, in [208], it has been shown that this relation fails for the scalar field because of the occurrence of a non-minimal coupling to the curvature. This seems to be a puzzle that, at this stage, has not been solved yet. We think that checking the validity of $f_\alpha(\pi/2) = \mathfrak{a}$ by employing other models is an interesting issue for future studies.

We mention also that using instead the restricted boundary conditions $K = \frac{d+1}{d} T$, the relations $\mathfrak{q} = \mathfrak{a} = f_\alpha(\pi/2)$ have been obtained [158–160]. Notice that the relation $\mathfrak{q} = \mathfrak{a}$ is not true for a free scalar [88, 91, 208].

We remark that, since the holographic corner function given by (3.2.7) and (3.2.12) has been found for a flat boundary, it should be the same for both the above AdS$_4$/BCFT$_3$ constructions, once the prescription (1.3.2) for the holographic entanglement entropy is accepted.

In the remaining part of this section we explore a relation involving the coefficient $f''_\alpha(\pi/2)$ of the expansion (3.1.2) of the holographic corner function as $\gamma \to \pi/2$.

In AdS$_4$/BCFT$_3$ we have found that $F''_\alpha(\pi/2) = 1/(\pi - \alpha)$ (see (3.2.19)); therefore for $\alpha = \pi/2$ we have

$$f''_\alpha(\pi/2) = \frac{R^2_{\text{AdS}}}{16\pi G_{\text{N}}} \, \frac{4\pi}{\pi - \alpha}. \tag{3.4.5}$$

By employing the AdS/BCFT construction of [89] and the standard approach to the holographic stress tensor [218, 270, 271], in Sec. 3.3 we have revisited the analysis of [266][3] finding the expression of A_T in AdS$_{d+2}$/BCFT$_{d+1}$ with the boundary conditions of [89] (see (3.3.27)). In the special case of $d = 2$, for $\alpha \in (0, \pi)$ we obtain (3.3.31).

From (3.4.5) and (3.3.31), we observe that in the AdS$_4$/BCFT$_3$ setup of [89] the ratio $f''_\alpha(\pi/2)/A_T$ is independent of the slope α, which should be related to the conformally invariant boundary conditions allowed for the dual BCFT$_3$. In particular this ratio reads

$$\frac{f''_\alpha(\pi/2)}{A_T} = -\,2\pi. \tag{3.4.6}$$

We find it very interesting to compute the ratio (3.4.6) also for other BCFT$_3$. Free quantum field theories are the simplest models to address in this direction. We mention that in [272] the numerical result of $f''_\alpha(\pi/2)$ for the free scalar boson with Dirichlet boundary conditions has been found, and it does not agree with our (3.4.6). However, the scalar boson seems to be anomalous due to the non-minimal coupling to the curvature mentioned above. It is certainly worth to test (3.4.6) also for the free fermions.

3.5 Transitions in the presence of corners

The main aim of this section is to discuss the vertices of the Q-type depicted in Fig. 3.1 in the AdS$_4$/BCFT$_3$ framework. In this case, two different extremal surfaces compete, and a transition occurs at a certain value of the angles $(\gamma, \omega) = (\gamma_c, \omega_c)$.

To begin with, we will consider the case of AdS$_4$/CFT$_3$ where similar transitions take place for two corners which share the same tip (see the right side of Fig. 3.1). Then, we move to the AdS$_4$/BCFT$_3$ setup where we find the analytic expression of $\mathcal{F}_\alpha(\omega, \gamma)$ discussed in the introduction of this chapter.

---

[3] In Sec. 3.3 the differences between our results and the ones obtained in [266] are discussed.

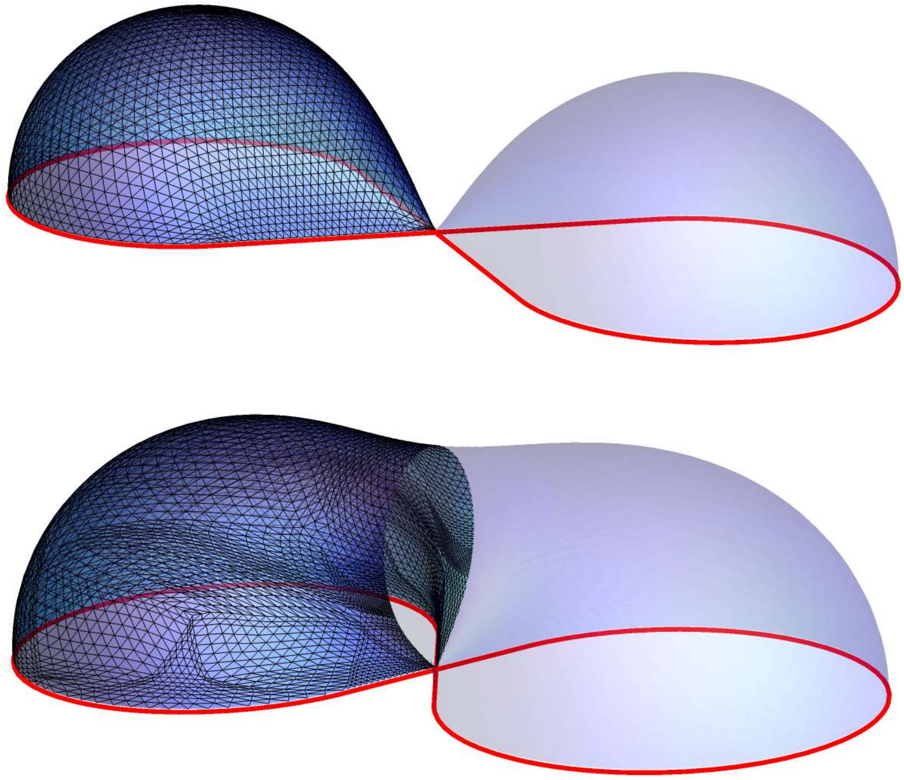

Figure 3.9: Triangulated surfaces in $\mathbb{H}_3$ approximating the minimal area surfaces $\hat{\gamma}_A$ which correspond to two different double drop regions A described in Sec. 3.5.1. For these domains $\phi_1 = \phi_2 \equiv \phi$ and $\varphi_1 = \varphi_2 = \pi - \phi$. The boundary ∂A (red curve) belongs to the $z = 0$ plane and the UV cutoff is $\varepsilon = 0.03$. Top: $L = 2$ and $\phi = 1.4$ (below $\phi_c = \pi/2$). Bottom: $L = 1$ and $\phi = 2.2$ (above $\phi_c = \pi/2$).

3.5.1 Two corners with the same tip

Let us consider the domain obtained as the union $A = A_1 \cup A_2$ of two single drop regions[4] A_1 and A_2, where A_1 and A_2 have the same tip W, as in the right side of Fig. 3.1. In particular, W is the only element of their intersection, i.e. $A_1 \cap A_2 = \{W\}$. The boundary ∂A is smooth except at the vertex W, where four lines join together. Considering the four adjacent corners with the common vertex W, let us denote by ϕ_1 and ϕ_2 the opening angles of the corners in A_1 and A_2 respectively and by φ_1 and φ_2 the opening angles of the other two corners which do not belong to A. We can assume $0 < \phi_1 \leqslant \phi_2$ and $0 < \varphi_1 \leqslant \varphi_2$ without loss of generality. The configuration of the corners around W can be characterised by the three angles $\vec{\phi} = (\phi_1, \varphi_1, \phi_2)$.

In Sec. 1.3.3 of chapter 1, by following [157] we have studied the minimal surfaces anchored to entangling curves with a single corner, finding the general expressions (1.3.23) and (1.3.24). In this section, we employ such expressions to compute the holographic entanglement entropy for "double drop" regions A. The coefficient of the logarithmic divergence of $\mathcal{A}[\hat{\gamma}_\varepsilon]$ comes

---

[4] We recall that the drop regions have been defined in the Sec. 1.3.3 of the first chapter.

from the contribution of the vertex W and it is given by $\widetilde{F}_{\text{tot}} = \widetilde{\mathcal{F}}(\vec{\phi}\,)$.

Symmetric configurations can be considered by imposing constraints among the components of $\vec{\phi}$. For instance, we can study domains such that A_1 and A_2 coincide after a proper rigid rotation of one of them. In these cases the configuration of the corners at the common tip W is determined by two parameters: the opening angle $\phi_1 = \phi_2 \equiv \phi$ and the relative orientation given by φ_1. Let us stress that the coefficient of the logarithmic term is determined by the local configuration of corners around the vertex W and it is not influenced by the shape of the entire domain A.

We consider first the configuration where the two drop regions A_1 and A_2 are symmetric with respect to their common tip W. This means that $\phi_1 = \phi_2 \equiv \phi$ and also $\varphi_1 = \varphi_2 \equiv \varphi$. The resulting domain A is symmetric w.r.t. two orthogonal straight lines whose intersection point is W. Since $\varphi + \phi = \pi$, the coefficient of the logarithmic divergence in (1.3.23) is determined only by the angle ϕ for these cases, namely $\widetilde{F}_{\text{tot}} = \widetilde{\mathcal{F}}(\phi)$. In particular, it is not difficult to realise that for these configurations the corner function is given by [273]

$$\widetilde{\mathcal{F}}(\phi) \;=\; 2\max\Big\{\widetilde{F}(\phi)\,,\,\widetilde{F}(\pi-\phi)\Big\} \tag{3.5.1}$$

being $\widetilde{F}(\phi)$ the corner function given by (1.3.26) and (1.3.28). The factor 2 in (3.5.1) is due to the fact that the two opposite wedges provide the same contribution.

A critical value ϕ_c for the common opening angle occurs when the two functions compared in (3.5.1) takes the same value. From the arguments of the $\widetilde{F}$'s in (3.5.1), it is straightforward to find that $\phi_c = \pi/2$.

In Fig. 3.9 we show two triangulations obtained with Surface Evolver which approximate the corresponding minimal surface $\hat{\gamma}_A$ in the two cases of $\phi < \phi_c$ (top panel) and $\phi > \phi_c$ (bottom panel). The crucial difference between them can be appreciated by focussing around the common tip W. Indeed, when $\phi < \phi_c$ the points of $\hat{\gamma}_A$ close to the tip have coordinates $(x, y) \in A$ and $\hat{\gamma}_A$ is made by the union of two minimal surfaces like the one in Fig. 1.7 which have the same tip. Instead, when $\phi > \phi_c$ the points of $\hat{\gamma}_A$ close to the tip have coordinates $(x, y) \notin A$. This leads to the expression (3.5.1) for the coefficient of the logarithmic divergence in the expansion of $\mathcal{A}[\hat{\gamma}_\varepsilon]$. The minimal surface $\hat{\gamma}_A$ is symmetric w.r.t. two half-planes orthogonal to the $z = 0$ plane whose boundaries are the two straight lines which characterise the symmetry of A. In Fig. 3.9 the symmetry w.r.t. one of these two half-planes is highlighted by the fact that the triangulation is shown only for half of the surface, while the remaining half-surface is shaded. This choice makes evident the curve given by the intersection between this half-plane and $\hat{\gamma}_A$ when $\phi > \phi_c$.

In Fig. 3.10 we show the results of our numerical analysis for this kind of symmetric regions. The points labeled by red triangles are obtained from triangulated surfaces like the one in the top panel of Fig. 3.9, while the points labeled by black circles correspond to triangulated surfaces like the one in the bottom panel of the same figure. The solid blue curve in Fig. 3.10 is obtained from the analytic expression (3.5.1). The agreement of our numerical results with the expected analytic curve is very good. This strongly encourages us to apply this numerical method to study more complicated configurations.

Another class of symmetric configurations is made by double drop regions A which are

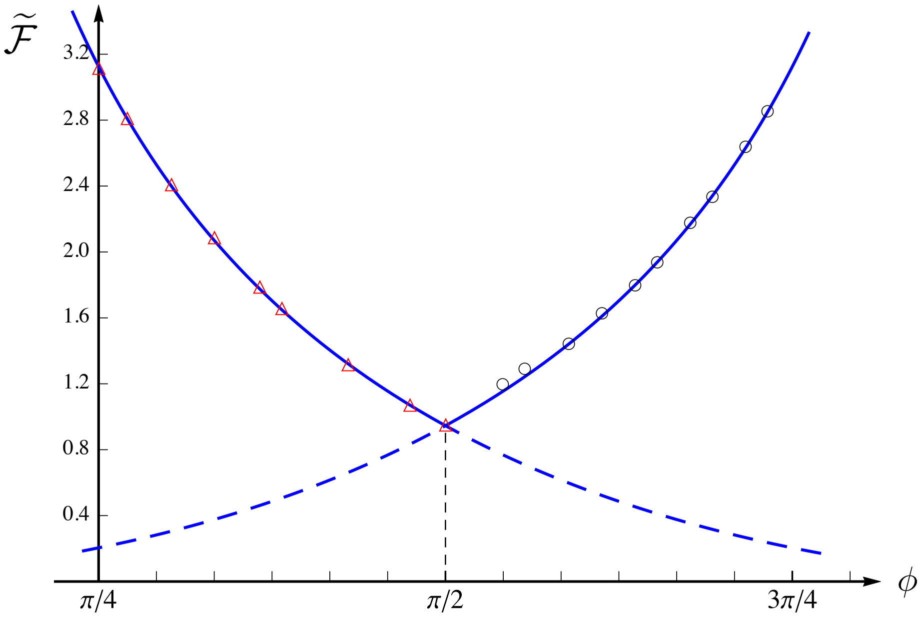

Figure 3.10: Corner function for a vertex with four edges in AdS$_4$/CFT$_3$ in the symmetric case where $\phi_1 = \phi_2 \equiv \phi$ and $\varphi_1 = \varphi_2 = \pi - \phi$ (see Sec. 3.5.1). The points labeled by the red triangles come from surfaces like the one in the top panel of Fig. 3.9, while the points labeled by the empty black circles are obtained from surfaces like the one in the bottom panel of Fig. 3.9. The solid curve corresponds to the analytic expression (3.5.1).

symmetric with respect to a straight line passing through the vertex W. There are two possibilities: either the intersection between this straight line and A is only the common tip (in this case $\phi_1 = \phi_2 \equiv \phi$) or such intersection is given by a finite segment belonging to A (in this case $\varphi_1 = \varphi_2 \equiv \varphi$). In both these cases, a constraint reduces the number of independent opening angles to two. Focussing on the coefficient of the logarithmic divergence, one can consider the limit of infinite wedges and employ the property $S_A = S_B$ of the pure states in this regime. This leads to conclude that these two options are equivalent and that the corresponding corner functions become the same because the property $S_A = S_B$ allows exchanging $\varphi_j \leftrightarrow \phi_j$. Nonetheless, we find it instructive to discuss both of them separately because they look very different when A is a finite domain.

As for the former class of configurations, by choosing the angles $\vec{\phi} = (\phi, \varphi_1)$ as independent variables, the remaining angle φ_2 is determined by the consistency condition $2\phi + \varphi_1 + \varphi_2 = 2\pi$. The area of the minimal surface anchored to this kind of regions is given by (1.3.23) where $\widetilde{F}_{\text{tot}} = \widetilde{\mathcal{F}}(\vec{\phi}\,)$ and the corner function reads

$$\widetilde{\mathcal{F}}(\vec{\phi}\,) \;=\; \max\Big\{2\,\widetilde{F}(\phi)\,,\, \widetilde{F}(\varphi_1) + \widetilde{F}(\varphi_2)\Big\} \tag{3.5.2}$$

where we remind that $\widetilde{F}(\varphi_2) = \widetilde{F}(\min[\varphi_2\,, 2\pi - \varphi_2])$. Also this case has been considered in [273]. When the two expressions occurring in the r.h.s. of (3.5.2) are equal, a transition occurs. This condition determines a critical value $\varphi_{1,c} = \varphi_{1,c}(\phi)$ in terms of $\phi < \pi$. In Fig. 3.11 we show two examples of minimal surfaces anchored to double drop regions that have this kind

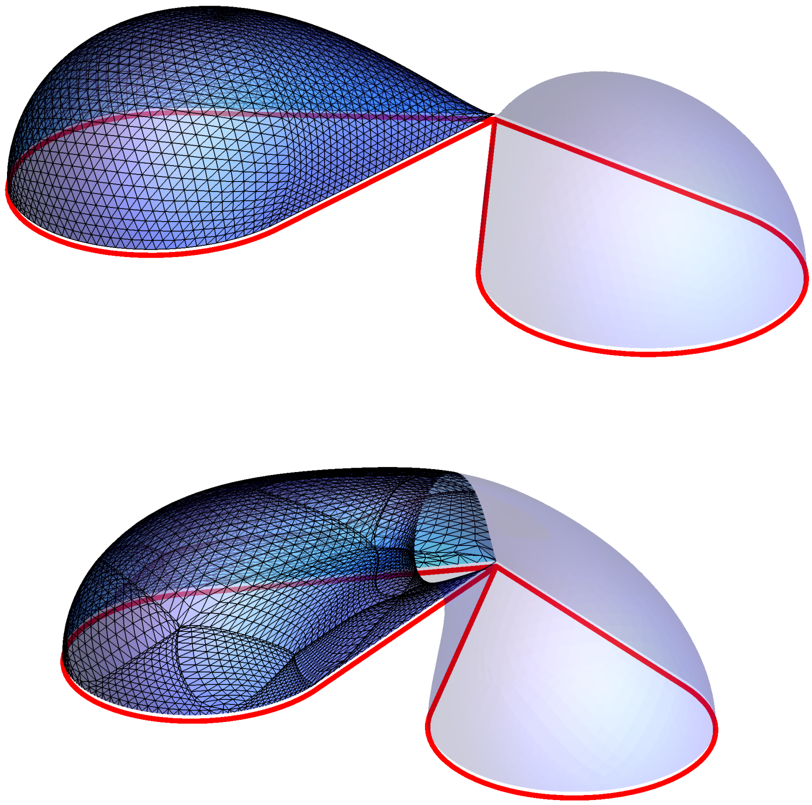

Figure 3.11: Triangulated surfaces in $\mathbb{H}_3$ which approximate the minimal area surfaces $\hat{\gamma}_A$ corresponding to two different double drop regions A which are symmetric w.r.t. a straight line passing through the vertex. For these domains $\phi_1 = \phi_2 \equiv \phi$ (see Sec. 3.5.1). The boundary ∂A (red curve) belongs to the $z = 0$ plane and the UV cutoff is $\varepsilon = 0.03$. Top: $L = 1.5$ with $\phi = 0.9$ and $\varphi_1 = 0.671$. Bottom: $L = 1.5$ with $\phi = 0.8$ and $\varphi_1 = 0.378$.

of symmetry. In particular $\varphi_1 > \varphi_{1,c}$ in the top panel and $\varphi_1 < \varphi_{1,c}$ in the bottom panel.

Considering the second class of configurations introduced above, where $\varphi_1 = \varphi_2 \equiv \varphi$, we have that $\phi_1 + \phi_2 + 2\varphi = 2\pi$ and therefore two angles fix the configurations of the corners in the neighbourhood of the common tip. One can choose e.g. $\vec{\phi} = (\phi_1, \phi_2)$. For this kind of double drop domains the coefficient of the logarithmic divergence in the area (1.3.23) is $\widetilde{F}_{\text{tot}} = \widetilde{\mathcal{F}}(\vec{\phi}\,)$ with

$$\widetilde{\mathcal{F}}(\vec{\phi}\,) \,=\, \max\Big\{ \widetilde{F}(\phi_1) + \widetilde{F}(\phi_2)\,,\, 2\,\widetilde{F}(\varphi) \Big\}. \tag{3.5.3}$$

As expected, also in this case two local solutions for the minimal surface exist and the global minimum provides the holographic entanglement entropy. The transition between the two kinds of solutions occurs when the two expressions in the r.h.s. of (3.5.3) are equal and this corresponds to a critical value for $\phi_{1,c} = \phi_{1,c}(\varphi)$. Notice that (3.5.2) and (3.5.3) exchange if $\phi_j \leftrightarrow \varphi_j$, as observed above.

For a generic double drop region A, we cannot employ symmetry arguments. Only the constraint $\phi_1 + \phi_2 + \varphi_1 + \varphi_2 = 2\pi$ holds; therefore the configuration of corners at W is

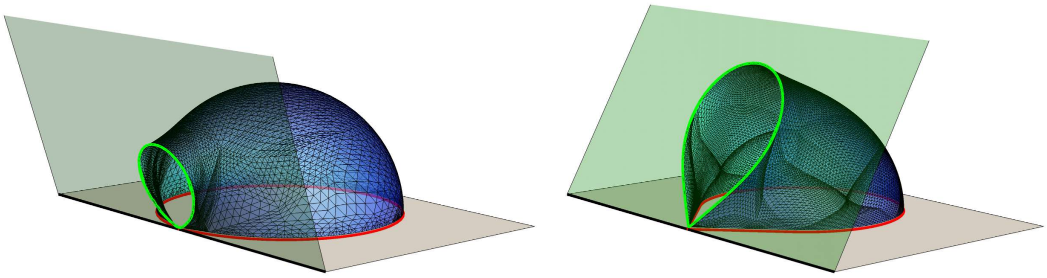

Figure 3.12: Minimal surfaces $\hat{\gamma}_A$ obtained with Surface Evolver and anchored to a single drop A (whose boundary is the solid red curve in the $z = 0$ grey half-plane) which has only the tip on the boundary. Here A has been chosen in a symmetric way (i.e. $\tilde{\gamma} = \gamma$). In the left panel $\alpha = \pi/2.5$, $\omega = 2.6$ and $L = 0.5$, while in the right panel $\alpha = 2\pi/3$, $\omega = \pi/2$ and $L = 1.5$. In both panels $\varepsilon = 0.03$. This kind of minimal surfaces have been constructed to find the data corresponding to $\omega > \omega_c$ in Fig. 3.13, which have been labeled by empty black circles.

determined by three independent angles, which are e.g. $\vec{\phi} = (\phi_1, \varphi_1, \phi_2)$. The expansion of the area of the corresponding $\hat{\gamma}_\varepsilon$ is (1.3.23) with $\widetilde{F}_{\text{tot}} = \widetilde{\mathcal{F}}(\vec{\phi})$, with the corner function given by

$$\widetilde{\mathcal{F}}(\vec{\phi}) = \max\left\{\widetilde{F}(\phi_1) + \widetilde{F}(\phi_2)\, ,\, \widetilde{F}(\varphi_1) + \widetilde{F}(\varphi_2)\right\}. \tag{3.5.4}$$

The transition occurs when the two expressions in the r.h.s. of (3.5.4) are equal. This condition provides a critical surface in the parameter space described by $(\phi_1, \varphi_1, \phi_2)$ with $\phi_1 \leqslant \phi_2$.

3.5.2 Corners with only the tip on the boundary

In this subsection, we consider the domain given by an infinite wedge having its tip on the boundary whose edges do not belong to it. In a generic BCFT$_3$ the entanglement entropy of this region contains a logarithmic divergence whose coefficient provides a corner function $\mathsf{F}_\alpha(\vec{\omega})$ which in general cannot be determined from the corner function $f_\alpha(\gamma)$ corresponding to the infinite wedge adjacent to the boundary. In the following, we explain that for the holographic entanglement entropy in AdS$_4$/BCFT$_3$ this analysis significantly simplifies and the corner function $\mathcal{F}_\alpha(\omega, \gamma)$ corresponding to this kind of wedge (see (3.0.4)) can be written in a form which involves the corner function $F_\alpha(\gamma)$ presented in Sec. 3.2.2 and the corner function $\widetilde{F}(\theta)$ reviewed in Sec. 1.3.3.

Let us consider the infinite wedge A with opening angle $\omega < \pi$ which has only the tip on the boundary $x = 0$. Domains containing this kind of corner occur in Fig. 3.2, where they are labeled by C and C_j. Setting the origin of the Cartesian coordinates in the tip of the wedge A, we have that the boundary $x = 0$ is split into two half-lines corresponding to $y < 0$ and $y > 0$. Denoting by $\gamma < \pi$ and $\tilde{\gamma} < \pi$ the opening angles of the corners in B, the supplementarity condition $\omega + \gamma + \tilde{\gamma} = \pi$ holds. We can assume that $\gamma \leqslant \tilde{\gamma}$ without loss of generality. Combining this inequality with the supplementarity condition, it is straightforward to observe that $\gamma \leqslant (\pi - \omega)/2$. Instead, since $\tilde{\gamma}$ is not restricted, we have that $\tilde{\gamma} \in (0, \pi)$. In the following we denote by $L \gg \varepsilon$ the length of the edges of A, as done in Sec. 3.2.2 for the wedge adjacent to the boundary.

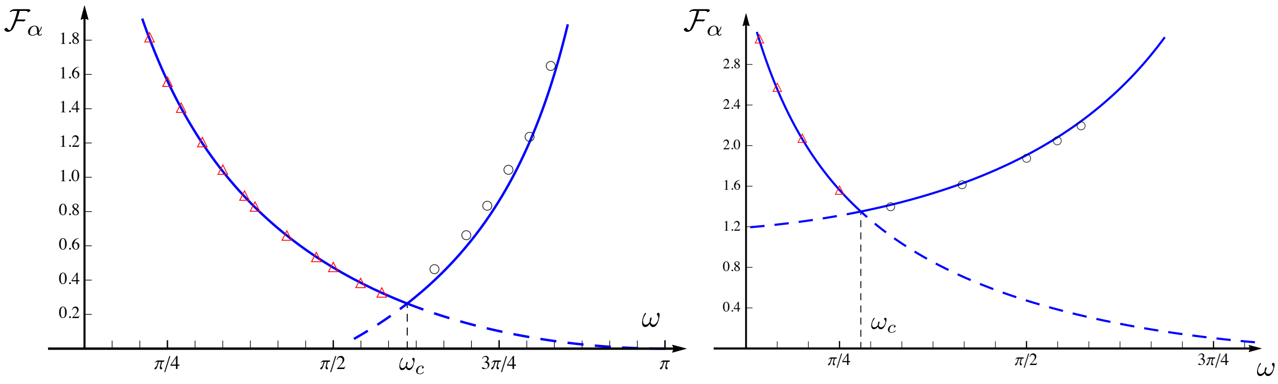

Figure 3.13: The corner function (3.5.6) for symmetric configurations of the infinite wedge (i.e. $\tilde{\gamma} = \gamma$). The slope α of $\mathcal{Q}$ is different in the two panels: $\alpha = \pi/2.3$ (left) and $\alpha = 2\pi/3$ (right). The solid blue line is obtained from the analytic expression (3.5.6). The data points have been found by constructing minimal surfaces with Surface Evolver anchored to single drop domains whose opening angle of the corner is ω. The minimal surfaces corresponding to the empty black circles are connected to $\mathcal{Q}$ (see e.g. Fig. 3.12), while the ones corresponding to the empty red triangles are disconnected from $\mathcal{Q}$. The critical value ω_c is defined by (3.5.7). Notice that $\omega_c > \pi/2$ when $\alpha < \pi/2$ and $\omega_c < \pi/2$ when $\alpha > \pi/2$.

Since the edges of A do not belong to the boundary $x = 0$, the minimal surface $\hat{\gamma}_A$ is anchored to both of them. Moreover, the expansion of the area of $\hat{\gamma}_\varepsilon$ is (3.0.3) with $P_{A,B} = 2L$ and the coefficient of the logarithmic divergence (3.0.4) is given by $F_{\alpha,\text{tot}} = \mathcal{F}_\alpha(\omega, \gamma)$.

It is not difficult to realise that there are two candidates for $\hat{\gamma}_A$ which are local solutions of the minimal area condition in presence of $\mathcal{Q}$. The first one is a surface $\hat{\gamma}_A^{\text{dis}}$ which connects the two edges of A through the bulk and is disconnected from the half-plane $\mathcal{Q}$. Since $\hat{\gamma}_A^{\text{dis}} \cap \mathcal{Q} = \emptyset$, we have that $\hat{\gamma}_A^{\text{dis}}$ is the minimal area surface found in [157], which has been discussed in Sec. 1.3.3. The second solution is a surface $\hat{\gamma}_A^{\text{con}}$ which connects the two edges of A to $\mathcal{Q}$ through the bulk. It is given by the union of two disjoint surfaces where each of them is like the one found in Sec. 3.2.2; therefore $\hat{\gamma}_A^{\text{con}} \cap \mathcal{Q}$ is made by two half-lines departing from the tip of the wedge.

The area $\mathcal{A}[\hat{\gamma}_\varepsilon]$, which provides the holographic entanglement entropy for this infinite wedge A, is the minimum between the area of $\hat{\gamma}_A^{\text{dis}} \cap \{z \geqslant \varepsilon\}$ and the area of $\hat{\gamma}_A^{\text{con}} \cap \{z \geqslant \varepsilon\}$. Being $P_{A,B} = 2L$ for both $\hat{\gamma}_A^{\text{dis}}$ and $\hat{\gamma}_A^{\text{con}}$, the minimal area surface $\hat{\gamma}_A$ must be found by comparing the coefficients of the subleading logarithmic divergence. This comparison leads to the following corner function

$$\mathcal{F}_\alpha(\omega, \gamma) \, = \, \max\Big\{ \widetilde{F}(\omega) \, , \, F_\alpha(\gamma) + F_\alpha(\tilde{\gamma}) \Big\} \qquad \tilde{\gamma} = \pi - (\omega + \gamma) \tag{3.5.5}$$

where the first function within the parenthesis corresponds to $\hat{\gamma}_A^{\text{dis}}$ and the second one to $\hat{\gamma}_A^{\text{con}}$. The corner function $\widetilde{F}(\omega)$ is the one found in [157] and reviewed in Sec. 1.3.3, while $F_\alpha(\gamma)$ is the corner function discussed in Sec. 3.2.2. Let us remind that, since $\tilde{\gamma} \in (0, \pi)$ in (3.5.5) we mean $F_\alpha(\tilde{\gamma}) = F_\alpha(\min[\,\tilde{\gamma}\,,\, \pi - \tilde{\gamma}\,])$, as stated in Sec. 3.1.

It could be useful to compare (3.5.5) with (3.5.2). Indeed, by extending the half-plane $x \geqslant 0$ to the whole $\mathbb{R}^2$ and including the reflected image of A obtained by sending $x \to -x$,

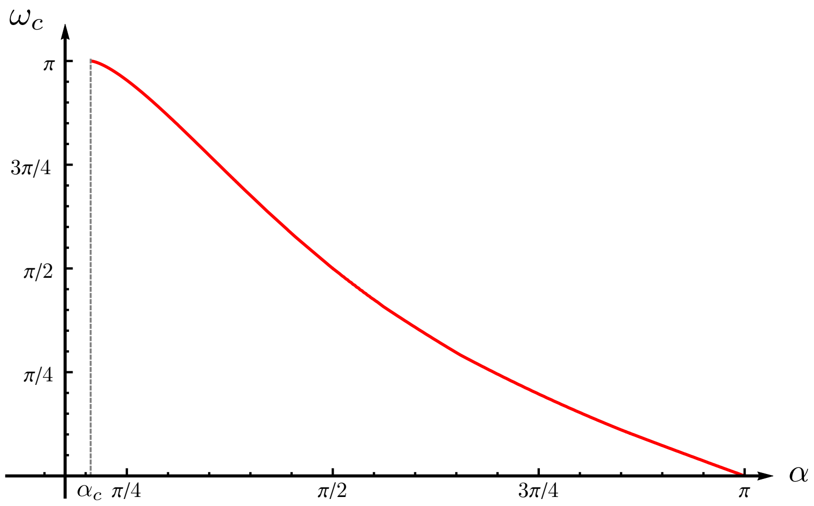

Figure 3.14: Infinite wedge with only the tip on the boundary and $\tilde{\gamma} = \gamma$: The critical opening angle ω_c as function of $\alpha \geqslant \alpha_c$. The curve has been found by solving (3.5.7) numerically.

one obtains the symmetric configuration of corners underlying (3.5.2). Nonetheless, let us stress that (3.5.5) with (3.5.2) are not equivalent because in (3.5.5) the boundary conditions (which correspond to α in this holographic setup) play a central role.

The corner function (3.5.5) occurs in the constraints from the strong subadditivity found in Sec. 3.1. In the appendix B.3 we show that the holographic corner functions $F_\alpha(\gamma)$ and $\mathcal{F}_\alpha(\omega,\gamma)$ fulfils these constraints.

For the sake of simplicity, let us consider first the subclass of infinite wedges which are symmetric with respect to the half-line departing from the tip and orthogonal to the boundary. For these wedges $\tilde{\gamma} = \gamma$; therefore the supplementarity condition implies that $\gamma = (\pi - \omega)/2$. Thus, these configurations are fully determined by ω (equivalently, one can adopt γ as the independent variable). By substituting $\omega = \pi - 2\gamma$ into (3.5.5), we find that for these symmetric wedges the corner function simplifies to

$$\mathcal{F}_\alpha(\omega,\gamma) \,=\, \max\Big\{\widetilde{F}(\omega)\,, 2F_\alpha(\gamma)\Big\} \qquad \gamma = \frac{\pi-\omega}{2}. \tag{3.5.6}$$

The maximisation procedure occurring in (3.5.5) and (3.5.6) chooses the first function for some configurations and the second function for other ones. In particular, there exist critical configurations such that the two functions in the r.h.s.'s of (3.5.5) and (3.5.6) provide the same result, namely both $\hat{\gamma}_A^{\text{dis}}$ and $\hat{\gamma}_A^{\text{con}}$ have the same coefficient of the logarithmic divergence.

In Fig. 3.12 we show two examples of minimal area surfaces obtained with Surface Evolver which correspond to single drop domains A (see Sec. 1.3.3) whose corners have the tip on the boundary and belong to this class of symmetric wedges having $\tilde{\gamma} = \gamma$. In a neighbourhood of the tips of these two domains, the minimal area surface $\hat{\gamma}_A$ is given by $\hat{\gamma}_A^{\text{con}}$.

In Fig. 3.13 the corner function (3.5.6) is plotted as function of ω for two particular values of α. The critical value ω_c, where the two functions in the r.h.s. of (3.5.6) are equal, is highlighted by the vertical dashed segments, and it depends on the slope α. For $\omega < \omega_c$ the minimal surface $\hat{\gamma}_A$ is disconnected from $\mathcal{Q}$ and it is like the one shown in Fig. 1.7, while for

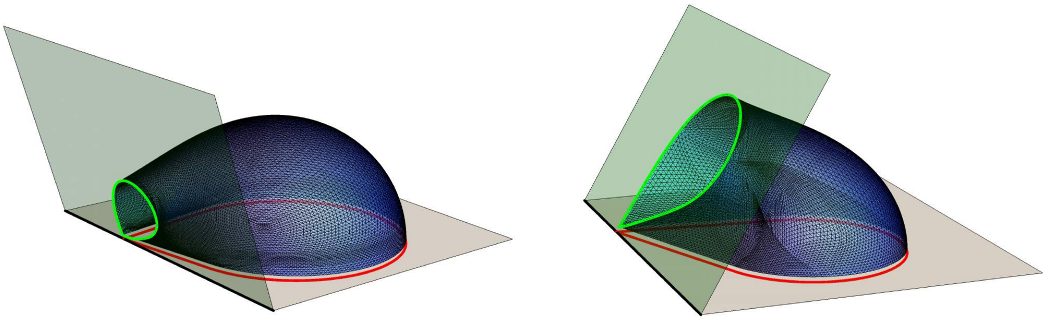

Figure 3.15: Minimal surfaces $\hat{\gamma}_A$ obtained with Surface Evolver and corresponding to a single drop A such that the entangling curve ∂A (solid red curve in the $z = 0$ grey half-plane) intersects the boundary at the tip of its corner. For these configurations of A, the corresponding minimal surface is the surface which intersects $\mathcal{Q}$ (green half-plane) orthogonally along the green curve. In the left panel $\alpha = \pi/2.5$, $\omega = \pi/2$, $\gamma = \pi/2 - \pi/5$ and $L = 0.75$, while in the right panel $\alpha = 2\pi/3$, $\omega = \pi/3$, $\gamma = \pi/2 - \pi/5$ and $L = 1$. In both panels $\varepsilon = 0.03$.

$\omega > \omega_c$ it is connected to $\mathcal{Q}$ and it looks like the minimal surfaces depicted in Fig. 3.12. The minimal surfaces in Fig. 3.12 are prototypical examples of the surfaces employed to find the numerical data corresponding to the empty circles in Fig. 3.13.

By applying the remark made above about (3.5.5) to this simpler situation, it could be instructive to compare (3.5.6) with (3.5.1), which has been found for the analogous situation in AdS$_4$/CFT$_3$, as it can be observed by using the image method. Nonetheless, we remark again that in (3.5.6) the parameter α enters in a crucial way. By performing the same analysis done for Fig. 3.13 setting $\alpha = \pi/2$, we have checked numerically the data shown in Fig. 3.10 are consistent with the relation (3.2.15).

In the remaining part of this section we describe the critical configurations corresponding to (3.5.5) and to (3.5.6).

Let us consider first the class of symmetric wedges where $\tilde{\gamma} = \gamma$. From (3.5.6), we have that the critical configuration is characterised by the opening angle $\omega_c = \omega_c(\alpha)$ which solves the following equation

$$\widetilde{F}(\omega_c) \,=\, 2\, F_\alpha\big((\pi - \omega_c)/2\big). \tag{3.5.7}$$

As consistency check we can set $\alpha = \pi/2$. In this case, by employing (3.2.15) in the r.h.s. of (3.5.7), the equation (3.5.7) becomes $\widetilde{F}(\omega_c) = \widetilde{F}(\pi - \omega_c)$, whose solution is $\omega_c = \pi/2$, as expected from the general fact the results in AdS$_4$/CFT$_3$ (see Fig. 3.10 for this quantity) are recovered in our AdS$_4$/BCFT$_3$ setup for $\alpha = \pi/2$.

We find it worth also focussing on the special value $\alpha = \alpha_c$. By employing the characteristic property of α_c given by (3.2.18) and the fact that $\widetilde{F}(\pi) = 0$ into (3.5.7), we find

$$\lim_{\alpha \to \alpha_c} \omega_c(\alpha) \,=\, \pi. \tag{3.5.8}$$

Since $\omega < \pi$, the limit (3.5.8) tells us that, within the class of symmetric wedges with $\tilde{\gamma} = \gamma$, the minimal area surface $\hat{\gamma}_A$ is always $\hat{\gamma}_A^{\text{dis}}$ when $\alpha \leqslant \alpha_c$. This observation can be inferred also from (3.5.6) because $F_\alpha(\gamma) \leqslant 0$ for $\alpha \leqslant \alpha_c$, while $\widetilde{F}(\omega) \geqslant 0$. Thus, when $\alpha \leqslant \alpha_c$, the

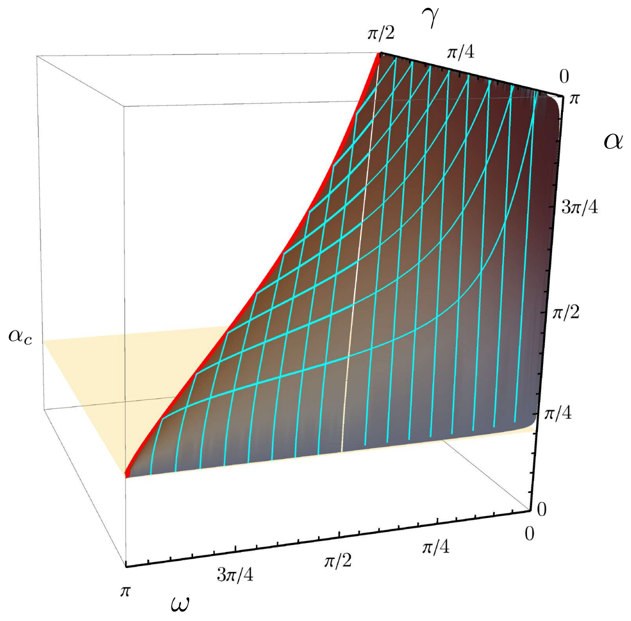

Figure 3.16: Infinite wedge with only the tip on the boundary: The surface described by the critical configurations, defined by (3.5.9) in the parameters space given by the angles ω, γ and α. The yellow plane is $\alpha = \alpha_c$. The red curve corresponds to the symmetric configurations having $\tilde{\gamma} = \gamma$ (see Fig. 3.14).

transition from $\hat{\gamma}_A = \hat{\gamma}_A^{\text{dis}}$ to $\hat{\gamma}_A = \hat{\gamma}_A^{\text{con}}$ as ω increases does not occur. The absence of this transition is a characteristic feature of the regime $\alpha \leqslant \alpha_c$ that can be detected with finite domains. We have not been able to get reliable numerical data from Surface Evolver for values of alpha close enough to α_c; therefore we have not observed (3.5.8) numerically. Hopefully, future analysis will address this numerical issue.

In Fig. 3.14 we show the curve $\omega_c(\alpha)$ of the critical opening angle for the symmetric wedges, which has been obtained by solving (3.5.7) numerically. Notice that the curve lies above the straight line tangent to it and passing through the point $\alpha = \pi/2$.

In the general case, $\tilde{\gamma} \geqslant \gamma$ and the configuration of the infinite wedge is characterised by the independent angles γ and ω. In Fig. 3.15 we show the minimal area surfaces constructed with Surface Evolver which are anchored to two different configurations of single drop domains A having the tip on the boundary and with $\tilde{\gamma} > \gamma$. For the configurations in Fig. 3.15, the minimal area surface $\hat{\gamma}_A$ in the neighbourhood of the tip is given by $\hat{\gamma}_A^{\text{con}}$.

As discussed above, critical configurations exist such that the two functions involved in the maximisation procedure of (3.5.5) have the same value. For a given slope α, we can equivalently characterise these configurations either by the critical value $\omega_c = \omega_c(\gamma, \alpha)$ in terms of γ or by the critical value $\gamma_c = \gamma_c(\omega, \alpha)$ in terms of ω. Choosing the former option, the critical value $\omega_c = \omega_c(\gamma, \alpha)$ is the solution of the following equation

$$\widetilde{F}(\omega_c) \;=\; F_\alpha(\gamma) + F_\alpha(\tilde{\gamma}) \qquad \tilde{\gamma} = \pi - (\omega_c + \gamma). \tag{3.5.9}$$

In Fig. 3.16 we show the surface which characterises the critical configurations, obtained by solving (3.5.9) numerically. Notice that the surface lies in the range $\alpha > \alpha_c$, as expected from the above considerations. The red solid curve in Fig. 3.16 corresponds to the symmetric case $\gamma = \tilde{\gamma}$, namely to the curve in Fig. 3.14. Furthermore, the section at $\alpha = \pi/2$ of the surface in Fig. 3.16 provides the critical configurations for the symmetric domains in a CFT_3 whose coefficient of the logarithmic divergence of the corresponding holographic entanglement entropy is (3.5.2), which have been described in Sec. 3.5.1.

3.6 Discussion

Considering a BCFT_3 with a flat boundary, in this chapter, we mainly focussed on the entanglement entropy of two-dimensional domains A in a constant time-slice whose entangling curve intersects the boundary of the BCFT_3. In particular, we have studied the cases where the singular points of ∂A belong to the boundary of the BCFT_3 (see e.g. the yellow region on the right panel of Fig. 3.1). The expansion of the entanglement entropy of these domains as the UV cutoff $\varepsilon \to 0$ contains a logarithmic divergence whose coefficient encodes the characteristic features of the BCFT_3 through some corner functions in a non-trivial way.

Our main result is the analytic expression of the corner function $F_\alpha(\gamma)$ for an infinite wedge adjacent to the boundary, which is given by (3.2.7) and (3.2.12) in a parametric form (see Fig. 3.7 and Fig. 3.8). This result and the corner function of [157] discussed in Sec. 1.3.3 lead to the analytic formula (3.5.5) for the corner function $\mathcal{F}_\alpha(\omega, \gamma)$, which corresponds to an infinite wedge having only its tip on the boundary.

Various checks have been done to test the analytic expressions of these two corner functions. The main one is the numerical analysis performed by employing Surface Evolver [152, 153], where minimal area surfaces corresponding to finite domains containing corners have been explicitly constructed. Further non-trivial consistency checks have been considered by studying the limiting regimes $\gamma \to 0^+$ and $\gamma \to \pi/2$ of the corner function $F_\alpha(\gamma)$. In the limit $\gamma \to 0^+$ the holographic entanglement entropy of the infinite strip adjacent to the boundary has been recovered, while taking the limit $\gamma \to \pi/2$ we have obtained the coefficient of the logarithmic divergence in the holographic entanglement entropy of the half-disk centered on the boundary, as expected.

We remark that interesting transitions have been observed in the analysis of the holographic entanglement entropy for the various domains. The main one occurs in the slope α at the critical value α_c given by (2.2.4). This transition can also be observed through the behaviour of the corner function $F_\alpha(\gamma)$ in the regime $\gamma \to 0^+$.

An interesting outcome of our analysis is the relation (3.4.6) found in the context of the $\mathrm{AdS}_4/\mathrm{BCFT}_3$ correspondence defined in [89], which involves the coefficient $f''_\alpha(\pi/2)$ obtained from the expansion of $F_\alpha(\gamma)$ as $\gamma \to \pi/2$ and the coefficient A_T characterising the behaviour of the one point function of the stress tensor $\langle T_{ij} \rangle$ close to the boundary (see (3.4.3)). In particular, (3.4.6) tells us that the ratio between these coefficients is independent of α. We stress that this relation does not hold if the prescriptions [158–161] for the gravitational dual of the BCFTs are employed. This is due to the fact that, even though the boundary corner function is the same in all the proposals, the value of A_T turns out to be different. In the future, we find it very interesting to explore the validity of this ratio in a generic BCFT.

Chapter 4

Shape Dependence of Holographic Entanglement Entropy in Asymptotically hvLif$_4$ Spacetimes

In this chapter, we explore the shape dependence of the holographic entanglement entropy in four-dimensional gravitational backgrounds having a non-trivial Lifshitz scaling (characterised by the parameter ζ) and a hyperscaling violation exponent θ (we find it more convenient to employ the parameter $d_\theta \equiv 2(d-1-\theta)/(d-1)$). This kind of backgrounds has been introduced for generic spacetime dimensions d in Sec. 1.5. In the following, we will focus mainly on $d = 2$, but we also consider generic dimensions in Sec. 4.2, where a formula for the area in terms of an integral along the boundary of the extremal surface $\hat{\gamma}_A$ will be derived.

Our analysis holds for smooth entangling curves ∂A, which can also be made by disjoint components. We consider $1 \leqslant d_\theta \leqslant 5$ for the sake of simplicity, although the method can be adapted to higher values of d_θ. In particular, we will study both the divergent terms and the finite term in the expansion of the holographic entanglement entropy as $\varepsilon \to 0$. Both analytic results and numerical data will be presented. For instance, in Fig. 4.1 we show the minimal area surface obtained with Surface Evolver whose area provides the holographic entanglement entropy of an elliptic region through (1.3.2), in the case where the gravitational background is a constant time slice of the four-dimensional hyperscaling violating Lifshitz spacetime (4.1.1).

The chapter is organised as follows. The main results about the finite term in the expansion of the holographic entanglement entropy as $\varepsilon \to 0$ for a generic static gravitational background are presented in Section 4.1, where also some important special cases like the four-dimensional hyperscaling violating Lifshitz spacetime (hvLif$_4$) defined in (4.1.1) and the asymptotically hvLif$_4$ black hole are explicitly discussed. In Section 4.2 we show that the finite term in the expression for the area of a minimal submanifold anchored on the boundary reduces to an integral over their intersection when the bulk geometry possesses a conformal Killing vector generating dilatations. In Section 4.3 we study the finite term of the holographic entanglement entropy for time-dependent backgrounds having $1 < d_\theta < 3$. In Section 4.4 we discuss explicitly the infinite strip, the disk and the ellipse. Some conclusions are drawn in

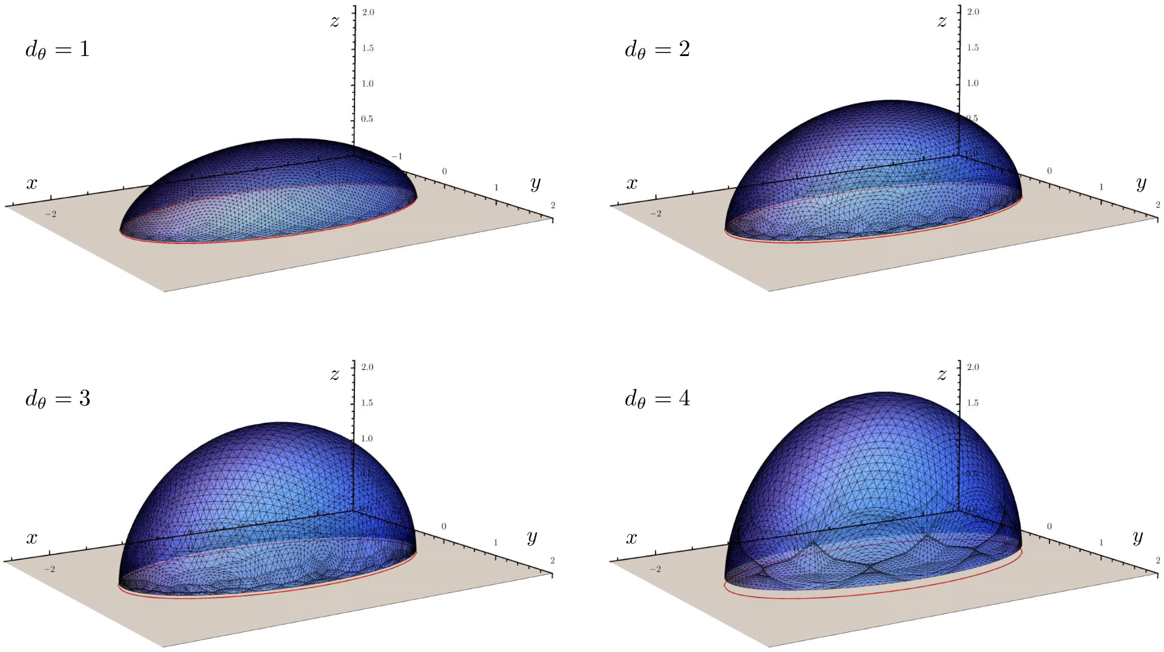

Figure 4.1: Minimal area surface obtained with Surface Evolver whose area provides the holographic entanglement entropy of an ellipse A delimited by the red curve. The minimal surface is embedded in a constant time slice of the four-dimensional hyperscaling violating Lifshitz spacetime (4.1.1), whose metric depends on the hyperscaling parameter d_θ.

Section 4.5. In appendices C.1, C.2, C.3, C.4, C.5 and C.6 we provide the technical details underlying the results presented in the main text.

4.1 Holographic entanglement entropy in asymptotically hvLif$_4$ backgrounds

In this chapter, we consider four-dimensional gravitational backgrounds $\mathcal{G}_4$ that depend on the hyperscaling violation exponent θ and on the Lifshitz scaling exponent $\zeta \geqslant 1$, and which have been discussed in Sec. 1.5. We recall that in Poincaré coordinates where $z > 0$ denotes the holographic coordinate, these backgrounds have a boundary at $z = 0$ and their asymptotic behaviour as $z \to 0^+$ is given by the following metric, that defines the four-dimensional hyperscaling violating Lifshitz spacetimes (hvLif$_4$) [123, 124, 126]

$$ds^2 = \frac{R_{\text{AdS}}^{d_\theta}}{z^{d_\theta}} \left(-\frac{z^{-2(\zeta-1)}}{R_{\text{AdS}}^{-2(\zeta-1)}}\, dt^2 + dz^2 + d\boldsymbol{x}^2 \right) \tag{4.1.1}$$

where $d\boldsymbol{x}^2 \equiv dx^2 + dy^2$ and $d_\theta \equiv 2 - \theta$. The length scale R_{AdS} is the analog of the AdS radius. When $d_\theta = 2$ and $\zeta = 1$, the background (4.1.1) becomes AdS$_4$ in Poincaré coordinates. In this chapter, we set R_{AdS} to one for simplicity, although it plays a crucial role in the dimensional analysis.

Moreover, to deal only with geometries admitting physically sensible dual field theories, the allowed values of the parameters in (4.1.1) are constrained by the null energy condition (1.5.10) introduces in Sec. 1.5.2. Specialising (1.5.10) to the case $d = 2$ we find

$$\begin{cases} (d_\theta + \zeta)(\zeta - 1) \geqslant 0 \\ d_\theta(d_\theta + 2\zeta - 4) \geqslant 0\,. \end{cases} \tag{4.1.2}$$

In the Appendix C.1 a detailed discussion of the NEC and its consequences is reported.

In this section we focus on static backgrounds; hence we can restrict our attention to the three-dimensional Euclidean section $\mathcal{C}_3$ obtained by taking a constant time slice of the asymptotically hvLif$_4$ bulk manifold $\mathcal{G}_4$. This submanifold is naturally endowed with a metric $g_{\mu\nu}$ such that

$$ds^2\big|_{t=\text{const}} \equiv g_{\mu\nu}\, dx^\mu dx^\nu \;\xrightarrow{z\to 0}\; \frac{1}{z^{d_\theta}}\big(dz^2 + dx^2 + dy^2\big)\,. \tag{4.1.3}$$

In the following, we give some definitions useful for the rest of the chapter. Those definitions have already been introduced in chapter Sec. 2.1 because they do not depend on the presence of the boundary $\mathcal{Q}$. Here, we recall them in order to facilitate the reading.

Given a two dimensional spatial region A in a constant time slice of the CFT$_3$ at $z = 0$, its holographic entanglement entropy is given by (1.3.2). Thus, first we must consider the class of two dimensional surfaces γ_A embedded in $\mathcal{C}_3$ whose boundary curve belongs to the plane $z = 0$ and coincides with the entangling curve, i.e. $\partial\gamma_A = \partial A$. Then, among these surfaces, we have to find the one having the minimal area, that provides the holographic entanglement entropy. As usual, we will denote by $\hat{\gamma}_A$ the extremal surfaces of the area functional, without introducing a particular notation for the global minimum.

Considering the unit vector n^μ normal to γ_A, the induced metric $h_{\mu\nu}$ on γ_A and the extrinsic curvature $K_{\mu\nu}$ are given in terms of n_μ respectively by

$$h_{\mu\nu} = g_{\mu\nu} - n_\mu n_\nu \qquad\qquad K_{\mu\nu} = h_\mu{}^\alpha h_\nu{}^\beta\, \nabla_\alpha n_\beta \tag{4.1.4}$$

being ∇_α the torsionless covariant derivative compatible with $g_{\mu\nu}$.

In our analysis, we find it convenient to introduce an auxiliary conformally equivalent three-dimensional space $\widetilde{\mathcal{C}}_3$ given by $\mathcal{C}_3$ with the same boundary at $z = 0$, but equipped with the metric $\tilde{g}_{\mu\nu}$, which is asymptotically flat as $z \to 0$ and Weyl related to $g_{\mu\nu}$, i.e.

$$g_{\mu\nu} = e^{2\varphi}\, \tilde{g}_{\mu\nu} \tag{4.1.5}$$

where φ is a function of the coordinates. The surface γ_A can be also viewed as a submanifold of $\widetilde{\mathcal{C}}_3$. Denoting by $\tilde{n}_\mu$ the unit normal vector to γ_A embedded in $\widetilde{\mathcal{C}}_3$, it is straightforward to find that $n_\mu = e^\varphi \tilde{n}_\mu$. The first and second fundamental form $\tilde{h}_{\mu\nu}$ and $\widetilde{K}_{\mu\nu}$ of $\gamma_A \subset \widetilde{\mathcal{C}}_3$ can be written in terms of the same quantities for $\gamma_A \subset \mathcal{C}_3$ (defined in (4.1.4)) as follows

$$h_{\mu\nu} = e^{2\varphi}\, \tilde{h}_{\mu\nu} \qquad\qquad K_{\mu\nu} = e^{\varphi}\big(\widetilde{K}_{\mu\nu} + \tilde{h}_{\mu\nu}\tilde{n}^\lambda \partial_\lambda \varphi\big)\,. \tag{4.1.6}$$

The two induced area elements $d\mathcal{A} = \sqrt{h}\, d\Sigma$ (of $\gamma_A \subset \mathcal{C}_3$) and $d\tilde{\mathcal{A}} = \sqrt{\tilde{h}}\, d\Sigma$ (of $\gamma_A \subset \widetilde{\mathcal{C}}_3$), where $d\Sigma$ is a shorthand notation for $d\sigma_1 d\sigma_2$ with σ_i some local coordinates on γ_A, are related as $d\mathcal{A} = e^{2\varphi} d\tilde{\mathcal{A}}$.

Since $\gamma_A \subset \mathcal{C}_3$ extends up to the boundary plane at $z = 0$, its area functional

$$\mathcal{A}[\gamma_A] = \int_{\gamma_A} \sqrt{h}\, d\Sigma \tag{4.1.7}$$

diverges when $d_\theta \geqslant 1$ because of the behaviour (4.1.3) near the conformal boundary. The holographic entanglement entropy is proportional to the area of the global minimum among the local extrema $\hat{\gamma}_A$ of (4.1.7) anchored to the entangling curve ∂A. These surfaces are obtained by solving the condition of vanishing mean curvature

$$\mathrm{Tr}K = 0 \tag{4.1.8}$$

with the Dirichlet boundary condition $\partial\gamma_A = \partial A$. In terms of the second fundamental form defined by the embedding in $\widetilde{\mathcal{C}}_3$, the extremal area condition (4.1.8) reads

$$\mathrm{Tr}\widetilde{K} = -\,2\,\tilde{n}^\lambda \partial_\lambda \varphi \qquad \Longleftrightarrow \qquad \mathrm{Tr}\widetilde{K} = d_\theta\,\frac{\tilde{n}^z}{z} \tag{4.1.9}$$

where in the last step we choose $e^{2\varphi} = 1/z^{d_\theta}$, as suggested by the asymptotic form (4.1.3).

4.1.1 Divergent terms

In our analysis, we consider only smooth entangling curves $\partial\gamma_A$. Furthermore, we restrict to two-dimensional surfaces γ_A that intersect the spatial boundary orthogonally at $z = 0$ of $\mathcal{C}_3$; and the extremal surfaces $\hat{\gamma}_A$ anchored to smooth entangling curves enjoy this property. In the following, we discuss the divergent contributions in the expansion of the holographic entanglement entropy as $\varepsilon \to 0$.

Since γ_A reaches the boundary and $d_\theta \geqslant 1$, its area is divergent; hence we have to introduce a UV cutoff plane at $z = \varepsilon$ and evaluate the functional (4.1.7) on the part of γ_A above the cutoff plane, i.e. on $\gamma_{A,\varepsilon} \equiv \gamma_A \cap \{z \geqslant \varepsilon\}$. The series expansion of $\mathcal{A}[\gamma_{A,\varepsilon}]$ as $\varepsilon \to 0$ contains divergent terms, a finite term and vanishing terms as $\varepsilon \to 0$. By exploiting the techniques discussed in [67, 76, 77] in Appendix C.2 we study the surface $\gamma_{A,\varepsilon}$, singling out the structure of the divergences in the expansion of $\mathcal{A}[\gamma_{A,\varepsilon}]$ as $\varepsilon \to 0$. In the following, we report only the results of this analysis. Let us stress that some of these results also hold for surfaces γ_A that are not minimal.

The leading divergence of $\mathcal{A}[\gamma_{A,\varepsilon}]$ as $\varepsilon \to 0$ is given by

$$\mathcal{A}[\gamma_{A,\varepsilon}] = \frac{P_A}{(d_\theta - 1)\,\varepsilon^{d_\theta - 1}} + \dots \qquad d_\theta \neq 1 \tag{4.1.10}$$

where P_A is the perimeter of the entangling curve ∂A, as pointed out in [124–126]. This leading divergence provides the area law of the holographic entanglement entropy for the asymptotically hvLif$_4$ backgrounds. When $d_\theta = 1$, the leading divergence is logarithmic

$$\mathcal{A}[\gamma_{A,\varepsilon}] = P_A \log(P_A/\varepsilon) + O(1) \qquad d_\theta = 1\,. \tag{4.1.11}$$

The apparent dimensional mismatch between the two sides of (4.1.11) is due to our choice to set $R_{\mathrm{AdS}} = 1$. The subleading terms in these expansions depend on the value of d_θ and we find it worth considering the ranges given by $2n+1 < d_\theta < 2n+3$, being $n \geqslant 0$ a positive integer.

When $1 < d_\theta < 3$, after the leading divergence (4.1.10), a finite term occurs

$$\mathcal{A}[\gamma_{A,\varepsilon}] = \frac{P_A}{(d_\theta - 1)\,\varepsilon^{d_\theta - 1}} - \mathcal{F}_A + O(\varepsilon) \qquad 1 < d_\theta < 3\,. \tag{4.1.12}$$

At this point, let us restrict our analysis to extremal surfaces $\hat{\gamma}_A$. When $\gamma_A = \hat{\gamma}_A$ is the minimal surface, in (4.1.12) we adopt the notation $\mathcal{F}_A = F_A$ for the finite term (see Section 4.1.2).

When $d_\theta = 3$, the subleading term diverges logarithmically [124–126]. In particular, for a generic smooth entangling curve we find

$$\mathcal{A}[\hat{\gamma}_{A,\varepsilon}] = \frac{P_A}{2\varepsilon^2} + \frac{\log \varepsilon}{8} \int_{\partial A} k^2(s)\, ds + O(1) \qquad d_\theta = 3 \tag{4.1.13}$$

where $k(s)$ is the geodesic curvature of $\partial\hat{\gamma}_A$ and s parameterises the entangling curve. When A is a disk of radius R, the geodesic curvature $k(s) = 1/R$ is constant, and the coefficient of the logarithmic divergence for this region has also been considered in [151].

In the range $3 < d_\theta < 5$, the subleading divergence is a power like; hence the finite term $\mathscr{F}_A$ is not changed by a global rescaling of the UV cutoff. The expansion of the area of $\hat{\gamma}_{A,\varepsilon}$ reads

$$\mathcal{A}[\hat{\gamma}_{A,\varepsilon}] = \frac{P_A}{(d_\theta - 1)\varepsilon^{d_\theta - 1}} + \frac{C_A}{\varepsilon^{d_\theta - 3}} - \mathscr{F}_A + O(\varepsilon) \qquad 3 < d_\theta < 5 \tag{4.1.14}$$

where the coefficient C_A is given by

$$C_A = -\frac{(d_\theta - 2)}{2(d_\theta - 3)(d_\theta - 1)^2} \int_{\partial A} k^2(s)\, ds\,. \tag{4.1.15}$$

For $d_\theta = 5$, a finite term in the expansion as $\varepsilon \to 0$ is not well defined because a logarithmic divergence occurs. In particular, we obtain

$$\mathcal{A}[\hat{\gamma}_{A,\varepsilon}] = \frac{P_A}{4\varepsilon^4} - \frac{3}{64\varepsilon^2} \int_{\partial A} k(s)^2\, ds + \frac{\log \varepsilon}{2048} \int_{\partial A} \Big(9\, k(s)^4 - 16\, k'(s)^2\Big) ds + O(1)\,. \tag{4.1.16}$$

The pattern outlined above seems to repeat also for higher values of d_θ: when $d_\theta = 2n+1$ is an odd integer with $n \geqslant 0$, one finds power like divergences $O(1/\varepsilon^{2n-2k})$ with integer $k \in [0, n-1]$ and a logarithmic divergence. Instead, in the range $2n+1 < d_\theta < 2n+3$ only power like divergencies $O(1/\varepsilon^{d_\theta - 1 - 2k})$ with integer $k \in [0, n]$ occur.

In Appendix C.2 we provide the derivations of the results reported above, and we also discuss their extensions to the class of surfaces that intersect the boundary plane orthogonally at $z = 0$, which includes the extremal surfaces.

4.1.2 Finite term

In this subsection, we investigate the finite term in (4.1.12) for surfaces γ_A that can be also non-extremal and in (4.1.14) only for $\hat{\gamma}_A$. The main result of this chapter is their expression as (finite) geometrical functionals over the two dimensional surface γ_A (or $\hat{\gamma}_A$ for $\mathscr{F}_A$) viewed as a submanifold of $\widetilde{\mathcal{C}}_3$. The procedure to obtain the finite terms extends the one developed in [76, 77] for AdS$_4$ and in [78] for asymptotically AdS$_4$ spacetimes. Since the specific details of this analysis depend on the type of divergences occurring in the expansion of the area functional as $\varepsilon \to 0$, we will treat the regimes $1 < d_\theta < 3$ and $3 < d_\theta < 5$ separately. In the following we report only the main results, collecting all the technical details of their derivation in Appendix C.3.

When $1 < d_\theta < 3$, the only divergence in the expansion of area functional $\mathcal{A}[\gamma_{A,\varepsilon}]$ is the area law term (4.1.10); hence our goal is to write an expression for the finite term $\mathcal{F}_A$ in (4.1.12).

In Appendix C.3.1 we adapt the analysis performed in [78] to this case, finding

$$\mathcal{F}_A = \frac{2}{d_\theta(d_\theta-1)}\int_{\gamma_A} e^{2\phi}\Big(2\tilde{h}^{\mu\nu}\partial_\nu\phi\,\partial_\mu\varphi - \frac{d_\theta(d_\theta-1)}{2}\,e^{2(\varphi-\phi)} + \widetilde{\nabla}^2\varphi - \tilde{n}^\mu\tilde{n}^\nu\widetilde{\nabla}_\mu\widetilde{\nabla}_\nu\varphi + (\tilde{n}^\lambda\partial_\lambda\varphi)^2\Big)d\tilde{\mathcal{A}} \\ + \frac{1}{2\,d_\theta(d_\theta-1)}\left[\int_{\gamma_A} e^{2\phi}\big(\mathrm{Tr}\widetilde{K}\big)^2 d\tilde{\mathcal{A}} + \int_{\gamma_A} e^{2\phi}\big(\mathrm{Tr}K\big)^2 d\mathcal{A}\right] \qquad (4.1.17)$$

where φ is the same conformal factor defined in (4.1.5), while ϕ is chosen so that $e^{-2\phi}g_{\mu\nu}$ is asymptotically AdS$_4$. In our explicit calculations we have employed the simplest choice for φ and ϕ, namely $\varphi = -\frac{d_\theta}{2}\log z$ and $\phi = \frac{2-d_\theta}{2}\log z$.

In the special case of $d_\theta = 2$, the field ϕ can be chosen to vanish (see (C.3.10)) and this leads us to recover the result obtained in [78] as a special case of our analysis.

When the functional (4.1.17) is evaluated on an extremal surfaces $\hat{\gamma}_A$, the forms (4.1.8) and (4.1.9) of the extremality condition imply respectively that the last term in (4.1.17) does not occur and that the term containing $(\tilde{n}^\lambda\partial_\lambda\varphi)^2$ can be written in terms of $(\mathrm{Tr}\widetilde{K})^2$. Finally, we can write

$$F_A = \frac{2}{d_\theta(d_\theta-1)}\int_{\hat{\gamma}_A} e^{2\phi}\Big(2\,\tilde{h}^{\mu\nu}\partial_\nu\phi\,\partial_\mu\varphi + \widetilde{\nabla}^2\varphi - \tilde{n}^\mu\tilde{n}^\nu\,\widetilde{\nabla}_\mu\widetilde{\nabla}_\nu\varphi \\ - \frac{d_\theta(d_\theta-1)}{2}\,e^{2(\varphi-\phi)} + \frac{1}{2}(\mathrm{Tr}\widetilde{K})^2\Big)\,d\tilde{\mathcal{A}}\,. \qquad (4.1.18)$$

The regime $3 < d_\theta < 5$ is more challenging because the expansion of the area functional $\mathcal{A}[\hat{\gamma}_{A,\varepsilon}]$ as $\varepsilon \to 0$ contains two power like divergent terms (see (4.1.14)). Let us remind that the structure of this expansion is dictated by the geometry of the entangling curve only for extremal surfaces (in this case, the coefficient of the subleading divergent term is (4.1.15)). For non-extremal surfaces, the structure of the divergent terms does not depend only on the geometry of the entangling curve, but also on the surface (see e.g. (C.2.8)).

In Appendix C.3.2 we find that the finite term in (4.1.14) for minimal surfaces reads

$$\mathscr{F}_A = F_A + \frac{2}{d_\theta^3(d_\theta-3)(d_\theta-1)}\int_{\hat{\gamma}_A} e^{2\psi}\Big((\mathrm{Tr}\widetilde{K})^2 f - \tilde{h}^{\mu\nu}\partial_\nu\varphi\,\partial_\mu(\mathrm{Tr}\widetilde{K})^2\Big)d\tilde{\mathcal{A}} \qquad (4.1.19)$$

being

$$f = \tilde{n}^\mu\tilde{n}^\nu\,\widetilde{\nabla}_\mu\widetilde{\nabla}_\nu\varphi - \widetilde{\nabla}^2\varphi - 2(\tilde{n}^\lambda\partial_\lambda\varphi)^2 - 2\tilde{h}^{\mu\nu}\partial_\mu\psi\,\partial_\nu\varphi \qquad (4.1.20)$$

where F_A is defined in (4.1.18). In (4.1.19) we have introduced a third conformal factor $e^{2\psi}$ that scales as z^{4-d_θ} when we approach the boundary at $z = 0$. The scaling of $e^{2\psi}$ with z (for small z) is fixed by requiring that the boundary terms in (C.3.13) match the divergence of order $1/\varepsilon^{d_\theta-3}$ appearing in (4.1.14) (see (C.3.18) and (C.3.19) for details).

4.1.3 HvLif$_4$

The simplest gravitation geometry to consider is hvLif$_4$, whose metric reads

$$ds^2 = \frac{1}{z^{d_\theta}}\Big(-\,z^{-2(\zeta-1)}dt^2 + dz^2 + dx^2 + dy^2\Big) \tag{4.1.21}$$

namely (4.1.1) with the length scale R_{AdS} set to one. In this background $\widetilde{g}_{\mu\nu} = \delta_{\mu\nu}$; hence the general formulae (4.1.18) and (4.1.19) take a compact and elegant form. In Appendix C.3.3 some details about these simplifications are provided.

When $1 < d_\theta < 3$, the expression (4.1.18) reduces to

$$F_A = \frac{1}{d_\theta - 1}\int_{\hat{\gamma}_A}\frac{(\tilde{n}^z)^2}{z^{d_\theta}}\,d\tilde{\mathcal{A}} \tag{4.1.22}$$

where we remind that $\tilde{n}^z$ is the z-component of the normal vector to $\hat{\gamma}_A$ in $\widetilde{\mathcal{C}}_3$. By employing the extremality condition (4.1.9), one can write F_A in terms of the second fundamental form in $\widetilde{\mathcal{C}}_3$ as follows

$$F_A = \frac{1}{d_\theta^2(d_\theta - 1)}\int_{\hat{\gamma}_A}\frac{(\mathrm{Tr}\widetilde{K})^2}{z^{d_\theta-2}}\,d\tilde{\mathcal{A}}\,. \tag{4.1.23}$$

This functional is a deformation of the Willmore functional parameterised by $1 < d_\theta < 3$. In the special case of $d_\theta = 2$ the functional (4.1.23) becomes the well known Willmore functional, as expected from the analysis of F_A in AdS$_4$ performed in [76, 77].

As a consistency check, we can show that in the limit $d_\theta \to 3$ the functional (4.1.22) reproduces the logarithmic divergence (4.1.13). This can be done by first plugging (C.3.17b) and (C.2.3) in (4.1.22), then expanding about $z = 0$ and finally using (C.2.12a). We find

$$F_A \;=\; \frac{1}{d_\theta - 1}\int_{\varepsilon}^{z_{\max}} dz\int_{\partial\hat{\gamma}_{A,\varepsilon}} ds\left[\frac{k^2(s)}{(d_\theta-1)^2\, z^{d_\theta-2}} + \mathcal{O}\big(z^{d_\theta-3}\big)\right] \tag{4.1.24}$$

$$\to\; -\,\frac{\log\varepsilon}{8}\int_{\partial A} k^2(s)\,ds + \mathcal{O}(1) \qquad\qquad d_\theta \to 3 \tag{4.1.25}$$

which is the logarithmic contribution occurring in (4.1.13).

In the regime $3 < d_\theta < 5$, the expression for $\mathscr{F}_A$ in (4.1.19) specified for (4.1.21) on a constant time slice becomes (see Appendix C.3.3 for details)

$$\mathscr{F}_A = -\,\frac{1}{(d_\theta-1)(d_\theta-3)}\int_{\hat{\gamma}_A}\left[\frac{3(\tilde{n}^z)^4}{z^{d_\theta}} - \frac{2\,\tilde{n}^z}{z^{d_\theta-2}}\,\tilde{h}^{z\mu}\,\partial_\mu\!\left(\frac{\tilde{n}^z}{z}\right)\right]d\tilde{\mathcal{A}} \tag{4.1.26}$$

where both the integrals are convergent; indeed, the former integrand scales as z^{4-d_θ}, while the latter one as z^{6-d_θ}. Following the same steps that lead to (4.1.24), we find that the expansion near to the boundary of (4.1.26) gives

$$\mathscr{F}_A = -\int_{\varepsilon}^{z_{\max}} dz\int_{\partial\hat{\gamma}_{A,\varepsilon}} ds\left\{\frac{\big[(9d_\theta - 2d_\theta^2 - 13)k(s)^4 - 2(d_\theta-1)^2 k(s)k''(s)\big]}{(d_\theta-3)^2(d_\theta-1)^5\, z^{d_\theta-4}} + \mathcal{O}(z^{6-d_\theta})\right\}. \tag{4.1.27}$$

Taking the limit $d_\theta \to 5$, we find the logarithmic divergent term

$$\mathscr{F}_A \to -\frac{\log\varepsilon}{2048}\int_{\partial A}\Big[16\,k(s)\,k''(s)+9\,k(s)^4\Big]ds+\mathcal{O}(1) \qquad d_\theta\to 5 \tag{4.1.28}$$

which becomes the logarithmic divergent term occurring in (4.1.16), after a partial integration.

4.1.4 Asymptotically hvLif$_4$ black hole

Another static background of physical interest is the asymptotically hvLif$_4$ black hole, whose metric reads [126, 133, 134]

$$ds^2=\frac{1}{z^{d_\theta}}\left(-\,z^{-2(\zeta-1)}f(z)dt^2+\frac{dz^2}{f(z)}+dx^2+dy^2\right) \qquad f(z)\equiv 1-(z/z_h)^{d_\theta+\zeta} \tag{4.1.29}$$

where the parameter z_h corresponds to the horizon, which determines the black hole temperature [126]

$$T=\frac{|d_\theta+\zeta|}{4\pi z_h^\zeta}\,. \tag{4.1.30}$$

Unlike hvLif$_4$, where the Lifshitz exponent ζ occurs only in the g_{tt} component of the metric, in (4.1.29) it enters also in $f(z)$; hence the minimal surface $\hat{\gamma}_A$ depends on ζ.

For $1<d_\theta<3$, specialising the general formula (4.1.18) to the black hole metric (4.1.29), for the finite term of the holographic entanglement entropy we find

$$F_A=\frac{1}{(d_\theta-1)}\int_{\hat{\gamma}_A}\frac{1}{z^{d_\theta}}\left[(d_\theta-1)(f(z)-1)-\frac{z f'(z)}{2}+(\tilde{n}^z)^2\left(1+\frac{z f'(z)}{2f(z)}\right)\right]d\tilde{\mathcal{A}}\,. \tag{4.1.31}$$

This functional reduces to (4.1.22) when $f(z)=1$ identically, as expected. For simplicity, here we do not consider the case $3<d_\theta<5$, but the corresponding computation to obtain $\mathscr{F}_A$ is very similar to the one leading to (4.1.31).

In the regime where the size of the domain A is very large with respect to the black hole horizon scale z_h, the extremal surface can be approximated by a cylinder $\hat{\gamma}_A^{\text{cyl}}$ with horizontal cross-section ∂A and the second base located at $z=z_*\sim z_h$. Within this approximation, the functional (4.1.31) simplifies to

$$\begin{aligned}F_A^{\text{cyl}}&=\frac{d_\theta[f(z_*)-1]+1}{(d_\theta-1)\,z_*^{d_\theta}}\,\text{Area}(A)+\frac{P_A}{d_\theta-1}\int_0^{z_*}\left[f(z)-\frac{z f'(z)}{2}-1\right]\frac{dz}{z^{d_\theta}}\\&=\frac{1-(z_*/z_h)^{d_\theta+\zeta}\,d_\theta}{z_*^{d_\theta}(d_\theta-1)}\,\text{Area}(A)+\frac{(d_\theta+\zeta-2)\,z_*^{1-d_\theta}}{2(\zeta+1)(d_\theta-1)}\left(\frac{z_*}{z_h}\right)^{d_\theta+\zeta}P_A\end{aligned} \tag{4.1.32}$$

where we used that $\tilde{n}^z=\sqrt{f(z_*)}$ on the base and $\tilde{n}^z=0$ on the vertical part of $\hat{\gamma}_A^{\text{cyl}}$. In the special case of $d_\theta=2$, the expression (4.1.32) reduces to the corresponding result of [78]. Taking the limit $z_*\to z_h$ of (4.1.32), we find

$$F_A^{\text{cyl}}=-\,\frac{\text{Area}(A)}{z_h^{d_\theta}}+\dots\,. \tag{4.1.33}$$

By using (4.1.30), this relation can be written as $F_A^{\text{cyl}}\simeq -\,T^{d_\theta/\zeta}\text{Area}(A)$ (up to a numerical coefficient), which tells us that $-F_A^{\text{cyl}}$ approaches the thermal entropy in this limit.

4.2 Finite term as an integral along the entangling curve

This section is devoted to showing that the finite term in the expansion of the entanglement entropy for the case hvLif$_{d+1}$ can be written as an integral over the entangling $(d-2)$ dimensional hypersurface. This analysis extends the result obtained in [77] for AdS$_4$. In Appendix C.4 we show that the same result can be obtained through a procedure on the area functional that is similar to the one leading to the Noether theorem.

The geometry of this spacetime is given by (4.1.1) with $d\boldsymbol{x}^2 = \sum_{i=1}^{d-1} dx_i^2$, $R_{\text{AdS}} = 1$ and $d_\theta = 2(d-1-\theta)/(d-1)$. This spacetime possesses a conformal Killing vector generating the following transformation

$$t \mapsto \lambda^{1-\zeta} t \qquad z \mapsto \lambda z \qquad \boldsymbol{x} \mapsto \lambda \boldsymbol{x} \tag{4.2.1}$$

under which the metric changes as $ds^2 \mapsto \lambda^{2-d_\theta} ds^2$, being $d_\theta \geqslant 1$.

An amusing consequence of the existence of this conformal Killing vector is the possibility to write the finite term (whenever a logarithmic divergence does not occur) as an integral over the entangling hypersurface independently of the number of divergent terms appearing in the expansion of the area and of the spacetime dimensionality. This can be shown by considering the variation of the induced area element for an infinitesimal transformation generated by the infinitesimal parameter $\lambda = 1 + \epsilon + \cdots$. From the scaling law of the metric, we find

$$\delta_\epsilon\big(\sqrt{h}\,\big) = \epsilon\, \frac{(2-d_\theta)m}{2}\, \sqrt{h} \tag{4.2.2}$$

where m is the dimension of the minimal hypersurface. Namely, if we perform the transformations (4.2.1) the volume of the hypersurface scales as $\mathcal{V} \to \lambda^{\frac{m(2-d_\theta)}{2}} \mathcal{V}$.

Since the transformation (4.2.1) can also be viewed as an infinitesimal diffeomorphism generated by a conformal Killing vector field V_μ acting on the bulk, its action on the induced metric can be cast into the following form

$$\delta h_{ab} = \big(\nabla_\mu V_\nu + \nabla_\nu V_\mu\big) \frac{\partial x^\mu}{\partial \sigma^a} \frac{\partial x^\nu}{\partial \sigma^b} = D_a V_b + D_b V_a + K^{(i)}_{ab}(n_{(i)} \cdot V) \tag{4.2.3}$$

where σ^a are the coordinates on the minimal surface, D_a is the induced covariant derivative on γ_A, the vector field $V_a = V_\mu \partial_a x^\mu$ is the pullback of V_μ on γ_A, $n_{(i)}$ are the normal vectors to the minimal surface and $K^{(i)}_{ab}$ the associated extrinsic curvature (the dot corresponds to the scalar product given by the bulk metric). Then, the variation of the volume form can be written as

$$\delta_\epsilon\big(\sqrt{h}\,\big) = \frac{1}{2}\sqrt{h}\, h^{ab} \delta_\epsilon h_{ab} = \frac{\epsilon}{2}\sqrt{h}\, \Big(2\, D_a V^a + K^{(i)}(n_{(i)} \cdot V)\Big) = \epsilon \sqrt{h}\,(D_a V^a) \tag{4.2.4}$$

where in the last step the extremality condition has been employed. If we compare (4.2.2) and (4.2.4), we find

$$\sqrt{h} = \frac{2}{(2-d_\theta)m} \sqrt{h}(D_a V^a) \tag{4.2.5}$$

which can be integrated over $\hat{\gamma}_{A,\varepsilon}$, finding

$$\mathcal{A}[\hat{\gamma}_{A,\varepsilon}] = \frac{2}{(2-d_\theta)m} \int_{\hat{\gamma}_{A,\varepsilon}} \sqrt{h}(D_a V^a)\, d^m\sigma = \frac{2}{(2-d_\theta)m} \int_{\partial\hat{\gamma}_{A,\varepsilon}} \sqrt{h}(b_a V^a)\, d^{m-1}\xi \tag{4.2.6}$$

where b^a is the unit vector normal to $\partial\hat{\gamma}_{A,\varepsilon}$ along the surface $\hat{\gamma}_{A,\varepsilon}$, and ξ^j denote the coordinates on the boundary of the minimal hypersurface. Actually, identities similar to (4.2.5) and (4.2.6) hold if the manifold admits a vector of constant divergence. The conformal Killing vector generating dilatations is just an example of this type. The above analysis is valid in any dimension and for generic codimension of the minimal submanifold. To complete our analysis, we need to know the behavior of the vector b_a close to the boundary. In the present paper, we have performed this analysis only for the case of interest, i.e. $d = 3$ and $m = 2$ (see Appendix C.2), but it can be extended to more general situations by means of the same techniques.

For $d = 3$ and $m = 2$, by plugging the expansion (C.2.5) into (4.2.6), for the finite term we find

$$F_A = -\frac{d_\theta + 1}{d_\theta - 2} \int_{\partial A} \big(\boldsymbol{x}_A \cdot \widetilde{N}\big)\, \mathcal{U}_{d_\theta+1}\, ds \qquad d_\theta \neq 2 \tag{4.2.7}$$

where $\mathcal{U}_{d_\theta+1}$ is the first non-analytic term encountered in the expansion (C.2.5), $\boldsymbol{x}_A$ is a shorthand notation for the parametric representation $\boldsymbol{x}_A \equiv (x(s), y(s))$ of the entangling curve and the vector $\widetilde{N}$ is the unit normal to this curve in the plane $z = 0$ in $\widetilde{\mathcal{M}}_3$ (see also Appendix C.2).

Further remarks about (4.2.7) are in order. The representation (4.2.7) for the finite term holds for any $d_\theta \neq 2$ and there is no restriction on the range of d_θ. Even though the expression (4.2.7) may suggest that F_A is completely characterized by the local behaviour of the extremal surface near the boundary, it turns out that the coefficient $\mathcal{U}_{d_\theta+1}$ cannot be determined only by solving perturbatively (4.1.8) about $z = 0$ (see Appendix C.2); hence it depends on the whole minimal surface $\hat{\gamma}_A$.

4.3 Time-dependent backgrounds for $1 < d_\theta < 3$

When the gravitational background is time-dependent, the covariant prescription for the holographic entanglement entropy introduced in [34] must be employed. The class of surfaces γ_A to consider is defined only by the constraint $\partial\gamma_A = \partial A$; hence γ_A is not restricted to lay on a slice of constant time, as in the static gravitational spacetimes.

In this section, we study the finite term in the expansion of the holographic entanglement entropy in time-dependent asymptotically hvLif$_4$ backgrounds. A crucial difference with respect to the case of static backgrounds is that surfaces in four dimensional spacetimes have two normal directions identified by the unit normal vectors $n^{(i)}_N$ (with $i = 1, 2$, whose squared norm $\epsilon_i = g^{MN} n^{(i)}_M n^{(i)}_N$ is either $+1$ or -1) and therefore two extrinsic curvatures $K^{(i)}_{MN}$. In this analysis, we need to extend the result obtained in [78] by including the Lifshitz scaling and the hyperscaling violation. The technical details of this computation are discussed in Appendix C.5 and in the following, we report only the final results.

In the range $1 < d_\theta < 3$, for surfaces γ_A that intersect orthogonally the boundary, the expansion (4.1.12) holds with the finite term given by

$$\begin{aligned}\mathcal{F}_A = c_1 \int_{\gamma_A} e^{2\phi} \bigg[& 2\,\tilde{h}^{MN} \partial_M \varphi\, \partial_N \phi - \sum_{i=1}^{2} \epsilon_i\, \tilde{n}^{(i)M} \tilde{n}^{(i)N} \Big(\widetilde{D}_M \widetilde{D}_N \varphi - \widetilde{D}_M \varphi \widetilde{D}_N \varphi \Big) + \widetilde{D}^2 \varphi \\ & + \frac{1}{4} \sum_{i=1}^{2} \epsilon_i \big(\mathrm{Tr} \widetilde{K}^{(i)}\big)^2 \bigg] d\tilde{\mathcal{A}} - \int_{\gamma_A} e^{2\varphi}\, d\widetilde{\mathcal{A}} - \frac{c_1}{4} \sum_{i=1}^{2} \epsilon_i \int_{\gamma_A} e^{2\phi} \big(\mathrm{Tr} K^{(i)}\big)^2 d\mathcal{A}\,. \end{aligned} \tag{4.3.1}$$

Specialising this expression to extremal surfaces $\hat{\gamma}_A$, that satisfy $\mathrm{Tr} K^{(i)} = 0$ and for which c_1 is given in (C.3.10), we find

$$\begin{aligned} F_A = \int_{\hat{\gamma}_A} \frac{2\, e^{2\phi}}{d_\theta (d_\theta - 1)} \bigg[& 2\,\tilde{h}^{MN} \partial_M \varphi\, \partial_N \phi - \sum_{i=1}^{2} \epsilon_i\, \tilde{n}^{(i)M} \tilde{n}^{(i)N} \widetilde{D}_M \widetilde{D}_N \varphi \\ & + \widetilde{D}^2 \varphi - \frac{d_\theta (d_\theta - 1)}{2}\, e^{2(\varphi - \phi)} + \frac{1}{2} \sum_{i=1}^{2} \epsilon_i \big(\mathrm{Tr} \widetilde{K}^{(i)}\big)^2 \bigg] d\tilde{\mathcal{A}}\,. \end{aligned} \tag{4.3.2}$$

In the special case of $d_\theta = 2$, the expressions (4.3.1) and (4.3.2) simplify to the ones obtained in [78] for time dependent asymptotically AdS$_4$ backgrounds. In the final part of Appendix C.5 we show that (4.3.2) becomes (4.1.18) for static backgrounds.

The temporal evolution of the holographic entanglement entropy in the presence of Lifshitz scaling and hyperscaling violation exponents has been studied in [147–151] by considering infinite strips and disks. It would be interesting to extend this numerical analysis to non-spherical finite domains, also to check the analytic expression (4.3.2).

4.4 Some particular regions

In the previous sections, we discussed expressions for the finite term in the expansion of the holographic entanglement entropy that hold for any smooth region A, independently of its shape. In this section we test these expressions by considering infinite strips (Section 4.4.1), disks (Section 4.4.2) and ellipses (Section 4.4.3).

4.4.1 Strip

The spatial region $A = \{(x, y) : |x| \leqslant \ell/2, |y| \leqslant L/2\}$ in the limit of $\ell \ll L$ can be seen as an infinite strip that is invariant under translations along the y-direction. The occurrence of this symmetry leads to a drastic simplification because the search of the minimal area surface $\hat{\gamma}_A$ can be restricted to the class of surfaces γ_A invariant under translations along the y-direction, which are fully characterised by the profile $z = z(x)$ of a section at $y = \text{const}$.

HvLif$_4$

The minimal surfaces anchored to the strip domain defined above have been studied in details in Sec. 1.5.2 of chapter 1 for generic spacetime dimension d. Here, we are interested in the case $d = 2$.

In Sec. 1.5.2 we discussed the most direct approach to obtain $\mathcal{A}[\hat{\gamma}_{A,\varepsilon}]$ consists in evaluating (1.5.14) on the profile (1.5.17). In the following, for $d = 2$ we reproduce the finite term of this expansion by specialising the expressions (4.1.22) and (4.1.26) to the strip (for the latter formula, the computation is reported in Appendix C.3.3).

Let us first consider the tangent and normal vectors to the surfaces anchored to the boundary of the infinite strip that are characterised by the profile $z = z(x)$. They read

$$\tilde{t}_1^{\mu} = \left(\frac{z'}{\sqrt{1+(z')^2}} \, , \frac{1}{\sqrt{1+(z')^2}} \, , 0 \right) \qquad \tilde{t}_2^{\mu} = (0,0,1) \qquad \tilde{n}^{\mu} = \left(\frac{-1}{\sqrt{1+(z')^2}} \, , \frac{z'}{\sqrt{1+(z')^2}} \, , 0 \right). \tag{4.4.1}$$

For $1 < d_\theta < 3$, we can plug the component $\tilde{n}^z$ into (4.1.22), that holds for the minimal surface $\hat{\gamma}_A$, finding that the finite term of the holographic entanglement entropy becomes

$$F_A = \frac{1}{d_\theta - 1} \int_{\hat{\gamma}_A} \frac{dx\, dy}{z^{d_\theta} \sqrt{1+(z')^2}} = \frac{4}{(d_\theta - 1)\, z_*^{d_\theta}} \int_0^{L/2} \!\! \int_0^{\ell/2} dx dy = \frac{L\, \ell}{(d_\theta - 1)\, z_*^{d_\theta}} \tag{4.4.2}$$

where (1.5.15) specialized to $d = 2$ has been used in the last step. By employing (1.5.16), the expression (4.4.2) can be written as [126]

$$F_A = \frac{L\, \ell^{1-d_\theta}}{d_\theta - 1} \left(\frac{2\sqrt{\pi}\, \Gamma\big((1+1/d_\theta)/2\big)}{\Gamma\big(1/(2d_\theta)\big)} \right)^{d_\theta} . \tag{4.4.3}$$

We have obtained this result for $1 < d_\theta < 3$, but it turns out to be valid for any $d_\theta > 1$ (in Appendix C.3.3 we have checked that (4.4.3) is recovered also by specialising to the strip the general formula (4.1.26) that holds for $3 < d_\theta < 5$). In fact, all the subleading divergences can be expressed recursively in terms of the geodesic curvature of ∂A and its derivatives (see Appendix C.2); and this quantity trivially vanishes for the straight line.

We find it instructive to specialise the method discussed in Section 4.2 to the infinite strip. The analytic profile (1.5.17) (for $d = 2$) allows us to determine the scalar function $u(z,s)$ used in Appendix C.2 to describe the minimal surface: $u(z,s) = \ell/2 - x(z)$. By expanding this result in powers of z and by comparing the expansion with (C.2.5), one finds the following coefficient

$$\mathcal{U}_{d_\theta+1} = \frac{1}{(d_\theta + 1)\, z_*^{d_\theta}} \, . \tag{4.4.4}$$

The expression (4.2.7) must be slightly modified for the infinite strip because, in this case, we evaluate the finite ratio $\mathcal{A}/L$ and the scaling in the direction along which the strip is infinitely long is not considered. Thus, the ratio $\mathcal{A}/L$ scales like $\mathcal{A}/L \to \lambda^{1-d_\theta} \mathcal{A}/L$ under (4.2.1). As a consequence, for the infinite strip (4.2.7) has to be replaced with

$$F_A = -\frac{d_\theta + 1}{d_\theta - 1} \int_{\partial A} \big(\boldsymbol{x}_A \cdot \tilde{N} \big)\, \mathcal{U}_{d_\theta+1}\, ds \, . \tag{4.4.5}$$

Plugging (4.4.4) into (4.4.5) and using that $\boldsymbol{x}_A \cdot \tilde{N} = -\ell/2$, we recover (4.4.2), and therefore also (4.4.3), which is the result found in [126] for the infinite strip in a generic number of spacetime dimensions.

Asymptotically hvLif$_4$ black hole

We find it worth also considering the finite term of the holographic entanglement entropy of an infinite strip A when the gravitational background is given by the asymptotically hvLif$_4$ black hole (4.1.29). This can be done by adapting the procedure described in Section 4.4.1 for hvLif$_4$.

The area functional restricted to the class of surfaces γ_A that are invariant under translations along the y-direction (which are fully determined by the profile $z = z(x)$ of any section at $y = \text{const}$) reads

$$\mathcal{A}[\gamma_A] = L \int_{-\ell/2}^{\ell/2} \frac{1}{z^{d_\theta}} \sqrt{1 + \frac{(z')^2}{f(z)}}\, dx \tag{4.4.6}$$

that simplifies to (1.5.14) when $f(z) = 1$ identically, as expected. Since x is a cyclic coordinate in (4.4.6), one obtains the following conservation law

$$z^{d_\theta} \sqrt{1 + \frac{(z')^2}{f(z)}} = z_*^{d_\theta} \tag{4.4.7}$$

being $(z, x) = (z_*, 0)$ the coordinates of the tip of the profile of the minimal surface $\hat{\gamma}_A$, where $z'(0) = 0$ holds. We also need the unit vector $\tilde{n}^\mu$ normal to the surface, whose components read

$$\tilde{n}^\mu = \left(\tilde{n}^z, \tilde{n}^x, \tilde{n}^y\right) = \left(\frac{f(z)}{\sqrt{f(z) + (z')^2}}\,, -\frac{z'}{\sqrt{f(z) + (z')^2}}\,, 0\right). \tag{4.4.8}$$

Now we can specialise (4.1.31), which holds for minimal surfaces, to the strip by employing (4.4.8), finding that

$$F_A = \frac{2L}{z_*^{d_\theta}(d_\theta - 1)} \int_0^{\ell/2} \left[\left((d_\theta - 1)(f(z) - 1) - \frac{z f'(z)}{2}\right) \frac{z_*^{2d_\theta}}{z^{2d_\theta}} + f(z) + \frac{z f'(z)}{2}\right] dx \tag{4.4.9}$$

where the emblacking factor $f(z)$ is given in (4.1.29). By employing the conservation law (4.4.7), it is straightforward to write (4.4.9) as an integral in z between 0 and z_*. Notice that, by setting $\zeta = 1$ and $d_\theta = 2$ in (4.4.9), we recover the result obtained in [78].

4.4.2 Disk

In this subsection, we study the holographic entanglement entropy of a disk A with radius R when the gravitational background is hvLif$_4$ (Section 4.4.2) or the asymptotically hvLif$_4$ black hole (Section 4.4.2). Fixing the origin of the Cartesian coordinates $(x, y, z > 0)$ in the center of A, the rotational symmetry of A about the z-axis implies that $\hat{\gamma}_A$ belongs to the subset of surfaces γ_A displaying this rotational symmetry; hence it is more convenient to adopt cylindrical coordinates (z, ρ, ϕ), where (ρ, ϕ) are polar coordinates in the plane at $z = 0$. In these coordinates, the entangling curve is given by $(\rho = R\,, \phi)$ in the plane at $z = 0$.

HvLif$_4$

When the gravitational background is hvLif$_4$ (now it is convenient to express the metric (4.1.21) in cylindrical coordinates), the area functional for the surfaces invariant under rotations about the z-axis that are defined by their radial profile $z = z(\rho)$ and that are anchored to the entangling curve $(\rho, \phi) = (R, \phi)$ (i.e. such that $z(R) = 0$) reads

$$\mathcal{A}[\gamma_A] \,=\, 2\pi \int_0^R \frac{\sqrt{1+(z')^2}}{z^{d_\theta}}\,\rho\, d\rho \tag{4.4.10}$$

where $z' = \partial_\rho z(\rho)$. Imposing the vanishing of the first variation of the functional (4.4.10) leads to the following second-order ordinary differential equation

$$\frac{z''}{1+(z')^2} + \frac{z'}{\rho} + \frac{d_\theta}{z} = 0 \tag{4.4.11}$$

where the boundary conditions $z(R) = 0$ and $z'(0) = 0$ hold. It is well known that, in the special case of $d_\theta = 2$, the hemisphere $z(\rho) = \sqrt{R^2 - \rho^2}$ is a solution of (4.4.11) [31, 32]. For $d_\theta \neq 2$, the solution of (4.4.11) has been studied numerically in [151].

In the following, we provide the finite term in the expansion of the holographic entanglement entropy for disks by specialising (4.1.22) and (4.1.26) to these domains. In terms of the cylindrical coordinates, the unit tangent and normal vectors to $\hat{\gamma}_A$ read

$$\tilde{t}^{\mu}_{\rho} = \left(\frac{z'}{\sqrt{1+(z')^2}}\,, \frac{1}{\sqrt{1+(z')^2}}\,, 0\right) \qquad \tilde{t}^{\mu}_{\phi} = \big(0,0,1\big) \qquad \tilde{n}^{\mu} = \left(\frac{1}{\sqrt{1+(z')^2}}\,, \frac{-\,z'}{\sqrt{1+(z')^2}}\,, 0\right) \tag{4.4.12}$$

where $z = z(\rho)$ satisfies (4.4.11). We remark that only the component $\tilde{n}^z$ occurs in (4.1.22) and (4.1.26). Thus, from (4.4.12), we easily find that for $1 < d_\theta < 3$ the expression (4.1.22) becomes

$$F_A = \frac{2\pi}{d_\theta - 1} \int_0^R \frac{\rho\, d\rho}{z^{d_\theta}\sqrt{1+(z')^2}}\,. \tag{4.4.13}$$

In the regime $3 < d_\theta < 5$, we have that (4.1.26) gives

$$\mathscr{F}_A = \frac{2\pi}{(d_\theta - 1)(d_\theta - 3)} \int_0^R \frac{2\big[(d_\theta - 1) + z\, z'/\rho\big](z')^2 - 3}{z^{d_\theta}\big[1+(z')^2\big]^{3/2}}\,\rho\, d\rho \tag{4.4.14}$$

where (4.4.11) has been used to rewrite z''.

Even though (4.4.11) is invariant under the scale transformation $(z, \rho) \to \lambda(z, \rho)$, the expressions in (4.4.13) and (4.4.14) do not enjoy this invariance. However, since the metric scales as $ds^2 \mapsto \lambda^{2-d_\theta} ds^2$, it is straightforward to observe that

$$F_A(R) = R^{2-d_\theta}\, F_A\big|_{R=1} \qquad\qquad \mathscr{F}_A(R) = R^{2-d_\theta}\, \mathscr{F}_A\big|_{R=1}\,. \tag{4.4.15}$$

Thus, the finite term in the holographic entanglement entropy decreases with the radius for $d_\theta > 2$, while it increases for $d_\theta < 2$. The case $d_\theta = 2$ corresponds to AdS$_4$, which is scale invariant, and $F_A = 2\pi$ for a disk, independently of the radius R, as expected.

In our numerical analysis we have employed *Wolfram Mathematica* and *Surface Evolver* [152, 153]. Wolfram Mathematica has been used to solve numerically ordinary differential

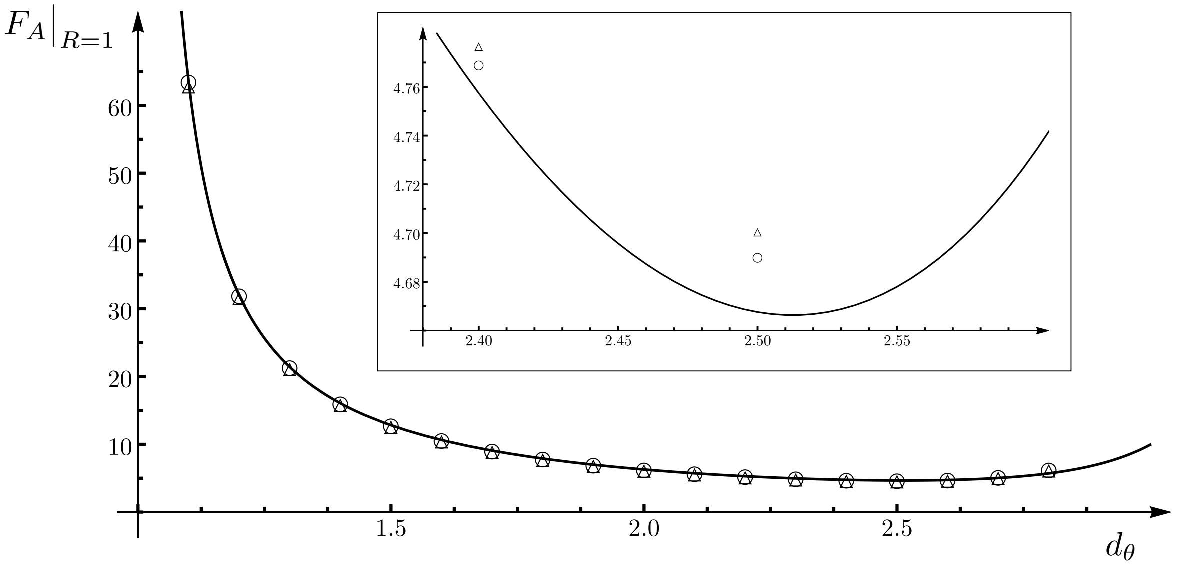

Figure 4.2: Finite term F_A in terms of $1 < d_\theta < 3$ for minimal surfaces anchored to a disk of radius $R = 1$ in the hvLif$_4$ geometry (4.1.21) at $t =$ const. The solid line is found by first solving numerically (with Wolfram Mathematica) the differential equation (4.4.11) and then plugging the resulting radial profile into (4.4.13). The data points labelled by the empty circles and the empty triangles have been obtained with Surface Evolver through the two formulas in (4.4.16) respectively. The inset contains a zoom close to the minimum of the curve, that corresponds to $(d_\theta, F_A) \simeq (2.52\,, 4.67)$.

equations, which can be written whenever the symmetry of A and of the gravitational background allows to parameterise γ_A only in terms of a function of a single variable. In this chapter, this is the case for the disk. Instead, Surface Evolver is more versatile in our three-dimensional gravitational backgrounds (on a constant time slice) because it provides an approximation of the minimal surface $\hat{\gamma}_A$ through triangulated surfaces without implementing any particular parameterisation of the surface. In particular, once the three-dimensional gravitational background has been introduced, given the UV cutoff ε and the entangling curve ∂A, only the trial surface (a rough triangulation that fixes the topology of the expected minimal surface) has to be specified as initial data for the evolution. This makes Surface Evolver suitable to study the holographic entanglement entropy in AdS$_4$/CFT$_3$ for entangling curve of generic shape, as already done in [78, 154, 155, 245] (we refer the interested reader to these works for technical details about the application of Surface Evolver in this context). We remark that, besides the position of the vertices of the triangulated surface, Surface Evolver can also provide the unit vectors normal to the triangles composing the triangulated surface. This information can be used to evaluate numerically the expressions discussed in Section 4.1.2.

Let us denote by $\hat{\gamma}_{A,\mathrm{SE}}$ the best approximation of the minimal surface obtained with Surface Evolver and by $\mathcal{A}_{\mathrm{SE}}$ its area, which depends on the value of ε adopted in the numerical analysis. These data allow to compute the finite term in the expansion of the holographic entanglement entropy in two ways: by subtracting the area law term from $\mathcal{A}_{\mathrm{SE}}$ or by plugging the numerical data provided by Surface Evolver into the general formulas discussed in Section 4.1.2. For

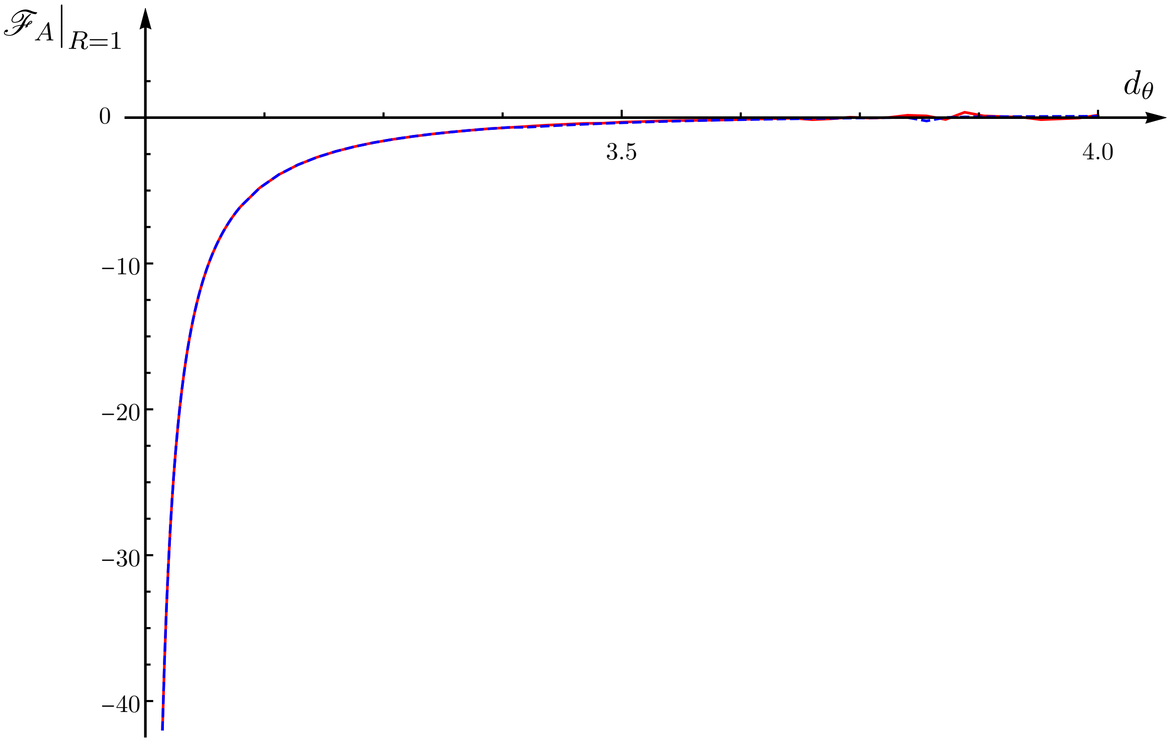

Figure 4.3: Finite term $\mathscr{F}_A$ in terms of $3 < d_\theta < 5$ for minimal surfaces anchored to a disk of radius $R = 1$ in the hvLif$_4$ geometry (4.1.21) at $t = \text{const}$. The two curves have been obtained by first solving numerically (with Wolfram Mathematica) the differential equation (4.4.11) and then plugging the resulting profile either in (4.4.14) (solid red line) or into (4.4.10) (dashed blue line), once the area law term has been subtracted.

$1 < d_\theta < 3$, these two ways to find the finite term are given by

$$F_{A,\text{SE}} \equiv -\Big(\mathcal{A}_{\text{SE}} - P_A/\varepsilon^{d_\theta - 1}\Big) \qquad\qquad \widetilde{F}_{A,\text{SE}} \equiv F_A\big|_{\hat{\gamma}_{A,\text{SE}}} \tag{4.4.16}$$

where F_A is the expression in (4.1.18). In the range $3 < d_\theta < 5$ we can write expressions similar to the ones in (4.4.16) starting from (4.1.14) and (4.1.19).

In Fig. 4.2 we show the finite term F_A for a disk of radius $R = 1$ as a function of the effective dimensionality d_θ, in the range $1 < d_\theta < 3$, when the gravitational background is hvLif$_4$. The solid black curve has been found with Mathematica, by solving numerically (4.4.11) first and then plugging the resulting radial profile for the minimal surface into (4.4.13). The data points have been found with Surface Evolver by using $F_{A,\text{SE}}$ (empty circles) and $\widetilde{F}_{A,\text{SE}}$ (empty triangles), introduced in (4.4.16). The very good agreement between the data points and the continuous curve provides a non-trivial check both of the analytic formula (4.1.22) and of the procedure implemented in Surface Evolver, that is sensible to the value of d_θ. For $d \simeq 3$ our numerical analysis fails; hence in Fig. 4.2 we have reported only the reliable results.

An interesting feature that can be observed in Fig. 4.2 is the occurrence of a minimum for F_A corresponding to $(d_\theta, F_A) \simeq (2.52\,, 4.67)$. When the gravitational background is AdS$_4$, the bound $F_A \geqslant 2\pi$ holds for any entangling curve and the inequality is saturated for the disks [78]. From Fig. 4.2 we notice that, for hyperscaling violating theories, F_A assumes also values lower than 2π for certain d_θ.

In Fig. 4.3 the finite term $\mathscr{F}_A$ for a disk of radius $R = 1$ is shown in terms of d_θ, in the range $3 < d_\theta < 5$, when the gravitational background is hvLif$_4$. The radial profile $z(\rho)$ for the minimal surface has been obtained by solving the equation of motion (4.4.11) numerically. Then, the finite term has been obtained by plugging this result either into the area functional regularised by subtracting the divergent terms (solid red line) or into the analytic expression (4.4.14) (dashed blue line). In the figure, we have reported only the reliable numerical data.

Asymptotically hvLif$_4$ black hole

It is worth studying the holographic entanglement entropy of a disk of radius R when the gravitational background is the black hole (4.1.29). By adopting the cylindrical coordinates, we can find the minimal surface among the surfaces γ_A invariant under rotations about the z-axis, characterised by their radial profile $z(\rho)$ such that $z(R) = 0$, as in Section 4.4.2. The area functional for this class of surfaces reads

$$\mathcal{A}[\gamma_A] \,=\, 2\pi \int_0^R \frac{1}{z^{d_\theta}} \sqrt{1 + \frac{(z')^2}{f(z)}}\; \rho\, d\rho\,. \tag{4.4.17}$$

Under the rescaling $(z,\rho) \to \lambda(z,\rho)$, we have that $z_h \to \lambda z_h$, $R \to \lambda R$ and $\mathcal{A}[\gamma_A] \to \lambda^{2-d_\theta}\mathcal{A}[\gamma_A]$ for (4.4.17). This rescaling leaves invariant both the equation of motion and the shape of the extremal surface $\hat{\gamma}_A$.

The unit vector normal to $\hat{\gamma}_A$ reads

$$\tilde{n}^\mu = \left(\tilde{n}^z, \tilde{n}^\rho, \tilde{n}^\phi\right) = \left(\frac{f(z)}{\sqrt{f(z)+(z')^2}}\,, -\frac{z'}{\sqrt{f(z)+(z')^2}}\,, 0 \right) \tag{4.4.18}$$

where $z(\rho)$ satisfies the equation of motion coming from (4.4.17). By employing the component $\tilde{n}^z$ in (4.4.18), we can specialise (4.1.31) to this case, finding that for $1 < d_\theta < 3$ the finite term of the holographic entanglement entropy of a disk in the black hole geometry (4.1.29) is proportional to

$$F_A = \frac{2\pi}{d_\theta - 1} \int_0^R \left[(d_\theta - 1)(f(z) - 1) - \frac{z f'(z)}{2} + \frac{f^2(z)}{f(z)+(z')^2} \left(1 + \frac{z f'(z)}{2 f(z)}\right) \right] \frac{\sqrt{1+(z')^2/f(z)}}{z^{d_\theta}}\, \rho\, d\rho\,. \tag{4.4.19}$$

This expression scales like $F_A \to \lambda^{2-d_\theta} F_A$ under the rescaling introduced above.

The radial profile characterising the minimal area surface $\hat{\gamma}_A$ can be found by solving the second order ordinary differential equation obtained by extremising the area functional (4.4.17). This can be done numerically for any d_θ (e.g. with Wolfram Mathematica). Then, the finite term F_A for $1 < d_\theta < 3$ can be found by plugging the resulting profile into the integral (4.4.17) properly regularised and subtracting the leading divergence (4.1.10),

In order to check our results, we have studied the finite term F_A as a function of the radius R for different values of ζ, where the gravitational background given by the black hole (4.1.29) with fixed $d_\theta = 2$ and the black hole horizon set to $z_h = 1$. The results are shown in Fig. 4.4, where the same quantity has been computed by employing analytic expressions and numerical

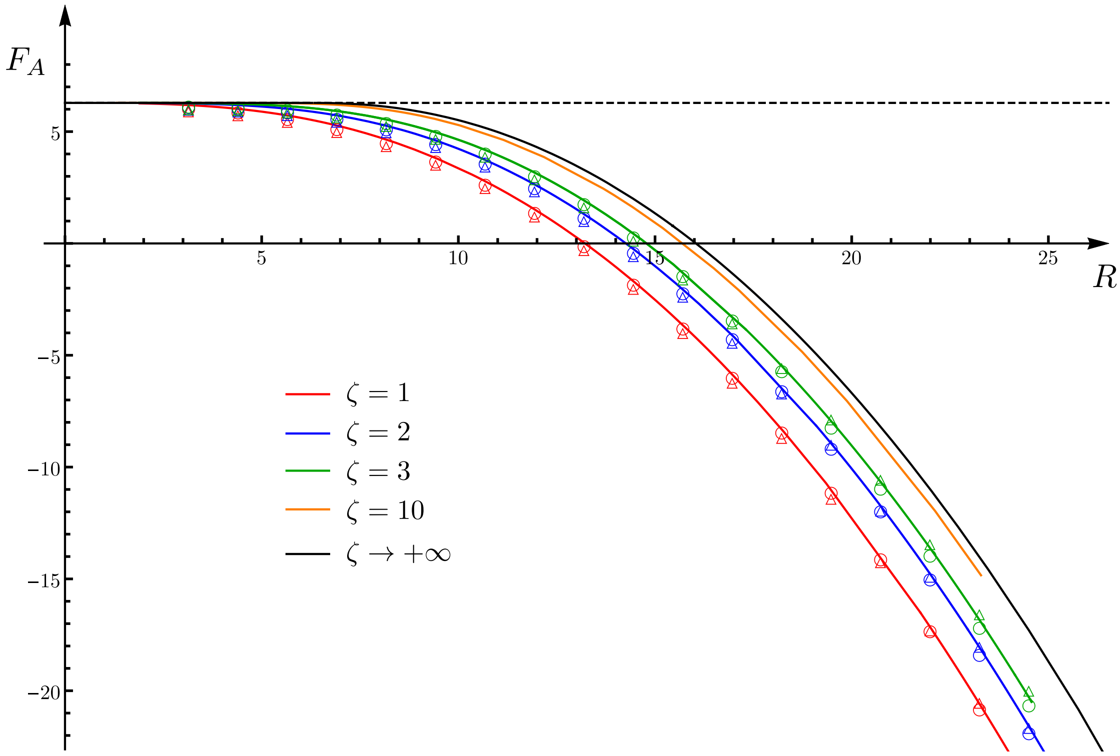

Figure 4.4: Finite term F_A for minimal surfaces anchored to a disk of radius R when the bulk metric is the black hole (4.1.29), with $d_\theta = 2$, different values of ζ and the horizon set to $z_h = 1$. The solid black curve corresponds to the analytic solution (4.4.24) described in Section 4.4.2, while the remaining coloured solid lines have been obtained by evaluating (4.4.19) on the minimal surface whose radial profile has been found by solving the equation of motion of (4.4.17) numerically. The data points labelled by the empty circles and the empty triangles have been obtained with Surface Evolver through the two formulas in (4.4.16) respectively. The horizontal black dashed line corresponds to $F_A = 2\pi$, that gives the finite term of the holographic entanglement entropy of disks when the gravitational background is AdS$_4$.

methods based either on Mathematica or on Surface Evolver, finding a remarkable agreement. For very small regions, F_A tends to 2π as in the AdS$_4$ and, in particular, it is independent on ζ. For very large regions we expect to obtain the behaviour (4.1.33), independent of ζ, while for intermediate sizes F_A depends on ζ in a non-trivial way.

Let us remark that, in Fig. 4.4, the curves having $d_\theta = 2$ and different ζ tend to accumulate toward a limiting curve as ζ increases. In Section 4.4.2 we provide the analytic expression of this limiting curve.

Analytic solution for $d_\theta = 2$ and $\zeta \to \infty$

Analytic solutions for the minimal surfaces anchored to the disk with radius R can be found for the black hole background (4.1.29) in the asymptotic regime given by $d_\theta = 2$ and large ζ. In this limit, the original black hole geometry collapses to AdS$_4$ for $z \leqslant z_h$, with an event

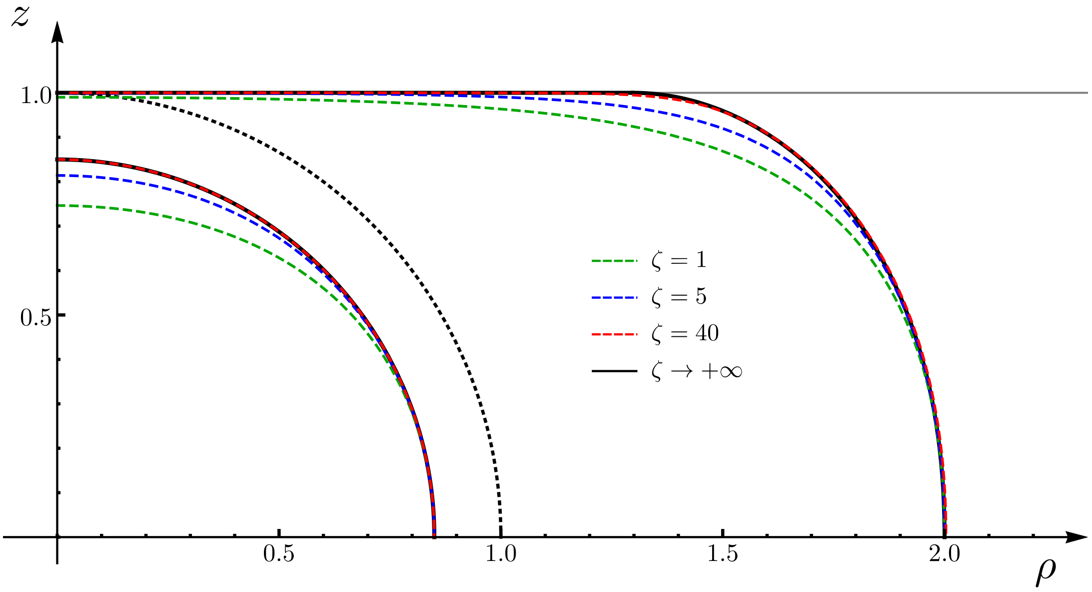

Figure 4.5: Radial profiles of minimal surfaces anchored to disks with $R = 0.85$ and $R = 2$ in the black hole background (4.1.29) for $d_\theta = 2$ and different values of ζ. The grey horizontal line is the black hole horizon at $z_h = 1$. The solid black lines correspond to the asymptotic regime $\zeta \to +\infty$: when $R \leqslant z_h$ they are hemispheres $z(\rho) = \sqrt{R^2 - \rho^2}$, otherwise they are given by (4.4.20). The coloured dashed lines, which correspond to some finite values of ζ, are radial profiles obtained numerically with Mathematica.

horizon located at $z = z_h$. The horizon prevents the minimal surface from entering the region $z > z_h$.

When $R/z_h \leqslant 1$, the minimal surface is provided by the usual hemisphere, that in cylindrical coordinates reads $z(\rho) = \sqrt{R^2 - \rho^2}$. When $R/z_h > 1$, the extremal surface consists of two branches: a non-trivial profile connecting the conformal boundary to the horizon and a flat disk that lies on the horizon. The detailed procedure to construct this minimal surface analytically is given in Appendix C.6 and below we summarize the main results.

In cylindrical coordinates, the profile of the minimal surface for $R/z_h > 1$ is parametrically defined by

$$(z, \rho) = \begin{cases} R\, e^{q_{+,k}(\hat{z})}(\hat{z}, 1) & 0 < \hat{z} < k^{1/4} \\ (z_h, \rho) & 0 < \rho < z_h/k^{1/4} \end{cases} \tag{4.4.20}$$

where $\hat{z} = z/\rho$ and k is an integration constant whose value as function of R/z_h is determined by the following condition

$$\frac{R}{z_h} = \frac{e^{q_{+,k}(k^{1/4})}}{k^{1/4}} \,. \tag{4.4.21}$$

The function $q_{+,k}(\hat{z})$ is one of the two functions emerging from the integration of the differential equation for the extremal surface (see Appendix C.6). They both can be written in terms of elliptic integrals of different kinds, and their expressions have already defined in (2.3.5).

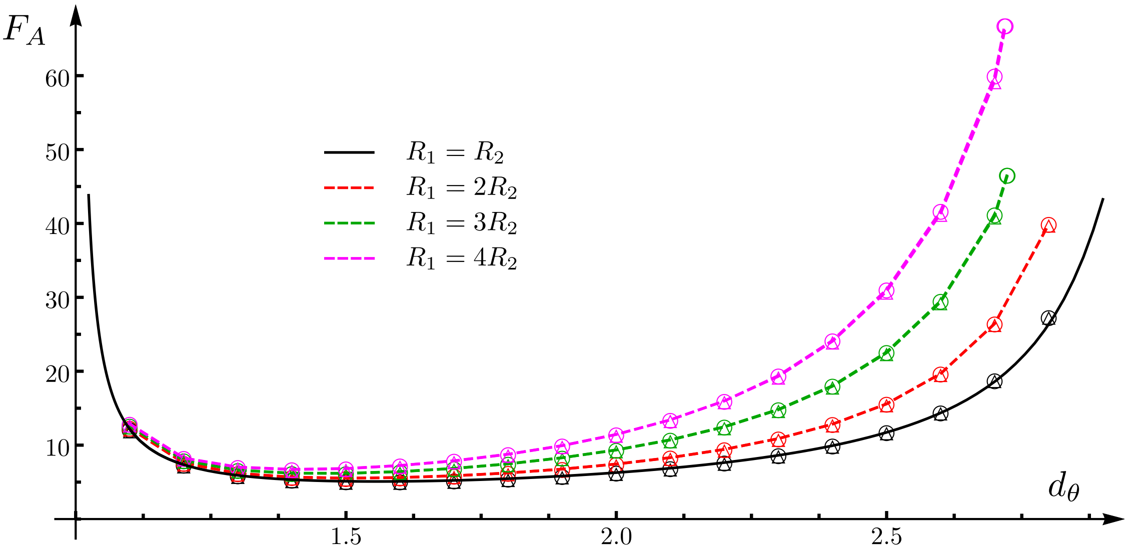

Figure 4.6: Finite term F_A in terms of d_θ in the range $1 < d_\theta < 3$ for minimal surfaces in hvLif$_4$ anchored to ellipses A having fixed perimeter $P_A = 1$. Different colours correspond to ellipses with different eccentricity. The data points have been obtained with Surface Evolver in the two ways described in (4.4.16) (the markers have been assigned as in the previous figures). The solid black curve, that corresponds to the disk, is the curve reported in Fig. 4.2 multiplied by $(P_A/(2\pi R))^{2-d_\theta}$.

However, for easier reading, we report again the result below:

$$q_{\pm,k}(\hat{z}) = \frac{1}{2}\log(1+\hat{z}^2) \pm \kappa\sqrt{\frac{1-2\kappa^2}{\kappa^2-1}}\Big[\Pi\big(1-\kappa^2, \Omega(\hat{z})|\kappa^2\big) - \mathbb{F}\big(\Omega(\hat{z})|\kappa^2\big)\Big] \tag{4.4.22}$$

with

$$\Omega(\hat{z}) \equiv \arcsin\left(\frac{\hat{z}/\hat{z}_m}{\sqrt{1+\kappa^2(\hat{z}^2/\hat{z}_m^2-1)}}\right) \qquad \kappa \equiv \sqrt{\frac{1+\hat{z}_m^2}{2+\hat{z}_m^2}} \tag{4.4.23}$$

where $\hat{z}_m^2 = (k+\sqrt{k(k+4)})/2$.

In Fig. 4.5, we have plotted the profile of the minimal surfaces in the limit $\zeta \to +\infty$ for two different radii $R = 0.85$ and $R = 2$ (continuous black lines). In the former case, the solution is the hemisphere, while in the latter one it is given by the profile (4.4.20). As a consistency check, we have obtained numerically (with Mathematica) the radial profiles for finite values of ζ (coloured dashed lines), finding that they approach the analytical solution as ζ increases.

We can now compute the finite term F_A for this family of surfaces, and the result reads

$$F_A = \begin{cases} 2\pi & \text{when} \quad R \leqslant z_h \\ 2\pi\left(\mathcal{F}_k(k^{1/4}) - \dfrac{1}{2\sqrt{k}}\right) & \text{when} \quad R > z_h \end{cases} \tag{4.4.24}$$

with

$$\mathcal{F}_k(\hat{z}) \equiv \frac{\sqrt{k(1+\hat{z}^2)-\hat{z}^4}}{\sqrt{k}\,\hat{z}} - \frac{\mathbb{F}(\arcsin(\hat{z}/\hat{z}_m)\,|-\hat{z}_m^2-1) - \mathbb{E}(\arcsin(\hat{z}/\hat{z}_m)\,|-\hat{z}_m^2-1)}{\hat{z}_m} \tag{4.4.25}$$

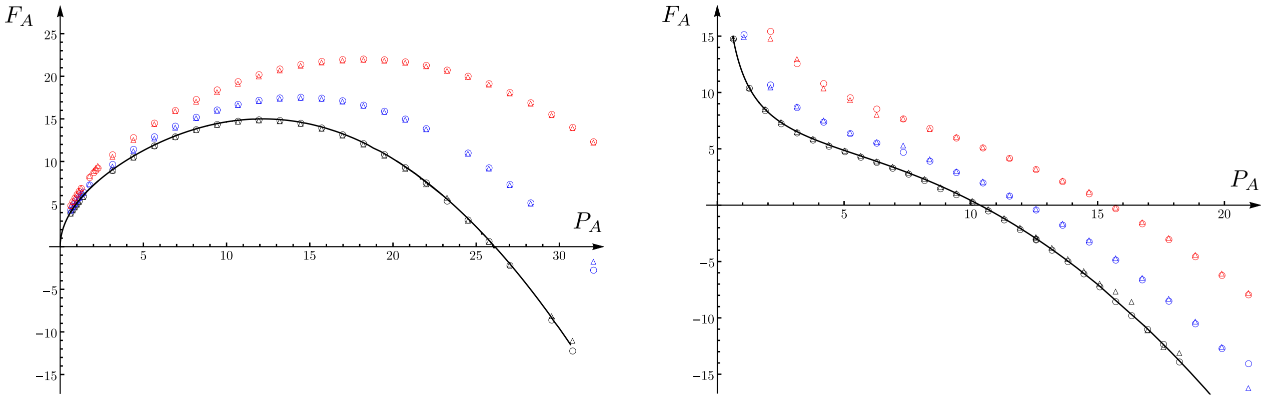

Figure 4.7: Finite term F_A in terms of the perimeter P_A for minimal surfaces in the asymptotically hvLif$_4$ black hole (4.1.29) anchored to ellipses A. The Lifshitz exponent is fixed to $\zeta = 1.5$, while $d_\theta = 1.5$ in the left panel and $d_\theta = 2.5$ in the right panel. Different colours correspond to ellipses with different eccentricity: disk (black), $R_2 = 2R_1$ (blue) and $R_2 = 3R_1$ (red). The data points labelled by the empty circles and the empty triangles have been obtained with Surface Evolver through the two formulas in (4.4.16) respectively. The solid black curves for disks have been found numerically by employing Mathematica. All the curves and the data points have been obtained by using (4.1.18).

where $\mathbb{F}$ and $\mathbb{E}$ are the first and second elliptic integral respectively. The curve (4.4.24) is a continuous function of R.

The solid black curve in Fig. 4.4 has been obtained by a parametric plot employing (4.4.21) and (4.4.24) (with $z_h = 1$) for $R > 1$, while $F_A = 2\pi$ for $R < 1$.

4.4.3 Ellipses

The main feature of the analytic expressions obtained in Section 4.1 and Section 4.3 for the finite term of the holographic entanglement entropy is that they hold for any smooth shape of the entangling curve. In order to evaluate these formulas for explicit domains, one needs to know the entire minimal surface $\hat{\gamma}_A$, and this task is usually very difficult, in particular when the entangling curve does not display some useful symmetry. Surface Evolver can be employed to study numerically $\hat{\gamma}_A$ for a generic smooth entangling curve ∂A, as already done in some asymptotically AdS$_4$ backgrounds in [78, 245], and in the chapters 2 and 3.

In this subsection, we consider the finite term of the holographic entanglement entropy of ellipses when the gravitational spacetime is hvLif$_4$ in (4.1.19) or the asymptotically hvLif$_4$ black hole (4.1.29).

In Fig. 4.6, we show the finite term F_A of elliptic regions having the same perimeter $P_A = 1$ as a function of the effective dimension $1 < d_\theta < 3$, when the bulk is hvLif$_4$. Ellipses with different eccentricity e have been considered (we recall that $e = \sqrt{1-(R_1/R_2)^2} \in [0, 1)$, being $R_1 \leqslant R_2$ the semi-axis of the ellipse). The numerical data have been obtained with Surface Evolver and F_A has been found through the two different methods described in (4.4.16). In particular, the empty circles and the empty triangles correspond respectively to $F_{A,\text{SE}}$ and $\widetilde{F}_{A,\text{SE}}$ (the coloured dashed lines just join the data points). The solid black line gives the finite term for disks, and it has been obtained by using Mathematica (it is the same curve shown in Fig. 4.2,multiplied by the factor $(P_A/(2\pi R))^{2-d_\theta}$).

The finite term F_A when the bulk metric is the black hole (4.1.29) also depends on d_θ. In Fig. 4.7 we show F_A for ellipses having different eccentricity in terms of their perimeter P_A for two different values of d_θ ($d_\theta = 1.5$ in the left panel and $d_\theta = 2.5$ in the right panel) and the same value of the Lifshitz parameter $\zeta = 1.5$. Also in this case, the data points have been found by evaluating numerically (4.1.31) on the approximated minimal surfaces obtained with Surface Evolver, while the solid black curve has been obtained numerically by using Mathematica. The very good agreement between the various methods provides a highly non-trivial check of the general formula (4.1.18).

A qualitative difference can be observed between the two panels in Fig. 4.7. Indeed, for very small regions, the behaviour of F_A depends on d_θ. In particular, when $P_A \to 0$, we have that $F_A \to 0$ for $d_\theta < 2$ while $F_A \to +\infty$ for $d_\theta > 2$. This can be understood by observing that the finite term F_A of small regions (whose maximal penetration in the bulk is very far from the horizon) is not influenced by the occurrence of the horizon; hence it scales approximately as in (4.4.15), which is valid in hvLif$_4$.

4.5 Discussion

In this chapter, we have explored the shape dependence of the holographic entanglement entropy in AdS$_4$/CFT$_3$ in the presence of Lifshitz scaling and hyperscaling violation. Both static and time-dependent backgrounds have been studied and, for the sake of simplicity, we focussed to smooth entangling curves and to the regime $1 \leqslant d_\theta \leqslant 5$ for the hyperscaling parameter. In the expansion of the holographic entanglement entropy as the UV cutoff ε vanishes, both the divergent terms and the finite term have been analysed.

Our main results are analytic expressions for the finite term that can be applied for any smooth entangling curve: for static backgrounds, they are given by (4.1.18) when $1 < d_\theta < 3$ and by (4.1.19) when $3 < d_\theta < 5$; for time-dependent backgrounds, we have obtained (4.3.2) when $1 < d_\theta < 3$. In the regime $1 < d_\theta < 3$, the finite term for static and time-dependent backgrounds has also been studied for surfaces that intersect the boundary orthogonally along smooth curves, finding the expressions (4.1.17) and (4.3.1) respectively. This class of surfaces includes the extremal surfaces providing the holographic entanglement entropy.

When $d_\theta \in \{1, 3, 5\}$, a logarithmic divergence occurs in the expansion of the holographic entanglement entropy. The coefficient of this divergence is determined only by the geometry of the entangling curve and its analytic expression for a generic smooth entangling curve has been reported in (4.1.11), (4.1.13) and (4.1.16) respectively.

The new results summarised above have been found by extending the analysis first performed in [76] and then further developed in [77, 78, 155] for gravitational backgrounds having $d_\theta = 2$.

We find it worth mentioning two other analytic results obtained. For hvLif$_{d+1}$ spacetime we showed that the finite term of the extremal surface can be expressed as an integral over the entangling surface, since the background metric admits a conformal Killing vector generating dilatations. Moreover, we have briefly discussed the extension of this result to more general geometries. By applying this result to hvLif$_{d+1}$, the simple expression (4.2.7) is found for the finite term, valid in any dimension and for any $d_\theta > 1$. Another result has been obtained for the asymptotically hvLif$_4$ black hole (4.1.29) in the asymptotic regime given by $d_\theta = 2$ and $\zeta \to \infty$, where we have found the analytic expression of the minimal surface anchored to a disk and of the finite term in the expansion of its area.

For the static backgrounds given by the hvLif$_4$ spacetime (4.1.21) and the asymptotically hvLif$_4$ black hole (4.1.29), a numerical analysis has been performed by considering disks and ellipses. Disks have been studied mainly through the standard Wolfram Mathematica, while for the ellipses we have employed Surface Evolver [152, 153]. A very good agreement between the analytic expressions in (4.1.18) and (4.1.19) and the numerical data has been observed.

Conclusions and Future Directions

The time has come for drawing the conclusions of this thesis and discussing some possible future directions.

The recurrent theme of this work is the shape dependence of the entanglement entropy. As already discussed in chapter 1, subleading terms with respect to the area law strongly depends on the shape of the region A. In four dimensions, the first subleading term is a logarithmic divergence whose coefficient is a universal quantity characterising the underlying CFT, and which contains the two anomalies a and c. It turns out that when the region A is a sphere, only the charge a appears in the logarithm and this provides a way to state the a-theorem in terms of the entanglement entropy. In the three-dimensional case, no logarithmic terms occur for smooth surfaces. Nonetheless, by considering a circular region A, the finite term (related to the free-energy on the sphere) provides the $F-$theorem. When the domain A is non-smooth, logarithmic terms arise as contributions from corners in A. The universal coefficient is a function of the opening angles of the corners and depends on the specific three-dimensional CFT. In particular, in the limit of vanishing angles, the coefficient of the quadratic term of the expansion of the corner function is proportional to the coefficient characterising the two-point function of the stress-energy tensor. All these results suggest that studying the dependence of the entanglement entropy on the shape of A can reveal important information about the theory. On the other hand, finding the entanglement entropy for a generic region is a formidable task also from the numerical perspective. For this reason, we employ the holographic setup, in which S_A can be found by computing the area of a minimal surface in a suitable asymptotically anti de-Sitter spacetime whose boundary supports the CFT. In this case, a change in the shape of the region A leads to a change of the corresponding minimal surface and, in turn, of its area. The holographic setup, which is conjectured to describe some strongly coupled CFTs, allows finding many analytical results, and it drastically simplifies the numerical analysis.

In chapters 2 and 3, we have considered the case of three-dimensional conformal field theories with boundaries (BCFT_3). Our strategy was to compute the entanglement entropy in the holographic setup introduced by Takayanagi [89]. In chapter 2, we have started deriving an *analytical formula for the finite term* F_A (see equation (2.1.18)) valid for any region A (also when it is made of disjoint components) and any static asymptotically AdS_4 metric with generic boundary $\mathcal{Q}$ that represents the gravitational counterpart of the boundary of the BCFT$_3$ (see Sec. 2.1). For gravitational backgrounds corresponding to AdS$_4$ spacetimes restricted by $\mathcal{Q}$, the functional (2.1.18) reduces to the *Willmore functional* over $\mathbb{R}^3$ with a proper boundary term (see equation (2.1.23)). When the gravitational spacetime is dual to the vacuum of the BCFT$_3$ with flat or circular boundaries, we found *explicit solutions* of the minimal surfaces from which we were able to check the general formula (2.1.18). These solutions correspond to *strip regions* (Sec. 2.2) when the boundary is flat, and to *circular regions* disjoint from either the flat or the circular boundary (Sec. 2.3). Both the domains show a particular feature of AdS$_{d+2}$/BCFT$_{d+1}$, namely for certain boundary conditions the minimal surfaces are never affected by the presence of the boundary $\mathcal{Q}$, not even for domains very closed to the boundary of the BCFT$_{d+1}$. In particular, in the holographic setup the boundary conditions are parametrized by the tension of $\mathcal{Q}$, or equivalently by the geometrical angle α setting the slope of $\mathcal{Q}$ when it is a hyperplane. Thus, below a certain *critical value* α_c of α, the minimal surfaces behave as in the absence of $\mathcal{Q}$. In contrast, above this value, the minimal surfaces can be either connected to $\mathcal{Q}$ or disconnected from it, depending on the distance of A from the boundary. This means that it exists a finite critical distance at which a *transition between extremal surfaces* occurs. This kind of transitions have been studied explicitly for circular regions in Sec. 2.3. Finally, in Sec. 2.4, numerical results for elliptic domains disjoint from the boundary have been studied by employing Surface Evolver [152, 153].

In chapter 3, we considered entangling curves intersecting the boundary at isolated points. For these bipartitions, a logarithmic term in the expansion of S_A arises as a contribution of corners adjacent to the boundary. The coefficient of the logarithm is a *boundary corner function* that depends on the opening angles of such corners. If more than one intersection occurs, the total coefficient is the sum of the functions due to the single intersections. By employing two simple domains, namely the half-disk (see Sec. 3.2.1) and the infinite wedge adjacent to the boundary (Sec. 3.2.3), we have found the analytic expression of the boundary corner function in the holographic setup. For such domains, the minimal surfaces are always affected by the boundary $\mathcal{Q}$. However, the critical value of α shows up in the limiting regime for which the opening angle of the infinite wedge tends to zero (see equation (3.2.17)). In this case, above the critical value, the boundary corner function displays a simple pole, while below that value it tends to a finite value (which is zero at the critical value). The other interesting limiting regime corresponds to the orthogonal intersection. In this case, from the expansion of the boundary corner function (3.2.19), we observed that the leading contribution $f_\alpha(\pi/2)$ *is proportional to the* $\mathfrak{a}$ *charge* of the boundary conformal anomaly (see Sec. 3.4) in agreement with the results [161, 208, 269], while the coefficient of the second-order $f''_\alpha(\pi/2)$ *is proportional to the coefficient* A_T, which appears in the leading order of the *one-point function of the stress-energy tensor* in its expansion near a curved boundary. We stress that this relation (3.4.6), which is independent of the boundary conditions, holds only in the setup proposed by Takayanagi. This is in contrast with the relation (3.2.19) that also holds for the other proposals [158–161]. Finally, numerical results have been found to check the analytic result of the boundary corner function, and transitions between extremal surfaces for domains with single tips located on the boundary have been studied in Sec. 3.5.

Many interesting directions can be explored in the future. An important conceptual issue to understand in the AdS/BCFT setup of [89] is the relation occurring between the geometrical parameter α and the space of the conformally invariant boundary conditions for the dual BCFT$_3$. As for the holographic entanglement entropy in AdS$_4$/BCFT$_3$, gravitational backgrounds dual to a BCFT$_3$ at finite temperature or to boundary RG flows could be considered. The expression (2.1.18) found in this chapter 2 also holds in these cases; nonetheless, it would be interesting to find explicit analytic expressions in some simple setups. Time-dependent gravitational backgrounds, which are relevant to study quenches, could be studied. Furthermore, an interesting issue that we find it worth exploring is the possibility that the relation (3.4.6) holds for other models of BCFT$_3$. A result in this direction has been discussed in [272], where this ratio has been obtained numerically for the free scalar boson with Dirichlet boundary condition. Their result shows a mismatch with our holographic computation (3.4.6). On the other hand, the free scalar boson seems to be a special case for the presence of non-minimal coupling to the scalar curvature. In particular, in [208] it has been discussed that this coupling spoils the relation $\mathfrak{a} = f_\alpha(\pi/2)$ that should be valid for any BCFTs [269]. It is certainly interesting to explore if such coupling is also the cause for the mismatch regarding the ratio (3.4.6). Furthermore, a deep understanding of the relation (3.4.6) could give insight on the possible different prescriptions for the holographic dual of BCFTs [89, 158–161]. The extension of the analysis performed in this thesis to higher dimensions, where different kinds of singular configurations occur, is certainly important to improve our understanding of the holographic entanglement entropy in AdS/BCFT. Furthermore, we find it interesting to explore in the future the holographic complexity [44–48] in the presence of boundaries. In particular, it has been recently found that the insertion of defects could give insights on the duals of the quantum complexity [274]. We remark that the results and the methods discussed in this thesis could be useful also in the context of the gauge/gravity correspondence in the presence of defects (AdS/dCFT) [262, 275].

In chapter 4, we considered asymptotically hvLif$_4$ background metrics. This kind of spacetimes are supposed to be dual to critical systems with anisotropic scale invariance (Lifshitz spacetime) characterised by the dynamical exponent ζ, and which display the violation of the hyperscaling relations driven by the exponent θ. These behaviours appear in quantum phase transitions of certain condensed matter systems. The holographic entanglement entropy of a region A in general depends on both ζ and θ (or $d_\theta = 2 - \theta$). In asymptotically hvLif$_4$ backgrounds, we computed the *divergent terms* for certain value of d_θ, i.e. $1 \leqslant d_\theta \leqslant 5$ for domains A. We showed that these terms are completely determined by the geodesics curvature of the entangling surface. In particular, for odd values of d_θ a logarithmic contribution appears, see for instance equations (4.1.11), (4.1.13) and (4.1.16) for $d_\theta = 1, 3, 5$, respectively. The case $d_\theta = 1$ is compelling because it shows a logarithmic violation of the area law, which characterises systems with a Fermi surface. The finite term has a more complicated structure since it also depends on the whole background metric. Despite that, we found *analytic expressions for the finite term in static backgrounds*. These expressions are different for the two ranges $1 < d_\theta < 3$ (see (4.1.18)) and $3 < d_\theta < 5$ (see (4.1.19)). Furthermore, for the case $1 < d_\theta < 3$

we have found the functional (4.3.1) which is valid for *time-dependent backgrounds* and extends the analysis of [78] which is recovered in the special case of $d_\theta = 2$. We find it worth mentioning two other analytic results obtained in that chapter. For hvLif$_{d+1}$ spacetimes, we showed that the finite term of an extremal surface can be expressed as an integral over the entangling surface because the background metric admits a conformal Killing vector generating dilatations. Then, numerical results have been found by employing Wolfram Mathematica (for circular shapes) and Surface Evolver (for elliptic domains) to check the analytic expressions (4.1.18) and (4.1.19). In particular, black-hole backgrounds have also been considered.

The results reported in chapter 4 can be extended in various directions. We find it worth exploring $d_\theta > 5$ because other divergent terms occur, and it is interesting to understand their dependence on the shape of the entangling curve. The numerical approach employed in chapter 4 deserves further studies. For instance, it is important to extend the application of Surface Evolver to time-dependent backgrounds, both to check on non-spherical finite regions the analytic expressions for the finite term in the expansions of the holographic entanglement entropy found in [78] and in Section 4.3, and to improve the current understanding of the shape dependence of the holographic entanglement entropy.

Appendices

Appendix **A**

Appendix of Chapter 2

A.1 Useful mappings

In this appendix we discuss two useful transformations employed in Sec. 2.1.1 and Sec. 2.3.

Let us consider the map $(x, y, z) \to (X, Y, Z)$ with $z > 0$ and $Z > 0$ defined by [246]

$$\begin{cases} X = \lambda \, \dfrac{x - a_x + c_x \left[(\boldsymbol{x} - \boldsymbol{a})^2 + z^2 \right]}{1 + 2\, \boldsymbol{c} \cdot (\boldsymbol{x} - \boldsymbol{a}) + \boldsymbol{c}^2 \left[(\boldsymbol{x} - \boldsymbol{a})^2 + z^2 \right]} \\[2ex] Y = \lambda \, \dfrac{y - a_y + c_y \left[(\boldsymbol{x} - \boldsymbol{a})^2 + z^2 \right]}{1 + 2\, \boldsymbol{c} \cdot (\boldsymbol{x} - \boldsymbol{a}) + \boldsymbol{c}^2 \left[(\boldsymbol{x} - \boldsymbol{a})^2 + z^2 \right]} \\[2ex] Z = \lambda \, \dfrac{z}{1 + 2\, \boldsymbol{c} \cdot (\boldsymbol{x} - \boldsymbol{a}) + \boldsymbol{c}^2 \left[(\boldsymbol{x} - \boldsymbol{a})^2 + z^2 \right]} \end{cases} \tag{A.1.1}$$

where $\lambda > 0$, the vectors $\boldsymbol{x} = (x, y)$, $\boldsymbol{a} = (a_x, a_y)$ and $\boldsymbol{c} = (c_x, c_y)$ belong to $\mathbb{R}^2$ and $\cdot$ denotes the standard scalar product between vectors in $\mathbb{R}^2$. The transformation (A.1.1) leaves the metric (2.1.22) invariant up to a conformal factor. On the conformal boundary, given by $Z = z = 0$, the map (A.1.1) becomes a special conformal transformation.

The first special case of (A.1.1) that we need is the map sending the right half-plane $\{(x, y) \in \mathbb{R}^2, x \geqslant 0\}$ at $z = 0$ into the disk $\{(X, Y) \in \mathbb{R}^2, X^2 + Y^2 \leqslant R_Q^2\}$ of radius R_Q at $Z = 0$. Since this transformation must send the straight line $(x, y, z) = (0, y, 0)$ into the circle $\mathcal{C}_Q$ given by $(X, Y, Z) = (R_Q \cos\phi, R_Q \sin\phi, 0)$ with $\phi \in [0, 2\pi)$, it can be constructed by first setting $a_y = a_z = 0$ and $x = z = 0$ in (A.1.1), and then imposing $X^2 + Y^2 = R_Q^2$. This leads to

$$\frac{\lambda^2 \left(a_x^2 + y^2\right)}{\left(a_x^2 + y^2\right)\left(c_x^2 + c_y^2\right) - 2 a_x c_x + 2 c_y y + 1} - R_Q^2 = 0 \qquad \forall y \in \mathbb{R} \tag{A.1.2}$$

which can be written as a quadratic equation in y that must hold $\forall y \in \mathbb{R}$; therefore we have to impose the vanishing of its coefficients. This procedure gives $a_x = \pm R_Q/(2\lambda)$ and $\boldsymbol{c} = (\pm \lambda/R_Q, 0)$, where the choice of the sign determines whether the right half-plane $x \geqslant 0$ is mapped in the region inside (positive sign) or outside (negative sign) the circle $\mathcal{C}_Q$. Considering the former option, we find that (A.1.1) becomes

$$\begin{cases} X = \dfrac{R_{\mathcal{Q}}\big[4\lambda^2(x^2+y^2+z^2)-R_{\mathcal{Q}}^2\big]}{R_{\mathcal{Q}}^2+4\lambda^2\,(x^2+y^2+z^2)+4\lambda R_{\mathcal{Q}}\,x} \\[2ex] Y = \dfrac{4\lambda R_{\mathcal{Q}}^2\,y}{R_{\mathcal{Q}}^2+4\lambda^2\,(x^2+y^2+z^2)+4\lambda R_{\mathcal{Q}}\,x} \\[2ex] Z = \dfrac{4\lambda R_{\mathcal{Q}}^2\,z}{R_{\mathcal{Q}}^2+4\lambda^2\,(x^2+y^2+z^2)+4\lambda R_{\mathcal{Q}}\,x} \end{cases} \qquad \begin{cases} x = \dfrac{R_{\mathcal{Q}}\big(R_{\mathcal{Q}}^2-X^2-Y^2-Z^2\big)}{2\lambda\big[(R_{\mathcal{Q}}-X)^2+Y^2+Z^2\big]} \\[2ex] y = \dfrac{R_{\mathcal{Q}}^2\,Y}{\lambda\big[(R_{\mathcal{Q}}-X)^2+Y^2+Z^2\big]} \\[2ex] z = \dfrac{R_{\mathcal{Q}}^2\,Z}{\lambda\big[(R_{\mathcal{Q}}-X)^2+Y^2+Z^2\big]} \end{cases} \tag{A.1.3}$$

where also the inverse map has been reported. The transformations in (A.1.3) relate the setups described in Sec. 2.1.1 and Sec. 1.4.2. Since in (A.1.3) the constant λ can be reabsorbed through the rescaling $(x,y,z)\to\lambda(x,y,z)$, which leaves $\mathbb{H}_3$ invariant, we are allowed to set $\lambda=1$ in (A.1.3) without loss of generality. The first transformation in (A.1.3) maps the half-plane (1.4.9) into the following spherical cap [90]

$$X^2+Y^2+(Z-R_{\mathcal{Q}}\cot\alpha)^2=\frac{R_{\mathcal{Q}}^2}{\sin^2\alpha} \qquad\qquad Z>0 \tag{A.1.4}$$

which has also been written in (1.4.11) by means of cylindrical coordinates. When $\alpha=\pi/2$, (A.1.4) reduces to the hemisphere of radius $R_{\mathcal{Q}}$.

The second map in (A.1.3) has been used in Sec. 2.3.2 to obtain the holographic entanglement entropy of a disk disjoint from a flat boundary starting from the holographic entanglement entropy of a disk concentric to a circular boundary computed in Sec. 2.3.1. Indeed, by considering the circle $(X,Y)=(b_\circ+R_\circ\cos\phi,R_\circ\sin\phi)$ with $\phi\in[0,2\pi)$ inside the disk delimited by $\mathcal{C}_{\mathcal{Q}}$, its image through the second map in (A.1.3) is the circle $(x,y)=(d+R+R\cos\phi,R\sin\phi)$ in the right half-plane at $z=0$, which has radius R and distance d from the straight boundary at $x=0$. We find that $(R_\circ,b_\circ)$ can be written in terms of (R,d) as follows

$$\frac{R_\circ}{R_{\mathcal{Q}}}=\frac{4\,R/R_{\mathcal{Q}}}{1+4(d/R_{\mathcal{Q}}+2R/R_{\mathcal{Q}})d/R_{\mathcal{Q}}+4(d/R_{\mathcal{Q}}+R/R_{\mathcal{Q}})} \tag{A.1.5}$$

$$\frac{b_\circ}{R_{\mathcal{Q}}}=1-\frac{2\big[1+2(d/R_{\mathcal{Q}}+R/R_{\mathcal{Q}})\big]}{\big[1+2(d/R_{\mathcal{Q}}+2R/R_{\mathcal{Q}})\big]\,\big[1+2d/R_{\mathcal{Q}}\big]} \tag{A.1.6}$$

where the r.h.s.'s depend only on the ratios $R/R_{\mathcal{Q}}$ and $d/R_{\mathcal{Q}}$. For a circle concentric to the circular boundary (considered e.g. in Sec. 2.3.1), $b_\circ=0$. The expressions in (2.3.21) have been obtained by solving (A.1.5) and (A.1.6) in this special case.

The second map in (A.1.3) has been also employed to obtain the analytic expressions for the extremal surfaces shown in Fig. 2.12 and Fig. 2.13.

The second transformation coming from (A.1.1) that we consider is the one mapping the disk delimited by $\mathcal{C}_{\mathcal{Q}}$ into itself. Let us rename $(x,y,z)=(X',Y',Z')$ in (A.1.1) for this case, where $Z=Z'=0$. By imposing that the circle $\mathcal{C}_{\mathcal{Q}}$ is mapped into itself in the coordinates (X',Y'), we find the following two options: either $\boldsymbol{a}=(\pm R_{\mathcal{Q}}\sqrt{(\lambda+1)/\lambda},0)$ and $\boldsymbol{c}=(\pm\sqrt{\lambda(1+\lambda)}/R_{\mathcal{Q}},0)$ or $\boldsymbol{a}=(\pm R_{\mathcal{Q}}\sqrt{(\lambda-1)/\lambda},0)$ and $\boldsymbol{c}=(\mp\sqrt{\lambda(\lambda-1)}/R_{\mathcal{Q}},0)$ with

$\lambda \geqslant 1$. Since the first option exchanges the interior and the exterior of the disk, we have to select the second one, where the lower or upper choice of the signs move the center of the disk along either $X' > 0$ or $X' < 0$ respectively. Being the disk invariant under a rotation of π about the origin, we can choose one of these two options without loss of generality. Considering e.g. $\boldsymbol{a} = -(R_{\mathcal{Q}}\sqrt{(\lambda-1)/\lambda}, 0)$ and $\boldsymbol{c} = (\sqrt{\lambda(\lambda-1)}/R_{\mathcal{Q}}, 0)$ with $\lambda \geqslant 1$, the resulting transformation maps the circle $(X, Y) = (R_\circ \cos\phi, R_\circ \sin\phi)$ with $R_\circ < R_{\mathcal{Q}}$ into the circle $(X', Y') = (b'_\circ + R'_\circ \cos\phi, R'_\circ \sin\phi)$, where

$$\frac{R'_\circ}{R_{\mathcal{Q}}} = \frac{R_\circ/R_{\mathcal{Q}}}{\lambda\big[1-(R_\circ/R_{\mathcal{Q}})^2\big] + (R_\circ/R_{\mathcal{Q}})^2} \qquad \frac{b'_\circ}{R_{\mathcal{Q}}} = \frac{\sqrt{(\lambda-1)\lambda}\,\big[1-(R_\circ/R_{\mathcal{Q}})^2\big]}{\lambda\big[1-(R_\circ/R_{\mathcal{Q}})^2\big] + (R_\circ/R_{\mathcal{Q}})^2}. \tag{A.1.7}$$

By inverting these relations, one gets $R_\circ/R_{\mathcal{Q}}$ and λ in terms of $R'_\circ/R_{\mathcal{Q}}$ and $b'_\circ/R_{\mathcal{Q}}$. We have checked that, under the transformation that we have constructed, the surface $\mathcal{Q}$ in (A.1.4) remains unchanged for any value of $\lambda \geqslant 1$.

The expression of $R_\circ/R_{\mathcal{Q}}$ obtained in this way and (2.3.13) provide the finite term F_A for the holographic entanglement entropy of a disk A inside the disk delimited by $\mathcal{C}_{\mathcal{Q}}$ in the cases where these two disks are not concentric.

A.2 On the Infinite strips in generic dimension

A.2.1 Infinite strip adjacent to the boundary

In this appendix, we study the holographic entanglement entropy for the d dimensional infinite strip of width ℓ adjacent to the boundary. The main results of this analysis specialised to $d = 2$ have been reported in Sec. 2.2.

Given a constant time slice of a BCFT$_{d+1}$, defined by $x \geqslant 0$ in proper Cartesian coordinates, let us consider the following spatial domain

$$A = \{(x, y_1, \dots, y_{d-1}) \,|\, 0 \leqslant x \leqslant \ell\,,\, 0 \leqslant y_i \leqslant L_\parallel\} \qquad L_\parallel \gg \ell \gg \varepsilon. \tag{A.2.1}$$

The invariance under translations along the y_i-axis (in a strict sense, this requires $L_\parallel \to +\infty$) allows us to assume that the minimal surface $\hat{\gamma}_A$ is characterised by its profile obtained by sectioning $\hat{\gamma}_A$ through an hyperplane defined by $y_i = \text{const}$. The profile of $\hat{\gamma}_A$ is given by either $x = \ell$ or by a non-trivial curve $z = z(x)$. Focussing on the latter case, let us denote by $P_* = (x_*, z_*)$ the intersection between the curve $z(x)$ and the section at $y_i = \text{const}$ of the half-hyperplane $\mathcal{Q}$, which is a half-line given by (1.4.9). The coordinates of P_* are constrained by imposing that $P_* \in \mathcal{Q}$, and this condition gives

$$x_* = -\,z_* \cot\alpha \tag{A.2.2}$$

where we recall that $\alpha \in (0, \pi)$. Since the curve $z(x)$ characterising the extremal surface intersects orthogonally the section at constant $y_i = \text{const}$ of the half-hyperplane $\mathcal{Q}$, it is not difficult to realise that $z'(x_*) = \cot\alpha$.

The profile $z(x)$ can be obtained by finding the extrema of the area functional among the surfaces γ_A anchored to the edge $x = \ell$ of the strip (A.2.1) which are invariant under translations along the y_i directions and intersect $\mathcal{Q}$ orthogonally.

Given a surface γ_A characterised by $z(x)$, by writing the metric induced on γ_A from the background (1.4.8), one obtains the following area functional

$$\mathcal{A}[\gamma_A] \,=\, L^d_{\mathrm{AdS}}\, L_{\parallel}^{d-1} \int_{x_*}^{\ell} \frac{\sqrt{1+(z')^2}}{z^d}\, dx. \tag{A.2.3}$$

Since the integrand does not depend on x explicitly, we can find the extremal surface $\hat{\gamma}_A$ by employing the fact that the first integral of motion is constant. For the functional (A.2.3) this condition tells us that $z^d\sqrt{1+(z')^2}$ is independent of x. By choosing the point (x_*, z_*), where $z'(x_*) = \cot\alpha$, the equation imposing the constancy of the first integral of motion reads

$$z^d\sqrt{1+(z')^2} \,=\, \frac{z_*^d}{\sin\alpha}. \tag{A.2.4}$$

In order to solve (A.2.4), we find it convenient to introduce the following parameterisation

$$z(\theta) \,=\, \frac{z_*}{(\sin\alpha)^{1/d}}\,(\sin\theta)^{1/d} \qquad\qquad 0 \leqslant \theta \leqslant \pi-\alpha \tag{A.2.5}$$

which respects the boundary conditions $z(\pi-\alpha) = z_*$ and $z(0) = 0$.

Plugging (A.2.5) into the square of (A.2.4), one gets $(\frac{dz}{dx})^2 = (\cot\theta)^2$, which gives $x'(\theta)^2 = z'(\theta)^2(\tan\theta)^2$. Then, by employing (A.2.5) into the latter differential equation, we obtain

$$x'(\theta) \,=\, -\,\frac{z_*}{d\,(\sin\alpha)^{1/d}}\,(\sin\theta)^{1/d} \tag{A.2.6}$$

where the physical condition that $x(\theta)$ decreases for increasing values of θ has been imposed.

The relation $(\frac{dz}{dx})^2 = (\cot\theta)^2$ and (A.2.5) leads to the geometrical meaning of the angle θ: it is the angle between the outgoing vector normal to the curve given by P_θ and the x semi-axis with $x \geqslant 0$. Thus, from (A.2.5) we have that $\theta = \pi/2$ corresponds to the point of the curve $z(x)$ having the maximum value $z_{\max} = z_*/(\sin\alpha)^{1/d}$.

By integrating (A.2.6) with the initial condition $x(0) = \ell$, we find

$$\begin{aligned} x(\theta) \,&=\, \ell - \frac{z_*}{d\,(\sin\alpha)^{1/d}} \int_0^\theta (\sin\tilde{\theta})^{1/d}\, d\tilde{\theta} && \text{(A.2.7)}\\ &=\, \ell - \frac{z_*}{(\sin\alpha)^{1/d}}\left[\frac{\sqrt{\pi}\,\Gamma\big(\frac{d+1}{2d}\big)}{\Gamma\big(\frac{1}{2d}\big)} - \frac{\cos\theta}{d}\;{}_2F_1\bigg(\frac{d-1}{2d}\,,\frac{1}{2}\,;\frac{3}{2}\,;(\cos\theta)^2\bigg)\right]. && \text{(A.2.8)}\end{aligned}$$

The expressions (A.2.5) and (A.2.8) depend on the coordinate z_* of the point P_*. We can relate z_* to the width ℓ of the strip (A.2.1) by imposing that (A.2.8) satisfies the consistency condition $x(\pi-\alpha) = x_*$, where x_* can be obtained from (A.2.2). This gives

$$\ell - \frac{z_*}{(\sin\alpha)^{1/d}}\left[\frac{\sqrt{\pi}\,\Gamma\big(\frac{d+1}{2d}\big)}{\Gamma\big(\frac{1}{2d}\big)} + \frac{\cos\alpha}{d}\;{}_2F_1\bigg(\frac{d-1}{2d}\,,\frac{1}{2}\,;\frac{3}{2}\,;(\cos\alpha)^2\bigg)\right] \,=\, -\,z_*\cot\alpha \tag{A.2.9}$$

which leads to the following relation

$$z_* \,=\, \frac{(\sin\alpha)^{1/d}}{\mathfrak{g}_d(\alpha)}\;\ell \tag{A.2.10}$$

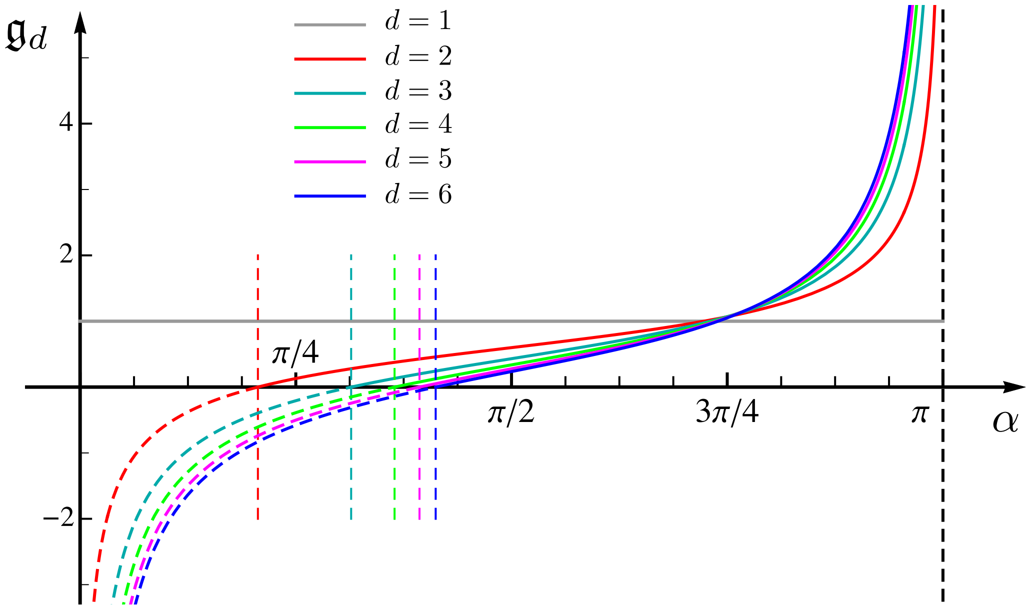

Figure A.1: The function $\mathfrak{g}_d(\alpha)$ defined in (A.2.11) for some values of d. For a given d, the critical value $\alpha_c(d)$ is the unique zero of $\mathfrak{g}_d(\alpha)$ (see (A.2.13)) and it has been highlighted through a vertical dashed segment having the same colour of the corresponding curve $\mathfrak{g}_d(\alpha)$.

where we have introduced

$$\mathfrak{g}_d(\alpha) \equiv \frac{\sqrt{\pi}\,\Gamma\left(\frac{d+1}{2d}\right)}{\Gamma\left(\frac{1}{2d}\right)} + \frac{\cos\alpha}{d}\,{}_2F_1\left(\frac{d-1}{2d}\,,\frac{1}{2}\,;\frac{3}{2}\,;(\cos\alpha)^2\right) - (\sin\alpha)^{1/d}\cot\alpha. \tag{A.2.11}$$

We remark that $z_* > 0$, therefore (A.2.10) is well defined only when $\mathfrak{g}_d(\alpha) > 0$, being $\alpha \in (0,\pi)$. For $d=2$, which is the case considered through the main text, the function (A.2.11) becomes the function $\mathfrak{g}(\alpha) \equiv \mathfrak{g}_2(\alpha)$ in (2.2.2).

The first derivative of $\mathfrak{g}_d(\alpha)$ with respect to α is very simple

$$\partial_\alpha\,\mathfrak{g}_d(\alpha) = \left(1-\frac{1}{d}\right)(\sin\alpha)^{1/d-2}. \tag{A.2.12}$$

This expression tells us that $\mathfrak{g}_1(\alpha)$ is constant and, in particular, one finds $\mathfrak{g}_1(\alpha) = 1$ identically. When $d>1$, we have that $\mathfrak{g}'_d(\alpha) > 0$ for $\alpha \in (0,\pi)$. Moreover, $\mathfrak{g}_d(\alpha) = -1/\alpha^{1-1/d} + O(1)$ as $\alpha \to 0^+$ and $\mathfrak{g}_d(\alpha) = 1/(\pi-\alpha)^{1-1/d} + o(1)$ as $\alpha \to \pi^-$. These observations allow to conclude that (A.2.11) has a unique zero $\alpha = \alpha_c$ for $d>1$, namely

$$\mathfrak{g}_d(\alpha_c) = 0. \tag{A.2.13}$$

Since $z_* > 0$ in (A.2.10), the condition (A.2.13) defines a critical value $\alpha_c(d)$ for the slope of $\mathcal{Q}$. Indeed, (A.2.10) is well defined only for $\alpha \in (\alpha_c, \pi)$. Moreover, from (A.2.10) and (A.2.13) we have that $z_* \to +\infty$ when $\alpha \to \alpha_c^+$. These observations allow us to conclude that for $\alpha \in (0, \alpha_c]$ the solution which intersects orthogonally the half-hyperplane $\mathcal{Q}$ at a finite value of z_* does not exist; therefore $\hat{\gamma}_A$ is the vertical half-hyperplane $x = \ell$ in this range of α.

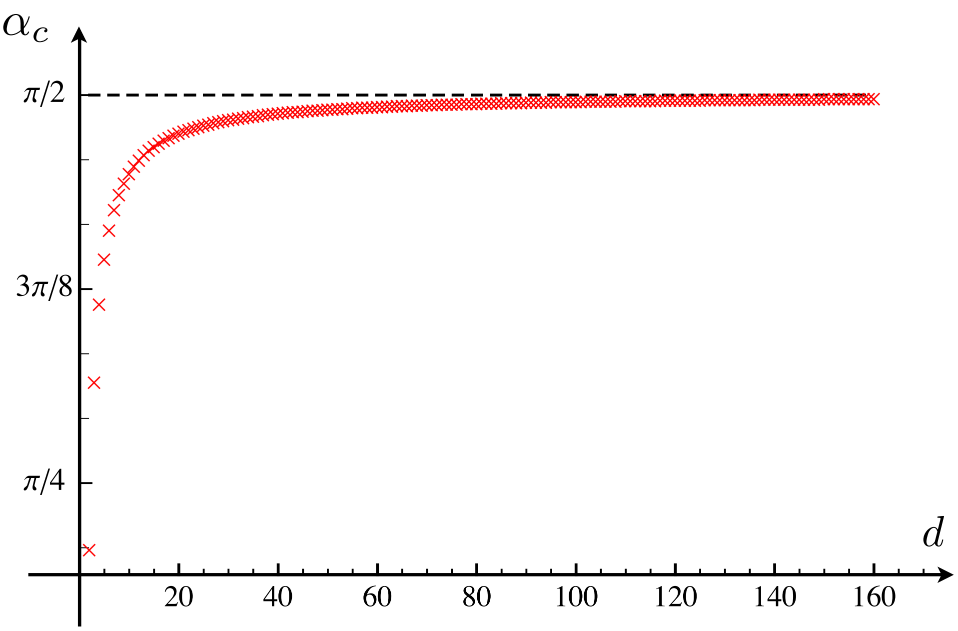

Figure A.2: The critical slope $\alpha_c(d)$ of the half-plane $\mathcal{Q}$ as function of the dimensionality parameter $d \geqslant 2$. These points have been found by solving (A.2.13). The value $\alpha_c(2)$ is given by (2.2.4). We find that $\alpha_c(d) \to \pi/2$ as $d \to +\infty$.

We remark that $\alpha_c \leqslant \pi/2$. Indeed, for $\alpha > \pi/2$ it is straightforward to observe that the vertical half-hyperplane $x = \ell$ is excluded because it does not intersect orthogonally the half-hyperplane $\mathcal{Q}$.

We find it worth considering the limit $d \to +\infty$ of (A.2.11). In this regime only the last term gives a non-vanishing contribution and, in particular, we have $\mathfrak{g}_d(\alpha) \to -\cot\alpha$, meaning that $\alpha_c(d) \to \pi/2$. Thus, α_c tends to its natural upper bound for large d.

In Fig. A.1 the function $\mathfrak{g}_d(\alpha)$ is shown for $1 \leqslant d \leqslant 6$. The corresponding critical values $\alpha_c(d)$ for $d \leqslant 2$ are highlighted through vertical dashed lines. The value of $\alpha_c(d = 3)$ has been found also in [159]. In Fig. A.2 we provide the critical slope $\alpha_c(d)$ as function of the dimensionality parameter d.

The profile $z(x)$ of the extremal solution intersecting $\mathcal{Q}$ orthogonally at a finite value z_* can be found by plugging (A.2.10) into (A.2.5) and (A.2.8). The result reads

$$\big(x(\theta)\,, z(\theta)\big) = \frac{\ell}{\mathfrak{g}_d(\alpha)} \left(\frac{\cos\theta}{d}\; {}_2F_1\!\left(\frac{d-1}{2d}\,, \frac{1}{2}\,; \frac{3}{2}\,; (\cos\theta)^2\right) - \frac{\sqrt{\pi}\,\Gamma\big(\frac{d+1}{2d}\big)}{\Gamma\big(\frac{1}{2d}\big)} + \mathfrak{g}_d(\alpha)\,,\; (\sin\theta)^{1/d} \right). \tag{A.2.14}$$

It is not difficult to check that this profile satisfies the required boundary conditions. Indeed for $\theta = 0$ and $\theta = \pi - \alpha$ we find $P_0 = (\ell, 0)$ and $P_* = z_*(-\cot\alpha\,, 1)$ respectively, being z_* given by (A.2.10). The expression of (A.2.14) specialised to $d = 2$ has been reported in (2.2.5).

An interesting point of the curve $z(x)$ is the one where $z'(x)$ vanishes. Denoting its coordinates by $P_{\max} = (x_{\max}, z_{\max})$, we have that $z'(x_{\max}) = 0$. From the latter condition and

(A.2.4) one finds a relation between $P_{\max}$ and P_* given by

$$z_{\max} = \frac{z_*}{(\sin\alpha)^{1/d}} = \frac{\ell}{\mathfrak{g}_d(\alpha)}. \tag{A.2.15}$$

The first equality can be obtained also from (A.2.5) for $\theta = \pi/2$, as remarked above, while in the last step (A.2.10) has been used. Notice that for $0 < \alpha < \pi/2$ we have that $z_{\max} > z_*$, being $\theta - \alpha \neq \pi/2$. Instead, $P_{\max} = P_*$ when $\alpha = \pi/2$, while $P_{\max}$ does not exist when $\alpha > \pi/2$. These features can be observed in Fig. 2.2 for the case $d = 2$.

In order to evaluate the area for $z \geqslant \varepsilon$ of the extremal surface characterised by the profile (A.2.14), let us compute the metric induced on this surface by the background metric of $\mathbb{H}_{d+1}$. By setting $t = \text{const}$ into (1.4.8) and employing the relation $x'(\theta)^2 = z'(\theta)^2(\tan\theta)^2$ derived above (see the text below (A.2.5)), we find that the induced metric reads

$$ds^2\big|_{\hat{\gamma}_A} = \frac{R^2_{\text{AdS}}}{z(\theta)^2}\left[\frac{z'(\theta)^2}{(\cos\theta)^2}\, d\theta^2 + d\vec{y}^{\,2}\right] \tag{A.2.16}$$

$$= \frac{R^2_{\text{AdS}}\,(\sin\alpha)^{2/d}}{z_*^2\,(\sin\theta)^{2/d}}\left[\frac{z_*^2}{d^2\,(\sin\alpha)^{2/d}\,(\sin\theta)^{2(1-1/d)}}\, d\theta^2 + d\vec{y}^{\,2}\right] \tag{A.2.17}$$

where $d\vec{y}^{\,2} = \sum_{j=1}^{d-1} dy_j^2$ and (A.2.5) have been used to obtain the last expression.

Let us focus on the cases with $d > 1$ first. From (A.2.17), for the area of $\hat{\gamma}_\varepsilon$ we find

$$\frac{\mathcal{A}[\hat{\gamma}_\varepsilon]}{L^d_{\text{AdS}}} = \frac{(\sin\alpha)^{1-1/d}}{d\, z_*^{d-1}} \int_0^{L_\parallel} dy_1 \dots dy_{d-1} \int_{\theta_\varepsilon}^{\pi-\alpha} \frac{d\theta}{(\sin\theta)^{2-1/d}} \tag{A.2.18}$$

$$= \frac{(\sin\alpha)^{1-1/d}}{d\, z_*^{d-1}}\, L_\parallel^{d-1}\left[{}_2F_1\!\left(\frac{3d-1}{2d}, \frac{1}{2}\,; \frac{3}{2}\,; (\cos\theta)^2\right)\cos\theta\,\right]\Bigg|_{\pi-\alpha}^{\theta_\varepsilon} \tag{A.2.19}$$

where the cutoff θ_ε is defined by imposing that $z(\theta_\varepsilon) = \varepsilon$, being $z(\theta)$ the expression in (A.2.5). This gives $\theta_\varepsilon = \arcsin(\varepsilon^d \sin\alpha / z_*^d)$.

Taking the limit $\varepsilon \to 0^+$ in (A.2.19) and neglecting terms which vanish in this limit, we find

$$\frac{\mathcal{A}[\hat{\gamma}_\varepsilon]}{L^d_{\text{AdS}}} = L_\parallel^{d-1}\left\{\frac{1}{(d-1)\,\varepsilon^{d-1}} - \frac{(\sin\alpha)^{1-1/d}}{z_*^{d-1}}\left[\frac{\sqrt{\pi}\,\Gamma\big(\frac{d+1}{2d}\big)}{(d-1)\,\Gamma\big(\frac{1}{2d}\big)} - \frac{\cos\alpha}{d}\; {}_2F_1\!\left(\frac{3d-1}{2d}, \frac{1}{2}\,; \frac{3}{2}\,; (\cos\alpha)^2\right)\right]\right\}. \tag{A.2.20}$$

We remark that the divergent part of the area $\mathcal{A}[\hat{\gamma}_\varepsilon]$ is due to the area term only.

The above analysis extends smoothly to the whole range of $\alpha \in (0, \pi)$ the results of [159] for the infinite strip adjacent to the boundary, which hold for $\alpha \in (0, \pi/2]$.

The finite term in (A.2.20) can be written in an insightful form by considering the following identity [276]

$$\big[(c-b)x - a\big]\; {}_2F_1(a+1, b\,; c+1\,; x) \;=\; (c-a)\; {}_2F_1(a, b\,; c+1\,; x) + c\,(x-1)\; {}_2F_1(a+1, b\,; c\,; x). \tag{A.2.21}$$

Specialising this identity to our case, we find

$$
{}_2F_1\!\left(\frac{3d-1}{2d}\,,\frac{1}{2}\,;\frac{3}{2}\,;(\cos\alpha)^2\right) \;=\; -\,\frac{1}{d-1}\left[\,{}_2F_1\!\left(\frac{d-1}{2d}\,,\frac{1}{2}\,;\frac{3}{2}\,;(\cos\alpha)^2\right) - d\,(\sin\alpha)^{1/d-1}\right]. \tag{A.2.22}
$$

By employing this result, it is straightforward to realise that the expression enclosed by the square brackets in (A.2.20) is $\mathfrak{g}_d(\alpha)/(d-1)$, being $\mathfrak{g}_d(\alpha)$ given by (A.2.11). This observation and (A.2.10) allow us to write (A.2.20) in terms of the width ℓ of the strip A as follows

$$
\frac{\mathcal{A}[\hat{\gamma}_\varepsilon]}{L_{\text{AdS}}^d} \;=\; \frac{L_\parallel^{d-1}}{d-1}\left(\frac{1}{\varepsilon^{d-1}} - \frac{\mathfrak{g}_d(\alpha)^d}{\ell^{d-1}} + O\big(\varepsilon^{d+1}\big)\right). \tag{A.2.23}
$$

The expression (2.2.6) in the main text corresponds to (A.2.23) specialised to $d = 2$.

The other extremal surface occurring in our analysis is the half-hyperplane defined by $x = \ell$. This can be observed by considering the extrinsic curvature of a half-hyperplane embedded in $\mathbb{H}_{d+1}$ whose normal vector has non-vanishing components only along z and x. Denoting by θ the angle between this normal vector and the positive x semi-axis, one finds $\mathrm{Tr}K \propto \cos\theta$ for the trace of the extrinsic curvature of the half-hyperplane. This implies that the vertical hyperplane, which has $\theta = 0$, is a local minimum for the area functional.

By also introducing an infrared cutoff z_{IR} beside the UV cutoff ε, it is straightforward to show that the portion of surface such that $\varepsilon \leqslant z \leqslant z_{\text{IR}}$ reads

$$
\frac{\mathcal{A}[\hat{\gamma}_\varepsilon]}{L_{\text{AdS}}^d} \;=\; \frac{L_\parallel^{d-1}}{d-1}\left(\frac{1}{\varepsilon^{d-1}} - \frac{1}{z_{\text{IR}}^{d-1}}\right). \tag{A.2.24}
$$

The divergent part of $\mathcal{A}[\hat{\gamma}_\varepsilon]$ is the same one occurring in (A.2.20), as expected. Let us stress that the finite term in (A.2.24) vanishes as $z_{\text{IR}} \to \infty$.

Summarising, for $\alpha \in (0, \alpha_c]$ the minimal surface $\hat{\gamma}_A$ is the vertical half-hyperplane $x = \ell$ because the surface characterised by (A.2.14) is not well defined. In the range $\alpha \in (\alpha_c, \pi/2]$ both the surface given by (A.2.14) and the vertical half-hyperplane $x = \ell$ are well defined extremal solutions of the area functional and, by comparing (A.2.23) with (A.2.24), we conclude that $\hat{\gamma}_A$ is the one characterised by (A.2.14). Instead, when $\alpha \in (\pi/2, \pi)$ the vertical half-hyperplane is not a solution anymore of our problem because it does not intersect $\mathcal{Q}$ orthogonally; therefore the minimal surface $\hat{\gamma}_A$ is again the surface corresponding to (A.2.14).

Putting these observations together, we find the following area for the restriction to $z \geqslant \varepsilon$ of the minimal surface corresponding to the strip adjacent to the boundary

$$
\frac{\mathcal{A}[\hat{\gamma}_\varepsilon]}{L_{\text{AdS}}^d} = L_\parallel^{d-1}\left[\frac{1}{(d-1)\,\varepsilon^{d-1}} + \frac{a_{0,d}(\alpha)}{(d-1)\,\ell^{d-1}} + o(1)\right] \tag{A.2.25}
$$

where

$$
a_{0,d}(\alpha) \equiv \begin{cases} -\,\mathfrak{g}_d(\alpha)^d & \alpha \geqslant \alpha_c(d) \\ \;0 & \alpha \leqslant \alpha_c(d) \end{cases}. \tag{A.2.26}
$$

Notice that $a_{0,d}(\alpha)$ and its first derivative are continuous functions of α. Also the higher order derivatives of $a_{0,d}(\alpha)$ are continuous until the d-th derivative of $a_{0,d}(\alpha)$, which is discontinuous at $\alpha = \alpha_c(d)$. In (2.2.7) we have specialised (A.2.25) and (A.2.26) to $d = 2$.

We find it interesting to discuss separately the $d = 1$ case. As already remarked below (A.2.11), in this case we have that $\mathfrak{g}_1(\alpha) = 1$ identically; therefore a critical value for α does not occur. Moreover, the profile (A.2.14) simplifies to $(x(\theta), z(\theta)) = \ell\,(\cos\theta\,, \sin\theta)$. This curve is an arc of circumference of radius ℓ; therefore it intersects orthogonally the half-line $\mathcal{Q}$ given by (1.4.9) which passes through the origin. We also have that $z_* = \ell\,\sin\alpha$, which corresponds to (A.2.10) for $d = 1$.

As for the length of this arc of circumference with opening angle $\pi - \alpha$ and for $z \geqslant \varepsilon$, it is straightforward to find that

$$\frac{\mathcal{A}[\hat{\gamma}_\varepsilon]}{L^d_{\text{AdS}}} = \int_{\theta_\varepsilon}^{\pi-\alpha} \frac{d\theta}{\sin\theta} = \log\left(\frac{\sin(\theta/2)}{\cos(\theta/2)}\right)\Bigg|_{\theta_\varepsilon}^{\pi-\alpha} = \log(\ell/\varepsilon) + \log\big(2\cot(\alpha/2)\big) + O(\varepsilon^2) \tag{A.2.27}$$

where the angular cutoff θ_ε is defined by requiring that $\varepsilon = \ell\sin\theta_\varepsilon$. As for the extremal curve given by the half-line $x = \ell$, by introducing the IR cutoff z_{IR}, for the length of the part of this straight line such that $\varepsilon \leqslant z \leqslant z_{\text{IR}}$ we find

$$\frac{\mathcal{A}[\hat{\gamma}_\varepsilon]}{L^d_{\text{AdS}}} = \log(\ell/\varepsilon) + \log(z_{\text{IR}}/\ell) \tag{A.2.28}$$

where the term $\log(z_{\text{IR}}/\ell)$ diverges when $z_{\text{IR}}/\ell \to +\infty$. Thus the minimal curve is always given by the arc of circumference. This is consistent with the observation that a critical slope does not occur when $d = 1$.

A.2.2 Infinite strip parallel to the boundary in generic dimension

In this appendix, we consider a strip A parallel to the boundary $x = 0$ and at a finite distance from it. Let us denote by ℓ_A the width of the strip and by d_A its distance from the boundary (see Fig. 2.4). We will focus on spacetimes having $d > 1$. For the case $d = 1$ we refer the reader to [159].

The main feature of the holographic entanglement entropy corresponding to this simple domain is the fact that two qualitatively different hypersurfaces are local extrema of the area functional; therefore, the minimum between them must be found. We recall that the case $d = 1$ has been discussed in Sec. 1.4.3.

One of these candidates is the minimal area surface in AdS_{d+2} corresponding to the infinite strip found in [31, 32] (see the blue solid curve in Fig. 2.4). Let us denote this hypersurface by $\hat{\gamma}_A^{\text{dis}}$, being disconnected from $\mathcal{Q}$. The second candidate $\hat{\gamma}_A^{\text{con}}$ is made by the union of two disjoint hypersurfaces. When $\alpha \leqslant \alpha_c$, we have that $\hat{\gamma}_A^{\text{con}}$ is the union of the vertical half-hyperplanes defined by $x = d_A$ and $x = d_A + \ell_A$. Instead, for $\alpha > \alpha_c$ the hypersurface $\hat{\gamma}_A^{\text{con}}$ is made by two disjoint hypersurfaces characterised by the profile (A.2.14) which depart from the edges of A and intersect $\mathcal{Q}$ orthogonally (see the green solid curves in Fig. 2.4 for a case with $\alpha > \alpha_c$).

Taking the part $z \geqslant \varepsilon$ of $\hat{\gamma}_A^{\text{dis}}$ and $\hat{\gamma}_A^{\text{con}}$, and evaluating the corresponding area as $\varepsilon \to 0^+$, one finds that the area law term is the same; therefore we have to compare the $O(1)$ terms to find $\hat{\gamma}_A$. By employing (A.2.25) and the well known result for the holographic entanglement entropy of the infinite strip in AdS_{d+2} [31, 32], one finds that the expansion of the area of $\hat{\gamma}_\varepsilon$ as $\varepsilon \to 0^+$ reads

$$\frac{\mathcal{A}[\hat{\gamma}_\varepsilon]}{L_{\mathrm{AdS}}^d} = \frac{L_\parallel^{d-1}}{d-1}\left(\frac{2}{\varepsilon^{d-1}} + \frac{1}{\ell_A^{d-1}}\min\left[h_d\,,\, a_{0,d}(\alpha)\left(\frac{1}{\delta_A^{d-1}} + \frac{1}{(\delta_A+1)^{d-1}}\right)\right] + o(1)\right). \tag{A.2.29}$$

The function $a_{0,d}(\alpha)$ has been introduced in (A.2.26), while the constant h_d is defined as [31, 32]

$$h_d \equiv -\,2^d \pi^{d/2}\left(\frac{\Gamma\big(\frac{d+1}{2d}\big)}{\Gamma\big(\frac{1}{2d}\big)}\right)^d. \tag{A.2.30}$$

The first term in the argument of the minimisation function occurring in the r.h.s. of (A.2.29) corresponds to $\hat{\gamma}_A^{\text{dis}}$, while the second one comes from $\hat{\gamma}_A^{\text{con}}$. Thus, $\hat{\gamma}_A = \hat{\gamma}_A^{\text{dis}}$ when $\delta_A \equiv d_A/\ell_A$ is large enough, while $\hat{\gamma}_A = \hat{\gamma}_A^{\text{con}}$ if the strip is close enough to the boundary. We remark that (A.2.29) holds for $\alpha \in (0,\pi)$. Notice that, when $\alpha \leqslant \alpha_c$, being $h_d < 0$ and $a_{0,d}(\alpha) = 0$, we have that $\hat{\gamma}_A = \hat{\gamma}_A^{\text{dis}}$.

The critical configurations correspond to the cases where the two terms occurring in the minimisation function of the $O(1)$ term of (A.2.29) are equal. The value $\delta_{A,c}$ of the ratio δ_A for these configurations can be found as a solution of the following equation

$$\delta_{A,c}^{d-1}\,(\delta_{A,c}+1)^{d-1} = \tilde{a}_{0,d}(\alpha)\Big[(\delta_{A,c}+1)^{d-1} + \delta_{A,c}^{d-1}\Big] \qquad \tilde{a}_{0,d}(\alpha) \equiv \frac{a_{0,d}(\alpha)}{h_d}. \tag{A.2.31}$$

We remark that $\tilde{a}_{0,d}$ is a positive and non-vanishing function of the slope α when $\alpha \in (\alpha_c, \pi)$, while $\tilde{a}_{0,d}(\alpha) = 0$ when $\alpha \in (0, \alpha_c]$. This implies that a strictly positive solution of (A.2.31) does not exist when $\alpha \leqslant \alpha_c$, as expected from the fact that $\hat{\gamma}_A = \hat{\gamma}_A^{\text{dis}}$. Instead, for $\alpha > \alpha_c$ we can show that $\delta_{A,c}$ always exists and it is also unique.

The equation (A.2.31) can be written as $p(\delta_{A,c}) = 0$, where the real polynomial $p(\delta_{A,c})$ in powers of $\delta_{A,c}$ schematically reads

$$p(\delta_{A,c}) = \delta_{A,c}^{2(d-1)} + (d-1)\delta_{A,c}^{2d-3} + \dots + \big[1 - 2\tilde{a}_{0,d}(\alpha)\big]\delta_{A,c}^{d-1} - \tilde{a}_{0,d}(\alpha)(d-1)\delta_{A,c}^{d-2} - \dots - \tilde{a}_{0,d}(\alpha). \tag{A.2.32}$$

The maximum number of positive roots of (A.2.32) can be determined by employing the Descartes' rule of signs. This rule states that the maximum number of positive roots of a real polynomial is bounded by the number of sign differences between consecutive nonzero coefficients of its powers, once they are set in decreasing order (the powers which do not occur must be just omitted). Since $\tilde{a}_{0,d}(\alpha) > 0$, the expression (A.2.32) shows that this number is equal to one in our case; therefore we have at most one positive real root. Its existence is guaranteed by the fact that $p(0) = -\,\tilde{a}_{0,d}(\alpha) < 0$ and $p(\delta) \to +\infty$ as $\delta \to +\infty$.

Since $\hat{\gamma}_A = \hat{\gamma}_A^{\text{dis}}$ when $\alpha \leqslant \alpha_c$, as remarked above, the critical configurations exist only for $\alpha \in (\alpha_c, \pi)$. Focussing on this range, an analytic expression for $\delta_{A,c}(\alpha)$ in terms of $\tilde{a}_{0,d}$ for a generic dimension d cannot be found. However, we find it instructive to determine it explicitly for $d = 2$ and $d = 3$ because (A.2.31) can be solved in closed form for these cases.

When $d = 2$ it is straightforward to obtain the result (2.2.9) reported in the main text. For $d = 3$ the algebraic equation (A.2.31) has degree four. A shift of the variable allows to

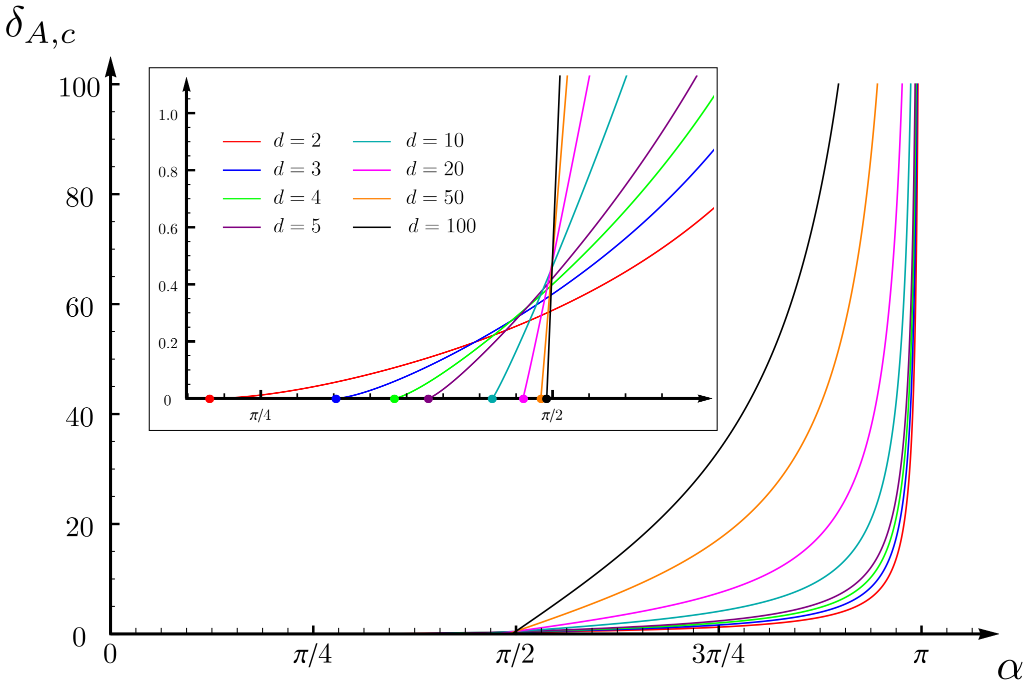

Figure A.3: Infinite strip of width ℓ_A parallel to the boundary at finite distance d_A from it: The ratio $\delta_A = d_A/\ell_A$ corresponding to the critical configurations in terms of $\alpha \in [\alpha_c, \pi)$ for some values of d. The curves are obtained by finding the unique positive root of (A.2.31). For $d = 2$ and $d = 3$ the expression of $\delta_{A,c}$ has been written analytically in (2.2.9) and (A.2.34) respectively, while for $d \geqslant 4$ the curves have been found by solving (A.2.31) numerically.

write it as follows

$$u^4 - \frac{4\,\tilde{a}_{0,3}(\alpha) + 1}{2}\,u^2 + \frac{1 - 8\,\tilde{a}_{0,3}(\alpha)}{16} = 0 \qquad \delta_{A,c} = u - \frac{1}{2} \tag{A.2.33}$$

which is a biquadratic equation. Its unique positive root reads

$$\delta_{A,c} = \frac{1}{2}\left(\sqrt{4\tilde{a}_{0,3}(\alpha) + 4\sqrt{\tilde{a}_{0,3}(\alpha)\big[\tilde{a}_{0,3}(\alpha) + 1\big]} + 1} - 1\right). \tag{A.2.34}$$

For $d \geqslant 4$ the root of (A.2.31) can be found numerically and the results for some values of d are shown in Fig. A.3, where the curves are defined for $\alpha > \alpha_c$ (see the inset, which contains a zoom of the main plot for small values of $\delta_{A,c}$).

A.3 On the disk concentric to a circular boundary

In this appendix, we provide some technical details underlying the derivation of the results reported in Sec. 2.3.1. Considering the setup introduced in Sec. 1.4.2, we are interested in the extremal surfaces anchored to the boundary of a disk A with radius $R_\circ$ concentric to the disk of radius $R_{\mathcal{Q}} > R_\circ$, which corresponds to a spatial slice of the spacetime where the BCFT$_3$ is defined. In the following we will adapt to this case the analysis reported in Appendix D.2

of [245] about the extremal surfaces anchored to the boundary of an annulus in $\text{AdS}_4/\text{CFT}_3$ (see also [243]).

A.3.1 Extremal surfaces

The invariance under rotations about the vertical axis z of this configuration significantly simplifies the analysis of the corresponding extremal surfaces. Indeed, by introducing the polar coordinates (ρ, ϕ) in the $z = 0$ plane, an extremal surface is determined by the curve $z = z(\rho)$ obtained by taking its section at a fixed angle ϕ. The area functional evaluated on these surfaces becomes

$$\mathcal{A} \,=\, 2\pi R_{\text{AdS}}^2 \int d\rho\, \rho\, \frac{\sqrt{z'^2+1}}{z^2}. \tag{A.3.1}$$

The equation of motion coming from the extremization of this functional reads

$$z\, z'' + \big(1+z'^2\big)\left(2+\frac{z\, z'}{\rho}\right) = 0. \tag{A.3.2}$$

By introducing the variable u and the function $\hat{z}(\rho)$ as follows

$$z(\rho) = \rho\, \hat{z}(\rho) \qquad u = \log \rho \qquad \hat{z}_u = \partial_u \hat{z} \tag{A.3.3}$$

the differential equation (A.3.2) becomes

$$\hat{z}\, \hat{z}_u (1+\partial_{\hat{z}} \hat{z}_u) + \big[1+(\hat{z}+\hat{z}_u)^2\big]\big[2+\hat{z}(\hat{z}+\hat{z}_u)\big] \,=\, 0. \tag{A.3.4}$$

Integrating this equation, one finds

$$\hat{z}_{u,\pm} = -\frac{1+\hat{z}^2}{\hat{z}}\left[1 \pm \frac{\hat{z}}{\sqrt{k(1+\hat{z}^2)-\hat{z}^4}}\right]^{-1} \qquad k>0 \tag{A.3.5}$$

where k is the integration constant. By employing that $du = d\hat{z}/\hat{z}_u$ and integrating (A.3.5) starting from an arbitrary initial point, we get

$$\log(\rho/\rho_{\text{in}}) = \int_{u_{\text{in}}}^{u} d\tilde{u} \,=\, -\int_{\hat{z}_{\text{in}}}^{\hat{z}} \frac{\lambda}{1+\lambda^2}\left[1 \pm \frac{\lambda}{\sqrt{k(1+\lambda^2)-\lambda^4}}\right] d\lambda. \tag{A.3.6}$$

Since the extremal surfaces are anchored to the boundary of the disk A of radius $R_\circ$ at $z=0$, from (A.3.3) we have $\hat{z}(R_\circ) = 0$ and $u = \log R_\circ$ when $\rho = R_\circ$. Choosing $\rho_{\text{in}} = R_\circ$ and the negative sign within the integrand in (A.3.6), one finds the first equation in the r.h.s. of (2.3.1), namely

$$\log(\rho/R_\circ) \,=\, -\,q_{-,k}(\hat{z}) \tag{A.3.7}$$

where $q_{-,k}(\hat{z})$ has been defined in (2.3.2). The choice of the negative sign in (A.3.7) will be discussed at the end of this subsection.

The solution (A.3.7) is well defined as long as the expression under the square root of (A.3.6) is positive. Such expression vanishes at the point $P_m = (\rho_m, \hat{z}_m)$, whose coordinates have been reported in (2.3.3). Following the curve given by (A.3.7) starting from $(\rho, z) = (R_\circ, 0)$, if it intersects $\mathcal{Q}$ before reaching P_m, then (A.3.7) fully describes the profile of $\hat{\gamma}_A^{\text{con}}$.

Otherwise, (A.3.7) provides the profile of $\hat{\gamma}_A^{\text{con}}$ until P_m and for the part between P_m and the point $P_* = (\rho_*, \hat{z}_*)$ (which fully characterises the curve $\partial\hat{\gamma}_{\mathcal{Q}} = \hat{\gamma}_A \cap \mathcal{Q}$ in this case) also the function defined by (A.3.6) with the positive sign must be employed. In particular, the profile between P_m and P_* reads

$$\log(\rho/R_\circ) \,=\, -\, q_{+,k}(\hat{z}) + q_{+,k}(\hat{z}_m) - q_{-,k}(\hat{z}_m) \tag{A.3.8}$$

which can also be written in the form given by the second expression in the r.h.s. of (2.3.1), once (2.3.4) has been used.

In order to justify (2.3.3) for the coordinates of P_m, let us consider the unit vectors $v_\pm^\mu$ tangent to the radial profile of $\hat{\gamma}_A^{\text{con}}$ along the two branches characterised by $q_{\pm,k}$. They read

$$v_\pm^\mu = \big(v_\pm^\rho, v_\pm^z, v_\pm^\phi\big) = \frac{\pm\, z}{\sqrt{(q'_{\pm,k})^2 + (1-\hat{z}\, q'_{\pm,k})^2}}\,\big(\, q'_{\pm,k}\,,\, \hat{z}\, q'_{\pm,k} - 1\,, 0\,\big) \tag{A.3.9}$$

where ± refers to the two different branches. At the matching point P_m, the tangent vector field defined by $v_\pm^\mu$ must be continuous, hence a necessary condition is that $g_{\mu\nu}\, v_+^\mu v_-^\nu = 1$ at P_m. From (A.3.9), one finds that this requirement gives $\hat{z}^4 = k(1+\hat{z}^2)$, whose only admissible solution is the first expression in (2.3.3).

The boundary condition along the curve $\partial\hat{\gamma}_{\mathcal{Q}} = \hat{\gamma}_A \cap \mathcal{Q}$ provides the parameter k. The condition to impose is that $\hat{\gamma}_A^{\text{con}}$ and $\mathcal{Q}$ intersects orthogonally along $\partial\hat{\gamma}_{\mathcal{Q}}$. This requirement is equivalent to impose that the vector v_μ tangent to $\hat{\gamma}_A^{\text{con}}$ and the vector u_μ tangent to $\mathcal{Q}$ are orthogonal along $\partial\hat{\gamma}_{\mathcal{Q}}$. From (1.4.11), we find

$$u^\mu = (u^\rho, u^z, u^\phi) = (\cot\alpha - \rho\, \hat{z}/R_{\mathcal{Q}}\,, \rho/R_{\mathcal{Q}}\,, 0)\,. \tag{A.3.10}$$

By using (A.3.9) and (A.3.10), we find that the orthogonality condition $v^\rho u^\rho + v^z u^z = 0$ at the intersection between $\hat{\gamma}_A^{\text{con}}$ and $\mathcal{Q}$ gives

$$q'_{\pm,k}(\rho_*) = \frac{\rho_*}{R_Q}\tan\alpha \tag{A.3.11}$$

where $q'_{\pm,k}$ can be read from (2.3.2) and $\rho_*/R_{\mathcal{Q}}$ can be obtained by specializing (1.4.12) to P_*. This leads to

$$\frac{\sqrt{\hat{z}_*^2 + \sin^2\alpha}}{\cos\alpha} = \pm\,\frac{\hat{z}_*^2}{\sqrt{k(1+\hat{z}_*^2) - \hat{z}_*^4}} \tag{A.3.12}$$

that allows us to write $\hat{z}_*$ as a function of k and α. Indeed, the first expression of (2.3.7) can be found by taking the square of (A.3.12). The ± in the r.h.s. of (A.3.12) correspond to the same choice of sign occurring in (A.3.11). From (A.3.12) and $\hat{z}_* \geqslant 0$, one observes that the orthogonality condition can be satisfied only by $q_{+,k}$ when $\alpha \leqslant \pi/2$, while for $\alpha \geqslant \pi/2$ the orthogonality condition leads to select $q_{-,k}$. Consequently, P_* belongs to the branch described $q_{-,k}$ for $\alpha \leqslant \pi/2$ and to the one characterised by $q_{+,k}$ for $\alpha \geqslant \pi/2$. When $\alpha \to \pi/2$ the l.h.s. of (A.3.12) diverges; therefore the argument of the square root in the r.h.s. must vanish in this limit. This means that $\hat{z}_* = \hat{z}_m$, being $\hat{z}_m$ given in (2.3.3). Thus, when $\alpha = \pi/2$, the extremal surface $\hat{\gamma}_A^{\text{con}}$ intersects $\mathcal{Q}$ at the matching point P_m of the two branches characterised by $q_{\pm,k}$.

In order to justify the choice of $q_{-,k}$ in (A.3.7), in the following we show that a contradiction is obtained if $q_{+,k}$ is assumed in (A.3.7) instead of $q_{-,k}$. In this case, the profile of $\hat{\gamma}_A$ can be obtained from (2.3.1) simply by exchanging the role of $R_\circ$ and R_{aux}, i.e.

$$\rho_\gamma(\theta) = \begin{cases} R_\circ \, e^{-q_{+,k}(\hat{z})} \\ R_{\text{aux}} \, e^{-q_{-,k}(\hat{z})} \end{cases} \tag{A.3.13}$$

where now $R_\mathcal{Q} > R_\circ > R_{\text{aux}}$. First, let us notice that the maximum value of $z(\hat{z})$ is realized in the $q_{+,k}$ branch because from (A.3.9) we have that $v_\pm^z = 0$ only for the $q_{+,k}$ branch (at $\hat{z} = \sqrt[4]{k}$). Since $R_\mathcal{Q} > R_\circ > R_{\text{aux}}$, this observation leads to conclude that $\mathcal{Q}$ cannot intersect the $q_{-,k}$ branch without intersecting the one described by $q_{+,k}$ (see e.g. the red and the black curves in the top panel of Fig. 2.8 as guidance). Thus, the only possibility is that $\mathcal{Q}$ intersects orthogonally the branch described by $q_{+,k}$. In this case, the condition (A.3.12) leads to $\alpha \leqslant \pi/2$. In order to find a contradiction, let us compare the quantity $\rho^2 + z^2$ for the branch $q_{+,k}$ with the one for $\mathcal{Q}$. For $\mathcal{Q}$ in the range $\alpha \leqslant \pi/2$ we get

$$\rho^2 + z^2 = R_\mathcal{Q}^2 (1+\hat{z}^2) Q_\alpha^2 = R_\mathcal{Q}^2 \frac{\left(\sqrt{\hat{z}^2(\csc\alpha)^2 + 1} + \hat{z}\cot\alpha\right)^2}{\hat{z}^2+1} \geqslant R_\mathcal{Q}^2 \tag{A.3.14}$$

being Q_α the function introduced in (1.4.12). As for the $q_{+,k}$ branch, from (A.3.13) and (A.3.3) we get $\rho_\gamma^2 + z^2 = (1+\hat{z}^2)\rho_\gamma^2 = R_\circ^2 \, e^{-2f_{+,k}}$ where $f_{+,k} \equiv q_{+,k} - \log\sqrt{1+\hat{z}^2}$ (see (2.3.5)). Since $f_{+,k} > 0$ for any $\hat{z}$ and $R_\circ > R_\mathcal{Q}$, we have $\rho_\gamma^2 + z^2 < R_\mathcal{Q}^2$. This means that the branch described by $q_{+,k}$ cannot intersect $\mathcal{Q}$ in the whole range $\alpha \leqslant \pi/2$, ruling out the possibility that $\hat{\gamma}_A$ is described by the profile (A.3.13).

A.3.2 Area

In this appendix we evaluate the area of $\hat{\gamma}_A^{\text{con}}$ in two ways: by a direct computation of the integral (A.3.1) and by specialising the general formula (2.1.24) to the extremal surfaces $\hat{\gamma}_A^{\text{con}}$.

The analysis performed in Sec. A.3.1 allows to write the area of $\hat{\gamma}_A^{\text{con}}$ from (A.3.1) and (A.3.3) as follows

$$\mathcal{A} = \begin{cases} 2\pi R_{\text{AdS}}^2 \left(\displaystyle\int_{\varepsilon/R_\circ}^{\hat{z}_m} \frac{d\hat{z}}{\hat{z}^2\sqrt{1+\hat{z}^2-\hat{z}^4/k}} + \int_{\hat{z}_*}^{\hat{z}_m} \frac{d\hat{z}}{\hat{z}^2\sqrt{1+\hat{z}^2-\hat{z}^4/k}} \right) & 0 < \alpha \leqslant \pi/2 \\ 2\pi R_{\text{AdS}}^2 \displaystyle\int_{\varepsilon/R_\circ}^{\hat{z}_*} \frac{d\hat{z}}{\hat{z}^2\sqrt{1+\hat{z}^2-\hat{z}^4/k}} & \pi/2 \leqslant \alpha < \pi \end{cases} \tag{A.3.15}$$

where the UV cutoff ε has been introduced to regularise $\mathcal{A}$, which is a divergent quantity as $\varepsilon \to 0$. Le us recall that $\hat{z}_* = \hat{z}_m$ for $\alpha = \pi/2$. The integrals in (A.3.15) can be explicitly written by using that

$$\int \frac{d\hat{z}}{\hat{z}^2\sqrt{1+\hat{z}^2-\hat{z}^4/k}} = -\mathcal{F}_k(\hat{z}) + \text{const} \tag{A.3.16}$$

where $\mathcal{F}_k(\hat{z})$ has been introduced in (2.3.14). The expression (2.3.13) for F_{con} can be found from (A.3.15) by employing the expansions of $\mathcal{F}_k(\hat{z})$ as $\hat{z} \to 0^+$, which reads

$$\mathcal{F}_k(\hat{z}) = \frac{1}{\hat{z}} + \frac{\hat{z}}{2} + O\left(\hat{z}^3\right). \tag{A.3.17}$$

In the remaining part of this appendix, we show that the analytic expression for F_{con} given in (2.3.13) can also be obtained by applying the general formula (2.1.24) in the special cases of the extremal surfaces $\hat{\gamma}_A^{\text{con}}$.

In order to evaluate the surface integral over $\hat{\gamma}_A$ in (2.1.24), we need the normal vector $\tilde{n}_\mu$ and the area element $d\tilde{\mathcal{A}}$, which are given respectively by

$$\tilde{n}^\mu = (n^\rho, n^z, n^\phi) = \frac{1}{\sqrt{1+z'^2}}\,\big(z', -1, 0\big) \qquad d\tilde{\mathcal{A}} \,=\, \sqrt{z'^2+1}\,\rho\, d\rho\, d\phi. \tag{A.3.18}$$

The evaluation of the surface integral over $\hat{\gamma}_A$ in (2.1.24) can be performed by using (A.3.3) and (A.3.18), finding

$$\int \frac{(\tilde{n}^z)^2}{z^2}\, d\tilde{\mathcal{A}} \,=\, \begin{cases} 2\pi\Big(\mathcal{F}_{k,-}(\hat{z}_m) + \mathcal{F}_{k,+}(\hat{z}_m) - \mathcal{F}_{k,+}(\hat{z}_*)\Big) & 0 < \alpha \leqslant \pi/2 \\[2ex] 2\pi\, \mathcal{F}_{k,-}(\hat{z}_*) & \pi/2 \leqslant \alpha < \pi \end{cases} \tag{A.3.19}$$

(which can be written as reported in (2.3.18)) where we have introduced the following functions

$$\mathcal{F}_{k,\pm}(\hat{z}) \equiv \frac{1}{\sqrt{k}} \int_0^{\hat{z}} \frac{\big(\sqrt{k(1+\xi^2)-\xi^4} \pm \xi\big)^2}{(\xi^2+1)^2\,\sqrt{k(1+\xi^2)-\xi^4}}\, d\xi \tag{A.3.20}$$

which can be written in terms of $\mathcal{F}_k(\hat{z})$ (see (2.3.19)). The relation (2.3.19) has been found by integrating the following identity

$$\frac{\big(\sqrt{k\,(\hat{z}^2+1)-\hat{z}^4} \pm \hat{z}\big)^2}{\sqrt{k}\,(\hat{z}^2+1)^2\,\sqrt{k\,(\hat{z}^2+1)-\hat{z}^4}} + \frac{1}{\sqrt{k}}\,\frac{\partial}{\partial\hat{z}}\left(\frac{\sqrt{k\,(\hat{z}^2+1)-\hat{z}^4} \pm \hat{z}}{\hat{z}(\hat{z}^2+1)}\right) = -\,\frac{1}{\hat{z}^2\sqrt{\hat{z}^2+1-\hat{z}^4/k}}. \tag{A.3.21}$$

The result of this indefinite integration contains an arbitrary integration constant which can be fixed by taking $\hat{z} \to 0$ and imposing that both sides of the equation are consistent in this limit (also (A.3.17) is useful in this computation).

In order to facilitate the recovering of the expression (2.3.13) for F_{con}, let us observe that, by employing (2.3.19), the expression (2.3.18) can be written as follows

$$\int_{\hat{\gamma}} \frac{(\tilde{n}^z)^2}{z^2}\, d\tilde{\mathcal{A}} \,=\, F_{\text{con}} - 2\pi\,\frac{\hat{z}_*^3 + \eta_\alpha\sqrt{k\,(\hat{z}_*^2+1)-\hat{z}_*^4}}{\sqrt{k}\,\hat{z}_*(\hat{z}_*^2+1)} \,=\, F_{\text{con}} - 2\pi\,\frac{\hat{z}_*^3 - \sqrt{k}\,\cos\alpha}{\sqrt{k}\,\hat{z}_*(\hat{z}_*^2+1)} \tag{A.3.22}$$

where in the last step we used the identity $\sqrt{k\,(\hat{z}_*^2+1)-\hat{z}_*^4} \,=\, -\sqrt{k}\,\eta_\alpha\cos\alpha$, which comes from the explicit form of $\hat{z}_*$ given in the first expression of (2.3.7).

As for the boundary term in (2.1.24), the vector $\tilde{b}^\mu$ can be obtained from the vector which is tangent to $\mathcal{Q}$ given in (A.3.10), finding

$$\tilde{b}^\mu = \big(\,\tilde{b}^\rho, \tilde{b}^z, \tilde{b}^\phi\,\big) = \left(\sqrt{1-\left(\frac{\rho_*}{R_{\mathcal{Q}}}\hat{z}_*\sin\alpha - \cos\alpha\right)^2}\,,\, \frac{\rho_*}{R_{\mathcal{Q}}}\,\hat{z}_*\sin\alpha - \cos\alpha\,,0\right) \tag{A.3.23}$$

that coincides with (A.3.9) evaluated at P_*. From the component $\tilde{b}^z$ in (A.3.23) and the fact that $d\tilde{s} = \rho_* d\phi$ along $\partial\hat{\gamma}_{\mathcal{Q}}$, we find that the boundary contribution in (2.1.24) becomes

$$\int_{\partial\hat{\gamma}_{\mathcal{Q}}} \frac{\tilde{b}^z}{z}\, d\tilde{s} \,=\, 2\pi\,\frac{\tilde{b}^z}{\hat{z}_*} \,=\, 2\pi\left(\frac{\rho_*}{R_{\mathcal{Q}}}\sin\alpha - \frac{\cos\alpha}{\hat{z}_*}\right) \tag{A.3.24}$$

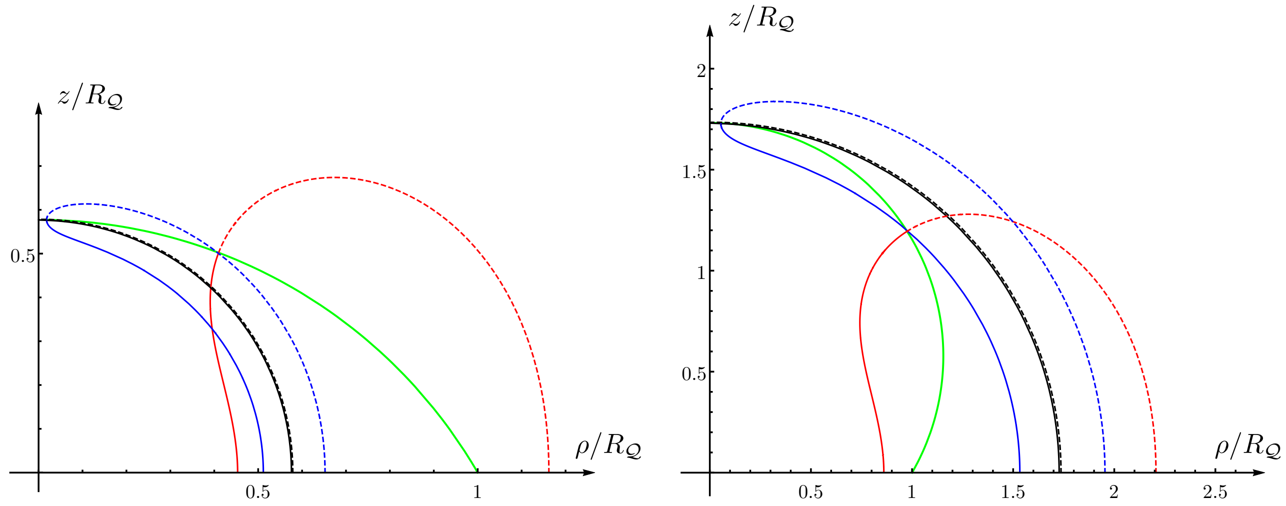

Figure A.4: Radial profiles of extremal surfaces $\hat{\gamma}_A^{\text{con}}$ intersecting $\mathcal{Q}$ (green curve) orthogonally and anchored to a disk A of radius $R_\circ$ concentric to a circular boundary with radius $R_{\mathcal{Q}}$ (see Sec. 2.3.1). Here $\alpha = 2\pi/3$ (left panel) and $\alpha = \pi/3$ (right panel). Any solid line provides $\hat{\gamma}_A^{\text{con}}$ and the dashed line with the same colour gives the radial profile of the corresponding auxiliary surface $\hat{\gamma}_{A,\,\text{aux}}^{\text{con}}$. Here the values of k associated to $\hat{\gamma}_A^{\text{con}}$ (see Fig. 2.7) are $k = 1$ (red), $k = 1000$ (blue) and $k = 10^7$ (black). For large k, both $\hat{\gamma}_A^{\text{con}}$ and the corresponding $\hat{\gamma}_{A,\,\text{aux}}^{\text{con}}$ tend to the hemisphere with radius $\cot(\alpha/2)$, which is tangent to $\mathcal{Q}$ at $\rho = 0$.

which reduces to (2.3.20), once the second expression of (2.3.7) has been employed. Then, plugging (A.3.22) and (2.3.20) into (2.1.24), one obtains

$$F_A \,=\, F_{\text{con}} - 2\pi\,\frac{\hat{z}_*^2 - \sqrt{k\big[\hat{z}_*^2 + (\sin\alpha)^2\big]}}{\sqrt{k}\,(\hat{z}_*^2 + 1)} \tag{A.3.25}$$

where, by using (A.3.12) and the identity given in the text below (A.3.22), it is straightforward to observe that the numerator in the r.h.s. vanishes.

A.3.3 Limiting regimes

In the remaining part of this appendix we provide some technical details about the limiting regimes $k \to 0$ and $k \to \infty$ of the analytic expressions for $R_\circ/R_{\mathcal{Q}}$ and F_{con} (see (2.3.9) and (2.3.13) respectively). The results of this analysis have been reported in (2.3.10), (2.3.11) and (2.3.16).

As for the ratio $R_\circ/R_{\mathcal{Q}}$, whose analytic expression is (2.3.9) with $\chi(\hat{z}_m)$ given by (2.3.4), we have to study $q_{\pm,k}(\hat{z}_*)$ and $q_{\pm,k}(\hat{z}_m)$ in these limiting regimes.

In order to find $q_{\pm,k}(\hat{z}_*)$ for $k \to 0$, let us write $q_{\pm,k}(\hat{z}_*)$ from the integral (2.3.2) evaluated for $\hat{z} = \hat{z}_*$ (see (2.3.7)) and adopt $\hat{z}_*\lambda$ as integration variable because it leads us to a definite integral whose extrema are 0 and 1. By first expanding the integrand of the resulting formula and then integrating the terms of the expansion separately, we find

$$q_{\pm,k}(\hat{z}_*) \,=\, \pm\Big[\mathbb{E}\big(\arcsin(\sqrt{\sin\alpha}\,)\big|-1\big) - \mathbb{F}\big(\arcsin(\sqrt{\sin\alpha}\,)\big|-1\big)\Big]\sqrt[4]{k} + \frac{\sin\alpha}{2}\,\sqrt{k} + O\big(k^{3/4}\big). \tag{A.3.26}$$

Adapting this analysis to $q_{\pm,k}(\hat{z}_m)$, we obtain

$$q_{\pm,k}(\hat{z}_m) \;=\; \pm\Big(\mathbb{E}(-1)-\mathbb{K}(-1)\Big)\sqrt[4]{k}+\frac{\sqrt{k}}{2}+\mathcal{O}(k^{3/4}). \tag{A.3.27}$$

By employing the expansions (A.3.26) and (A.3.27) into (2.3.4) and (2.3.9), one gets the result (2.3.10).

As for the $k\to\infty$ regime, for the integrals (2.3.2) we have

$$q_{\pm,k}(\hat{z}) = \frac{1}{2}\log(1+\hat{z}^2)+\mathcal{O}\big(1/\sqrt{k}\,\big). \tag{A.3.28}$$

Moreover, from (2.3.3) and (2.3.7) notice that both $\hat{z}_*$ and $\hat{z}_m$ diverge, with $\hat{z}_*/\hat{z}_m\to 1$. Thus, being $\hat{z}=z/\rho$ with finite z for the surfaces that we are considering, we have that $\rho_*\to 0$ and $\rho_m\to 0$. These observations tell us that, in the regime of large k, the two branches in (2.3.1) become the same arc of circle from $\rho = R_\circ$ to $\rho = 0$ (see the black curves in Fig. A.4). In particular, we have $R_{\textrm{aux}}\to R_\circ$. By taking the limit of (1.4.12) for large $\hat{z}$ and employing the identity $\cot\alpha+\csc\alpha=\cot(\alpha/2)$, one finds that $P_* = P_m = R_{\mathcal{Q}}(0,\cot(\alpha/2))$ in this regime. Then, being the limiting curve a circle of radius $R_\circ$, we have that $R_{\mathcal{Q}}\cot(\alpha/2) = R_\circ$. The latter relation provides (2.3.11), which is the asymptotic behaviour of the curves in Fig. 2.7. In Fig. A.4 we show some examples of extremal surfaces (which are not necessarily the global minimum of the area) as k increases for two fixed values of α, highlighting the limit of large k, which corresponds to the black curves.

In order to study the subleading term of area of the extremal surfaces as $k\to 0$ or $k\to\infty$, we find it convenient to employ the expressions (2.1.24), (2.3.18) and (2.3.20). Indeed, since $\mathcal{F}_{k,\pm}(\hat{z}_*)$ and $\mathcal{F}_{k,\pm}(\hat{z}_m)$ can be written through the integral representation (A.3.20) of the functions $\mathcal{F}_{k,\pm}(\hat{z})$, we can adapt the above analysis to this case (e.g. for $\mathcal{F}_{k,\pm}(\hat{z}_*)$ one first introduces $\hat{z}_*\xi$ as integration variable, obtaining a definite integral between 0 and 1, then expands the integrand of the resulting expression and finally integrates the various terms of the expansion), finding

$$\begin{aligned}\mathcal{F}_{k,\pm}(\hat{z}_*) \;=\; & \frac{1}{\sqrt[4]{k}}\Big[\mathbb{E}\big(\arcsin(\sqrt{\sin\alpha}\,)\big|-1\big)-\mathbb{F}\big(\arcsin(\sqrt{\sin\alpha}\,)\big|-1\big)\Big]\pm\sin\alpha\\ &+\bigg(\frac{1}{4}\,\mathbb{F}\big(\arcsin(\sqrt{\sin\alpha}\,)\big|-1\big)-\eta_\alpha\cos\alpha\,\sqrt{\sin\alpha}\,\bigg)\sqrt[4]{k}+\mathcal{O}\big(\sqrt{k}\,\big)\end{aligned} \tag{A.3.29}$$

and

$$\mathcal{F}_{k,\pm}(\hat{z}_m) \;=\; \frac{\mathbb{E}(-1)-\mathbb{K}(-1)}{\sqrt[4]{k}}\pm 1+\frac{\mathbb{K}(-1)}{4}\,\sqrt[4]{k}+\mathcal{O}(\sqrt{k}). \tag{A.3.30}$$

By using these expansions into (2.3.18), together with (2.3.20) into (2.1.24), the expansion (2.3.16) is obtained.

The asymptotic value 2π for large k in Fig. 2.9 can be found by employing that the profile of $\hat{\gamma}_A^{\textrm{con}}$ in this regime is the one of the hemisphere in $\mathbb{H}_3$ anchored to $R_\circ$ (see also the Appendix D in [245]). Since the finite term of the area for the hemisphere in $\mathbb{H}_3$ is 2π, we can easily conclude that the curves in Fig. 2.9 tend to this value as $k\to\infty$.

A.4 Auxiliary surfaces

In this appendix, we discuss a way to relate an extremal surface $\hat{\gamma}_A$ anchored to the entangling curve of a region A in AdS$_4$/BCFT$_3$ to an extremal surface in AdS$_4$/CFT$_3$ anchored to a corresponding entangling curve in $\mathbb{R}^2$, which is the spatial slice of the CFT$_3$, being the gravitational background the one obtained by removing $\mathcal{Q}$. We will discuss only the simplest cases where a spatial section of the gravitational spacetimes is given by $\mathbb{H}_3$ or part of it.

In AdS$_{d+2}$/BCFT$_{d+1}$ setups of Sec. 1.4.1 and Sec. 1.4.2, if the extremal surface $\hat{\gamma}_A$ does not intersect the boundary $\mathcal{Q}$, then it can be also seen as an extremal surface in $\mathbb{H}_{d+1}$. Instead, when $\hat{\gamma}_A$ intersects orthogonally $\mathcal{Q}$ along some curve $\partial\hat{\gamma}_{\mathcal{Q}}$ (since we mainly consider extremal surfaces intersecting $\mathcal{Q}$ orthogonally, in this appendix we denote by $\hat{\gamma}_A$ the surfaces $\hat{\gamma}_A^{\text{con}}$ of Sec. 2.3.1), we can consider the unique auxiliary surface $\hat{\gamma}_{A,\,\text{aux}}$ such that $\hat{\gamma}_A \cup \hat{\gamma}_{A,\,\text{aux}}$ is an extremal surface in $\mathbb{H}_{d+1}$ and $\hat{\gamma}_{A,\,\text{aux}}$ is orthogonal to $\mathcal{Q}$ along $\partial\hat{\gamma}_{\mathcal{Q}}$. The extremal surface $\hat{\gamma}_A \cup \hat{\gamma}_{A,\,\text{aux}}$ in $\mathbb{H}_{d+1}$ is anchored to $\partial A_{\,\text{aux}}$ of some auxiliary region $A_{\,\text{aux}}$ in the plane $\mathbb{R}^d$ at $z = 0$.

As first example, let us consider the infinite strip A of width ℓ adjacent to the flat boundary discussed in Sec. 2.2.1. The minimal surface $\hat{\gamma}_A$ characterised by the profile (A.2.14) is part of an auxiliary surface $\hat{\gamma}_{A,\text{aux}}$ which has minimal area in the hyperbolic space $\mathbb{H}_{d+1} = \text{AdS}_{d+2}\big|_{t\,=\,\text{const}}$ and which is anchored to an infinite strip $A_{\,\text{aux}}$ of width ℓ_{aux} belonging to the boundary $z = 0$ of $\mathbb{H}_{d+1}$. The auxiliary infinite strip $A_{\,\text{aux}}$ includes A and it shares with A the edge at $x = \ell$. The minimal surface $\hat{\gamma}_{A,\text{aux}}$ has been computed in [31, 32], and their result can be recovered from the more general expression (1.5.18) by setting $\theta = 0$. Then, by imposing that (A.2.15) is also the largest value assumed by the coordinate z for the points of $\hat{\gamma}_{A,\text{aux}}$, we find that

$$\ell_{\text{aux}} = 2\,\frac{\sqrt{\pi}\,\Gamma(\frac{d+1}{2d})}{\Gamma(\frac{1}{2d})\,\mathfrak{g}_d(\alpha)}\,\ell \tag{A.4.1}$$

where $\mathfrak{g}_d(\alpha)$ has been defined in (A.2.11). In particular, ℓ_{aux} depends on α. As consistency check of (A.4.1), we observe that $\ell_{\text{aux}} = \ell - x(\pi)$, where $x(\theta)$ has been written in (A.2.14). We remark that the strip A is not necessarily a subset of the $A_{\,\text{aux}}$. Indeed, for $\alpha \leqslant \alpha_{c,\,\text{aux}}$ we have that $A \subseteq A_{\,\text{aux}}$, while $A_{\,\text{aux}} \subseteq A$ when $\alpha \geqslant \alpha_{c,\,\text{aux}}$. The value of $\alpha_{c,\,\text{aux}}$ is defined by imposing that $\ell_{\text{aux}} = \ell$, which gives $\mathfrak{g}_d(\alpha_{c,\,\text{aux}}) = 2\sqrt{\pi}\,\Gamma(\frac{d+1}{2d})/\Gamma(\frac{1}{2d})$. From the latter result and (A.2.11), for $\alpha \in (0,\pi)$ we have

$$\mathfrak{g}(\pi-\alpha) \;=\; \mathfrak{g}(\alpha_{c,\,\text{aux}}) - \mathfrak{g}(\alpha). \tag{A.4.2}$$

By specifying this relation to $\alpha = \alpha_c$, the critical value of α defined as the zero of $\mathfrak{g}_d(\alpha)$, one finds that $\alpha_{c,\,\text{aux}} = \pi - \alpha_c$.

Regarding the strip parallel to the boundary studied in Sec. 2.2.2, the auxiliary domain $A_{\,\text{aux}} = A \cup A'$ in $\mathbb{R}^d$ is made by two parallel and disjoint infinite strips and the corresponding minimal surface in $\hat{\gamma}_{A,\text{aux}} \subset \mathbb{H}_{d+1}$ has been studied e.g. in [142]. Denoting by ℓ' the width of A' and by d_{aux} the separation between A and A', from Fig. 2.4 and (A.4.1) it is not difficult to realise that

$$\ell' = 2\,\frac{\sqrt{\pi}\,\Gamma(\frac{d+1}{2d})}{\Gamma(\frac{1}{2d})\,\mathfrak{g}_d(\alpha)}\,\ell_A \qquad\qquad d_{\text{aux}} = 2\,\frac{\sqrt{\pi}\,\Gamma(\frac{d+1}{2d})}{\Gamma(\frac{1}{2d})\,\mathfrak{g}_d(\alpha)}\,d_A. \tag{A.4.3}$$

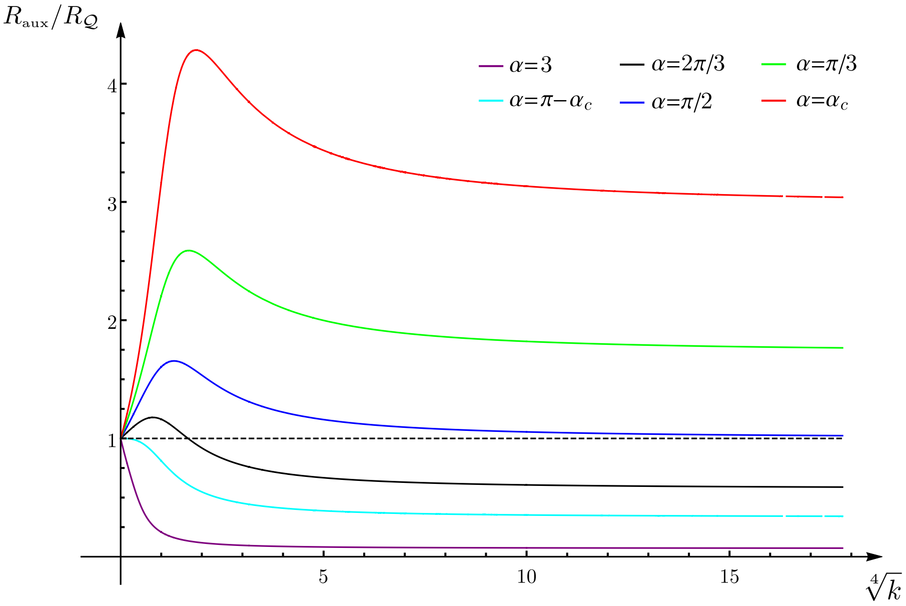

Figure A.5: The ratio $R_{\rm aux}/R_{\mathcal{Q}}$ for a disk A concentric to a circular boundary of radius $R_{\mathcal{Q}}$ (see Sec. 2.3.1 and Appendix A.4) in terms of the parameter k, obtained by combining (2.3.4) and (2.3.9). For $\alpha \geqslant \pi - \alpha_c$ we have that $R_{\rm aux} \leqslant R_{\mathcal{Q}}$, therefore part of $\hat{\gamma}_{A,\,\rm aux}$ belongs to the gravitational spacetime bounded by $\mathcal{Q}$.

Another interesting configuration is given by a disk A disjoint from the boundary which is either flat or circular (see Sec. 2.3). In these cases the extremal surfaces $\hat{\gamma}_{A,\,\rm aux} \cup \hat{\gamma}_A$ are anchored to a pair of circles and they have been studied in [241–245] for the gravitational background given by $\mathbb{H}_3$. In the setup of Sec. 1.4.2, considering a disk A of radius $R_\circ$ concentric to a circular boundary of radius $R_{\mathcal{Q}}$ as in Sec. 2.3.1, we have that $\hat{\gamma}_A \cup \hat{\gamma}_{A,\,\rm aux}$ is an extremal surface in $\mathbb{H}_3$ anchored to the boundary of an annulus characterised by the radii $R_\circ$ and $R_{\rm aux} > R_\circ$ (see also (2.3.1)). The ratio $R_\circ/R_{\rm aux}$ is given by (2.3.4).

Partitioning $\mathbb{H}_3$ into the part $\mathcal{C}_3$, introduced in Sec. 2.1, and its complement $\overline{\mathcal{C}}_3$, we have that part of $\hat{\gamma}_{A,\,\rm aux}$ belongs to $\overline{\mathcal{C}}_3$ because $\hat{\gamma}_{A,\,\rm aux} \perp \mathcal{Q}$ along $\partial\hat{\gamma}_{\mathcal{Q}}$. It can happen that the intersection between $\hat{\gamma}_{A,\,\rm aux}$ and $\mathcal{C}_3$ is non-trivial (see e.g. the right panel in Fig. 2.12). In Fig. A.5 we show the ratio $R_{\rm aux}/R_{\mathcal{Q}}$ as function of k for some values of α. Let us introduce the critical value $\alpha_{c,\,\rm aux}$ such that $R_{\rm aux}/R_{\mathcal{Q}} < 1$ for every k at fixed $\alpha > \alpha_{c,\,\rm aux}$. For this configuration we observe numerically that $\alpha_{c,\,\rm aux} = \pi - \alpha_c$, namely, the same relation found above for the strip adjacent to the flat boundary. Three qualitatively different situations are observed (see Fig. A.5): when $\alpha \leqslant \pi/2$ we have $R_{\rm aux} > R_{\mathcal{Q}}$ and $\hat{\gamma}_{A,\,\rm aux} \cap \mathcal{C}_3 = \emptyset$, for $\pi/2 \leqslant \alpha \leqslant \pi - \alpha_c$ it is possible that $\hat{\gamma}_{A,\,\rm aux} \cap \mathcal{C}_3 \neq \emptyset$, while when $\alpha \geqslant \pi - \alpha_c$ we have that some part of $\hat{\gamma}_{A,\,\rm aux}$ always belongs to $\mathcal{C}_3$ because $R_{\rm aux} < R_{\mathcal{Q}}$.

By employing the map (A.1.3), analogous considerations can be done for the extremal surfaces anchored to a disk A disjoint from a flat boundary, considered in Sec. 2.3.2. The extremal surface is anchored to a pair of circles in $\mathbb{R}^2$ and one of them is ∂A. For this configuration explicit examples are given in Fig. 2.12 and Fig. 2.13, where $\hat{\gamma}_{A,\,\rm aux}$ are the shaded surfaces.

Appendix **B**

Appendix of Chapter 3

B.1 On the half-disk

In this appendix, we report the computation of the area $\mathcal{A}[\hat{\gamma}_\varepsilon]$, which provides the holographic entanglement entropy of half-disk of radius R centered on the boundary, according to the prescription (1.3.2). The main result derived here is (3.2.1), which is discussed in Sec. 3.2.1.

Given the half-disk $A = \{(x,y) \in \mathbb{R}^2 \,|\, x^2 + y^2 \leqslant R^2,\, x \geqslant 0\}$, which is centered on the boundary $x = 0$, the entangling curve $\partial A \cap \partial B$ is $\{(x,y) \in \mathbb{R}^2 \,|\, x^2 + y^2 = R^2,\, x \geqslant 0\}$. In Sec. 3.2.1 we have discussed for this domain $\hat{\gamma}_{A,\text{aux}}$ is the hemisphere $x^2 + y^2 + z^2 = R^2$ in $\mathbb{H}_3$ and that $\hat{\gamma}_A$ is just the part of $\hat{\gamma}_{A,\text{aux}}$ identified by the constraint $x \geqslant -(\cot\alpha)z$. In Fig. 3.3, the minimal surface $\hat{\gamma}_A$ is shown in a case having $\alpha < \pi/2$ and in a case where $\alpha > \pi/2$.

The holographic entanglement entropy is obtained by evaluating the area $\mathcal{A}[\hat{\gamma}_\varepsilon]$ of the surface $\hat{\gamma}_A \cap \{z \geqslant \varepsilon\}$, which is the part of $\hat{\gamma}_A$ above the yellow line in Fig. 3.3. This area can be written as follows

$$\frac{\mathcal{A}[\hat{\gamma}_\varepsilon]}{R^2_{\text{AdS}}} = \begin{cases} \mathcal{A}_\perp + \mathcal{A}_\angle & 0 < \alpha \leqslant \pi/2 \\ \mathcal{A}_\perp - \mathcal{A}_\angle & \pi/2 \leqslant \alpha < \pi \end{cases} \tag{B.1.1}$$

where $\mathcal{A}_\perp$ is the area of the half-hemisphere restricted to $z \geqslant \varepsilon$ with $x \geqslant 0$ and $\mathcal{A}_\angle \geqslant 0$ is the area of the part of the hemisphere restricted to $z \geqslant \varepsilon$ enclosed between the vertical half-plane $x = 0$ and the half-plane $\mathcal{Q}$. Notice that, in the right panel of Fig. 3.3, the area $\mathcal{A}_\angle$ corresponds to the shaded part of $\hat{\gamma}_{A,\text{aux}}$.

The area $\mathcal{A}_\perp$ can be easily computed by adopting the usual spherical coordinates (θ,ϕ), where $\theta = 0$ is the positive z semi-axis and $\phi = 0$ is the positive y semi-axis. The change of coordinates between these polar coordinates and the Cartesian coordinates reads

$$z = R\,\cos\theta \qquad x = R\,\sin\theta\,\sin\phi \qquad y = R\,\sin\theta\,\cos\phi. \tag{B.1.2}$$

In terms of the polar coordinates (θ,ϕ), the induced metric on $\hat{\gamma}_A$ from $\mathbb{H}_3$ is given by

$$ds^2\big|_{\hat{\gamma}_A} = \frac{R^2_{\text{AdS}}}{(\cos\theta)^2}\big(d\theta^2 + (\sin\theta)^2 d\phi^2\big). \tag{B.1.3}$$

By employing this metric, for $\mathcal{A}_\perp$ we find

$$\mathcal{A}_\perp = \int_0^{\theta_\varepsilon} d\theta \int_0^{\pi} d\phi \, \frac{\sin\theta}{(\cos\theta)^2} = \frac{\pi}{\cos\theta}\bigg|_0^{\theta_\varepsilon} = \frac{\pi R}{\varepsilon} - \pi \tag{B.1.4}$$

where the condition defining θ_ε is $\varepsilon = R\cos\theta_\varepsilon$.

In order to compute $\mathcal{A}_\angle$, let us parameterise the hemisphere by employing spherical coordinates (θ,ϕ), where $\theta = 0$ is the positive y semi-axis and $\phi = 0$ is the positive z semi-axis. Now from the change of coordinates (3.2.22), we obtain $\varepsilon = R\sin\theta_\varepsilon\cos\phi$, which relates the UV cutoff ε to the cutoff θ_ε of the angular variable. This relation leads to $\sin(\theta_\varepsilon/2) = \varepsilon[1+O(\varepsilon^2)]/(2R\cos\phi)$.

When $\alpha \in (0,\pi/2)$, the area $\mathcal{A}_\angle$ is given by the following integral

$$\begin{aligned}
\mathcal{A}_\angle &= 2\int_0^{\pi/2-\alpha} d\phi \int_{\theta_\varepsilon}^{\pi/2} d\theta\, \frac{1}{(\cos\phi)^2\sin\theta} \;=\; -2\int_0^{\pi/2-\alpha} d\phi\, \frac{\log(\tan\theta_\varepsilon/2)}{(\cos\phi)^2} \\
&= 2\int_0^{\pi/2-\alpha} d\phi\, \frac{\frac{1}{2}\log(1-[\sin(\theta_\varepsilon/2)]^2) - \log[\sin(\theta_\varepsilon/2)]}{(\cos\phi)^2} \\
&= 2\int_0^{\pi/2-\alpha} d\phi\, \frac{1}{(\cos\phi)^2}\left(\frac{1}{2}\log\left(1-\varepsilon^2/[2R\cos\phi]^2\right) - \log(\varepsilon/R) + \log(2\cos\phi)\right) + O(\varepsilon^2) \\
&= 2(\cot\alpha)\log(R/\varepsilon) + O(1)
\end{aligned} \tag{B.1.5}$$

where in (B.1.5) the relation between θ_ε and ε has been employed, and the $O(\varepsilon^2)$ terms have been neglected. The $O(1)$ term in (B.1.5) can be found explicitly, but we do not report it here because we are interested only in the logarithmic divergence. When $\alpha \in (\pi/2,\pi)$, being $\mathcal{A}_\angle > 0$, the resulting integral for $\mathcal{A}_\angle$ is like (B.1.5), except for the domain of integration for the integral in ϕ, which is $(0, \alpha - \pi/2)$.

Summarising, the term $\mathcal{A}_\angle$ provides the following logarithmic divergence

$$\mathcal{A}_\angle = \begin{cases} 2(\cot\alpha)\log(R/\varepsilon) + O(1) & 0 < \alpha \leqslant \pi/2 \\ -2(\cot\alpha)\log(R/\varepsilon) + O(1) & \pi/2 \leqslant \alpha < \pi \end{cases}. \tag{B.1.6}$$

Finally, by plugging (B.1.4) and (B.1.6) into (B.1.1), we obtain the area $\mathcal{A}[\hat{\gamma}_\varepsilon]$ given by (3.2.1), which is the main result of this appendix.

Let us stress that the holographic entanglement entropy for this domain provides the corner function $F_\alpha(\pi/2)$ for the special value $\gamma = \pi/2$ and for any $\alpha \in (0,\pi)$. This is an important benchmark for the analytic expression of the corner function $F_\alpha(\gamma)$ presented in Sec. 3.2.2, whose derivation is described in the appendix B.2.

B.2 On the infinite wedge adjacent to the boundary

In this appendix, we provide the technical details underlying the computation of the holographic entanglement entropy of the infinite wedge A adjacent to the boundary. The main results have been collected and discussed in Sec. 3.2.2.

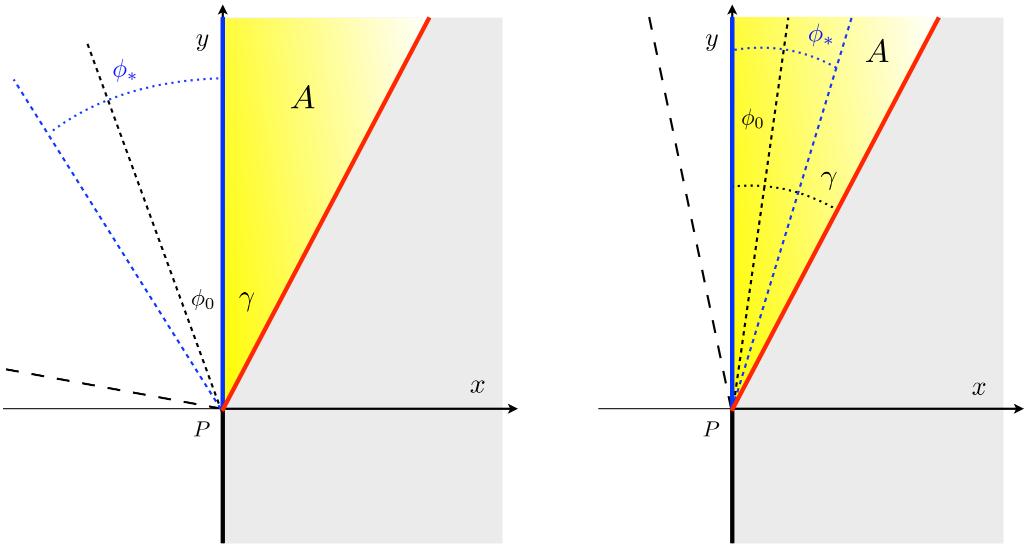

Figure B.1: The opening angles occurring in the construction of the minimal surface $\hat{\gamma}_A$ anchored to the infinite wedge A adjacent to the boundary with opening angle γ, which has been discussed in Sec. 3.2.2 and in the appendix B.2. In the left panel $\alpha \in (0, \pi/2]$ and in the right panel $\alpha \in [\pi/2, \pi)$. The wedge A is the yellow region, whose edges are the red and the solid blue half-lines, given by $\phi = \gamma$ and $\phi = 0$ respectively. The auxiliary wedge A_{aux} is the infinite wedge in $\mathbb{R}^2$ containing A whose tip is P and whose edges are the red half-line and the black dashed line with the largest dashing. The black dashed line with the smallest dashing at $\phi = \phi_0$ corresponds to the bisector of A_{aux}. The blue dashed half-line at $\phi = \phi_*$ corresponds to the projection of $\hat{\gamma}_A \cap \mathcal{Q}$ in the $z = 0$ plane.

In the half-plane $\{(x, y) \in \mathbb{R}^2\,,\, x \geqslant 0\}$, let us introduce the polar coordinates (ρ, ϕ) such that $\phi = 0$ is the half-line given by $x = 0$ and $y > 0$, namely

$$x = \rho\, \sin\phi \qquad y = \rho\, \cos\phi. \tag{B.2.1}$$

In terms of these coordinates, the infinite wedge A having one of its two edges on the boundary $x = 0$ can be described without loss of generality as follows

$$A = \big\{(\rho, \phi)\,|\, 0 \leqslant \phi \leqslant \gamma\,,\, \rho \leqslant L\big\} \qquad L \gg \varepsilon. \tag{B.2.2}$$

In order to study the holographic entanglement entropy of the infinite wedge A within the AdS$_4$/BCFT$_3$ setup described in Sec. 1.4.3, let us consider the surfaces anchored to the edge $\{(\rho, \phi)\,|\, \phi = \gamma\}$ of A and embedded in the region of $\mathbb{H}_3$ restricted by $x \geqslant -(\cot\alpha) z$. The symmetry under dilatations tells us that $\hat{\gamma}_A$ belongs to the class of surfaces γ_A described by (3.2.3) with $q(\phi) > 0$. The metric induced on γ_A from $\mathbb{H}_3$ reads

$$ds^2\big|_{\gamma_A} = R^2_{\text{AdS}} \left(\frac{1+q^2}{\rho^2}\, d\rho^2 - \frac{2\, q'}{\rho\, q}\, d\rho\, d\phi + \frac{(q')^2 + q^4}{q^2}\, d\phi^2 \right). \tag{B.2.3}$$

Our analysis heavily relies on [157], where the authors have found the minimal area surface in $\mathbb{H}_3$ anchored to both the edges of an infinite wedge. Indeed, we study $\hat{\gamma}_A$ by introducing an auxiliary wedge A_{aux} in the $z = 0$ boundary of $\mathbb{H}_3$ such that $A \subsetneq A_{\text{aux}}$ and $\{(\rho, \phi)\,|\, \phi = \gamma\}$ is a common edge of both A and A_{aux}. Considering the minimal area surface $\hat{\gamma}_{A,\text{aux}}$ in $\mathbb{H}_3$ anchored to the edges of A_{aux}, the minimal area surface $\hat{\gamma}_A$ anchored to the edge $\{(\rho,\phi)\,|\,\phi=\gamma\}$ of A and intersecting $\mathcal{Q}$ orthogonally is the part of $\hat{\gamma}_{A,\text{aux}}$ identified by the constraint $x \geqslant -(\cot\alpha)z$. Thus, finding $\hat{\gamma}_A$ corresponds to find the proper $\hat{\gamma}_{A,\text{aux}}$.

In Fig. B.1 we show the relevant angles occurring in our construction, by distinguishing the two cases of $\alpha \in (0,\pi/2]$ (left panel) and $\alpha \in [\pi/2,\pi)$ (right panel). The infinite wedge A adjacent to the boundary $x=0$ is the yellow region, which is embedded into the grey half-plane $x \geqslant 0$. The edges of the auxiliary wedge A_{aux} are the red half-line $\{(\rho,\phi)\,|\,\phi=\gamma\}$ and the half-line denoted by the large black dashing. The bisector of A_{aux} is the black dashed half-line at $\phi=\phi_0$; therefore the opening angle of A_{aux} is $2(\gamma-\phi_0)$. The half-line corresponding to the small black dashing is the bisector of the auxiliary wedge, while the blue dashed half-line is the projection on the $z=0$ plane of the half-line given by $\hat{\gamma}_A \cap \mathcal{Q}$.

B.2.1 Minimal surface condition

The metric (B.2.3) induced on the surfaces γ_A leads to the following area functional

$$\frac{\mathcal{A}[\gamma_A]}{R^2_{\text{AdS}}} = \int_{\gamma_A} \frac{1}{\rho}\sqrt{q'^2+q^2+q^4}\,d\phi\,d\rho = \int_{\gamma_A}\frac{1}{\rho}\,\mathcal{L}\,d\phi\,d\rho \qquad \mathcal{L}\equiv\sqrt{q'^2+q^2+q^4}. \tag{B.2.4}$$

The functions $q(\phi)$ characterising the extrema of this functional can be found by observing that its integrand is independent of ϕ. The first integral associated with this invariance provides a quantity which is independent of ϕ. It reads

$$\frac{\partial\mathcal{L}}{\partial q'}\,q' - \mathcal{L} \;\propto\; \frac{q^4+q^2}{\sqrt{(q')^2+q^4+q^2}}. \tag{B.2.5}$$

Let us introduce the angle ϕ_0 such that

$$q'(\phi_0)=0 \qquad q(\phi_0)\equiv q_0 \qquad q_0>0. \tag{B.2.6}$$

The angle ϕ_0 provides the bisector of the auxiliary wedge A_{aux}.

By employing (B.2.6) into the condition that (B.2.5) is independent of ϕ, one obtains the following first order differential equation

$$\frac{q^4+q^2}{\sqrt{(q')^2+q^4+q^2}} = \sqrt{q_0^4+q_0^2}. \tag{B.2.7}$$

Taking the square of this expression, one gets

$$\frac{(q')^2}{q^2} = (q^2+1)\left(\frac{q^4+q^2}{q_0^4+q_0^2}-1\right) \qquad q\geqslant q_0. \tag{B.2.8}$$

Separating the variables in (B.2.8), one finds $d\phi = \mathcal{P}_\phi(q,q_0)\,dq$. Then, by integrating the latter expression, we get

$$|\phi-\phi_0| = \int_{q_0}^{q}\mathcal{P}_\phi(\hat{q},q_0)\,d\hat{q} = P(q,q_0) \qquad \mathcal{P}_\phi(q,q_0)\equiv\frac{\sqrt{q_0^4+q_0^2}}{q\,\sqrt{(q^2+1)(q^2-q_0^2)(q^2+q_0^2+1)}} \tag{B.2.9}$$

where $q \geqslant q_0$ and $P(q, q_0)$ has been written in (3.2.8). From (B.2.9), it is straightforward to realise that $P(q_0, q_0) = 0$ and that the function $P(q, q_0) \geqslant 0$ is an increasing function of $q \geqslant q_0$. The minimal area surface $\hat{\gamma}_A$ is described by (3.2.3) with the proper $q(\phi)$ obtained by inverting (B.2.9).

The opening angle of the auxiliary wedge A_{aux} is $2(\gamma - \phi_0)$, as already observed above from Fig. B.1. This angle can be found from (B.2.9) as follows

$$\gamma - \phi_0 = \int_{\phi_0}^{\gamma} d\phi \;=\; \int_{q_0}^{\infty} \mathcal{P}_\phi(\tilde{q}, q_0)\, d\tilde{q} \;=\; \lim_{q \to +\infty} P(q, q_0) \;\equiv\; P_0(q_0). \tag{B.2.10}$$

Equivalent expressions of $P_0(q_0)$ have been reported in (1.3.28) and (3.2.10).

The next step of our analysis consists in studying the intersection $\hat{\gamma}_A \cap \mathcal{Q}$ and the opening angle of A_{aux}.

B.2.2 Intersection between the minimal surface and $\mathcal{Q}$

In order to find the extremal surface $\hat{\gamma}_A$ anchored to the edge $\{(\rho, \phi) \,|\, \phi = \gamma\}$ of A and ending on the half-plane $\mathcal{Q}$, beside the differential equation (B.2.7) we also have to impose that $\hat{\gamma}_A$ and $\mathcal{Q}$ intersect orthogonally.

By writing the equation (1.4.9) for $\mathcal{Q}$ in terms of the polar coordinates (B.2.1) and intersecting the resulting expression with the ansatz (3.2.3) for γ_A, we find

$$q_* \sin\phi_* = -\cot\alpha \qquad q_* \equiv q(\phi_*). \tag{B.2.11}$$

This relation defines the angle $\phi = \phi_*$ at which γ_A and $\mathcal{Q}$ intersect. Thus, $\gamma_A \cap \mathcal{Q}$ is the half-line whose points have coordinates $(z, \rho, \phi) = (\rho/q_*, \rho, \phi_*)$, with $\rho > 0$. Since $q_* > 0$, from (B.2.11) we have that $\phi_* \leqslant 0$ when $\alpha \in (0, \pi/2]$, and $\phi_* \geqslant 0$ when $\alpha \in [\pi/2, \pi)$. This is shown in Fig. B.1, where the blue dashed half-line corresponds to the projection of $\hat{\gamma}_A \cap \mathcal{Q}$ on the $z = 0$ plane. The relation (B.2.11) tells us that $\phi_* = 0$ when $\alpha = \pi/2$, as expected.

In order to impose that γ_A and $\mathcal{Q}$ intersect orthogonally along the half-line at $\phi = \phi_*$, we have to find the unit vector normal to γ_A and the unit vector normal to the $\mathcal{Q}$. The surfaces γ_A described by the ansatz (3.2.3) can be equivalently written as $\mathcal{C} = 0$, with $\mathcal{C} \equiv z - \rho/q(\phi)$. Thus, the unit vector normal to γ_A is

$$n_\mu = \frac{\partial_\mu \mathcal{C}}{\sqrt{g^{\alpha\beta}\, \partial_\alpha \mathcal{C}\, \partial_\beta \mathcal{C}}} \;=\; \frac{R_{\text{AdS}}}{z\,\sqrt{(q')^2 + q^4 + q^2}}\, \big(q^2\,, -q\,,\, \rho\, q'\big) \tag{B.2.12}$$

where the components of the vector have been ordered according to $\mu \in \{z, \rho, \phi\}$. As for the half-plane $\mathcal{Q}$, its definition in (1.4.9) can be written as $\mathcal{C}_{\mathcal{Q}} = 0$, with $\mathcal{C}_{\mathcal{Q}} \equiv z + \rho \sin\phi \tan\alpha$, where the first relation in (B.2.1) has been used. This tells us that the unit vector normal to the half-plane $\mathcal{Q}$ is

$$b_\mu = \frac{\partial_\mu \mathcal{C}_{\mathcal{Q}}}{\sqrt{g^{\alpha\beta}\, \partial_\alpha \mathcal{C}_{\mathcal{Q}}\, \partial_\beta \mathcal{C}_{\mathcal{Q}}}} = \frac{R_{\text{AdS}} \cos\alpha}{z}\, \big(1\,,\, \sin\phi \tan\alpha\,,\, \rho \cos\phi \tan\alpha\big). \tag{B.2.13}$$

Given the unit vectors (B.2.12) and (B.2.13), we have to impose that they are orthogonal (namely $g^{\mu\nu} n_\mu b_\nu = 0$) along the half-line $\gamma_A \cap \mathcal{Q}$ at $\phi = \phi_*$. This requirement leads to the following relation

$$q_*^2 + \left[\, q_*' \cos\phi_* - q_* \sin\phi_* \right] \tan\alpha = 0 \qquad q_*' \equiv q'(\phi_*) \tag{B.2.14}$$

which can be written also as

$$\frac{q_*'}{q_*} = \tan\phi_* - \frac{q_*}{\cos\phi_*} \cot\alpha. \tag{B.2.15}$$

Taking the square of (B.2.15) first and then employing (B.2.8) to write $(q_*'/q_*)^2$ in terms of q_* and q_0, we have

$$\left(\tan\phi_* - \frac{q_*}{\cos\phi_*} \cot\alpha\right)^2 = (q_*^2+1)\left(\frac{q_*^4+q_*^2}{q_0^4+q_0^2} - 1\right). \tag{B.2.16}$$

This expression can be simplified by using (B.2.11) to rewrite q_* in terms of ϕ_*, finding

$$(\tan\phi_*)^2 \left[\frac{(\cot\alpha)^2}{(\sin\phi_*)^2} + 1\right] = \frac{1}{q_0^4+q_0^2}\,\frac{(\cot\alpha)^2}{(\sin\phi_*)^2}\left[\frac{(\cot\alpha)^2}{(\sin\phi_*)^2} + 1\right] - 1. \tag{B.2.17}$$

This relation leads to the following biquadratic equation

$$q_0^4 + q_0^2 = \left[1 + \frac{(\cot\alpha)^2}{(\sin\phi_*)^2}\right] (\cos\alpha)^2\,(\cot\phi_*)^2 \tag{B.2.18}$$

which has only one positive root in terms of q_0^2. This solution allows us to write q_0 in terms of ϕ_* as follows

$$q_0 = \frac{1}{\sqrt{2}}\left(\sqrt{1 + 4\big[1 + (\cot\alpha)^2(\csc\phi_*)^2\big](\cos\alpha)^2\,(\cot\phi_*)^2} - 1\right)^{1/2}. \tag{B.2.19}$$

Instead of ϕ_*, we prefer to adopt q_0 as fundamental parameter; therefore let us consider the biquadratic equation in terms of $\sin\phi_*$ obtained from (B.2.18), namely

$$\left[1 + \frac{q_0^4+q_0^2}{(\cos\alpha)^2}\right](\sin\phi_*)^4 - \big[1 - (\cot\alpha)^2\big](\sin\phi_*)^2 - (\cot\alpha)^2 = 0 \tag{B.2.20}$$

whose positive solution for $(\sin\phi_*)^2 \equiv s_*(\alpha, q_0)^2$ reads

$$\begin{aligned} s_*(\alpha,q_0)^2 \;&= \\ &= \frac{1}{2}\left(1 + \frac{q_0^4+q_0^2}{(\cos\alpha)^2}\right)^{-1}\left[1 - (\cot\alpha)^2 + \sqrt{\big[1-(\cot\alpha)^2\big]^2 + 4\left(1 + \frac{q_0^4+q_0^2}{(\cos\alpha)^2}\right)(\cot\alpha)^2}\;\right]. \end{aligned} \tag{B.2.21}$$

Notice that $s_*(\pi-\alpha, q_0)^2 = s_*(\alpha, q_0)^2$. We denote by $s_*(\alpha, q_0) > 0$ the positive root of (B.2.21), which has been written explicitly in (3.2.4). Plugging $s_*(\alpha, q_0)$ into (B.2.11), one obtains (3.2.6).

Since $\phi_* \leqslant \phi_0 \leqslant 0$ when $\alpha \in (0, \pi/2]$, while $0 \leqslant \phi_0 \leqslant \phi_*$ when $\alpha \in [\pi/2, \pi)$ (see Fig. B.1), we find it convenient to introduce $\eta_\alpha \equiv -\,\mathrm{sign}(\cot\alpha)$, as done in (3.2.4). Then, the expression for $\phi_* = \phi_*(q_0, \alpha)$ in (3.2.5) can be written straightforwardly. Furthermore, (B.2.9) leads to

$$\big|\phi_* - \phi_0\big| = \int_{q_0}^{q_*} \mathcal{P}_\phi(q, q_0)\, dq = P(q_*, q_0) = \begin{cases} \phi_0 - \phi_* & 0 < \alpha \leqslant \pi/2 \\ \phi_* - \phi_0 & \pi/2 \leqslant \alpha < \pi \end{cases}. \tag{B.2.22}$$

This provides the angle $\phi_0 = \phi_0(q_0, \alpha)$ as follows

$$\phi_0 \,=\, \phi_*(q_0,\alpha) - \eta_\alpha \, P\big(q_*(\alpha,q_0),q_0\big) \,=\, \eta_\alpha\big(\arcsin[s_*(\alpha,q_0)] - P(q_*,q_0)\big) \tag{B.2.23}$$

where the last step has been obtained by using $\phi_*(q_0,\alpha)$ in (3.2.5). Notice that ϕ_0 characterises the opening angle of the auxiliary wedge $A_{\textrm{aux}}$.

Finally, an expression for the opening angle γ in terms of α and q_0 can be written. Indeed, from (B.2.10) one first finds that $\gamma = P_0(q_0) + \phi_0$; then (B.2.23) can be used to get (3.2.7).

Summarising, we have determined the angles ϕ_*, ϕ_0 and γ as functions of α and q_0. They are given in (3.2.5), (B.2.23) and (3.2.7) respectively.

B.2.3 Area of the minimal surface

The minimal surface $\hat{\gamma}_A$ anchored to the edge $\{(\rho,\phi)\,|\,\phi=\gamma\}$ of the infinite wedge adjacent to the boundary given by (B.2.2) is non-compact; therefore we have to compute the area of its restriction $\hat{\gamma}_\varepsilon$ to $z \geqslant \varepsilon$. We stress that $\hat{\gamma}_A \subsetneq \hat{\gamma}_{A,\textrm{aux}}$ is the part of the auxiliary minimal surface $\hat{\gamma}_{A,\textrm{aux}}$ identified by the constraint $x \geqslant -(\cot\alpha)z$, as discussed in Sec. 3.2.2 and in the beginning of the appendix B.2 (see also Fig. B.1). The auxiliary infinite wedge $A_{\textrm{aux}}$ and the corresponding minimal surface $\hat{\gamma}_{A,\textrm{aux}}$ have been obtained through the analysis of the appendices B.2.1 and B.2.2. The area of $\hat{\gamma}_{\varepsilon,\textrm{aux}} \equiv \hat{\gamma}_{A,\textrm{aux}} \cap \{z \geqslant \varepsilon\}$ has been computed in [157].

We compute $\mathcal{A}[\hat{\gamma}_\varepsilon]$ by considering two parts of $\hat{\gamma}_{A,\textrm{aux}}$, that we denote by $\hat{\gamma}^{\infty}_{A,\textrm{aux}}$ and $\hat{\gamma}^{*}_{A,\textrm{aux}}$.

The surface $\hat{\gamma}^{\infty}_{A,\textrm{aux}}$ corresponds to the part of $\hat{\gamma}_{A,\textrm{aux}}$ such that with $\phi_0 \leqslant \phi \leqslant \gamma$. We remark that $\hat{\gamma}^{\infty}_{A,\textrm{aux}}$ reaches the half-plane at $z=0$ along the edge at $\phi=\gamma$ and it corresponds to half of $\hat{\gamma}_{A,\textrm{aux}}$. The surface $\hat{\gamma}^{*}_{A,\textrm{aux}}$ is the part of $\hat{\gamma}_{A,\textrm{aux}}$ having $\phi_* \leqslant \phi \leqslant \phi_0$ when $\alpha \in (0,\pi/2]$ and $\phi_0 \leqslant \phi \leqslant \phi_*$ when $\alpha \in [\pi/2,\pi)$ (see respectively the left and right panel of Fig. B.1). Notice that $\hat{\gamma}^{*}_{A,\textrm{aux}} = \emptyset$ when $\alpha = \pi/2$.

The restrictions of $\hat{\gamma}^{\infty}_{A,\textrm{aux}}$ and $\hat{\gamma}^{*}_{A,\textrm{aux}}$ to $z \geqslant \varepsilon$ provide $\hat{\gamma}^{\infty}_{\varepsilon,\textrm{aux}}$ and $\hat{\gamma}^{*}_{\varepsilon,\textrm{aux}}$ respectively, and we denote their areas by $R^2_{\textrm{AdS}}\,\mathcal{A}_\infty$ and $R^2_{\textrm{AdS}}\,\mathcal{A}_*$ respectively. From (B.2.4), one finds

$$\mathcal{A}_\infty \equiv \int_{\hat{\gamma}^{\infty}_\varepsilon} \frac{1}{\rho}\,\sqrt{q'^2+q^2+q^4}\,d\phi\,d\rho \qquad \mathcal{A}_* \equiv \int_{\hat{\gamma}^{*}_\varepsilon} \frac{1}{\rho}\,\sqrt{q'^2+q^2+q^4}\,d\phi\,d\rho \tag{B.2.24}$$

which give the area of $\hat{\gamma}_\varepsilon$ as follows

$$\frac{\mathcal{A}[\hat{\gamma}_\varepsilon]}{R^2_{\textrm{AdS}}} = \begin{cases} \mathcal{A}_\infty + \mathcal{A}_* & \quad 0 < \alpha \leqslant \pi/2 \\ \mathcal{A}_\infty - \mathcal{A}_* & \quad \pi/2 \leqslant \alpha < \pi \end{cases}. \tag{B.2.25}$$

By using (B.2.7) and (B.2.9), the angular part of the integrands in (B.2.24) can be written as

$$\sqrt{q'^2+q^2+q^4}\,\frac{dq}{|q'|} \,=\, \frac{q^4+q^2}{\sqrt{q_0^4+q_0^2}}\;\mathcal{P}_\phi(q,q_0)\,dq \,=\, \frac{\sqrt{q^4+q^2}}{\sqrt{q^4+q^2-q_0^4-q_0^2}}\,dq \tag{B.2.26}$$

which leads us to introduce the following function

$$\int_{q_0}^{q} \frac{\sqrt{\hat{q}^4+\hat{q}^2}}{\sqrt{\hat{q}^4+\hat{q}^2-q_0^4-q_0^2}}\,d\hat{q} \,\equiv\, \mathcal{G}(q,q_0) \qquad q \geqslant q_0. \tag{B.2.27}$$

Performing explicitly this integral, we obtain

$$\mathcal{G}(q,q_0) \equiv -\,\mathrm{i}\sqrt{q_0^2+1}\;\mathbb{E}\Bigg(\mathrm{i}\,\mathrm{arcsinh}\sqrt{\frac{q^2-q_0^2}{1+2q_0^2}}\;\Bigg|\;\frac{2q_0^2+1}{q_0^2+1}\Bigg) \tag{B.2.28}$$

which satisfies the condition $\mathcal{G}(q_0,q_0) = 0$, as expected from (B.2.27). By employing the following identity [277]

$$\begin{aligned}\mathbb{E}(\mathrm{i}\psi|m) = \mathrm{i}\,\mathbb{F}\big(\arctan(\sinh\psi)\,\big|\,1-m\big) - \mathrm{i}\,\mathbb{E}\big(\arctan(\sinh\psi)\,\big|\,1-m\big)\\ +\mathrm{i}\sqrt{1-(1-m)\tanh^2\psi}\;\sinh\psi\end{aligned} \tag{B.2.29}$$

we can write (B.2.28) in a form that does not contain the imaginary unit, finding the real expression reported in (3.2.13).

Since $\hat{\gamma}^{\infty}_{A,\mathrm{aux}}$ is half of $\hat{\gamma}_{A,\mathrm{aux}}$, the area $\mathcal{A}_\infty$ has been already computed in [157]. First, we have to expand (B.2.28) for large q, finding

$$\mathcal{G}(q,q_0) = q - F(q_0) + O(1/q^3) \qquad q \gg 1 \qquad q \gg q_0 \tag{B.2.30}$$

where $F(q_0)$ has been explicitly written in (1.3.27). In order to get the area $\mathcal{A}_\infty$, a large cutoff $\rho_{\mathrm{max}} \gg 1$ in the radial direction must be introduced. Then, we have

$$\varepsilon = \frac{\rho_{\mathrm{min}}}{q_0}\,, \qquad \varepsilon = \frac{\rho_{\mathrm{max}}}{q(\gamma-\delta_\varepsilon)}\,, \qquad L = \rho_{\mathrm{max}}\cos\delta_\varepsilon\,, \tag{B.2.31}$$

where $\delta_\varepsilon \sim 0^+$ is the angle between the edge of A at $\phi = \gamma$ and the straight line in the $z=0$ half-plane connecting the tip of the wedge to the intersection point between the circumference given by $\rho = \rho_{\mathrm{max}}$ and the projection of $\partial\hat{\gamma}_\varepsilon \cap \{z=\varepsilon\}$ on the $z=0$ half-plane. By employing the expansion (B.2.30) and (B.2.31), the area $\mathcal{A}_\infty$ is obtained as follows [157]

$$\begin{aligned}\mathcal{A}_\infty &= \int_{\rho_{\mathrm{min}}}^{\rho_{\mathrm{max}}} \frac{d\rho}{\rho}\int_{q_0}^{\rho/\varepsilon} \frac{\sqrt{q^4+q^2}}{\sqrt{q^4+q^2-q_0^4-q_0^2}}\,dq \;=\; \int_{\rho_{\mathrm{min}}}^{\rho_{\mathrm{max}}} \frac{\mathcal{G}(\rho/\varepsilon,q_0)}{\rho}\,d\rho\\ &= \int_{\rho_{\mathrm{min}}}^{\rho_{\mathrm{max}}} \frac{1}{\rho}\left[\frac{\rho}{\varepsilon} - F(q_0) + O\big((\varepsilon/\rho)^3\big)\right] d\rho \;=\; \frac{\rho_{\mathrm{max}}-\rho_{\mathrm{min}}}{\varepsilon} - F(q_0)\,\log(\rho_{\mathrm{max}}/\rho_{\mathrm{min}}) + \dots\\ &= \frac{L}{\varepsilon} - F(q_0)\,\log(L/\varepsilon) + \dots\end{aligned} \tag{B.2.32}$$

where the dots correspond to finite terms for $\varepsilon \to 0^+$. We remark that $\mathcal{A}_\infty$ provides the expected linear divergence (area law term) whose coefficient is the length of the entangling curve $\partial A \cap \partial B$. Furthermore, the coefficient of the subleading logarithmic divergence is half of the corresponding coefficient (1.3.26) found for the wedge in AdS$_4$/CFT$_3$, as expected, being $\hat{\gamma}^{\infty}_{A,\mathrm{aux}}$ half of $\hat{\gamma}_{A,\mathrm{aux}}$.

The computation of the surface integral $\mathcal{A}_*$ in (B.2.24) is similar to the one of $\mathcal{A}_\infty$, with a crucial difference in the angular integral. In particular, we find

$$\begin{aligned}\mathcal{A}_* &= \int_{\rho_{\mathrm{min}}}^{\rho_{\mathrm{max}}} \frac{d\rho}{\rho}\int_{q_0}^{q_*} \frac{\sqrt{q^4+q^2}}{\sqrt{q^4+q^2-q_0^4-q_0^2}}\,dq \;=\; \int_{\rho_{\mathrm{min}}}^{\rho_{\mathrm{max}}} \frac{\mathcal{G}(q_*,q_0)}{\rho}\,d\rho\\ &= \mathcal{G}(q_*,q_0)\,\log(\rho_{\mathrm{max}}/\rho_{\mathrm{min}}) \;=\; \mathcal{G}(q_*,q_0)\,\log(L/\varepsilon) + \dots\end{aligned} \tag{B.2.33}$$

Notice that the double integral in $\mathcal{A}_*$ factorises into the product of two integrals that can be computed separately. This simplification does not occur in the computation of $\mathcal{A}_\infty$.

Finally, plugging (B.2.32) and (B.2.33) into (B.2.25), we find the total corner function F_α in terms of α and q_0, whose explicit expression has been reported in (3.2.12). Combining this formula with (3.2.7), we obtain $F_\alpha(\gamma)$ parametrically through the real parameter $q_0 > 0$. This function is the main result of this chapter. It is shown in Fig. 3.7 and Fig. 3.8.

A considerable simplification occurs in the expressions obtained above when $\alpha = \pi/2$. Indeed, being $q_* > 0$, the relation (B.2.11) tells us that $\phi_* = 0$. Then, since $0 \leqslant |\phi_0| \leqslant |\phi_*|$, we have that $\phi_* = \phi_0 = 0$, and this implies $q_* = q_0$. By substituting $\phi_0 = 0$ into (B.2.10), we can conclude that $\gamma = P_0(q_0)$ in this special case. As for the corner function, the condition $q_* = q_0$ tells us that $\mathcal{G}(q_*, q_0) = \mathcal{G}(q_0, q_0) = 0$. Plugging this result in (3.2.12), we find that $F_{\pi/2} = F(q_0)$. Thus, when $\alpha = \pi/2$ we have that the minimal surface $\hat{\gamma}_A$ is half of the minimal surface found in [157], namely $\hat{\gamma}_A = \hat{\gamma}^\infty_{A,\text{aux}}$ as expected. This is also stated in (3.2.14).

B.2.4 On the limiting regimes of the corner function

We find it worth considering some interesting regimes of the corner function $F_\alpha(\gamma)$, whose analytic expression is given by (3.2.7) and (3.2.12). In particular, we focus on the limits $\gamma \to 0$ and $\gamma \to \pi/2$, which correspond to $q_0 \to +\infty$ and $q_0 \to 0$ respectively. The main results derived in the following are also discussed in Sec. 3.2.2.

In order to expand $\gamma(q_0)$ in (3.2.7) for small and large values of q_0, we find it convenient to write it as follows

$$\gamma \,=\, P_0(q_0) + \int_{\pi/2}^{\alpha} \partial_{\tilde{\alpha}} \gamma \, d\tilde{\alpha} \tag{B.2.34}$$

where (3.2.14) has been used and $P_0(q_0)$ is given by (1.3.28) or (3.2.10). From (3.2.7) we have that the integrand in (B.2.34) reads

$$\partial_\alpha \gamma = \eta_\alpha \Big(\partial_\alpha \arcsin[s_*(\alpha, q_0)] - \partial_\alpha P\big(q_*(\alpha, q_0), q_0\big) \Big) \tag{B.2.35}$$

where $s_*(\alpha, q_0)$ in the first term is given by (3.2.4). Then, (B.2.9) tells us that $P(q_*(\alpha, q_0), q_0)$ depends on α only through its first argument $q_*(\alpha, q_0)$, which is also the upper extremum in the integral defining $P(q, q_0)$.

Thus, for the second term in (B.2.35) with $\alpha \in (0, \pi)$ we find

$$\begin{aligned} \partial_\alpha P\big(q_*(\alpha, q_0), q_0\big) \,&=\, \partial_\alpha \big(q_*(\alpha, q_0)\big)\, \mathcal{P}_\phi(q, q_0)\big|_{q = q_*(\alpha, q_0)} \\ &=\, \frac{\sqrt{q_0^4 + q_0^2}}{\sqrt{(q_*^2(\alpha, q_0) + 1)(q_*^2(\alpha, q_0) - q_0^2)(q_*^2(\alpha, q_0) + q_0^2 + 1)}}\; \frac{\partial_\alpha\big(q_*(\alpha, q_0)\big)}{q_*(\alpha, q_0)} \\ &=\, -\,\eta_\alpha\, \frac{\sqrt{q_*^2(\alpha, q_0) - (\cot\alpha)^2}}{\big(q_*^2(\alpha, q_0) + 1\big)\, q_*(\alpha, q_0)}\; \partial_\alpha\big(q_*(\alpha, q_0)\big) \tan\alpha . \end{aligned} \tag{B.2.36}$$

We remark that the combination $(\tan\alpha)\, \partial_\alpha q_*(\alpha, q_0)$ in the last expression is regular when $\alpha \to \pi/2$. Similarly, for the first term in (B.2.35) we find

$$\partial_\alpha \arcsin[s_*(\alpha, q_0)] \,=\, \partial_\alpha \arcsin\left[\frac{|\cot\alpha|}{q_*(\alpha, q_0)} \right] \,=\, \eta_\alpha\, \frac{\cot\alpha\; \partial_\alpha q_*(\alpha, q_0) + (\csc\alpha)^2\, q_*(\alpha, q_0)}{q_*(\alpha, q_0)\, \sqrt{q_*^2(\alpha, q_0) - (\cot\alpha)^2}} . \tag{B.2.37}$$

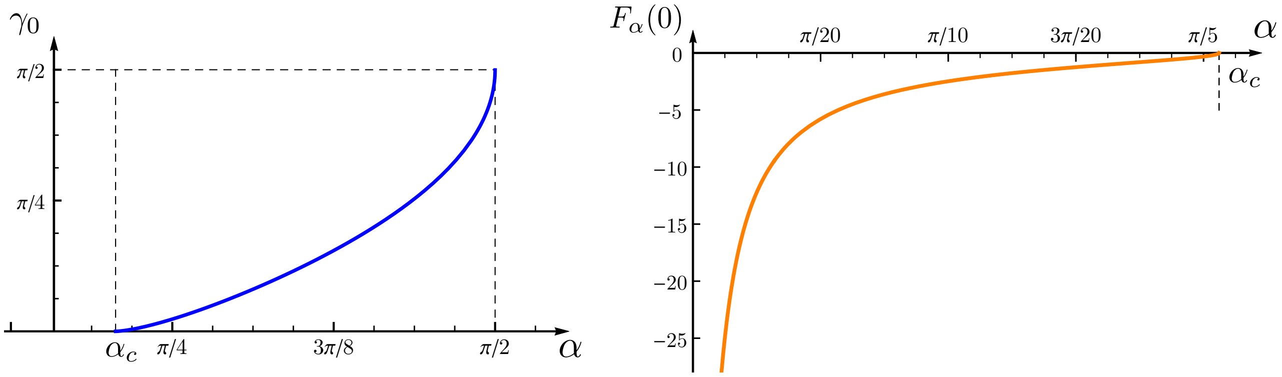

Figure B.2: Left: The function $\gamma_0(\alpha)$ for $\alpha \in [\alpha_c, \pi/2]$, being γ_0 defined by $F_\alpha(\gamma_0) = 0$. Right: The function $F_\alpha(0)$ in terms of $\alpha \leqslant \alpha_c$.

It is important to observe that the factor η_α in (B.2.36) and (B.2.37) simplify with the analogous one in (B.2.35). Thus, it becomes evident that (B.2.35) is smooth for $\alpha \in (0, \pi)$.

To study γ for small and large values of q_0, we first employ (B.2.35) and (B.2.36) for the integrand in (B.2.34); then we expand the resulting expression in the regime we are interested in, and only at the end, we integrate the coefficients of the expansion.

The corner function $F_\alpha(q_0)$ in (3.2.12) can be treated in the same way. First, by employing (3.2.14), we write F_α as

$$F_\alpha \;=\; F(q_0) - \int_\alpha^{\pi/2} \partial_{\tilde\alpha} F_{\tilde\alpha}\, d\tilde\alpha. \tag{B.2.38}$$

Then, from the derivative of (3.2.12) with respect to α, the integral representation of $\mathcal{G}(q, q_0)$ in (B.2.27) and the expression of $q_*(\alpha, q_0)$ in (3.2.6), we find that

$$\begin{aligned} \partial_\alpha F_\alpha \;&=\; \eta_\alpha \big(\partial_\alpha q_*(\alpha, q_0)\big)\, \partial_q \mathcal{G}(q, q_0)\big|_{q = q_*(\alpha, q_0)} \\ &=\; \eta_\alpha \,\frac{\sqrt{q_*^4(\alpha, q_0) + q_*^2(\alpha, q_0)}}{\sqrt{q_*^4(\alpha, q_0) + q_*^2(\alpha, q_0) - q_0^4 - q_0^2}}\; \partial_\alpha\big(q_*(\alpha, q_0)\big) \\ &=\; \eta_\alpha \,\frac{|\sec\alpha\,|\, q_*(\alpha, q_0)}{\sqrt{1 + q_*^2(\alpha, q_0)}}\; \partial_\alpha\big(q_*(\alpha, q_0)\big) \;=\; -\,\frac{q_*(\alpha, q_0)}{\cos\alpha\, \sqrt{1 + q_*^2(\alpha, q_0)}}\; \partial_\alpha\big(q_*(\alpha, q_0)\big) \end{aligned} \tag{B.2.39}$$

where, like in (B.2.36), we observe again the occurrence of $(\partial_\alpha q_*(\alpha, q_0))/\cos\alpha$, which is finite and regular when $\alpha = \pi/2$. Thus, also in this case η_α simplifies; therefore it becomes evident that $\partial_\alpha F_\alpha$ is a smooth function in $\alpha \in (0, \pi)$.

By plugging (B.2.39) into (B.2.38), we obtain an expression which can be easily expanded for $q_0 \to 0$ and $q_0 \to +\infty$. Only at the end, one integrates the coefficients of the expansion as prescribed in the r.h.s. of (B.2.38). We remark that the analysis presented here holds for any $\alpha \in (0, \pi)$.

Before considering the regimes $\gamma \to 0$ and $\gamma \to \pi/2$ of the corner function, we find it worth remarking that when $\alpha \in [\alpha_c, \pi/2]$ the corner function $F_\alpha(\gamma)$ has a unique zero (see Fig. 3.7), as already discussed in Sec. 3.2.2. Denoting by γ_0 the value of γ such that $F_\alpha(\gamma_0) = 0$, the function $\gamma_0(\alpha)$ in terms of $\alpha \in [\alpha_c, \pi/2]$ can be obtained numerically and the result is shown in the left panel of Fig. B.2.

Large q_0 regime

Let us consider the limit $q_0 \to +\infty$ of the opening angle $\gamma(q_0)$ written in the form (B.2.34). For the first term, which is given by (1.3.28) or (3.2.10), we find

$$P_0(q_0) = \frac{1}{\sqrt{2\pi}\,\Gamma(\frac{3}{4})^2}\left(\frac{\Gamma(\frac{3}{4})^4}{q_0} + \frac{\pi^2 - 6\,\Gamma(\frac{3}{4})^4}{24\,q_0^3} + \frac{16\,\Gamma(\frac{3}{4})^4 - 5\pi^2}{160\,q_0^5} + O(1/q_0^7)\right). \tag{B.2.40}$$

As for the second term in (B.2.34), the integrand can be expanded by employing (B.2.35), obtaining

$$\partial_\alpha \gamma = \frac{(\csc\alpha)^{3/2}}{2\,q_0} - \frac{(1+\csc\alpha)\,(\csc\alpha)^{3/2}}{8\,q_0^3} + O(1/q_0^5). \tag{B.2.41}$$

Finally, by plugging (B.2.40) and (B.2.41) into (B.2.34), and integrating separately the coefficients of the resulting expansion, one finds the first expression in (3.2.16).

The limit $q_0 \to +\infty$ of the corner function $F_\alpha(q_0)$ can be studied in a similar way, starting from (B.2.38). As for the first term, whose explicit expression has been reported in (1.3.27), its expansion reads

$$F(q_0) = \frac{1}{\sqrt{2\pi}\,\Gamma(\frac{3}{4})^2}\left(\Gamma(\tfrac{3}{4})^4\,q_0 - \frac{\pi^2 - 2\,\Gamma(\frac{3}{4})^4}{8\,q_0} + \frac{\pi^2}{32\,q_0^3} + O(1/q_0^5)\right). \tag{B.2.42}$$

The second term in (B.2.38) can be addressed by using (B.2.39), whose expansion is

$$\partial_\alpha F_\alpha = \frac{(\csc\alpha)^{3/2}}{2}\,q_0 + \frac{(3\csc\alpha+1)\,(\csc\alpha)^{3/2}}{8\,q_0} + \frac{\big(3\cos(2\alpha) - 12\sin\alpha + 7\big)(\csc\alpha)^{7/2}}{128\,q_0^3} + O(1/q_0^5). \tag{B.2.43}$$

The coefficient of the leading term in this expansion coincides with the coefficient of the leading term in the expansion (B.2.41), while the subleading terms are different. By inserting the expansions (B.2.42) and (B.2.43) into (B.2.38) first and then integrating the coefficient of the leading term of the resulting expression, one obtains the second expression in (3.2.16).

As discussed in detail in Sec. 3.2.2, a peculiar feature of the corner function $F_\alpha(\gamma)$ as $\gamma \to 0^+$ is that $F_\alpha(\gamma) \to +\infty$ when $\alpha > \alpha_c$, while it tends to a finite value $F_\alpha(\gamma) \to F_\alpha(0)$ when $\alpha \leqslant \alpha_c$. The function $F_\alpha(0)$ in terms of $\alpha \leqslant \alpha_c$ can be obtained numerically and the result is shown in the right panel of Fig. B.2. In particular, (3.2.18) holds for the critical slope α_c, and this feature has been employed to get (3.5.8) for an infinite wedge which has only its tip on the boundary.

We find it worth also discussing the behaviour of the angle ϕ_* characterising the half-line $\hat{\gamma}_A \cap \mathcal{Q}$ as $\gamma \to 0^+$. When $\alpha > \alpha_c$, from the expansion of (3.2.5) as $q_0 \to +\infty$ and (3.2.16) we find that

$$\phi_* = -\frac{\cos\alpha\,\sqrt{\csc\alpha}}{\mathfrak{g}(\alpha)}\,\gamma + \dots \qquad \alpha > \alpha_c \tag{B.2.44}$$

which implies that $\phi_* \to 0$ when $\gamma \to 0^+$. Instead, when $\alpha \leqslant \alpha_c$, we have to consider the value $\hat{q}_0$ introduced in Sec. 3.2.2 and plug it into (3.2.5). The result is a negative and increasing function of α which takes the value $-\pi/2$ for $\alpha \to 0^+$ and vanishes for $\alpha = \alpha_c$.

Small q_0 regime

The method described in the appendix B.2.4 can be adapted to study the limit $q_0 \to 0^+$ of the functions $\gamma(q_0)$ and $F_\alpha(q_0)$, once they are written in the form given by (B.2.34) and (B.2.38) respectively.

Considering the opening angle γ, for the first term of (B.2.34) we find

$$P_0(q_0) = \frac{\pi}{2} - \frac{\pi}{2}\, q_0 + \frac{3\pi}{8}\, q_0^3 - \frac{61\pi}{128}\, q_0^5 + O(q_0^7). \tag{B.2.45}$$

As for the expansion of the integrand in (B.2.34), we find

$$\partial_\alpha \gamma = q_0 + \frac{5\cos(2\alpha) - 3}{4}\, q_0^3 + \frac{63\cos(4\alpha) - 132\cos(2\alpha) + 61}{64}\, q_0^5 + O(q_0^7). \tag{B.2.46}$$

Plugging (B.2.45) and (B.2.46) into (B.2.34) first and then integrating the coefficients of the resulting expansion, we find that

$$\gamma = \frac{\pi}{2} - (\pi - \alpha)\, q_0 + \frac{3(\pi-\alpha) + 5\sin\alpha\cos\alpha}{4}\, q_0^3 + O(q_0^5) \tag{B.2.47}$$

which can be inverted obtaining

$$q_0 = \frac{\pi/2 - \gamma}{\pi - \alpha} - \frac{6(\pi-\alpha) + 5\sin(2\alpha)}{8(\pi-\alpha)^4}\,(\pi/2-\gamma)^3 + O\big((\pi/2-\gamma)^5\big) \qquad \gamma \to \frac{\pi}{2}. \tag{B.2.48}$$

The limit $q_0 \to 0^+$ of the corner function $F_\alpha(q_0)$ in the form (B.2.38) can be studied in the same way. The first term in the r.h.s. of (B.2.38) is (1.3.27) and its expansion reads

$$F(q_0) = \frac{\pi}{4}\, q_0^2 - \frac{7\pi}{32}\, q_0^4 + O(q_0^6). \tag{B.2.49}$$

As for the integrand occurring in (B.2.38), from (B.2.39) we obtain

$$\partial_\alpha F_\alpha = \frac{1}{(\sin\alpha)^2} - \frac{1}{2}\, q_0^2 + \frac{7 - 15\cos(2\alpha)}{16}\, q_0^4 + O(q_0^6). \tag{B.2.50}$$

By inserting (B.2.49) and (B.2.50) into (B.2.38) first and then integrating separately the coefficients of the resulting expansion, we find

$$F_\alpha = -\cot\alpha + \frac{\pi - \alpha}{2}\, q_0^2 - \frac{7(\pi-\alpha) + 15\cos\alpha\sin\alpha}{16}\, q_0^4 + O(q_0^6). \tag{B.2.51}$$

Finally, by employing (B.2.48) into (B.2.51), we obtain

$$F_\alpha(\gamma) = -\cot\alpha + \frac{(\pi/2-\gamma)^2}{2(\pi-\alpha)} + \frac{5(\pi - \alpha + \cos\alpha\,\sin\alpha)}{16(\pi-\alpha)^4}\,(\pi/2-\gamma)^4 + O\big((\pi/2-\gamma)^6\big) \tag{B.2.52}$$

which is one of our main results. In (3.2.19) the first two terms of (B.2.52) have been reported.

B.2.5 A relation between the infinite wedge and the infinite strip

In the expansion (3.2.17) of the holographic corner function $F_\alpha(\gamma)$ for $\gamma \to 0$ and in the $O(1)$ term of the holographic entanglement entropy of the infinite strip adjacent to the boundary in (2.2.7), the same function $\mathfrak{g}(\alpha)$ given by (2.2.2) occurs. In the following, we explain this connection by exploiting a conformal map that relates the infinite wedge adjacent to the boundary in the half-plane and the infinite strip adjacent to a border of a half-cylinder. This analysis has been done by adapting to our case in a straightforward way the analogue relation in the absence of the boundary, which involves the infinite wedge in $\mathbb{R}^2$ and the infinite strip on the surface of an infinite cylinder [189, 247, 265].

Consider a BCFT$_3$ defined on $\mathbb{R}^3_+ \equiv \{(t_{\textrm{E}}, x, y) \in \mathbb{R}^3 \,|\, x \geqslant 0\}$ endowed with the usual Euclidean metric $ds^2 = dt_{\textrm{E}}^2 + dx^2 + dy^2$. By adopting the polar coordinates introduced in (B.2.1), where we recall that $0 \leqslant \phi \leqslant \pi$, this metric becomes $ds^2 = dt_{\textrm{E}}^2 + d\rho^2 + \rho^2 d\phi^2$. We define $t_{\textrm{E}} = 0$ the slice containing the infinite wedge A adjacent to the boundary introduced in Sec. 3.2.2, whose edges are given by $\phi = 0$ and $\phi = \gamma$. By introducing the coordinates $(\tilde{r}, \chi)$ through the relations $t_{\textrm{E}} = \tilde{r}\cos\chi$ and $\rho = \tilde{r}\sin\chi$, where $\tilde{r} \geqslant 0$ and $0 \leqslant \chi \leqslant \pi$, the flat metric becomes

$$ds^2 = d\tilde{r}^2 + \tilde{r}^2\big(d\chi^2 + (\sin\chi)^2 d\phi^2\big). \tag{B.2.53}$$

Let us define the coordinate $\tau \in \mathbb{R}$ as $\tilde{r} = L_0\, e^{\tau/L_0}$. The tip of the wedge A corresponds to $\tau \to -\infty$, being $\rho = 0 = \tilde{r}$ in the previous coordinates. In terms of the coordinates (τ, χ, ϕ), the metric (B.2.53) reads

$$ds^2 = e^{2\tau/L_0} d\tilde{s}^2 \qquad d\tilde{s}^2 \equiv d\tau^2 + L_0^2\big(d\chi^2 + (\sin\chi)^2 d\phi^2\big) \tag{B.2.54}$$

i.e. the flat metric on $\mathbb{R}^3_+$ is conformally equivalent to $d\tilde{s}^2$, which is the metric $\mathbb{R} \times S^2_+$, being S^2_+ a two dimensional hemisphere whose radius is L_0. The condition $t_{\textrm{E}} = 0$ corresponds to $\chi = \pi/2$ and the metric induced on this slice from $d\tilde{s}^2$ is given by $d\tilde{s}^2|_{\chi=\pi/2} = d\tau^2 + L_0^2\, d\phi^2$, which characterises the external surface of a half-cylinder of radius L_0, whose boundaries are defined by $\phi = 0$ and $\phi = \pi$ (see Fig. B.3). Thus, on this surface, the infinite wedge A corresponds to the infinite strip adjacent to the boundary and enclosed by the generatrices given by $\phi = 0$ and $\phi = \gamma$ (the yellow region in Fig. B.3). The width of this infinite strip measured along the surface of the cylinder is $\ell = L_0 \gamma$.

In terms of the coordinates (ρ, ϕ) in $\mathbb{R}^3_+|_{t_{\textrm{E}}=0}$, the entanglement entropy of the infinite wedge A adjacent to the boundary can be written as

$$S_A \,=\, b\,\frac{\rho_{\textrm{max}} - \rho_{\textrm{min}}}{\varepsilon} - f_\alpha(\gamma)\,\log(\rho_{\textrm{max}}/\rho_{\textrm{min}}) + O(1) \tag{B.2.55}$$

where $\rho_{\textrm{max}} = L$ and $\rho_{\textrm{min}} = \varepsilon$, being $L \gg \varepsilon$ the infrared regulator introduced in the beginning of Sec. 3.2.2. We remark that (B.2.55) is a special case of the general expression (3.0.1) (see (3.2.11) for the holographic case). Since at $\chi = \pi/2$ we have that $\rho = \tilde{r} = L_0\, e^{\tau/L_0}$, in terms of this coordinate τ one finds that (B.2.55) becomes

$$S_A \,=\, b\, L_0\,\frac{e^{\tau_+/L_0} - e^{\tau_-/L_0}}{\varepsilon} - f_\alpha(\gamma)\,\frac{\tau_+ - \tau_-}{L_0} + O(1) \tag{B.2.56}$$

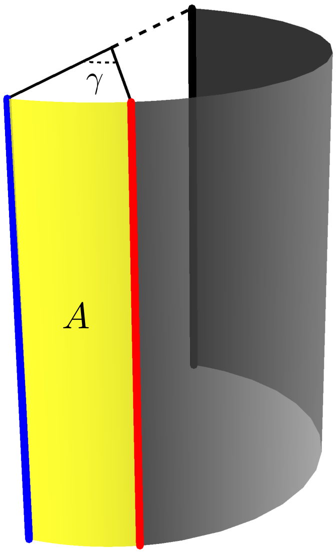

Figure B.3: Part of the surface of a half-cylinder, introduced in the appendix B.2.5 (see $d\tilde{s}^2$ in (B.2.54) for $\chi = \pi/2$). This surface corresponds to the conformal boundary of the gravitational spacetimes depicted in Fig. B.4. The yellow region is an infinite strip A adjacent to the boundary.

where we used that $\rho_{\text{max}} = L = L_0\, e^{\tau_+/L_0}$ and $\rho_{\text{min}} = \varepsilon = L_0\, e^{\tau_-/L_0}$. These relations and the condition $L/\varepsilon \gg 1$ imply that $(\tau_+ - \tau_-)/L_0 \gg 1$.

In order to relate (B.2.56) to the expansion of the entanglement entropy of the infinite strip adjacent to the boundary, we take $L_0 \to +\infty$ and $\gamma \to 0^+$ such that $\ell = L_0\gamma$ is kept constant. Notice that the width $L_0(\pi - \gamma)$ of the complementary region B in the half-cylinder of Fig. B.3 diverges in this limit. Moreover, since $L_0 \to +\infty$ we have that $L_0(e^{\tau_+/L_0} - e^{\tau_-/L_0}) \to \tau_+ - \tau_-$ in the r.h.s. of (B.2.56). Thus, in this regime (B.2.56) becomes

$$S_A = b\,\frac{L_\parallel}{\varepsilon} + A_0\, L_\parallel + O(1) \qquad \tau_+ - \tau_- = L_\parallel \gg L_0 \tag{B.2.57}$$

where $O\big((\tau_+^2 - \tau_-^2)/L_0^2\big)$ term has been neglected and A_0 is defined as follows

$$-\,\frac{f_\alpha(\gamma)}{L_0} \to A_0 \qquad \text{as} \qquad \begin{cases} L_0 \to +\infty \\ \gamma \to 0^+ \\ L_0\gamma = \ell \end{cases} . \tag{B.2.58}$$

The expression (B.2.57) in a BCFT$_3$ corresponds to the entanglement entropy of an infinite strip ($L_\parallel \gg \varepsilon$) of width ℓ adjacent to the boundary.

The above discussion holds for any BCFT$_3$ with a flat boundary. In the following, we focus on the case of AdS$_4$/BCFT$_3$, where this relation between the infinite wedge and the infinite strip adjacent to the boundary can be explicitly checked.

In order to address the holographic case, let us consider a part of the Euclidean AdS$_4$ spacetime in global coordinates, whose spacetime interval reads

$$ds^2 = \frac{dr^2}{1 + r^2/R_{\text{AdS}}^2} + \big(1 + r^2/R_{\text{AdS}}^2\big)d\tau^2 + r^2\big(d\chi^2 + (\sin\chi)^2 d\phi^2\big) \tag{B.2.59}$$

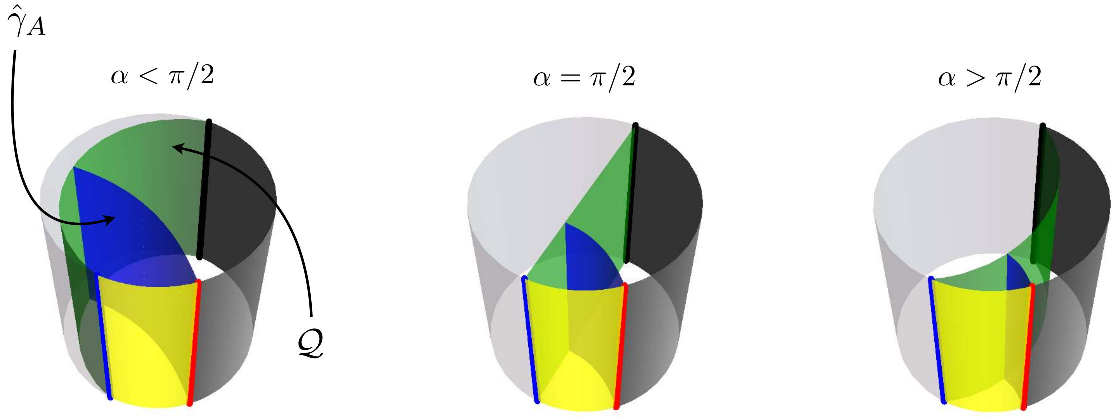

Figure B.4: The spacetime (B.2.60), whose boundary is the union of the surface in Fig. B.3 and of the green surface $\mathcal{Q}$ in (B.2.63), which depends on the parameter $\alpha \in (0, \pi)$. The blue surface is the minimal area surface $\hat{\gamma}_A$ corresponding to the infinite strip adjacent to the boundary (yellow region). The parameter α changes in the various panels: $\alpha = \pi/10$ (left), $\alpha = \pi/2$ (middle) and $\alpha = 3\pi/4$ (right).

where $\tau \in \mathbb{R}$, $\chi \in [0, \pi]$, $r \geqslant 0$ and $\phi \in [0, 2\pi)$, but the ranges of the last two coordinates are influenced by the occurrence of $x \geqslant -(\cot\alpha) z$. Indeed, we have that the conformal boundary corresponds to $r \to +\infty$ and $0 \leqslant \phi \leqslant \pi$. On the $\chi = \pi/2$ slice, the induced metric is given by

$$ds^2 = \frac{dr^2}{1 + r^2/R_{\text{AdS}}^2} + \big(1 + r^2/R_{\text{AdS}}^2\big) d\tau^2 + r^2 d\phi^2. \tag{B.2.60}$$

By introducing the coordinates (z, ρ) as follows

$$r \,=\, R_{\text{AdS}} \,\frac{\rho}{z} \qquad \tanh\big(\tau/R_{\text{AdS}}\big) = \frac{z^2 + \rho^2 - R_{\text{AdS}}^2}{z^2 + \rho^2 + R_{\text{AdS}}^2} \tag{B.2.61}$$

one finds that (B.2.60) becomes

$$ds^2 = \frac{R_{\text{AdS}}^2}{z^2}\,\big(dz^2 + d\rho^2 + \rho^2 d\phi^2\big) \tag{B.2.62}$$

which is the metric of $\mathbb{H}_3$ in terms of the polar coordinates (B.2.1), whose conformal boundary corresponds to $z \to 0^+$.

From the definition (1.4.9) of half-plane $\mathcal{Q}$ written in terms of the polar coordinates (B.2.1) and the first expression of (B.2.61), we find that the position of $\mathcal{Q}$ in the spacetime (B.2.60) is given by

$$\mathcal{Q} \;:\; \qquad r \,=\, -\,R_{\text{AdS}}\,\frac{\cot\alpha}{\sin\phi} \qquad\qquad \begin{cases} \pi \leqslant \phi \leqslant 2\pi & \alpha \in (0, \pi/2) \\ 0 \leqslant \phi \leqslant \pi & \alpha \in (\pi/2, \pi) \end{cases}. \tag{B.2.63}$$

In Fig. B.4 the spacetime defined by (B.2.60) and constrained by (B.2.63) is the internal part of the cylinder enclosed by the green surface, which corresponds to $\mathcal{Q}$ and the darker half of the cylindrical surface, which is the conformal boundary of the spacetime (B.2.60) (see also

Fig. B.3). Since the conformal boundary is defined by $r \to +\infty$, in Fig. B.4 the radial variable $\hat{r} = (2R_{\text{AdS}}/\pi) \arctan r$ has been employed. Notice that for $\alpha = \pi/2$ half of the global AdS$_4$ must be considered, as expected.

Close to this boundary the second expression of (B.2.61) becomes

$$\tanh\left(\tau/R_{\text{AdS}}\right) = \frac{\rho^2 - R^2_{\text{AdS}}}{\rho^2 + R^2_{\text{AdS}}} \qquad \Longleftrightarrow \qquad \rho = R_{\text{AdS}}\, e^{\tau/R_{\text{AdS}}} \tag{B.2.64}$$

i.e. we recover the exponential change of coordinate reported in the text above (B.2.56), once the identification $R_{\text{AdS}} = L_0$ is assumed.

In AdS$_4$/BCFT$_3$, by computing the holographic entanglement entropy of the infinite wedge adjacent to the boundary (Sec. 3.2.2), we have found that (B.2.55) holds with $b = R^2_{\text{AdS}}/(4G_{\text{N}})$ and $f_\alpha(\gamma) = \frac{R^2_{\text{AdS}}}{4G_{\text{N}}}\, F_\alpha(\gamma)$, being $F_\alpha(\gamma)$ given by (3.2.7) and (3.2.12). By employing the results discussed in Sec. 3.2.2 for the regime $\gamma \to 0^+$ of $F_\alpha(\gamma)$ (namely (3.2.17) and the fact that $F_\alpha(\gamma) \to F_\alpha(0)$ when $\alpha \leqslant \alpha_c$) and the identification $R_{\text{AdS}} = L_0$, we find that (B.2.58) in this case gives

$$A_0 = \frac{R^2_{\text{AdS}}}{4G_{\text{N}}}\, \frac{a_0(\alpha)}{\ell} \tag{B.2.65}$$

where $\ell = R_{\text{AdS}}\, \gamma$ and $a_0(\alpha)$ has been defined in (2.2.7). Plugging these results into (B.2.57), we recover the holographic entanglement entropy (2.2.7) of the infinite strip adjacent to the boundary, as expected.

As further consistency check of the relation between the infinite wedge and the infinite strip adjacent to the boundary, we find it worth considering the quantity $R_{\text{AdS}}\, \phi_*$ in the limit defined in (B.2.58) with $L_0 = R_{\text{AdS}}$. By employing (B.2.44) and the corresponding result for $\alpha \leqslant \alpha_c$, we find

$$\begin{cases} R_{\text{AdS}}\, \phi_* = -\dfrac{\cos\alpha\,\sqrt{\csc\alpha}}{\mathfrak{g}(\alpha)}\, R_{\text{AdS}}\, \gamma + \dots = -\dfrac{\cos\alpha\,\sqrt{\csc\alpha}}{\mathfrak{g}(\alpha)}\, \ell + \dots & \alpha > \alpha_c \\ R_{\text{AdS}}\, \phi_* \to -\infty & \alpha \leqslant \alpha_c \end{cases} . \tag{B.2.66}$$

In Sec. 2.2 we have found that $x_* = -\, z_* \cot\alpha$ when $\alpha > \alpha_c$, with z_* given by (2.2.1), while $x_* \to -\infty$ when $\alpha \leqslant \alpha_c$. Comparing these results with (B.2.66), we have that $x_* = R_{\text{AdS}}\, \phi_*$ in the limit that we are considering. This identification allows to interpret the transition between $\hat{\gamma}_A^{\text{con}}$ and $\hat{\gamma}_A^{\text{dis}}$ at $\alpha = \alpha_c$ for the infinite strip adjacent to the boundary (see Sec. 2.2) in terms of the behavior of ϕ_* for $\gamma \to 0$. Indeed, when $\alpha > \alpha_c$, from (B.2.44) we have $\phi_* \to 0$ as $\gamma \to 0$, therefore x_* remains finite and the minimal surface for the infinite strip is $\hat{\gamma}_A^{\text{con}}$. Instead, when $\alpha \leqslant \alpha_c$ the angle ϕ_* remains finite and negative, as discussed below (B.2.44). This means that $x_* \to -\infty$ for large R_{AdS}, which tells us that the minimal area surface for the infinite strip adjacent to the boundary is the vertical half-plane $\hat{\gamma}_A^{\text{dis}}$.

B.2.6 Recovering the corner function from (2.1.23)

In the gravitational setup described in Sec. 2.1.1, let us consider an infinite wedge A in (B.2.2), which is adjacent to the flat boundary and whose opening angle is γ. As for the corresponding holographic entanglement entropy, in the main text the area $\mathcal{A}[\hat{\gamma}_\varepsilon]$ of $\hat{\gamma}_\varepsilon$ it has been found by a direct computation and the analytic expression of the boundary corner function $F_\alpha(\gamma)$ has been extracted. In this appendix, we provide some technical details underlying the discussion of Sec. 3.2.3, where we have shown that the analytic expression for $F_\alpha(\gamma)$ can also be recovered through (3.2.20).

Let us consider first the line integral over $\partial\hat{\gamma}_{\mathcal{Q}}$ occurring in (3.2.20). The curve $\partial\hat{\gamma}_{\mathcal{Q}}$ is a line on $\mathcal{Q}$ which can be parameterised as follows

$$\partial\hat{\gamma}_{\mathcal{Q}}: \quad (z,x,y) = \rho\left(-\sin\phi_*\tan\alpha\,,\,\sin\phi_*\,,\,\cos\phi_*\right) \qquad 0 \leqslant \rho \leqslant L \tag{B.2.67}$$

where ϕ_* is the angular coordinate characterising the projection of $\partial\hat{\gamma}_{\mathcal{Q}}$ on the $z=0$ plane. The line element $d\tilde{s}$ induced by the flat metric reads

$$d\tilde{s} = \sqrt{x'^2+y^2+z'^2}\,d\rho = \frac{\sqrt{x'^2+\cos^2\alpha\,y'^2}\,d\rho}{|\cos\alpha|} = -\frac{\eta_\alpha}{\cos\alpha}\sqrt{\sin^2\phi_*+\cos^2\alpha\,\cos^2\phi_*}\,d\rho. \tag{B.2.68}$$

By employing (B.2.67) and (B.2.68), the line integral over $\partial\hat{\gamma}_{\mathcal{Q}}$ in (3.2.20) becomes

$$-\cos\alpha\int_{\partial\hat{\gamma}_{\mathcal{Q}}}\frac{1}{z}\,d\tilde{s} = -\cot\alpha\int_{\rho_\varepsilon}^{L}\frac{\sqrt{1+\cos^2\alpha\cot^2\phi_*}}{\rho}\,d\rho \tag{B.2.69}$$

where $\mathrm{sign}(\sin\phi_*) = \eta_\alpha$ has been used. The integral in the r.h.s. of (B.2.69) has been regularised by introducing the lower extremum ρ_ε, which is defined by the condition $\varepsilon = -\rho_\varepsilon\sin\phi_*\tan\alpha$, obtained by intersecting $\partial\hat{\gamma}_{\mathcal{Q}}$ in (B.2.67) with the plane $z=\varepsilon$. The radial integral (B.2.69) can be easily evaluated, finding (3.2.26) at leading order as $\varepsilon\to 0$.

In order to compute the surface integral over $\hat{\gamma}_\varepsilon$ in (3.2.20), we need the unit normal vector $\tilde{n}_\nu$. Up to a normalization factor, this vector is given by the gradient of the equation $\mathcal{C} = z - \rho/q(\phi) = 0$, where $q(\phi)$ has been introduced in (3.2.3) and characterises the minimal surface. By imposing the normalization condition $\tilde{n}_\mu\tilde{n}^\mu = 1$, we get

$$\tilde{n}_\mu = \frac{1}{\sqrt{q^4+q^2+q'^2}}\left(q^2,-q,q'\rho\right) \tag{B.2.70}$$

where the index μ spans the cylindrical coordinates (z,ρ,ϕ) defined in Sec. 3.2.3. We saw in appendix B.2.1 the first derivative q' of q with respect to ϕ can be expressed in term of q and q_0 with the help of the integral of motion associated to the cyclic coordinate ϕ, i.e. by means of equation (B.2.8). Thus, by using (B.2.70) and (B.2.8) the integrand of the integral over $\hat{\gamma}_\varepsilon$ in (3.2.20) can be written as

$$\frac{(\tilde{n}^z)^2}{z^2} = \frac{q^6}{\rho^2\left(q^4+q^2+q'^2\right)} = \frac{q^2(q_0^4+q_0^2)}{(q^2+1)^2\rho^2}. \tag{B.2.71}$$

In terms of the cylindrical coordinates introduced in Sec. 3.2.3, the area element induced by the flat metric reads

$$d\tilde{\mathcal{A}} = \frac{\sqrt{q'^2+q^4+q^2}}{q^2}\,\rho\,d\rho\,d\phi = \frac{q^2+1}{\sqrt{q_0^4+q_0^2}}\,\rho\,d\rho\,d\phi. \tag{B.2.72}$$

Plugging (B.2.71) and (B.2.72) into the surface integral over $\hat{\gamma}_\varepsilon$ in (3.2.20), it reduces to the following double integral

$$\int_{\hat{\gamma}_\varepsilon} \frac{(\tilde{n}^z)^2}{z^2}\, d\tilde{\mathcal{A}} = \int_{\rho_{\min}}^{\rho_{\max}} \frac{1}{\rho}\, d\rho \int_{\phi_*}^{\gamma_\varepsilon} \frac{q^2\sqrt{q_0^4+q_0^2}}{q^2+1}\, d\phi. \tag{B.2.73}$$

The integration domain in the angular integral is defined by the angle ϕ_* characterising $\partial\hat{\gamma}_{\mathcal{Q}}$ and $\gamma_\varepsilon \equiv \gamma - \delta_\varepsilon$, where $\delta_\varepsilon \sim 0$ is the angle between the border of the wedge at $\phi = \gamma$ and the straight line in the $z = 0$ half-plane connecting the tip of the wedge to the intersection point between the circle given by $\rho = \rho_{\max}$ and the projection of $\hat{\gamma}_A \cap \{z = \varepsilon\}$ on the half-plane $z = 0$. In the radial direction we have introduced the large cutoff $\rho_{\max}$ to regulate the infrared divergences of this integral, while the lower extremum $\rho_{\min} = q_0\,\varepsilon$ (being q_0 the minimum value of q) controls the UV behaviour. The cutoff $\rho_{\max}$ is related to L in (B.2.2) and to δ_ε through the relation $L = \rho_{\max}\cos\delta_\varepsilon$, and to ε through the condition

$$\rho_{\max} = \varepsilon\, q(\gamma - \delta_\varepsilon). \tag{B.2.74}$$

In order to perform the angular integration in (B.2.73), it is convenient to change the integration variable from ϕ to q. However, since q is not monotonic as a function of ϕ for some values of α, we have to split the integral into two separate contributions (depending on the sign of $\cot\alpha$) as follows

$$\int_{\hat{\gamma}} \frac{(\tilde{n}^z)^2}{z^2}\, d\tilde{\mathcal{A}} = \int_{\rho_{\min}}^{\rho_{\max}} \frac{d\rho}{\rho} \left(\int_{q_0}^{\rho/\varepsilon} \frac{q^2\sqrt{q_0^4+q_0^2}}{(q^2+1)\, q'}\, dq - \eta_\alpha \int_{q_0}^{q_*} \frac{q^2\sqrt{q_0^4+q_0^2}}{(q^2+1)\, q'}\, dq \right) \tag{B.2.75}$$

where (B.2.8) can be used to express q'. By introducing the integration variable $\tilde{\rho} = \rho/\varepsilon$ in the radial integration, we get

$$\int_{\hat{\gamma}} \frac{(\tilde{n}^z)^2}{z^2}\, d\tilde{\mathcal{A}} = \int_{\rho_{\min}/\varepsilon}^{\rho_{\max}/\varepsilon} \frac{d\tilde{\rho}}{\tilde{\rho}} \left(\int_{\rho_{\min}/\varepsilon}^{\tilde{\rho}} \frac{q^2\sqrt{q_0^4+q_0^2}}{(q^2+1)\, q'}\, dq - \eta_\alpha \int_{q_0}^{q_*} \frac{q^2\sqrt{q_0^4+q_0^2}}{(q^2+1)\, q'}\, dq \right) \equiv I_1 - \eta_\alpha\, I_2 \tag{B.2.76}$$

where I_2 is defined as the integral multiplying η_α, while I_1 is the remaining one.
Considering I_1 first, in order to single out the logarithmic divergence we exchange the order of integration between $\tilde{\rho}$ and q, finding that

$$I_1 = \int_{\rho_{\min}/\varepsilon}^{\rho_{\max}/\varepsilon} \frac{q^2\sqrt{q_0^4+q_0^2}}{(q^2+1)\, q'}\, dq \int_{q}^{\rho_{\max}/\varepsilon} \frac{d\tilde{\rho}}{\tilde{\rho}}. \tag{B.2.77}$$

Now the integration over ρ can be easily performed, obtaining

$$I_1 = \int_{\rho_{\min}/\varepsilon}^{\rho_{\max}/\varepsilon} \sqrt{q_0^4+q_0^2} \left(\frac{q^2}{(q^2+1)\, q'} \log(\rho_{\max}/\varepsilon) - \frac{q^2\log q}{(q^2+1)\, q'} \right) dq. \tag{B.2.78}$$

Since L is large, the dominant contribution comes from the first integral (the second one is finite in this limit). In particular, we find

$$I_1 = \left(\int_{q_0}^{+\infty} \frac{q^2\sqrt{q_0^4+q_0^2}}{(q^2+1)\, q'}\, dq \right) \log(L/\varepsilon) + \cdots \tag{B.2.79}$$

where the integral multiplying the logarithmic divergence provides an integral representation of the function $F(q_0)$ given in (1.3.27) in terms of elliptic function, i.e.

$$\int_{q_0}^{+\infty} \frac{q^2\sqrt{q_0^4+q_0^2}}{(q^2+1)\,q'}\, dq = F(q_0). \tag{B.2.80}$$

The second integral I_2 in (B.2.76) can be also calculated in closed form in terms of elliptic functions. Expanding the result for large L, one finds that the dominant contribution is the following logarithmic divergence

$$I_2 = \left(S(q_*, q_0) + \sqrt{\frac{\left(q_*^2 - q_0^2\right)\left(q_*^2 + q_0^2 + 1\right)}{q_*^2+1}} \right) \log(L/\varepsilon) + \cdots \tag{B.2.81}$$

where $S(q_*, q_0)$ has been defined in (3.2.29).

Combining (B.2.79) and (B.2.81) into (B.2.76), we get the logarithmic divergence provided by the surface integral over $\hat{\gamma}_\varepsilon$ in (3.2.20), which is given by (3.2.27) and (3.2.28). By taking into account also the logarithmic divergence provided by the line integral over $\partial\hat{\gamma}_Q$ (see (3.2.26)), for the coefficient of $\log(L/\varepsilon)$ in the subleading term F_A we find

$$\begin{aligned} F_\alpha(q_0) \,=\, & F(q_0) - \eta_\alpha S(q_*(\alpha, q_0), q_0) \\ & - \eta_\alpha \sqrt{\frac{\left(q_*^2 - q_0^2\right)\left(q_*^2 + q_0^2 + 1\right)}{q_*^2+1}} - \sqrt{1+\cos^2\alpha\cot^2\phi_*(\alpha,q_0)}\;\cot\alpha \end{aligned} \tag{B.2.82}$$

where the last two terms in (B.2.82) cancel, once the explicit expressions for $\phi_*(\alpha, q_0)$ and $q_*(\alpha, q_0)$ (see (3.2.5) and (3.2.4)) have been used. Hence, $F_\alpha(q_0)$ simplifies to

$$F_\alpha(q_0) = F(q_0) - \eta_\alpha\, S(q_*(\alpha, q_0), q_0). \tag{B.2.83}$$

In order to show that (B.2.83) coincides with (3.2.12), we have to prove that $S(q_*, q_0) = -\mathcal{G}(q_*, q_0)$. This follows from two observations that can be easily verified: the function obtained by taking the derivative of (3.2.13) with respect to q and then evaluating it for $q = q_*$ is the opposite of the derivative of (3.2.29) with respect to q_* and $S(q_0, q_0) = \mathcal{G}(q_0, q_0) = 0$ for any α.

B.3 Check of the constraints for the corner functions

In this appendix we check that the holographic corner functions derived in Sec. 3.2.2 and Sec. 3.5 for $\text{AdS}_4/\text{BCFT}_3$ satisfy the constraints found in Sec. 3.1.

The corner function (3.5.5) fulfils the inequality (3.1.6) in a trivial way. Indeed, whenever the maximisation procedure selects $\widetilde{F}(\omega)$ (namely for either $\alpha \leqslant \alpha_c$ or $\omega \leqslant \omega_c$ when $\alpha > \alpha_c$), this constraints simply tells us that the corner function $\widetilde{F}(\omega)$ is convex. The property $\tilde{f}''(\theta) \geqslant 0$ for the generic corner function $\tilde{f}(\theta)$ has been derived from the strong subadditivity in [178] and, in the special case of the holographic corner function $\widetilde{F}(\omega)$ found in [157], the convexity is evident from its plot (see the solid curve in Fig. 1.8). When the second function in the r.h.s. of (3.5.5) is selected, the inequality (3.1.6) is saturated, as one can straightforwardly observe by using that $\tilde{\gamma} = \pi - (\omega + \gamma)$.

As for the constraint obtained from the configuration shown in the middle panel of Fig. 3.2, we find it worth specialising the inequality (3.1.7) to the holographic corner functions. By employing (3.5.5), we find

$$F_\alpha(\omega_1 + \omega_2 + \gamma) - F_\alpha(\omega_1 + \gamma) \geqslant \\ \max\Big\{\widetilde{F}(\omega_1 + \omega_2)\,,\, F_\alpha(\gamma) + F_\alpha(\omega_1 + \omega_2 + \gamma)\Big\} - \max\Big\{\widetilde{F}(\omega_1)\,,\, F_\alpha(\gamma) + F_\alpha(\omega_1 + \gamma)\Big\}. \tag{B.3.1}$$

For the configurations such that in both the maximisations occurring in the r.h.s. of (B.3.1) the second function is selected, $F_\alpha(\gamma)$ simplifies in the r.h.s. and this inequality becomes a trivial identity. As for other configurations, the inequality (B.3.1) is a non-trivial inequality. We checked numerically for some cases that it is verified but, unfortunately, we do not have a general proof.

The last constraint to check is (3.1.10). Specifying this inequality for the holographic corner function (3.5.5), we obtain

$$F_\alpha(\gamma + \omega) + F_\alpha(\gamma) \leqslant \max\Big\{\widetilde{F}(\omega)\,,\, F_\alpha(\gamma) + F_\alpha(\omega + \gamma)\Big\}. \tag{B.3.2}$$

It is straightforward to observe that this inequality is trivially true.

Appendix **C**

Appendix of Chapter 4

C.1 Null Energy Condition

In this appendix, we discuss the constraints for the Lifshitz and the hyperscaling exponents imposed by the Null Energy Condition (NEC), which has been introduced in Section 4.1.

Let us consider spacetimes whose metric has the following form

$$ds^2 = e^{2A(z)}\left(-e^{2B(z)}f(z)dt^2 + \frac{dz^2}{f(z)} + dx^2 + dy^2\right) \tag{C.1.1}$$

for some $A(z)$, $B(z)$ and $f(z)$, being $z > 0$ the holographic coordinate. In [126], it is shown that the NEC leads to the following constraints

$$(2A' + 3B')f' + 2f(2A'B' + B'^2 + B'') + f'' \geqslant 0 \tag{C.1.2}$$

$$f(A'^2 + A'B' - A'') \geqslant 0\,. \tag{C.1.3}$$

Since we are mainly interested in the black hole metric (4.1.29), let us fix the functions $A(z)$, $B(z)$ and $f(z)$ as follows

$$A(z) = -\frac{d_\theta}{2}\log z \qquad B(z) = (1-\zeta)\log z \qquad f(z) = 1 - \left(\frac{z}{z_h}\right)^{\chi_1} + a\, z^{\chi_2} \tag{C.1.4}$$

where a is a constant. Plugging (C.1.4) into (C.1.2) and (C.1.3), one obtains respectively

$$d_\theta(d_\theta + 2\zeta - 4)f \geqslant 0 \tag{C.1.5}$$

$$2(d_\theta+\zeta)(\zeta-1) + \left(\frac{z}{z_h}\right)^{\chi_1}(d_\theta+\zeta-\chi_1)(2-2\zeta+\chi_1) - a\, z^{\chi_2}\,(d_\theta+\zeta-\chi_2)\,(2-2\zeta+\chi_2) \geqslant 0. \tag{C.1.6}$$

Restricting to the region of spacetime outside the horizon, where $f > 0$, one observes that (C.1.5) provides the same constraint holding in the hvLif$_4$, that is the first inequality in (4.1.2). The constraint (C.1.6) is more involved because it depends on the coordinate z in a non-trivial way. Notice that the second inequality in (4.1.2) is recovered by taking $z \to 0$ in (C.1.6).

Let us focus on the simple case given by $a = 0$ and assume that $\chi_1 \geqslant 0$, in order to have an asymptotically hvLif$_4$ background (this class of metrics includes (4.1.29)). Taking the limit $z \to z_h$ in the inequality (C.1.6) with $a = 0$, one finds $\chi_1 \leqslant d_\theta + 3\zeta - 2$. Setting $\chi_1 = d_\theta + \zeta \geqslant 0$ as in (4.1.29), one obtains $\zeta - 1 \geqslant 0$ corresponding to the first constraint in (4.1.2).

C.2 Expansion of the area near the boundary

This appendix is devoted to reviewing the derivation of the expansion near the boundary of the area functional $\mathcal{A}[\gamma_A]$ for two-dimensional surfaces γ_A that intersect the boundary $\partial\mathcal{C}_3$ orthogonally. In the following, we adapt the analysis reported in [77] to the gravitational backgrounds of our interest. Since the structure of this expansion depends only on the local geometry of γ_A near $\partial\mathcal{C}_3$, we may as well suppose that $\mathcal{C}_3$ is conformally flat (i.e. $\widetilde{\mathcal{C}}_3 = \mathbb{R}^3$) and that the form (4.1.3) of the metric is valid for any value of the coordinate z. The analysis below can also be adapted directly to spaces whose metric is only asymptotically of the form (4.1.3), though the equations involve higher-order correction terms and the procedure becomes more complicated.

The boundary curve $\partial\gamma_A \subset \partial\widetilde{\mathcal{C}}_3 \equiv \mathbb{R}^2$ is taken to be smooth and its parametric form $\boldsymbol{x}_A(s)$ is given by $(x(s), y(s))$, being s the affine parameter. At each non-singular point of $\partial\gamma_A$ the unit tangent vector $\widetilde{T} = \boldsymbol{x'}_A(s)$ and the normal one $\widetilde{N}$ provide a basis for the boundary plane $\partial\widetilde{\mathcal{C}}_3$. Then, let us consider the vertical cylinder $\Gamma \subset \widetilde{\mathcal{C}}_3$ constructed over the curve $\boldsymbol{x}_A(s)$, which is given by $\{(z, x, y) \in \mathcal{C}_3 \,|\, (z, \boldsymbol{x}_A(s))\}$. Near $\partial\widetilde{\mathcal{C}}_3$, i.e. close to the boundary plane $z = 0$, we can parametrize the surface γ_A as a horizontal graph over Γ. This means that we can introduce a scalar function $u(s, z)$ so that the embedding $E(s, z)$ of γ_A takes the form

$$E(s, z) = \big(\, z \,, \boldsymbol{x}_A(s) + u(s, z)\widetilde{N} \,\big) \,. \tag{C.2.1}$$

The function $u(s, z)$ in (C.2.1) describes the displacement of γ_A from the vertical cylinder over $\partial\gamma_A$. The boundary condition $E(s, 0) = \boldsymbol{x}_A(s)$ implies that $u(s, 0) = 0$, and thus the partial derivative with respect to s at $z = 0$ vanishes as well, i.e. $u_s(s, 0) = 0$. From (C.2.1) one finds the two vectors tangent to the surface by taking the derivative with respect to s and z

$$t_1 = E_s(s, z) = \big(0, w(s, z)\widetilde{T} + u_s\widetilde{N}\big) \qquad\qquad t_2 = E_z(s, z) = \big(1, u_z\widetilde{N}\big) \tag{C.2.2}$$

where we have introduced $w(s, z) = 1 - k(s)u(s, z)$, being $k(s)$ the geodesic curvature of the entangling curve $\boldsymbol{x}_A(s)$.

The scalar product of the vectors in (C.2.2) provides the metric $\tilde{h}_{ab}$ (and the its inverse $\tilde{h}^{ab}$) induced on the surface by the embedding (C.2.1)

$$\tilde{h}_{ab} = \begin{pmatrix} w^2 + u_s^2 & u_z u_s \\ u_z u_s & 1 + u_z^2 \end{pmatrix} \qquad\qquad \tilde{h}^{ab} = \frac{1}{\tilde{h}} \begin{pmatrix} 1 + u_z^2 & -u_z u_s \\ -u_z u_s & w^2 + u_s^2 \end{pmatrix} \tag{C.2.3}$$

where $\tilde{h} = \det(\tilde{h}_{ab}) = u_s^2 + w^2(1 + u_z^2)$. The inward unit normal vector $\tilde{n}_\mu$ can be evaluated by taking the normalized wedge product of t_1 and t_2, finding that

$$\tilde{n}^\mu = \frac{(t_1 \wedge t_2)^\mu}{|t_1 \wedge t_2|} = \frac{1}{\sqrt{\tilde{h}}} \Big(- u_z w \,, - u_s \widetilde{T} + w\widetilde{N} \Big) \,. \tag{C.2.4}$$

In order to study the behaviour of the minimal surface $\hat{\gamma}_A$ near the boundary $z = 0$, we expand the function $u = u(s,z)$ in a power series of z about $z = 0$ as follows

$$u(s,z)=\frac{U_2(s)}{2}\,z^2+\frac{U_3(s)}{3!}\,z^3+\frac{U_4(s)}{4!}\,z^4+\dots+z^{\alpha}\left[\mathcal{U}_{\alpha}(s)+\mathcal{U}_{\alpha+1}(s)\,z+\mathcal{U}_{\alpha+2}(s)\,\frac{z^2}{2!}+\dots\right] \tag{C.2.5}$$

where we have assumed that this expansion may contain both an analytic and a non-analytic part, in order to be consistent with the non-analytic behaviour of the bulk metric near the boundary. The non-analytic component is controlled by a real exponent α. The boundary condition $u(s,0) = 0$ has been employed to set $U_0(s) = 0$ in (C.2.5). Instead, the requirement that γ_A intersects orthogonally the plane $z = 0$ leads to $U_1(s) = 0$ and $\alpha > 1$. In fact, if we use the expression in (C.2.2) for t_2^{μ}, we immediately recognize that this condition translates into $u_z(s,0) = 0$, which in turn entails the above two constraints. In the following we shall adopt the stronger requirement $\alpha \geqslant d_\theta + 1$. This ensures that the structure of the divergences is determined only by the analytical part of the expansion and, moreover, it is automatically satisfied by a minimal surface, as discussed below.

From (C.2.3), we can easily write the regularized area functional as follows

$$\mathcal{A}[\gamma_{A,\varepsilon}] = \int_{\gamma_{A,\varepsilon}} \frac{1}{z^{d_\theta}}\,\sqrt{\tilde{h}}\,d\Sigma \,=\int_{\gamma_{A,\varepsilon}} \frac{1}{z^{d_\theta}}\,\sqrt{u_s^2+w^2(1+u_z^2)}\,ds\,dz \tag{C.2.6}$$

where $\gamma_{A,\varepsilon} \equiv \gamma_A \cap \{z \geqslant \varepsilon\}$. Assuming that the embedding function $u(s,z)$ can be expanded as in (C.2.5) (with $\alpha \geqslant d_\theta + 1$), for the leading contributions as $z \to 0$ we obtain

$$\begin{aligned}\mathcal{A}[\gamma_{A,\varepsilon}] \,=& \int_{\partial\gamma_{A,\varepsilon}} ds \int_{\varepsilon}^{z_{\max}} \frac{1}{z^{d_\theta}} \Big[1+\frac{z^2}{4}\big(-2k(s)\,U_2(s)+U_2'(s)+2\,U_2(s)^2\big) \\ &+\frac{z^3}{12}\big(-2k(s)\,U_3(s)+6\,U_2(s)U_3(s)+U_3'(s)\big)+\mathcal{O}\big(z^4\big)\Big]\,dz\end{aligned} \tag{C.2.7}$$

which contains divergent terms only if $d_\theta \geqslant 1$. The integration of the first term within the expansion between square bracket provides the leading divergence (4.1.10), where the perimeter P_A of the entangling curve comes from the integration over s. The subleading terms are obtained by performing the integration over z in the remaining terms in the expansion (C.2.7). This leads to

$$\begin{aligned}\mathcal{A}[\gamma_A] \,=&\, \frac{P_A}{(d_\theta-1)\varepsilon^{d_\theta-1}}+\frac{1}{2(d_\theta-3)\varepsilon^{d_\theta-3}}\int_{\partial A}[U_2(s)-k(s)]\,U_2(s)\,ds \\ &+\frac{1}{6(d_\theta-4)\varepsilon^{d_\theta-4}}\int_{\partial A}[3U_2(s)-k(s)]\,U_3(s)\,ds+\mathcal{O}\big(\max\{1/\varepsilon^{d_\theta-5},1\}\big) \qquad d_\theta\notin\mathbb{N}\,.\end{aligned} \tag{C.2.8}$$

When $d_\theta = n \in \mathbb{N}$ is a positive integer, this expansion still holds except for a crucial modification of the $O(\varepsilon^{n-d_\theta})$ term, where $1/[(d_\theta-n)\varepsilon^{d_\theta-n}]$ has to be replaced with $\log\varepsilon$. For instance, when $d_\theta = 3$ we obtain

$$\mathcal{A}[\gamma_A] = \frac{P_A}{2\,\varepsilon^2}-\frac{\log\varepsilon}{2}\int_{\partial A} ds\;[U_2(s)-k(s)]\,U_2(s)+\mathcal{O}(1)\,. \tag{C.2.9}$$

In the above analysis, we considered surfaces γ_A whose smooth boundary is $\partial\gamma_A = \partial A$, that intersect orthogonally the boundary plane $z = 0$ and which are not necessarily minimal.

Moreover, we have assumed that the embedding function $u(s,z)$ defined in (C.2.1) admits an expansion of the form (C.2.5) close to $z=0$ with $\alpha \geqslant 0$. In the following we specialize to surfaces $\hat{\gamma}_A$ that are extrema of the area functional (4.1.7), namely to surfaces whose mean curvature vanishes everywhere (see (4.1.8)) or, equivalently, which obey (4.1.9).

In terms of the parameterisation introduced in (C.2.1), the second fundamental form $\widetilde{K}_{ab}$ reads

$$\widetilde{K}_{ab} = -\,\tilde{h}^{-1} \begin{pmatrix} w(u_{ss}+kw)-u_s(w_s-ku_s) & wu_{zs}+ku_z u_s \\ wu_{zs}+ku_z u_s & wu_{zz} \end{pmatrix} . \tag{C.2.10}$$

Taking the trace of (C.2.10), we can translate the extremality condition (4.1.8) into the following second order partial differential equation for $u(s,z)$

$$\begin{aligned} &(1+u_z^2)\big[w(u_{ss}+k\,w)-u_s(w_s-k\,u_s)\big]-2\,u_z\,u_s\big(w\,u_{zs}+k\,u_z u_s\big)+w\,u_{zz}\big(w^2+u_s^2\big) \\ &= d_\theta \frac{u_z w}{z}\left[u_s^2+w^2(1+u_z^2)\right] \end{aligned} \tag{C.2.11}$$

with the boundary conditions $u(s,0)=0$.

We can employ the expansion (C.2.5) to solve the equation (C.2.11) order by order in z. Even if $U_1(s)=0$ is not assumed in (C.2.5), the vanishing of the leading term in the sector of the expansion of (C.2.11) with integer powers implies $U_1(s)=0$. In other words, an extremal surface is necessarily orthogonal to the boundary. Instead, the vanishing of the leading term in the non-analytic sector of the expansion of (C.2.11), where the powers depend on α, determines the value of α to be $d_\theta+1$. The associated coefficient $\mathcal{U}_\alpha(s)$ in (C.2.5) cannot be determined through this local analysis near the boundary because it encodes global properties of $\hat{\gamma}_A$. On the other hand, (C.2.11) allows us to determine the analytical part of the expansion (C.2.5) recursively. For the lowest coefficients of an extremal surface $\hat{\gamma}_A$, we find

$$U_2(s) = \frac{k(s)}{d_\theta - 1} \qquad d_\theta \neq 1 \tag{C.2.12a}$$

$$U_3(s) = 0 \qquad d_\theta \neq 2 \tag{C.2.12b}$$

$$U_4(s) = \frac{3k''(s)}{(d_\theta-1)(d_\theta-3)} + \frac{3(d_\theta^2-2d_\theta-1)}{(d_\theta-1)^3\,(d_\theta-3)}\,k^3(s) \qquad d_\theta \neq 1,3 \tag{C.2.12c}$$

$$U_5(s) = 0 \qquad d_\theta \neq 4\,. \tag{C.2.12d}$$

The integer values of d_θ require a separate analysis. For even values of d_θ, the non-analytical sector in (C.2.5) disappears and in general the odd coefficients $U_{d_\theta+2n+1}(s)$ (with $n \geqslant 0$) can be non-vanishing. In particular, this local analysis leaves $U_{d_\theta+1}(s)$ undetermined, as above. When d_θ is an odd integer, it is necessary to introduce terms of the form $z^{d_\theta+1+n}\log z$ in the expansion (C.2.5) in order to satisfy the extremality condition (C.2.11). However, these additional terms do not contribute to the divergent part of $\mathcal{A}[\gamma_A]$, hence they can be neglected in the present discussion.

Finally, by plugging the expressions in (C.2.12) into the expansions (C.2.8) and (C.2.9), one obtains the subleading divergent contributions in (4.1.13) and (4.1.14).

C.2.1 Asymptotic hvLif$_4$ black hole

In the above analysis, we have investigated the UV divergent terms in the expansion of the holographic entanglement entropy when the bulk metric $\tilde{g}_{\mu\nu}$ of $\widetilde{\mathcal{C}}_3$ is flat. However, since the leading divergence in (4.1.10) is completely determined by the value of $\sqrt{\tilde{h}}$ on the boundary curve $\partial\hat{\gamma}_A$, i.e. $\tilde{h}|_{z=0} = 1$, the expansion of the area of the minimal surface is given by (4.1.10) for any metric $g_{\mu\nu}$ satisfying (4.1.3). Instead, the subleading divergent terms in the expansion (4.1.10) can be different from the ones occurring for the hvLif$_4$ spacetime. Thus, in the expansion $g_{\mu\nu}(z,\boldsymbol{x}) = g^{\text{hvLif}}_{\mu\nu}(\boldsymbol{x}) + \delta g^{(1)}_{\mu\nu}(\boldsymbol{x})z + \delta g^{(2)}_{\mu\nu}(\boldsymbol{x})z^2 + \dots$ of the metric near the plane $z=0$, the occurrence of the terms $\delta g^{(n)}_{\mu\nu}$ might lead to important modifications of the analysis presented above (e.g. (C.2.12) are expected to be modified). In this appendix, we address this issue in a concrete example where the asymptotic behaviour of the metric near the boundary is given by a black hole geometry with hyperscaling violation.

Considering the general metric (C.1.1) with $A(z), B(z)$ and $f(z)$ given by (C.1.4), the induced metric $g_{\mu\nu}$ on $\mathcal{C}_3$ reads

$$ds^2 = \frac{1}{z^{d_\theta}}\left(\frac{dz^2}{f(z)} + dx^2 + dy^2\right) \qquad\qquad f(z) = 1 - (z/z_h)^{\chi_1} + a\, z^{\chi_2}\,. \tag{C.2.13}$$

The parametrization (C.2.1) for $\hat{\gamma}_A \subset \widetilde{\mathcal{C}}_3$ allows to write the unit normal vector as follows

$$\tilde{n}^\mu = \frac{1}{\sqrt{u_s^2 + w^2[1+u_z^2 f(z)]}}\Big(-\,u_z\, w f(z)\,,\, -\,u_s\,\widetilde{T} + w\widetilde{N}\Big)\,. \tag{C.2.14}$$

By expressing $\tilde{n}^\mu$ in terms of the unit normal vector $\tilde{n}^\mu_{\text{hvLif}}$ corresponding to $f(z)\equiv 1$, one finds

$$\tilde{n}^\mu = C\big(\,\tilde{n}^z_{\text{hvLif}}\, f(z)\,,\, \tilde{n}^{\boldsymbol{x}}_{\text{hvLif}}\,\big) \qquad\qquad C \equiv \frac{\sqrt{\tilde{h}_{\text{hvLif}}}}{\sqrt{u_s^2 + w^2[1+u_z^2 f(z)]}} \tag{C.2.15}$$

where $\tilde{h}_{\text{hvLif}}$ is the determinant of the induced metric for hvLif$_4$. Thus, for the trace of the second fundamental form we have

$$\begin{aligned} \text{Tr}\widetilde{K} = \widetilde{\nabla}_\alpha \tilde{n}^\alpha &= C^{-1}\tilde{n}^\alpha \partial_\alpha C + C\,\widetilde{\nabla}_\alpha\big(C^{-1}\tilde{n}^\alpha\big) \\ &= C^{-1}\tilde{n}^\alpha \partial_\alpha C + C\big(\partial_{\boldsymbol{x}}\tilde{n}^{\boldsymbol{x}}_{\text{hvLif}} + \partial_z \tilde{n}^z_{\text{hvLif}} f(z) + \frac{1}{2}\tilde{n}^z_{\text{hvLif}} f'(z)\big) \end{aligned} \tag{C.2.16}$$

where we used that, for the metric (C.2.13), the following result holds

$$\Gamma^\alpha_{\alpha\mu}\,\tilde{n}^\mu = -\,\frac{C}{2}\, f'(z)\,\tilde{n}^z_{\text{hvLif}}\,. \tag{C.2.17}$$

The extremal surfaces $\hat{\gamma}_A$ fulfil (4.1.9), which can be written as

$$C^{-2}\,\tilde{n}^\alpha\partial_\alpha C + \partial_{\boldsymbol{x}}\tilde{n}^{\boldsymbol{x}}_{\text{hvLif}} + f(z)\,\partial_z\tilde{n}^z_{\text{hvLif}} + \frac{1}{2}\, f'(z)\,\tilde{n}^z_{\text{hvLif}} = d_\theta\,\frac{f(z)}{z}\,\tilde{n}^z_{\text{hvLif}}\,. \tag{C.2.18}$$

Specialising (C.2.18) to the expression of $f(z)$ given in (C.2.13), we find that the equation solved by extremal surfaces in hvLif$_4$ gets modified by $O(z^{\chi_1})$ and $O(z^{\chi_2})$ terms. Thus, for arbitrary exponents χ_1 and χ_2, the divergent terms in $\mathcal{A}[\hat{\gamma}_{A,\varepsilon}]$ are different from the ones discussed in Section 4.1.1. However, in the following, we show that for black hole geometries new divergencies do not occur because of the NEC.

The black hole geometry corresponds to $a = 0$ and $\chi_1 = d_\theta + \zeta$ in (C.2.13). In this case the NEC inequalities in (C.1.5) and (C.1.6) reduce to ones in (4.1.2). Since $d_\theta + \zeta \geqslant 0$, we also have $\zeta \geqslant 1$; hence for the cases of interest, where $d_\theta > 1$, we can assume $d_\theta + \zeta > 2$. Now we are ready to analyze the behaviour of the solution of (C.2.18) for small z. Since the leading behaviour of $\tilde{n}^z_{\text{hvLif}}$ for $z \to 0$ (see (C.2.5) and (C.2.4)) is given by $\tilde{n}^z_{\text{hvLif}} \simeq -U_2\, z + O(z^3)$, the extremality equation (C.2.18) in a black hole geometry differs from (C.2.11) by $O(z^{d_\theta+\zeta})$ terms. This implies that the putative expansion for the function $u(s,z)$, which solves (C.2.18), must also contain terms of the form $z^{d_\theta+\zeta+n}$ with $n \in \mathbb{N}$. An explicit calculation shows that the first new non-vanishing term occurs for $n = 2$ and its coefficient reads

$$\frac{d_\theta - \zeta - 2}{2(d_\theta - 1)(d_\theta + \zeta + 2)(d_\theta + \zeta + 1)}\, k(s)\,. \tag{C.2.19}$$

These new terms, which scale at least like $z^{d_\theta+\zeta+2}$, cannot contribute to the divergent part of the holographic entanglement entropy. Thus, the analysis performed for hvLif$_4$ remains valid also for the black hole geometry.

C.3 On the finite term

In this appendix, we describe the details of the derivation of the results presented in Section 4.1.2.

Considering a constant time slice $\mathcal{C}_3$ of an asymptotically hvLif$_4$ spacetime endowed with the metric $g_{\mu\nu}$, the asymptotically flat metric $\tilde{g}_{\mu\nu}$ of the conformally equivalent space $\widetilde{\mathcal{C}}_3$ is related to $g_{\mu\nu}$ through the relation $g_{\mu\nu} = e^{2\varphi}\tilde{g}_{\mu\nu}$. At the beginning of 2 we have shown, by following [78], that for any surface (not necessarily anchored to a curve on the boundary) the following identity holds (see equation (2.1.10))

$$\Big(\widetilde{\mathcal{D}}^2\varphi - \widetilde{\nabla}^2\varphi + \tilde{n}^\mu\tilde{n}^\nu\widetilde{\nabla}_\mu\widetilde{\nabla}_\nu\varphi - (\tilde{n}^\lambda\partial_\lambda\varphi)^2 - \frac{1}{4}(\mathrm{Tr}\widetilde{K})^2\Big)d\tilde{\mathcal{A}} + \frac{1}{4}(\mathrm{Tr}K)^2 d\mathcal{A} = 0 \tag{C.3.1}$$

where the tilded quantities are evaluated considering $\widetilde{\mathcal{C}}_3$ as embedding space, while $\mathcal{C}_3$ is the embedding space for the untilded ones. In particular, $\mathrm{Tr}K$ and $\mathrm{Tr}\widetilde{K}$ are the mean curvatures of γ_A computed in the two embedding spaces, while $d\mathcal{A}$ and $d\widetilde{\mathcal{A}}$ are the two area elements. Denoting by $\tilde{n}^\nu$ the versor perpendicular to the surface γ_A viewed as a submanifold of $\widetilde{\mathcal{C}}_3$, the covariant derivative $\widetilde{\nabla}$ is the one defined in $\widetilde{\mathcal{C}}_3$ while $\widetilde{\mathcal{D}}$ is the one induced on the surface γ_A by the embedding space $\widetilde{\mathcal{C}}_3$.

Let us focus on surfaces γ_A anchored orthogonally to ∂A, which are not necessarily extremal surfaces. The first term in the left-hand side of (C.3.1) is a total derivative; hence it yields a boundary term when integrated over γ_A. As we will discuss in detail later in this Appendix, the main step to construct a finite area functional is to multiply both sides of (C.3.1) by a suitable term that makes this total derivative the only source of the type of divergences discussed in Section 4.1.1 when the integration over γ_A is carried out. Our analysis follows slightly different paths, depending on the ranges of d_θ. In particular, we consider separately the ranges $1 < d_\theta < 3$ and $3 < d_\theta < 5$. The special cases $d_\theta = 3$ and $d_\theta = 5$, where a logarithmic divergence occurs, can be studied as limiting cases.

C.3.1 Regime $1 < d_\theta < 3$

In order to find the finite term in the expansion (4.1.12) of the area of the surfaces γ_A anchored orthogonally to ∂A (not necessarily extremal), first we multiply the identity (C.3.1) by a factor $c_1 e^{2\phi}$, where ϕ is a function of the coordinates and c_1 is a numerical constant to be determined. Then, integrating the resulting expression over the surface $\gamma_{A,\varepsilon} \equiv \gamma_A \cap \{z \geqslant \varepsilon\}$, one finds

$$\begin{aligned}
0 = {}& c_1 \int_{\gamma_{A,\varepsilon}} e^{2\phi}\Big(\widetilde{\mathcal{D}}^2\varphi - \widetilde{\nabla}^2\varphi + \tilde{n}^\mu\tilde{n}^\nu\widetilde{\nabla}_\mu\widetilde{\nabla}_\nu\varphi - (\tilde{n}^\lambda\partial_\lambda\varphi)^2 - \frac{1}{4}(\mathrm{Tr}\widetilde{K})^2\Big)d\tilde{\mathcal{A}} \\
&+ c_1 \int_{\gamma_{A,\varepsilon}} e^{2\phi}\frac{1}{4}(\mathrm{Tr}K)^2 d\mathcal{A}\,. \qquad \text{(C.3.2)}
\end{aligned}$$

By adding the area functional of γ_A to both sides of this identity, we get

$$\begin{aligned}
\mathcal{A}[\gamma_{A,\varepsilon}] = {}& c_1 \int_{\gamma_{A,\varepsilon}} e^{2\phi}\Big(\widetilde{\mathcal{D}}^2\varphi - \widetilde{\nabla}^2\varphi + \tilde{n}^\mu\tilde{n}^\nu\widetilde{\nabla}_\mu\widetilde{\nabla}_\nu\varphi - (\tilde{n}^\lambda\partial_\lambda\varphi)^2 - \frac{1}{4}(\mathrm{Tr}\widetilde{K})^2\Big)d\tilde{\mathcal{A}} \\
&+ \int_{\gamma_{A,\varepsilon}} e^{2\varphi} d\tilde{\mathcal{A}} + \frac{c_1}{4}\int_{\gamma_{A,\varepsilon}} e^{2\phi}(\mathrm{Tr}K)^2\, d\mathcal{A}\,. \qquad \text{(C.3.3)}
\end{aligned}$$

The first term of the first integrand can be arranged as a divergence minus a term that does not contain second derivatives as follows

$$e^{2\phi}\,\widetilde{\mathcal{D}}^2\varphi = \widetilde{\mathcal{D}}^\mu(e^{2\phi}\partial_\mu\varphi) - 2\,e^{2\phi}\tilde{h}^{\mu\nu}\partial_\nu\phi\,\partial_\mu\varphi\,. \qquad \text{(C.3.4)}$$

At this point, Stokes' theorem can be employed to transform the integration over the divergence in (C.3.4) into an integral over the boundary of $\gamma_{A,\varepsilon}$. Thus, (C.3.3) becomes

$$\begin{aligned}
\mathcal{A}[\gamma_{A,\varepsilon}] = {}& c_1 \int_{\partial\gamma_{A,\varepsilon}} e^{2\phi}\,\tilde{b}^\mu\partial_\mu\varphi\, d\tilde{s} + \int_{\gamma_{A,\varepsilon}} e^{2\varphi}d\tilde{\mathcal{A}} + \frac{c_1}{4}\int_{\gamma_{A,\varepsilon}} e^{2\phi}(\mathrm{Tr}K)^2 d\mathcal{A} \qquad \text{(C.3.5)} \\
&- c_1\int_{\gamma_{A,\varepsilon}} e^{2\phi}\Big(2\tilde{h}^{\mu\nu}\partial_\nu\phi\partial_\mu\varphi + \widetilde{\nabla}^2\varphi - \tilde{n}^\mu\tilde{n}^\nu\widetilde{\nabla}_\mu\widetilde{\nabla}_\nu\varphi + (\tilde{n}^\lambda\partial_\lambda\varphi)^2 + \frac{1}{4}(\mathrm{Tr}\widetilde{K})^2\Big)d\tilde{\mathcal{A}}
\end{aligned}$$

where $\tilde{b}^\mu$ is the outward pointing unit vector normal to the boundary curve. The function ϕ and the constant c_1 can be fixed by requiring that the divergence originating from the boundary term in (C.3.5) as $\varepsilon \to 0$ matches the divergence in (4.1.12). The limit $\varepsilon \to 0$ of the remaining terms provides the finite contribution $\mathcal{F}_A$ in (4.1.12).

As for the vector $\tilde{b}^\mu$ normal to the boundary of $\gamma_{A,\varepsilon}$, it has the same direction of the vector t_2^μ in (C.2.2). This gives

$$\tilde{b}^\mu = \frac{-1}{\sqrt{1+u_z^2}}\,\big(1, u_z\widetilde{N}\big) \qquad \text{(C.3.6)}$$

whose expansion as $\varepsilon \to 0$ reads

$$\tilde{b}^\mu = \Big(-1 + \frac{\varepsilon^2}{2}\,U_2^2 + O(\varepsilon^4), -U_2\,\widetilde{N}\,\varepsilon + O\big(\varepsilon^3\big)\Big)\,. \qquad \text{(C.3.7)}$$

This expansion can be used to determine the behaviour of the boundary term in (C.3.5), finding

$$c_1 \int_{\partial\gamma_{A,\varepsilon}} e^{2\phi}\, \tilde{b}^\mu \partial_\mu \varphi \, d\tilde{s} = -\frac{c_1 d_\theta P_A}{2\varepsilon}\, e^{2\phi(\varepsilon)} + O(\varepsilon^a) \tag{C.3.8}$$

where

$$\varphi = -\frac{d_\theta}{2} \log z \tag{C.3.9}$$

and a is determined by the specific choice of ϕ. By imposing consistency between the leading divergence in (4.1.12) and (C.3.8), one obtains

$$\phi = \frac{2 - d_\theta}{2} \log z + O(z^2) \qquad c_1 = \frac{2}{d_\theta(d_\theta - 1)}\,. \tag{C.3.10}$$

By considering the expressions of φ in (C.3.9) and of ϕ in (C.3.10), together with the expansion in (C.3.7), the integral (C.3.8) leads to $a = 3 - d_\theta$. Notice that the leading singular behaviour of ϕ vanishes identically when $d_\theta = 2$. The sum of the remaining terms in (C.3.5) must be finite; hence we can safely remove the cutoff ε, obtaining the expression (4.1.17) for the finite term.

We remark that (4.1.17) holds for surfaces γ_A that intersect orthogonally $\partial\mathcal{C}_3$ and that this class includes the extremal surfaces. For extremal surfaces, (4.1.8) and (4.1.9) can be employed to simplify (4.1.17), which reduces to (4.1.18). In the special case of $d_\theta = 2$, the expression (4.1.18) simplifies further to the formula valid for the asymptotically AdS$_4$ backgrounds found in [78].

C.3.2 Regime $3 < d_\theta < 5$

In this range of d_θ we limit our analysis to the case of extremal surfaces because the condition of orthogonal intersection with the boundary does not fix the structure of the divergences completely. Instead, for extremal surfaces anchored to ∂A we can have only two types of divergences as $\varepsilon \to 0$, and they are of the form occurring in (4.1.14). To single out these singular terms, we multiply both sides of the identity (C.3.1) by the following factor

$$c_1 e^{2\phi} + c_2 e^{2\psi} (\mathrm{Tr}\widetilde{K})^2 \tag{C.3.11}$$

where c_1 ans c_2 are numerical coefficients and $e^{2\phi}$ and $e^{2\psi}$ are functions of the coordinates to be determined. Integrating the resulting expression over $\hat{\gamma}_{A,\varepsilon}$ and then adding the area $\mathcal{A}[\hat{\gamma}_{A,\varepsilon}]$ to both sides, we obtain

$$\begin{aligned}\mathcal{A}[\hat{\gamma}_A] = & \int_{\hat{\gamma}_{A,\varepsilon}} \Big(c_1 e^{2\phi} + c_2 e^{2\psi} (\mathrm{Tr}\widetilde{K})^2 \Big) \Big(\widetilde{\mathcal{D}}^2 \varphi - \widetilde{\nabla}^2 \varphi + \tilde{n}^\mu \tilde{n}^\nu \widetilde{\nabla}_\mu \widetilde{\nabla}_\nu \varphi - (\tilde{n}^\lambda \partial_\lambda \varphi)^2 - \frac{1}{4} (\mathrm{Tr}\widetilde{K})^2 \Big) d\tilde{\mathcal{A}} \\ & + \int_{\hat{\gamma}_{A,\varepsilon}} e^{2\varphi}\, d\tilde{\mathcal{A}} \end{aligned} \tag{C.3.12}$$

where the equation of motion $\mathrm{Tr}K = 0$ has been used. As done in Section C.3.1, let us rewrite the term proportional to $\widetilde{\mathcal{D}}^2\varphi$ as a total divergence minus residual contributions. In particular, we have

$$\begin{aligned}\Big(c_1 e^{2\phi} + c_2 e^{2\psi} (\mathrm{Tr}\widetilde{K})^2 \Big) \widetilde{\mathcal{D}}^2 \varphi = \; & \widetilde{\mathcal{D}}^\mu \big[\, c_1\, e^{2\phi} \partial_\mu \varphi + c_2\, e^{2\psi} \big(\mathrm{Tr}\widetilde{K}\big)^2 \partial_\mu \varphi \,\big] - 2\, c_1\, e^{2\phi} \tilde{h}^{\mu\nu} \partial_\mu \phi \partial_\nu \varphi \\ & - 2\, c_2\, e^{2\psi} (\mathrm{Tr}\widetilde{K})^2 \tilde{h}^{\mu\nu} \partial_\mu \psi \partial_\nu \varphi - 2\, c_2\, e^{2\psi} \big(\mathrm{Tr}\widetilde{K}\big)\, \tilde{h}^{\mu\nu} \partial_\mu \big(\mathrm{Tr}\widetilde{K}\big) \partial_\nu \varphi\,. \end{aligned}$$

Plugging this expression back into (C.3.12), we can write the area of $\hat{\gamma}_{A,\varepsilon}$ in the following form

$$\mathcal{A}[\hat{\gamma}_{A,\varepsilon}] = \int_{\hat{\gamma}_{A,\varepsilon}} \widetilde{\mathcal{D}}^{\mu} J_{\mu} \, d\tilde{\mathcal{A}} - \mathscr{F}_{A,\varepsilon} \tag{C.3.13}$$

where

$$J_{\mu} = c_1 \, e^{2\phi} \partial_{\mu}\varphi + c_2 \, e^{2\psi} \big(\mathrm{Tr}\widetilde{K}\big)^2 \partial_{\mu}\varphi \tag{C.3.14}$$

and $\mathscr{F}_{A,\varepsilon}$ contains all the remaining terms. By Stokes' theorem, the integral of the divergence turns into a line integral over the boundary curve

$$\int_{\hat{\gamma}_{A,\varepsilon}} \widetilde{\mathcal{D}}^{\mu} J_{\mu} \, d\tilde{\mathcal{A}} = \int_{\partial\hat{\gamma}_{A,\varepsilon}} \tilde{b}^{\mu} J_{\mu} d\tilde{s} = \int_{\partial\hat{\gamma}_{A,\varepsilon}} \Big(c_1 \, e^{2\phi} \, \tilde{b}^{\mu} \partial_{\mu}\varphi + c_2 \, e^{2\psi} \big(\mathrm{Tr}\widetilde{K}\big)^2 \, \tilde{b}^{\mu} \partial_{\mu}\varphi \Big) d\tilde{s} \, . \tag{C.3.15}$$

The first term occurs also in (C.3.8) and it contains the leading divergence of $\mathcal{A}[\hat{\gamma}_{A,\varepsilon}]$. Thus, we must choose $e^{2\phi}$ and c_1 as in (C.3.10). Then we fix c_2 and $e^{2\psi}$ so that the boundary term (C.3.15) reproduces also the subleading divergence in (4.1.14). Specifically, if we use the explicit expressions of c_1, of $e^{2\phi}$ and the extremal equation (4.1.9), we can rewrite the above boundary term as follows

$$\int_{\partial\hat{\gamma}_{A,\varepsilon}} \tilde{b}^{\mu} J_{\mu} d\tilde{s} = - \int_{\partial\hat{\gamma}_{A,\varepsilon}} \tilde{b}^{z} \left(\frac{\varepsilon^{1-d_\theta}}{d_\theta - 1} + c_2 \, e^{2\psi} d_\theta^3 \, \frac{(\tilde{n}^z)^2}{2\varepsilon^3} \right) d\tilde{s} \, . \tag{C.3.16}$$

From the analysis reported in Appendix 4.1.1, we obtain the following expansions as $z \to 0$

$$\tilde{b}^z = -1 + \frac{U_2(s)^2}{2} \, z^2 + O(z^4) \tag{C.3.17a}$$

$$\tilde{n}^z = -U_2(s) \, z + O(z^3) \tag{C.3.17b}$$

$$d\tilde{s} = \left(1 - \frac{k(s) \, U_2(s)}{2} \, z^2 + O(z^4) \right) ds \tag{C.3.17c}$$

where $U_2(s)$ is given in (C.2.12a). Plugging (C.3.17) into (C.3.16) and collecting the terms containing $k(s)^2$, we get

$$\begin{aligned} \int_{\partial\hat{\gamma}_{A,\varepsilon}} \tilde{b}^{\mu} J_{\mu} \, d\tilde{s} &= \int_{\partial\hat{\gamma}_{A,\varepsilon}} \left(1 - \frac{U_2^2}{2} \, \varepsilon^2 \right) \left(\frac{\varepsilon^{1-d_\theta}}{d_\theta - 1} + c_2 \, e^{2\psi} d_\theta^3 \, \frac{U_2^2}{2\varepsilon} \right) \left(1 - \frac{U_2 \, k}{2} \, \varepsilon^2 \right) ds \\ &= \frac{P_A}{(d_\theta - 1) \, \varepsilon^{d_\theta - 1}} - \int_{\partial\hat{\gamma}_{A,\varepsilon}} \left(\frac{\varepsilon^{3-d_\theta}}{2(d_\theta - 1)^3} - \frac{c_2 \, d_\theta^3 \, e^{2\psi}}{2(d_\theta - 1)^2 \varepsilon} + \frac{\varepsilon^{3-d_\theta}}{2(d_\theta - 1)^2} \right) k^2 \, ds \\ &= \frac{P_A}{(d_\theta - 1) \, \varepsilon^{d_\theta - 1}} + \frac{1}{2(d_\theta - 1)^2 \, \varepsilon^{d_\theta - 3}} \left(c_2 d_\theta^3 e^{2\psi} \varepsilon^{d_\theta - 4} - \frac{d_\theta}{d_\theta - 1} \right) \int_{\partial\hat{\gamma}_{A,\varepsilon}} k^2 \, ds \, . \end{aligned} \tag{C.3.18}$$

The simplest choice to obtain the right subleading divergence in (4.1.14) is given by

$$c_2 = -\frac{2}{d_\theta^3 (d_\theta - 3)(d_\theta - 1)} \qquad e^{2\psi} = z^{4-d_\theta} \big(1 + O(z^2) \big) \, . \tag{C.3.19}$$

Since the boundary integral (C.3.18) with the substitutions (C.3.19) yields all the correct divergences of the area as $\varepsilon \to 0$, the sum of the remaining terms is finite in this limit and provides the finite contribution $\mathscr{F}_A$ to $\mathcal{A}[\hat\gamma_{A,\varepsilon}]$. After some simple algebraic manipulations, $\mathscr{F}_A$ can be expressed as in (4.1.19).

The procedure to subtract the divergences and consequently to write down a finite functional F_A is not unique. Instead of adding a second exponential weighted by the $(\mathrm{Tr}K)^2$, we could have achieved the same result by tuning the subleading in the expansion of ϕ. For instance, if we choose

$$\phi = \frac{2-d_\theta}{2}\,\log z - \frac{k(s)^2}{(d_\theta-3)(d_\theta-1)^2}\,z^2 + O(z^4) \tag{C.3.20}$$

the functional (4.1.18) would produce the correct result in the entire interval $1 < d_\theta < 5$. It would be interesting to find a geometrical interpretation of (C.3.20).

C.3.3 HvLif$_4$

In hvLif$_4$, we have that $\tilde g_{\mu\nu} = \delta_{\mu\nu}$ and this leads to drastic simplifications in (4.1.18) and (4.1.19).

As for F_A in (4.1.18), we observe that the following combination of terms vanishes identically (for any d_θ)

$$\widetilde{\nabla}^2\varphi + 2\,\tilde g^{\mu\nu}\,\partial_\nu\phi\,\partial_\mu\varphi - \frac{d_\theta(d_\theta-1)}{2}\,e^{2(\varphi-\phi)} = \frac{1}{2z^2}\Big(d_\theta + d_\theta(d_\theta-2) - d_\theta(d_\theta-1)\Big) = 0\,. \tag{C.3.21}$$

The remaining terms can be written through $\tilde n^z$ as follows

$$\tilde n^\mu\tilde n^\nu\widetilde{\nabla}_\mu\widetilde{\nabla}_\nu\varphi = d_\theta\,\frac{(\tilde n^z)^2}{2z^2}\qquad (\mathrm{Tr}\widetilde{K})^2 = d_\theta^2\,\frac{(\tilde n^z)^2}{z^2}\qquad \tilde n^\mu\tilde n^\nu\partial_\nu\phi\,\partial_\mu\varphi = d_\theta(d_\theta-2)\,\frac{(\tilde n^z)^2}{4z^2}\,. \tag{C.3.22}$$

The above observations allow to write F_A in the form (4.1.22) or (4.1.23).

Next, we show that $\mathscr{F}_A$ in (4.1.19) simplifies to (4.1.26) for the hvLif$_4$ geometry. First, we find it useful to decompose f in (4.1.20) as the following sum

$$f = f_0 + f_n \tag{C.3.23}$$

where f_0 includes the terms that do not contain the vector $\tilde n^\mu$, namely

$$f_0 = -\,\widetilde{\nabla}^2\varphi - 2\,\tilde g^{\mu\nu}\partial_\mu\psi\,\partial_\nu\varphi \tag{C.3.24}$$

while the terms containing $\tilde n^\mu$ are collected into f_n. Then, the combination

$$F_A - c_2\int_{\hat\gamma_A} e^{2\psi}(\mathrm{Tr}\widetilde{K})^2 f_0\, d\tilde{\mathcal{A}} \tag{C.3.25}$$

in $\mathscr{F}_A$ can be shown to vanish identically when $\tilde g_{\mu\nu} = \delta_{\mu\nu}$ with the help of (4.1.22) and (C.3.22). In fact, we find

$$F_A - c_2\int_{\hat\gamma_A} e^{2\psi} f_0(\mathrm{Tr}\widetilde{K})^2 d\tilde{\mathcal{A}} = \frac{1}{d_\theta-1}\int_{\hat\gamma_A}\frac{(\tilde n^z)^2}{z^{d_\theta}}\,d\tilde{\mathcal{A}} + c_2\frac{d_\theta^3(d_\theta-3)}{2}\int_{\hat\gamma_A}\frac{(\tilde n^z)^2}{z^{d_\theta}}\,d\tilde{\mathcal{A}}\; = 0 \tag{C.3.26}$$

where in the last equality we used the value of c_2 in (C.3.19). Thus the functional (4.1.19) for $\mathscr{F}_A$ collapses to

$$\mathscr{F}_A = -\,c_2 \int_{\hat{\gamma}_A} e^{2\psi}\Big(\big(\mathrm{Tr}\widetilde{K}\big)^2 f_n - 2(\mathrm{Tr}\widetilde{K})\tilde{h}^{\mu\nu}\partial_\mu(\mathrm{Tr}\widetilde{K})\partial_\nu\varphi\Big)d\tilde{\mathcal{A}} \tag{C.3.27}$$

with

$$f_n = \tilde{n}^\mu\tilde{n}^\nu\,\widetilde{\nabla}_\mu\widetilde{\nabla}_\nu\varphi - 2(\tilde{n}^\lambda\partial_\lambda\varphi)^2 + 2\tilde{n}^\mu\tilde{n}^\nu\partial_\mu\psi\partial_\nu\varphi \tag{C.3.28}$$

and reduces to (4.1.26) when $\tilde{g}_{\mu\nu}$ is the flat metric. We can also explicitly verify that the result (4.1.26) is finite in the limit $\varepsilon \to 0$. If we use the near boundary expansion (C.3.17b) of the normal vector, we can easily check that the integrand in first term of (4.1.26) is of order z^{4-d_θ} and it is convergent for $d_\theta < 5$. Then, assuming the parametrization (C.2.1), for the integrand in the second term of (4.1.26) one gets

$$\frac{\tilde{n}^z}{z^{d_\theta-2}}\,\tilde{h}^{z\mu}\,\partial_\mu\bigg(\frac{\tilde{n}^z}{z}\bigg) = \frac{\tilde{n}^z}{z^{d_\theta-2}}\,\tilde{h}^{zz}\,\partial_z\bigg(\frac{\tilde{n}^z}{z}\bigg) + \frac{\tilde{n}^z}{z^{d_\theta-2}}\,\tilde{h}^{zs}\,\partial_s\bigg(\frac{\tilde{n}^z}{z}\bigg)\,. \tag{C.3.29}$$

From (C.2.3) we know that near $z=0$ the inverse metric components are $\tilde{h}^{zz}=1+O(z^2)$ and $\tilde{h}^{zs} = O(z^3)$, so that we have the following behaviours

$$\frac{\tilde{n}^z}{z^{d_\theta-2}}\,\tilde{h}^{zz}\,\partial_z\bigg(\frac{\tilde{n}^z}{z}\bigg) \propto \frac{1}{z^{d_\theta-3}}\,\partial_z\bigg(\frac{U_2 z + O(z^3)}{z}\bigg) \propto z^{4-d_\theta} \qquad \frac{\tilde{n}^z}{z^{d_\theta-2}}\,\tilde{h}^{zs}\,\partial_s\bigg(\frac{\tilde{n}^z}{z}\bigg) \propto z^{6-d_\theta} \tag{C.3.30}$$

and both scalings provide convergent integrals for $d_\theta < 5$.

Consistency check of $\mathscr{F}_A$ for the strip

In this section we show that the functional $\mathscr{F}_A$ in (4.1.26) gives the expected result when $\hat{\gamma}_A$ is the extremal surface anchored to the infinite strip discussed in 4.4.1, when the gravitational background is (4.1.21) with $3 < d_\theta < 5$.

By employing the parametrization of Section 4.4.1, we find that (4.1.26) becomes

$$\begin{aligned}\mathscr{F}_A = \frac{4}{(d_\theta-1)(d_\theta-3)}\int_0^{L/2}\!\!\int_0^{\ell/2}\Bigg[\frac{2}{z^{d_\theta-2}}\bigg(1-\frac{1}{1+(z')^2}\bigg)\frac{1}{z'}\,\partial_x\bigg(\frac{1}{z\sqrt{1+(z')^2}}\bigg) \\ -\frac{3}{z^{d_\theta}}\,\frac{1}{(1+(z')^2)^{\frac{3}{2}}}\Bigg]\,dxdy\end{aligned} \tag{C.3.31}$$

where $\tilde{h}^{z\mu}\partial_\mu = \tilde{h}^{zz}\partial_z + \tilde{h}^{zy}\partial_y = (1-\tilde{n}^z\tilde{n}^z)(1/z')\partial_x$ has been used. The conserved quantity (1.5.15) allows to rewrite the (C.3.31) as

$$\mathscr{F}_A = -\,\frac{4}{(d_\theta-1)(d_\theta-3)}\int_0^{L/2}\!\!\int_0^{\ell/2}\Bigg[\frac{3}{z_*^{d_\theta}(1+(z')^2)} - \frac{2(d_\theta-1)\,(z')^2}{z_*^{d_\theta}(1+(z')^2)}\Bigg]\,dxdy \tag{C.3.32}$$

which can be further simplified by eliminating z' with the help of (1.5.15):

$$\mathscr{F}_A = -\,\frac{2L\,(2d_\theta+1)}{(d_\theta-1)(d_\theta-3)\,z_*^{3d_\theta}}\int_0^{\ell/2} z^{2d_\theta}\,dx + \frac{2L\ell}{(d_\theta-3)\,z_*^{d_\theta}}\,. \tag{C.3.33}$$

Now, we perform the integral in (C.3.33)

$$\int_0^{\ell/2} z^{2d_\theta} dx = \int_0^{z_*} \frac{z^{2d_\theta}\, dz}{\sqrt{(z_*/z)^{2d_\theta} - 1}} = \frac{\sqrt{\pi}\,\Gamma\Big(\frac{3}{2} + \frac{1}{2d_\theta}\Big)}{2d_\theta\,\Gamma\Big(2 + \frac{1}{2d_\theta}\Big)}\, z_*^{2d_\theta+1} = \frac{\ell(d_\theta+1)}{2(2d_\theta+1)}\, z_*^{2d_\theta} \tag{C.3.34}$$

where in the first step we changed integration variable first and then we used (1.5.15) again, while in the last step we employed the expression (1.5.16) for $\ell/2$. Finally, by plugging (C.3.34) in (C.3.33) we obtain the r.h.s. of (4.4.2).

We stress that the same result can be achieved by starting from the more general functional (4.1.19). Since the functional F_A in (4.1.19) is the same as the one in (4.1.18), it is sufficient to show that the remaining integral in (4.1.19) vanishes. This can be shown through a calculation similar to the one performed in this section.

C.4 On the finite term as an integral along the entangling curve

This appendix is devoted to an alternative and more field theoretical derivation of the expression (4.2.7) for the finite term written as an integral along the entangling curve. The method employed below is also discussed in [278].

Let us denote with $\hat\gamma$ an extremal m dimensional hypersurface embedded in $\mathcal{G}_{d+1}$ with tangent vectors t^μ_a, where $a = 1 \cdots m$. The area of $\hat\gamma$ is the integral

$$\mathcal{I} = \int_{\hat\gamma} \mathcal{L}[x^\mu(\sigma), \partial_b x^\mu(\sigma)] d^m\sigma \qquad \mathcal{L}[x^\mu(\sigma), \partial_b x^\mu(\sigma)] \equiv \sqrt{h} \tag{C.4.1}$$

where σ is a set of local coordinates on $\hat\gamma$ and $h = \det(t^\mu_a t^\nu_b g_{\mu\nu})$. Next, we assume that the metric $g_{\mu\nu}$ is endowed with a conformal Killing vector V^μ, namely, a vector field obeying the equation

$$\nabla_\mu V_\nu + \nabla_\nu V_\mu = \frac{2}{d}\, g_{\mu\nu} \nabla_\rho V^\rho \,. \tag{C.4.2}$$

This vector generates the infinitesimal coordinate transformation $x^\mu \to x^\mu + \epsilon V^\mu$, under which the volume form on $\hat\gamma$ transforms as

$$\delta\sqrt{h} = \frac{1}{2}\sqrt{h}\, h^{ab}\, \delta h_{ab} = \frac{1}{2}\sqrt{h}\, h^{ab}\, t^\mu_a t^\nu_b\, \delta g_{\mu\nu} \,. \tag{C.4.3}$$

The variation of the metric $g_{\mu\nu}$ is given by $\delta g_{\mu\nu} = \epsilon\, g_{\mu\nu} \nabla_\rho V^\rho$, hence the variation (C.4.3) can be rewritten as

$$\delta\sqrt{h} = \frac{\epsilon}{2}\sqrt{h}\, h^{ab} h_{ab} \nabla_\rho V^\rho = \epsilon\, \frac{m\,(2-d_\theta)}{2}\, \sqrt{h} \,. \tag{C.4.4}$$

Let us now suppose that the divergence of the vector V^μ is a constant c. The transformation law of the area of $\hat\gamma$ becomes

$$\delta\mathcal{I} = \epsilon\, \frac{m\, c}{2}\, \mathcal{I} \,. \tag{C.4.5}$$

The left-hand side of (C.4.5) can be cast into a total divergence as follows

$$\begin{aligned}\delta\mathcal{I} &= \int_{\hat\gamma}\left[\frac{\delta\mathcal{L}}{\delta x^\mu}\delta x^\mu + \frac{\delta\mathcal{L}}{\delta\partial_a x^\mu}\,\delta\partial_a x^\mu\right]d^m\sigma \\ &= \int_{\hat\gamma}\left[\left(\frac{\delta\mathcal{L}}{\delta x^\mu} - \partial_a\frac{\delta\mathcal{L}}{\delta\partial_a x^\mu}\right)\delta x^\mu + \partial_a\left(\frac{\delta\mathcal{L}}{\delta\partial_a x^\mu}\,\delta x^\mu\right)\right]d^m\sigma \\ &= \int_{\hat\gamma}\partial_a\left(\frac{\delta\mathcal{L}}{\delta\partial_a x^\mu}\,\delta x^\mu\right)d^m\sigma = \epsilon\int_{\hat\gamma}\partial_a\left(\frac{\delta\mathcal{L}}{\delta\partial_a x^\mu}\,V^\mu\right)d^m\sigma\end{aligned} \tag{C.4.6}$$

where the equations of motions and $\delta x^\mu = \epsilon\, V^\mu$ have been used. By employing the Stokes' theorem, we can write (C.4.6) as the following integral over $\partial\hat\gamma$

$$\delta\mathcal{I} = \epsilon\int_{\partial\hat\gamma} b_a\left(\frac{\delta\mathcal{L}}{\delta\partial_a x^\mu}\,V^\mu\right)d^{m-1}s \tag{C.4.7}$$

where b^a is the unit normal vector to $\partial\hat\gamma$. Finally, by plugging (C.4.7) into (C.4.5), we get

$$\mathcal{I} = \frac{2}{m\,c}\int_{\partial\hat\gamma} b_a\left(\frac{\delta\mathcal{L}}{\delta\partial_a x^\mu}\,V^\mu\right)d^{m-1}s\,. \tag{C.4.8}$$

This result tells us that the area of an extremal hypersurface can be expressed as a boundary integral whenever the ambient metric exhibits a conformal Killing vector with constant divergence.

Let us now specialize (C.4.8) to our case of interest, namely to a two dimensional extremal surface $\hat\gamma_A$ anchored to ∂A embedded into $\mathcal{C}_3$ with metric $g_{\mu\nu}$ given by (4.1.21) (thus, $m = 2$ and $d = 3$). This metric has a conformal Killing vector $V^\mu = x^\mu$ with constant divergence that generates scale transformations $x^\mu \to \lambda x^\mu$. Under dilation the metric acquires an overall factor $g_{\mu\nu} \to \lambda^{2-d_\theta} g_{\mu\nu}$, i.e. $c = 2 - d_\theta$. Thus, in the case of hvLif$_4$ geometry we can rewrite (C.4.8) as

$$\mathcal{I} = \frac{1}{2-d_\theta}\int_{\partial\hat\gamma_A} b_a\left(\frac{\delta\mathcal{L}}{\delta\partial_a x^\mu}x^\mu\right)ds\,. \tag{C.4.9}$$

The expression (C.4.9) can be further simplified by employing the parametrization (C.2.1) for the minimal surface $\hat\gamma_A$; hence $\sigma = \{z, s\}$. The derivative of $\mathcal{L} = \sqrt{h} = e^{2\varphi}\sqrt{\tilde h}$ yields

$$\frac{\delta\mathcal{L}}{\delta\partial_a x^\mu} = \frac{e^{2\varphi}}{2}\,\sqrt{\tilde h}\,\tilde h^{bc}\frac{\delta\tilde h_{bc}}{\delta\partial_a x^\mu} = e^{2\varphi}\sqrt{\tilde h}\,\tilde h^{ab}\partial_b x^\nu \tilde g_{\mu\nu}\,. \tag{C.4.10}$$

In order to compute the vector b_a we remind that the integral (C.4.9) is defined on[1] $\mathbb{R}^2$, so it is simply the normal vector to the boundary of the coordinate domain of the surface $\hat\gamma_A$. The integral is divergent, and therefore, we need to introduce a cutoff. In particular, this means the line integral (C.4.9) has to be performed over the curve $\partial\hat\gamma_{A,\varepsilon} = \{z = \varepsilon\}\cap\hat\gamma_A$. Finally, by plugging (C.4.10) into (C.4.9), using the explicit expression of $\tilde h^{ab}$ in (C.2.3) and $\tilde g_{\mu\nu} = \delta_{\mu\nu}$, for the area of extremal surfaces in hvLif$_4$ in terms of the function $u(z, s)$ we obtain

$$\mathcal{I} = \frac{1}{d_\theta - 2}\int_{\partial\hat\gamma_{A,\varepsilon}} \frac{(w^2 + u_s^2)(z + u_z\,\boldsymbol{x}_A\cdot\widetilde N + u_z u) - u_z u_s(w\,\tilde T\cdot\partial\gamma + u_s\,\boldsymbol{x}_A\cdot\widetilde N + u_s\,u)}{z^{d_\theta}\,\sqrt{u_s^2 + w^2(1+u_z^2)}\,.}\,ds \tag{C.4.11}$$

---

[1] Notice that. the index a in b_a is not associated with the metric on $\hat\gamma_A$ but with the metric of $\mathbb{R}^2$.

Although this form is not very illuminating, it is interesting to observe that, once we expand the integrand near to $z = 0$, only the term $u_z \, \boldsymbol{x}_A \cdot \widetilde{N}$ gives a finite contribution to $\mathcal{I}$. By writing the area of the regularized extremal surface $\gamma_{A,\varepsilon}$ in the following form

$$\mathcal{A}[\hat{\gamma}_{A,\varepsilon}] = P_A(\varepsilon) - F_A + \mathcal{O}(\varepsilon) \tag{C.4.12}$$

where $P_A(\varepsilon)$ is a shorthand for all the divergent terms in (C.4.11), and employing the expansion of $u(z, s)$ given in (C.2.5), we find (4.2.7).

C.5 Time-dependent backgrounds

In this appendix we derive the expressions (4.3.1) and (4.3.2), which generalize the results found in the Appendix C.3.1 to time dependent backgrounds.

Let us consider a two-dimensional spacelike surface γ_A embedded in a four-dimensional Lorentzian spacetime $\mathcal{G}_4$, endowed with the metric g_{MN}. Given the two unit vectors $n^{(i)}$ (with $i = 1, 2$) normal to γ_A and orthogonal between them, the induced metric (the projector) on the surface is

$$h_{MN} = g_{MN} - \sum_{i=1}^{2} \epsilon_i \, n^{(i)}_M n^{(i)}_N \tag{C.5.1}$$

where $\epsilon_i = g^{MN} n^{(i)}_M n^{(i)}_N$ is either $+1$ or -1. The surface γ_A is now a codimension two surface in the full spacetime $\mathcal{G}_4$ and we can compute its two extrinsic curvatures as

$$K^{(i)}_{MN} = h_M{}^A h_N{}^B \, \nabla_A n^{(i)}_B \, . \tag{C.5.2}$$

We introduce an auxiliary conformally equivalent four dimensional space $\widetilde{\mathcal{G}}_4$ given by $\mathcal{G}_4$ with the same boundary at $z = 0$, but equipped with the metric $\tilde{g}_{MN}$, which is asymptotically flat as $z \to 0$ and Weyl related to g_{MN}, i.e.

$$g_{MN} = e^{2\varphi} \, \tilde{g}_{MN} \tag{C.5.3}$$

where φ is a function of the coordinates. Within this framework, in [78] the following identity was shown to hold for any surface (not necessarily anchored to a curve on the boundary)

$$\begin{aligned} 0 = &\left[\widetilde{\mathcal{D}}^2 \varphi + \sum_{i=1}^{2} \epsilon_i \widetilde{N}^{(i)M} \tilde{n}^{(i)N} \Big(\widetilde{D}_M \widetilde{D}_N \varphi - \widetilde{D}_M \varphi \widetilde{D}_N \varphi \Big) - \widetilde{D}^2 \varphi - \frac{1}{4} \sum_{i=1}^{2} \epsilon_i \big(\mathrm{Tr} \widetilde{K}^{(i)} \big)^2 \right] d\tilde{\mathcal{A}} \\ &+ \frac{1}{4} \sum_{i=1}^{2} \epsilon_i \big(\mathrm{Tr} K^{(i)} \big)^2 d\mathcal{A} \end{aligned} \tag{C.5.4}$$

where the tilded quantities are evaluated considering $\widetilde{\mathcal{G}}_4$ as embedding space, while for the untilded ones the embedding space is $\mathcal{G}_4$. In particular $\mathrm{Tr}K^{(i)}$ and $\mathrm{Tr}\widetilde{K}^{(i)}$ are the mean curvatures of the surface computed in the two embedding spaces, while $d\mathcal{A}$ and $d\widetilde{\mathcal{A}}$ are the two area elements. The vectors $\tilde{n}^{(i)M}$ are versors perpendicular to the surface viewed as a submanifold of $\widetilde{\mathcal{G}}_4$. The covariant derivative $\widetilde{\nabla}$ is the one defined in $\widetilde{\mathcal{G}}_4$ while $\widetilde{\mathcal{D}}$ is the one induced on the surface by the embedding space $\widetilde{\mathcal{G}}_4$.

At this point, let us consider the surfaces γ_A anchored to some smooth entangling curve ∂A and orthogonal to the boundary. Similarly to the static case considered in Section C.3.1, we multiply (C.5.4) by $c_1 e^{2\phi}$, integrate over $\gamma_{A,\varepsilon}$ and add the regularized area function to both sides of (C.5.4). Thus, we obtain

$$\begin{split}\mathcal{A}[\gamma_{A,\varepsilon}] = c_1 \int_{\gamma_{A,\varepsilon}} e^{2\phi} \Bigg[\widetilde{\mathcal{D}}^2\varphi + \sum_{i=1}^{2} \epsilon_i \tilde{n}^{(i)M} \tilde{n}^{(i)N} \Big(\widetilde{D}_M \widetilde{D}_N \varphi - \widetilde{D}_M \varphi \widetilde{D}_N \varphi \Big) - \widetilde{D}^2 \varphi \\ - \frac{1}{4} \sum_{i=1}^{2} \epsilon_i \big(\mathrm{Tr}\widetilde{K}^{(i)}\big)^2 \Bigg] d\tilde{\mathcal{A}} + \int_{\gamma_{A,\varepsilon}} e^{2\varphi} d\widetilde{\mathcal{A}} + \frac{c_1}{4} \sum_{i=1}^{2} \epsilon_i \int_{\gamma_{A,\varepsilon}} e^{2\phi} \big(\mathrm{Tr}K^{(i)}\big)^2 d\mathcal{A}\,.\end{split} \tag{C.5.5}$$

When we evaluate the first term in the r.h.s. of (C.5.5) over $\gamma_{A,\varepsilon}$ with the same procedure of the static case, it provides the divergent contribution to $\mathcal{A}[\gamma_{A,\varepsilon}]$. Thus, the expansion (4.1.12) is obtained, with $\mathcal{F}_A$ given by (4.3.1).

For non-static geometries, the holographic entanglement entropy of a region A belonging to the asymptotic boundary of $\mathcal{G}_4$ can be computed by employing the prescription [34]. One has to compute the area of the minimal surface $\hat{\gamma}_A$ anchored to the boundary of the region A. Since $\hat{\gamma}_A$ has codimension two, we have the following two extremality conditions

$$\mathrm{Tr}K^{(i)} = 0 \qquad \Longleftrightarrow \qquad \big(\mathrm{Tr}\widetilde{K}^{(i)}\big)^2 = 4\big(\tilde{n}^{(i)M}\partial_M\varphi\big)^2\,. \tag{C.5.6}$$

By specialising (4.3.1) to an extremal surface $\hat{\gamma}_A$, we find the expression (4.3.2) for the finite term in the expansion of the area.

For scale invariant theories, where $d_\theta = 2$, the first term in (4.3.2) vanishes because ϕ can be set to 0; hence the expression for F_A reduces to [78]

$$F_A = \int_{\hat{\gamma}_A} \Bigg[\widetilde{D}^2\varphi - \sum_{i=1}^{2} \epsilon_i \tilde{n}^{(i)M} \tilde{n}^{(i)N} \widetilde{D}_M \widetilde{D}_N \varphi - e^{2\varphi} + \frac{1}{2} \sum_{i=1}^{2} \epsilon_i \big(\mathrm{Tr}\widetilde{K}^{(i)}\big)^2 \Bigg] d\tilde{\mathcal{A}}\,. \tag{C.5.7}$$

We shall now briefly discuss how to recover the result (4.1.18) for the static cases from (4.3.2). The most general static metric can be written as

$$ds^2 = -\,N^2 dt^2 + g_{\mu\nu} dx^\mu dx^\nu \tag{C.5.8}$$

where N and $g_{\mu\nu}$ are functions of the spatial coordinates $x^\mu = (z, \boldsymbol{x})$ only. In this background metric, the two unit normal vectors can be written as $n^{(1)}_M = (N, 0, \mathbf{0})$ and $n^{(2)}_M = (0, n_\mu)$. With the choice of coordinates (C.5.8), the only non-vanishing Christoffel symbols are

$$\Gamma^t_{\mu t} = \frac{1}{2N^2}\partial_\mu N \qquad \Gamma^\mu_{tt} = \frac{1}{2} g^{\mu\nu}\partial_\nu N \qquad \Gamma^\mu_{\nu\rho} = {}^{(3)}\Gamma^\mu_{\nu\rho} \tag{C.5.9}$$

where ${}^{(3)}\Gamma^\mu_{\nu\rho}$ denotes the Christoffel computed with the three dimensional metric $g_{\mu\nu}$ of the constant time hypersurface. Combining (C.5.9) with the observation that the time components h_{tM} of the projector (C.5.1) vanish, we easily conclude that the extrinsic curvature in the timelike direction $K^{(1)}_{MN}$ is zero. Thus, the first equation of motion in (C.5.6) is identically satisfied. Instead the second equation of motion in (C.5.6) reduces to (4.1.8) because only the spatial components of the extrinsic curvature $K^{(2)}_{MN}$ are non-vanishing; hence $\mathrm{Tr}K^{(2)} = \mathrm{Tr}K$. Similar conclusions can be reached for the tilded quantities: $\widetilde{K}^{(1)}_{MN} = 0$, $\widetilde{K}^{(2)}_{\mu\nu} = \widetilde{K}_{\mu\nu}$ and $\widetilde{K}^{(2)}_{tt} = 0$, being φ independent of t. Finally, due to (C.5.9), $\tilde{n}^{(2)\,M}\tilde{n}^{(2)\,N}\widetilde{D}_M\widetilde{D}_N\varphi = \widetilde{\nabla}_M\widetilde{\nabla}_N\varphi$, while the Laplacian $\widetilde{D}^2\varphi$ and the term $\tilde{n}^{(1)\,M}\tilde{n}^{(1)\,N}\widetilde{D}_M\widetilde{D}_N$ sum to $\widetilde{\nabla}^2\varphi$.

C.6 On the analytic solution for a disk when $d_\theta = 2$ and $\zeta \to \infty$

In this appendix, we analytically study minimal surfaces $\hat{\gamma}_A$ anchored to circular regions A in spacetimes equipped with the metric (4.1.29) in the limit $\zeta \to +\infty$ and for $d_\theta = 2$. The background metric becomes the AdS$_4$ metric for $z \leqslant z_h$ with an event horizon located at $z = z_h$. The only effect of the horizon is to forbid the minimal surface enters the region $z > z_h$. As discussed below, for regions large enough, the minimal surfaces reach and stick to the horizon sharing a portion of the surface with it.

For small regions A, the minimal surfaces do not reach the horizon, and their profile is the same as in AdS$_4$ case, i.e., it is given by the hemisphere: $z(\rho) = \sqrt{R^2 - \rho^2}$. This occurs as long as the surface does not intersect the horizon, namely for $R < z_h$. For $R = z_h$ the hemisphere is tangent to the event horizon at the point $(z, \rho) = (z_h, 0)$. As the radius R increases further, a certain portion of the dome would cross the horizon; hence, in this regime, the hemispheres cannot be the extremal surfaces. The actual minimal surfaces consist of two parts: a flat disk that lies on the horizon and a non-trivial surface connecting the conformal boundary to the horizon. The aim of the following discussion is to find the latter one analytically.

Let us consider the most general solution of the differential equation (4.4.11) for $d_\theta = 2$, which has already been found in Sec. A.3.1 in the context of the minimal surfaces anchored to the disk disjoint from the circular boundary. The profile can be found from the equation (A.3.6) also in this case. Now, by imposing the boundary condition $\rho(z = 0) = R$ we find the equation

$$\rho = R\, e^{-q_{\pm,k}(\hat{z})} \qquad \hat{z} = z/\rho \tag{C.6.1}$$

where again the function $q_{\pm,k}(\hat{z})$ is defined in (2.3.5) and (4.4.22), and k is an integration constant. Below we will fix both k and the plus/minus ambiguity by imposing the boundary condition on the horizon $z = z_h$.

Let us denote by $P_* = (\rho_*, z_h)$ the intersection point between (C.6.1) and the horizon. For $\rho < \rho_*$, the minimal surface is a disk lying exactly on the horizon. The position of P_* and the constant k are then determined by requiring that the solution is continuous and differentiable at P_*. Since the tangent vector to the surface for $\rho \geqslant \rho_*$ is $t^\mu_\rho = (t^\rho_\rho, t^z_\rho) = (\rho', \rho + \hat{z}\rho')$, the condition of being tangent to the horizon reads $\rho + \hat{z}\rho' = 0$. Being $\rho' = -\rho\, q'_{\pm,k}$, we obtain $\hat{z}_*\, q'(\hat{z}_*)_{\pm,k} = 1$, that implies $\pm\hat{z}_*^3 = \sqrt{k(1+\hat{z}_*^2) - \hat{z}_*^4}$; and this is meaningful only if the plus sign is chosen in (C.6.1). This choice, in turn, gives $\hat{z}_* = k^{1/4}$. Finally, the value of k is evaluated by imposing that $z = z_h$ when $\hat{z} = \hat{z}_*$. This leads to (4.4.21), which implicitly determines k in terms of R/z_h. The possibility of inverting (4.4.21) is controlled by its derivative with respect to k. We find

$$\frac{d}{dk}\left(\frac{R}{z_h}\right) = -\frac{R}{z_h}\int_0^{k^{1/4}} \frac{\lambda^2}{2\left[k(1+\lambda^2) - \lambda^4\right]^{3/2}} \leqslant 0\,. \tag{C.6.2}$$

Since R/z_h is a monotonic function of k, the condition (4.4.21) has at most one solution for any value of R/z_h. On the other hand, in Section C.6.2 we show that $R/z_h \to +\infty$ for $k \to 0$, while $R/z_h \to 1$ for $k \to +\infty$. Thus (4.4.21) admits exactly one solution in the range

$R/z_h \in (1, +\infty)$ which leads to the profile (4.4.20). Instead, let us remind that in the range $R/z_h \in (0, 1]$ the solution is the hemisphere $z(\rho) = \sqrt{R^2 - \rho^2}$.

C.6.1 Area

As for the area of the minimal surface $\hat{\gamma}_A$, when $R < z_h$ it is the area of the hemisphere $z(\rho) = \sqrt{R^2 - \rho^2}$ regularised by the condition $z \geqslant \varepsilon$, namely

$$\mathcal{A} = \frac{2\pi R}{\varepsilon} - 2\pi \qquad R < z_h \, . \tag{C.6.3}$$

For $R > z_h$, the area is $\mathcal{A} = \mathcal{A}_1 + \mathcal{A}_2$, where $\mathcal{A}_1$ corresponds to a flat disk located at z_h and with radius $\rho_* = z_h/\hat{z}_* = k^{1/4}/z_h$; hence it reads

$$\mathcal{A}_1 = \frac{\pi \rho_*^2}{z_h^2} = \frac{\pi}{\sqrt{k}} \, . \tag{C.6.4}$$

The contribution $\mathcal{A}_2$ is the area of the profile (C.6.1) between $\hat{z} = 0$ and $\hat{z}_* = k^{1/4}$. In terms of the variables introduced in (A.3.3), the area functional (4.4.17) in the limit $\zeta \to +\infty$ and for $d_\theta = 2$ reduces to

$$\mathcal{A}_2 = 2\pi \int_{\varepsilon/R}^{\hat{z}_*} \frac{d\lambda}{\lambda^2 \sqrt{1 + \lambda^2 - \lambda^4/k}} \tag{C.6.5}$$

where we introduced the UV cutoff ε. The primitive $\mathcal{F}_k(\lambda)$ of the integrand in (C.6.5) can be written explicitly in terms of elliptic integrals and it has been reported in (2.3.14) and (4.4.25). In order to single out the UV divergence, one employs its expansion as $\lambda \to 0^+$

$$\mathcal{F}_k(\lambda) = \frac{1}{\lambda} + \frac{\lambda}{2} + \mathcal{O}(\lambda^3) \tag{C.6.6}$$

which gives

$$\mathcal{A}_2 = \frac{2\pi R}{\varepsilon} - 2\pi \mathcal{F}_k(k^{1/4}) + \mathcal{O}(\varepsilon/R) \tag{C.6.7}$$

where also $\hat{z}_* = k^{1/4}$ has been used. By adding (C.6.7) to (C.6.4), we find that the area of $\hat{\gamma}_A$ for $R > z_h$ reads

$$\mathcal{A} = \frac{2\pi R}{\varepsilon} - 2\pi \left(\mathcal{F}_k(k^{1/4}) - \frac{1}{2\sqrt{k}} \right) \qquad R > z_h \tag{C.6.8}$$

which provides (4.4.24).

C.6.2 Limiting regimes

Let us consider the limit of (4.4.21) and (C.6.8) for $R/z_h \to +\infty$, which corresponds to $k \to 0$. The expansion of (C.6.8) is straightforward, and we find

$$\mathcal{A} = \frac{2\pi R}{\varepsilon} - 2\pi \left[-\frac{1}{2\sqrt{k}} + \frac{\sqrt{2}\,\pi^{3/2}}{\Gamma(1/4)^2 \sqrt[4]{k}} + \frac{1}{2} \right] + \mathcal{O}\big(k^{1/4}\big) \, . \tag{C.6.9}$$

In order to expand (4.4.21) for small k, we find it more convenient to use the integral representation (2.3.5). First one performs the change of variable $\lambda \to k^{1/4}\lambda$, obtaining a definite integral between the two extrema in $\lambda = 0$ and $\lambda = 1$. Then, we expand the integrand as $k \to 0$, and we integrate term by term, finding

$$q_{+,k}(k^{1/4}) = \frac{\sqrt{2}\,\pi^{3/2}}{\Gamma(1/4)^2}\,k^{1/4} + \frac{\sqrt{k}}{2} + \dots \tag{C.6.10}$$

that leads to

$$\frac{R}{z_h} = \frac{1}{k^{1/4}} + \frac{\sqrt{2}\,\pi^{3/2}}{\Gamma(1/4)^2} + \left(\frac{\pi^3}{\Gamma(1/4)^4} + \frac{1}{2}\right) k^{1/4} + \dots . \tag{C.6.11}$$

Now, by plugging (C.6.11) into (C.6.9) we get

$$\mathcal{A} = \frac{2\pi R}{\varepsilon} + \left(\frac{\pi R^2}{z_h^2} + \frac{4\pi\sqrt{2}\,\pi^{3/2} R}{\Gamma(1/4)^2\, z_h}\right) + \mathcal{O}(1) \tag{C.6.12}$$

where the leading term in R agrees with (4.1.33).

In the regime given by $k \to +\infty$, from the definition of $\hat{z}_m$ we have $\hat{z}_m \to +\infty$, and therefore the surface reaches $\rho = 0$. Moreover from (2.3.5) we obtain

$$q_{\pm,k}(\hat{z}) = \int_0^{\hat{z}} \frac{\lambda}{1+\lambda^2}\, d\lambda = \frac{1}{2}\log(1+\hat{z}^2) \tag{C.6.13}$$

that gives the profile of the hemisphere $z(\rho) = \sqrt{R^2 - \rho^2}$. By means of (C.6.13) we find that $q_{+,k}(k^{1/4}) = \log k^{1/4} + \dots$ as $k \to \infty$, which leads to $R/z_h \to 1$ in the same limit. Notice that $R = z_h$ is the value of the radius corresponding to the transition between the two minimal surfaces. Since we showed that the solution reduces to the hemisphere with radius $R = z_h$ in this limit, we conclude that (C.6.8) reduces to $\mathcal{A} \to 2\pi R/\varepsilon - 2\pi$ as $k \to \infty$. In particular, this means that the function $F_A(R)$ given in (4.4.24) is continuous in R.

Bibliography

[1] E. Schrödinger, *Probability relations between separated systems*, *Proceedings of the Cambridge Philosophical Society* **32** (1936) 446.

[2] A. Einstein, B. Podolsky and N. Rosen, *Can quantum-mechanical description of physical reality be considered complete?*, *Phys. Rev.* **47** (1935) 777.

[3] C. H. Bennett, G. Brassard, C. Crépeau, R. Jozsa, A. Peres and W. K. Wootters, *Teleporting an unknown quantum state via dual classical and einstein-podolsky-rosen channels*, *Phys. Rev. Lett.* **70** (1993) 1895.

[4] C. H. Bennett, D. P. DiVincenzo, J. A. Smolin and W. K. Wootters, *Mixed state entanglement and quantum error correction*, *Phys. Rev.* **A54** (1996) 3824 [`quant-ph/9604024`].

[5] C. H. Bennett, H. J. Bernstein, S. Popescu and B. Schumacher, *Concentrating partial entanglement by local operations*, *Phys. Rev.* **A53** (1996) 2046 [`quant-ph/9511030`].

[6] J. D. Bekenstein, *Black holes and the second law*, *Lett. Nuovo Cim.* **4** (1972) 737.

[7] J. D. Bekenstein, *Black holes and entropy*, *Phys. Rev.* **D7** (1973) 2333.

[8] J. D. Bekenstein, *Generalized second law of thermodynamics in black hole physics*, *Phys. Rev.* **D9** (1974) 3292.

[9] S. W. Hawking, *Particle Creation by Black Holes*, *Commun. Math. Phys.* **43** (1975) 199.

[10] L. Bombelli, R. K. Koul, J. Lee and R. D. Sorkin, *A Quantum Source of Entropy for Black Holes*, *Phys. Rev.* **D34** (1986) 373.

[11] M. Srednicki, *Entropy and area*, *Phys. Rev. Lett.* **71** (1993) 666 [`hep-th/9303048`].

[12] C. G. Callan, Jr. and F. Wilczek, *On geometric entropy*, *Phys. Lett.* **B333** (1994) 55 [`hep-th/9401072`].

[13] C. Holzhey, F. Larsen and F. Wilczek, *Geometric and renormalized entropy in conformal field theory*, *Nucl. Phys.* **B424** (1994) 443 [`hep-th/9403108`].

[14] S. N. Solodukhin, *The Conical singularity and quantum corrections to entropy of black hole*, *Phys. Rev.* **D51** (1995) 609 [`hep-th/9407001`].

[15] S. N. Solodukhin, *On 'Nongeometric' contribution to the entropy of black hole due to quantum corrections*, *Phys. Rev.* **D51** (1995) 618 [`hep-th/9408068`].

[16] D. V. Fursaev and S. N. Solodukhin, *On the description of the Riemannian geometry in the presence of conical defects*, *Phys. Rev.* **D52** (1995) 2133 [`hep-th/9501127`].

[17] J. Polchinski, *Dirichlet Branes and Ramond-Ramond charges*, *Phys. Rev. Lett.* **75** (1995) 4724 [`hep-th/9510017`].

[18] A. Strominger and C. Vafa, *Microscopic origin of the Bekenstein-Hawking entropy*, *Phys. Lett.* **B379** (1996) 99 [`hep-th/9601029`].

[19] L. Amico, R. Fazio, A. Osterloh and V. Vedral, *Entanglement in many-body systems*, *Rev. Mod. Phys.* **80** (2008) 517 [`quant-ph/0703044`].

[20] J. Eisert, M. Cramer and M. B. Plenio, *Area laws for the entanglement entropy - a review*, *Rev. Mod. Phys.* **82** (2010) 277 [`0808.3773`].

[21] P. Calabrese, J. Cardy and B. Doyon, *Entanglement entropy in extended quantum systems*, *J. Phys. A* **42** *(2009) special issue* .

[22] G. Vidal, J. I. Latorre, E. Rico and A. Kitaev, *Entanglement in quantum critical phenomena*, *Phys. Rev. Lett.* **90** (2003) 227902 [`quant-ph/0211074`].

[23] P. Calabrese and J. L. Cardy, *Entanglement entropy and quantum field theory*, *J. Stat. Mech.* **0406** (2004) P06002 [`hep-th/0405152`].

[24] P. Calabrese and J. Cardy, *Entanglement entropy and conformal field theory*, *J. Phys.* **A42** (2009) 504005 [`0905.4013`].

[25] R. Islam, R. Ma, P. Preiss, M. Eric Tai, A. Lukin, M. Rispoli et al., *Measuring entanglement entropy in a quantum many-body system*, *Nature* **528** (2015) 77.

[26] A. M. Kaufman, M. E. Tai, A. Lukin, M. Rispoli, R. Schittko, P. M. Preiss et al., *Quantum thermalization through entanglement in an isolated many-body system*, *Science* **353** (2016) 794.

[27] A. Lukin, M. Rispoli, R. Schittko, M. E. Tai, A. M. Kaufman, S. Choi et al., *Probing entanglement in a many-body–localized system*, *Science* **364** (2019) 256.

[28] H. Casini and M. Huerta, *Universal terms for the entanglement entropy in 2+1 dimensions*, *Nucl. Phys.* **B764** (2007) 183 [`hep-th/0606256`].

[29] A. Kitaev and J. Preskill, *Topological entanglement entropy*, *Phys. Rev. Lett.* **96** (2006) 110404 [`hep-th/0510092`].

[30] M. Levin and X.-G. Wen, *Detecting Topological Order in a Ground State Wave Function*, *Phys. Rev. Lett.* **96** (2006) 110405 [`cond-mat/0510613`].

[31] S. Ryu and T. Takayanagi, *Holographic derivation of entanglement entropy from AdS/CFT*, *Phys. Rev. Lett.* **96** (2006) 181602 [`hep-th/0603001`].

[32] S. Ryu and T. Takayanagi, *Aspects of Holographic Entanglement Entropy*, *JHEP* **08** (2006) 045 [`hep-th/0605073`].

[33] J. M. Maldacena, *The Large N limit of superconformal field theories and supergravity*, *Int. J. Theor. Phys.* **38** (1999) 1113 [`hep-th/9711200`].

[34] V. E. Hubeny, M. Rangamani and T. Takayanagi, *A Covariant holographic entanglement entropy proposal*, *JHEP* **07** (2007) 062 [`0705.0016`].

[35] B. Swingle, *Entanglement Renormalization and Holography*, *Phys. Rev.* **D86** (2012) 065007 [`0905.1317`].

[36] M. Van Raamsdonk, *Comments on quantum gravity and entanglement*, `0907.2939`.

[37] M. Van Raamsdonk, *Building up spacetime with quantum entanglement*, *Gen. Rel. Grav.* **42** (2010) 2323 [`1005.3035`].

[38] J. Maldacena and L. Susskind, *Cool horizons for entangled black holes*, *Fortsch. Phys.* **61** (2013) 781 [`1306.0533`].

[39] A. Almheiri, X. Dong and D. Harlow, *Bulk Locality and Quantum Error Correction in AdS/CFT*, *JHEP* **04** (2015) 163 [`1411.7041`].

[40] F. Pastawski, B. Yoshida, D. Harlow and J. Preskill, *Holographic quantum error-correcting codes: Toy models for the bulk/boundary correspondence*, *JHEP* **06** (2015) 149 [`1503.06237`].

[41] X. Dong, D. Harlow and A. C. Wall, *Reconstruction of Bulk Operators within the Entanglement Wedge in Gauge-Gravity Duality*, *Phys. Rev. Lett.* **117** (2016) 021601 [`1601.05416`].

[42] A. Hamilton, D. N. Kabat, G. Lifschytz and D. A. Lowe, *Local bulk operators in AdS/CFT: A Boundary view of horizons and locality*, *Phys. Rev.* **D73** (2006) 086003 [`hep-th/0506118`].

[43] A. Hamilton, D. N. Kabat, G. Lifschytz and D. A. Lowe, *Holographic representation of local bulk operators*, *Phys. Rev.* **D74** (2006) 066009 [`hep-th/0606141`].

[44] L. Susskind, *Computational Complexity and Black Hole Horizons*, *Fortsch. Phys.* **64** (2016) 44 [`1403.5695`].

[45] D. Stanford and L. Susskind, *Complexity and Shock Wave Geometries*, *Phys. Rev.* **D90** (2014) 126007 [`1406.2678`].

[46] L. Susskind and Y. Zhao, *Switchbacks and the Bridge to Nowhere*, `1408.2823`.

[47] A. R. Brown, D. A. Roberts, L. Susskind, B. Swingle and Y. Zhao, *Holographic Complexity Equals Bulk Action?*, *Phys. Rev. Lett.* **116** (2016) 191301 [`1509.07876`].

[48] A. R. Brown, D. A. Roberts, L. Susskind, B. Swingle and Y. Zhao, *Complexity, action, and black holes*, *Phys. Rev.* **D93** (2016) 086006 [`1512.04993`].

[49] J. Watrous, *Quantum Computational Complexity*, *arXiv e-prints* (2008) arXiv:0804.3401 [`0804.3401`].

[50] T. J. Osborne, *Hamiltonian complexity*, *Reports on Progress in Physics* **75** (2012) 022001 [`1106.5875`].

[51] S. Gharibian, Y. Huang, Z. Landau and S. W. Shin, *Quantum Hamiltonian Complexity*, *arXiv e-prints* (2014) arXiv:1401.3916 [`1401.3916`].

[52] S. Chapman, H. Marrochio and R. C. Myers, *Complexity of Formation in Holography*, *JHEP* **01** (2017) 062 [`1610.08063`].

[53] D. Carmi, R. C. Myers and P. Rath, *Comments on Holographic Complexity*, *JHEP* **03** (2017) 118 [`1612.00433`].

[54] R. Jefferson and R. C. Myers, *Circuit complexity in quantum field theory*, *JHEP* **10** (2017) 107 [`1707.08570`].

[55] D. Carmi, S. Chapman, H. Marrochio, R. C. Myers and S. Sugishita, *On the Time Dependence of Holographic Complexity*, *JHEP* **11** (2017) 188 [`1709.10184`].

[56] H. Casini and M. Huerta, *A Finite entanglement entropy and the c-theorem*, *Phys. Lett.* **B600** (2004) 142 [`hep-th/0405111`].

[57] R. C. Myers and A. Sinha, *Holographic c-theorems in arbitrary dimensions*, *JHEP* **01** (2011) 125 [`1011.5819`].

[58] D. L. Jafferis, I. R. Klebanov, S. S. Pufu and B. R. Safdi, *Towards the F-Theorem: N=2 Field Theories on the Three-Sphere*, *JHEP* **06** (2011) 102 [`1103.1181`].

[59] H. Liu and M. Mezei, *A Refinement of entanglement entropy and the number of degrees of freedom*, *JHEP* **04** (2013) 162 [`1202.2070`].

[60] H. Casini and M. Huerta, *On the RG running of the entanglement entropy of a circle*, *Phys. Rev.* **D85** (2012) 125016 [`1202.5650`].

[61] H. Casini, E. Testé and G. Torroba, *Markov Property of the Conformal Field Theory Vacuum and the a Theorem*, *Phys. Rev. Lett.* **118** (2017) 261602 [`1704.01870`].

[62] H. Casini, R. Medina, I. Salazar Landea and G. Torroba, *Renyi relative entropies and renormalization group flows*, *JHEP* **09** (2018) 166 [`1807.03305`].

[63] P. Bueno, R. C. Myers and W. Witczak-Krempa, *Universality of corner entanglement in conformal field theories*, *Phys. Rev. Lett.* **115** (2015) 021602 [`1505.04804`].

[64] P. Bueno and R. C. Myers, *Universal entanglement for higher dimensional cones*, *JHEP* **12** (2015) 168 [`1508.00587`].

[65] T. Faulkner, R. G. Leigh and O. Parrikar, *Shape Dependence of Entanglement Entropy in Conformal Field Theories*, *JHEP* **04** (2016) 088 [`1511.05179`].

[66] L. Bianchi, M. Meineri, R. C. Myers and M. Smolkin, *Rényi entropy and conformal defects*, *JHEP* **07** (2016) 076 [`1511.06713`].

[67] C. R. Graham and E. Witten, *Conformal anomaly of submanifold observables in AdS/CFT correspondence*, *Nucl. Phys.* **B546** (1999) 52 [`hep-th/9901021`].

[68] S. N. Solodukhin, *Entanglement entropy, conformal invariance and extrinsic geometry*, *Phys. Lett.* **B665** (2008) 305 [`0802.3117`].

[69] I. R. Klebanov, T. Nishioka, S. S. Pufu and B. R. Safdi, *On Shape Dependence and RG Flow of Entanglement Entropy*, *JHEP* **07** (2012) 001 [`1204.4160`].

[70] V. E. Hubeny, *Extremal surfaces as bulk probes in AdS/CFT*, *JHEP* **07** (2012) 093 [`1203.1044`].

[71] A. F. Astaneh, G. Gibbons and S. N. Solodukhin, *What surface maximizes entanglement entropy?*, *Phys. Rev.* **D90** (2014) 085021 [`1407.4719`].

[72] A. Allais and M. Mezei, *Some results on the shape dependence of entanglement and Rényi entropies*, *Phys. Rev.* **D91** (2015) 046002 [`1407.7249`].

[73] M. Mezei, *Entanglement entropy across a deformed sphere*, *Phys. Rev.* **D91** (2015) 045038 [`1411.7011`].

[74] S. Fischetti and T. Wiseman, *A Bound on Holographic Entanglement Entropy from Inverse Mean Curvature Flow*, *Class. Quant. Grav.* **34** (2017) 125005 [`1612.04373`].

[75] T. Willmore, *Riemannian Geometry*. Oxford University Press, 1996.

[76] M. Babich and A. Bobenko, *Willmore tori with umbilic lines and minimal surfaces in hyperbolic space*, *Duke Mathematical Journal* **72** (1993) .

[77] S. Alexakis and R. Mazzeo, *Renormalized area and properly embedded minimal surfaces in hyperbolic 3-manifolds*, *Commun. Math. Phys.* **297** (2010) 621.

[78] P. Fonda, D. Seminara and E. Tonni, *On shape dependence of holographic entanglement entropy in* AdS_4/CFT_3, *JHEP* **12** (2015) 037 [`1510.03664`].

[79] J. L. Cardy, *Conformal Invariance and Surface Critical Behavior*, *Nucl. Phys.* **B240** (1984) 514.

[80] J. L. Cardy, *Boundary Conditions, Fusion Rules and the Verlinde Formula*, *Nucl. Phys.* **B324** (1989) 581.

[81] J. L. Cardy, *Boundary conformal field theory*, `hep-th/0411189`.

[82] D. M. McAvity and H. Osborn, *Asymptotic expansion of the heat kernel for generalized boundary conditions*, *Class. Quant. Grav.* **8** (1991) 1445.

[83] D. M. McAvity and H. Osborn, *Quantum field theories on manifolds with curved boundaries: Scalar fields*, *Nuclear Physics B* **394** (1993) 728 [`cond-mat/9206009`].

[84] D. M. McAvity and H. Osborn, *Energy momentum tensor in conformal field theories near a boundary*, *Nucl. Phys.* **B406** (1993) 655 [`hep-th/9302068`].

[85] D. M. McAvity and H. Osborn, *Conformal field theories near a boundary in general dimensions*, *Nucl. Phys.* **B455** (1995) 522 [`cond-mat/9505127`].

[86] I. Affleck and A. W. W. Ludwig, *Universal noninteger 'ground state degeneracy' in critical quantum systems*, *Phys. Rev. Lett.* **67** (1991) 161.

[87] D. Friedan and A. Konechny, *On the boundary entropy of one-dimensional quantum systems at low temperature*, *Phys. Rev. Lett.* **93** (2004) 030402 [`hep-th/0312197`].

[88] K. Jensen and A. O'Bannon, *Constraint on Defect and Boundary Renormalization Group Flows*, *Phys. Rev. Lett.* **116** (2016) 091601 [`1509.02160`].

[89] T. Takayanagi, *Holographic Dual of BCFT*, *Phys. Rev. Lett.* **107** (2011) 101602 [`1105.5165`].

[90] M. Fujita, T. Takayanagi and E. Tonni, *Aspects of AdS/BCFT*, *JHEP* **11** (2011) 043 [`1108.5152`].

[91] M. Nozaki, T. Takayanagi and T. Ugajin, *Central Charges for BCFTs and Holography*, *JHEP* **06** (2012) 066 [`1205.1573`].

[92] M. Billò, V. Gonçalves, E. Lauria and M. Meineri, *Defects in conformal field theory*, *JHEP* **04** (2016) 091 [`1601.02883`].

[93] P. Liendo, L. Rastelli and B. C. van Rees, *The Bootstrap Program for Boundary* CFT_d, *JHEP* **07** (2013) 113 [`1210.4258`].

[94] A. Gadde, *Conformal constraints on defects*, `1602.06354`.

[95] T. Quella, I. Runkel and G. M. T. Watts, *Reflection and transmission for conformal defects*, *JHEP* **04** (2007) 095 [`hep-th/0611296`].

[96] M. Fukuda, N. Kobayashi and T. Nishioka, *Operator product expansion for conformal defects*, *JHEP* **01** (2018) 013 [1710.11165].

[97] J. Kondo, *Resistance Minimum in Dilute Magnetic Alloys*, *Progress of Theoretical Physics* **32** (1964) 37.

[98] I. Affleck, *Conformal field theory approach to the Kondo effect*, *Acta Phys. Polon.* **B26** (1995) 1869 [cond-mat/9512099].

[99] B. Bellazzini, M. Burrello, M. Mintchev and P. Sorba, *Quantum Field Theory on Star Graphs*, *Proc. Symp. Pure Math.* **77** (2008) 639 [0801.2852].

[100] B. Bellazzini and M. Mintchev, *Quantum Fields on Star Graphs*, *J. Phys.* **A39** (2006) 11101 [hep-th/0605036].

[101] G. Y. Cho, K. Shiozaki, S. Ryu and A. W. W. Ludwig, *Relationship between symmetry protected topological phases and boundary conformal field theories via the entanglement spectrum*, *Journal of Physics A Mathematical General* **50** (2017) 304002 [1606.06402].

[102] J. R. Fliss, X. Wen, O. Parrikar, C.-T. Hsieh, B. Han, T. L. Hughes et al., *Interface Contributions to Topological Entanglement in Abelian Chern-Simons Theory*, *JHEP* **09** (2017) 056 [1705.09611].

[103] B. Han, A. Tiwari, C.-T. Hsieh and S. Ryu, *Boundary conformal field theory and symmetry protected topological phases in* $2+1$ *dimensions*, *Phys. Rev.* **B96** (2017) 125105 [1704.01193].

[104] A. Karch and L. Randall, *Locally localized gravity*, *JHEP* **05** (2001) 008 [hep-th/0011156].

[105] O. DeWolfe, D. Z. Freedman and H. Ooguri, *Holography and defect conformal field theories*, *Phys. Rev.* **D66** (2002) 025009 [hep-th/0111135].

[106] J. Erdmenger, Z. Guralnik and I. Kirsch, *Four-dimensional superconformal theories with interacting boundaries or defects*, *Phys. Rev.* **D66** (2002) 025020 [hep-th/0203020].

[107] J. Erdmenger, C. Hoyos, A. O'Bannon and J. Wu, *A Holographic Model of the Kondo Effect*, *JHEP* **12** (2013) 086 [1310.3271].

[108] J. Estes, K. Jensen, A. O'Bannon, E. Tsatis and T. Wrase, *On Holographic Defect Entropy*, *JHEP* **05** (2014) 084 [1403.6475].

[109] J. Erdmenger, M. Flory, C. Hoyos, M.-N. Newrzella and J. M. S. Wu, *Entanglement Entropy in a Holographic Kondo Model*, *Fortsch. Phys.* **64** (2016) 109 [1511.03666].

[110] J. Erdmenger, M. Flory, C. Hoyos, M.-N. Newrzella, A. O'Bannon and J. Wu, *Holographic impurities and Kondo effect*, *Fortsch. Phys.* **64** (2016) 322 [1511.09362].

[111] J. Erdmenger, C. Hoyos, A. O'Bannon, I. Papadimitriou, J. Probst and J. M. S. Wu, *Two-point Functions in a Holographic Kondo Model*, *JHEP* **03** (2017) 039 [1612.02005].

[112] J. Erdmenger, C. Hoyos, A. O'Bannon, I. Papadimitriou, J. Probst and J. M. S. Wu, *Holographic Kondo and Fano Resonances*, *Phys. Rev.* **D96** (2017) 021901 [1611.09368].

[113] R. M. Hornreich, M. Luban and S. Shtrikman, *Critical behavior at the onset of* $\vec{\mathrm{k}}$*-space instability on the* λ *line*, *Phys. Rev. Lett.* **35** (1975) 1678.

[114] G. Grinstein, *Anisotropic sine-gordon model and infinite-order phase transitions in three dimensions*, *Phys. Rev. B* **23** (1981) 4615.

[115] E. Fradkin, D. A. Huse, R. Moessner, V. Oganesyan and S. L. Sondhi, *Bipartite rokhsar–kivelson points and cantor deconfinement*, *Phys. Rev. B* **69** (2004) 224415 [cond-mat/0311353].

[116] A. Vishwanath, L. Balents and T. Senthil, *Quantum criticality and deconfinement in phase transitions between valence bond solids*, *Phys. Rev. B* **69** (2004) 224416 [cond-mat/0311085].

[117] E. Ardonne, P. Fendley and E. Fradkin, *Topological order and conformal quantum critical points*, *Annals Phys.* **310** (2004) 493 [cond-mat/0311466].

[118] D. S. Fisher, *Scaling and critical slowing down in random-field Ising systems*, *Phys. Rev. Lett.* **56** (1986) 416.

[119] S. Kachru, X. Liu and M. Mulligan, *Gravity duals of Lifshitz-like fixed points*, *Phys. Rev.* **D78** (2008) 106005 [0808.1725].

[120] K. Balasubramanian and J. McGreevy, *Gravity duals for non-relativistic CFTs*, *Phys. Rev. Lett.* **101** (2008) 061601 [0804.4053].

[121] M. Taylor, *Non-relativistic holography*, 0812.0530.

[122] C. Charmousis, B. Gouteraux, B. S. Kim, E. Kiritsis and R. Meyer, *Effective Holographic Theories for low-temperature condensed matter systems*, *JHEP* **11** (2010) 151 [1005.4690].

[123] B. Gouteraux and E. Kiritsis, *Generalized Holographic Quantum Criticality at Finite Density*, *JHEP* **12** (2011) 036 [1107.2116].

[124] L. Huijse, S. Sachdev and B. Swingle, *Hidden Fermi surfaces in compressible states of gauge-gravity duality*, *Phys. Rev.* **B85** (2012) 035121 [1112.0573].

[125] N. Ogawa, T. Takayanagi and T. Ugajin, *Holographic Fermi Surfaces and Entanglement Entropy*, *JHEP* **01** (2012) 125 [1111.1023].

[126] X. Dong, S. Harrison, S. Kachru, G. Torroba and H. Wang, *Aspects of holography for theories with hyperscaling violation*, *JHEP* **06** (2012) 041 [`1201.1905`].

[127] K. Goldstein, S. Kachru, S. Prakash and S. P. Trivedi, *Holography of Charged Dilaton Black Holes*, *JHEP* **08** (2010) 078 [`0911.3586`].

[128] S. S. Gubser and F. D. Rocha, *Peculiar properties of a charged dilatonic black hole in* AdS_5, *Phys. Rev.* **D81** (2010) 046001 [`0911.2898`].

[129] N. Iizuka, N. Kundu, P. Narayan and S. P. Trivedi, *Holographic Fermi and Non-Fermi Liquids with Transitions in Dilaton Gravity*, *JHEP* **01** (2012) 094 [`1105.1162`].

[130] K. Narayan, *On Lifshitz scaling and hyperscaling violation in string theory*, *Phys. Rev.* **D85** (2012) 106006 [`1202.5935`].

[131] M. Ammon, M. Kaminski and A. Karch, *Hyperscaling-Violation on Probe D-Branes*, *JHEP* **11** (2012) 028 [`1207.1726`].

[132] J. Bhattacharya, S. Cremonini and A. Sinkovics, *On the IR completion of geometries with hyperscaling violation*, *JHEP* **02** (2013) 147 [`1208.1752`].

[133] M. Alishahiha, E. O Colgain and H. Yavartanoo, *Charged Black Branes with Hyperscaling Violating Factor*, *JHEP* **11** (2012) 137 [`1209.3946`].

[134] P. Bueno, W. Chemissany, P. Meessen, T. Ortin and C. S. Shahbazi, *Lifshitz-like Solutions with Hyperscaling Violation in Ungauged Supergravity*, *JHEP* **01** (2013) 189 [`1209.4047`].

[135] J. Gath, J. Hartong, R. Monteiro and N. A. Obers, *Holographic Models for Theories with Hyperscaling Violation*, *JHEP* **04** (2013) 159 [`1212.3263`].

[136] B. Gouteraux and E. Kiritsis, *Quantum critical lines in holographic phases with (un)broken symmetry*, *JHEP* **04** (2013) 053 [`1212.2625`].

[137] M. H. Christensen, J. Hartong, N. A. Obers and B. Rollier, *Boundary Stress-Energy Tensor and Newton-Cartan Geometry in Lifshitz Holography*, *JHEP* **01** (2014) 057 [`1311.6471`].

[138] M. H. Christensen, J. Hartong, N. A. Obers and B. Rollier, *Torsional Newton-Cartan Geometry and Lifshitz Holography*, *Phys. Rev.* **D89** (2014) 061901 [`1311.4794`].

[139] J. Hartong, N. A. Obers and M. Sanchioni, *Lifshitz Hydrodynamics from Lifshitz Black Branes with Linear Momentum*, *JHEP* **10** (2016) 120 [`1606.09543`].

[140] M. M. Wolf, *Violation of the entropic area law for Fermions*, *Phys. Rev. Lett.* **96** (2006) 010404 [`quant-ph/0503219`].

[141] D. Gioev and I. Klich, *Entanglement Entropy of Fermions in Any Dimension and the Widom Conjecture*, *Phys. Rev. Lett.* **96** (2006) 100503 [`quant-ph/0504151`].

[142] E. Tonni, *Holographic entanglement entropy: near horizon geometry and disconnected regions*, *JHEP* **05** (2011) 004 [1011.0166].

[143] E. Shaghoulian, *Holographic Entanglement Entropy and Fermi Surfaces*, *JHEP* **05** (2012) 065 [1112.2702].

[144] K. Narayan, T. Takayanagi and S. P. Trivedi, *AdS plane waves and entanglement entropy*, *JHEP* **04** (2013) 051 [1212.4328].

[145] M. Alishahiha, A. F. Astaneh, P. Fonda and F. Omidi, *Entanglement Entropy for Singular Surfaces in Hyperscaling violating Theories*, *JHEP* **09** (2015) 172 [1507.05897].

[146] R. Mishra and H. Singh, *Entanglement entropy at higher orders for the states of* $a = 3$ *Lifshitz theory*, *Nucl. Phys.* **B938** (2019) 307 [1804.01361].

[147] V. Keranen, E. Keski-Vakkuri and L. Thorlacius, *Thermalization and entanglement following a non-relativistic holographic quench*, *Phys. Rev.* **D85** (2012) 026005 [1110.5035].

[148] H. Liu and S. J. Suh, *Entanglement Tsunami: Universal Scaling in Holographic Thermalization*, *Phys. Rev. Lett.* **112** (2014) 011601 [1305.7244].

[149] H. Liu and S. J. Suh, *Entanglement growth during thermalization in holographic systems*, *Phys. Rev.* **D89** (2014) 066012 [1311.1200].

[150] M. Alishahiha, A. Faraji Astaneh and M. R. Mohammadi Mozaffar, *Thermalization in backgrounds with hyperscaling violating factor*, *Phys. Rev.* **D90** (2014) 046004 [1401.2807].

[151] P. Fonda, L. Franti, V. Keränen, E. Keski-Vakkuri, L. Thorlacius and E. Tonni, *Holographic thermalization with Lifshitz scaling and hyperscaling violation*, *JHEP* **08** (2014) 051 [1401.6088].

[152] K. A. Brakke, *The surface evolver*, *Experimental Mathematics* **1** (1992) 141 [`https://doi.org/10.1080/10586458.1992.10504253`].

[153] "*Surface Evolver*." `http://www.susqu.edu/brakke/evolver/evolver.html`.

[154] D. Seminara, J. Sisti and E. Tonni, *Corner contributions to holographic entanglement entropy in* $AdS_4/BCFT_3$, *JHEP* **11** (2017) 076 [1708.05080].

[155] D. Seminara, J. Sisti and E. Tonni, *Holographic entanglement entropy in* $AdS_4/BCFT_3$ *and the Willmore functional*, *JHEP* **08** (2018) 164 [1805.11551].

[156] G. Cavini, D. Seminara, J. Sisti and E. Tonni, *On shape dependence of holographic entanglement entropy in* AdS_4/CFT_3 *with Lifshitz scaling and hyperscaling violation*, 1907.10030.

[157] N. Drukker, D. J. Gross and H. Ooguri, *Wilson loops and minimal surfaces*, *Phys. Rev.* **D60** (1999) 125006 [`hep-th/9904191`].

[158] R.-X. Miao, C.-S. Chu and W.-Z. Guo, *New proposal for a holographic boundary conformal field theory*, *Phys. Rev.* **D96** (2017) 046005 [`1701.04275`].

[159] C.-S. Chu, R.-X. Miao and W.-Z. Guo, *On New Proposal for Holographic BCFT*, *JHEP* **04** (2017) 089 [`1701.07202`].

[160] A. Faraji Astaneh and S. N. Solodukhin, *Holographic calculation of boundary terms in conformal anomaly*, *Phys. Lett.* **B769** (2017) 25 [`1702.00566`].

[161] A. Faraji Astaneh, C. Berthiere, D. Fursaev and S. N. Solodukhin, *Holographic calculation of entanglement entropy in the presence of boundaries*, *Phys. Rev.* **D95** (2017) 106013 [`1703.04186`].

[162] S. N. Solodukhin, *Entanglement entropy of black holes*, *Living Rev. Rel.* **14** (2011) 8 [`1104.3712`].

[163] M. Rangamani and T. Takayanagi, *Holographic Entanglement Entropy*, *Lect. Notes Phys.* **931** (2017) pp.1 [`1609.01287`].

[164] G. Vidal and R. F. Werner, *Computable measure of entanglement*, *Phys. Rev.* **A65** (2002) 032314 [`quant-ph/0102117`].

[165] P. Calabrese, J. Cardy and E. Tonni, *Entanglement negativity in quantum field theory*, *Phys. Rev. Lett.* **109** (2012) 130502 [`1206.3092`].

[166] B. M. Terhal, M. Horodecki, D. W. Leung and D. P. DiVincenzo, *The entanglement of purification*, *Journal of Mathematical Physics* **43** (2002) 4286 [`quant-ph/0202044`].

[167] M. Mezard, G. Parisi and M. Virasoro, *Spin Glass Theory and Beyond*. WORLD SCIENTIFIC, 1986, 10.1142/0271, [`https://www.worldscientific.com/doi/pdf/10.1142/0271`].

[168] J. L. Cardy, O. A. Castro-Alvaredo and B. Doyon, *Form factors of branch-point twist fields in quantum integrable models and entanglement entropy*, *J. Statist. Phys.* **130** (2008) 129 [`0706.3384`].

[169] M. B. Hastings, *An area law for one-dimensional quantum systems*, *J. Stat. Mech.* **2007** (2007) P08024 [`0705.2024`].

[170] A. B. Zamolodchikov, *Irreversibility of the Flux of the Renormalization Group in a 2D Field Theory*, *JETP Lett.* **43** (1986) 730.

[171] P. Calabrese, J. Cardy and E. Tonni, *Entanglement entropy of two disjoint intervals in conformal field theory*, *J. Stat. Mech.* **0911** (2009) P11001 [`0905.2069`].

[172] P. Calabrese, J. Cardy and E. Tonni, *Entanglement entropy of two disjoint intervals in conformal field theory II*, *J. Stat. Mech.* **1101** (2011) P01021 [`1011.5482`].

[173] C. De Nobili, A. Coser and E. Tonni, *Entanglement entropy and negativity of disjoint intervals in CFT: Some numerical extrapolations*, *J. Stat. Mech.* **1506** (2015) P06021 [`1501.04311`].

[174] A. Coser, E. Tonni and P. Calabrese, *Spin structures and entanglement of two disjoint intervals in conformal field theories*, *J. Stat. Mech.* **1605** (2016) 053109 [`1511.08328`].

[175] H. Casini, C. D. Fosco and M. Huerta, *Entanglement and alpha entropies for a massive Dirac field in two dimensions*, *J. Stat. Mech.* **0507** (2005) P07007 [`cond-mat/0505563`].

[176] H. Casini and M. Huerta, *Entanglement and alpha entropies for a massive scalar field in two dimensions*, *J. Stat. Mech.* **0512** (2005) P12012 [`cond-mat/0511014`].

[177] H. Casini, M. Huerta, R. C. Myers and A. Yale, *Mutual information and the F-theorem*, *JHEP* **10** (2015) 003 [`1506.06195`].

[178] T. Hirata and T. Takayanagi, *AdS/CFT and strong subadditivity of entanglement entropy*, *JHEP* **02** (2007) 042 [`hep-th/0608213`].

[179] H. Casini, M. Huerta and L. Leitao, *Entanglement entropy for a Dirac fermion in three dimensions: Vertex contribution*, *Nucl. Phys.* **B814** (2009) 594 [`0811.1968`].

[180] H. Elvang and M. Hadjiantonis, *Exact results for corner contributions to the entanglement entropy and Rényi entropies of free bosons and fermions in 3d*, *Phys. Lett.* **B749** (2015) 383 [`1506.06729`].

[181] E. Fradkin and J. E. Moore, *Entanglement entropy of 2D conformal quantum critical points: hearing the shape of a quantum drum*, *Phys. Rev. Lett.* **97** (2006) 050404 [`cond-mat/0605683`].

[182] E. M. Stoudenmire, P. Gustainis, R. Johal, S. Wessel and R. G. Melko, *Corner contribution to the entanglement entropy of strongly interacting O(2) quantum critical systems in 2+1 dimensions*, *Phys. Rev.* **B90** (2014) 235106 [`1409.6327`].

[183] A. B. Kallin, E. M. Stoudenmire, P. Fendley, R. R. P. Singh and R. G. Melko, *Corner contribution to the entanglement entropy of an O(3) quantum critical point in 2 + 1 dimensions*, *J. Stat. Mech.* **1406** (2014) P06009 [`1401.3504`].

[184] A. B. Kallin, K. Hyatt, R. R. P. Singh and R. G. Melko, *Entanglement at a two-dimensional quantum critical point: A numerical linked-cluster expansion study*, *Phys. Rev. Lett.* **110** (2013) 135702.

[185] T. Devakul and R. R. P. Singh, *Quantum critical universality and singular corner entanglement entropy of bilayer heisenberg-ising model*, *Phys. Rev. B* **90** (2014) 064424.

[186] J. Helmes, L. E. Hayward Sierens, A. Chandran, W. Witczak-Krempa and R. G. Melko, *Universal corner entanglement of Dirac fermions and gapless bosons from the continuum to the lattice*, *Phys. Rev.* **B94** (2016) 125142 [`1606.03096`].

[187] H. Osborn and A. C. Petkou, *Implications of conformal invariance in field theories for general dimensions*, *Annals Phys.* **231** (1994) 311 [`hep-th/9307010`].

[188] P. Bueno, R. C. Myers and W. Witczak-Krempa, *Universal corner entanglement from twist operators*, *JHEP* **09** (2015) 091 [`1507.06997`].

[189] R. C. Myers and A. Singh, *Entanglement Entropy for Singular Surfaces*, *JHEP* **09** (2012) 013 [`1206.5225`].

[190] P. Bueno, H. Casini and W. Witczak-Krempa, *Generalizing the entanglement entropy of singular regions in conformal field theories*, `1904.11495`.

[191] L. E. H. Sierens, P. Bueno, R. R. P. Singh, R. C. Myers and R. G. Melko, *Cubic trihedral corner entanglement for a free scalar*, *Phys. Rev.* **B96** (2017) 035117 [`1703.03413`].

[192] G. Bednik, L. E. Hayward Sierens, M. Guo, R. C. Myers and R. G. Melko, *Probing trihedral corner entanglement for dirac fermions*, *Phys. Rev. B* **99** (2019) 155153.

[193] N. Andrei et al., *Boundary and Defect CFT: Open Problems and Applications*, 2018, `1810.05697`.

[194] J. Cardy, *Conformal Field Theory and Statistical Mechanics*, in *Les Houches Summer School: Session 89: Exacts Methods in Low-Dimensional Statistical Physics and Quantum Computing Les Houches, France, June 30-August 1, 2008*, 2008, `0807.3472`.

[195] A. Sagnotti, *Open Strings and their Symmetry Groups*, in *NATO Advanced Summer Institute on Nonperturbative Quantum Field Theory (Cargese Summer Institute) Cargese, France, July 16-30, 1987*, pp. 0521–528, 1987, `hep-th/0208020`.

[196] C. Angelantonj and A. Sagnotti, *Open strings*, *Phys. Rept.* **371** (2002) 1 [`hep-th/0204089`].

[197] K. Hori, S. Katz, A. Klemm, R. Pandharipande, R. Thomas, C. Vafa et al., *Mirror symmetry*, vol. 1 of *Clay mathematics monographs*. AMS, Providence, USA, 2003.

[198] A. Recknagel and V. Schomerus, *Boundary Conformal Field Theory and the Worldsheet Approach to D-Branes*, Cambridge Monographs on Mathematical Physics. Cambridge University Press, 2013, 10.1017/CBO9780511806476.

[199] D. Deutsch and P. Candelas, *Boundary Effects in Quantum Field Theory*, *Phys. Rev.* **D20** (1979) 3063.

[200] R.-X. Miao, *Casimir Effect, Weyl Anomaly and Displacement Operator in Boundary Conformal Field Theory*, *JHEP* **07** (2019) 098 [`1808.05783`].

[201] S. Deser and A. Schwimmer, *Geometric classification of conformal anomalies in arbitrary dimensions*, *Phys. Lett.* **B309** (1993) 279 [`hep-th/9302047`].

[202] R. A. Bertlmann, *Anomalies in quantum field theory*. 1996.

[203] K. Fujikawa and H. Suzuki, *Path integrals and quantum anomalies*. 2004, 10.1093/acprof:oso/9780198529132.001.0001.

[204] A. Bilal, *Lectures on Anomalies*, `0802.0634`.

[205] S. N. Solodukhin, *Boundary terms of conformal anomaly*, *Phys. Lett.* **B752** (2016) 131 [`1510.04566`].

[206] C. P. Herzog, K.-W. Huang and K. Jensen, *Universal Entanglement and Boundary Geometry in Conformal Field Theory*, *JHEP* **01** (2016) 162 [`1510.00021`].

[207] D. Fursaev, *Conformal anomalies of CFT's with boundaries*, *JHEP* **12** (2015) 112 [`1510.01427`].

[208] D. V. Fursaev and S. N. Solodukhin, *Anomalies, entropy and boundaries*, *Phys. Rev.* **D93** (2016) 084021 [`1601.06418`].

[209] H. Casini, I. S. Landea and G. Torroba, *The g-theorem and quantum information theory*, *JHEP* **10** (2016) 140 [`1607.00390`].

[210] C. Berthiere and S. N. Solodukhin, *Boundary effects in entanglement entropy*, *Nucl. Phys.* **B910** (2016) 823 [`1604.07571`].

[211] S. S. Gubser, I. R. Klebanov and A. M. Polyakov, *Gauge theory correlators from noncritical string theory*, *Phys. Lett.* **B428** (1998) 105 [`hep-th/9802109`].

[212] E. Witten, *Anti-de Sitter space and holography*, *Adv. Theor. Math. Phys.* **2** (1998) 253 [`hep-th/9802150`].

[213] O. Aharony, S. S. Gubser, J. M. Maldacena, H. Ooguri and Y. Oz, *Large N field theories, string theory and gravity*, *Phys. Rept.* **323** (2000) 183 [`hep-th/9905111`].

[214] O. Aharony, O. Bergman, D. L. Jafferis and J. Maldacena, *N=6 superconformal Chern-Simons-matter theories, M2-branes and their gravity duals*, *JHEP* **10** (2008) 091 [`0806.1218`].

[215] J. D. Brown and M. Henneaux, *Central Charges in the Canonical Realization of Asymptotic Symmetries: An Example from Three-Dimensional Gravity*, *Commun. Math. Phys.* **104** (1986) 207.

[216] N. Seiberg, *Notes on theories with 16 supercharges*, *Nucl. Phys. Proc. Suppl.* **67** (1998) 158 [`hep-th/9705117`].

[217] J. M. Maldacena, *Wilson loops in large N field theories*, *Phys. Rev. Lett.* **80** (1998) 4859 [`hep-th/9803002`].

[218] S. de Haro, S. N. Solodukhin and K. Skenderis, *Holographic reconstruction of space-time and renormalization in the AdS / CFT correspondence*, *Commun. Math. Phys.* **217** (2001) 595 [`hep-th/0002230`].

[219] M. Bianchi, D. Z. Freedman and K. Skenderis, *Holographic renormalization*, *Nucl. Phys.* **B631** (2002) 159 [`hep-th/0112119`].

[220] K. Skenderis, *Lecture notes on holographic renormalization*, *Class. Quant. Grav.* **19** (2002) 5849 [`hep-th/0209067`].

[221] J. de Boer, E. P. Verlinde and H. L. Verlinde, *On the holographic renormalization group*, *JHEP* **08** (2000) 003 [`hep-th/9912012`].

[222] J. de Boer, *The Holographic renormalization group*, *Fortsch. Phys.* **49** (2001) 339 [`hep-th/0101026`].

[223] M. Headrick and T. Takayanagi, *A Holographic proof of the strong subadditivity of entanglement entropy*, *Phys. Rev.* **D76** (2007) 106013 [`0704.3719`].

[224] H. Casini, M. Huerta and R. C. Myers, *Towards a derivation of holographic entanglement entropy*, *JHEP* **05** (2011) 036 [`1102.0440`].

[225] A. Lewkowycz and J. Maldacena, *Generalized gravitational entropy*, *JHEP* **08** (2013) 090 [`1304.4926`].

[226] D. V. Fursaev, *Proof of the holographic formula for entanglement entropy*, *JHEP* **09** (2006) 018 [`hep-th/0606184`].

[227] M. Headrick, *Entanglement Renyi entropies in holographic theories*, *Phys. Rev.* **D82** (2010) 126010 [`1006.0047`].

[228] M. Freedman and M. Headrick, *Bit threads and holographic entanglement*, *Commun. Math. Phys.* **352** (2017) 407 [`1604.00354`].

[229] M. Headrick and V. E. Hubeny, *Riemannian and Lorentzian flow-cut theorems*, *Class. Quant. Grav.* **35** (2018) 10 [`1710.09516`].

[230] S. X. Cui, P. Hayden, T. He, M. Headrick, B. Stoica and M. Walter, *Bit Threads and Holographic Monogamy*, `1808.05234`.

[231] T. Faulkner, A. Lewkowycz and J. Maldacena, *Quantum corrections to holographic entanglement entropy*, *JHEP* **11** (2013) 074 [`1307.2892`].

[232] M. Banados, C. Teitelboim and J. Zanelli, *The Black hole in three-dimensional space-time*, *Phys. Rev. Lett.* **69** (1992) 1849 [`hep-th/9204099`].

[233] V. E. Hubeny, H. Maxfield, M. Rangamani and E. Tonni, *Holographic entanglement plateaux*, *JHEP* **08** (2013) 092 [`1306.4004`].

[234] J. Abajo-Arrastia, J. Aparicio and E. Lopez, *Holographic Evolution of Entanglement Entropy*, *JHEP* **11** (2010) 149 [1006.4090].

[235] V. Balasubramanian, A. Bernamonti, J. de Boer, N. Copland, B. Craps, E. Keski-Vakkuri et al., *Holographic Thermalization*, *Phys. Rev.* **D84** (2011) 026010 [1103.2683].

[236] V. Balasubramanian, A. Bernamonti, N. Copland, B. Craps and F. Galli, *Thermalization of mutual and tripartite information in strongly coupled two dimensional conformal field theories*, *Phys. Rev.* **D84** (2011) 105017 [1110.0488].

[237] A. Allais and E. Tonni, *Holographic evolution of the mutual information*, *JHEP* **01** (2012) 102 [1110.1607].

[238] R. Callan, J.-Y. He and M. Headrick, *Strong subadditivity and the covariant holographic entanglement entropy formula*, *JHEP* **06** (2012) 081 [1204.2309].

[239] V. E. Hubeny, M. Rangamani and E. Tonni, *Thermalization of Causal Holographic Information*, *JHEP* **05** (2013) 136 [1302.0853].

[240] A. C. Wall, *Maximin Surfaces, and the Strong Subadditivity of the Covariant Holographic Entanglement Entropy*, *Class. Quant. Grav.* **31** (2014) 225007 [1211.3494].

[241] K. Zarembo, *Wilson loop correlator in the AdS/CFT correspondence*, *Phys. Lett.* **B459** (1999) 527 [hep-th/9904149].

[242] P. Olesen and K. Zarembo, *Phase transition in Wilson loop correlator from AdS/CFT correspondence*, hep-th/0009210.

[243] N. Drukker and B. Fiol, *On the integrability of Wilson loops in $AdS_5 \times S^5$: Some periodic ansatze*, *JHEP* **01** (2006) 056 [hep-th/0506058].

[244] A. Dekel and T. Klose, *Correlation Function of Circular Wilson Loops at Strong Coupling*, *JHEP* **11** (2013) 117 [1309.3203].

[245] P. Fonda, L. Giomi, A. Salvio and E. Tonni, *On shape dependence of holographic mutual information in AdS_4*, *JHEP* **02** (2015) 005 [1411.3608].

[246] D. E. Berenstein, R. Corrado, W. Fischler and J. M. Maldacena, *The Operator product expansion for Wilson loops and surfaces in the large N limit*, *Phys. Rev.* **D59** (1999) 105023 [hep-th/9809188].

[247] J. K. Erickson, G. W. Semenoff and K. Zarembo, *Wilson loops in N=4 supersymmetric Yang-Mills theory*, *Nucl. Phys.* **B582** (2000) 155 [hep-th/0003055].

[248] O.-Y. Zhong-Can, L. Ji-Xing and X. Yu-Zhang, *Geometric Methods in the Elastic Theory of Membranes in Liquid Crystal Phases*. WORLD SCIENTIFIC, 1999, 10.1142/3579, [https://www.worldscientific.com/doi/pdf/10.1142/3579].

[249] G. Hayward, *Gravitational action for space-times with nonsmooth boundaries*, *Phys. Rev.* **D47** (1993) 3275.

[250] S. W. Hawking and C. J. Hunter, *The Gravitational Hamiltonian in the presence of nonorthogonal boundaries*, *Class. Quant. Grav.* **13** (1996) 2735 [`gr-qc/9603050`].

[251] M. Henningson and K. Skenderis, *The Holographic Weyl anomaly*, *JHEP* **07** (1998) 023 [`hep-th/9806087`].

[252] M. Bianchi, D. Z. Freedman and K. Skenderis, *How to go with an RG flow*, *JHEP* **08** (2001) 041 [`hep-th/0105276`].

[253] S. N. Solodukhin, *Entanglement Entropy in Non-Relativistic Field Theories*, *JHEP* **04** (2010) 101 [`0909.0277`].

[254] X. Chen, G. Y. Cho, T. Faulkner and E. Fradkin, *Scaling of entanglement in 2 + 1-dimensional scale-invariant field theories*, *J. Stat. Mech.* **1502** (2015) P02010 [`1412.3546`].

[255] T. Zhou, X. Chen, T. Faulkner and E. Fradkin, *Entanglement entropy and mutual information of circular entangling surfaces in the 2 + 1-dimensional quantum Lifshitz model*, *J. Stat. Mech.* **1609** (2016) 093101 [`1607.01771`].

[256] M. R. Mohammadi Mozaffar and A. Mollabashi, *Entanglement in Lifshitz-type Quantum Field Theories*, *JHEP* **07** (2017) 120 [`1705.00483`].

[257] J. Angel-Ramelli, V. G. M. Puletti and L. Thorlacius, *Entanglement Entropy in Generalised Quantum Lifshitz Models*, `1906.08252`.

[258] C. Berthiere and W. Witczak-Krempa, *Relating bulk to boundary entanglement*, `1907.11249`.

[259] P. M. Chaikin and T. C. Lubensky, *Principles of Condensed Matter Physics*. Sept., 2000.

[260] S. A. Hartnoll, J. Polchinski, E. Silverstein and D. Tong, *Towards strange metallic holography*, *JHEP* **04** (2010) 120 [`0912.1061`].

[261] K. Balasubramanian and K. Narayan, *Lifshitz spacetimes from AdS null and cosmological solutions*, *JHEP* **08** (2010) 014 [`1005.3291`].

[262] K. Nagasaki, H. Tanida and S. Yamaguchi, *Holographic Interface-Particle Potential*, *JHEP* **01** (2012) 139 [`1109.1927`].

[263] S. Kobayashi and K. Nomizu, *Foundations of Differential Geometry*, no. v. 2 in A Wiley Publication in Applied Statistics. Wiley, 1996.

[264] K. Jensen and A. O'Bannon, *Holography, Entanglement Entropy, and Conformal Field Theories with Boundaries or Defects*, *Phys. Rev.* **D88** (2013) 106006 [`1309.4523`].

[265] P. Bueno and R. C. Myers, *Corner contributions to holographic entanglement entropy*, *JHEP* **08** (2015) 068 [`1505.07842`].

[266] R.-X. Miao and C.-S. Chu, *Universality for Shape Dependence of Casimir Effects from Weyl Anomaly*, *JHEP* **03** (2018) 046 [`1706.09652`].

[267] H. Liu and A. A. Tseytlin, *D = 4 superYang-Mills, D = 5 gauged supergravity, and D = 4 conformal supergravity*, *Nucl. Phys.* **B533** (1998) 88 [`hep-th/9804083`].

[268] A. Buchel, J. Escobedo, R. C. Myers, M. F. Paulos, A. Sinha and M. Smolkin, *Holographic GB gravity in arbitrary dimensions*, *JHEP* **03** (2010) 111 [`0911.4257`].

[269] K. Jensen, A. O'Bannon, B. Robinson and R. Rodgers, *From the Weyl Anomaly to Entropy of Two-Dimensional Boundaries and Defects*, *Phys. Rev. Lett.* **122** (2019) 241602 [`1812.08745`].

[270] V. Balasubramanian and P. Kraus, *A Stress tensor for Anti-de Sitter gravity*, *Commun. Math. Phys.* **208** (1999) 413 [`hep-th/9902121`].

[271] R. C. Myers, *Stress tensors and Casimir energies in the AdS/CFT correspondence*, *Phys. Rev.* **D60** (1999) 046002 [`hep-th/9903203`].

[272] C. Berthiere, *Boundary-corner entanglement for free bosons*, *Phys. Rev.* **B99** (2019) 165113 [`1811.12875`].

[273] M. R. Mohammadi Mozaffar, A. Mollabashi and F. Omidi, *Holographic Mutual Information for Singular Surfaces*, *JHEP* **12** (2015) 082 [`1511.00244`].

[274] S. Chapman, D. Ge and G. Policastro, *Holographic Complexity for Defects Distinguishes Action from Volume*, *JHEP* **05** (2019) 049 [`1811.12549`].

[275] C. Kristjansen, G. W. Semenoff and D. Young, *Chiral primary one-point functions in the D3-D7 defect conformal field theory*, *JHEP* **01** (2013) 117 [`1210.7015`].

[276] H. Bateman and A. Erdélyi, *Higher transcendental functions*, Calif. Inst. Technol. Bateman Manuscr. Project. McGraw-Hill, New York, NY, 1955.

[277] M. Abramowitz and I. A. Stegun, *Handbook of Mathematical Functions with Formulas, Graphs, and Mathematical Tables*. Dover, New York, ninth dover printing, tenth gpo printing ed., 1964.

[278] N. Ogawa, *A Note on the scale symmetry and Noether current*, `hep-th/9807086`.